# Local Heat Transfer and Stress Analysis during Quenching of Moving Metal Plates using Array of Jets

**Dissertation**

For the award of the degree

Doktoringenieur

**(Dr.-Ing.)**

submitted by

**M.Sc. Suresh Babu Gopalkrishna**

Date of Birth: 08.07.1993

in Vijayapura, Karnataka, India

Accepted by

The Faculty of Process and Systems Engineering

of the Otto von Guericke University Magdeburg

Reviewer:

Prof. Dr. -Ing. Eckehard Specht
Institute of Fluid Dynamics and Thermodynamics,
Otto von Guericke University Magdeburg

Prof. Dr. -Ing. Udo Fritsching
Leibniz-Institute für Werkstofforientierte Technologien,
University Bremen

Prof. Dr. -Ing. Ashok Kumar Nallathambi
Department of Mechanical Engineering,
National Institute of Technology, Tiruchirapalli, India

Submission on: 07.06.2022
Doctoral Colloquium on: 24.10.2022

# Preface

This dissertation is submitted to Otto von Guericke University, Magdeburg for the degree of Doctor of Philosophy. The research described herein was conducted under the supervision of Prof. Dr.-Ing. Eckehard Specht between December 2018 and May 2022. To the best of my knowledge, this work is original, except where suitable references are made to previous works. Neither this, nor any substantially similar dissertation had been submitted for any degree, diploma, or qualification at any other university or institution.

<div align="right">

Suresh Babu Gopalkrishna
Magdeburg, 24.10.2022

</div>

# Abstract

Cooling of hot metal plates during the many heat treatment process, the casting process and hardening processes is highly challenging as the material undergoes large deformation and leads to the formation of cracks. The high residual stresses, initiation of the cracks occur with cooling water from an array of jets. The local heat transfer mechanism in such processes leads to larger non-uniform temperature distribution across the material for various quench time. Therefore, the accurate knowledge of the thermal boundary conditions due to water impingement in the transient phenomenon leads to better optimizing the process to lower the deformation.

To estimate heat transfer mechanism on the quenched side, we conducted experiments using infrared thermography to measure the surface temperatures on the surface of the quenched side. Experiments are conducted in a laboratory setup and two-dimensional spatial temperature measurements are highly beneficial for understanding the local heat transfer phenomena. The thermal history on the back side of quenching was used for the accurate prediction of the heat fluxes on the quenched side and further more to characterize the boiling curve. A non-linear inverse heat transfer method is developed and verified accurately with the experimental surface temperatures for the two-dimensional directions and furthermore the three-dimensional inverse heat conduction problem is developed. The developed inverse model employes the Tikhonov regularization parameter to accurately stabilize the non-linearities of the experimental measurements. A finite element program is developed for the coupling of the direct heat transfer problem and the inverse heat conduction problem using *MATLAB* programming language. The coupled finite element program predicts the heat fluxes accurately with the usage of the experimental surface temperatures. The developed method can be easily employed to the estimation of the heat fluxes with the know surface measured temperatures. This type of heat flux prediction should replace the large fluid simulation to understand the accurate local heat transfer.

The influence of different process parameters such as water jet velocity, plate velocity, initial temperature, metal thickness, and types of metal are investigated to understand the heat transfer mechanism. The local heat transfer in the full jet quenching process demonstrates the maximum heat transfer occurs nearly in the stagnation position of the water jet. The high intensity of the heat transfer can be extracted in the water impingement position. The variation of the different process parameters reveals that the increase in the magnitude proportionally higher the rate of heat transfer and the position of the departure nucleate boiling occurs exactly near the water impingement position. Therefore, the local position of the water jet impingement is highly responsible for the heat extraction from the hot moving metal plates and the fixed plates.

An accurate prediction of the thermal boundary conditions can be further used in the thermo-mechanical modeling to estimate the mechanical behavior of the material in the cooling process. For this, coupled finite element programming in two-dimensions was developed in *MATLAB* programming language and three-dimensional model in *COMSOL* multiphysics. To predict the thermal deformation and residual stresses, an accurate material model was used from the literature. The further variation of different process parameters such as the configuration of water jets, water jet velocity, plate velocity, initial temperature

of the plate, metal thickness on the thermal deformation and the formation of the thermal stresses.

The thermo-mechanical model coupled with the estimation of the thermal boundary conditions with the inverse heat conduction model for the measured surface temperatures as an input is validated. This work mainly focused to understand the thermal boundary conditions locally during quenching of moving hot metal plates and further more to estimating the evolution of the thermal stresses. A brief understanding of the influencing process parameters on the heat transfer mechanism is reported in detail and observed the definition of the local position of the water impingement plays a crucial role in the maximum heat transfer intensity. The themo-mechanical modeling of the quenching process is a powerful tool for estimating the thermal stresses, deformation and local heat transfer to optimize the process in industrial applications.

**Keywords**: Quenching Process, Water Jet Impingement, Inverse Heat Conduction Method, Finite Element Method, Boiling Curve, Thermo-Mechanical Modeling, Three-Dimensional Finite Element Modeling

# Zussammenfassung

Die Abkühlung heißer Metallplatten während verschiedener Wärmebehandlungsverfahren, des Gießens und der Härtung ist eine große Herausforderung, da das Material stark verformt wird, was zur Bildung von Rissen führen kann. Die Entwicklung hoher Eigenspannungen während der Abkühlung heißer Platten mit Hilfe von Kühlwasser aus einer Reihe von Düsen führt zur Rissbildung. Der lokale Wärmeübertragungsmechanismus führt bei solchen Prozessen zu einer großen ungleichmäßigen Temperaturverteilung über das Material. Daher ist die genaue Kenntnis der instationären thermischen Randbedingungen von entscheidender Bedeutung. Ziel dieser Arbeit ist es, die Prozessparameter zu optimieren, um die Eigenspannung und die Verformung zu verringern.

Um den Wärmeübertragungsmechanismus während des Abschreckens abzuschätzen, werden Experimente durchgeführt und die Oberflächentemperatur auf der abgeschreckten Seite mit Hilfe der Infrarot-Thermografie gemessen. Die Experimente werden in einem Laboraufbau durchgeführt, und zweidimensionale räumliche Temperaturmessungen sind für das Verständnis der lokalen Wärmeübertragungsphänomene von großem Vorteil. Der Wärmeverlauf auf der Rückseite der Abschreckplatte wurde für die genaue Vorhersage des Wärmestroms auf der abgeschreckten Seite und zur Charakterisierung der Siedekurve verwendet. Eine nichtlineare inverse Wärmeübertragungsmethode wird entwickelt und mit den experimentellen Oberflächentemperaturen für die zweidimensionalen Richtungen genau verifiziert, und darüber hinaus wird das dreidimensionale inverse Wärmeleitungsproblem entwickelt. Das entwickelte inverse Modell verwendet den Tikhonov-Regularisierungsparameter, um die Nichtlinearitäten der experimentellen Messungen genau zu stabilisieren. Für die Kopplung des direkten Wärmeübertragungsproble-ms und des inversen Wärmeleitungsproble-ms wird ein Finite-Elemente-Programm in der Programmiersprache *MATLAB* entwickelt. Das gekoppelte Finite-Elemente-Programm sagt den Wärmestrom unter Verwendung der experimentellen Oberflächentemperatur genau voraus. Die entwickelte Methode kann leicht zur Abschätzung des Wärmestroms mit der bekannten gemessenen Oberflächentemperatur eingesetzt werden. Diese Art der Wärmestromvorhersage ersetzt die großflächige Strömungssimulation und ermöglicht eine genaue Vorhersage des lokalen Wärmeübergangs.

Der Einfluss verschiedener Prozessparameter wie Wasserstrahlgeschwindigkeit, Plattengeschwindigkeit, Anfangstemperatur, Metalldicke und Metallarten wird untersucht, um den Wärmeübertragungsmechanismus während dieses Prozesses zu verstehen. Der lokale Wärmeübergang bei der Vollstrahlabschreckung zeigt, dass der maximale Wärmeü-bergang nahezu in der Stagnationsposition des Wasserstrahls stattfindet. Die hohe Intensität des Wärmeübergangs kann in der Nähe des Wasseraufprallbereichs ermittelt werden. Die Variation der verschiedenen Prozessparameter zeigt, dass die Zunahme der Größe proportional die Wärmeübertragungsrate erhöht und die Position des Abgangs vom Keimsieden genau in der Nähe der Wasseraufprallposition auftritt. Daher ist die lokale Position der Wasserstrahlbeaufschlagung in hohem Maße für den Wärmeentzug sowohl aus den heißen, sich bewegenden Metallplatten als auch aus den festen Platten verantwortlich.

Die vorhergesagten thermischen Randbedingungen werden in der thermomechanischen Modellierung weiter verwendet, um das mechanische Verhalten des Materials während des Abkühlungsprozesses abzuschätzen. Hierfür wird eine gekoppelte Finite-Elemente-Programmierung in zwei Dimensionen in der Programmiersprache *MATLAB* und ein dreidimensionales Modell in *COMSOL* Multiphysics entwickelt. Für die Modellierung der Mechanik werden Kriech- und viskoplastische Konstitutivbeziehungen verwendet. Die Variation verschiedener Prozessparameter wie die Konfiguration der Wasserstrahlen, die Geschwindigkeit des Wasserstrahls, die Geschwindigkeit des Blechs, die

Anfangstemperatur des Blechs und die Dicke des Metalls auf die thermische Verformung und die Bildung der thermischen Spannungen wird im Detail untersucht.

Das thermomechanische Modell, gekoppelt mit der Abschätzung der thermischen Rand-bedingungen mit dem inversen Wärmeleitungsmodell für die gemessenen Oberflächentemp-eraturen als Input, wird validiert. Das Hauptaugenmerk dieser Arbeit lag auf dem Verständ-nis der lokalen thermischen Randbedingungen während des Abschreckens von sich bewegenden heißen Metallplatten und der Abschätzung der Entwicklung der thermischen Spannungen. Ein kurzes Verständnis der Prozessparameter, die den Wärmeübertrag-ungsmechanismus beeinflussen, wird im Detail beschrieben. Die lokale Position des Wasseraufpralls spielt eine entscheidende Rolle für die maximale Wärmeübertragungsintensität. Einige wenige industrielle Anwendungen der entwickelten Modelle werden in dieser Arbeit diskutiert.

**Schlüsselwörter**: Abschreckprozess, Wasserstrahlbeaufschlagung, Inverses Wärmele-itungsproblem, Finite-Elemente-Methode, Siedekurve, thermomechanische Modellierung, Dreidimensionale Finite-Elemente-Modellierung

# Contents

# Chapter 1

# Introduction

## 1.1 Motivation

Quenching is employed in many heat treatment processes for the rapid cooling of high-temperature metals to improve its mechanical properties and microstructure. Consequently, quenching provokes residual stresses, which distorts the material. The initiation of cracks occurs, and the service life of the metal product is shortened as a result of high residual stresses. Therefore, higher residual stresses are further reduced by an additional process such as stretching or tempering. The methods like straightening, grinding, and surface polishing are utilized in practice to remove the distortion, when it exceeds the specified tolerance. The aim of rapid cooling is to set the required material properties, the so-called C-curve of an aluminium alloy is shown in **Fig. 1.1**. The illustrated inner region cannot be passed through to prevent inter-granular corrosion on cooling. Here the material from 500 $°C$ to below 300 $°C$ is cooled in a maximum of 0.2s. For other materials, the objectives are defined based on the required hardness of the workpiece. Higher cooling rates can result in high residual stresses in the workpiece. Thus leads the component to deformation and, un-favourable conditions and cracks. Therefore another critical requirement of the cooling process is defining a local heat transfer in order to delay and avoid material damages. The challenge for all cooling methods is to achieve high heat transfer that the required mechanical properties are guaranteed at greater depths. With the increasing demands on the materials which satisfies the requirements of a sophisticated heat treatment technology for the targeted cooling technology. For designing a cooling section, a variety of questions arises e.g., nozzle type: full jet, and full cone. This kind of decision is arrived based on the basic understanding of the different types of nozzles. Then, the positioning of the individual nozzles is set in the cooling zone.
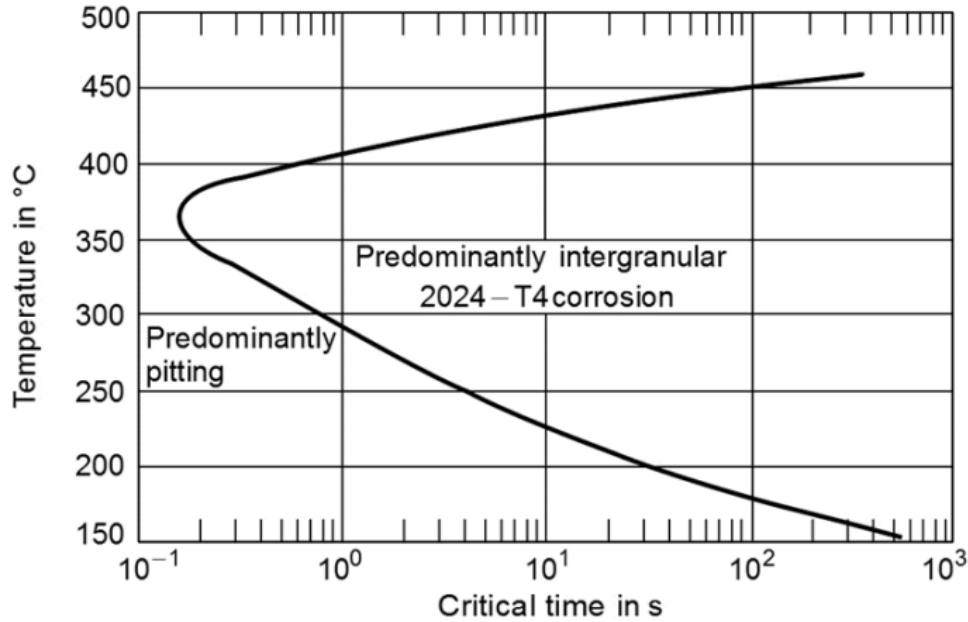
Figure 1.1: Hardness diagram for aluminium according to Evancho and Staley (1974)

## 1.2   Boiling Curve

Nukiyama (1934) constructed a boiling curve in an experiment of a pool boiling with water; henceforth, the boiling curve is also defined as Nukiyama's curve. The typical boiling curve as obtained from the work of Nukiyama as shown in the four characteristic regimes is defined as follows:

**1.   Film Boiling:** For a certain experimental condition in the quenching process, the surface temperature above the re-wetting phenomena and the region between the initial surface temperature and that of the re-wetting temperature are termed as film boiling regime. At the liquid-vapour interface, vapour propagates into the liquid once generated. The conduction through the vapour layer is the most dominant heat transfer mechanism in the film boiling region. The film boiling region exists once the surface temperature approaches the Leidenfrost or the minimum heat flux point, in other terms re-wetting point.

**2.   Transition Boiling:** The transition from the film boiling regime to the nucleate boiling with faster cooling is characterized as transition boiling. The intermittent contact between the liquid and the heated surface enhances the heat transfer, as shown in **Fig. 1.2**. The progressive decrease in the surface temperature is inversely proportional to the heat transfer, i.e., heat flux. The heat flux reaches a peak at the end of the transition boiling region, which is named maximum heat flux (MHF).

**3.  Nucleate Boiling** The region starts at maximum heat flux resulting in a vigorous boiling of the liquid. With the formation of the bubble, further, the nucleation of the bubbles takes place extensively, consequently growing and departing from the heated wall. The end of this region is characterized by the onset of nucleate boiling (ONB).

**4.  Single Phase Convection:** As the surface superheat reduces, generated vapour bubble is condensed immediately to the surrounding liquid. The liquid is forced to flow over the hot surface in the jet impingement quenching process. The effect of the hydrodynamics of the jet is significant on the overall heat transfer.
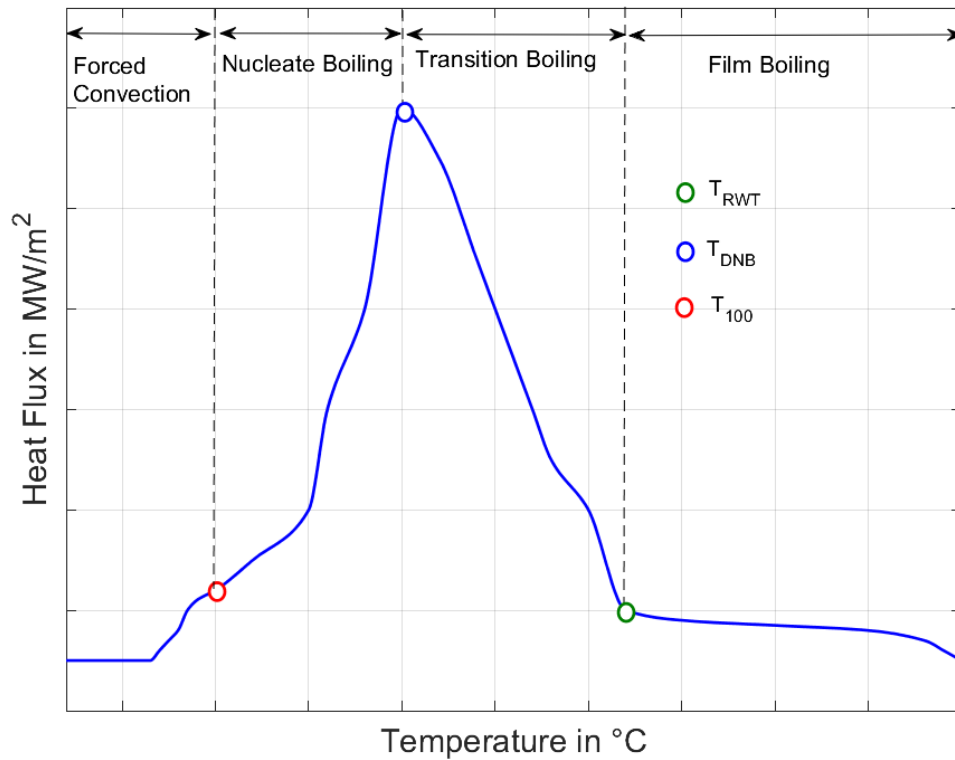
Figure 1.2: Characteristic boiling curve for the quenching process

## 1.3 Industrial Quenching of Hot Metals

### 1.3.1 Heat Treatment

In material science, quenching is the rapid cooling of a workpiece in water, oil or air to obtain the required material properties. Quenching prevents undesired low-temperature processes, such as phase transformations, to occur. The quenching process takes a short amount of time, which reduces the undesired reactions promoting both thermodynamically favourable and kinetically accessible; for instance, quenching can reduce the crystal grain size of metallic and plastic materials, increasing their hardness. In metallurgy, quenching is most commonly used to harden the steel by inducing martensite transformation, where the steel must be rapidly cooled through its eutectoid point, the temperature at which austenite becomes unstable. In steel alloyed metals such as nickel and manganese, the eutectoid temperature becomes much lower, but the kinetic barriers to phase transformation remain the same. This allows quenching to start at a lower temperature, making the process much easier. Heat treatment is the controlled heating and cooling of metal alloy in the solid-state to alter the physical and mechanical properties. To influence the properties of the material heat treatment technique is a well-established technique by the controlled diffusion rate within the microstructure. The cooling rate influences the formation of different microstructures on the same alloy. To obtain the maximum strength and hardness: rapid cooling is employed in which the austenite will transform to martensite, a hard little crystalline structure is formed and necessitates a tempering to precipitate inter-metallic particles. The desired mechanical properties at room temperature for a specific alloy can be achieved by a designed heat treatment process which requires an understanding of phase transfer within the alloy Kayamak (2007). A typical heat treatment process can be seen in the **Fig. 1.3** for the variation of the material temperature. The temperature drop during the quenching process is maximum compared to the heating rate. The duration of the austenitization may vary from minutes to hours and usually tempering duration from

hours to days. The tempering stage involves lower heating and cooling rate to avoid stress and distortion.

In the quenching process, several mechanisms like phase transformation, thermal shrinkage, transformation induced plasticity, and yielding of metals occurs. The non-uniform temperature distribution of the material causes the volume change accompanied by phase transformation to rearrange the atoms in the crystal structure. Therefore, due to thermal shrinkage and phase transformation, the total strain field becomes non-uniform. The material is exposed to a higher residual stresses. Below the yield point, the transformation induced plasticity strain amplifies the distortion.

A process like stretching and tempering alters the material state with a reduction of residual stress. Stretching induces a uniform and equalized distribution of the plastic stress field, the internal state throughout the product. The method restricts specific applications like plates and long profiles. Tempering is employed to relieve internal stress by lowering hardness to a certain extent to increase ductility. The creep phenomena can explain the stress relief mechanism in tempering. Creep (Stress relaxation) is defined as the material moving slowly (or) deforms permanently to relieve stress in time. Although it takes a very long time at room temperature, the effect of creep increases substantially as the temperature approaches the material's melting point.

- Heat treatment is an indispensable method in many large-scale manufacturing industries such as automotive, transportation, aerospace, construction, marine, military, material handling (casting, forging, machinery), and medical/pharmaceutical industries.

- Heat treatment provides a great advantage, such as reduced cast, weight and nose, and increased strength, durability, dependability, toughness, wear, and fatigue resistance.
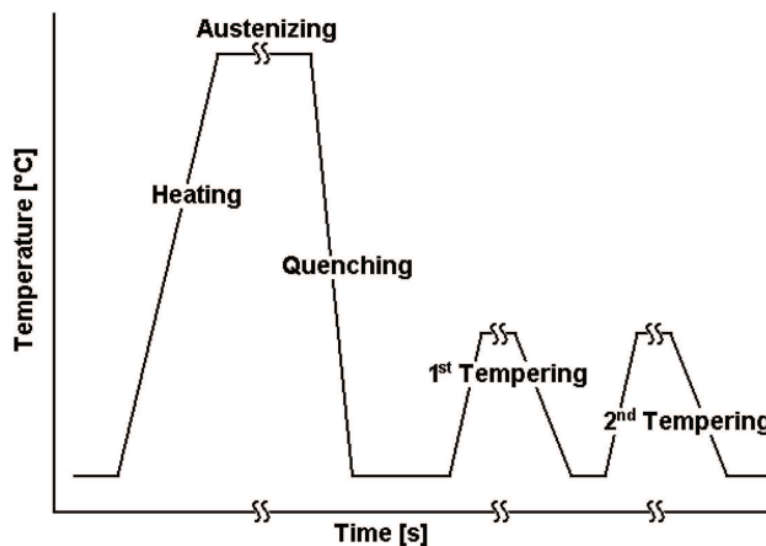


Figure 1.3: Typical heat treatment process in practice Kayamak (2007)

## 1.3.2  Quench Hardening

For Ferrous metals and alloys, the quench hardening is typically applied to strengthen and harden the steel and cast-iron alloys. The process is carried out by heating the material to the required temperature depending on the material. The surface hardening or

through-hardening varying at the rate of cooling the material produces the harder material. The material is often tempered to reduce the brittleness that may increase from the quench hardening process. The work parts that are most quenched include gears, shafts, and wear blocks.

**Purpose**

Cast steels and iron are uniform and lamellar (or layered) pearlite grain structures. This mixture of ferrite and cementite forms when the steel or cast iron is manufactured and cooled at a slow rate. Pearlite becomes insignificant for the ideal choice of material for many common applications of steel alloys because of its soft behaviour. While heating pearlite past its eutectoid transition temperature of 727°C and then rapidly cooling, some of the material's crystal structure can be transformed into a much harder structure known as martensite. Steels with this martensitic structure are often used when the workpiece must be highly resistant to deformation, such as blades' cutting edge.

**Process**

Heating the sample between the $800°C$ to $900°C$ temperature while maintaining the uniform temperature throughout that workpiece. To obtain the desired material properties, the uneven heating and overheating of the material should be avoided or minimized. The second step of the quenching process is soaking. The workpiece can be soaked in the air (air furnace), a liquid bath, or a vacuum. The temperature during the soaking process should remain as uniform as possible throughout its period. The workpiece is moved to the cooling section, where the part is submerged into the quenching fluid or, depending on the kind of quench technique, the fluid is applied on the hot surface to cool the workpiece. Water is one of the most efficient quenching media to attain maximum hardness, but there are chances of distortion and cracks of the workpiece taking place. Mineral oils are often used to obtain the workpiece with compromised hardness, and these oil-based fluids often oxidize and form sludge during quenching, which consequently lowers the efficiency of the process. The cooling rate of the oil is much less than water, and the intermediate cooling rates between the water and the oil. Inert gases like nitrogen and noble gases are used for the quenching process, and to minimize the distortion in the workpiece, the long cylindrical workpieces are quenched vertically; flat workpieces are quenched on edge. After the quenching process, an iron or steel alloy will be rigid and brittle due to an overabundance of martensite. In this situation, another heat treatment technique known as tempering is performed on the quenched material. The tempering process takes place by heating the workpiece to the temperature below the critical point for a particular point of time, then allowing it to cool in still air.

Quenching of hot surface is a complex phenomenon involving a two-phase boiling process. The heat transfer process during water impact on the hot surface is dominated mainly by the phase-change process during the cooling process of the hot sheet with multiple water jets, as shown in the **Fig. 1.4**, a large number of vapour bubbles are rapidly formed, grown and departed during the quenching period. Schweizer (2010) proposed several reasons for the enhancement of heat transfer during boiling compared with that of single-phase forced convection.

- A thin liquid micro-layer is formed at beneath the bubble, which improves the heat transfer rate proportionately.

- The motion of the vapour bubbles contribute to the enhancement of the single-phase convection by agitating the liquid near the surface.

- The thermal resistance is lowered due to the removal of the thermal boundary layer at each bubble cycle.
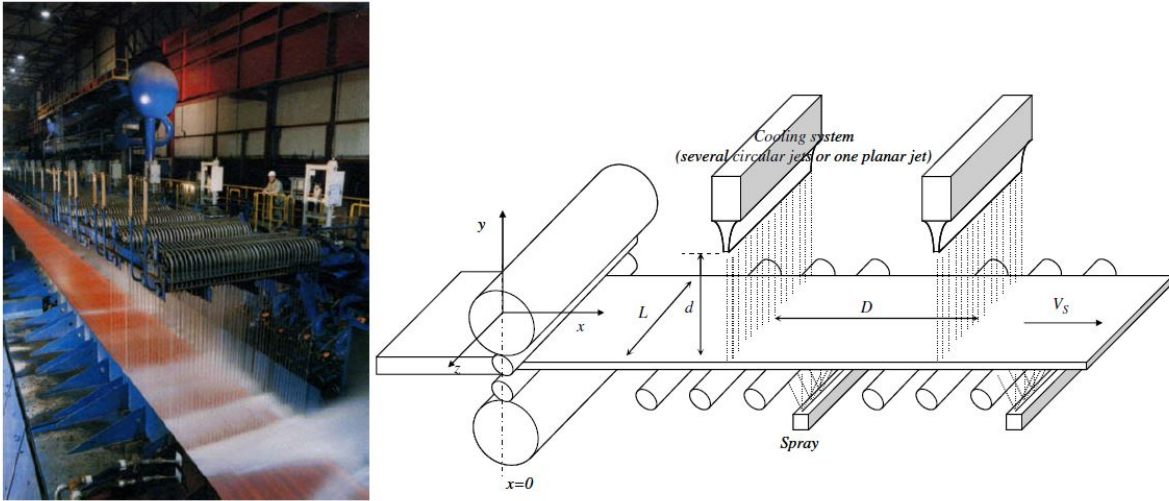
Figure 1.4: Industrial process for continuous cooling of the hot metal sheet Gradeck et al. (2009b)

### 1.3.3   Direct Chill Casting Process

The schematic diagram of the direct chill casting process is shown in the **Fig.  1.5**. Although with larger availability of the casting process, like Direct chill (DC) casting, Electromagnetic (EM) casting, melt level control, Electromagnetic stirring of liquid metal at advanced solidification stage, casting with multiple alloy layers.  The semi-continuous vertical DC casting process is depicted in Fig.  1.5.  The casting process occurs by pouring the liquid molten metal into a bottom block, and then the bottom block is withdrawn at a certain velocity with a certain level of molten metal maintained in the tundish or launder. In the DC casting process, the liquid metal undergoes primary cooling at the outer part of the solid.  Complex heat transfer occurs in the primary cooling, depending on the casting technology, contact heat transfer between the outer shell of the molten metal and the liquid water and forming a gap between the mould and ingot owing to contradiction.  After the primary cooling process, the DC casting is caused by the secondary cooling with direct impingement of the water with an array of jets on the hot, partially solidified material as the ingot emerges from the primary cooling. For the optimization of the DC casting process, the analysis of the heat transfer in the secondary cooling becomes very much significant since the majority of the heat transfer takes place in this region, accounting for nearly 80-90 % of the total heat extraction from the hot movement of the plate.
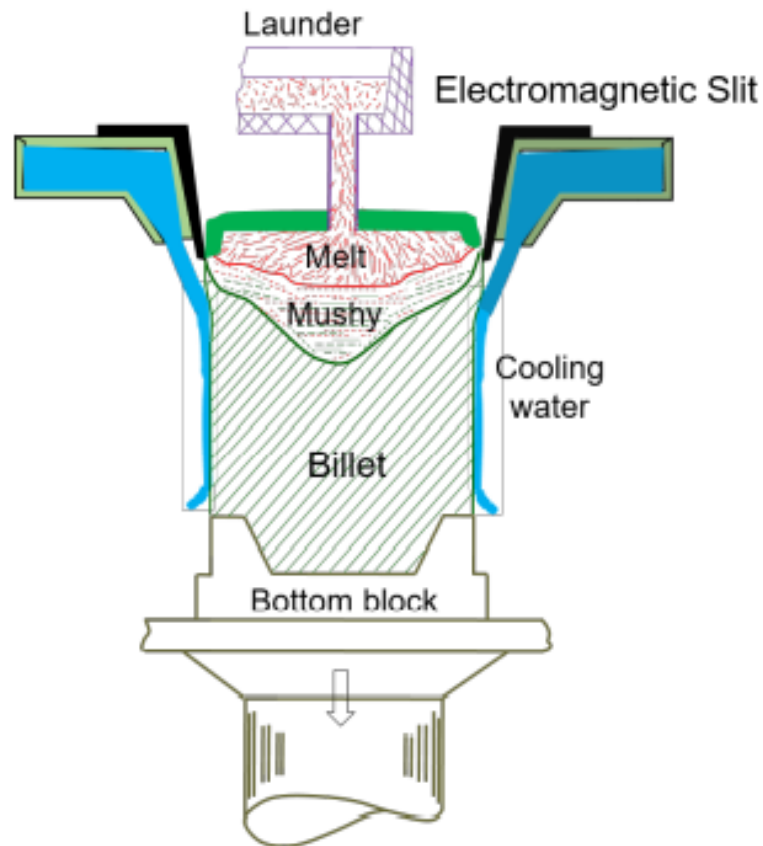
Figure 1.5: Schematic of Direct Chill casting process Kulkarni (2019)

## 1.4 Problems Faced by Industries

### 1.4.1 Heat Treatment

A non-uniform temperature field promotes distortion in the material. The distortion occurs by the thermal shrinkage and solid-state transformation. Before the phase transformation begins at the initial cooling stages, the low-temperature region shrinks more and causes bending in profile. Distortion is typically defined by the curvature, which is contact throughout the length of the profile and defined as the reciprocal of the arc radius. Typical profile cross-section and typical arc-shaped distortion. Typical profiles cross-section and arc-shaped distortion are shown in **Fig. 1.6**. The problem during the cooling process is to be minimized through the controlled and optimal design of the cooling process. The residual stresses generated during the heat treatment process caused the buckling of the plate. As the plate undergoes cooling from the top and bottom surface from the high initial temperature at the same cooling rate, the tension and compression in the surface and core of the plate take place, respectively. The resulting stresses, i.e., tension and compression, allow the plate to deform, exceeding the yield limit and resulting in plastic deformation at high cooling rates.

Figure 1.6: Typical distortion in quenching of hot metal plates

## 1.4.2  Direct Chill (DC) Casting

New alloys are developed to obtain the properties like corrosion, resistance, and higher strength, which may impose constraints on the production process. Even though a large number of the problem arise during casting problems, overcoming the casting hardness should become mandatory for improved casting efficiency. The typical casting (DC) problems are as follows Nallathambi (2010):

1. Hot tearing:
   The hot tearing is usually at a high-temperature region or above the solidus temperature. The origin of the hot tear occurs in the mushy region, where the higher solid fraction is responsible for the vulnerability of the ingot. In the worst condition, the propagation of hot tear in the axial direction or the extension to the lateral direction divides the ingot into two parts wherein liquid metal flow passes between the cross-section.

   - The thermally induced deformation due to the non-uniform cooling contradiction is a major reason for hot tearing.
   - At the start-up phase in DC casting, extensive tensile residual stresses, circumferential stresses, and inelastic strains are tensile at solidus temperature near the centre of the ingot is the most favourable to the formation of hot cracks.



Figure 1.7: Typical hot tears which occur during pseudo steady state phase Suyitno et al. (2004)

2. Cold Cracking

   The formation of the cold cracking takes place well below the solidus temperature or when the material is in a complete solidified condition. Due to higher thermal stresses, the cold crack generally occurs in the atmospheric condition in high-strength alloys. Poor thermal and mechanical properties of 7xxx series aluminium alloys experience rapid propagation of micro-cracks in tensile thermal stresses leading to catastrophic failure of ingots in the solid state.

   - Low thermal conductivity material results in higher temperature gradients with the occurrence of the non-uniform distribution of thermal stresses at various ingot locations with different signs and magnitude of the stress state.

   - At the centre of the billet, the stress state is tensile for all time. On the billet's surface, initially, the stress is tensile at the water impingement region and turns into compressive upon further cooling.

   - With the higher cooling rates, the extensive compressive stress state avoids the formation of cracks at the surface. Henceforth, the susceptibility of the cold cracks is high at the centre of the ingot.
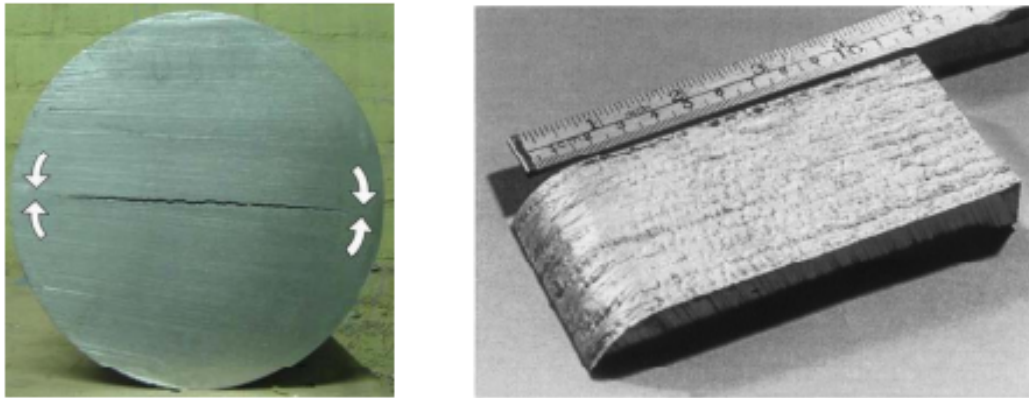


Figure 1.8: Cold cracks during DC casting process Thevik et al. (1999)

## 1.5 Purpose of the Thesis

The rapid cooling of the hot plate results in uneven or non-uniform temperature distribution on the material, resulting in a higher amount of residual stresses and deformation. To reduce problems such as thermal shrinkage, transformation induced plasticity, and residual stresses which are prone to initiation and propagation of cracks, the cooling strategies should be investigated, and an optimal cooling method should be designed. Cooling methodology was investigated with an experiment method using infrared thermography. The experimental method provides a surface temperature in spatial and temporal directions during different quenching techniques.

The surface temperature is measured on the other side of the quenching process. Since the other measuring technique, such as thermocouples below the quenched side, are more prone to experimental error. To understand the heat transfer distribution, the measured temperature is utilized to estimate the heat fluxes. The two-dimensional transient inverse heat conduction method is formulated and developed for the hot moving plate and fixed conditions of different quenching techniques. The finite element method is solved numerically with computer code development in the *MATLAB* program to solve the associated partial differential equation of the inverse problem.

The inverse problem solution provides heat flux as a function of time and space during the

cooling process of the corresponding measured surface. The boiling curve for the moving plate condition are quantified at the quasi-steady state condition from the inverse problem. To construct the boiling curve as proposed in Specht (2017), the peak values i.e., $T_{DNB}$, $T_{RWT}$, $q_{max}$, $q_{RWT}$ are given input to the parabolic function as shown in **Fig. 1.9**.
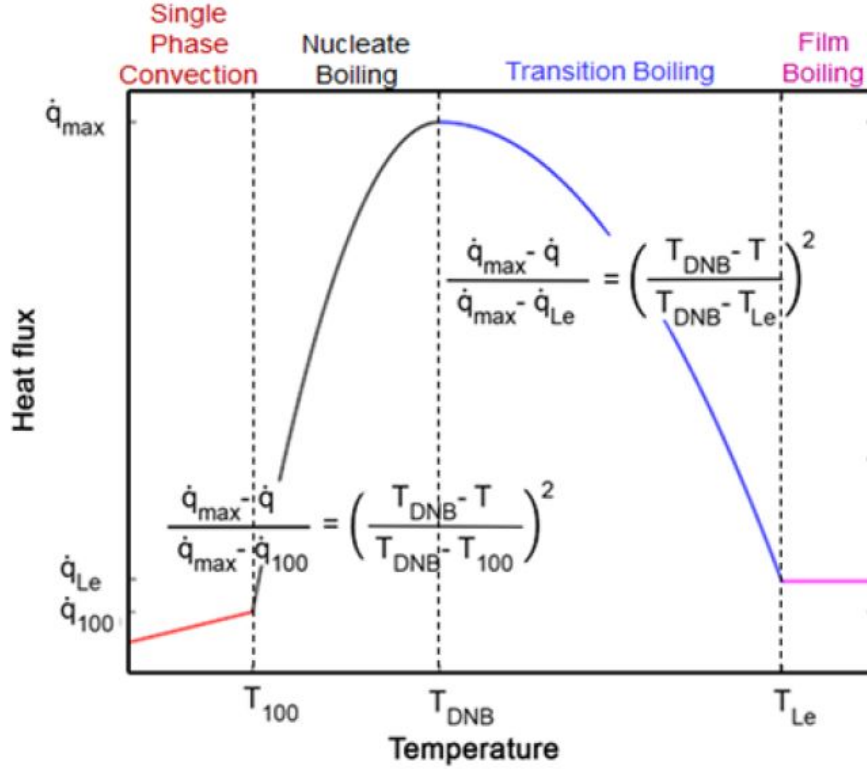


Figure 1.9: Characteristic approximation boiling curve with peak points Specht (2017)

The thermo-mechanical model is solved using the boiling curve formulated from the solution of the inverse problem to determine the thermal stresses and displacements (i.e., deformation /distortion) field in the material during the cooling process. The detailed view of the present work is given in the **Fig. 1.10**
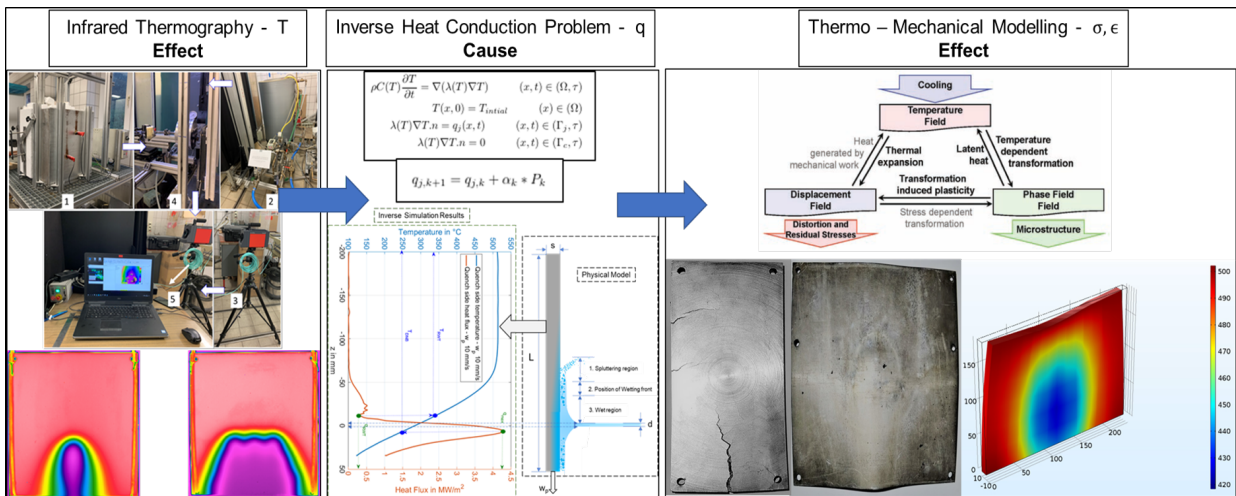


Figure 1.10: Purpose of the thesis: Infrared thermography (**T**), Inverse heat conduction problem (**q**), Thermo-mechanical modelling ($\sigma$, $\epsilon$)

# Chapter 2

# Experimental Analysis of Quenching Process

## 2.1  Introduction

The focus of this chapter is confined to the temperature measurements during the quenching of hot metals. For the purpose of the temperature measurements during quenching process, the infrared thermography is utilized in order to obtain the temperatures in both space and time direction. The experimental method consists of both fixed plate and moving plate conditions to better understand the overall heat transfer behaviour in quenching process. Quenching of the hot fixed and moving plate is carried out with different kinds of nozzles and in this study, three different kinds of nozzles mainly full jet nozzle, array of jets (mold), and full cone nozzle were utilized. Further, different configuration of the full jet nozzle are investigated with inline and staggered arrangement. From the experimental temperature measurement, it can be observed that the quasi-steady state condition is retained in the case of moving plate condition and the movement of the wetting front suggests the quasi-steady temperature drop in fixed plate condition.

## 2.2  Kinds of Quenching Technique

**Fig. 2.1** shows that the overview of the kinds of quenching method adopted in the present research work. In principle, all different kinds of the quenching technique can be categorised into two kinds of real quenching techniques: 1. Full jet quenching process, 2. Horizontal array of jets (mold). The aim of different quenching techniques is to change the fluid flow pattern during quenching process in order to higher the cooling efficiency, reduce the thermal/residual stresses, avoid the deformation and importantly for the final product output which relates to different kinds of applications.

The quenching techniques were applied in the industrial plants mainly to extract the larger amount of heat depending on the kind of process or application in general. Each of the quenching method aims to provide, promote the effectiveness of the cooling of hot metal plate.
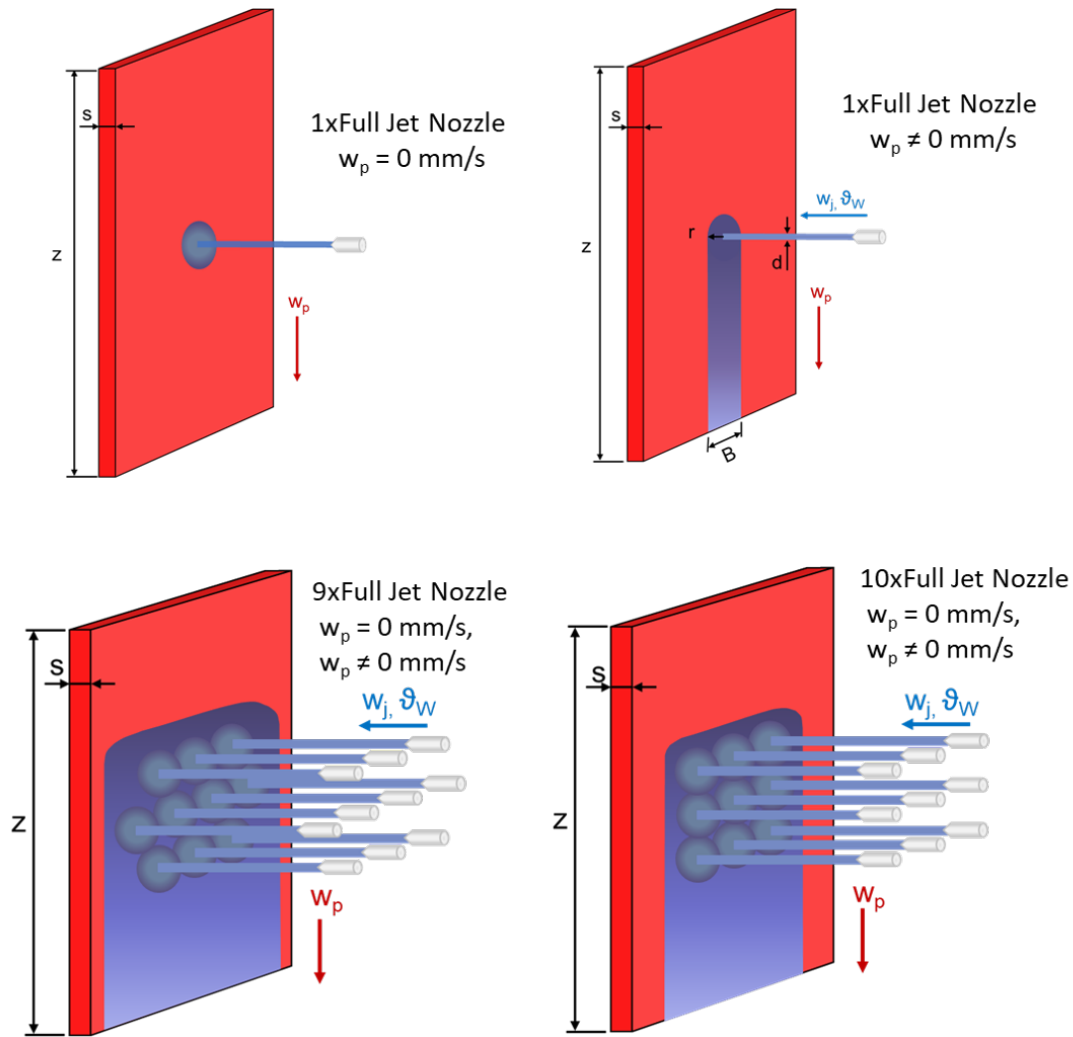
Figure 2.1: Overview of the quenching methods used in the present work

Full jet nozzle are primarily adopted to obtain the faster cooling in the water impingement region with higher amount of water flow rate. Whereas the spray or full cone nozzle extracts the larger amount of heat in the spatial direction with lower water flow rates and aims to give uniform temperature distribution across the spray impingement region. The primary difference in both kinds of cooling techniques is the existence of the vapour film and collapse of the vapour film, which strongly affects the cooling rate of the hot metal in the startup phase of the quenching process. In spray cooling, the water droplets accumulates on the impingement surface for certain time period until the surface temperature reaches a below Leidenfrost point and the vapour film collapses after certain temperature. Then, the plate experiences a transition, nucleate boiling phase where tremendous amount of heat transfer takes place. In case of full jet quenching, the Leidenfrost effect can't be observed instead the re-wetting phenomena takes place. As the water jet impinges on the hot metal surface, the jet starts to move instantaneously lowering the surface temperature of the plate. During the wetting front movement, are can observe two different boiling regimes, film boiling, and nucleate boiling. Since, the wetting front with certain velocity experiences continuously new hot region at the outer edge of the wetting front where the vapour film also exists. Henceforth, this phenomena in practice named as re-wetting.

## 2.3 Experimental Techniques
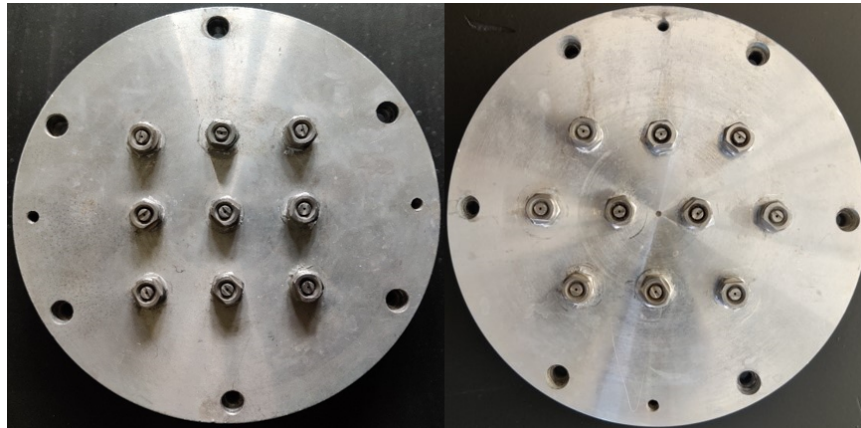
### 2.3.1 Nozzle for Quenching



Figure 2.2: Left:Inline configuration mold with array of 9 jets, Right: Staggered configuration mold with array of 10 jets
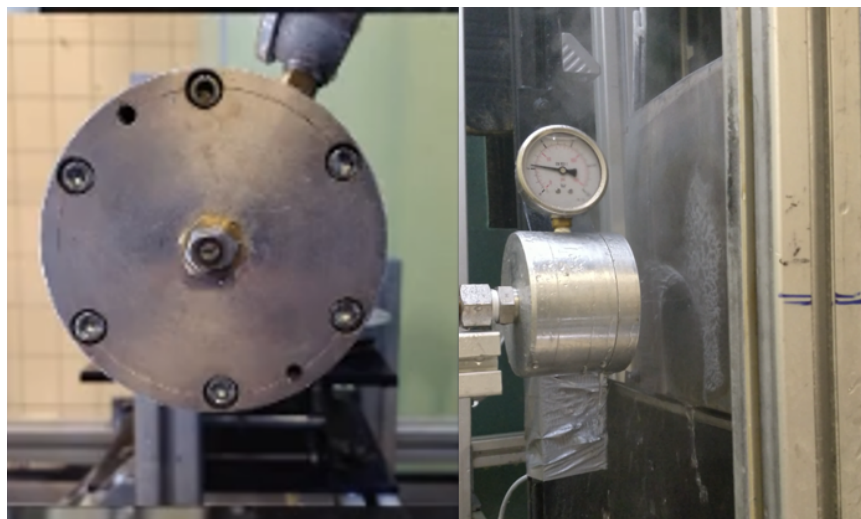


Figure 2.3: Left:Single water jet mould, Right: Quenching process with single jet moving plate at quench time of 5s

A small section of a real mold consisting of array of jets was used for the experimental works in order to mimic the real time continuous cooling process as practised in industries. It consists of an array of jets that creates a circular zone of water impingement along the hot surface during the quenching process. The mold hold a diameter of 70 mm to accommodate several water jet nozzles. In the present work, we adopt 9 and 10 full jet nozzle fields, each of 1.05 $mm$ in diameter as shown in **Fig. 2.2** which are equally spaced at 35 mm distance apart. **Fig. 2.3** shows the mold utilized for the single water jet on the left mounted to circular mould which accommodates pressurized liquid water before it exists through the nozzle. Also the mould is headed with pressure indicator to control the water pressure through the nozzle exit and the water jet velocity. On the right we can observe the quenching process with single water jet nozzle with moving plate condition at quench time of 5s for AA6082 aluminium alloy plate with water jet velocity of 12 $m/s$ (2 bar), initial temperature of 520 °$C$, with plate velocity of 10 $mm/s$. The fluid flow on the hot moving plate can be clearly captured during the process.

Figure 2.4: Left) Water Jet Mold used for cooling with 11 orifices, Right) Photographic visualization of quench side

**Fig. 2.4** demonstrates the photographic view of the experimental water jet quenching with the usage of array of jets. The left part of the Fig. 2.4 shows the water jet mold with 11 orifices each of 2 mm in diameter equally spaced at 2 mm apart, whereas on the right part of the Fig. 2.4 shows the quenched side view of the array of water jets or mold similar to the left image. The water jet impingement clearly shows the wetting front movement, dynamics of water jet on the hot surface, hydraulic jump near the water jet impingement for 45 ° impingement angle would alter the mechanism of the heat transfer.

## 2.3.2 Experimental Sample

A rectangular sheet of aluminium alloy AA6082, with length and width as 250 *mm* and 230 *mm* respectively and a thickness ranging from 2 - 20 *mm* was used for experimental investigation. The surface of the plate is cleaned with appropriate agents to attain uniform surface condition. The samples were painted black on the measuring side in order to increase the emissivity, for a more accurate temperature measurement. From the calibration of emissivity, it was found that the emissivity of the coating was stable in the range of 0.90 to 0.93 and independent from surface temperature. A detailed review is available in the work by Alam et al. (2008). Thermo-physical properties of material like, density, thermal conductivity, specific heat capacity are listed in **Tab. 2.1** for the AA6082 material.

| Density | 2700 $kg/m^3$ |
|---|---|
| Thermal Conductivity | 170 $W/m.K$ |
| Specific Heat Capacity | 1050 $J/kg.K$ |

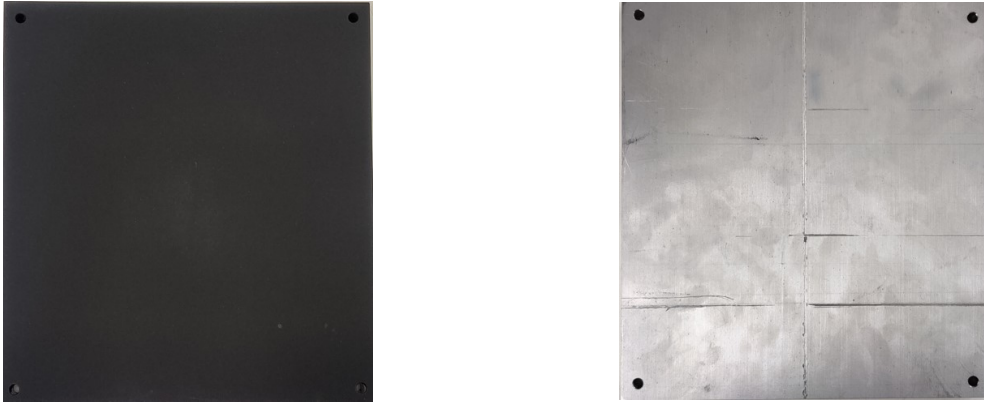Table 2.1: Material property of Aluminium Alloy AA6082

Figure 2.5: Left: Measuring side sample metal plate, Right: Quenching side sample metal plate

## 2.4 Experimental Setup

The experimental analysis of secondary cooling in the DC casting of Aluminium alloy was investigated using a test rig as shown in **Fig. 2.6**. The same test facility can be adopted to various kinds of quenching techniques as shown in Fig. 2.1. The test facility can be distinguished into three different sections, namely, heating section, quenching chamber, data acquisition. In the heating section, an electric furnace is responsible for heating the plate to the desired initial temperature before shifting to the quenching chamber. The thermocouples inside the electrical furnace are coupled with the limiting switch to avoid the overheating of the test plate in the oven. The limiting switch can be manually controlled to achieve desired temperature of the plate for the experiments. In the quenching chamber, 2 phase steeper motor is responsible for the movement of the plate, which holds the horizontal heated plate with the vertical bar that acts as a cantilever beam. The vertical movement of the sample plate can be controlled with an IT 116 flash controller, similar to the movement of the ingot or billet in a real DC casting process. The cooling water is supplied to the water jet mold through the centrifugal pump, which flows through the array of orifices to produce an array of water jets. A mold of width 120 mm consists of 11 orifices equally spaced at its base was used to resemble the secondary cooling of real DC casting process as in **Fig. 2.4**. For any kind of quenching techniques, the suitable nozzle type is utilized for the experimental work as shown schematically in Fig. 2.2. A metallic separator was used between the water jets and the hot metal plate to avoid the initial contact at undesired temperature. As the plate reaches a desired value, the separator is dropped at high speed to ensure that jet makes contact with the plate. Cooling water impinges at the bottom when the plate moves with certain plate velocity. Data acquisition section consists of infrared thermography, a data acquisition system to control and store the experimental data. Infrared camera records the temperature in terms of thermal images, which have high spatial resolution of 610 x 560 pixels with a frame rate capacity of up to 200 images per second. The infrared camera measures the temperature distribution on the back of the water impingement region.
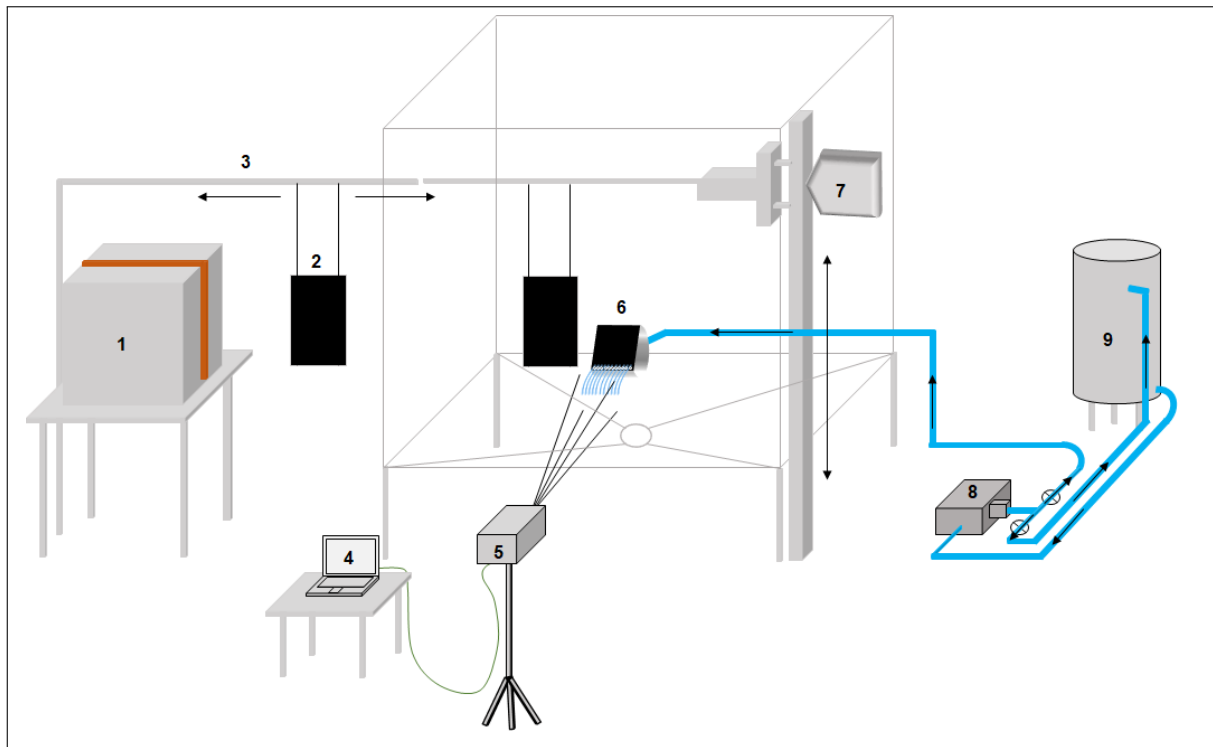
**Experimental Section: 1.** Electrical furnace, **2.** Test plate, **3.** Sliding rail, **4.** Data acquisition system, **5.** Infrared thermography, **6.** Mold with array of jets, **7.** Motor for vertical movement of the plate, **8.** Gear pump, **9.** Water Tank

Figure 2.6: Experimental setup of moving sheet mechanism

## 2.5   Experimental Infrared Thermography

### 2.5.1   Mold Quenching

Temperature will vary at different times and at different locations. This gives rise to the local heat transfer and the problem becomes two dimensional for high thermal conductivity. In the present work, two dimensional inverse method is solved to quantify the heat transfer. **Fig. 2.7** shows the thermal images obtained from the infrared camera and the temperature distribution in the central vertical position for different times during the quenching process. $x_e$ is the Eulerian position recorded by the infrared camera. Boiling phenomena during the quenching process can be distinguished as pre-cooling, transition, and nucleate boiling regions. The temperature profiles in Fig. 2.7 agree well for different times (e.g., 5, 6, 7 seconds) and thus we say a steady state of the cooling process is obtained.
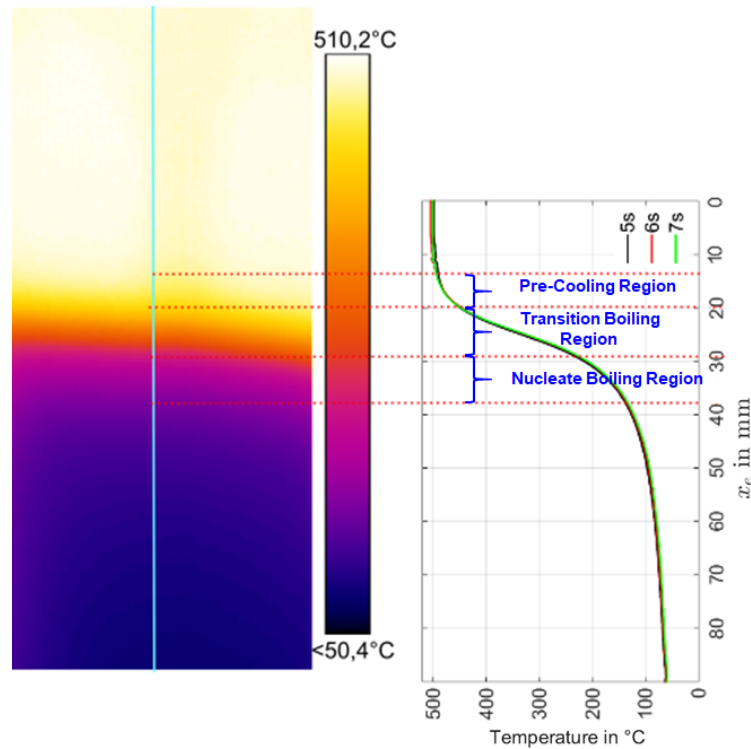
Figure 2.7: Thermal images from infrared thermography and corresponding temperature profiles at different time instants Kulkarni et al. (2019)

The steady state condition is observed in real DC casting process after a cast length of 0.5 - 1 $m$, where similar phenomena were obtained in the experiments of hot moving plate. The region of interest is in an Eulerian position are considered, the temperature away from the impingement point there is no much spatial variation in temperature is noted. **Fig. 2.8** presents the temperature profiles in the horizontal direction for different vertical positions decreases the quasi-steady state of the plate quenching. The temperature profiles in the range of $-10mm$ to $10mm$ was found to be uniform. Since, the heat conduction from the extreme edges of the plate has an insignificant effect on the cooling at centre region of water impingement, the temperature profiles on this region were chosen for further analysis in this work.
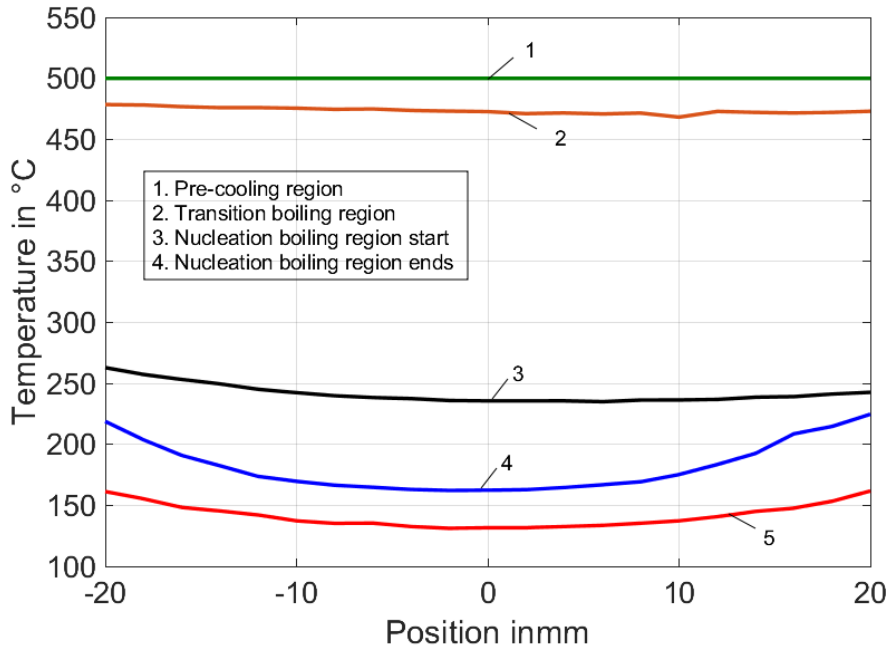
Figure 2.8: Temperatures of the plate at quasi-steady state for different horizontal lines

## 2.5.2   Full Jet Quenching

The schematic physical model of the single full jet quenching is represented in the **Fig. 2.9**. As seen from the diagram, the single circular water jet impinges on the hot metal surface at certain start temperature with water jet velocity $w_j$. After the water jet impact on the hot surface, the water jet velocity diminishes and wetting front travels on the surface of the hot metal plate. Across the wetting front, different phases of boiling attains especially transition, nucleate boiling, film boiling with higher temperature gradient between the wet region and dry region. Henceforth, we can clearly distinguish the quenching process with single full jet into three different sections 1. wet region, 2. wetting front, 3. spluttering region. In the wet region, the temperature lies below the 100-150°$C$ as most of the heat is already extracted at the wetting front movement and this region consequently lies in the single phase convection. Whereas, the most heat transfer occurs in the wetting front movement with high thermal gradient between the hot region and cold region. The spluttering region is the consequence of the film boiling, excess of superheat between the hot metal and the cooling water make the water vapour film not to wet the surface. At the start of the quenching process, the wetting front with high momentum encounters the hot region at higher temperature. When the vapour production rate is higher than the water jet momentum orthogonal to the plate, the droplets are ejected from the hot surface. In the quasi-steady state region, the effect of water ejection reduces since the wetting front velocity becomes constant and the water wets along the gravity direction.
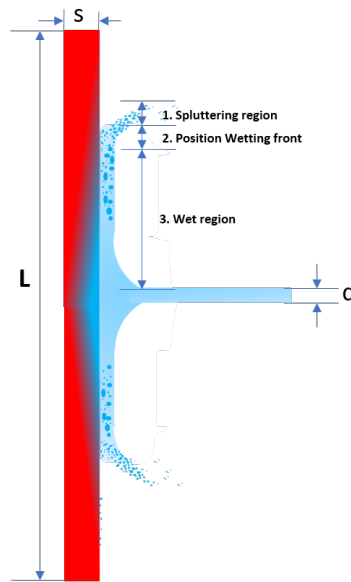
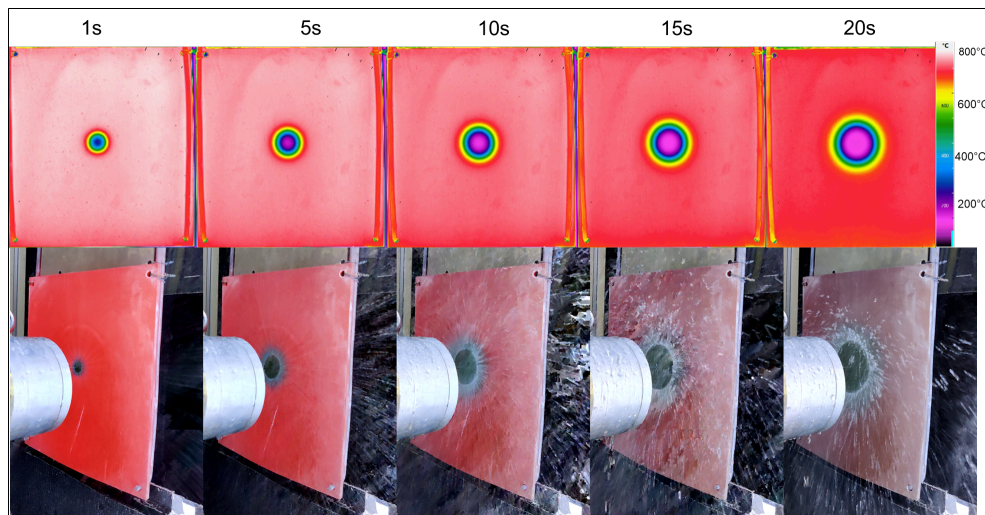Figure 2.9: Schematic diagram of stationary full jet impingement quenching



Figure 2.10: Experimental results of single full jet nozzle: (Top): Infrared images for different time instants, (Bottom): Quenched side images for different images

**Fig. 2.10** gives a view from the water impingement side of hot nickel plate quenched with full jet nozzle. The Fig. 2.10 shows a snapshots of the transient cooling process for 6 time instants i.e. 1, 5, 10, 15, 20 s respectively. Over the time, the growth of the wetting front is clearly observed. Due to the heat conduction from dry to wet region, wetting front velocity delays to grow from the impingement point. The growth of the wet region gives a clear view of the nucleate boiling phenomenon. As the wetting front grows, the nucleate or the re-wetting extracts large part of the heat stored in the thermal body.
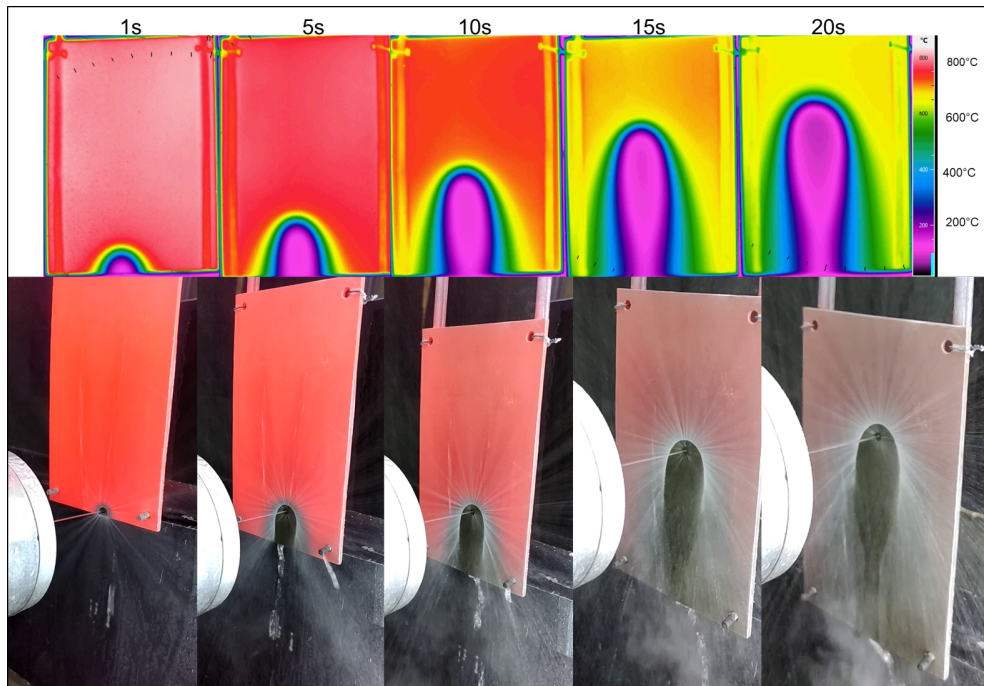
Figure 2.11: Experimental results of single full jet nozzle of moving plate condition: (Top): Infrared images for different time instants, (Bottom): Quenched side images for different images

**Fig. 2.11** depicts the measurement side and the quenched side images for different time instants for the plate movement. Water jet with high momentum impinges initially at the bottom of plate and instantly surface temperature of the plate drops to 150 °$C$. The movement of wetting front in semi-circular shape happens below the jet impingement position water wets the surface due to gravitational effect. As the plate moves from bottom to top, the most of temperature drop occurs in the water jet impingement position and the wetting front propagates in the downward direction. At higher cooling period, the heat conduction from the dry region affects the wetting front movement and the water jet gets ejected from the plate surface in the downward direction.
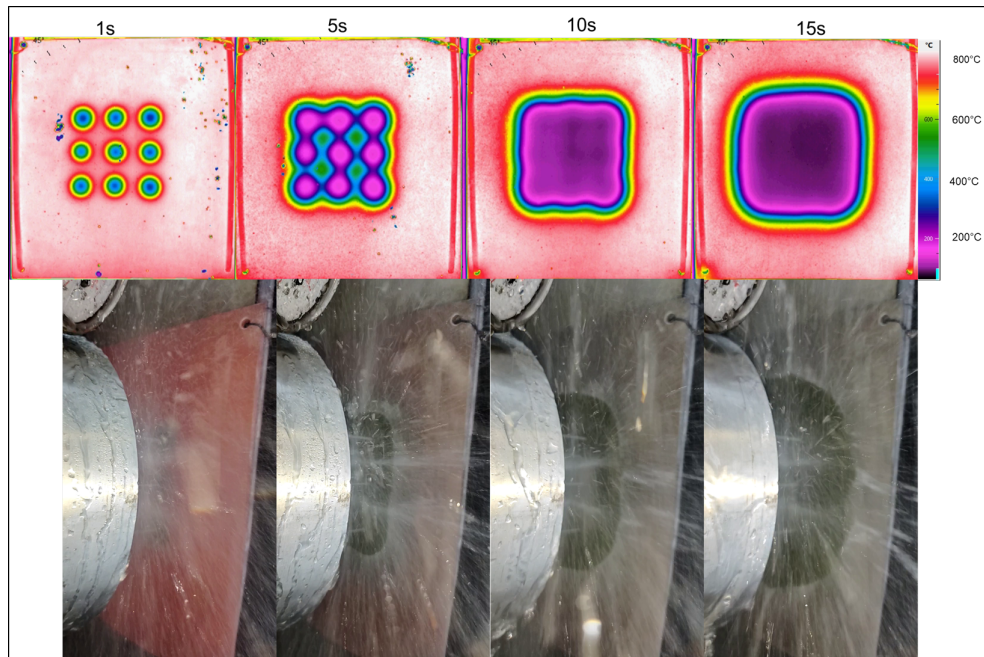
Figure 2.12: Experimental results of Inline full jet nozzle configuration of fixed plate condition: (Top): Infrared images for different time instants, (Bottom): Quenched side images for different images

Configuration of the water jets in inline arrangement with 9 circular shaped nozzles were utilized to cool the hot metal plate under fixed condition as shown in the **Fig. 2.12**. The cooling process shown for 4 consecutive time steps of 1s, 5s, 10s, 15s respectively. The complex interaction of configuration of water jets spaced equally at 35 mm with each other on the hot metal plate occurs with larger amount of water ejects from the surface. For 1s, the influence of the water jets can be seen with almost same wetting front radius for all the 9 jets of the inline configuration. Whereas, at 5s we can clearly see the start of the water jet interaction with the adjacent jets causing the water fountain at this location. The high turbulent behaviour can be observed as seen from the quenched side images as shown in the Fig. 2.12. The uniform cooling of the plate occurs after the 10s while wetting front moves in rectangular shaped orientation.
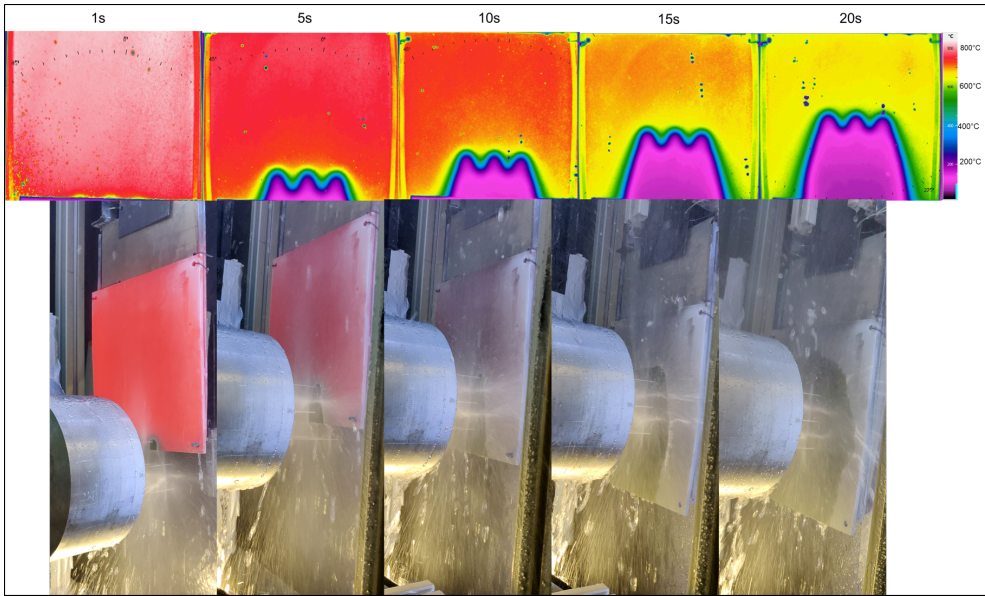
Figure 2.13: Experimental results of Inline full jet nozzle configuration of moving plate condition: (Top): Infrared images for different time instants, (Bottom): Quenched side images at the corresponding time instants.

For the same experimental condition as that of fixed plate, the inline configuration with plate movement is depicted as shown in **Fig. 2.13**. The continuous movement of the hot metal plate with certain velocity strictly changes the fluid structure interaction and the phenomena of the heat transfer. As seen from the infrared images and the quenched side images, the fluid is highly turbulent and the water jet ejects strictly away from the metal plate for larger time steps. The turbulent water jet favours the cooling behaviour and the uniformity of the cooling occurs in the downward direction. Whereas, the non-uniform distribution occurs at the first row of waters due to the continuous movement of the plate.
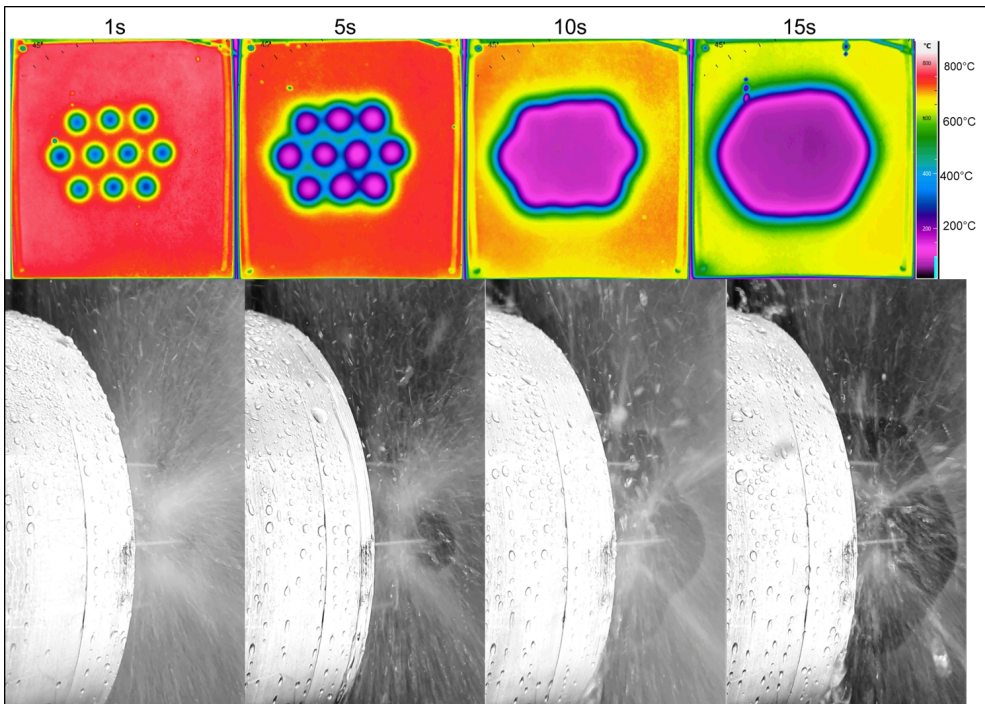


Figure 2.14: Experimental results of staggered full jet nozzle configuration of fixed plate condition: (Top): Infrared images for different time instants, (Bottom): Quenched side images for different images

Staggered configuration of the 10 water jets equally spaced at 35 mm distance apart were water cooled with a fixed plate condition as shown in the **Fig. 2.14**. Similar to the inline configuration, the wetting front radius of the 10 water jets with similar magnitude can be found and consequently the interaction of the water jets can be seen at cooling time of 5s. In the water jet quenching side, the tremendous amount of water jet interaction takes place and the effect of jet interaction or the hot quenched plate can be seen accurately.
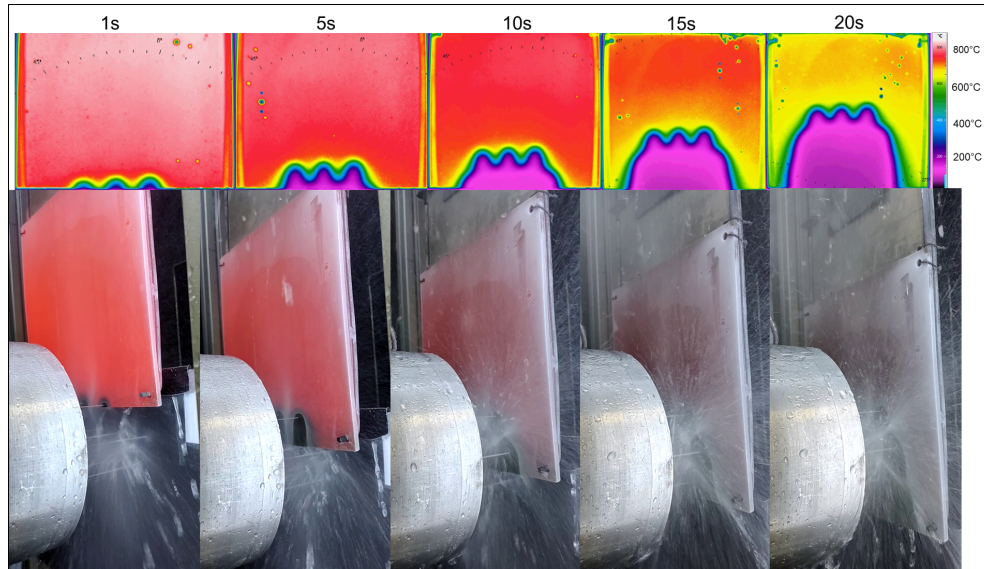


Figure 2.15: Experimental results of staggered full jet nozzle configuration of moving plate condition: (Top): Infrared images for different time instants, (Bottom): Quenched side images for different images

For the plate movement, in case of staggered configuration with similar experimental conditions, the experiments were performed as shown in the **Fig. 2.15**. The local temperature distribution becomes uniform and overall temperature of the plate becomes equal in the water impingement region. As the continuous movement of the plate occurs, the water jet arranged in three rows strongly affects the cooling behaviour and the new incoming hot surface cooled intensively. Except at the first row of jets, the other parts of the plate attains almost same temperatures.

# Chapter 3

# Inverse Heat Conduction Problem

## 3.1 Introduction

The majority of the researchers in the literature focus to investigate the heat transfer during quenching of the hot metals using the inverse heat conduction method. Since, the temperature distribution on the water impingement region is unable to measure by using both the non-contact and contact measuring techniques. The complex fluid-structure interaction adds more error in the temperature measurement and hence the temperatures are measured below or on the other side of the plate. Using the thermocouples, the temperature is recorded below some distance from the water impingement side and further the measured temperatures were utilized for the evaluation of the heat transfer. In contrast to the contact temperature measurements, the infrared thermography is implemented to capture the thermal images on the back side of the water impingement region with spatial and temporal resolution. In case of the thicker metal plates, the time delay between the quenched side and the temperature variation on the measured side can be clearly observed. So, the heat transfer in delay time period is unable to calculate and this acts as a main disadvantage to the measurements as well as the inverse problems. Although, the temperature distribution in most of the applications occurs at steady state condition and hence the inverse problems are well applied to solve those kinds of problems. Even though, most of the researchers propose, develop, formulate the inverse heat conduction method to estimate the heat flux during the quenching process. The main question arises, for what kind of applications the model is suitable? Is the proposed model is verified against the experimental temperatures? These questions are unanswered in most of the papers published. Although, the papers discuss on the verification of the proposed model against the exact heat fluxes, the validation should be made with the experimental temperatures and the error should be quantified. The validation of the inverse heat conduction method as proposed in this research work is done with the surface temperatures obtained from inverse solution and the experimental method. Also, the proposed model is well suitable for any kind of application, given the governing partial differential equation should be modified based on the application or the process involved before formulation of the inverse heat conduction method.

Huang and Wang (1999) presents a three-dimensional inverse heat conduction problem in estimating heat flux using conjugate gradient method. The transient surface heat flux is estimated, but the validation of the mathematical model is not discussed and the surface temperature are not given. Kim and Oh (2001) presents a solution method for non-linear 3D inverse method using sequential gradient method with cubic spline function. The proposed method deviates from the exact temperature and surface heat fluxes. Although the sequential gradient method is restricted with the cubic spline function, the solution without the use of cubic spline function is not presented. Groß et al.

(2005) consider a 3D in a falling film experiment. The IHCP is solved with conjugate gradient method. Step theta method and piecewise linear finite elements on a tetrahedral grid for the time and space discretization, respectively and the resulting sparse system is solved with Krylov subspace method. The numerical validation is presented against the input heat flux rather temperature validation would give a better understanding of the model verification. Raynaud and Bransier (1986) developed a space marching finite difference algorithm to solve non-linear one-dimensional inverse heat conduction problem. The verification of the proposed numerical model is not discussed and the application of the presented method to other physical process is unknown and detailed study on the limitation of the method should be presented. Beck et al. (1996) compares the several other inverse methods using experimental data like function specification with several function approximation, Tikhonov regularization, iterative regularization and specified function over time region with Green's function. The comparison of measured temperature and the temperature from computations were not discussed although the comparison of the surface heat fluxes was reported. The heat flux comparison shows a clear agreement with other kinds of inverse techniques. Jarny et al. (2001) presents the non-linear inverse method for two-dimensional heat flow. The well-known conjugate gradient method is implemented to solve the two-dimensional IHCP. The validation of the measured temperature and the estimated temperature agrees well. Su and Hewitt (2004) solved the inverse heat conduction method using Alifanov's iterative algorithm method to estimate the heat transfer coefficient for boiling over hot surface of heated tube. The author proposes a one-dimensional model for the calculation of heat flux using inverse method. Although, the numerical validation is discussed with the heat transfer coefficient profiles along the time direction, the temperature validation should be made for better understanding. The extension of one-dimension model to the two-dimensional would provide a better result. Kim and Oh (2001) develop a two-dimensional inverse heat transfer method to estimate a heat transfer coefficient on various surface locations of the specimen. In order to avoid the fluctuations on the heat flux estimation, the concept of spatial regularization and future time information were introduced in their formulation to get more realistic heat transfer. The validation with other researchers is insignificant and deviates from their results. The method of heat flux estimation was not discussed efficiently. Abou Khachfe and Jarny (2000) provide a numerical solution of 2-D non-linear inverse problem using FEM and emphasizes an attention on the calculation of the gradient of the functional for non-linear problem. The author gives three general situations (media, force or boundary data) which are shown for the computation of the gradient equation for the CGM approach. Yang et al. (1997) proposed an inverse method based on the symbolic approach for 3-dimensional heat conduction problem. The elimination of the nonlinear optimization process is emphasized with the usage of the linear domain. The proposed method is also applicable to other kinds of inverse problem such as initial estimation and source strength estimation in the three-dimensional heat conduction problem. Chantasiriwan (2001) proposed an algorithm for solving multi-dimensional inverse heat conduction problem. The sequential function specification method using the assumption that the heat fluxes varies linearly with time. The verification of the model is not reported and the merits and demerits of the proposed algorithm is not clear. Lüttich et al. (2005) design the multi-dimensional inverse heat conduction problem. The author reveals the necessity to develop a formulation for unifying error in the measurements and to obtain the suitable estimation of the unknown quantities. The algorithm or the solution steps seems to be complexed in comparison to the other available methods in literature and also the method is limited to the particular application. The application of this method to other physical process is not reported. Jarny et al. (1991) presents a multi-dimensional optimization method using adjoint method coupled with conjugate gradient method to estimate the surface condition (heat flux or temperature),

space dependent thermal conductivity and heat capacity with the known temperature measurements. The author specifies that no prior information is needed for the solution of the inverse method, whereas it describes with known prior information about unknown function, the problem becomes a special case from that general approach. Hadała et al. (2017) developed a solution strategy for the inverse determination of spatially varying heat transfer co-efficient. The HTC is approximated with non-linear shape function in space and time direction. Even though, the temperature solution is verified against the measured profiles. The method is restricted to only certain experimental conditions due to the approximation of the heat transfer co-efficient.

Duda (2015) formulated a space marching method to solve inverse axi-symmetric heat conduction problem in thick walled complex shaped elements. The presented method used to identify the temperature in a heated steam gate valve. The present method is validated efficiently with the measured temperature and provide a flexibility to apply to other process as well. Many authors studied the quenching of hot metals and the methods used to estimate the heat flux are listed briefly: Beck (1970) solved the one dimensional heat conduction model with the inverse method using the temperatures measured inside the copper block. Huang and Wu (2006), Xue and Yang (2005) estimated the surface heat flux using the conjugate gradient method. Nallathambi and Specht (2009b) implemented the non-iterative method to predict the surface heat flux during the array of jet impingement quenching. Kulkarni et al. (2019) proposed an Eulerian steady state solution to obtain the heat flux during quenching process. The experimental temperature data were used to estimate the surface heat flux with iterative two dimensional inverse method by Robidou et al. (2003). Ciofalo et al. (1999) employed the one dimensional inverse heat conduction to estimate the heat flux and the heat transfer coefficient. Jarny et al. (1991) formulated the three dimensional inverse heat conduction method for general optimization problem. The author used the adjoint equation along with the conjugate gradient algorithm to obtain the inverse solution. The inverse problem is ill posed and is very sensitive to the temperature measurement errors. Thus, the sophisticated numerical techniques are used for the computations. In this work, the experiments were performed to measure the temperatures on the other side of the quenching process. To understand the heat transfer mechanism on the quenching region the two dimensional finite element method is developed and the corresponding coupled adjoint equation along with the conjugate gradient method is implemented. Since the inverse problem is highly sensitive to the temperature error or fluctuations, Tikohonov regularization is used and the solution algorithm is presented.

## 3.2  Finite Element Formulation

From the experimental analysis, it is clear that the surface temperature drop in case of full jet quenching process observed to be axi-symmetric. The mathematical formulation of the quenching process becomes easier. In quenching process, the temperature field in the body is modelled by Fourier's law of heat conduction. The source terms such as transformation enthalpies, mechanical energy dissipation are negligibly small and hence are not considered in the mathematical formulation. From the energy balance, we obtain the following partial differential equation.

$$\nabla(\lambda \nabla T) = \rho(T)c(T)\frac{\partial T}{\partial t} \qquad (x,t) \in (\Omega, \tau) \tag{3.1a}$$

$$T(x,0) = T_{intial} \qquad (x) \in (\Omega) \tag{3.1b}$$

$$\lambda(T)\nabla T.n = q_j(x,t) \qquad (x,t) \in (\Gamma_j, \tau) \tag{3.1c}$$

$$\lambda(T)\nabla T.n = 0 \qquad (x,t) \in (\Gamma_c, \tau) \tag{3.1d}$$

Where $\rho$ is the density, $c_p$ is the specific heat capacity, and the $\lambda$ is the thermal conductivity of the material as a function of temperature. $q_j$ is the unknown spatio-temporal dependent heat flux due to the convection phenomena of the quenching process, T is the temperature distribution of the whole domain, x represents the spatial co-ordinate, $\Omega$ represents the spatial domain, $\tau$ is the time domain $[0, t_{max}]$ and n is the outward pointing unit normal vector. **Fig. 3.1** gives the overview of the finite element model, boundary 1, 2, 3 are insulated and radiation effects are neglected.

The schematic description of finite element modelling for quenching process is as shown in Fig. 3.1. In this work, we consider the two-dimensional part of the quenching process in length and thickness direction. The width direction is simplified as plain strain condition, due to the circular movement of wetting front. The axisymmetric two-dimensional finite element model is valid only for the circular propagation of wetting front. The domain is discretized into four different boundaries. The boundary at the water impingement side is considered to be Neumann condition.
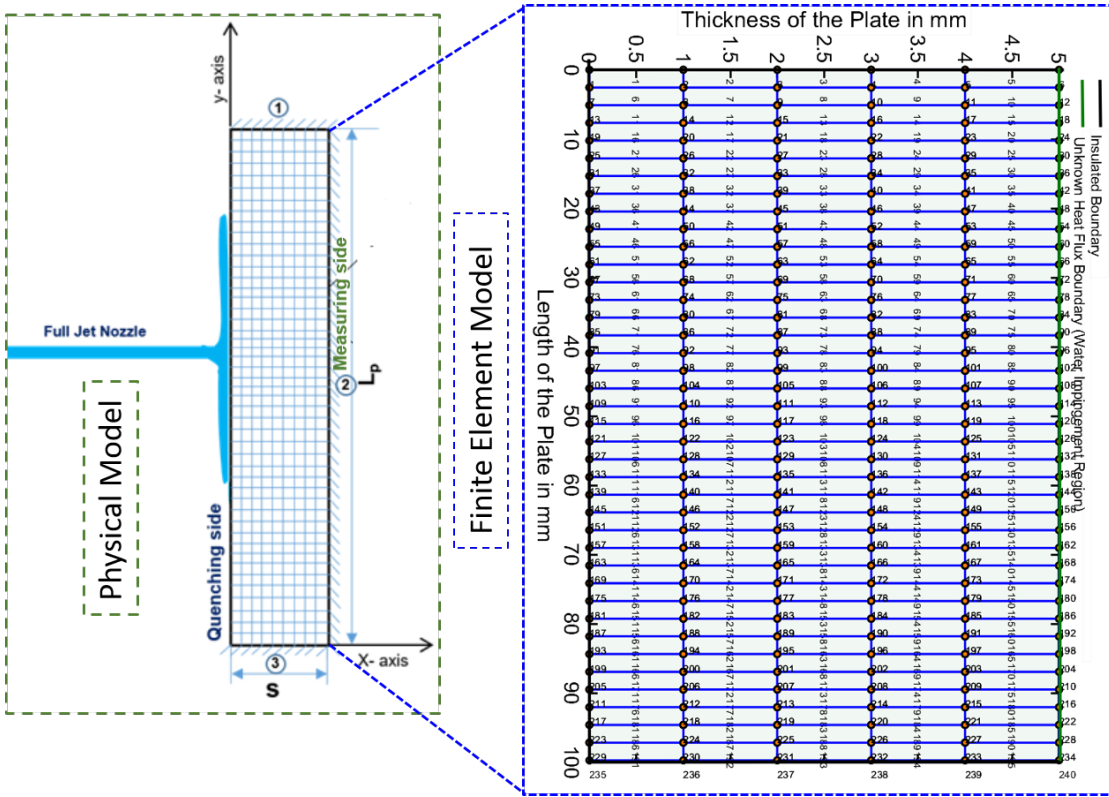


Figure 3.1: Moving sheet mechanism experimental setup

For an arbitrarily choosen temperature profiles, integration of the heat conduction is expressed with the help of principle of virtual temperature stated as

$$\int_V [\nabla(k\nabla T) - \rho c_p \dot{T}] \tilde{T} dV = 0 \tag{3.2}$$

Application of the divergence theorem ,

$$\nabla(\tilde{T}\ k\ \nabla T) = k\ \nabla T\ .\ \nabla \tilde{T} + \nabla(k\nabla T)\tilde{T} \tag{3.3}$$

**3.2** can be rewritten according to **3.3** as follows,

$$\int_V [\nabla(\tilde{T}\ k\ \nabla T) - (k\ \nabla T)\ \nabla \tilde{T}\ - \rho\ c_p\ \dot{T}\ \tilde{T}] dV = 0 \tag{3.4}$$

with the use of divergence theorem, and appropriate boundary conditions the first term becomes,

$$\int_V [\nabla(\tilde{T} \ k \ \nabla T)] dV = \int_s [n^s(\tilde{T} \ k \ \nabla T)] ds = -\int_s [q^s(\dot{T})] ds \tag{3.5}$$

Applying the **Eg. 3.5** into **Eg. 3.4** we get,

$$\int_V [\nabla \dot{T}( \ k \ \nabla T)] dV - \int_s [\dot{T} \ \alpha \ T)] ds + \int_V [\rho \ c_p(\dot{T})] dV = 0 \tag{3.6}$$

**Eq. 3.5** is satisfied over the whole domain, and sub-domain for arbitrarily temperature distribution $\dot{T}$.

The thermal body under consideration was discretized with finite number of elements. The temperature field on each element were interpolated for nodal temperature. The temperature field and its gradient for $e^{th}$ element are

$$T_e = N_e^T \ T_e \tag{3.7a}$$

$$\frac{\partial T_e}{\partial x_i} = \frac{\partial N_e^T}{\partial x_i} \ T_e = H_e T_e \tag{3.7b}$$

where $T_e$ is the vector of the nodal point temperature at eth element with n-nodes.

$$T_e = [T_1, \ T_2, \ T_3, \ ...... \ T_n]^T \tag{3.8}$$

The operators in **Eq. 3.7b** i.e., $N_e$ and $H_e = [\frac{\partial N_e}{\partial x} \frac{\partial N_e}{\partial y}]^T$ and the element temperature and temperature-gradient interpolation operators, respectively. The integral form can be rearranged as follows:

$$\sum_e \int_V [\dot{T}_e^T \ H_e^T \ k \ H_e \ T_e] dV + \sum_e \int_{s_e} [\dot{T}_e^T \ N_e^S \ \alpha(N_e^T) \ T_e)] ds + \sum_e \int_{V_e} [\dot{T}_e^T \ N_e \ \rho \ c_p \ N_e^T \ \dot{T}_e] dV = 0 \tag{3.9}$$

where $N_e^S$ is the interpolation functions on the element surface and $\dot{T}_e$ is an arbitrary vector of virtual nodal temperatures. After the assemblage of finite elements, a linear system of equations is obtained with unknown nodal temperature Newton-Raphson method used for the time-discretization and for the solution at current time $t + dt$ Kayamak (2007). The nodal temperature and its derivatives (Euler backward approximation) for the current ith iteration are

$$T_i^{t+\Delta t} = T_{i-1}^{t+\Delta t} + \Delta T \tag{3.10a}$$

$$T_i^{t+\Delta t} = \frac{T_{i-1}^{t+\Delta t} + \Delta T - T^t}{\Delta t} \tag{3.10b}$$

The final form of the integral equations becomes

$$(\sum_e \int_{V_e} [H_e^T \ k \ H_e)] dV + \sum_e \int_{S_e} [N_e \ \alpha_{i-1}^{t+\Delta t} \ (N_e^s)^T] ds)(T_{i-1}^{t+\Delta t} \tag{3.11a}$$

$$+\Delta T) + (\sum_e \int_{V_e} [N_e \ \rho c_p N_e^T] dV)(\frac{T_{i-1}^{t+\Delta t} + \Delta T - T^t}{\Delta t}) = 0 \tag{3.11b}$$

After rearrangement, unknown nodal temperature are kept on the left-hand side for simplicity reason,

$$(\sum_e \int_{V_e} [H_e^T \ k \ H_e)] dV + \sum_e \int_{S_e} [N_e \ \alpha \ (N_e^s)^T] ds)(\Delta T) + (\sum_e \int_{V_e} [N_e \ \rho c_p N_e^T] dV) \tag{3.12a}$$

$$(\frac{\Delta T}{\Delta t}) = -(\sum_e \int_{V_e} [H_e^T \ k \ H_e)] dV + \sum_e \int_{S_e} [N_e \ \alpha \ (N_e^s)^T] ds)(T_{i-1}^{t+\Delta t}) - (\sum_e \int_{V_e} [N_e \ \rho c_p N_e^T] dV)(\frac{T_{i-1}^{t+\Delta t} - T^t}{\Delta t}) \tag{3.12b}$$

The matrices form of the **Eq. 3.12** can be written as follows:

$$_kK_{i-1}^{t+\Delta t} + {}_cK_{i-1}^{t+\Delta t} + \frac{1}{\Delta t}C_{i-1}^{t+\Delta t} \ \Delta T = -_kQ_{i-1}^{t+\Delta t} - {}_{c_p}Q_{i-1}^{t+\Delta t} \tag{3.13}$$

The global matrices are assembled using element connectivity from the numerical integrated element matrices. The finite element matrices of non-linear heat transfer analysis are stated below:

$$_kK_{i-1}^{t+\Delta t} = \sum_e \int_{V_e} [H_e^T \ k \ H_e)]dV \tag{3.14a}$$

$$_cK_{i-1}^{t+\Delta t} = \sum_e \int_{S_e} [N_e \ \alpha \ (N_e^s)^T]ds \tag{3.14b}$$

$$C_{i-1}^{t+\Delta t} = \sum_e \int_{V_e} [N_e \ \rho c_p N_e^T]dV \tag{3.14c}$$

$$_kQ_{i-1}^{t+\Delta t} = (\sum_e \int_{V_e} [H_e^T \ k \ H_e)]dV + \sum_e \int_{S_e} [N_e \ \alpha \ (N_e^s)^T]ds)(T_{i-1}^{t+\Delta t}) \tag{3.14d}$$

$$_{c_p}Q_{i-1}^{t+\Delta t} = (\sum_e \int_{V_e} [N_e \ \rho c_p N_e^T]dV)(\frac{T_{i-1}^{t+\Delta t} - T^t}{\Delta t}) \tag{3.14e}$$

Gauss-Quadrature is applied for calculation of the integrals. In 2D elements, nine integration point in the area and the integration points on each side were selected for computation. In this work, we choose quadrilateral elements for the discretization of the domain. The typical mapping from the natural coordinate system to the physical co-ordinate system is done through the mathematical mapping called iso-parametric elements.

## 3.3 Inverse Heat Conduction method

The conjugate gradient method with the coupled gradient equation is presented here based on Bergagio et al. (2018) The inverse method is to be solved with the aim of minimizing the following objective function:

$$J_{q_j} = \frac{1}{2} \int_0^{t_f} \int_{\Gamma_c} (T - T_{exp})^2 d\Gamma dt + \frac{\gamma_k}{2} \int_0^{t_f} \int_{\Gamma_q} (q_j)^2 d\Gamma dt \tag{3.15}$$

where, $\Gamma_c$ represents temperature measured region, $\Gamma_q$ represents heat flux boundary condition. The first term on the right hand side of the equation $T_{exp}$ is from the experimentally measured temperatures from the infrared camera and T is obtained from the direct heat conduction problem. $\gamma_k$ in second term of the equation indicates the regularization term. The second order Tikhonov regularization method is used to stabilize the inverse method. The solution of the direct problem obtained from the below partial differential equations.

$$\rho(T)c(T)\frac{\partial T}{\partial t} = \nabla(\lambda(T)\nabla T) \qquad (x,t) \in (\Omega, \tau) \tag{3.16a}$$

$$T(x,0) = T_i \qquad (x) \in (\Omega) \tag{3.16b}$$

$$\lambda(T)\nabla T.\vec{n} = q_j(\vec{x}, t) \qquad (x,t) \in (\Gamma_q, \tau) \tag{3.16c}$$

$$\lambda(T)\nabla T.n = 0 \qquad (x,t) \in (\Gamma_c, \tau) \tag{3.16d}$$

This equation can be solved with a 2D-Finite Element Method. On the quenching side, the heat flux as a function of the position and time needs to be assumed at the start of

the iteration as a means of thermal boundary condition and whereas on the remaining boundaries, the insulation boundary conditions were applied. Since the problem considered here is two dimensional and along with time dimension the problem necessitated to develop an adjoint problem for the computation of the gradient $\nabla J_{q_j}$ in order to minimize the function.

## 3.3.1 Adjoint equation

Adjoint function $\phi(x,t)$ are needed to determine the gradient of the objective function $\nabla J(q_j)$ in addition to the sensitivity function $\theta(x,t)$. For this, we first develop an adjoint problem and then follows the gradient equation. Henceforth, the adjoint problem is defined as follows:

$$e_m(t) = T(x_m, t; q) - T_{exp}(t), \quad m = 1, \ .....M \tag{3.17a}$$

$$\rho C(T)\frac{\partial \phi}{\partial t} = -\lambda(T)\nabla^2\phi \qquad (x,t) \in (\Omega, \tau) \tag{3.17b}$$

$$\phi(x, t_{max}) = 0 \qquad (x) \in (\Omega) \tag{3.17c}$$

$$\lambda(T)\nabla\phi.n = 0 \qquad (x,t) \in (\Gamma_j, \tau) \tag{3.17d}$$

$$\lambda(T)\nabla\phi.n = T(x,t; q_j) - T_{exp} \qquad (x,t) \in (\Gamma_c, \tau) \tag{3.17e}$$

- The adjoint problem has zero solution with no clear errors.

- We must observe that the adjoint problem is solved backwards in time with zeros as the initial conditions.

- However, the definition of a new variable $\tau = t_f - t$ for the computation should simplify the problem.

## 3.3.2 Gradient Equation

**Definition of the gradient function**

The gradient of the objective function $J(q_j)$ at point $q_j$, can be denoted by $\nabla J(q_j)$, which relates to the variable $J$ as discussed according to Jarny et al. (1991) as follows:

$$J(q_j + \epsilon \ \Delta q_j) - J(q_j) \ = < \nabla J(q_j), \epsilon \ \nabla\tau >_E +(terms \ non-linear \ in ||\Delta||) \tag{3.18}$$

where $(q_j + \epsilon \ \nabla q_j) \in E$ and $\epsilon$ is the real number.
The derivative of the objective function $J$ at $q_j$ in the direction of $\nabla q_j$, can be denoted by $D_{\nabla q_j} J(q_j)$ as

$$D_{\nabla q_j} J(q_j) = \lim_{\epsilon \to 0} \frac{J(q_j + \epsilon \ \Delta q_j) - J(q_j)}{\epsilon} \tag{3.19}$$

the gradient of the objective function $\nabla J(q_j)$ is given by

$$D_{\nabla q_j} J(q_j) =< \nabla J(q_j), \epsilon \ \nabla\tau >_E \tag{3.20}$$

**Sensitivity Problem**

Let $\nabla T_{\epsilon \Delta q_j}$ accounts for the change of temperature resulting from the unknown boundary condition $q_j$ in the amount $\epsilon \Delta q_j$, that is

$$\Delta T_{\epsilon \Delta q_j} = T(x, t; q_j + \epsilon \Delta q_j) - T(x, t; q_j) \tag{3.21}$$

The directional derivative of T, $D_{\nabla q_j} J(q_j)$ evaluated at $(x, t)$ in the direction $\Delta q_j$, is defined in the same way as in **Eq. 3.19 - 3.20** Jarny et al. (1991), that is

$$D_{\nabla z} T(x, t; q_j) = \lim_{\epsilon \to 0} \frac{T(x, t; q_j + \epsilon \ \Delta q_j) - T(x, t; q_j)}{\epsilon} \tag{3.22}$$

We note that $D_{\nabla q_j} T(x, t; q_j)$ is a sensitivity function which can be represented as $\theta(x, t)$, that is

$$D_{\nabla z} T(x, t; q_j) = \theta(x, t) \tag{3.23}$$

To formulate the definition of sensitivity function, the direct problem is formulated first for $(q_j + \epsilon \Delta q_j)$, then for $q_j$, both the equations are subtracted, and the limiting process defined by **Eq. 3.22** is applied. In order to determine the sensitiveness of the direct problem, the sensitive function is derived as described by Jarny et al. (1991) The variation of $q_j(x, t)$ undergoes a change of $\nabla q_j(x, t)$ and T is perturbed by $\nabla T$. The sensitivity function is obtained simply by replacing $\nabla q_j(x, t)$ and $\nabla T$ in place of $q_j(x, t)$ and T in **Eq. 5.7**. The sensitivity problem is described as

$$\rho \frac{\partial(C(T)\theta)}{\partial t} = \nabla^2(\lambda(T)\theta) \qquad (x, t) \in (\Omega, \tau) \tag{3.24a}$$

$$\theta(x, 0) = 0 \qquad (x) \in (\Omega) \tag{3.24b}$$

$$\lambda(T)\nabla\theta.n = P(x, t) \qquad (x, t) \in (\Gamma_j, \tau) \tag{3.24c}$$

$$\lambda(T)\nabla\theta.n = 0 \qquad (x, t) \in (\Gamma_c, \tau) \tag{3.24d}$$

$$D_{\nabla q_j} J(q_j) = \int_0^{t_f} (\sum_{m=1}^M T(d_m, t; q_j) - T_{exp}(t)) * (D_{\Delta q_j} T(d_m, t; q_j))dt + \alpha_0 < q_j - q_{est}, \Delta q_j >_E \tag{3.25}$$

The integral on the right hand side of the **Eq. 3.25** can be written in the form as follows:

$$\int_0^{t_f} (\sum_{m=1}^M T(d_m, t; q_j) - T_{exp}(t)) * (D_{\Delta q_j} T(d_m, t; q_j))dt$$
$$= \int_0^{t_f} \int_R \sum_{m=1}^M (T(d_m, t; q_j) - T_{exp}(t)) * \delta(x - d_m)\theta(x, t)dxdt \tag{3.26}$$

we utilize the definition of the delta function at $x = x_m$ and the sensitivity function. The **Eq. 3.26** takes the form,

$$D_{\nabla z} J(q_j) = \int_0^{t_f} \int_R (\sum_{m=1}^M T(d_m, t; q_j) - T_{exp}(t)) * \delta(x - d_m) \theta(x, t) \ dx \ dt + \alpha_0 < q_j - q_{est}, \Delta q_j >_E \tag{3.27}$$

**Eq. 3.17a & 3.17b** are now utilized to write as follows:

$$D_{\nabla z} J(q_j) = \int_0^{t_f} \int_R [-\rho \ C(T) \ \frac{\partial \phi}{\partial t} - \lambda(T) \ \nabla^2 \ \phi(x, t)] \ \theta(x, t) \ dx \ dt \ + \ \alpha_0 < q_j - q_{est}, \Delta q_j >_E \tag{3.28}$$

Application of integration by parts with respect to $t$ and using Green's formula **Eq. 3.28** takes the final form

$$D_{\nabla_{q_j}} J(q_j) = \int_0^{t_f} \int_R [-\rho \, C(T) \, \frac{\partial \phi}{\partial t} - \lambda(T) \, \nabla^2 \, \theta(x,t)] \, \phi(x,t) \, dx \, dt +$$

$$\sum_i \int_0^{t_f} \int_{A_i} [\lambda(T) \, \frac{\partial \theta(x,t)}{\partial n_i} \, \phi(x,t) - \lambda(T)\theta(x,t)\frac{\partial \phi(x,t)}{\partial n_i}] \, dA \, dt \qquad (3.29)$$

$$- \int_R \rho \, C(T) \, \phi(x,t) \, \theta(x,t_f) - \rho \, \phi(x,0) \, \theta(x,0) \, dx + \alpha_0 < q_j - q_{est}, \Delta q_j >_E$$

Apply the boundary conditions **Eq. 3.17c - 3.17d** and the final condition given by **Eq. 3.17e** results as follows:

$$D_{\nabla_{q_j}} J(q_j) = \int_0^{t_f} \int_R [-\rho \, C(T) \, \frac{\partial \theta(x,t)}{\partial t} - \lambda(T) \, \nabla^2 \, \theta(x,t)] \, \phi(x,t) \, dx \, dt +$$

$$\int_0^{t_f} \int_{A_1} [\lambda(T) \, \frac{\partial \theta(x_1,t)}{\partial n_1} -$$

$$(T(x,t;q_j) - T_{exp})] \, \phi(x,t) \, dx \, dt + \int_0^{t_f} \int_{A_2} [\lambda(T)\frac{\partial \theta(x,t)}{\partial n_2}\phi(x,t)] \, dA \, dt \qquad (3.30)$$

$$+ \int_R \rho \, \phi(x,0) \, \theta(x,0) \, dx + \alpha_0 < q_j - q_{est}, \Delta z >_E$$

The sensitivity function $\theta(x,t)$ is obtained from the solution of the sensitivity problem and the adjoint function $\phi(x,t)$ determined from the solution of the adjoint problem Eq. 5.10, the directional derivative is computed from **Eq. 3.30**. From the definition of $D_{\Delta_{q_j}} J(q_j)$, it can be expressed in the scalar form as

$$D_{\Delta_{q_j}} J(q_j) = < \nabla J(q_j), \nabla q_j >_E \qquad (3.31)$$

The physical significance of the result given by **Eq. 3.31**.

$$D_{\Delta_{q_j}} J(q_j) = \int_0^{t_f} \int_{A_1} \Delta q_j(x,t)\phi(x,t) \, dA \, dt + \alpha_0 < q_j - q_{est}, \Delta q_j >_E \qquad (3.32)$$

From the definition of the least-square, we get $E = L^2(A_i]_0, t_f[) =$ all square integrable functions defined on $A_1 \, * \, |0, t_f|$, with the scalar product

$$< q_{j,i}, q_{j,i} >_E = \int_0^{t_f} \int_{A_i} q_{j,i}(x,t)dxdt \qquad (3.33)$$

Utilizing the condition **Eq. 3.33** in the **Eq. 3.32** becomes

$$D_{\Delta_{q_j}} J(q_j) = < phi, \Delta q_j >_E + \alpha_0 < q_j - q_{est}, \Delta q_j >_E \qquad (3.34)$$

From **Eq. 3.31**, we get the expression for the gradient of $J$ as a function of $(x,t)$ defined as follows:

$$\nabla J(x,t;q_j) = \phi(x,t) + \alpha_0(q_j(x,t) - q_{est}(x,t)) \qquad (3.35)$$

Henceforth, the gradient of the objective function is defined as

$$\nabla J_{q_j} = \phi + \gamma_k \, q_j \qquad (3.36)$$

The expressions for the optimal step size or length $\alpha_k$ is proved in Jarny et al. (1991) and the conjugate coefficient $\beta_k$ reads as follows:

$$\alpha_k = - \frac{\int_0^{t_f} \int_{\Gamma_c}(T - T_{exp})\theta_k d\Gamma dt + \int_0^{t_f} \int_{\Gamma_j} P_k q_j d\Gamma dt}{\int_0^{t_f} \int_{\Gamma_c} \theta_k^2 d\Gamma dt + \gamma_{k+1} \int_0^{t_f} \int_{\Gamma_j} P_k^2 d\Gamma dt} \qquad (3.37)$$

and

$$\beta_k = \{ \begin{array}{cc} 0 & if\, k = 0 \\ max(0, \beta^{PR}) & otherwise \end{array} \tag{3.38}$$

where $\beta^{PR}$ is the conjugation coefficient in the Polak-Ribiere version of the CGM.

$$\beta^{PR} = -\frac{\int_0^{t_f} \int_{\Gamma_j} \nabla J_{q_{j,k}} (\nabla J_{q_{j,k}} - \nabla J_{q_{j,k-1}}) d\Gamma dt}{\int_0^{t_f} \int_{\Gamma_j} (\nabla J_{q_{j,k-1}})^2 d\Gamma dt} \tag{3.39}$$

Conjugate search direction in **Eq.5.11** was determined as follows:

$$P_k = \{ \begin{array}{cc} \nabla J_{q_{j,k}} & if\, k = 0 \\ \nabla J_{q_{j,k}} + \beta_k P_{k-1} & otherwise \end{array} \tag{3.40}$$

The regularization parameter as simplified in Bozzoli et al. (2014) was used in this work:

$$\gamma_{k+1} = \frac{\int_0^{t_f} \int_{\Gamma_c} (T - T_{exp}) d\Gamma dt}{\int_0^{t_f} \int_{\Gamma_j} (q_{j,k})^2 d\Gamma dt} \tag{3.41}$$

## 3.4   Computational Algorithm

To solve the partial differential equation, a transient two-dimensional finite element method were implemented as discussed earlier. To estimate the unknown heat flux, initially the heat fluxes were approximated as zeros and for the adjoint problem, gradient of the objective function are initialized before the start of iteration. The experimental temperatures are used to determine the optimal search direction to estimate the unknown heat flux through iterative process. The detailed computational algorithm to estimate the surface heat flux and the distribution of surface temperature can be found as follows: The following steps describe the brief overview of the equations used in solving the inverse heat conduction problem.

1. Initialize the unknown heat flux on quenching region

2. Solve the adjoint problem as shown in **Eq. 5.10**.

3. Computation of the gradient of the objective function $\nabla J_{q_j}$ as in **Eq. 5.8**
   where $\phi$ is the solution of the adjoint problem and
   $\gamma_k$ is the regularization parameter
   **Iteration Start**

4. Solve the direct heat problem as in **Eq. 5.7**

5. Solve the adjoint problem as in step 2. But boundary condition $T(x, t; q_j)$ as in **Eq. 5.10** is from the solution of step 4.

6. Solve the gradient of the objective equation as in step 3 **Eq. 5.8**. $\phi$ is from the solution of step 5.

7. Compute conjugate coefficient $\beta_k$ from **Eq. 5.12**

8. Compute conjugate search direction (descent direction) as shown in **Eq. 5.14**

9. Solve the sensitivity problem from **Eq. 5.9**

10. Compute Regularization parameter from **Eq. 5.15**

11. Compute the Optimal step size as in **Eq. 5.11**

12. Compute $q_{j,k+1}$ as

$$q_{j,k+1} = q_{j,k} + \alpha_k * P_k \tag{3.42}$$

13. Set k to k+1 while $\int_0^{t_{max}} \int_{\Gamma_j} (\alpha_k P_k)^2$ is larger than the preset tolerance; stop the iteration
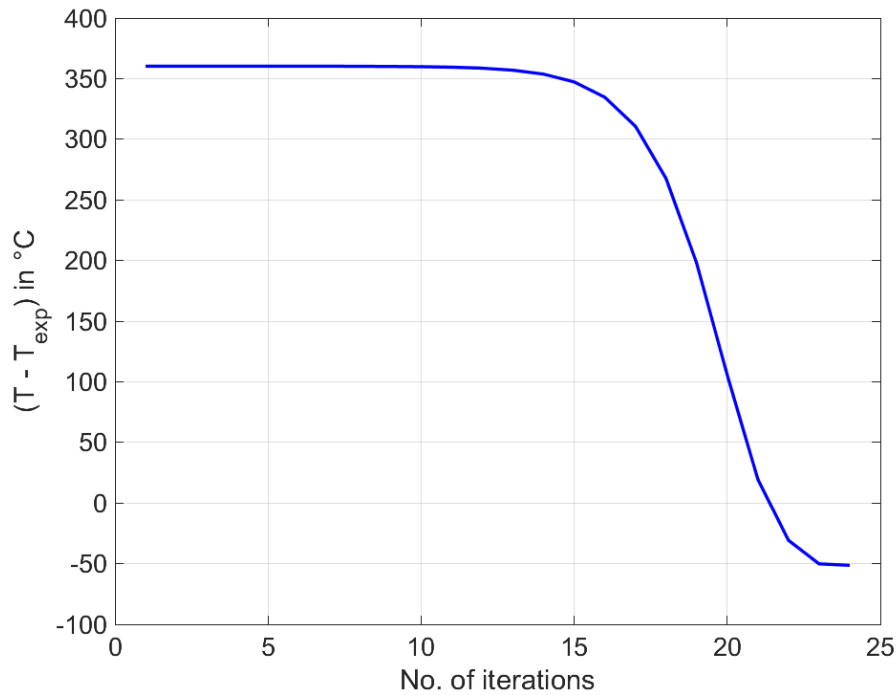


Figure 3.2: Comparison of the temperature difference between simulation and experimental for different iterations

**Fig. 3.2** explains the comparison of the temperature difference for the number of iteration in order to estimate the exact heat flux. The temperature difference $(T - T_{exp})$ curve shows the difference between the solution from the direct problem with the estimated heat fluxes according to the inverse heat transfer method and the experimentally measured temperature on the back of the quenched surface. The temperature variation between the experimental and simulation has no influence until iteration number 15. With further continue in the estimation of the heat flux, the inverse method promotes a steady temperature drop and temperature difference is approximately zero.

**Fig. 3.3** shows the profile of the minimization of the objective function for different iterations. The increase of the number of iterations, the objective function minimizes significantly and the accuracy of the estimation starts well above the iteration number 5. The objective function only reduce in the order of approximately $10^2$, whereas the significant drop can only be observed at iteration number 21.
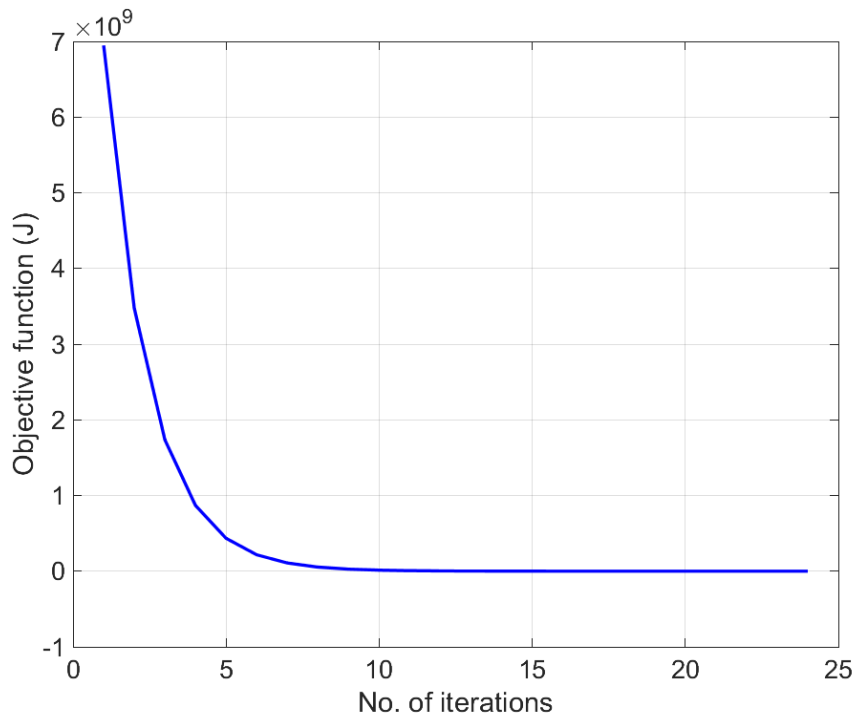
Figure 3.3: Minimization of the objective function for different iterations

## 3.5   Results and Discussion

**Validation of the Inverse Heat Conduction Problem**

**Fig. 3.4** shows the temperature profiles of experimentally measured nickel plate at fixed condition for 19 $m/s$ water jet velocity, jet angle of 90°, initial temperature of 800°$C$. The temperature profiles from the solution of two-dimensional regularized inverse problem shows a promising outcome in comparison to the experimentally measured temperature on the other side of the quenched surface using infrared thermography. Henceforth, the proposed inverse method in combination to the Tikhonov regularization and conjugate gradient method for the iteration along with adjoint and sensitivity function can be effectively for the quenching problem. Fig. 3.4 also discuss the temperature distribution obtained from the two-dimensional inverse model at location of 5 $mm$ from the stagnant jet impingement point. The quenched side temperature drops faster in comparison to the other side of the plate at the same location. At nearly 0.01$s$, the temperature between quenched side and the measured side is about 400°$C$ and the temperature gradient gradually decreases as the time instant raises. At 1$s$, we can see a thermal gradient of 250°$C$ and reason for the significant difference is mainly due to the thermal conductivity of the material. Nickel has lower thermal conductivity when compared to that of the aluminium alloy which has highest conductivity. After 4$s$, the temperature is almost constant and the difference between water quenched side and the measured side is gradually reduced.
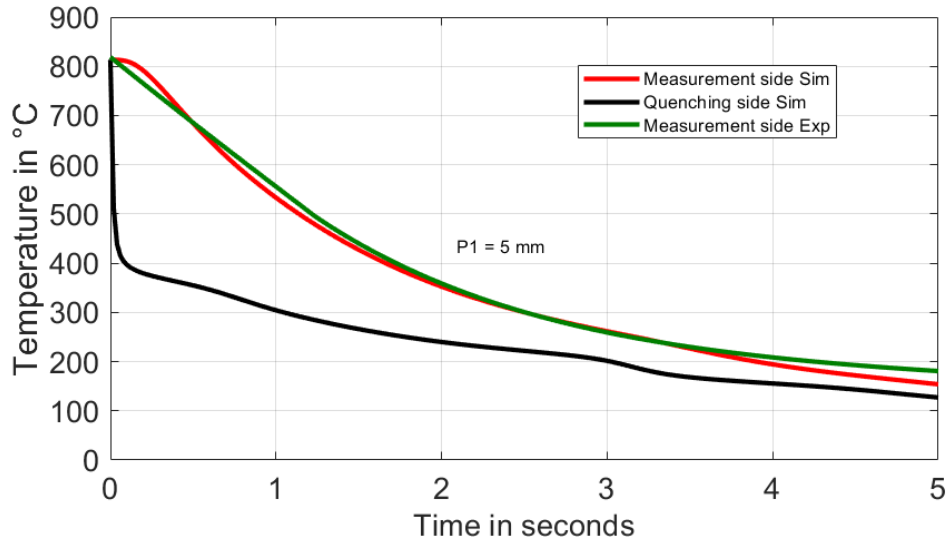
Figure 3.4: Temperature validation on the measuring side of the single jet nozzle

## 3.5.1 Comparison of Measuring side and Quenching side:

The goal is to measure the temperature distribution in space and time direction on the back of water impingement side in order to known the heat transfer or to quantify the unknown heat flux on the quenching region. For this, temperature profiles against the heat flux on the quenched surface is showed in the **Fig. 3.5**. The experimental conditions of AA6082 material with 5 $mm$ thick plate of length 250 $mm$ and width of 230 $mm$, initial temperature of the plate is 550 $°C$ for jet velocity of 19 $m/s$. Fig. 3.5, depicts the boiling curves obtained from the one-dimensional analytical model as proposed in the present work for the experimental condition as mentioned earlier. Boiling curve for two consecutive points at 5 $mm$ and 10 $mm$ distance from the stagnation point is presented in Fig. 3.5. Using two-dimensional inverse method and one-dimensional analytical method. The results show a significant difference between the quenched side and the other side of the plate. From the physical understanding of the water quenching process, we know that the boiling curve can be distinguished into four regimes i.e., film boiling, transition boiling, nucleate boiling and single-phase convection. The measured side boiling curve indicates the peak of the maximum heat flux at 7 $MW/m^2$ lies in the temperature ranging from 410°$C$ to 380°$C$. Due to the thermal gradient between the measured side and the water impingement side, the shift of maximum heat flux towards lower surface temperature are obtained from inverse results. Heat flux at the quenched side is around 230°$C$ with maximum heat flux of 8.8 $MW/m^2$ for 5 mm location point. The re-wetting temperature is around 400°$C$ on the water impingement side and on the opposite side at same location temperature of departure nucleate boiling is observed. From this discussion, we observe the necessity of two-dimensional inverse method to find the exact heat transfer during the impingement of water on the hot surface. Henceforth, the comparison of the temperature on the measuring side from experiments using infrared thermography and surface temperatures from the numerical solution of the inverse problem proves to match quite well. The inverse solution also provides the clear thermal gradient between the water impingement side and the measuring side. Further, the boiling curves for the measured temperature and the water impingement are presented showing the significant difference in the peak heat fluxes and corresponding temperature. The two-dimensional model is necessary and it should be mandatory for the analysis of heat transfer distribution in water cooling systems. The reason for the shift in nucleate boiling from 1D to 2D is the temperature gradient between

the water impingement and the measurement region. On the water impingement, the cooling is more effective and further when compared to that of measurement side. Due to the two-dimensional model, the heat conduction in x and y direction restrict the maximum heat flux at lower temperatures. Whereas, in the one-dimensional case, the heat conduction is insignificant, the heat transport is faster and thus provides the maximum heat flux at higher temperature.
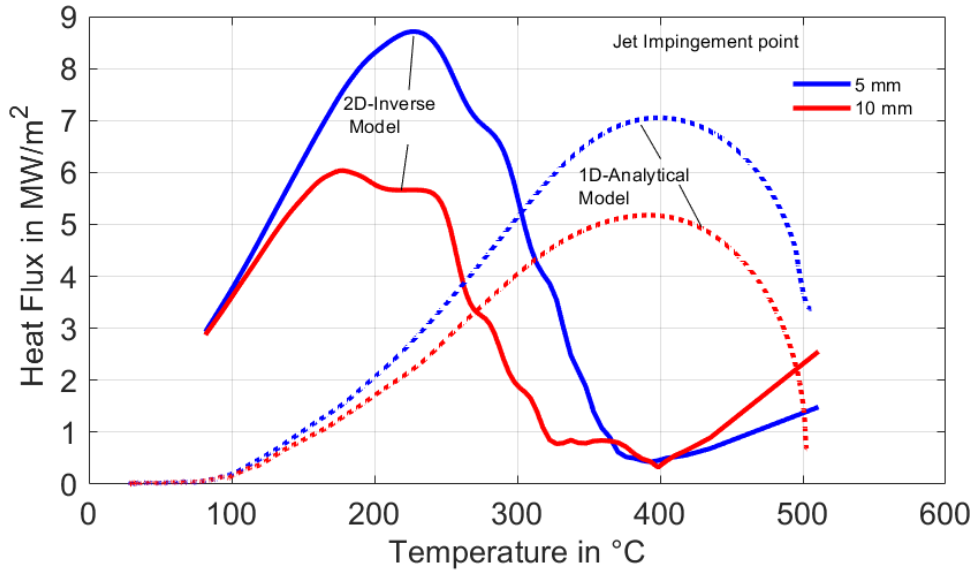


Figure 3.5: Boiling curve obtained from 2D inverse heat conduction problem and 1D analytical model

### 3.5.2   Estimated heat flux

To avoid the experimental error in the numerical computation of the inverse heat conduction problem, regularization techniques should be incorporated in the objective function to obtain the un-disturbed heat flux distribution. In this work, Tikhonov regularization with fixed point iteration is used to stabilize the estimation of surface heat flux. **Fig. 3.6** presents the boiling surface heat fluxes in comparison with surface temperature on the quenched side for Nickel material for 5 mm thick plate, at 19 $m/s$ jet velocity for the stationary plate condition. The peak of heat flux decreases along the position away from the jet impingement point. The similar trend or fact is also observed in the various literature works with single full jet nozzle.
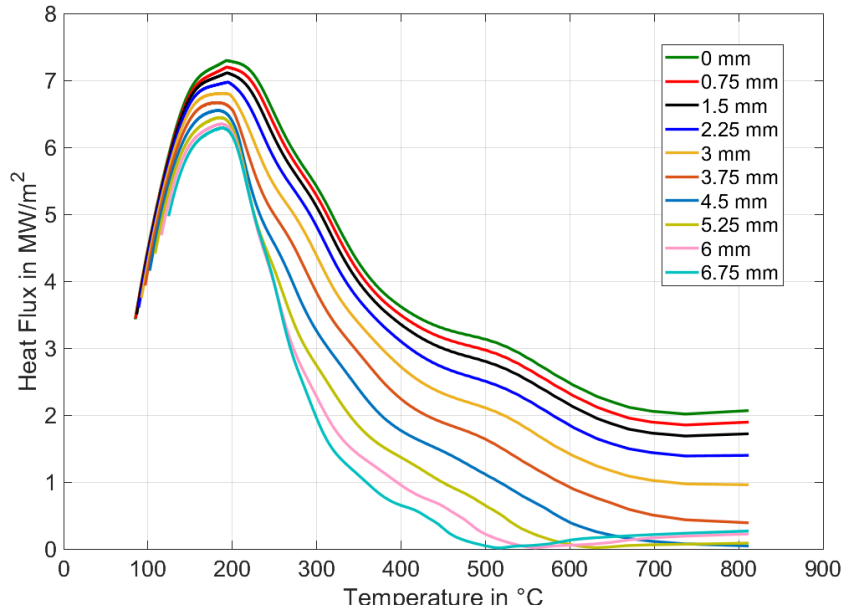
Figure 3.6: Boiling curve at different points from the impingement for nickel plate

### 3.5.3 AA6082 material
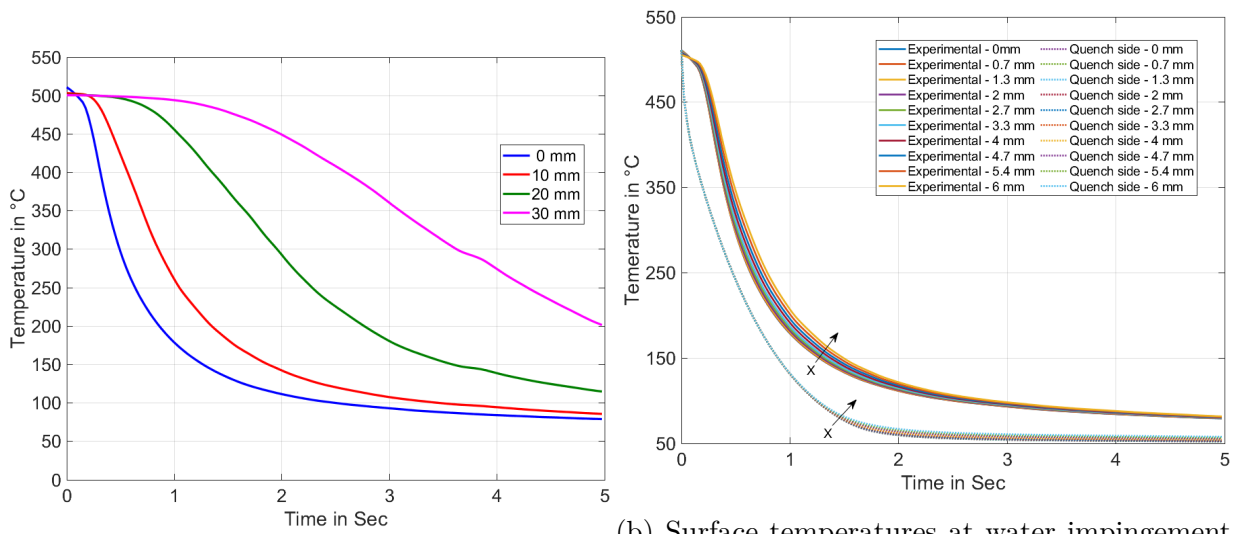


(a) Cooling curves for various locations on plate and measurement side of plate



(b) Surface temperatures at water impingement

Figure 3.7: Surface temperature profiles of the AA6082 plate at fixed plate condition

**Fig. 3.7a - 3.7b** shows the surface temperature distribution versus time for various location on the length of the plate. Temperature profiles for 0 mm shows a sharp decrease in magnitude from 500 °C to 180 °C in just 1 sec. Whereas, for measuring points between 10 mm and 30 mm observed to show a delay in the temperatures. At 30 mm from th e centre of the impingement region, the temperature remains to be 200 °C after 5 sec from the start of the cooling which experiences the departure nucleate boiling. **Fig. 3.7b** indicates the surface temperature profiles for quenched side and measured side regions for various points from the centre of the water jet impingement region until 6 mm. The profiles shows the clear thermal gradient between the water jet side and measured side of about 50°C at 1 sec from the start of the cooling.
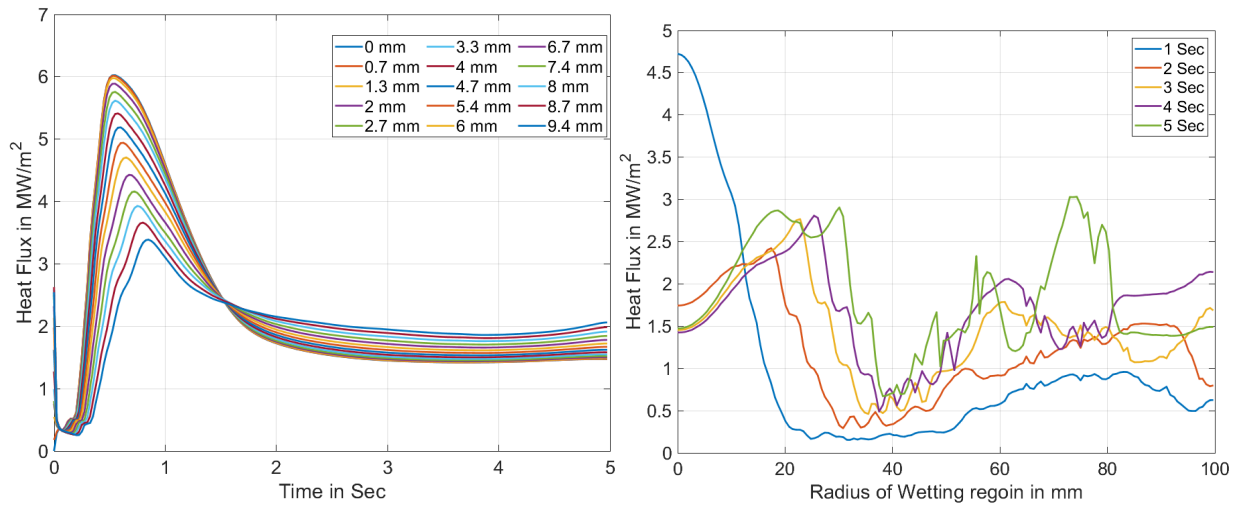
(a) Heat flux curves for various locations on the plate length

(b) Heat flux curves over the plate length for various time instants

Figure 3.8: Surface heat fluxes obtained from inverse simulations on water impingement side for AA6082 material

**Fig. 3.8a - 3.8b** gives the heat flux curves versus time and heat flux curves over the length of the plate for various locations on the plate and for different time instants respectively. As seen from the Fig. 3.8a, peak of the heat flux decreases from 6 $MW/m^2$ to 3.2 $MW/m^2$ between 0 to 9.4 mm for various time instants. The heat flux gradually decreases once the wetting front starts to move over to the next position and becomes steady as seen from the profiles after 2 sec. Similar situation arises for heat fluxes over length of the plate as in Fig. 3.8b for various time instants. The peak of heat flux decreases from 4.7 $MW/m^2$ to 2.9 $MW/m^2$ for 1 sec and 5 sec respectively. The heat flux remains steady at 2.9 $MW/m^2$ for above 2 sec until 5 sec. From these two profiles, we can observe a quasi-steady heat transfer along the plate length and for various time instants.
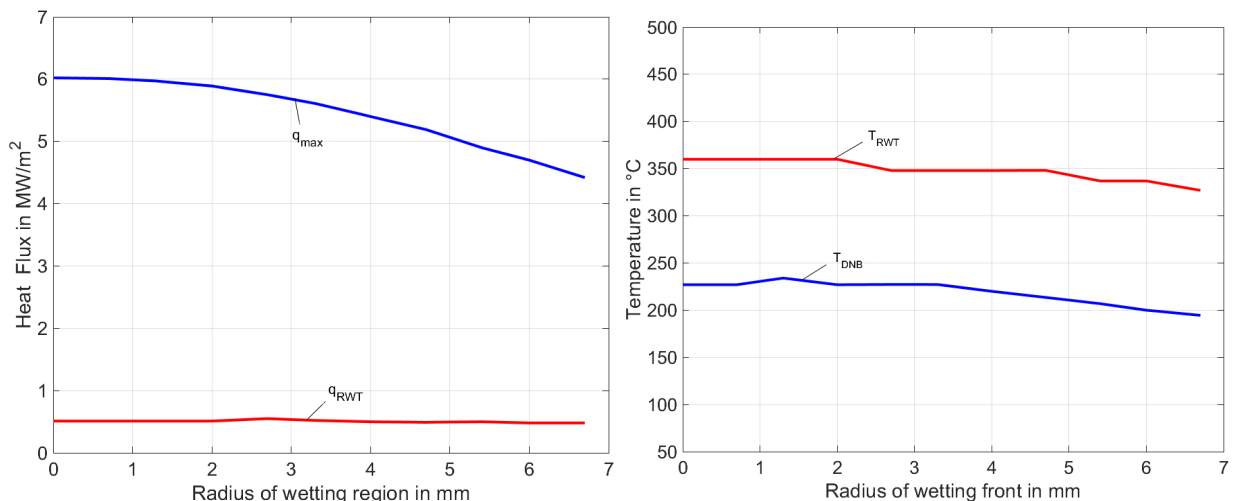


(a) $q_{max}$ and $q_{RWT}$ profiles over the length of the plate

(b) $T_{DNB}$ and $q_{RWT}$ profiles over the length of the plate

Figure 3.9: Quenched side profiles obtained from inverse simulations on water impingement side for AA6082 material

The heat transfer characteristics for AA6082 plate material were shown in **Fig. 3.9a - 3.9b**. Maximum heat flux ($q_{max}$) and the heat flux at the re-wetting point ($q_{RWT}$) are

described in Fig. 3.9a. The $q_{max}$ decreases gradually from 6 $MW/m^2$ to 4 $MW/m^2$ over the wetting region, whereas the heat flux at the re-wetting point remains almost constant at 0.5 $MW/m^2$. Fig. 3.9b described the re-wetting and departure from nucleate boiling temperature along the wetting front region. The re-wetting and the departure nucleate boiling temperature remains constant in the water impingement region at around 350 °C and 230 °C respectively and a steady drop in temperature occurs away from the centre of the jet region. Also, the **Tab. 3.1** gives characteristic values for the widths of boiling region as well as the wetting front velocities for the AA6082 material plate. The increase of the nucleate boiling and overall boiling region takes place for various time instants. The position of re-wetting point changes continuously from 24.8 $mm$ to 38.8 $mm$ while the wetting front velocity abruptly decreases from 24.8 to 1.3 $mm/s$.
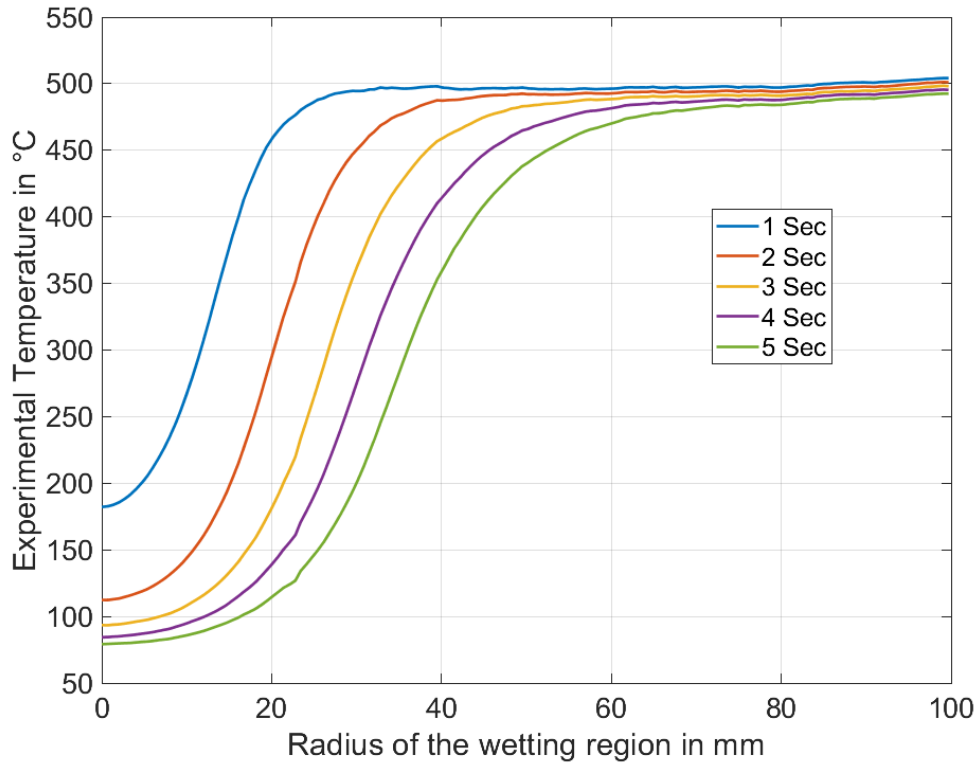


Figure 3.10: Temperature validation on the measuring side of the single jet nozzle

The surface measurement temperature profiles for various time instants i.e., 1 sec to 5 sec are presented in **Fig. 3.10**. For time instant 1 sec, the temperature at the jet impingement region drops to below 200 °C and for higher time instants the temperature attains a steady state and the temperature drop is almost constant. These temperature profiles clearly indicates a quasi-steady state.

| Time | 1 sec | 2 sec | 3 sec | 4 sec | 5 sec |
|---|---|---|---|---|---|
| Width of $T_{DNB}$ in mm | 3.3 | 7.4 | 10 | 10.7 | 16.1 |
| Width of Boiling in $mm$ | 15.4 | 20.1 | 22.8 | 26.1 | 30.1 |
| $w_f$ in $mm/s$ | 24.8 | 6 | 4.7 | 2 | 1.3 |
| Position of Wetting front in $mm$ | 24.8 | 31 | 35.5 | 37.5 | 38.8 |

Table 3.1: Width of boiling region of AA6082 plate at fixed plate condition

### 3.5.4    Nickel material
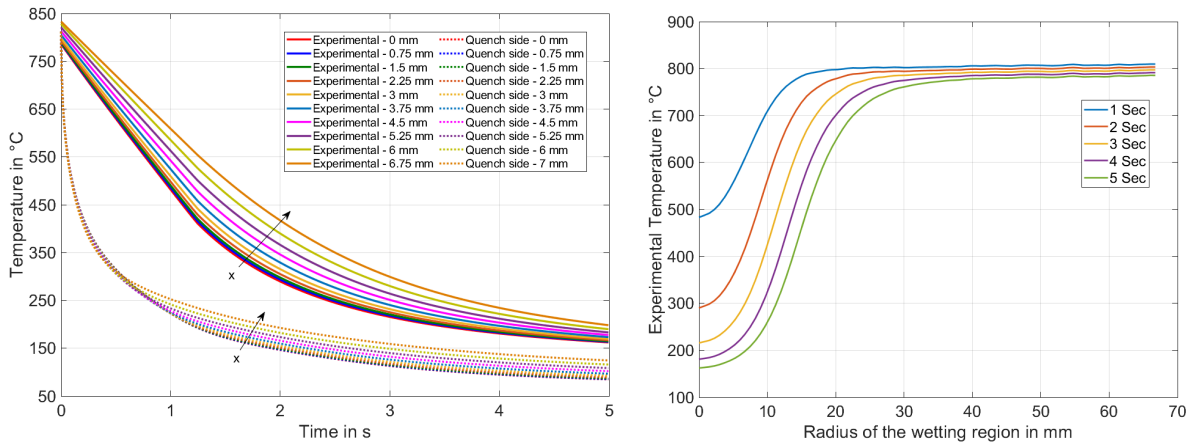


(a) Cooling curves for various locations on the (b) Surface temperatures at water impingement
plate length                                                             and measurement side of the plate

Figure 3.11: Surface temperature profiles of Nickel material at fixed plate condition

Surface temperature for Nickel material for stationary plate condition is depicted in the
**Fig.3.11a - 3.11b**. The quench side and the measured side temperature for various points
in the water impingement region clearly shows a higher temperature gradient of about 200
$°C$ at 1 sec. The surface temperature at various locations away from the impingement
region shows lower gradient or in other words takes longer time to cool. The temperature
profiles along the wetting region for various time instants shown in Fig. 3.11b. For time
instant of 1 sec, the temperature drops to 500 $°C$ from initial temperature of 800 $°C$. The
steady drop in temperature exists for above 3 sec.
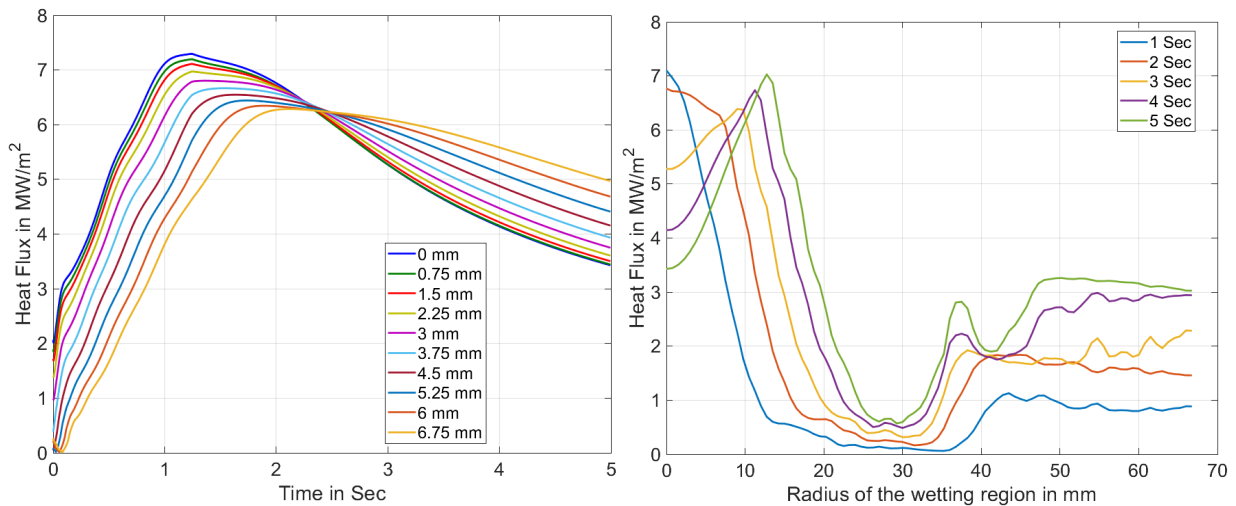


(a) Heat flux curves for various locations on the (b) Heat flux curves over the plate length for
plate length                                                             various time instants

Figure 3.12: Surface heat fluxes obtained from inverse simulations on water impingement
side for Nickel material

Heat flux from the two-dimensional inverse solutions indicate that a decrease in the peak of
the maximum heat flux from 7.2 $MW/m^2$ to 6.2 $MW/m^2$ as represented in **Fig. 3.12a**. In
similar way, the peak of the maximum heat flux decreases from 7 $MW/m^2$ to 6.2 $MW/m^2$
correspondingly for 1 sec to 3 sec. Contradictorily, the peak of the maximum heat flux

| Time | 1 sec | 2 sec | 3 sec | 4 sec | 5 sec |
|---|---|---|---|---|---|
| Width of $T_{DNB}$ in $mm$ | 3 | 7.5 | 11.25 | 2 | 2 |
| Width of Boiling in $mm$ | 9.75 | 12.75 | 15 | 17.25 | 18 |
| $w_f$ in $mm/s$ | 13.5 | 4.5 | 7.5 | 0.75 | 0.75 |
| Position of Wetting front in $mm$ | 13.5 | 18 | 25.5 | 26.25 | 27 |

Table 3.2: Width of boiling for the Nickel plate during quenching at stationary plate condition

increases for 4 to 5 sec, since during this time the plate experiences a nucleate boiling and hence the peak of maximum heat flux increases.
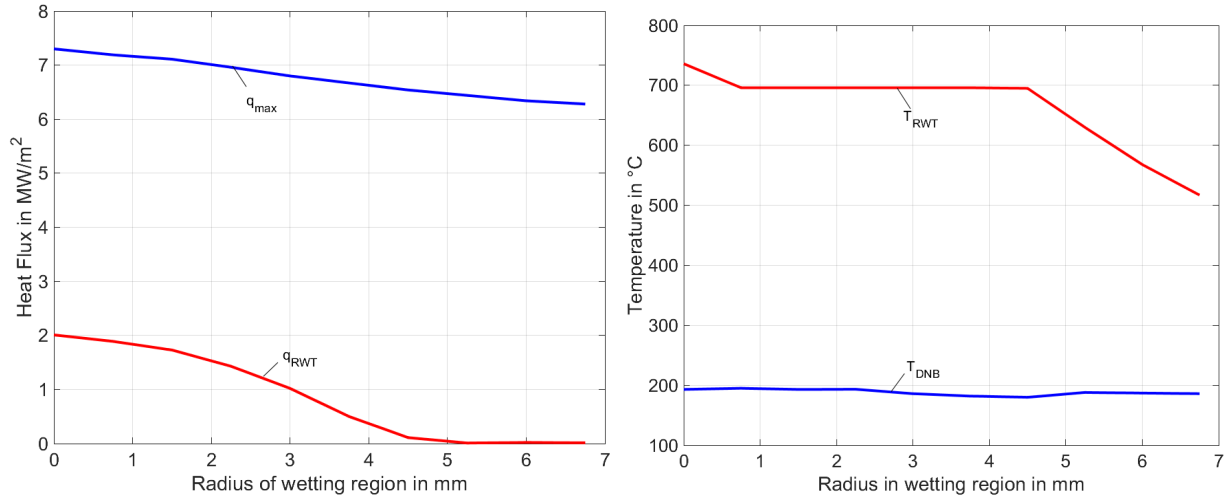


(a) $q_{max}$ and $q_{RWT}$ profiles over the length of the plate

(b) $T_{DNB}$ and $q_{RWT}$ profiles over the length of the plate

Figure 3.13: Quenched side heat flux and temperature data obtained from inverse simulations for Nickel material

The heat transfer characteristics for the Nickel material is presented in the **Fig. 3.13a - 3.13b**. The maximum heat flux decreases steadily away from the wetting region from 7.3 $MW/m^2$ to 6.8 $MW/m^2$ and the similar phenomena is seen in the re-wetting point where the heat flux decreases from 2 $MW/m^2$ to 0.01 $MW/m^2$. Similar to the condition in the AA6082 material, the re-wetting temperature nearly constant at 700 $°C$ which further decreases to 500 $°C$ and the departure nucleate boiling temperature remains nearly constant at about 200 $°C$.

The characteristics widths of the boiling region and the wetting front is listed in the **Tab. 3.2**. The width of departure nucleate boiling increases from 3 mm to 11.25 mm correspondingly between 1 sec and 3 sec. Further increase in the time of cooling leads to the less steeper width of the nucleate boiling region. Whereas, the width of the boiling region increases from 9.75 $mm$ to 18 $mm$. The velocity of the wetting front decreases from 13.5 $mm/s$ to 0.75 $mm/s$.

# 3.6 Numerical Implementation of the Physical Problem

## 3.6.1 Fixed Plate $(w_p = 0 \ mm/s)$
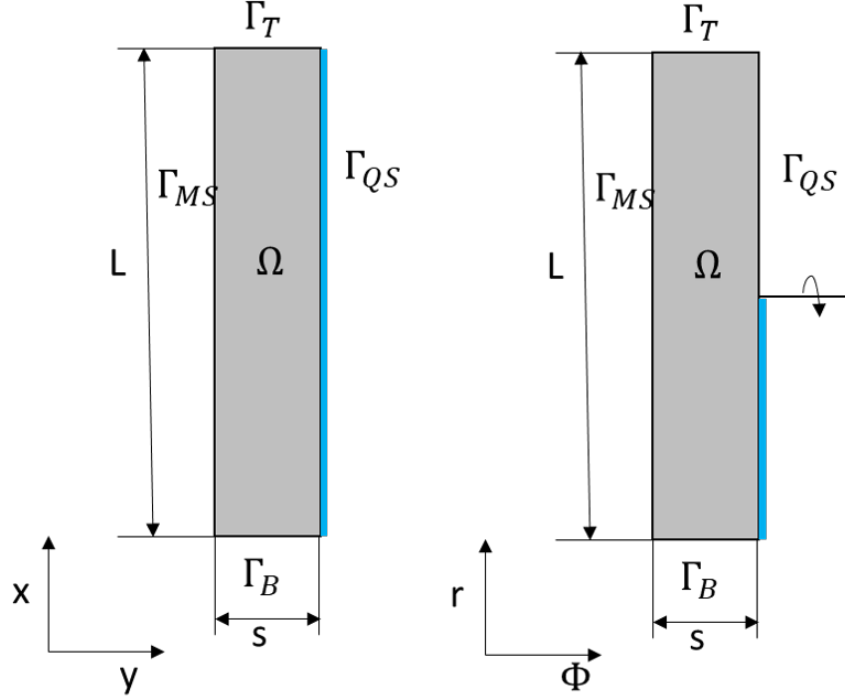


Figure 3.14: Physical model for the fixed plate condition in case of Cartesian co-ordinate (left) and cylindrical co-ordinate or axi-symmetric condition (right)

The analysis of the surface temperature for the estimation of heat flux in quenching process is categorize into fixed plate and moving plate condition. The application of thermal boundary condition on the hot metal plate eventually changes for both conditions and therefore the boundary conditions should be modified.

**For Cartesian coordinate:**

The governing partial differential equation are applicable as given in **Fig. 3.14** (left part) for Cartesian co-ordinate system, in case of fixed plate condition. The **Eq. 3.43** is valid for the non-axisymmetric condition during quenching of hot metal plate.

$$\rho c_p \frac{\partial T}{\partial t} = \lambda \left( \frac{\partial^2 T}{\partial y^2} + \frac{\partial^2 T}{\partial x^2} \right) \qquad (x,t) \in (\Omega, \tau) \qquad \text{(3.43a)}$$

$$T(x,0) = T_{intial} \qquad (x) \in (\Omega) \qquad \text{(3.43b)}$$

$$\lambda \frac{\partial T}{\partial x} = q_j(x,t) \qquad (x,t) \in (\Gamma_j, \tau) \qquad \text{(3.43c)}$$

$$\frac{\partial T}{\partial x} = 0 \qquad (x,t) \in (\Gamma_c, \tau) \qquad \text{(3.43d)}$$

$$\frac{\partial T}{\partial y} = 0 \qquad (x,t) \in (\Gamma_T, \tau) \qquad \text{(3.43e)}$$

$$\frac{\partial T}{\partial y} = 0 \qquad (x,t) \in (\Gamma_B, \tau) \qquad \text{(3.43f)}$$

**For Cylindrical coordinate:**

The governing partial differential equation are applicable as given in **Fig. 3.14** (right part) for cylindrical co-ordinate system, in case of fixed plate condition. The **Eq. 3.44** is valid for the axisymmetric condition during quenching of hot metal plate.

$$\rho c_p \frac{\partial T}{\partial t} = \frac{1}{r} \frac{\partial}{\partial r}(r\lambda \frac{\partial T}{\partial r}) + \frac{1}{r} \frac{\partial}{\partial \phi}(\frac{1}{r}\lambda \frac{\partial T}{\partial \phi}) \qquad (x,t) \in (\Omega, \tau) \qquad (3.44a)$$

$$T(x,0) = T_{intial} \qquad (x) \in (\Omega) \qquad (3.44b)$$

$$\lambda \frac{\partial T}{\partial \phi} = q_j(x,t) \qquad (x,t) \in (\Gamma_j, \tau) \qquad (3.44c)$$

$$\frac{\partial T}{\partial \phi} = 0 \qquad (x,t) \in (\Gamma_c, \tau) \qquad (3.44d)$$

$$\frac{\partial T}{\partial r} = 0 \qquad (x,t) \in (\Gamma_T, \tau) \qquad (3.44e)$$

$$\frac{\partial T}{\partial r} = 0 \qquad (x,t) \in (\Gamma_B, \tau) \qquad (3.44f)$$

## 3.6.2 Moving Plate ($w_p \neq 0$ $mm/s$)

The movement of hot surface during quenching process can be seen as depicted in **Fig. 3.15**. The mathematical model of the moving boundary is complicated to solve analytically or numerically. To simplify the mathematical modelling of the moving boundary, the movement of the plate can be reduced to stationary (fixed plate condition) plate condition. While the tracking of the plate position at every time using $x' = L * w_p t$. With the preceding method, the surface temperature can be stored for every time. The tracking of the movement of the plate at every time and thus the movement of the plate is made stationary. Hence the plate velocity becomes zero and the Euler equation in **Eq. 3.45** reduces as follows:
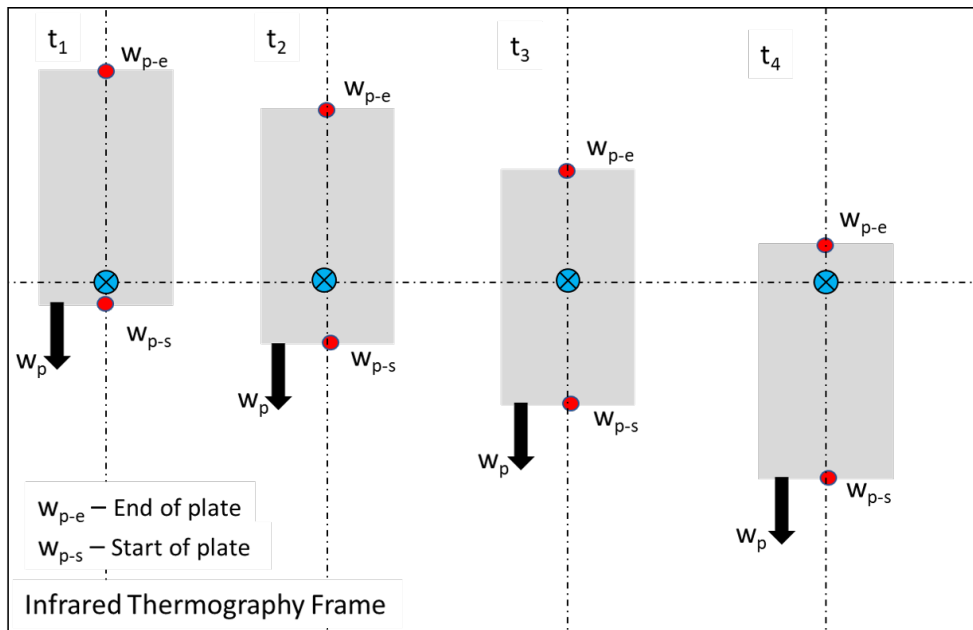


Figure 3.15: Physical model for the moving plate condition in case of Cartesian co-ordinate

$$\frac{DT}{Dt} = w_p \frac{\partial T}{\partial x} + \frac{\partial T}{\partial t} \qquad (3.45)$$

If $w_p = 0mm/s$, then Eq. 3.45 becomes as follows

$$\frac{DT}{Dt} = \frac{\partial T}{\partial t} \tag{3.46}$$

The modified governing partial differential equation for Lagrangian description of the plate becomes as shown in **Eq. 3.47** and the **Fig. 3.16** depicts the physical model in case of moving plate condition.
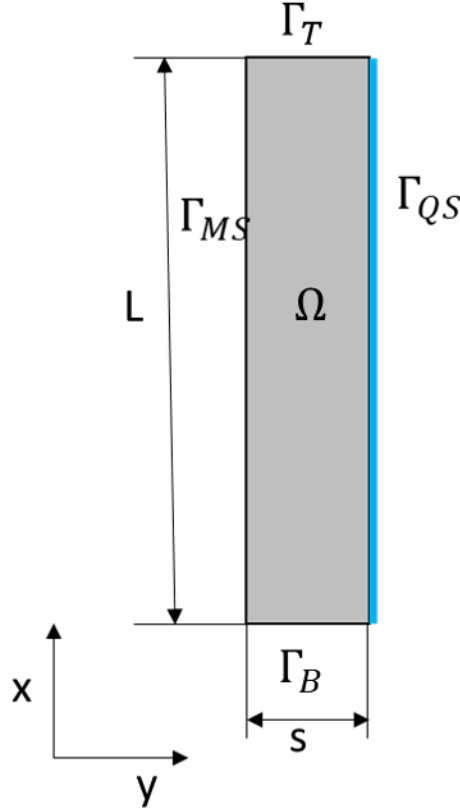


Figure 3.16: Physical model for the moving plate condition in case of Cartesian co-ordinate

$$\rho c_p \frac{\partial T}{\partial t} = \lambda(\frac{\partial^2 T}{\partial y^2} + \frac{\partial^2 T}{\partial x^2}) \qquad (x, t) \in (\Omega, \tau) \tag{3.47a}$$

$$T(x, 0) = T_{intial} \qquad (x) \in (\Omega) \tag{3.47b}$$

$$\lambda \frac{\partial T}{\partial x} = q_j(x, t) \qquad (x, t) \in (\Gamma_j, \tau) \tag{3.47c}$$

$$\frac{\partial T}{\partial x} = 0 \qquad (x, t) \in (\Gamma_c, \tau) \tag{3.47d}$$

$$\frac{\partial T}{\partial y} = 0 \qquad (x, t) \in (\Gamma_T, \tau) \tag{3.47e}$$

$$\frac{\partial T}{\partial y} = 0 \qquad (x, t) \in (\Gamma_B, \tau) \tag{3.47f}$$

Eq. 3.47 represents the governing partial differential equation for the moving plate condition while adopting the new concept of moving boundary condition on the hot plate. The initial temperature of the plate is $T_{in}$ in $°C$ based on experimental conditions. The boundary condition i.e., on quenched side $\lambda \frac{\partial T}{\partial x} = q$ is unknown, where the temperature distribution on

the other side of the water impingement side is known. The problem is ill-posed in nature, because the moving boundary conditions are unknown. The heat fluxes are estimated with the computation of the inverse heat conduction problem. Therefore, the tracking of experimental temperature on the hot plate are stored in a large matrix of (x, t). The x represents the position of the plate from 0 $mm$ to 250 $mm$ (length of the plate), t represents the time direction from 0s to the end or certain time of interest. Henceforth, the numerical prediction of the unknown heat fluxes becomes less complicated and the governing partial differential equation can be used for this kind of problem.

In the present work,

**Fixed plate**

1. $q_{max}$ occurs at stagnation point

2. Liquid jet impinges and forms a circular zone on a stationary plate surface

**Moving Plate**

1. The liquid layer is stretched in the moving direction because of the viscous effect between the moving plate and the liquid flow

2. The stagnation point fixed directly below the jet. The heat transfer is enhanced downstream of the stagnation point and is weakened upstream.
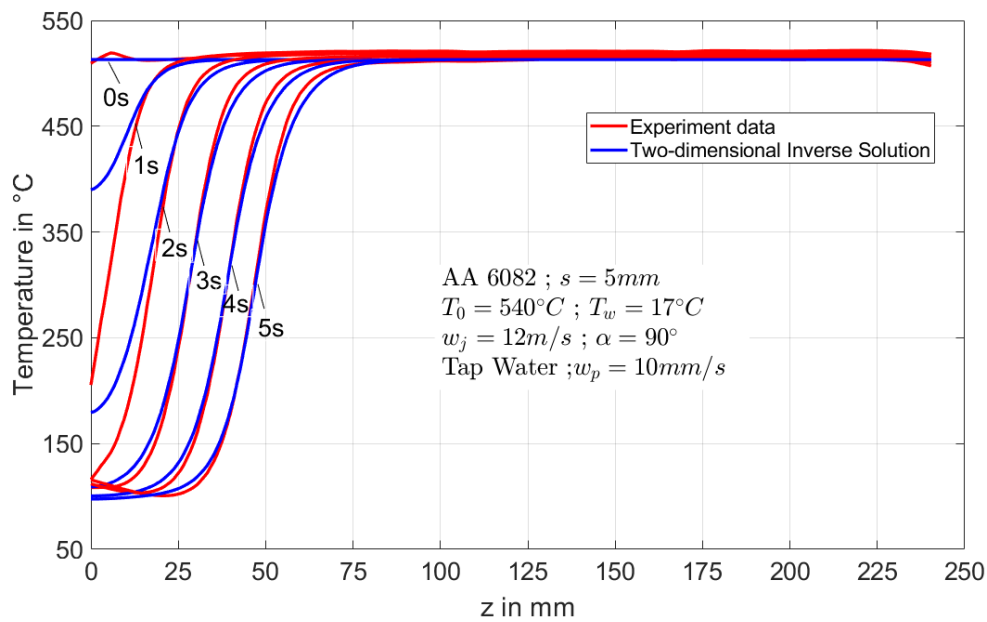


Figure 3.17: Surface temperature verification of the measured and simulated from the solution of the two-dimensional inverse heat conduction problem
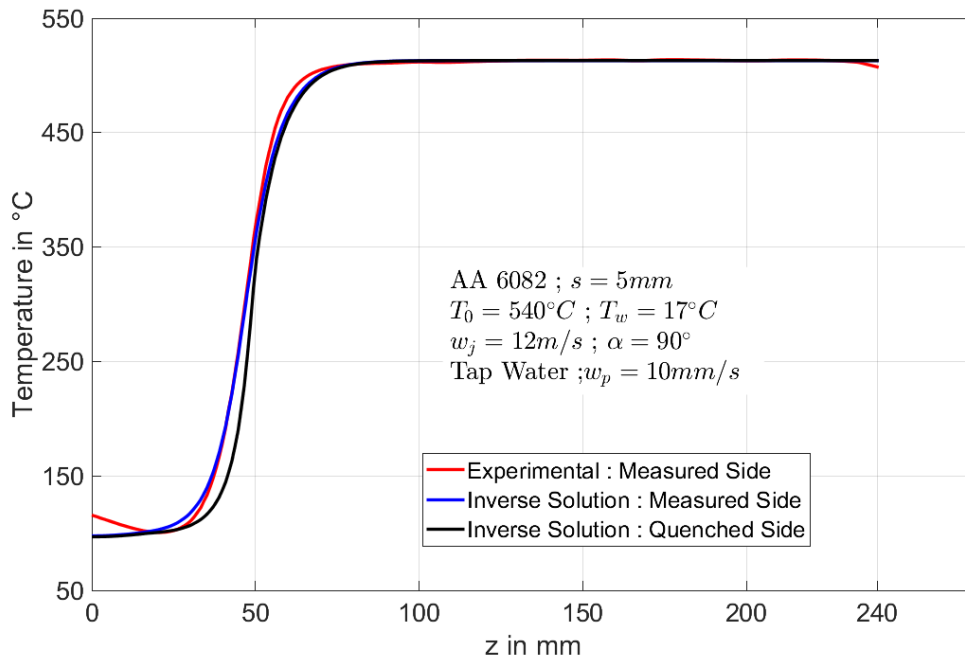
Figure 3.18: Measured side and quenched side surface temperatures from the solution of the two-dimensional inverse heat conduction problem

**Fig. 3.17** shows the verification of the surface temperature along the plate length for different time instants from experimental measurements and solution from the inverse algorithm. The profiles tend to match exactly well after certain quench time in the range of quasi-steady state when the temperature gradient becomes almost constant. However, the temperature profiles deviate in the initial phase of the cooling process because of larger temperature gradient and exact reason for the fluctuations can't be reported. **Fig. 3.18** depicts the surface temperatures distribution on the measured and quenched side for the same experimental conditions. The temperature gradient between the measured side and the quenched side observed to be relatively lower. Although the temperature shows a slight variation in the range of nucleate boiling. Therefore, the inverse solution can be employed in the estimation of the surface heat fluxes for the quenching process and typically in the cooling process.

## 3.7 Heat Flux Approximation with Gaussian Curve
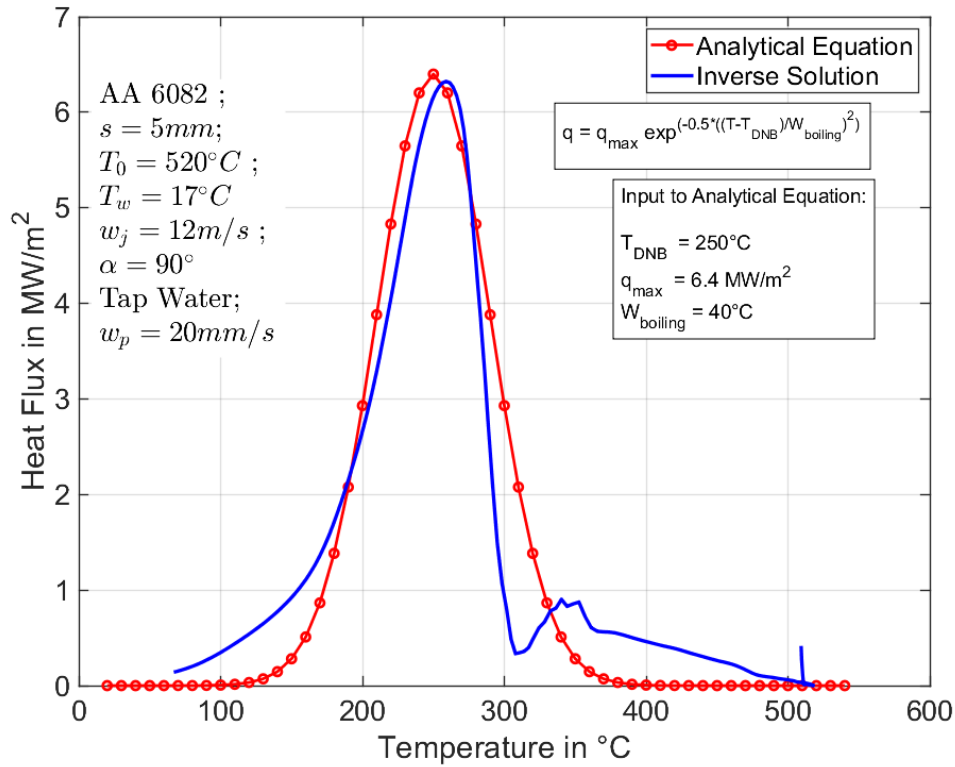


Figure 3.19: Approximation of the heat flux as a function of temperature using Gaussian Curve with inverse heat conduction problem

**Fig. 3.19** depicts the comparison of the boiling curve which indicates the surface heat flux on the water impingement side as a function of surface temperature is approximated using the Gaussian equation. The two profiles tend to show the similar heat fluxes for the surface temperatures at quasi-steady state condition. Although, the heat flux tend to deviate from the solution of the two-dimensions in below the peak heat flux or the two ends of the nucleate boiling range. The heat fluxes in the nucleate boiling shows a nearly similar heat fluxes with the help of analytical equation. The input to the equation as shown in the Fig. 3.19 are $T_{DNB}$, $q_{max}$, and $W_{boiling}$ which indicates the DNB temperature, maximum heat flux, and the width of the boiling in $°C$, $MW/m^2$, and $°C$ respectively. From our perspective, most important factor would be the width of the boiling, which varies depending on the different experimental conditions, even though the maximum heat flux, and DNB has a significant influence. In addition to those, width of the boiling also influences the rate of heat transfer during quenching process. In the upcoming chapters, the definition of the width of the boiling at approximately $0.75 \times q_{max}$ should reveal its importance.

## 3.8 Conclusion

To estimate the unknown surface heat fluxes during quenching of hot metals, a two dimensional and three-dimensional inverse heat conduction method incorporated with Tikhonov regularization is presented. The proposed model stabilizes the error in the experimental measurements and found to be accurate in predicting the surface heat fluxes and temperatures are verified against the experimental measurements. Henceforth the proposed mathematical model can predict the surface temperature and heat flux based on the measured surface temperature. Comparison of the temperature profiles indicate that

the quenched side and the measured side profiles show a significant difference up to 400 $^\circ C$ to about 200 $^\circ C$ over the quenching process which last around 5s for nickel material. The boiling curve obtained from the inverse heat conduction method is compared with the solution from the one-dimensional analytical method based on the measured temperature profiles. The clear shift in the maximum heat flux and the corresponding temperature i.e., departure nucleate boiling shifts to higher heat fluxes and lower temperatures respectively. Hence, computation of the two-dimensional inverse heat conduction method becomes necessary. The maximum heat flux reduces its magnitude away from the water impingement region, since the impingement velocity diminishes as the wetting front moves on the hot plate. The proposed method can be well implemented to any kind of practical application provided that the governing partial differential equation should be modified. However, to further study the influence of different configurations of nozzle fields, three-dimensional heat conduction model is developed and implemented successfully for the single full jet nozzle and array of jets in the Chapter 6.1.

# Chapter 4

# Full Jet Quenching

## 4.1   Introduction

Full jet impingement quenching is the primary heat transfer enhancement technique in the convective heat transfer process since it promotes high local heat fluxes. This kind of technique can be entirely integrated with the process system through a simple design involving water chamber and orifice to remove large amount of heat.

- Gas turbine cooling: For the leading edge of the rotor air foil, where the thermal load is highest and thicker cross-section enables accommodation of a coolant plenum and impingement holes.

- Turbine guide vanes (stators), combustion chamber wall, steam generator, ion thrusters, tempering of glass, electronic devices cooling and paper drying, etc.

For the high heat removal rate in the application of cooling of hot metals, electronic equipment, nuclear reactors. The thermo-physical configuration of water, jet and surface plate configuration primarily influences the rate of heat removal from the surface. The impinging water jet progresses away from the jet with the reduction in the surface temperature. The reduction in the surface temperature gives rise to the occurrence of the different kinds of boiling regimes on the hot surface simultaneously. In this chapter, single full jet quenching with fixed and moving plate condition is investigated for water quenching of hot metal. To further investigate the mechanism of heat transfer during full jet quenching, we underwent to perform the numerous experiments with various influencing process parameters. The in-house experimental setup as discussed in the Chapter 2 were utilized. The surface temperature was captured using the infrared thermography with high resolution in space and time direction. The two-dimensional inverse heat conduction method was implemented as developed in the chapter 3 for the estimation of the surface heat fluxes during the quenching process. Experimental study with the water jet impingement during quenching process for different metal samples of nicrofer, nickel, AA6082 material has been investigated with the initial temperature of 500, 700, 850 $°C$. The temperature measurements on the quenched side is highly complicated and with the utilization of conventional thermocouples below the quenched surface is more prone to experimental errors. Henceforth, we adopt the infrared thermography to measure the surface temperature during the quenching process in a two-dimensional space and in time direction on the back side of the quenching surface. The surface measurements were utilized to estimate the surface heat fluxes during the quenching surface with the two-dimensional inverse heat conduction method. Furthermore, the maximum heat flux, re-wetting heat flux and corresponding departure nucleate boiling temperature, re-wetting temperature were determined. Boiling region size decreases with increasing liquid jet velocity and initial

temperature. On the contrary, region of boiling increases with increasing material thermal conductivity.

## 4.2   Phenomena of Full Jet Quenching Process

**Fig. 4.1** shows a diagram of the single full jet quenching process for a fixed plate condition. Initially, the cooling of hot metal plate commences with low temperature drop due to the continuous vapour generation at higher temperature between the liquid and solid surface. The wetting of the hot surface with liquid occurs and this condition typically termed as re-wetting condition. The wetting delay or residence time is termed as the elapsed time between the initiation of jet and the surface re-wetting. The fluid flow accelerates with the rise in the enthalpy after the impingement on the hot plate for certain distance away from the stagnation point. With the further travel of the wetting front on the metal surface, the flow field retards due to the strong resistance forces from the vapours generated with the accumulation of the spent fluid enthalpy. The reduction in the fluid flow promotes stronger decrease in the local start temperature in the dry zone of the quenching process. Fluid Flow Situation The flow situation in full jet quenching process can be observed in the Fig. 4.1, where wetting front gradually flow towards the circumference. The fluid flow can be characterized into three different condition: In the first region i.e., convection with no splashing of droplets can be seen, as the heat transfer mainly occurs due to the single-phase convection i.e., surface temperature lies below 100°C. The droplet ejected from the surface under high surface superheat and the droplet hovers over the surface without the physical contact quickly ejected away from the metal surface. The formation of the hydraulic jump hinders the wetting front velocity even though the expansion area is higher. Second region can be categorized as the wetting front region, the intense heat transfer mechanism happens with formation of transition boiling, and nucleate boiling regime. Similarly, the third region is the unaffected region or dry region. The temperature in this region always maintains a initial temperature and depending on the experimental condition start temperature varies in this region. The three regions can be distinguished based on the temperature i.e., $T_{sat}$, $T_{DNB}$, $T_{REW}$ from experimental observations. The position of $T_{REW}$ can be called as wetting front. The surface temperature greater than the saturation temperature of the water at ambient pressure tends to generate a thin layer of bubbles on the surface. The bubbles in the thin layer condense when the surface temperature of the plate reaches below 100 $°C$ i.e., below saturation temperature of water. The bulk liquid impinging on the hot surface increase its temperature gradually in the flow direction. The spent liquid significantly increases its enthalpy while lowering the surface temperature at the stagnation position. Consequently, the fluid flow, temperature drop attains a steady state condition with the formation of the three regions as mentioned earlier.
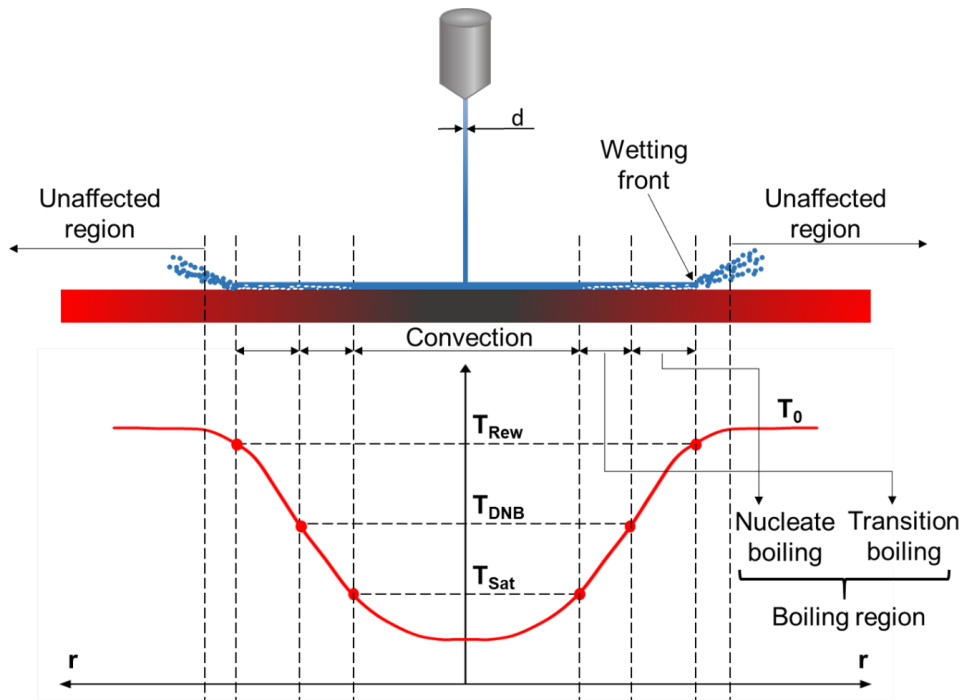
Figure 4.1: Temperature profile along hot surface under liquid jet impingement

## 4.3 Fixed Plate: Literature Review

In many industrial processes, such as fuel bundle cooling post-loss-of-coolant-accident in nuclear reactors, heat treatment of metal parts post hot processing, and further thermal processing of metals. At moderate flow rates, the liquid jets extracts high heat flux from metal parts for the higher initial temperature of the metal part. The heat transfer mechanism during quenching of water jet impingement is bit complex to understand, therefore the description of the heat flux estimation in spatio-temporal region is desirable. Among all the quenching methods, liquid jet impingement is applied where a very high heat transfer rate is required. This is the case in thermal treatment processes such as hardening and direct chill casting of non-ferrous metals Specht (2017). Timm et al. (2003) has observed heat fluxes with values higher than 10 $MW/m^2$ in the stagnation zone during a liquid jet impinging on a red hot steel plate. The heat transfer mechanism involved in a liquid jet impingement on hot surfaces was extensively studied by different authors and groups. Preliminary work was published mainly in Japanese research journals during 1980's HATTA et al. (1983); Hatta et al. (1989a); Ishida et al. (1989). Although these works have given insight into the jet impingement cooling, the proposed correlations and predictions have their limitation due to the inadequate measurement methods. Numerous efforts have been conducted since then in order to improve the understanding of thermo-physical mechanism occurred in this high-temperature quenching process. HAMMAD et al. (2004) conducted experiments for the metal blocks with initial temperature from 250 to 300 °$C$. They determined the average wetting front velocity based on estimation from video images. It was found out that average wetting front velocity increased with liquid jet velocity and decreased with increasing block initial temperature and liquid jet temperature. And the wetting front velocity was maximum for steel with lowest thermal conductivity among three materials (copper, brass and steel). Mozumder et al. (2005, 2006b, 2007a) investigated the effect of various parameters on maximum heat flux and wetting front during liquid jet impingement. The residence time was also defined as the time from when the jet first strikes the hot surface until the wetting front starts moving. However, the wetting front moves outwards immediately after the initial impact between the liquid jet and hot

surface in this study. Wang et al. (2016b) reported that the re-wetting temperature was not susceptible to the jet velocity, which is in congruence with results obtained by Lee and Shen (1985). Some re-wetting temperatures reported in literature is compiled in **Table 4.1**. These studies have shed light on the understanding of liquid jet impingement cooling for further development of corresponding models. The focus of the present work is the size of boiling region within the wetted area. **Fig. 4.1** depicts the temperature profile along the hot surface under liquid jet impingement at a specific cooling instance. Boiling region consists of nucleate and transition boiling and develops with the radial movement of the wetting front. The straightforward nomenclature of Departure from Nucleate Boiling temperature ($T_{DNB}$) is the temperature at which boiling regime shifts between nucleate and transition boiling. And re-wetting temperature ($T_{Rew}$) is the temperature where re-wetting initializes. It is vital to study the influential parameters on boiling region size, because it is believed and validated that the heat flux tends to be highest in this region and a strong coupling among surface temperatures, heat flux and boiling phenomena exists Woodfield et al. (2009). Experimental determination of the wetting front region can also improve the accuracy of the model predictions, since the boiling mechanism in the boiling region is totally different from that in one-phase forced convection region. The definition of wetting front is the first step towards determination of the boiling region. Lienhard et al. (1992) found that liquid splattering occurs only within a narrow radial band, rather than being distributed at all radii in the wetted area. Meanwhile, this narrow band also moves to the circumference region as quenching continues. Dua and Tien (1978) defined that surface re-wetting refers to the establishment of direct liquid contact with a solid surface whose initial temperature is higher than the sputtering temperature. Filipovic et al. (1995) proposed a mathematical method to determine the position of wetting front. The minimum of the second derivative of the temperature could be used to position the leading edge of the wetting front. Wang et al. (2016a) investigated the jet impingement quenching for continuous cooling for the development of ultra-fast cooling system. For this top and bottom surface were cooled with the single circular jet. The heat transfer and wetting front propagation are noticeable. The temperature measurements was performed with the 3mm K type chromel-alumel thermocouples were embedded 2 mm beneath the impact surface to monitor the temperature. The one-dimensional heat equation in thickness direction were considered to calculate the surface temperature and the inverse heat conduction formulation were developed to find the surface heat fluxes. The heat transfer performance increases with increase in the water flow rate. Chen et al. (1991a) studied a hybrid scheme of combining experimental and numerical method to study heat transfer on stationary and moving plate and the experiments were intend to resemble the cooling process in steel rolling. For the purpose of temperature measurement, 0.0127 mm K type thermocouples were used. Three-dimensional co-ordinate system with Lagrangian description for the heat equation were implemented to calculate the surface temperature. The authors observed the flow in the moving direction, resulting in enhancement of the heat transfer downstream of the jet. The study reveals that the maximum heat flux occur at the initial contact with the cooling zone i.e., at stagnation zone. For initial temperature of 250 $°C$, boiling is observed away from the stagnation region. The temperature profiles in the hot metal plates were calculated with the solution of the axi-symmetric condition. The heat fluxes were evaluated from an energy balance. At the stagnation zone, a high thermal transient occurs during a high initial peak heat flux. For this they recommend to compare the heat flux in the boiling region except the thermal transient with literature. Xu and Gadala (2006) studied the heat transfer behaviour under circular water jet in the impingement zone. Type K thermocouple used in the experimental for the measurement of the surface length. For the heat transfer calculation two-dimensional, iterative and sequential inverse heat transfer analysis is developed and implemented using finite element program. From the analysis

of heat transfer rate at the stagnation is significantly affected by the water temperature and are slightly affected by the steel grade and water flow rate shows significantly low effect on the heat transfer. The verification of the inverse problem is not discussed and the reported heat fluxes are prone to experimental and numerical errors. Sharma et al. (2018) report the heat transfer characterization and re-wetting behaviour of 0.15 mm thick plate, with circular jet impinges from bottom side. The temperature measurements were mainly performed using energy balance. The results indicate that the peak heat flux attains at the stagnation point and reduces in the radial direction away fro the stagnation point. The maximum heat flux found to increase with the increase in the Reynolds number and remains maximum at the stagnation point irrespective of Reynolds number and jet to plate distance. Karwa and Stephan (2013) investigated experimentally jet impingement quenching process of stationary steel plate with 800 - 1000 $°C$ initial temperature. Type-K class 1, grounded thermocouples were utilized to measure the temperature profiles in quenching process. In order to estimate the surface boundary condition, 2 dimensional inverse heat conduction software were adopted. The local maximum occurs at the upstream of the wetting front were observed in the heat transfer calculation. Mozumder et al. (2007b) characterizes the maximum heat flux propagation during quenching of hot cylindrical block with 250 - 600 $°C$ initial temperature with sub-cooled water jet. Convection thermocouples are adopted for the temperature measurements inserted along the radial direction at edge length. Two-dimensional inverse solution of the heat conduction was adopted from Monde et al.. The maximum heat flux propagation velocity increases with increase in jet velocity was sub-cooled and decreases with high start temperature. Hammad et al. (2004) carried out the experimental work on the hot transfer characteristics of jet impingement quenching on the hot cylindrical block. The heat transfer was estimated using a two-dimensional inverse heat transfer solution with the help of surface temperature measured using the thermocouple. They found the maximum heat flux occurs when the surface temperature reaches less than 170 $°C$. The maximum heat flux strongly depends on the radial location from the jet impingement point. Lee et al. investigated the heat transfer analysis with stainless steel initially heated up to 900 $°C$. 2D inverse heat conduction problem helps to estimate the temperature and surface heat flux. The another observed a quasi-steady state with the increase of radial wetting front location increases linearly with time. Also, at the quasi-steady state, the liquid is ejected as droplets at the wetting front and the importance of the evaporation cooling due to the ejected droplets on the dry region were reported. Agrawal et al. (2012). investigated the mist jet impingement in case of hot horizontal stainless steel plate for initial temperature of 255, 355, 565 $°C$. One-dimensional and energy balance equation were solved to conjugate the surface heat flux. The re-wetting temperature increases with the increase of start temperature on the water impingement region. For the influence of initial temperature, maximum helps remain constant up to 4 mm and drops significantly. Wang et al. (2012) performed heat transfer analysis of hot stationary plate under multiple top circular jets on run-out table. Local surface heat fluxes were calculated using inverse heat conduction model based on two-dimensional finite difference program. The authors observed that the cooling flow rate has no effect on the heat transfer in the water stagnation region. Mozumder et al. (2006a) investigated the jet impingement quenching of hot cylindrical block made of copper, brass, and steel. The local surface heat fluxes were calculated using two-dimensional inverse method adopted from **?** For this study, the maximum heat flux as a function of jet velocity and thermal properties of the material. Chester et al. (2012b) performed the experimental analysis on the bottom jet cooling of a steel plate. Inverse heat conduction in conjunction with the experimental measurements were studied to estimate the unknown heat fluxes during quenching process. Effect of inclination, water flow rate on the heat transfer was studied and both the parameter have significant effect on the heat transfer, since the water flow

rate improves the rate of

Table 4.1: List of experimental studies on re-wetting temperature, $T_{Rew}$, during quenching with flowing liquid (arranged chronologically)

| Author | Material | $T_{in}$ [°C] | Exp. Conditions | Analysis Result |
|---|---|---|---|---|
| Agrawal et al. (2012) | SS-316 | 800 | d:2.5 mm, 0.59-2.84 l/min, s:0.25 mm | $T_{DNB}$-550°C, $T_{RWT}$-780°C $q_{max}$-2 $MW/m^2$ |
| Wang et al. (2016a) | SS-304l | 670 | d:4 mm, 1.5-25 l/min, s:20 mm | $T_{DNB}$-350°C, $T_{RWT}$-670°C $q_{max}$-3.75 $MW/m^2$ |
| Chen et al. (1991a) | SS | 240 | d:4.76 mm, 2.45 l/min, s:6.75 mm | $T_{DNB}$:185°C, $T_{RWT}$:240°C $q_{max}$:22 $MW/m^2$ |
| Xu and Gadala (2006) | SS-316 | 900 | d:19 mm, 15-45 l/min, s:10 mm | $T_{DNB}$:350-450°C, $T_{RWT}$:900°C $q_{max}$:14 $MW/m^2$ |
| Sharma et al. (2018) | SS-304 | 500 | d:1 mm, 0.11-0.47 l/min, s:0.15 mm | $T_{DNB}$:300°C, $T_{RWT}$:430°C $q_{max}$:8.5 $MW/m^2$ |
| Karwa and Stephan (2013) | AISI-314 | 1000 | d:3 mm, 1.05 - 4.23 l/min, s:1 mm | $T_{DNB}$:400°C, $T_{RWT}$:850°C $q_{max}$:9.5 $MW/m^2$ |
| Mozumder et al. (2007b) | Steel | 600 | d:2 mm, 0.942 l/min, s:59 mm | $T_{DNB}$:150°C, $T_{RWT}$:380°C $q_{max}$:3.5 $MW/m^2$ |
| Hammad et al. (2004) | Steel, Copper, Brass | 300 | d:2 mm, 1.88 l/min, s:59 mm | $T_{DNB}$:150°C, $T_{RWT}$:300°C $q_{max}$:4.5 $MW/m^2$ |
| Lee et al. (2017) | Steel | 900 | d:3 mm, 2.33 l/min, s:20 mm | $T_{DNB}$:230-680°C, $T_{RWT}$:625-875°C $q_{max}$:7 $MW/m^2$ |
| Agrawal and Sahu (2013) | Steel | 255-565 | d:0.5 mm, 0.024 l/min, s:0.25 mm | $T_{DNB}$:80-140°C, $T_{RWT}$:160-250°C $q_{max}$:0.25 $MW/m^2$ |
| Wang et al. (2012) | Steel | 900 | d:2 mm, 15-25 l/min, s:25 mm | $T_{DNB}$:400°C, $T_{RWT}$:700°C $q_{max}$:7.5 $MW/m^2$ |
| Mozumder et al. (2006a) | Steel Brass Copper | 250-400 | d:2 mm, 0.56-2.82 l/min, s:59 mm | $T_{DNB}$:141°C, $T_{RWT}$:380°C $q_{max}$:2.1 $MW/m^2$ |

wetting front progress across the impingement surface. Wang et al. (2012) studied the jet impingement quenching to investigate the effect of initial surface temperature, water temperature, and jet velocity. An inverse heat conduction based on the sequential function specification method was adopted to estimate the temperature and the surface heat flux. The results indicate that the initial temperature significantly affects the heat transfer in the stagnation and parallel region, where as the water temperature and jet velocity show merely low effect. The main objective of this article is to study the characteristics of the

size of boiling region due to the vigorous boiling occurring in this region. Meanwhile, the propagation of the size of boiling region is also given. The dominating variables such as jet velocity, material type and solid initial temperature will also be discussed. Especially, the boiling region size is recorded. This is only possible because the temperature field is measured with an infrared camera. Thermocouples are used in all previous mentioned studies. Therewith the temperature can be measured at specific locations. However, the exact determination of the boiling region size and wetting front can only be realized by temperature measurement with a high local resolution.

## 4.4 Results and Discussion

### 4.4.1 Repeatability of the Experiments

The surface temperature from the experimental work are primarily performed with infrared thermography for accurate and precise data in space and time direction. To ensure the accuracy of the experimental repeatability on the test material, experiments were conducted with similar experimental conditions for 3 consecutive times. Henceforth, we observed a overall accuracy of the measured surface temperature of around 3% which is illustrated by repeated temperature measurements under the same experimental conditions as shown in **Fig. 4.2** . Consequently, all the experiments which are included in this work have been repeated at least twice in order to avoid the experimental error. The validation of the experimental repeatability at location of 19 mm from the stagnation point is discussed in Fig. 4.2 and the temperature drop from start temperature of $500°C$ to $100°C$ occur in the time span of around $6s$. The time delay of the wetting front to cool the surface below $100°C$ is about $5s$ and this delay in time is termed as the residence time.
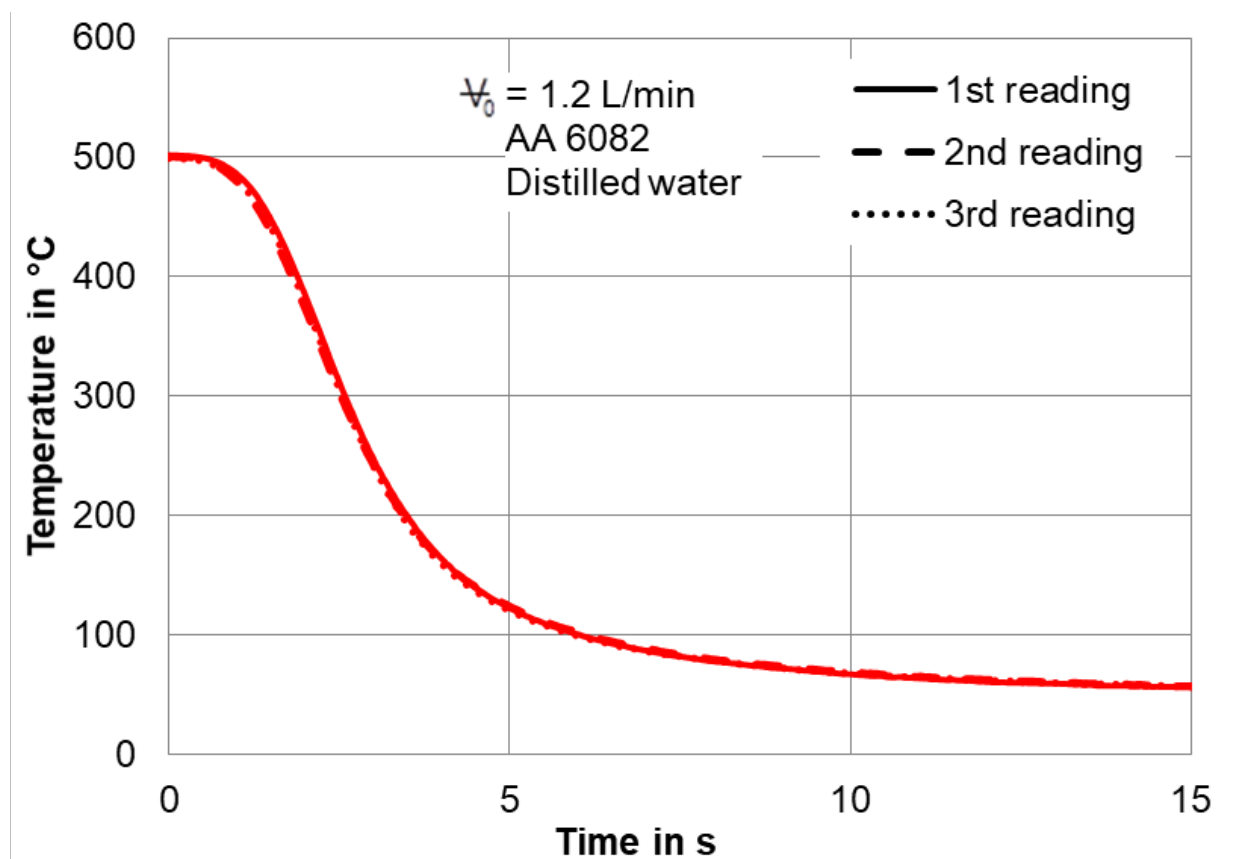


Figure 4.2: Validation of experimental repeatability for full jet nozzle at 19 mm

### 4.4.2   Boiling region width and Radial heat flux

The width of wetting front region develops on the hot surface while the wetting front moves radially towards the circumferential region. The exact definition of the boiling width is difficult to characterize visually and numerically based on heat fluxes and temperature measurements. Although, the heat flux distribution along with the temperature profile at three different times (1, 1.8, and 2.8 s) are depicted as shown in **Fig. 4.3**. in order to clarify the development of boiling region size. Obviously with the elapsed time, the heat flux distribution becomes wider and the temperature gradient correspondingly at the maximum heat flux are determined to be $65°C/min$, $61°C/min$, $50°C/min$ respectively. The width of the wetting front region at the three times, however, increases from 17 mm through 21 mm to 24 mm, which means a steeper gradient leads to narrower wetting front region. The physical significant of high heat transfer increases temperature gradient steep in the boiling region which significantly reduces the area of the boiling region size. Henceforth, the magnitude of the heat transfer is primarily responsible for the temperature gradient and consequently the width of the boiling region. In addition, the longer width of the wetting front region causes the initiation of the conduction from the dry region to the wet region thereby reduce the temperature on the dry region. At the time instant of 2.8s, the start temperature drops to below $600°C$ from nearly $700°C$ at 0.8s.
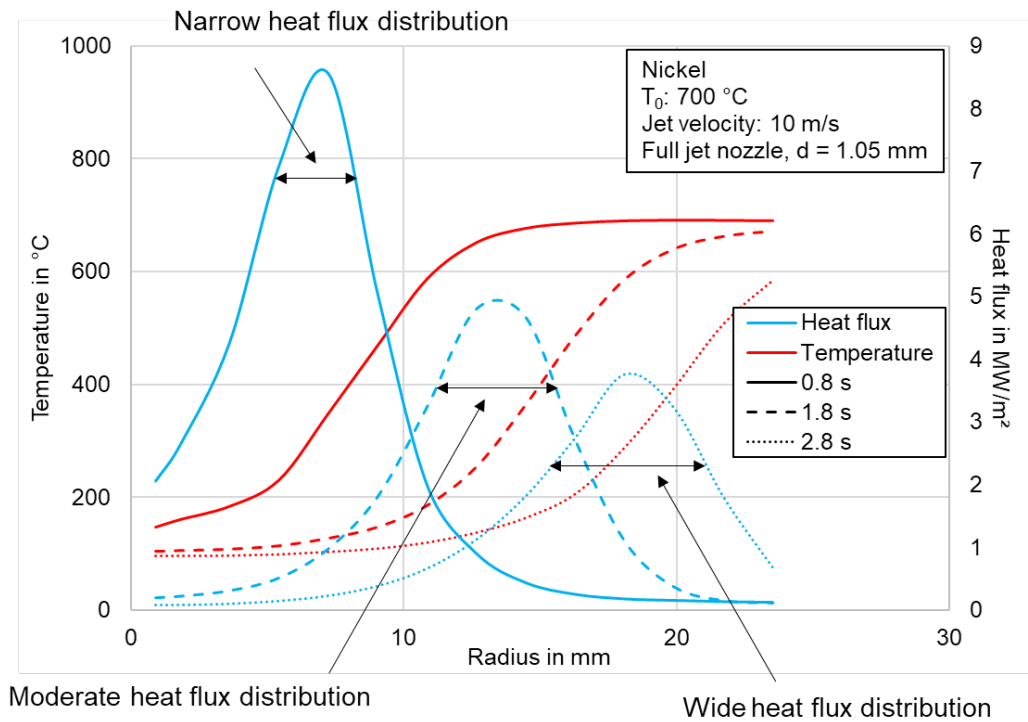


Figure 4.3: Variation of heat flux with wetting front movement

### 4.4.3   Influence of Material

The materials investigated to understand the heat transfer mechanism are Nickel, Nicrofer, and AA6082. The nomenclature and thermophysical properties are included in **Tab. 4.2** and **Tab. 4.3** respectively. The heat extraction from the hot surface for the above specified materials are determined are as shown in the **Fig. 4.4**. The peak of the maximum heat flux is always found at the stagnation point of the water jet and the position of the maximum heat flux always changes relative to the stagnation point. As we know, the water jet with 19 $m/s$ hits the hot metal surface of $500°C$ of 4 $mm$ thick plate at the stagnation point i.e., 0 $mm$. The water jet velocity losses some of its kinetic energy at the stagnation point

Table 4.2: Nomenclature of the used materials

| Name in text and figures | Detailed representation of the metals |
|---|---|
| Nickel | LC-Nickel 99.2 - alloy 201 (UNS*:N02201) |
| Nicrofer | Nicrofer 6020 hMo - alloy 625 (UNS:N06625) |
| AA6082 | Aluminium Alloy AA6082 |
| *UNS: Unified Numbering System (USA) | |

and tends to propagate with lower jet velocity below 19 $m/s$ in a circular manner across the hot metal surface of 500°$C$ with 4 $mm$ thickness. After 5s, the water jet velocity losses its momentum and the further propagation of the wetting front stops gradually. The stronger heat conduction from the dry region is mainly responsible for the decrease in the wetting front velocity further over time to attain steady state condition. At the stagnation point of the water jet (0 mm), the maximum heat flux of nickel is 1.9 times higher than nicrofer material and almost 3 times higher than the AA6082 material i.e., 15.8 $MW/m^2$ and 8.7 $MW/m^2$, 6 $MW/m^2$ respectively. Furthermore the heat flux decreases in a radial manner. The peak heat flux almost reaches a steady state after reaching a radius of 20 mm from the stagnation position. The nickel and nicrofer, AA6082 material relatively shows the similar tendency in the maximum heat flux extraction. Whereas the heat flux in the re-wetting region is almost uniform and no significant influence can be observed. The significant increase in the maximum heat flux for the nickel material is mainly due to the heat penetration coefficient in comparison to the nicrofer material. The higher conductivity of material can supply heat quickly to the surface and the temperature and surface heat flux remains high so the maximum heat flux propagates significantly low. A high conductivity and a longer wetting delay contribute to an overall cooling of the block prior to the movement, which ultimately results in the fastest maximum heat flux propagation velocity among the others. Xu and Gadala (2006) studied the influence of different material on the heat transfer mechanism in full jet quenching. The thermal conductivity incites the cooling effect at the plate surface and instigates the faster decrease of the temperature at the target location. On the other hand, the heat from the bottom part is also easily transferred to the target location and this tends to increase the target temperature. To reduce the temperature at the target location to a same value, higher heat flux may be needed for cooling the material with higher conductivity. Also, this indicates the cooling is more confined at the top surface and it is easier to cool down the surface with higher conductivity than with lower conductivity i.e., less heat is needed to reduce the surface temperature to a given value for the material with higher conductivity than that with lower conductivity. Mozumder et al. (2007b) investigated the influence of material on heat transfer and they observe the following: In terms of temperature distribution within the solid, quenching results in localized cooling near the surface for low thermal conductive material in contrast to high conductive material whenever the entire heated test piece quickly feels the effect of maximum heat flux on the surface. The temperature difference is partly responsible for the peculiar effect of radial position on $q_{max}$ for low conductive material.

Table 4.3: Thermo-physical properties of the used materials

| Material | AA6082 | | Nicrofer | | Nickel | |
|---|---|---|---|---|---|---|
| Temperature [$°C$] | 300 | 500 | 300 | 500 | 300 | 500 |
| Density [$kg/m^3$] | 2700 | 2700 | 8400 | | 8900 | |
| Thermal conductivity [$W/m/K$] | 232 | 219 | 14.4 | 17.3 | 60 | 58.5 |
| Specific capacity [J/kg/K] | 1028 | 1130 | 480 | 525 | 570 | 525 |
| Heat penetration coefficient or Thermal Effusivity [$W\sqrt{s}/m^2/K$] | 22000 | 22000 | 7600 | 8700 | 17450 | 16500 |
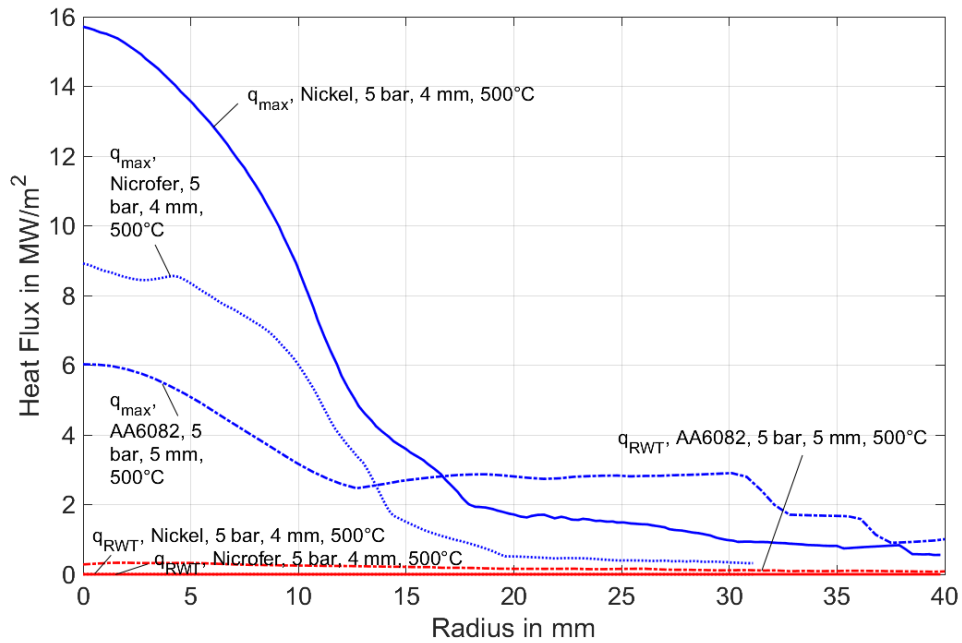


Figure 4.4: $q_{max}$ and $q_{RWT}$ for different materials
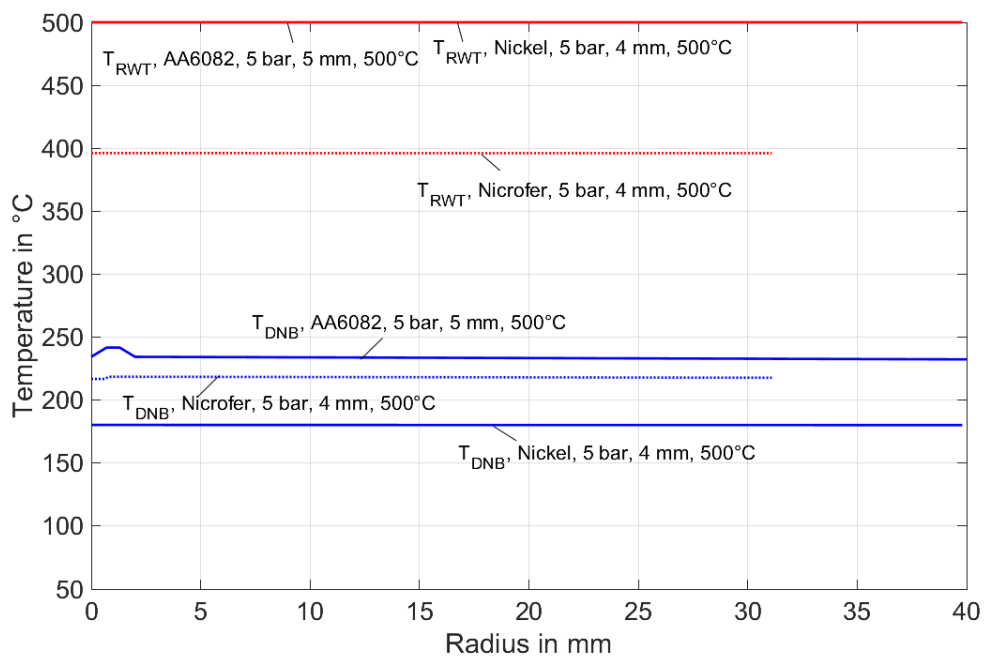


Figure 4.5: Departure nucleate boiling and re-wetting temperatures for different materials

**Fig. 4.5** discuss the variation of the temperatures at departure nucleate boiling and re-wetting condition for different kinds of materials. The re-wetting temperature remains constant for nickel at 500 °$C$ and for nicrofer the temperature fluctuates from 450 to 400 °$C$. Meanwhile, the DNB temperature decreases initially from 210 °$C$ to 100 °$C$ for nicrofer material and for nickel it decreases from 180 °$C$ until 15 mm. Contradictorily, the departure nucleate boiling temperature above 15 mm start to increase above 150 °$C$ for both nickel and nicrofer material.

### 4.4.4   Influence of Initial Temperature

The initial temperature of the sample determines how much thermal energy is stored. Investigated sample with a higher initial temperature provides more thermal energy to be extracted by the coolant. Meanwhile, sample with higher initial temperature also promotes more vigorous local cooling at wetting front, since it can conduct more thermal energy from the dry region to the wetted region, which again creates a steeper temperature gradient. This will as described above inevitably result in narrower boiling region as shown in **Fig. 4.6**. The maximum heat flux for the nicrofer start temperature 850 °$C$, 700 °$C$, the maximum heat flux is almost equal below 10 mm and whereas in the stagnation jet position heat flux shows a difference of 2 $MW/m^2$. Consequently, away from the stagnation position the maximum heat flux for the 850 °$C$ increases when compared to 700 °$C$. For the start temperature of 500 °$C$, the heat flux with magnitude lower than that of initial temperature 700 °$C$, 850 °$C$ shows a similar tendency.
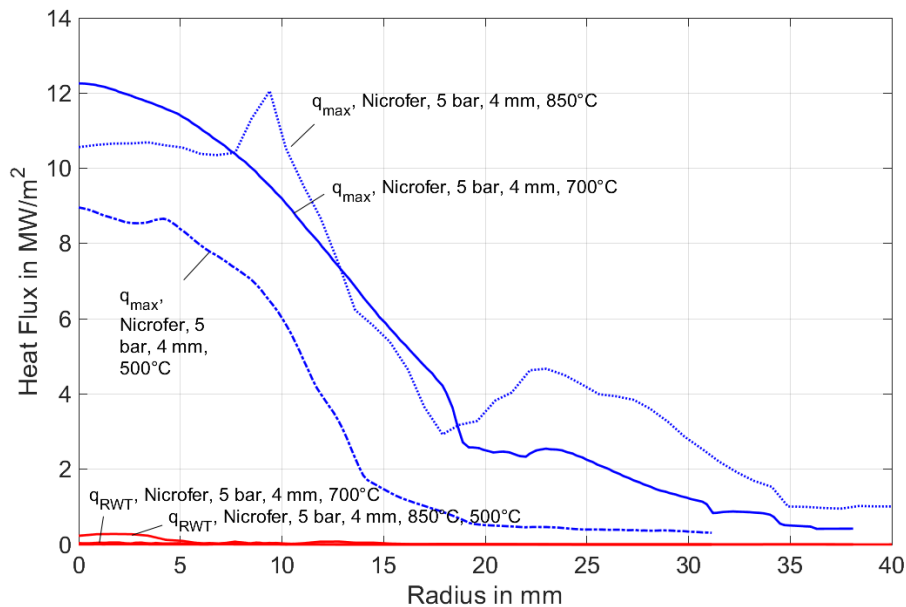


Figure 4.6: $q_{max}$ and $q_{RWT}$ for different initial temperature of the plate
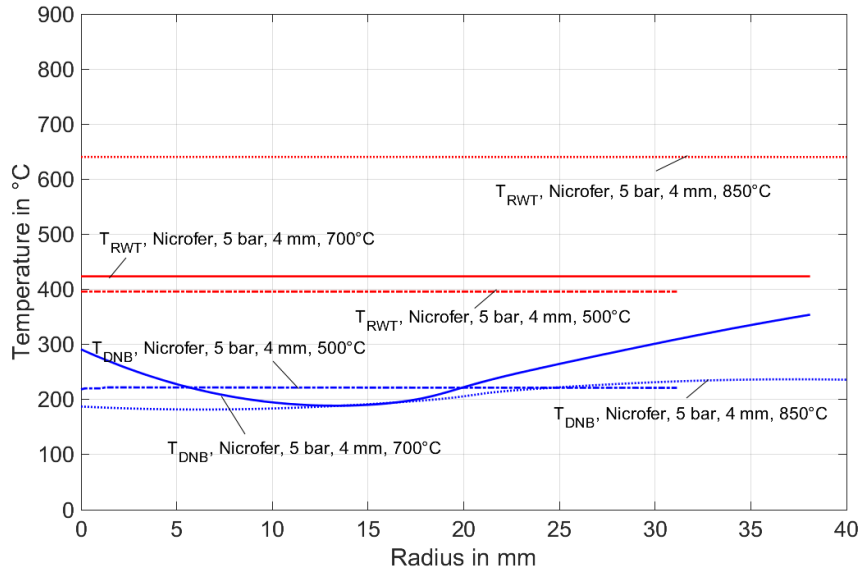
Figure 4.7: Departure nucleate boiling and re-wetting temperatures for different initial temperature of the plate

The effect of initial temperature on re-wetting temperatures can be further found in **Fig. 4.7**. It is noticeable that with increasing radius away from the stagnation region, the re-wetting temperature fluctuates slightly. The start temperature primarily lowers the re-wetting temperature and for 850 ° start temperature re-wetting temperature lies between $600\,°C$ to $650\,°C$ but whereas for start temperature 700, $500\,°C$ the re-wetting temperature significantly drops to $400\,°C$. In contrast, the start temperature has no significant effect on the departure nucleate boiling rather it remains constant at around $200\,°C$ for all the cases.

The effect of solid temperature is higher due to increasing the heat flux leads to unexpected effects such as long resident time. The increase of the start temperature promotes a stronger heat transfer to the impinging liquid and the vapour layer thickness would decrease and the re-wetting temperature occurs relative higher temperatures. The rise in the fluid enthalpy at lower surface temperature, the retardation of the fluid flow, and the effect of precursory cooling for the downstream radial location are mainly responsible for the spatial drop in the re-wetting temperature. Contradictorily, at the higher start temperature we observe the rise in the re-wetting temperature due to the void fraction in the impingement jet for the downstream direction. As the jet comes in contact with the hot surface at high temperature the water droplet immediately evaporates, resulting in reduced liquid fraction in the spent-out fluid, which for the leads to a reduction of vapour layer thickness on the hot surface. The rate of evaporation is further enhanced for the surface of the higher initial temperature and hence the vapour quickly leaves the hot surface, which further enhances the process of thinning of vapour layer thickness over the hot surface. With the reduced vapour layer thickness, the impinging fluid is able to penetrate the vapour layer much earlier and can establish contact with the hot surface even at the higher temperature. Perhaps at lower surface initial temperature this phenomenon of vapour layer thinning is not able to overcome the effect of flow retardation and rise in spent out fluid enthalpy. Thus, the results reported here indicate a diverse effect on the spatial variation of the re-wetting temperature for different initial surface temperature.

### 4.4.5 Influence of Thickness of the Material

The effect of sample thickness on the propagation of maximum heat flux is illustrated in **Fig. 4.8**. It can be clearly seen that the maximum heat flux near the stagnation region for plate with thickness of 2 $mm$, 3 $mm$, 4 $mm$ is approximately around 12 $MW/m^2$. Whereas for the location away from the stagnation point, the heat transfer significantly varies. The higher plate thickness posses larger heat fluxes of around 10 - 12 $MW/m^2$ but for lower plate thickness the heat flux significantly drops to 3 $MW/m^2$. Panda and Prasad Panda and Prasad (2011) have performed computational and experimental investigations with a shower head of impinging liquid jets. They concluded that the temperature gradient is larger for thicker plate than thinner plate. Similar effect can be found for current research, the re-wetting state for a 2 $mm$ plate can be attained earlier than a 4 $mm$ plate which makes the liquid temperature rise more for plate with 4 mm thickness. All these factors will impede the wetting front movement from stagnation point to the downstream locations as well as heat transfer rate for the thicker samples. The thermal energy of the material would be higher for the larger plate thickness compared to lower plate thickness. The material would resist the heat transport within the body for the fluid impingement on the hot surface. As the water jet strikes the plate at stagnation point, due to the large internal energy of the body the initial contact of the fluid with the hot metal plate occurs faster. The vapour generation in the spent-out fluid increases drastically and the evaporation rates significantly increases with the replacement of the fresh incoming liquid. Thus, the vapour layer thickness between the hot surface and fluid becomes insignificant and therefore the re-wetting temperature increases. The higher plate thickness delays the heat propagation from the other side of the quenched surface and the with high jet velocity homogeneous cooling takes place for larger conductive materials.
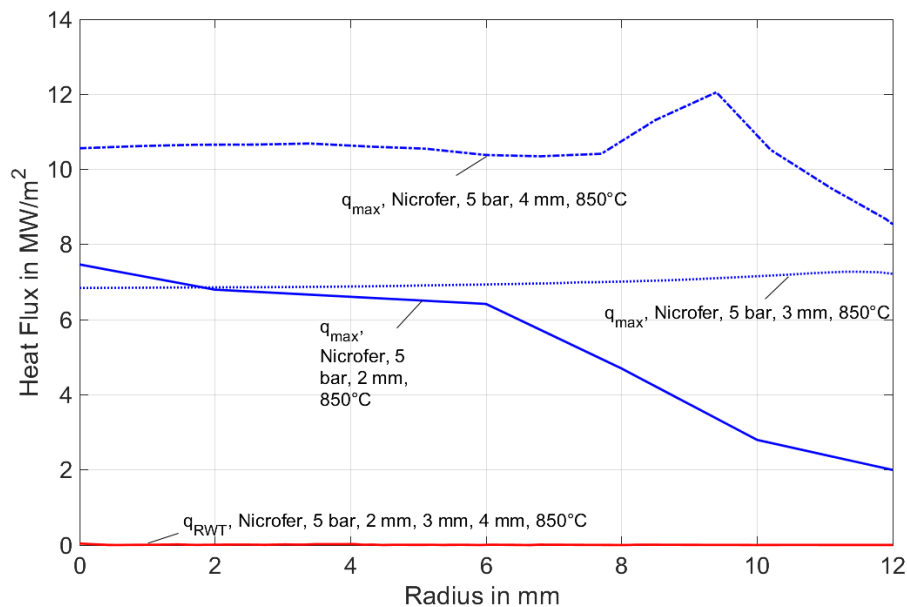


Figure 4.8: $q_{max}$ and $q_{RWT}$ for different metal thickness of the plate
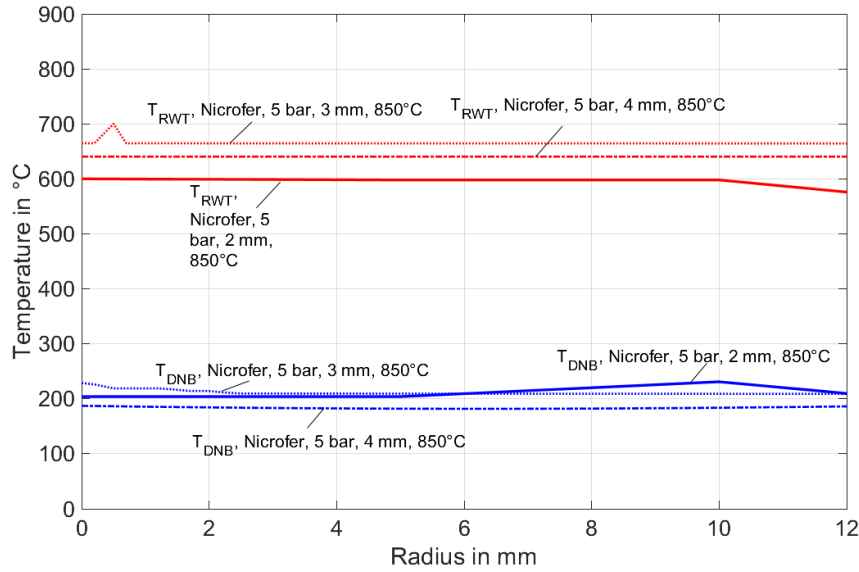
Figure 4.9:  Departure nucleate boiling and re-wetting temperatures for different metal thickness

**Fig. 4.9** shows the temperature variation for the departure nucleate boiling and re-wetting temperature for different metal thickness. The re-wetting temperature for nicrofer at 2 *mm* and 3 *mm* shows a temperature range of 600 - 670 $°C$ whereas for higher plate thickness the re-wetting temperature decreases to around 400 $°C$ and the fluctuation are obtained to be experimental and numerical methods. The similar effect can be observed in case of departure nucleate boiling at around 200 $°C$ for 2 to 3 *mm* and for 4 *mm* the DNB temperature decreases to around 150 $°C$.

### 4.4.6   Influence of Water Flow Rate

The influence of the water flow rate in case of full jet quenching with fixed plate condition are depicted in the **Fig. 4.10** explains the heat flux variation. The maximum heat flux for 5 bar and 9 bar pressure significantly varies away from the stagnation position. For 9 bar water pressure, the heat flux varies slightly and maximum heat flux decreases from 11.5 $MW/m^2$ to 10 $MW/m^2$. Whereas for the 5 bar water pressure, the heat flux decreases significantly to around 3 $MW/m^2$. The maximum heat flux variation for 9 bar is about 2.5 times that of 9 bar water pressure. The re-wetting heat flux has no significant influence for the water flow rate influence.
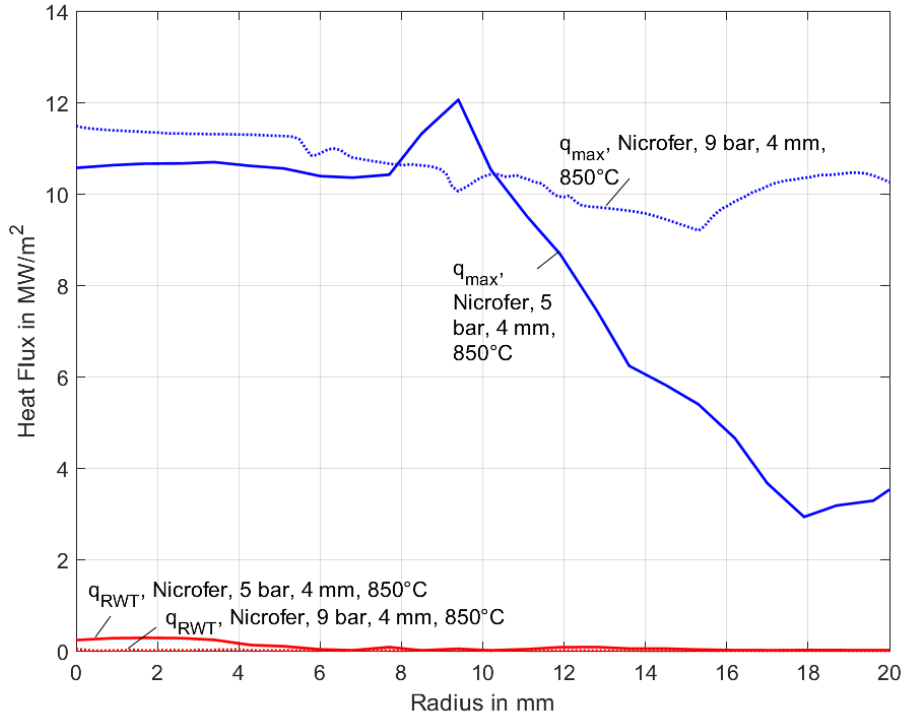
Figure 4.10: $q_{max}$ and $q_{RWT}$ for different water flow rates

The high-water jet velocity promotes a shorter resident time and hence a higher start temperature was observed during the wetting front movement. The high start temperature responsible for the faster movement of the wetting front. The fresh liquid possesses lower enthalpy and the enthalpy of the fluid rises as it travels on the hot surface. The fluid enthalpy rises high due to low water jet velocity and the enthalpy continues to rise unless it is replaced by fresh liquid. Henceforth, the heat absorbing capacity significantly drops with the generation of vapour layer occurs at the liquid movement and surface interface since the liquid poses larger part of enthalpy. Further, the vapour layer thickness rises on the hot surface. The surface conduction pre-dominates as the liquid flow reduces the heat absorbing capacity at the wetting front movement. Therefore, the significant drop in the re-wetting temperature takes place.

- The opposite phenomena can be interpreted for the rise in the water flow rate or the Reynolds number. At the higher water flow rate, the jet velocity is higher, then, spent out fluid is quickly replaced by the fresh liquid. Henceforth, the effect of the flow retardation and rise in enthalpy is lower for higher water flow rate. In addition, the effect of boundary layer thickness is insignificant for higher water flow rates.

- The development of boundary layer thickness, reduces the ability of liquid to condense the vapour bubble at the wetting front. Further results in the hindrance of heat removal rate by the liquid and the internal heat conduction.

The re-wetting temperature downstream location away from the stagnation point might be due to flow retardation and rise in enthalpy of spent fluid after impinging onto the hot surface. The reduction in the water jet velocity, the surface re-wetting temperature goes down. The reason for the decrease in re-wetting temperature is mainly due to the lesser fluid over the hot surface is higher for low water jet velocity compared to higher water jet velocity. The fresh liquid continuously replaces the spent fluid on the hot surface at higher water jet velocities. The heat absorbing capacity of the fluid for high velocity mainly responsible for the occurrence of the re-wetting phenomena at higher temperature. Where

the lower water jet velocity, the fluid losses the heat absorbing capacity after certain radial distance and the large portion of heat generates the vapour layer between the hot surface and the fluid. The thickness of the vapour layer rises and thus conduction through the vapour layer is significantly low and the re-wetting temperature occurs at relatively lower value. The localized drop in re-wetting temperature at extreme position is also due to the entire conduction effect. The temperature of downstream region gets reduced due to the conduction heat transfer towards the stagnation region after the jet strikes the hot metal surface. Xu et al. noticed a little effect of water flow rate on the heat transfer. The boiling curve profiles clearly indicates the non-existence of the film boiling regime and the water flow rate has no significance effect on the transition region and convection. Alternatively, the nucleate boiling region fluctuates between $\pm$ 5 $MW/m^2$ for water flow rate of 15-45 $l/min$.
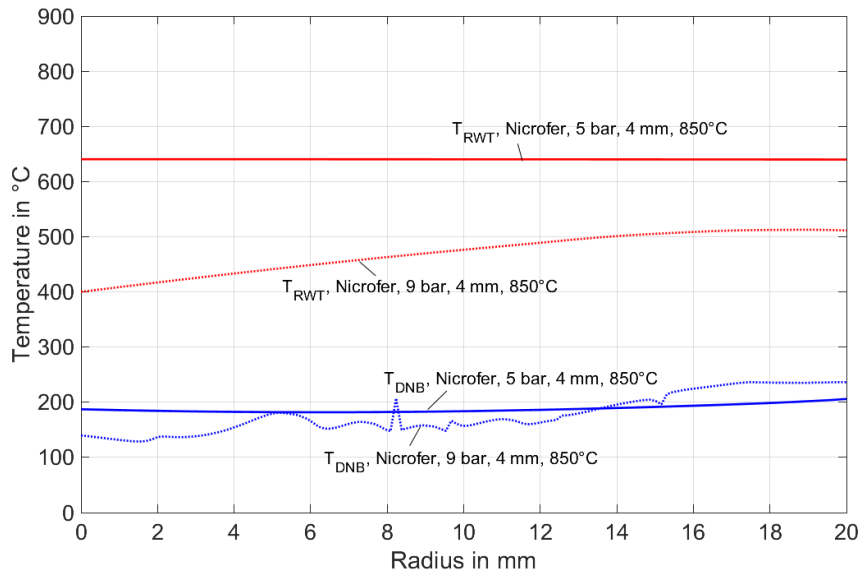


Figure 4.11: Departure nucleate boiling and re-wetting temperatures for different water flow rates

**Fig. 4.11** shows the departure nucleate boiling and the re-wetting temperatures for different water flow rates. The re-wetting temperature for 5 bar and 9 bar water pressure shows stronger influence and the magnitude for 9 bar pressure shows lower value of around 400 °$C$ whereas for 5 bar water pressure it is around 650 ∘ respectively. The higher amount of water induces the reduction of the surface temperature and the enhances the movement of the wetting front. Consequently, the departure nucleate boiling temperature for 5 bar is little higher compared to 9 bar water pressure. For 5 bar water pressure, the departure nucleate boiling temperature is about 200 °$C$, whereas for the 9 bar water pressure it is around 150 °$C$.

## 4.4.7   Influence of Process Parameters from Literature

The heat transfer during wetting front movement posses relatively strong influence and quantifying the influencing parameters are to be discussed. The boiling parameters like $T_{DNB}$, $T_{RWT}$, $q_{max}$ and $q_{RWT}$ were listed and are shortly discussed on the process parameters like impingement radius, water flow rate, initial temperature of the plate.
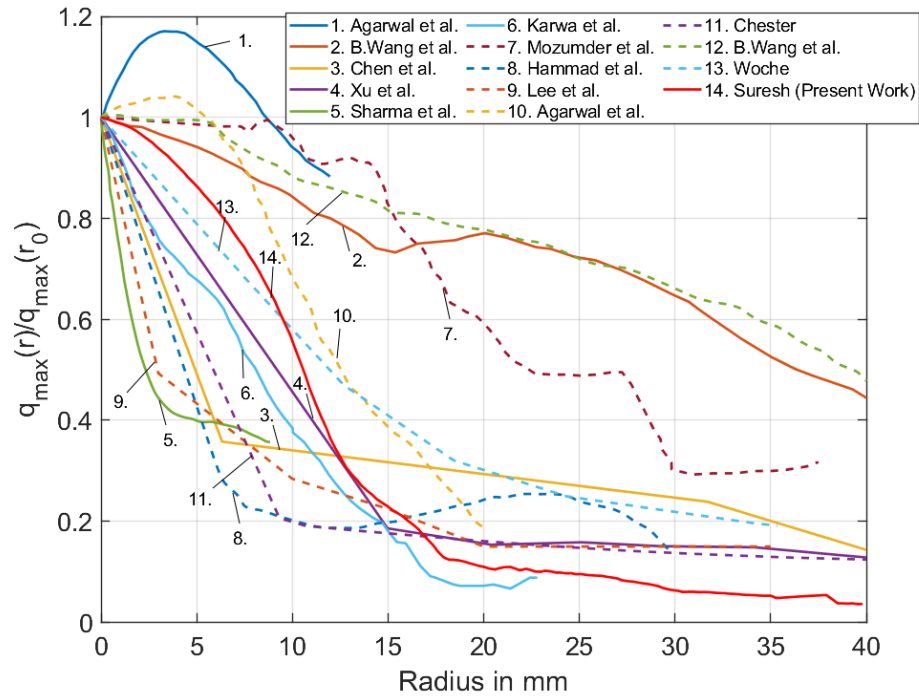
Figure 4.12: $q_{max}$ comparison as a function of radius from different authors in literature

**Fig. 4.12** shows a comparison for the ratio of maximum heat flux to the maximum heat flux at stagnation point $(q_{max}/q_{max}(r_0))$. The ratio of maximum heat fluxes normalizes the heat flux variation from different authors over the impingement radius are shown for simplification. The profiles indicate the variation of the tendency of the maximum heat flux and experimental conditions shows a stronger influence on the heat flux extraction until 15 $mm$ from the stagnation position. Above 20 $mm$, the maximum heat flux is almost constant. Most of the authors indicate that maximum heat extraction of about $q_{max}/q_{max}(r_0) = 0.6$, takes place for the radius up to 5 mm from the stagnation position. Otherwise, all the authors suggest that maximum heat transfer of approximately $q_{max}/q_{max}(r_0) = 0.6$ should takes place within 15 mm from the stagnation position. From this heat flux profiles we can clearly understand the dependency of the maximum heat flux on the radius or the impingement position.
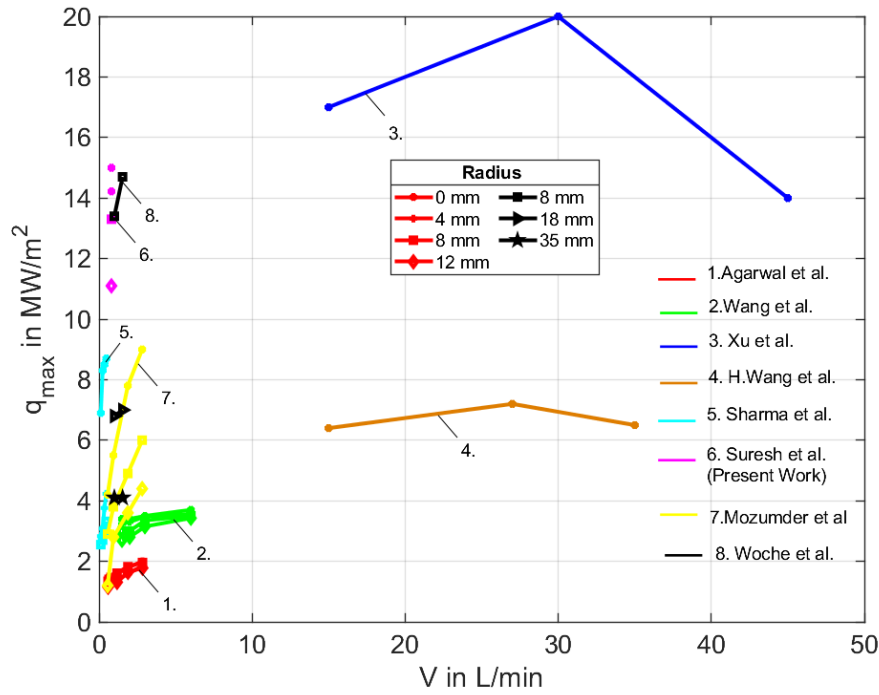
Figure 4.13: $q_{max}$ in comparison with different authors from literature for different water flow rates
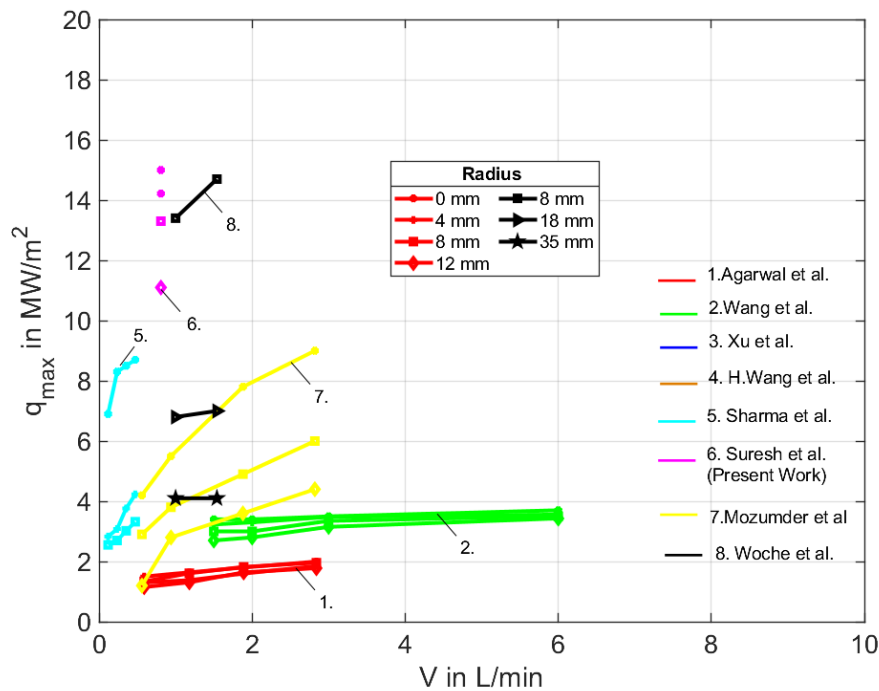


Figure 4.14: $q_{max}$ in comparison with different authors from literature for different water flow rates

The literature study from various research authors were listed in the schematic **Fig. 4.13** and **Fig. 4.14** explains for different water flow rates. The heat flux variation clearly indicates no significant change rather the very few authors demonstrates the higher heat transfer changes. Except Mozumder et al. (2007b) all other authors demonstrates the significantly low influence of water flow rate on maximum heat transfer during full jet

quenching. For the higher water flow rates, the movement or the wetting front velocity and henceforth the heat transfer should proportionately increase. From the observation, it is clear that the heat transfer increases proportionally whereas the intensity of the rise in heat flux is insignificant and it lies in the range of about $\pm$ 2 $MW/m^2$.
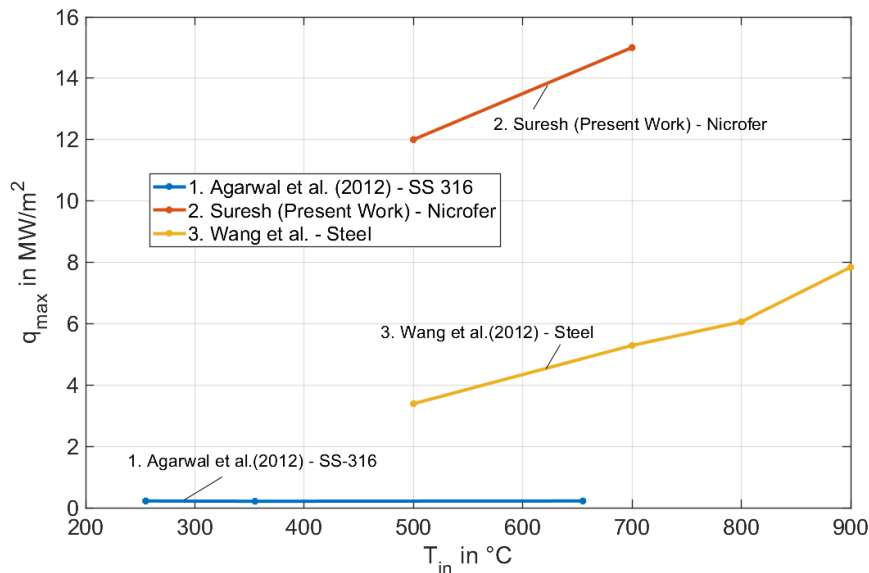


Figure 4.15: $q_{max}$ in comparison with different authors from literature for different start temperatures

The influence of start temperature on the maximum heat flux is clearly discussed in **Fig. 4.15** and the maximum heat flux increases for increase in the temperature due to the higher thermal capacity of the plate increases. The higher energy of the plate rises the surface superheat and promotes the faster movement of the wetting front. The high temperature promotes generation of the vapour drastically when wetting front encounters a hot surface. The large amount of vapour ejects away from the surface leaving space for the new incoming liquid to extract the heat from the surface. Henceforth, the increase of the thermal energy of the body should promote a linear increase of the heat flux as discussed in the earlier Fig. 4.15.
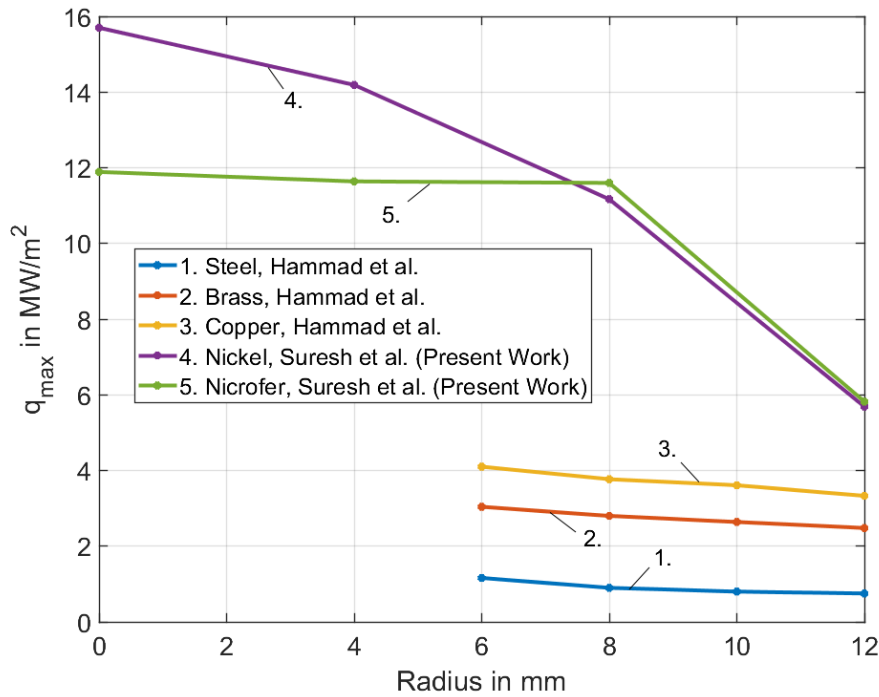
Figure 4.16: $q_{max}$ in comparison with different authors from literature for different material of the plate

**Fig. 4.16** shows a schematic of the different material influence on the radius from various authors. The steel obtains the lower magnitude compared to brass and copper because of lower thermal conductivity. In similar way, nickel obtains the highest magnitude compared to nicrofer material. The reason for the increase in heat flux for the nickel material is mainly the thermal conductivity and conductivity of the nickel is three times that of the nicrofer. Therefore the heat transfer at the stagnation point is higher than the nicrofer material. The similar phenomena can be seen under similar experimental condition in case of Hammad et al. (2004) for copper, brass, steel in the order of the magnitude of thermal conductivity.
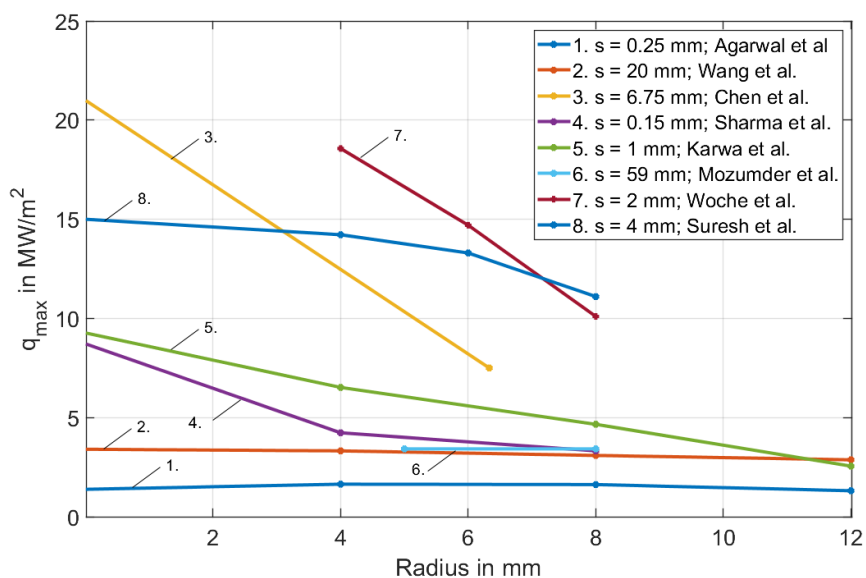


Figure 4.17: $q_{max}$ in comparison with different authors from literature for different thickness of the plate

**Fig. 4.17** shows the maximum heat flux profiles from different authors in literature with respect to the thickness of the plate. The thickness varied from 0.25 *mm* to 59 *mm* depending on the respective experimental conditions. Although each author utilized different experimental condition and the exact range of influence is hard to correlate. However, we can observe the heat flux fluctuations at the impingement point of about 4 mm and the maximum heat flux reported goes up to 20 $MW/m^2$.
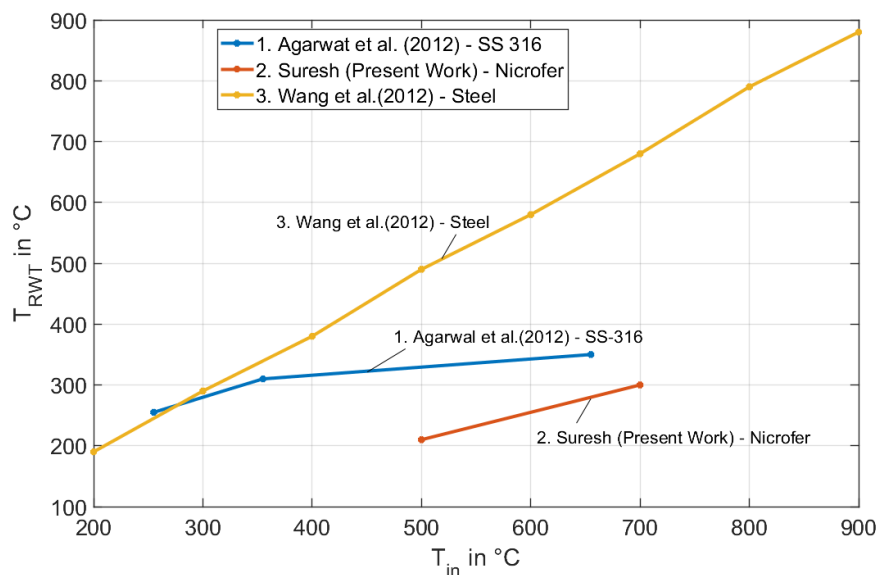


Figure 4.18: $T_{RWT}$ in comparison with different authors from literature for different start temperatures

Re-wetting temperature as a function of start temperature is depicted in the schematic **Fig. 4.18**. As seen from the profiles, the re-wetting temperature strongly increases with the start temperature as a function of the impingement position. The higher plate temperature significantly increases the thermal capacity of the plate which directly proportional to the higher magnitude of the re-wetting temperature.

**Fig. 4.19** and **Fig. 4.20** clearly demonstrates the variation of the re-wetting and departure nucleate boiling temperature as a function of radius. The temperature profiles clearly indicates the constant trend except some authors also observed the decrease in the magnitude of the temperature for position away from the impingement.
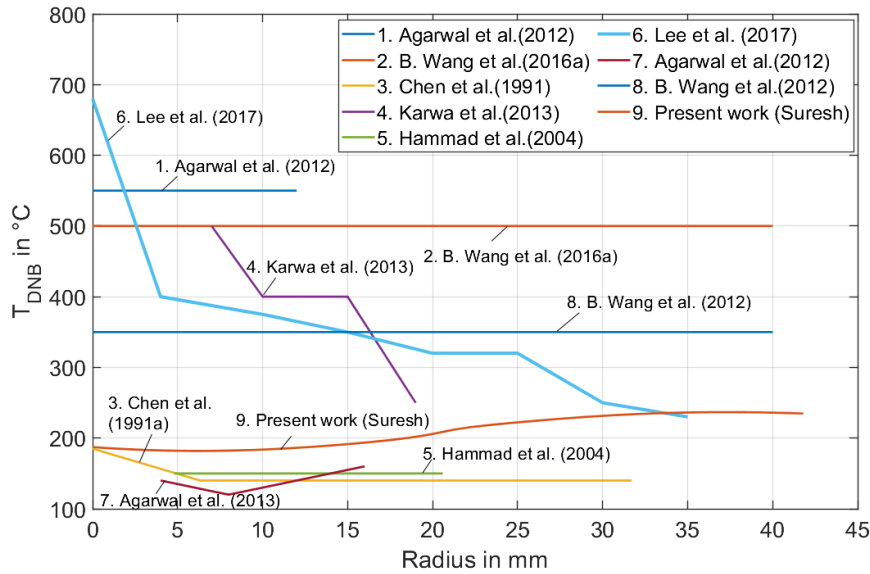
Figure 4.19: $T_{DNB}$ in comparison with different authors from literature for different material of the plate

**Fig. 4.19** gives the information about the departure nucleate boiling as a function of radius from different authors from literature. The observation clearly demonstrates that the departure nucleate boiling has no dependency on the radius of the metal plate. Except Lee et al. (2017) wherein they observed the high temperature drop from 700 ot 400 $°C$ up to 4 mm from the impingement point and decreases gradually up ot 250 $°C$. All the authors show a steady temperature value depending on the respective experimental conditions. Although, most authors report the departure nucleate boiling temperature to lie in the range of 200 $∘C$.
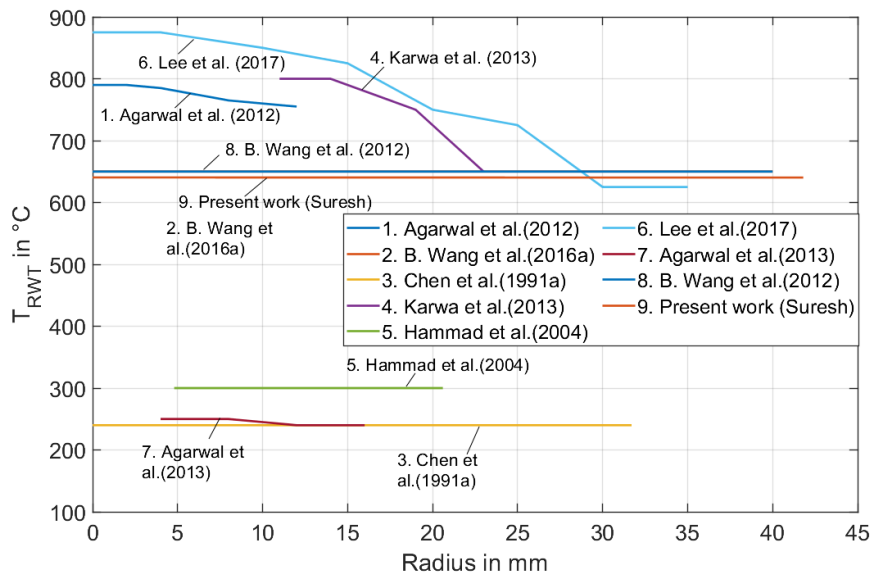


Figure 4.20: $T_{RWT}$ in comparison with different authors from literature for different material of the plate

**Fig. 4.20** shows the variation of the re-wetting temperature as a function of the radius from different authors in the literature. The re-wetting temperature remains nearly constant over the radius and from earlier in the Fig. 4.18 we observe that the re-wetting temperature is a

strong function of the initial temperature. The exact phenomena can be understood with this profiles.

## 4.5   Conclusion: Fixed Plate

Liquid jet impingement on hot metal surface is a very complicated phenomenon, since boiling occurs and brings complexity due to the occurence of two-phase flow on surface. This section of the chapter is focused on the determination of the maximum heat flux, departure nucleate boiling, rewetting temperature, which is of vital importance, because the highest heat transfer and most vigorous boiling activity occurs in this region, also the rewetting temperature influence the start of wetting front on the hot surface.

- High heat transfer rate will increases temperature gradient steep in the boiling region and consequently the width of the boiling region reduces. Henceforth, the magnitude of heat transfer is primarily responsible for the temperature gradient and the reduction in the heat transfer lowers the temperature difference between dry region and the wet region.

- For higher thermal conductivity of the material, the maximum heat flux decreases. The conductivity instigates faster decrease of the temperature at the target location and needs less heat is needed to reduce the surface temperature. Also the lower thermal conductive material promotes a localized cooling near the surface in contrast to the higher thermal conductive where the influence of maximum heat flux can be felt on the entire surface quickly. Therefore, Nickel with low thermal conductivity posses high maximum heat flux of 16 $MW/m^2$, whereas AA6082 posses 6 $MW/m^2$ respectively. Although, the DNB temperature remains independent of the radial and fluctuates around 200 °$C$ within the range of 50 °$C$.

- The maximum heat flux is a strong function of the start temperature of the plate which highers the rate of heat transfer with a factor of 1.5 times than 500°$C$ for 700 and 850 °$C$ respectively. Although, the DNB temperature lies significantly within the range of 200 °$C$, whereas the RWT temperature is a strong function of the start temperature and significantly increases with the higher start temperature.

- The higher plate thickness offers a high intensity of heat transfer and the heat transfer reduces for lower plate thickness. This can be evident in terms of the rewetting temperature, where the increase of plate thickness lowers the RWT temperature because transfer of heat occurs faster.

- Influence of water flow rate on the maximum heat flux is relatively less significant in the stagnation region of the water jet impingement. With further away from the jet impingement region, the high water flow rate posses high heat flux magnitude. Decrease of the rewetting temperature occurs for higher water flow rate, and further the high heat transfer is attained at higher water flow rates. Whereas the DNB temperature remains to be constant for all the water flow rates nearly around 200 °$C$.

## 4.6   Single Full Jet Quenching: Moving Plate

### 4.6.1   Introduction for Moving Plate

Movement of the plate with the single full jet quenching can be primarily seen in the continuous rolling process for the heat treatment of the material at higher temperatures. The hot material movement changes fluid motion on the quenched surface.   Large temperature gradient occurs across the quenched surface which promotes the development of thermal stresses and are prone to induce deformation. To minimize the local stresses and large deformation of the heat treated body during quenching stage in industrial processes, it is very important to investigate the local heat transfer. In this subchapter, we perform several experimental study on the plate movement with single full jet quenching. For this, we choose the flat plate with dimensions 230 mm width, 250 mm length and thickness vary from 5 – 20 mm were water cooled with fixed single jet nozzle. The surface temperature distribution was captured with the help of infrared camera on the back of the quenched surface in both space and temporal direction. The process parameters like thickness, plate velocity, initial temperature, water jet velocity was successfully studied and the results shows a steady increase in the heat extraction.

**Phenomena of Full Jet Quenching**
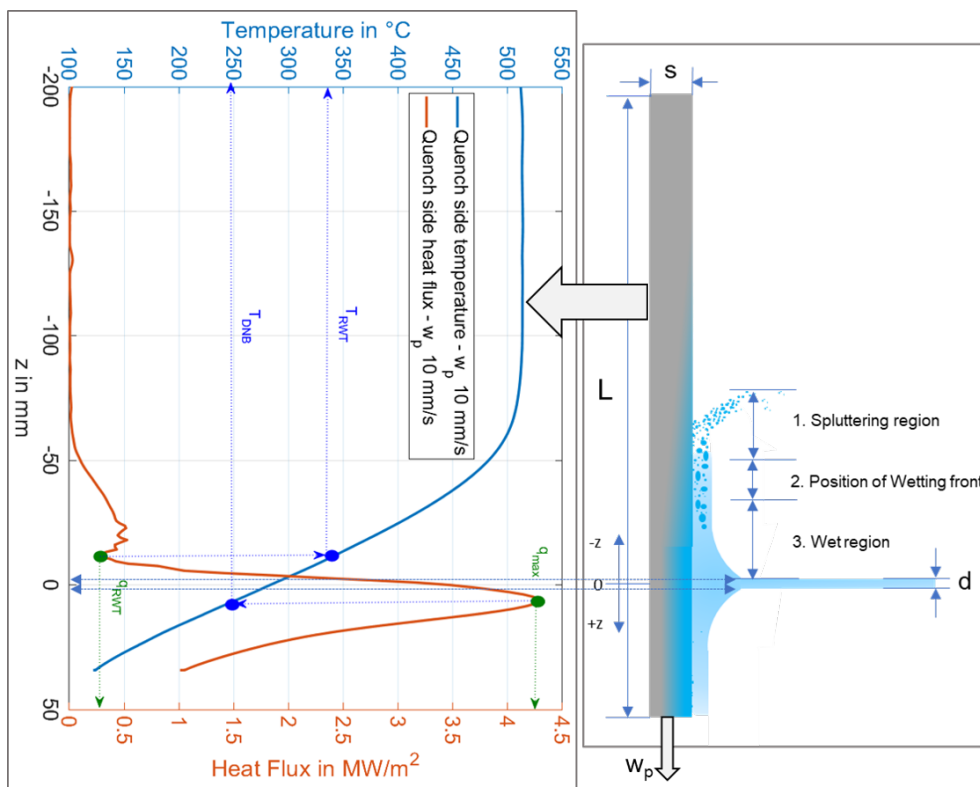


Figure 4.21: Schematic diagram of Single Full Jet Quenching with Movement

**Fig.  4.21** shows the schematic diagram of the full jet impingement on the hot moving plate at velocity of 10 $mm/s$, jet velocity of 12 $m/s$, plate thickness of 5 $mm$ for AA6082 plate.  The left part of the figures indicates the results from inverse simulation at the quasi-steady state condition and right part depicts the physical model on the water jet impingement side. The inverse results present the quenched side temperature profiles and the corresponding heat flux on the length of the plate. At z = 0 $mm$, indicates the nozzle position, minus sign $(-z)$ and plus sign $(+z)$ are above the water jet impingement and below

the jet impingement region respectively. The boiling parameters on the surface of the plate are determined as shown in the schematic Fig. 4.21 which are indicated as $T_{RWT}$, $T_{DNB}$ and $q_{RWT}$, $q_{max}$ respectively. The corresponding values of boiling parameters are found to be 330°C for $T_{RWT}$, 250°C for $T_{DNB}$, and 0,35 $MW/m^2$ for $q_{RWT}$, 4.3 $MW/m^2$. From the physical perspective, the movement of the hot plate occurs from top to bottom direction when water jet at an impingement angle of 90° acts at a fixed position in space. Whereas, the plate with velocity of 10 $mm/s$ continuously moves indicating that the material point of the body changes with time while the jet position remains in stationary. Further, the fixed condition of the water jet and the constant plate movement from top to bottom direction facilitate the quenching process to attain quasi-steady state condition after certain elapsed time. The velocity of the plate is relatively low compared to the water jet velocity and henceforth the water makes a direct contact at the stagnation point of the plate as seen from the fixed plate condition. The high momentum of the water jet after striking the hot metal surface tend to move in a circular manner, but the motion of the plate from top to bottom alters the circular motion of the water jet. In Fig. 4.21 shows the three different regions of the quenching process in case of plate movement. First region is the spluttering region, where most of the fluid is ejected away from the surface due to the large amount of vapour generation. The continuous forced movement of the plate promotes stronger ejection of the water droplets although the hot solid temperature at the interface of the dry region and the fluid resist direct contact with the surface. Second region is classified as the position of the wetting front and this region typically combination of re-wetting , transition boiling. The region between the spluttering and the wet is mainly responsible for the increase of heat transfer during quenching process and also initiates the movement of the wetting front. Finally, the wet region lies between water jet and the wetting front. The high heat transfer takes place below the jet position and downstream the jet position fluid moves along with the plate. In other words, the motion of the plate enlarges or stretches the wetting front to the downward direction. Interestingly, the velocity of the wetting front and the plate should be considerably similar and further investigation should reveal more information.
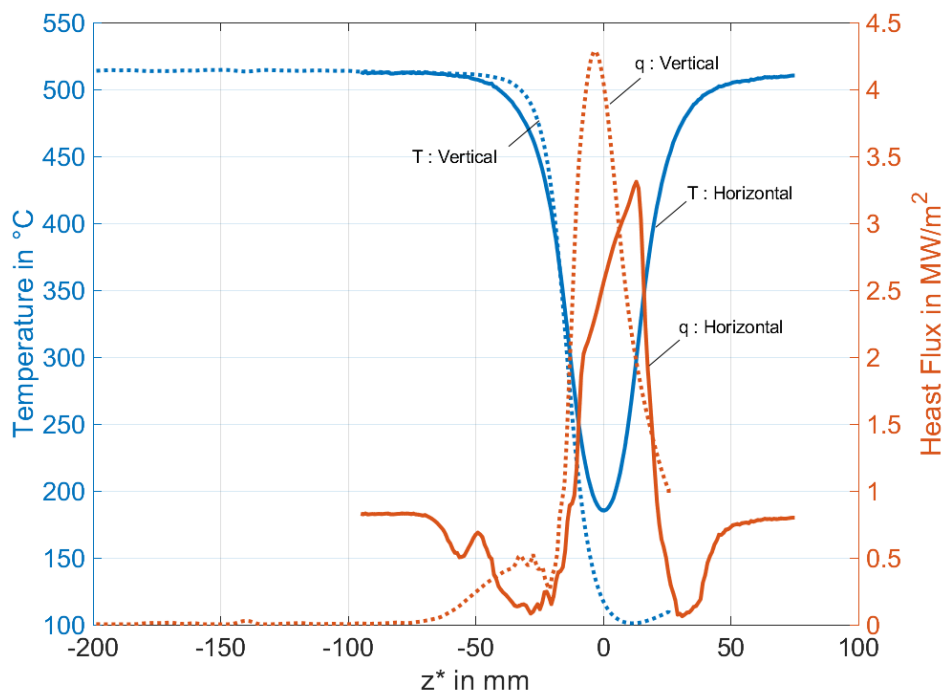


Figure 4.22: Variation of the surface temperature with the heat flux with respect to position

**Fig. 4.22** demonstrates the difference between the horizontal and vertical position at the impingement location. In addition, the measured surface temperatures and the heat fluxes on the quenched surface were compared for the same experimental condition as in Fig. 4.21.The temperature profiles for the vertical direction and the horizontal direction superimposed and seems to coincide approximately with $\pm$ 10% in the upward direction only i.e., wetting front movement above $200°C$. The peak of the maximum heat flux lies in the range of the $\pm$ 10 mm from the stagnation position. The magnitude of maximum heat flux for vertical line is 4.3 $MW/m^2$ and that for horizontal line is 3.3 $MW/m^2$ and a difference of 1 $MW/m^2$ would be mainly due to the end temperature of the plate. For horizontal line, the heat conduction from the circumferential area is significantly strong compared to the vertical line. The heat flux profile tend to inversely proportional to the surface temperatures and is approximately obtained to be symmetric although the numerical instabilities are responsible for such fluctuations.

## 4.6.2   Literature Review

Heat transfer mechanism in moving of hot metal plate most primarily changes as compared to the fixed plate mechanism. The plate movement moves from top to bottom with specific velocity, the water jet impinges at a specific location on the plate. The hot moving plate tries to elongates the impinging water jet and the fluid dynamics, heat transfer behaviour of the wetting front in the downward region as well as the upward region changes. The influence of process parameters like thickness of the plate, initial temperature, water jet velocity, plate velocity and material on the heat transfer in single full jet quenching is to be understood. The literature search should provide some basic understanding of the heat transfer behaviour in single full jet quenching.

| **Author** | $s$ $mm$ | $d_j$ $mm$ | $w_j$ or $Q$ $m/s$ or $l/min.m$ | $w_p$ $mm/s$ | $T_{in}$ $°C$ | $q_{max}$ $MW/m^2$ |
|---|---|---|---|---|---|---|
| Franco (2008) | 6.65 | 25 | 15* | 350, 1000 | 700 | 14.4 |
| Fujimoto et al. (2014) | 0.3 | 5 | 0.4, 0.8, 1.2 | 500-1500 | 100, 250 | 14 |
| Fujimoto et al. (2015b) | 0.3 | 5 | 0.4,1.2 | 500-1500 | 100-500 | 28 |
| Fujimoto et al. (2016) | 0.3 | 5 | 0.8 | 1500 | 300-500 | - |
| Chen et al. (1991b) | 6.35 | 4.76 | 2.3 | 500 | 240 | 17.5 |
| Morisawa et al. (2018) | 0.3 | 4 | 0.97,1.19,1.49 | 500-1500 | 700 | 26 |
| Leocadio (2018) | 10 | 8 | 1 | 166.7 | 900 | 6.5 |
| Jha et al. (2016) | 6 | 6 | 14* | 500, 800 | 900 | 2.47 |
| Gradeck et al. (2009a) | 37.5 | 17 | 1.2 | 500-1300 | 500 | 3 |
| Jha et al. (2015a) | 6 | 6 | 15* | 600 | 900 | 3 |
| Wang et al. (2019b) | 20 | 2 | 15* | 10, 15 | 700 | 4.8 |
| Hatta et al. (1989b) | 10 | 1 | 50* | 40 | 800 | - |
| Sharma and Sahu (2019b) | 0.15 | 1 | 2.5, 5 ,7.5 ,10 | 10, 20, 40 | 500 | 8.1 |
| Caron and Wells (2009b) | 100 | 4.75 | 31* | 10, 20 | 500 | 6.9 |

Table 4.4: Results reported from various authors

| Author | Comments |
| --- | --- |
| Franco (2008) | Heat flux increase with the increase in initial temperature and with higher the jet line spacing. Lower speeds attain higher heat flux. |
| Fujimoto et al. (2015b) | The maximum heat flux increased monotonically with increasing initial temperature of the sheet. Peak heat flux is higher for larger jet velocities, and peak increase slightly with increasing mean jet velocity. The critical heat flux is higher for larger sheet velocity. |
| Fujimoto et al. (2014) | Heat flux is large for higher temperature of solid. Heat flux increase with the increase in the sheet velocity. The peak value of heat flux shifts upstream as jet velocity increases. |
| Fujimoto et al. (2016) | Heat flux increases with an increase in initial temperatures up to a certain value. Still, it decreases after a temperature where it is close to the minimum heat flux point for two jets. The size of wetting areas in width direction reduced as the nozzle spacing decreased, indicating total heat removal depends on nozzle spacing. |
| Chen et al. (1991b) | Heat flux increases with increase in initial temperature. The heat transfer coefficient remains the same for both stationary and moving. Heat flux values are higher in moving compared to stationary cases. |
| Morisawa et al. (2018) | Maximum heat flux for the upward jets increases with an initial increased temperature of solid. Critical heat flux increased for large jet impact velocities or smaller sheet velocities for upward jets. The steel plate's temperature drop for a downward-imping jet was more significant than that for the upward jet because of the residual liquid. |
| Leocadio (2018) | Heat flux increases with increase in initial temperature. Higher radial velocity yields higher heat transfer capacity. |
| Jha et al. (2016) | With the increasing jet velocity and plate speed, critical heat flux increases initially, attains maximum value and then decreases. The cooling rate decreases monotonically by increasing the amplitude of oscillation. |
| Gradeck et al. (2009a) | Heat flux is maximum at the stagnation point, and it decreases when it moves away from the stagnation point. Heat flux increases with increase in sub cooling temperature. Critical heat flux increase with increase in plate velocity. |
| Sharma and Sahu (2019b) | With the increase in the plate velocity, the local surface temperature decreases in the upstream direction and increases in the downstream direction. The cooling at the farthest location away from the stagnation point takes place faster with the rise in the plate velocity. Maximum heat flux increases with an increase in jet velocity. |

| Caron and Wells (2009b) | Maximum heat flux increases with an increase in water flow rate. It also increases with an increase in plate velocity, and DNB temperature shifts right. |
|---|---|
| Hatta et al. (1989b) | Tend- end temperature is high for higher plate velocities, so cooling rate is high for lower velocities. |
| Jha et al. (2015a) | On increasing the surfactant concentration, the cooling rate gradually falls. The jet cooling technique provides a higher cooling rate in comparison to air atomized spray cooling.The value of heat transfer coefficient at high surface temperature $(900°C)$ almost identical, but as the temperature decreases, significant differences are observed. |
| Wang et al. (2019b) | Maximum heat flux decrease with decrease in jet moving velocity. An increase in the impact jet angle significantly improved the heat transfer capacity of the forward-moving inclined slit jet impingement cooling process. |

Table 4.5: Conclusions of different authors

Franco (2008): The stagger between nozzles, jet line spacing and plate speed is systematically varied to investigate their effects on the cooling of hot moving steel plates. Slower moving plates tend to have higher heat flux and total heat extracted. Short distances between jet lines are found to extract more heat per unit length. At higher surface entry temperatures, heat flux increases with a decrease in temperature, consistent with transition boiling. Higher heat extraction is attained at lower speeds. Higher the jet line spacing higher the total heat extracted but, in narrow jet line spacing(25.4 $cm$) extracts more heat per unit length than the wider jet line spacing (50.8 $cm$).

Fujimoto et al. (2015b): The hydrodynamics and heat transfer characteristics of a circular water jet impinging on a heated moving surface were investigated experimentally. For initial temperatures, heat flux reached a peak at approximately $Ts=400°C$. It decreased at higher temperatures, caused by forming a vapour layer in the jet impact region, which prevented direct contact between the coolant and the solid. The maximum heat flux is not a parameter representing the total heat flux from the moving sheet to the coolant. The wetting area is much wider for larger jet velocities. The moving velocity of the sheet is seen to have a strong influence on the heat transfer characteristics in the jet impingement region. Fujimoto et al. (2014): The effects on the heat transfer characteristics of varying the initial temperature of the solid, the sheet velocity, and the mean jet velocity were examined. Heat flux is minimal in an upstream dry region, increase steeply at front edge liquid film where liquid-solid direct contact occurs, and peaks in the hydraulic jump region. Boiling bubbles also enhance heat transfer. At the lower sheet velocity, the liquid-solid contact time becomes longer, and the size of the wet area on the front side is larger. The wetting area is larger for larger jet velocity. The mean jet velocity has a small effect on peak value. Fujimoto et al. (2016): Heat flux distribution on the cooled surface estimated by inverse heat conduction analysis. This study investigates the boiling heat transfer characteristics on a hot plate cooled by multiple pipe laminar jets. The initial sheet temperature, number of jets, and distance between nozzles are varied in the experiments. The heat flux in the jet impact regions are high owing to strong nucleate boiling. At $T_s = 450$ and $500°C$, the heat flux is smaller than that at $T_s = 300$ and $350°C$ because the vapour bubbles/ films with small thermal conductivity prevent direct contact between the water and solid. In three-jet impingement, enormous local thermal stress is induced, resulting in unwanted local buckling of the sheet. A small nozzle spacing is desirable to achieve moderately uniform cooling in actual run-on-table cooling. Chen et al. (1991b): In this study, the thermal behaviour of stationary and moving metal plates cooled by a circular water jet with and without

boiling was studied. Using surface temperature measurements coupled with numerical data reduction techniques, local heat fluxes and heat transfer coefficients were evaluated. Higher surface temperature increases the speed of film propagation. Overall, heat transfer rates are higher for higher initial temperatures. The maximum heat transfer coefficient is similar for both stationary and moving cases. Overall heat transfer and cooling efficiencies for moving plates are about four times those for a stationary plate at the same initial temperature. Morisawa et al. (2018): This study experimentally investigated the cooling characteristics of a moving hot plate due to the impingement of both upward and downward jets. The peak heat fluxes for the upward- and downward- impinging jets were compared under identical jet impact velocity and cross-section of the jet at the solid surface. Leocadio (2018): This work aimed at understanding the heat transfer and boiling regimes(re-wetting, maximum heat flux, nucleate transition and film boiling) in water jet impingement quenching on a high-temperature steel surface. Higher initial temperature increases the amount of energy stored in the plate, increasing the time needed to extract energy and, thus, reducing the quench front velocities. Re-wetting temperature is used interchangeably with minimum film boiling temperature, corresponding to minimum heat flux. After the peak heat flux, the heat transfer coefficient increases due to a decrease in the number of vapour bubbles on the surface. Cooling efficiency in the impingement zone is significantly higher than in other zones. Low velocities result in larger wet areas and, thus, a higher heat removal. With increasing jet cooling, the vapour layer thickness decreases, causing an increase in re-wetting temperature and re-wetting time. A higher radial jet velocity increases bubbles removal from the surface and increases heat transfer capacity. The air concentration has no effect on heat transfer behaviour during the quenching process. Jha et al. (2016): Cooling experiments have been conducted on the moving steel/plate to correlate the independent parameters with dependent variables (cooling rate and CHF) by using a response surface methodology. An increase in water flow rate results in a corresponding increase in jet velocity. CHF is maximum at 0.43m nozzle height, after which it decreases. An increase in potential energy increase jet velocity due to its subsequent conversion into kinetic energy. The lower speed of the plate accelerates the speeding of the water layer on the surface, making the evaporation faster and thereby increasing the cooling rate and CHF. Increasing the amplitude of oscillation, the plate is exposed to air for a longer period of time, natural cooling occurs, decreasing the cooling rate and CHF. Gradeck et al. (2009a): Thermocouples are used to measure the surface temperatures. The inverse method is used to solve the heat equation. So Beck's future time steps have been implemented in his inverse code to stabilize the solution. A good comparison is obtained between the heat flux estimated through this semi-analytical solution and those estimated through the method developed by Blanc. The Leidenfrost point depends only on sub-cooling. It varies between 260 and $290°C$ for a range of sub-cooling lying between 18 and 34 $K$. The second effect is the decrease of CHF. The cooling zone begins beneath the jet and develops only downstream at the beginning of cooling. Moreover, the maximum heat transfer is not located beneath the jet and moves during the cooling. Hatta et al. (1989b): Thermocouples are used to measure the surface temperatures. The temperature history is calculated by rewriting the two-dimensional equation for non-steady heat conduction into explicit finite-difference. The effect of the plate velocity on the cooling intensity has been examined from a numerical point of view, and the result has suggested that there exists a discontinuous change in the cooling the intensity in the neighbourhood of plate velocity of 1.2 $m/min$ in the present range, which is considered to correspond to the critical velocity whether the film boiling occurs or not. Sharma and Sahu (2019b): Thermal imaging camera is used to record the surface temperatures. Local surface heat flux is higher for moving plates. It may be noted that the heat removal from the surface may depend on various factors, namely, the thickness of the test surface and nozzle diameter.

Caron and Wells (2009b): E-type subsurface thermocouples inserted from the back of the sample to measure surface temperatures. IHC algorithm used to convert the temperature history measured by the subsurface thermocouples into a boiling curve was based on Beck's function specification method.The effect of the cooling-water flow rate, water temperature, water-jet velocity, and initial sample temperature on segments of the boiling curve was investigated. Jha et al. (2015a): K-type thermocouples are used to record the surface temperature. Inverse heat conduction analysis is conducted by using the commercial inverse heat conduction software INTEMP. 2D planar model has been applied to estimate the surface heat flux. Increasing the surfactant concentration, the surface tension decreases, consequently the spread-ability of water on the surface increases.As the thermal the conductivity of surfactant is less in comparison to steel, therefore the heat transfer from the steel surface is reduced.

Wang et al. (2019b): K-type thermocouples are used to record the surface temperature. The surface heat flux and temperature calculations were performed using a one-dimensional heat equation in the thickness direction. $q_{max}$ decreased from 4.83–4.95 to 4.55–4.66 $MW/m^2$ at 15°$C$ impact angle and 15 $L/min$ water flow as the nozzle moving speed decreased from 20 to 15 $mm/s$

In the present work, many experiments have performed to study the influence of various process parameters during quenching of moving hot metal plate. Quenching water through an array of jets is impinged on the front side of the heated metal plate The temperatures are measured with the use of Infrared camera on the other side of the plate surface. These temperature are used as an input to the inverse heat conduction algorithm to find the boundary heat flux variations in space and time across the width and along the length of the moving flat plate. From the literature it is mainly observed that lot of authors have studied the heat transfer for steels and very few studied the aluminium alloy. In this study, initially we investigated four different kinds of metal to show the influence of the kind of metal. Aluminium with high thermal conductivity is preferred and experiments were performed to observe the influence of various process parameters on the heat transfer. The heat transfer is quantified and boiling curve is showed using the Eulerian steady state condition which is developed from previous work of authors.

### 4.6.3   Influence of Plate Velocity

**For 5 mm Thick Plate**

**Fig. 4.23** shows the infrared images for three different plate velocities of 5 $mm/s$, 10 $mm/s$ and 20 $mm/s$ at quasi-steady state condition of cooling time 4s from the start of the quenching process for AA6082 plate material with water jet velocity of 12 $m/s$, plate thickness of 5 mm. The infrared images clearly show the measured surface temperature distribution of the back of the quenched surface. As the cooling of metal progresses, the infrared images clearly show the horizontal and vertical movement of the wetting front. In reality, the hot plate moves from top to bottom while the full jet nozzle is kept at a stagnant position in space. The temperature distribution shows a clear affect at higher plate velocities i.e., 40 $mm/s$ on the heat extraction. As the plate velocity is lowered, the wetting front in the width direction grows and the heating effect is significantly reduced promoting the cooling of the plate. Although, the water jet velocity in all three experimental cases are maintained at $w_j = 12$ $m/s$ (Re = 12000) which typically lies in the turbulent region is relatively high in the order of $10^3$ compared to plate velocity. As we know from the physical understandings, the fluid layer in contact with the hot surface tries to dry along the plate length due to friction force. The effect of the plate velocity on the fluid motion on the hot plate can be depicted in the infrared images.

AA6082 $s = 5mm$, $T_0 = 520°C$, $T_w = 17°C$, $\alpha = 90°$, Tap water, $w_j = 12m/s$
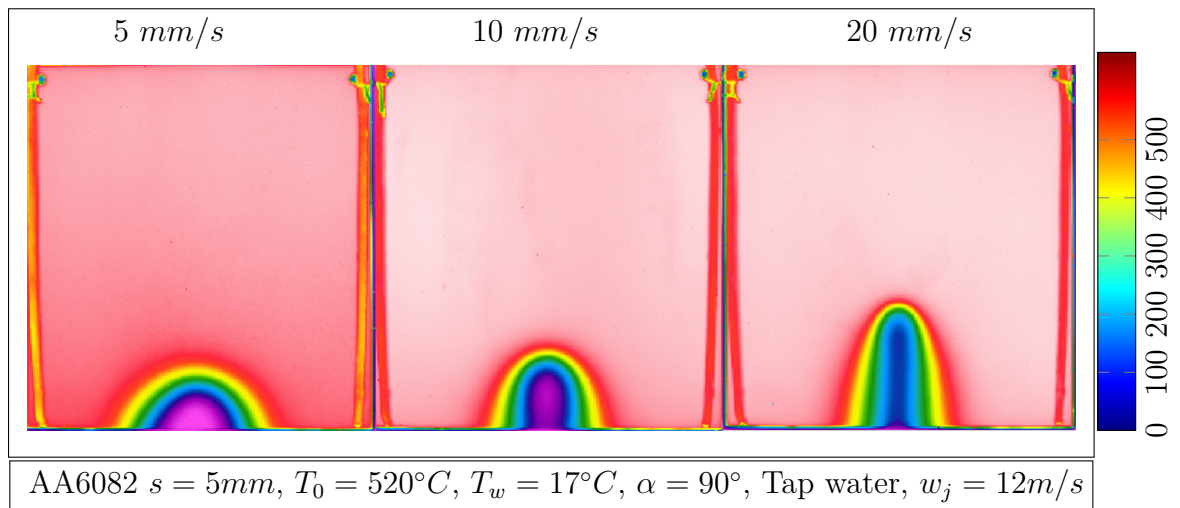
Figure 4.23: Infrared temperatures for plate velocity of 5 mm/s, 10 mm/s, 20 mm/s at quasi-steady state condition
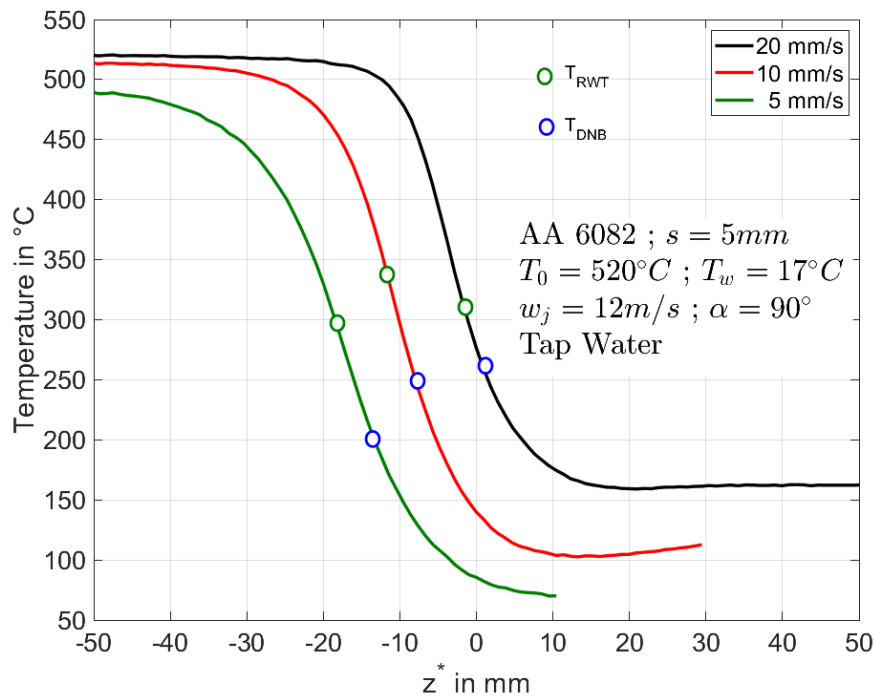


Figure 4.24: Measured surface temperature distribution for the different plate velocities at quasi-steady state

**Fig. 4.24** shows the measured surface temperature profiles at the centre vertical line of the water jet impingement position for three different plate velocities of 5 $mm/s$, 10 $mm/s$ and 20 $mm/s$ of AA6082 material for plate thickness of 5 mm and water jet velocity of 12 m/s. The temperature profiles clearly suggested the significant variation of the cooling process on the temperature distribution for higher plate velocities. The higher plate velocities show stronger effect on the end temperature of the cooling. At nozzle position $z^* = 0$ $mm$, the temperature for plate velocity of 5 $mm/s$ is 80°C which is lower compared to plate velocity of 10 $mm/s$ and 20 $mm/s$ that corresponds to 140°C and 280°C respectively. The next question is to estimate the re-wetting temperature or pre-cooling temperature, DNB temperature for the specific temperature profile of the experiment. This could be probably answered through the solution of two-dimensional inverse heat conduction method.

Although, from the temperature profiles in Fig. 4.24, we can clearly see the variation of the temperature gradient in the film boiling, transition boiling, nucleate boiling and finally in single phase convection. At higher plate velocities, the front part of the liquid film shifts downward because of the large viscous wall friction and drag forces between the cooling water and boiling vapour bubbles. In the same manner for lower plate velocities, the liquid/solid contact time becomes longer and the size of the wet area on the front side is larger. As a consequence, the temperature of the solid reduced compared to that of a higher plate velocity. This effect can be clearly seen in the surface measured temperatures as in Fig. 4.24. The position where the temperature first begins to decrease on the length of the plate can be located more upstream for the lower plate velocity. 1. The temperature is related to the position of the front part of the liquid film, which is affected by wall friction and dry forces. These forces are small where the plate velocity is low. 2. The plate moved only a shorter distance at low plate velocity, the time available to diffuse from dry region to wet side becomes significant.
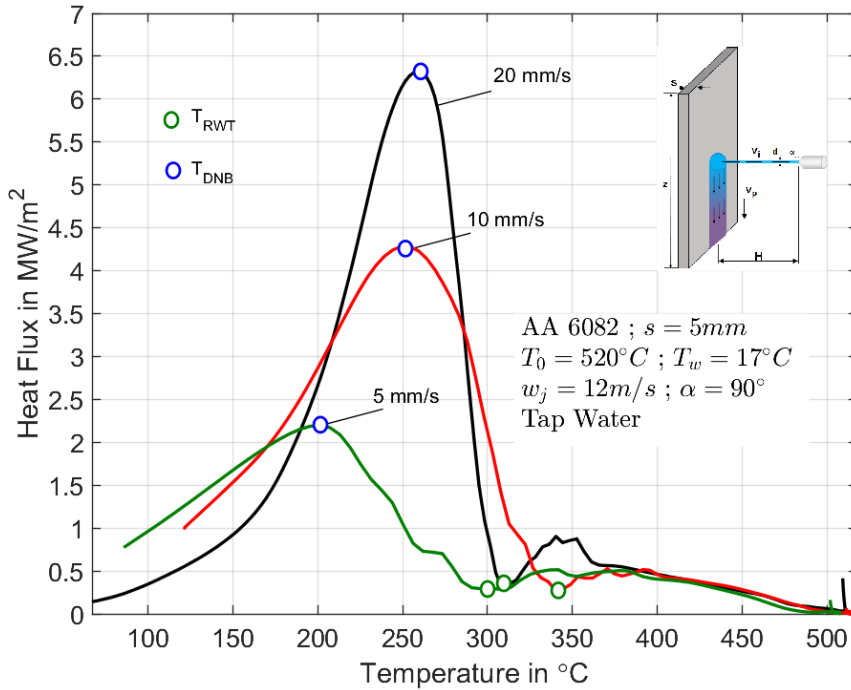


Figure 4.25: Boiling curve for the different plate velocity at quasi-steady state condition

| $w_p$ | $q_{max}$ in $MW/m^2$ | $q_{RWT}$ in $MW/m^2$ | $T_{DNB}$ in $°C$ | $T_{RWT}$ in $°C$ | $z^*_{DNB}$ in $mm$ | $z^*_{RWT}$ in $mm$ | $w_b = 0.75 * q_{max}$ in $°C$ |
|---|---|---|---|---|---|---|---|
| $5\ mm/s$ | 2.19 | 0.29 | 201 | 300 | -13.3 | -18.05 | 90 |
| $10\ mm/s$ | 4.27 | 0.26 | 254 | 340 | -7.6 | -11.4 | 90 |
| $20\ mm/s$ | 6.12 | 0.34 | 260 | 310 | 0.95 | -1.9 | 40 |

Table 4.6: Boiling parameters for influence of plate velocity on 5 mm thick plate for single full jet nozzle quenching

In **Fig. 4.25** and **Tab. 4.6**, shows the boiling trend on the quenched surface for the plate velocity of 5 $mm/s$, 10 $mm/s$ and 20 $mm/s$ at the quasi-steady state condition. The typical characteristic curve for the boiling shows that the maximum heat flux increases from 2.3 $MW/m^2$ to 6.4 $MW/m^2$ and corresponding temperature also increases from 200°$C$ to 260°$C$ respectively. Contradictorily, the width of nucleate boiling reduces for the higher

plate velocities. This affects the heat extraction from film boiling to nucleate boiling, the re-wetting temperature for higher plate velocities of 10 $mm/s$ and 20 $mm/s$. The re-wetting temperature for plate velocity of 5 $mm/s$ corresponds to 300°$C$, but whereas for the plate velocity of 10 $mm/s$ it is 340°$C$ and for plate velocity of 20 $mm/s$ it is 310°$C$. As the position of the wetting front shifts to the jet impingement position with the increase in the plate velocity significantly promotes the heat extraction to higher magnitudes. Henceforth, we can observe increase in the departure nucleate boiling temperature to higher values. The important conclusion for the increase in the maximum heat flux for the different plate velocity is mainly due to the shift in the DNB temperature towards the centre of the nozzle, while reducing the pre-cooling effect or the axial conduction from the outer region of the water impingement region. The position of the heat flux decreases downstream with the increase in the plate velocity. The width of the boiling reduces with the higher plate velocities with steep temperature exists with high maximum heat flux.

**For 10 mm Thick Plate**



AA6082 $s = 10mm$, $T_0 = 520°C$, $T_w = 17°C$, $\alpha = 90°$, Tap water, $w_j = 12m/s$
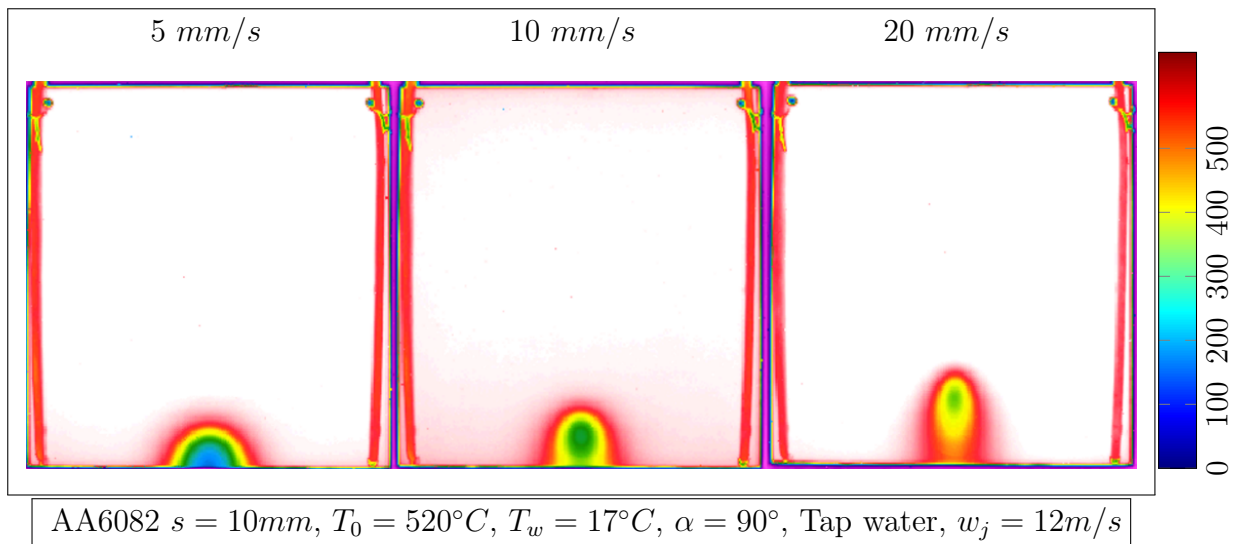
Figure 4.26: Infrared images for different plate velocities of 10 mm thick plate at quasi-steady state condition

The infrared thermal images of the 10 $mm$ thick plate for different plate velocities are shown in **Fig. 4.26**. From the thermal images, we can observe that the water jet moves further away for higher plate velocities and the wetting front also moves in both horizontal and vertical directions. Whereas for higher plate velocities, the cooling at the water impingement region is quite insignificant because of less contact time over the length of the plate. Contradictorily for lower plate velocities, the temperature at the jet impingement region is quite significant and cools the plate efficiently. The wetting front for the plate velocity of 5 $mm/s$ grows wider in the lateral direction compared to the longitudinal direction.

Figure 4.27: Measured surface temperature profiles for different plate velocities of 10 mm thick plate at quasi-steady state condition

Temperature profiles for the 10 $mm$ thick plate for different plate velocities are shown at quasi-steady state condition. The effect of reheating is stronger for higher plate velocities and the heat transfer significantly influences. The width of cooling decreases for higher plate velocities from 40 $mm$ to 10 $mm$ in the range of 5 to 20 $mm/s$ plate velocity. At nozzle position $z^* = 0$ $mm$, the temperature increases from $170°C$ to $440°C$ for 5 $mm/s$ to 20 $mm/s$ respectively. The faster plate velocity plays an insignificant role in homogeneous cooling of the plate in the longitudinal direction. The lower plate velocity promotes stronger diffusion of heat from dry region to wetting region and this effect can be seen as similar to the 5 mm thick plate. The increase of the plate velocity offers strong wall friction to the fluid motion and shifts the departure nucleate boiling near to nozzle position. For plate velocity 10 $mm/s$ and 20 $mm/s$, the departure nucleate boiling position lies exactly below nozzle position and influence of thickness can be seen with the heat conduction from the bottom affects the fluid to eject away from plate.

Figure 4.28: Boiling curve and characteristic curve for the different plate velocities of 10 mm thick plate at quasi-steady state

| $w_p$ | $q_{max}$ in $MW/m^2$ | $q_{RWT}$ in $MW/m^2$ | $T_{DNB}$ in $°C$ | $T_{RWT}$ in $°C$ | $z^*_{DNB}$ in $mm$ | $z^*_{RWT}$ in $mm$ | $w_b = 0.75 * q_{max}$ in $°C$ |
|---|---|---|---|---|---|---|---|
| 5 $mm/s$ | 4.6 | 0.34 | 274 | 402 | -9.5 | -19 | 110 |
| 10 $mm/s$ | 4.03 | 0.26 | 334 | 413 | 0 | -6.65 | 60 |
| 20 $mm/s$ | 3.7 | 0.13 | 420 | 476 | 1.9 | -2.85 | 50 |

Table 4.7: Boiling and characteristic parameters for influence of plate velocity on 10 mm thick plate for single full jet nozzle quenching

In **Fig. 4.28** and **Tab. 4.7**, the typical boiling curves for the plate thickness of 10 $mm$ of different plate velocities were shown. The heat transfer rate significantly reduces for the increase in the plate velocity, due to the reheating phenomena from the edges of the hot moving plate. Also, the higher thermal conductivity of the plate promotes the heat from the other regions to the water-cooled region which increases the temperature of the plate. The departure nucleate boiling at the corresponding maximum heat flux point also shifts to higher temperatures from $270°C$ to $420°C$ for the plate velocities of 5 $mm/s$ to 20 $mm/s$, due to insignificant cooling of the plate. The decrease in the heat flux is only about 1 $MW/m^2$. The reheating phenomena can also be observed in the surface heat fluxes for the 20 $mm/s$ and 10 $mm/s$ plate velocity at below $300°C$ and $250°C$ respectively. For plate velocity above 10 $mm/s$, 20 $mm/s$, the typical characteristic curve can be seen similar to the boiling curve of 5 $mm/s$. Approximately around $350°C$, the fluid should be in vapour phase and the heat transfer profiles for 10 and 20 $mm/s$ should not be misunderstood as boiling curve. Even though the profile looks like boiling curve, the mechanism of the heat transfer is different. The water jet velocity of 12 $m/s$ impinges on the hot metal of 10 mm promotes the stronger ejection of water droplets with the higher enthalpy at higher temperature. The new incoming liquid at the stagnation point further promotes the rise in the enthalpy of the fluid and heat transfer rate increases. This should be the reason for the

maximum heat flux peak at 340 and 430°$C$ for 10 $mm/s$ and 20 $mm/s$ respectively but the heat flux intensity is lower compared to the 5 $mm/s$.

### 4.6.4   Influence of Water Jet Velocity

**For 5 mm Thick Plate**



AA6082 $s = 5mm$, $T_0 = 540$°$C$, $T_w = 17$°$C$, $\alpha = 90$°, Tap water, $w_p = 10mm/s$
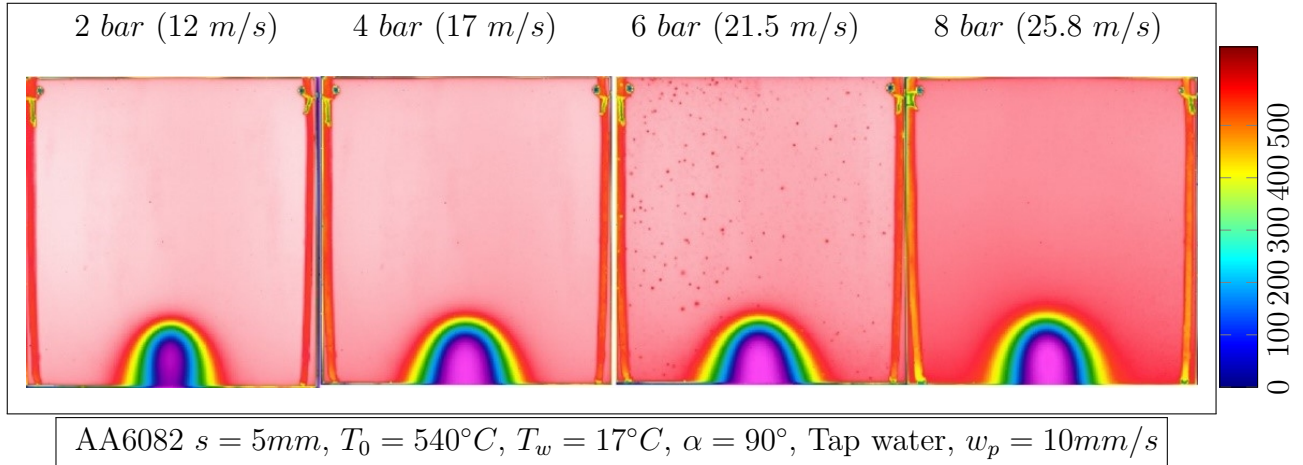
Figure 4.29: Infrared images for different water jet velocity at quasi-steady state condition of 5 mm thick plate

**Fig.   4.29**, shows the infrared images for four different water jet velocities for 5 $mm$ thick plate at quasi-steady state condition.  The wetting front in the width direction increases slight consistently from 2 $bar$ to 4 $bar$ water pressure, whereas for higher water jet velocity the width remains constant. The wet area is considerably larger for the larger jet velocity, which is associated with greater impact inertia of the jet. Consequently, the low-temperature area on the reverse side is wider, and the front side of the low-temperature area shifts upstream.  The peak value of heat flux shifts upstream as Vj increases.  In addition, the mean jet velocity has a small effect on the peak value. The peaks are located near the front wet edge where the apparent bulk velocity of the liquid in the x-direction is very small.

Figure 4.30: Measured surface temperature profiles for different water jet velocities at quasi-steady state condition of 5 mm thick plate

From the **Fig. 4.30**, temperature profiles for different water jet velocities of $12\ m/s$, $17\ m/s$, $21.5\ m/s$ and $25.8\ m/s$ were studied. The temperature profiles attain steady state for water jet velocity of $17\ m/s$ and $21.5\ m/s$, but for jet velocity of $25.8\ m/s$ temperature increase only slightly. The pre-cooling effect is stronger for higher water jet velocity in comparison with lower jet velocity. At the nozzle position i.e., $z* = 0\ mm$, the temperature seems to be constant at about 110° for higher jet velocities and whereas for lower jet velocity it is about 140°.

Figure 4.31: Boiling curve for different water jet velocities at quasi-steady state condition of 5 mm thick plate

| $w_j$ | $q_{max}$ in $MW/m^2$ | $q_{RWT}$ in $MW/m^2$ | $T_{DNB}$ in $^\circ C$ | $T_{RWT}$ in $^\circ C$ | $z^*_{DNB}$ in $mm$ | $z^*_{RWT}$ in $mm$ | $w_b = 0.75 * q_{max}$ in $^\circ C$ |
|---|---|---|---|---|---|---|---|
| 12 $m/s$ | 4.3 | 0.26 | 254 | 340 | -8.55 | -12.35 | 80 |
| 17 $m/s$ | 5.57 | 0.23 | 268 | 358 | -15.2 | -17.1 | 80 |
| 26 $m/s$ | 5.75 | 0.22 | 269 | 358 | -15.2 | -19.95 | 80 |

Table 4.8: Boiling parameters for influence of water jet velocity on 5 mm thick plate for single full jet nozzle quenching

**Fig. 4.31** and **Tab. 4.8**shows the characteristic boiling curve for different water jet velocities at quasi-steady state condition. The jet velocity has stronger effect on heat extraction and remains almost constant for increase in higher jet velocities. The corresponding maximum heat flux is 4.3 $MW/m^2$ for 12 $m/s$ and for 17 to 26 $m/s$ it is nearly constant at 5.7 $MW/m^2$. The departure nucleate boiling increases from $250^\circ C$ to $280^\circ C$ for 12 to 26 $MW/m^2$ respectively. However, the re-wetting temperature at the wetting front remains consistently at $350^\circ C$.

**For 10 mm Thick Plate**
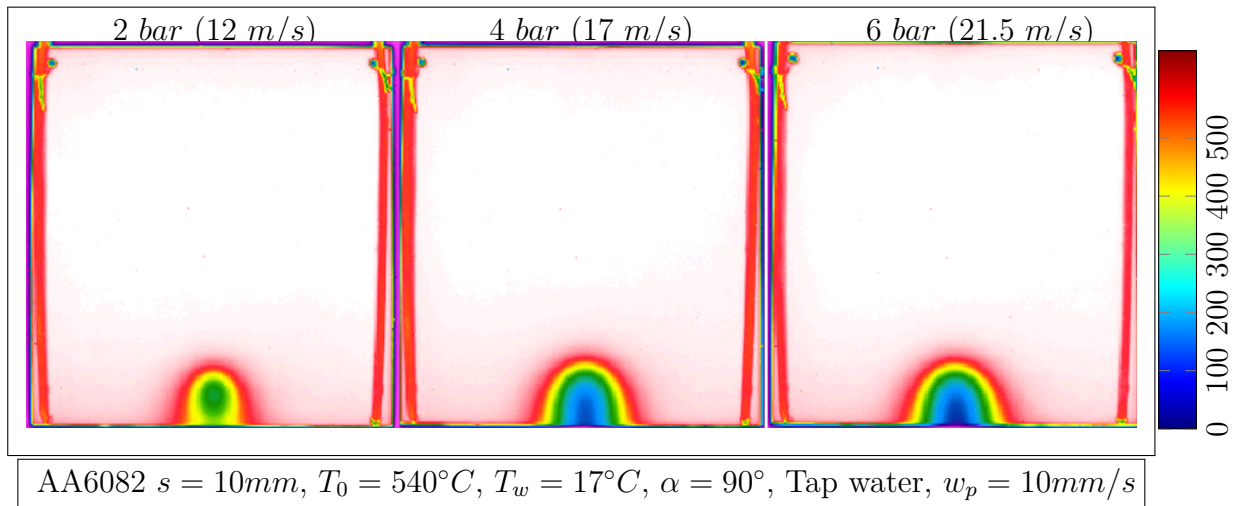


Figure 4.32: Infrared images for different water jet velocities of 10 mm thick plate at quasi-steady state condition

In **Fig. 4.32**, the thermal images from the infrared camera for 10 $mm$ thick plate is seen and from the images we can clearly observe the growth of wetting front for increase in the water jet velocities. Correspondingly, the higher water jet velocity accounts for increase in the temperature gradient at the water jet impingement which further increases the cooling efficiency and heat transfer.
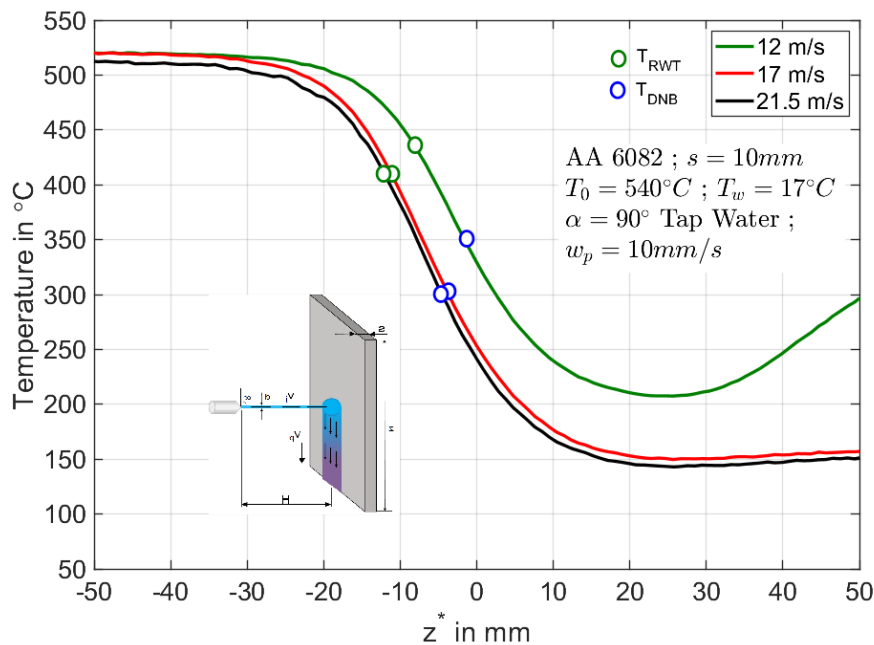


Figure 4.33: Measured surface temperature profiles for the different water jet velocities of 10 mm thick plate at quasi-steady state condition

**Fig. 4.33** shows the surface temperature for different water jet velocities of 10 $mm$ thick plate at quasi-steady state condition. From the temperature profiles, it is clear that the higher jet velocity cools the plate faster with larger thermal gradient in the impingement

region.  The temperature at the nozzle position i.e.  $z* = 0\ mm$ for $12\ m/s$ corresponds to $330°C$ and lowers for higher jet velocities of about $250°C$.  In the lower jet velocity of $12\ m/s$, the effect of reheating is stronger and the increase in the temperature can be seen clearly below $20\ mm$ of the plate length.
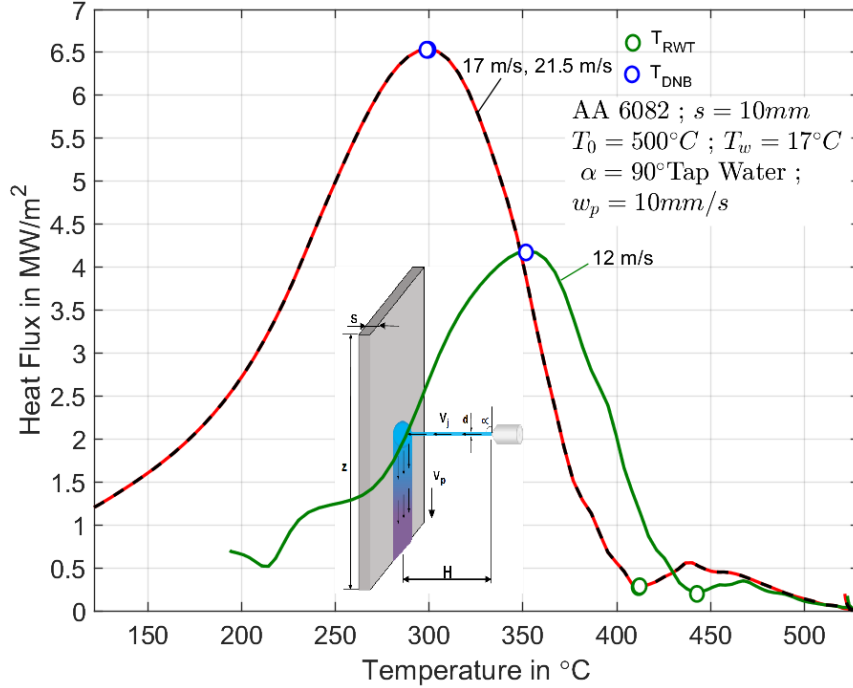


Figure 4.34:  Boiling curve and characteristic curve for different water jet velocities of 10 mm plate thick at quasi-steady state condition

| $w_j$ | $q_{max}$ in $MW/m^2$ | $q_{RWT}$ in $MW/m^2$ | $T_{DNB}$ in $°C$ | $T_{RWT}$ in $°C$ | $z^*_{DNB}$ in $mm$ | $z^*_{RWT}$ in $mm$ | $w_b = 0.75 * q_{max}$ in $\circ C$ |
|---|---|---|---|---|---|---|---|
| $12\ m/s$ | 4.18 | 0.21 | 352 | 444 | -1.9 | -8.55 | 70 |
| $17\ m/s$ | 4.27 | 0.27 | 300 | 412 | -3.8 | -11.4 | 150 |
| $26\ m/s$ | 6.53 | 0.27 | 300 | 310 | 0.95 | -1.9 | 150 |

Table 4.9:  Boiling and characteristic parameters for influence of plate velocity on 10 mm thick plate for single full jet nozzle quenching

Boiling curve for different water jet velocities for $10\ mm$ thick plate are shown in **Fig. 4.34** and **Tab. 4.9**.  From the boiling curve we can clearly see the increase in the heat flux intensity for higher water jet velocities at quasi-steady state condition.  The shift in the departure nucleate boiling takes place from $350°C$ to $300°C$ for 2 *bars* to 4 and 6 *bars* respectively.  From these results, we clearly understand the direct relation between the water jet velocity and the heat flux extraction rate.  Significantly, the re-wetting temperature also shifts towards the lower temperatures for higher water jet velocities.

### 4.6.5  Influence of Initial Temperature of the plate



| 250°C | 350°C | 450°C | 520°C |

AA6082 $s = 5mm$, $T_w = 17°C$, $w_j = 12m/s$, $\alpha = 90°$, Tap water, $w_p = 10mm/s$
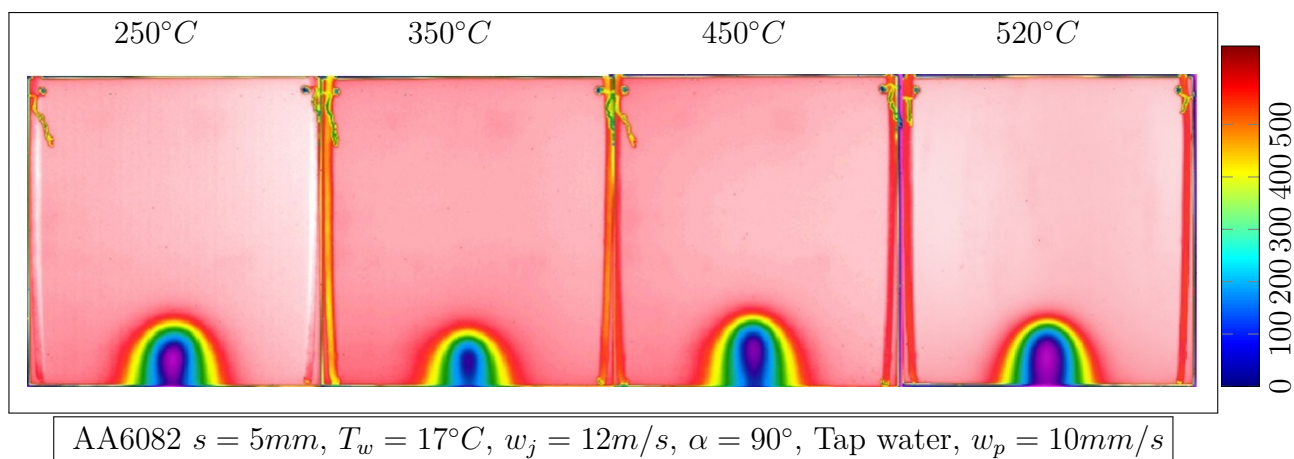
Figure 4.35: Infrared images of different initial temperature of the plate at quasi-steady state condition

In **Fig.  4.35**, we can clearly see the infrared images recorded for different initial temperature of the plate at quasi-steady state condition. The infrared camera images at quasi-steady condition suggests that the temperature distribution varies for every start temperature of the plate. The cause for the fluctuation is difficult to explain and the further investigation of the surface temperature should be analysed further.

At this liquid film is formed near the impact point. The thin film area is small on the upstream side and expands in the downstream region. A bow-shaped hydraulic jump is observed on the upstream side. The liquid film is thick at its periphery. As expected, the area outside the hydraulic jump is dry. The initial temperature of the solid is higher then the saturation temperature of water, and boiling vapour bubbles are seen at the liquid/solid interface. Some dry are appear in the thin liquid film as indicated by the circle. These areas are formed due to the bursting of boiling vapour bubbles whose sizes are almost the same as the film thickness The abrupt heating of water at the front edge gives rise to the rapid formation of the vapour bubbles, which are transported downstream by the sheet motion. The drag forces of the bubbles acting on the liquid works in the direction of motion. Because the bubble increase in size and number with increase in the initial temperature of the solid, the drag force increases as well. As a consequence, the front edge of the liquid is located closer to the jet impact point. The presence of the boiling vapour bubbles also prevents the expansion of the width of this liquid film.

Figure 4.36: Measured surface temperature profiles for different initial temperature of the plate at quasi-steady state condition

From **Fig. 4.36**, it can be clearly seen that the start temperature of the plate is increased from $250°C$ to $520°C$. The temperature profiles indicate that cooling is more effective as the start temperature of the plate reduces, whereas the for start temperature of $350°C$ and $520°C$ temperature gradient in the nozzle impingement position remains constant. The reason for the similar cooling tendency is difficult to explain and further understanding of the heat transfer should be made.



Figure 4.37: Boiling curve for different initial temperature of the plate at quasi-steady state condition

| $T_{in}$ | $q_{max}$ in $MW/m^2$ | $q_{RWT}$ in $MW/m^2$ | $T_{DNB}$ in °C | $T_{RWT}$ in °C | $z^*_{DNB}$ in $mm$ | $z^*_{RWT}$ in $mm$ | $w_b = 0.75 * q_{max}$ in °C |
|---|---|---|---|---|---|---|---|
| 250°C | 1.27 | 0.03 | 164 | 220 | -25.58 | -31.35 | 50 |
| 450°C | 3.01 | 0.18 | 214 | 290 | -12.35 | -17.1 | 70 |
| 520°C | 4.5 | 0.3 | 227 | 305 | -7.6 | -11.4 | 70 |

Table 4.10: Boiling parameters for influence of initial temperature on 5 mm thick plate for single full jet nozzle quenching

In **Fig. 4.37** and **Tab. 4.10**, shows the typical boiling curve for different initial temperature of the plate at quasi-steady state condition. The maximum heat transfer increases with the initial temperature of the plate. The DNB temperature for 350°C and 520°C start temperature is almost constant at 230°C. This could be the reason for the similar temperature gradient at the nozzle impingement position. The re-wetting temperature decreases from 300°C to 220°C for start temperature of 520°C to 250°C.

### 4.6.6 Influence of Thickness of the Plate



AA6082 $T_0 = 540°C$, $T_w = 17°C$, $w_j = 12m/s$, $\alpha = 90°$, Tap water, $w_p = 10mm/s$
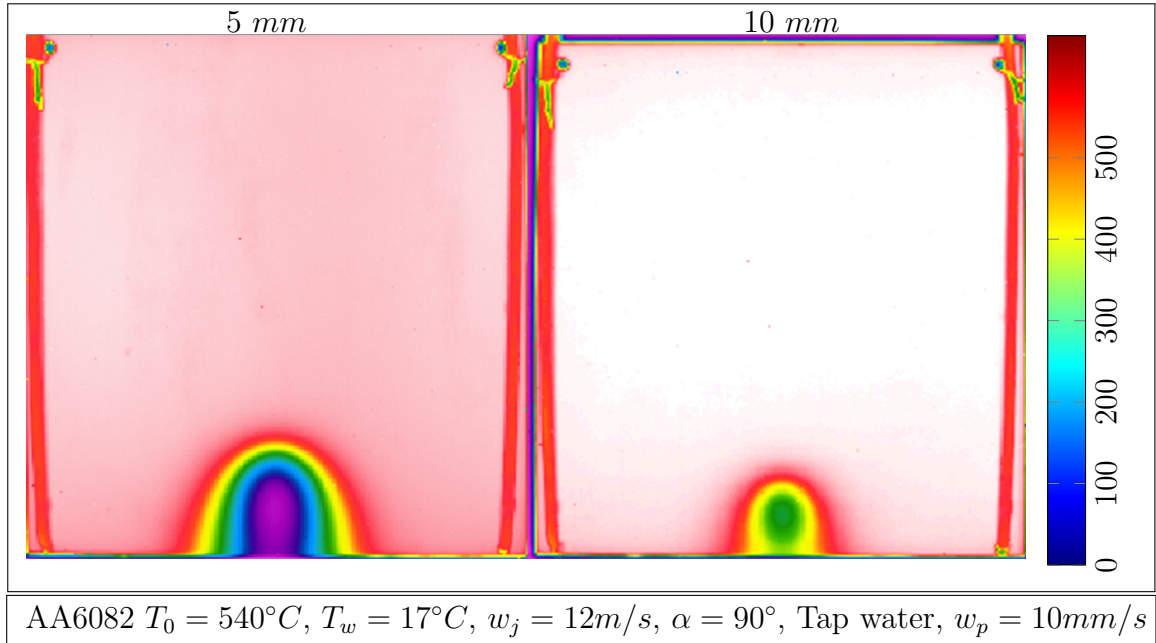
Figure 4.38: Infrared images of different thickness of the plate at quasi-steady state condition

**Fig. 4.38** depicts the infrared images for different thickness of the plate at quasi-steady state condition. The infrared images clearly shows the effect of plate thickness on the spatial temperature distribution in both width and length direction. For 5 mm plate thickness, the uniform temperature drop takes place at the nozzle or water jet impingement region. Whereas for 10 mm plate thickness, the reheating effect can be seen in the lower portion of the nozzle impingement region.
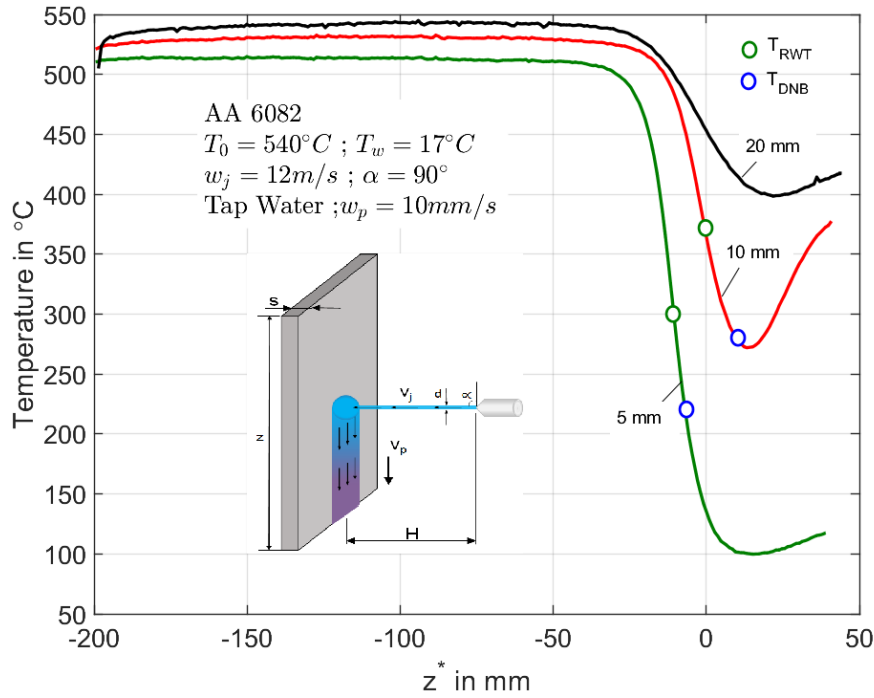
Figure 4.39: Measured surface temperature profiles for different thickness of the plate at quasi-steady state condition

**Fig. 4.39**, shows the surface temperature profiles for different thickness of the plate at quasi-steady state condition. From the temperature distribution, we clearly understand that the increase in plate thickness, the temperature of the plate is higher because of increase in thermal energy of the body. The plate thickness of 5 $mm$ cools faster, since it possesses lower thermal energy compared to higher plate thickness. The effect of reheating is stronger for higher plate thickness as seen from the temperature profile of 10 $mm$ thick plate in the range of $0 - 30$ $mm$.
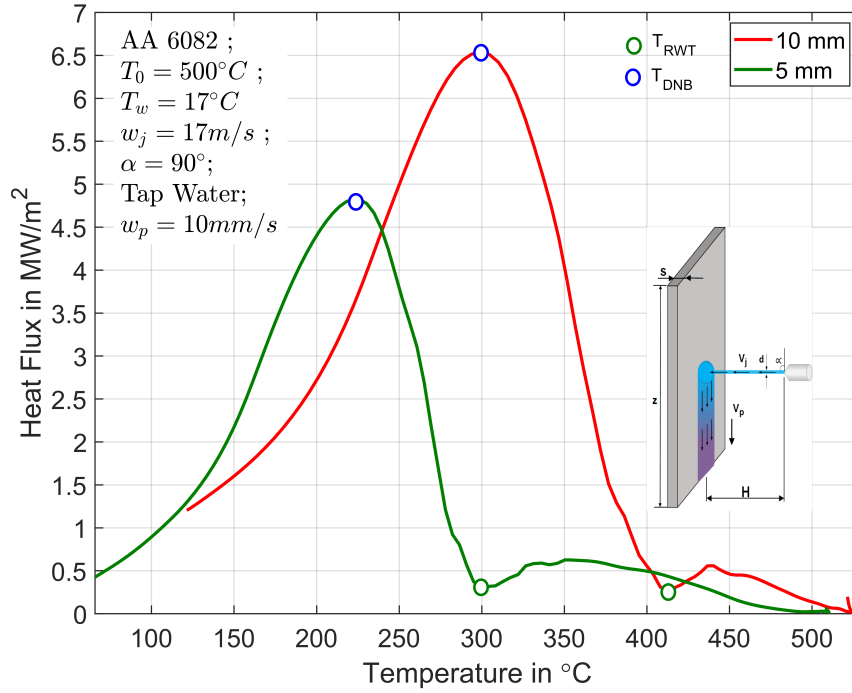
Figure 4.40: Boiling curve and characteristic curve for different plate thickness at quasi-steady state condition

| $s$ | $q_{max}$ in $MW/m^2$ | $q_{RWT}$ in $MW/m^2$ | $T_{DNB}$ in $°C$ | $T_{RWT}$ in $°C$ | $z^*_{DNB}$ in $mm$ | $z^*_{RWT}$ in $mm$ | $w_b = 0.75 * q_{max}$ in $°C$ |
|---|---|---|---|---|---|---|---|
| 5 $mm$ | 4.82 | 0.3 | 201 | 300 | -6.65 | -10.45 | 70 |
| 10 $mm$ | 5.9 | 0.38 | 272 | 371 | 12.35 | -0.95 | 110 |

Table 4.11: Boiling and characteristic parameters for influence of plate thickness for single full jet nozzle quenching

From **Fig. 4.40** and **Tab. 4.11**, we can clearly see the characteristic boiling curve for 5 $mm$ and 10 $mm$ plate thickness at quasi steady state condition. The boiling curve indicates the shift in the maximum heat flux and its corresponding temperature from 4.9 $MW/m^2$ to 6.5 $MW/m^2$ and $230°C$ to $300°C$ respectively. The re-wetting temperature also gets shifted from $300°C$ to $410°C$ for 5 $mm$ and 10 $mm$ respectively. The direct relation between the stored thermal energy to the extracted thermal energy and physically which makes sense.
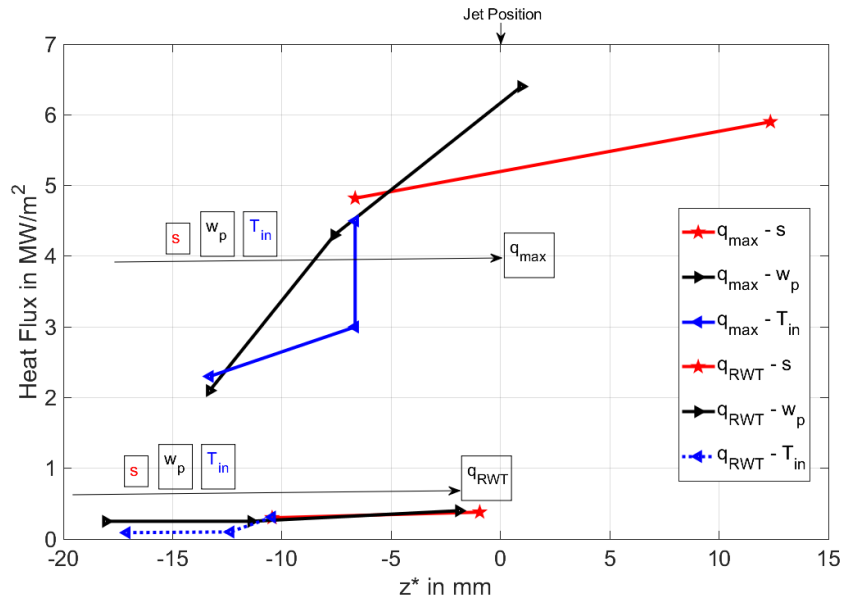
Figure 4.41: Heat flux with respect to nozzle position for different process parameters

**Fig. 4.41** shows the influence of the heat flux for different process parameters such as $w_j$, $s$, $w_p$, $T_{in}$ with respect to nozzle position. The heat transfer intensity increases for increasing the plate thickness, plate velocity, and initial temperature and shifts toward the nozzle position and in some cases below nozzle position up to 10 mm from jet position. To obtain the high heat transfer rate with the reduction of the pre-cooling region, the increase in the initial temperature, plate velocity should be solution and with decrease in the above said parameters promotes stronger heat diffusion while pre-cooling width, maximum heat flux reduces significantly. Consequently, the re-wetting heat flux remains constant at 0.5 $MW/m^2$ irrespective of process parameters.
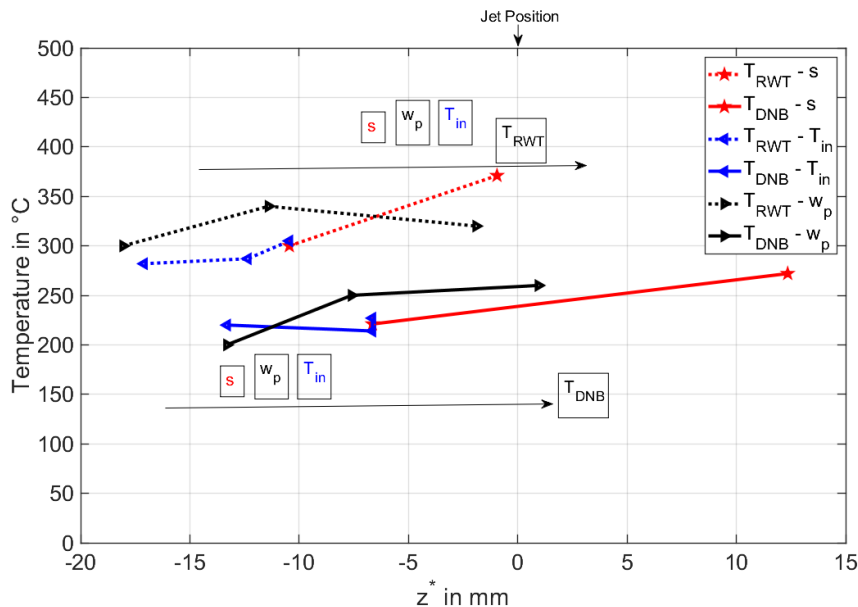


Figure 4.42: Temperature with respect to nozzle position for different process parameters

**Fig. 4.42** shows the temperature variation with respect to the nozzle position for the different process parameters. Irrespective of the process parameters such as $w_p$, $s$, $T_in$ the temperature remains constant and for higher magnitude the position of the temperature shifts towards the nozzle position while the temperature remains to be same. The departure nucleate boiling for all the process parameters lies around $200°C$ with $\pm 50°C$ and for the

re-wetting temperature the magnitude is about $300°C \pm 50°C$ and shifts the location to the nozzle position.

The influencing process parameters from the literature are studied in comparison with the present work and the detailed description and the heat flux profiles are listed.
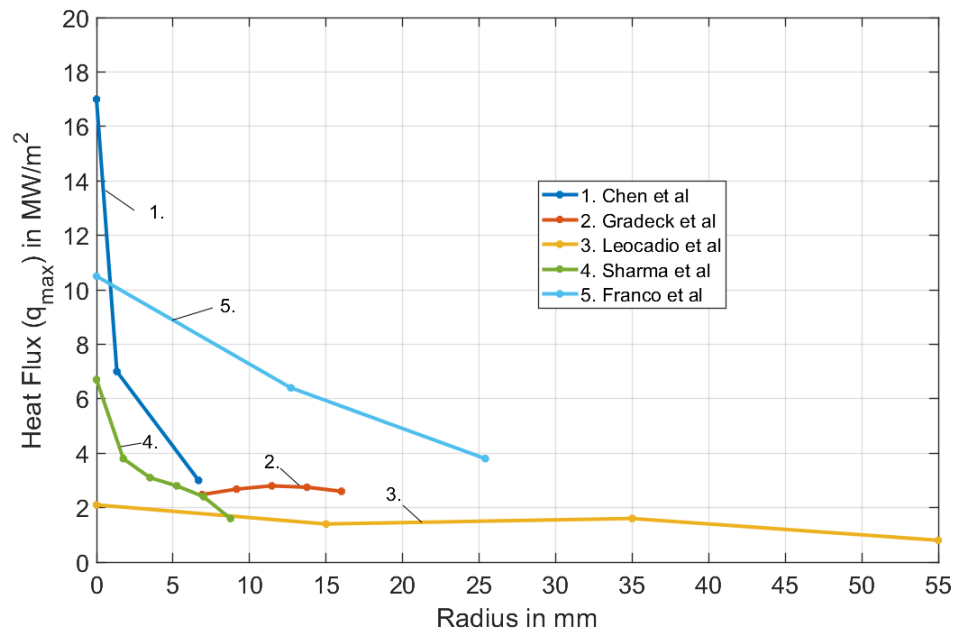


Figure 4.43: Comparison of maximum heat flux values with distance from stagnation point

**Fig. 4.43** shows the heat flux variation with respect to the radius i.e., distance from the nozzle position. The various authors report the heat flux values differently based on their respective experimental conditions. Interestingly, the maximum heat flux for all the heat flux profiles lies at the stagnation position or the nozzle impingement position. The heat transfer intensity decreases drastically from higher magnitude (16, 10, 7 $MW/m^2$) to below 4 $MW/m^2$ within 10 mm from the nozzle position. Thus, it can be understood that the nozzle position is the most influencing parameter for the heat transfer extraction from the plate.
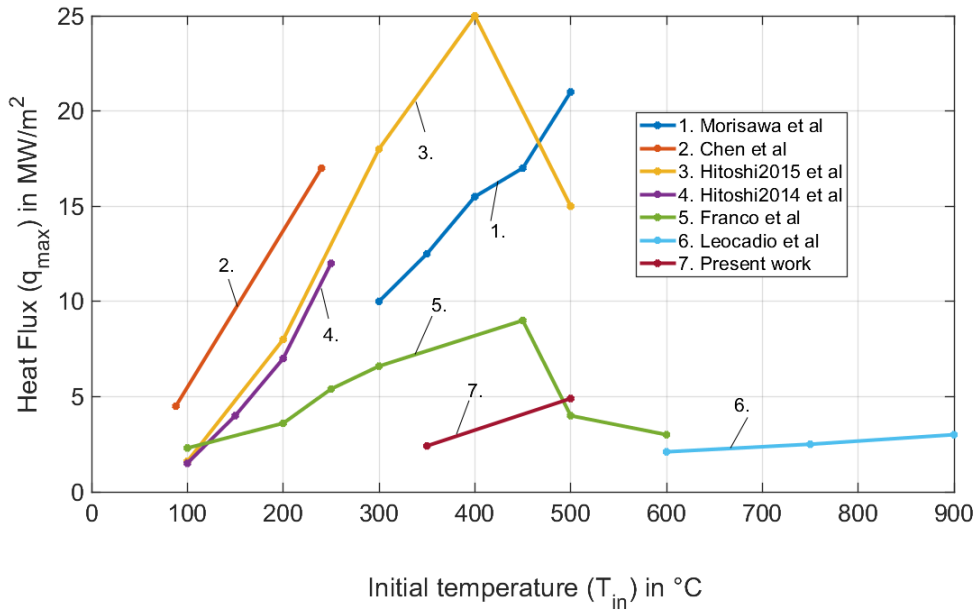
Figure 4.44: Comparison of maximum heat flux values with initial temperatures of the plate

**Fig. 4.44** shows the comparison of the maximum heat flux with the initial temperature of the plate at the jet impingement position. From the heat flux profiles, we can observe that the heat flux increases as reported from all the authors in the literature. The main reason for this should be the increase in the rate of vaporization at high temperature, promotes the faster propagation of the wetting front or in other words the position of the heat flux shifts to nozzle position since the pre-cooling region can be reduced with the continuos ejection of the vapour generated.
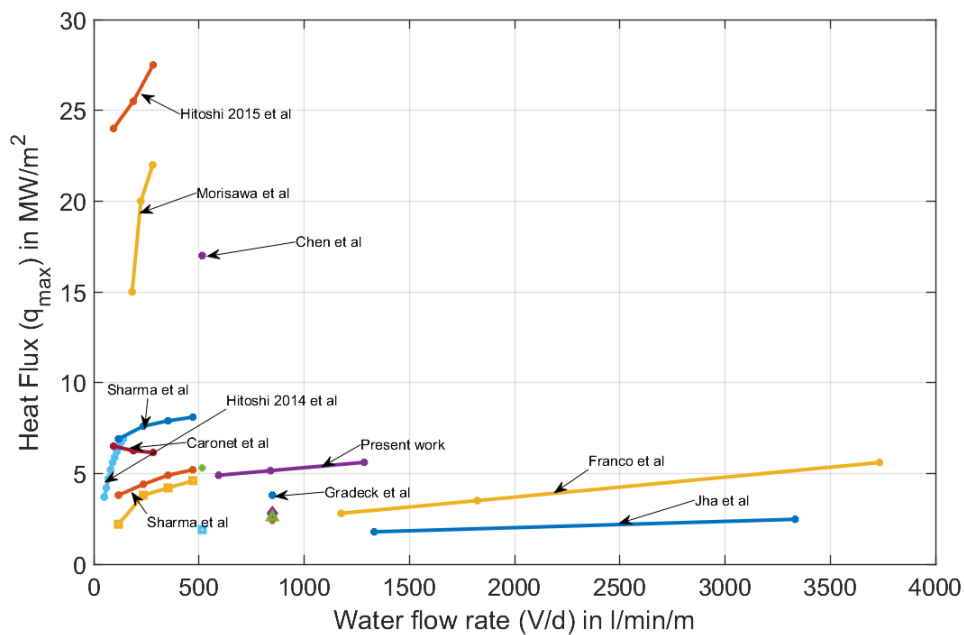


Figure 4.45: Comparison of maximum heat flux with water flow rate

**Fig. 4.45** shows the variation of the heat flux with respect to the water flow rate from different authors shows a slight variation in the magnitude of the maximum heat flux as

similar to the fixed plate condition. Even though the higher water flow rates promote stronger pre-cooling region, the heat conduction from the dry region to the wet region should influence the magnitude of the peak heat flux value. Although the higher momentum tends to increase fresh incoming fluid into the water impingement region and thus the heat transfer intensity increases.
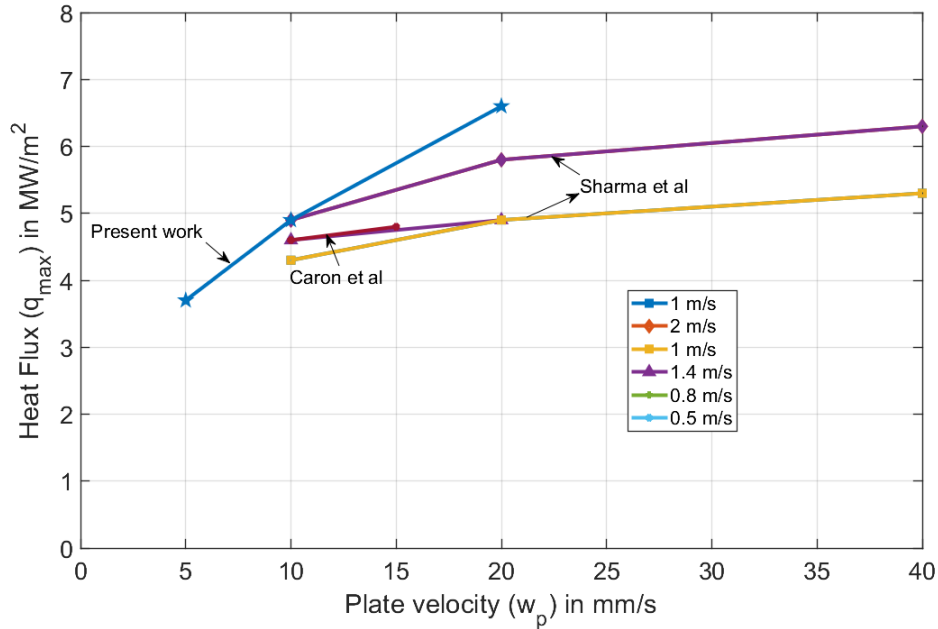


Figure 4.46: Comparison of maximum heat flux for different plate velocities up to 40 $mm/s$
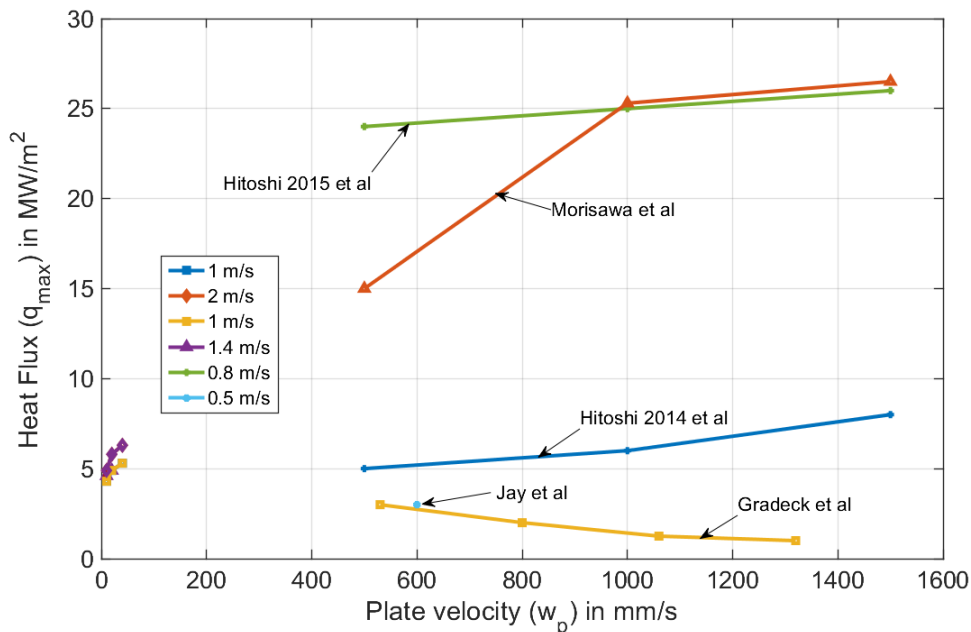


Figure 4.47: Comparison of maximum heat flux for different plate velocities up to 1600 $mm/s$

**Fig. 4.46** and **Fig. 4.47** shows the variation of the maximum heat flux with respect to the different plate velocities from the literature. Both the profiles shows the influence of the maximum heat flux on the heat transfer intensity up to 1500 $mm/s$. In the Fig. 4.46 the heat transfer intensity increases from 4 $MW/m^2$ to above 6 $MW/m^2$ about 1.5 times

the lower plate velocity. From Fig. 4.47, we can also observe the same increase in heat transfer intensity of about 1.5 times in case of higher plate velocities i.e., 1500 $mm/s$.

### 4.6.7   Influence of Material

**Nickel Material**
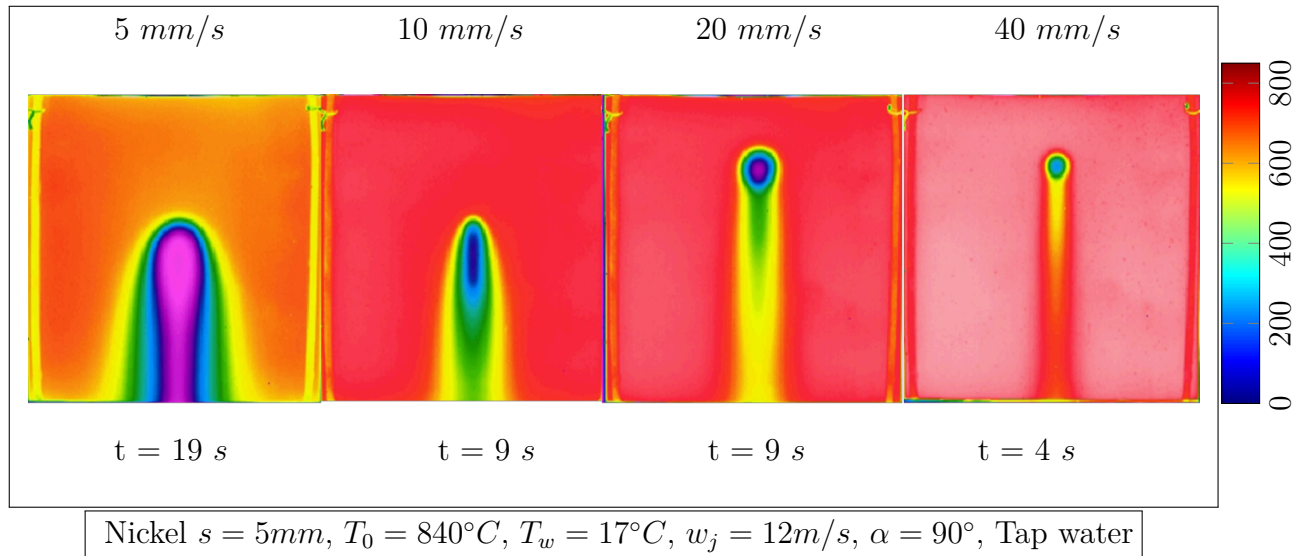


Figure 4.48: Infrared images for nickel material of different plate velocities at quasi-steady state

Infrared images for different plate velocities in case of 5 mm thick nickel material were shown in **Fig. 4.48**. The thermal images clearly indicates the surface temperature distribution and we can clearly observe the stronger cooling takes place in case of 5 $mm/s$, 10 $mm/s$ whereas for lower plate velocities the cooling shows no influence on the surface temperature of the plate.
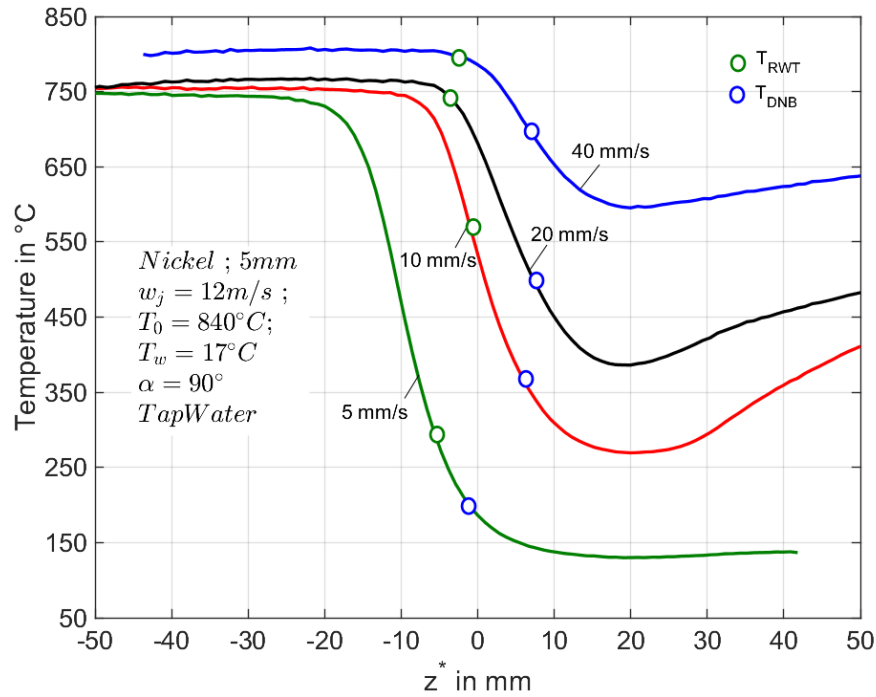
Figure 4.49: Measured surface temperatures for nickel material of different plate velocities at quasi-steady state

Surface temperature for four different plate velocities 5, 10, 20, and 40 $mm/s$ are depicted in the **Fig. 4.49**. The lower plate velocities shows better cooling behaviour in the water impingement region compared to the higher plate velocities. The end temperatures increases from $140°C$, $260°C$, $380°C$ and $580°C$ for plate velocities 5, 10, 20, and 40 $mm/s$ respectively.
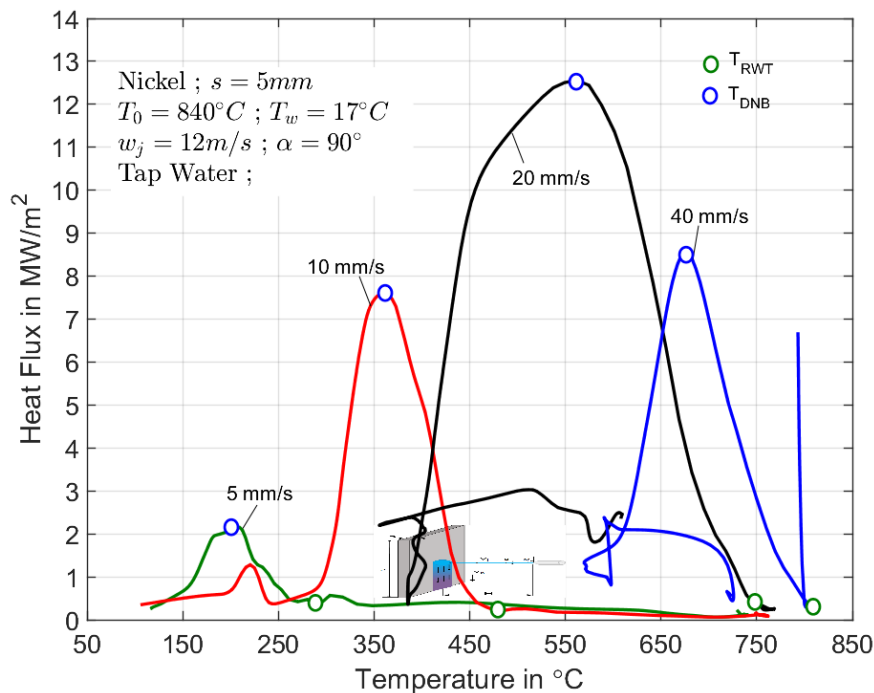


Figure 4.50: Boiling curve and characteristic curves for nickel material of different plate velocities at quasi-steady state

Boiling curve for the different plate velocities at quasi-steady state condition for nickel material of 5 mm thick plate in the **Fig. 4.50** and **Tab. 4.12**. The heat flux profiles clearly shows the shift in the maximum heat flux from lower temperature i.e., $206°C$ to $676°C$ for 5 $mm/s$ to 40 $mm/s$ respectively as depicted in the following **Tab. 4.12**

| $w_p$ | $q_{max}$ in $MW/m^2$ | $q_{RWT}$ in $MW/m^2$ | $T_{DNB}$ in $°C$ | $T_{RWT}$ in $°C$ | $z^*_{DNB}$ in $mm$ | $z^*_{RWT}$ in $mm$ | $w_b = 0.75 * q_{max}$ in $°C$ |
|---|---|---|---|---|---|---|---|
| 5 $mm/s$ | 2.15 | 0.33 | 206 | 291 | -0.95 | -5.7 | 50 |
| 10 $mm/s$ | 7.6 | 0.19 | 361 | 480 | 6.65 | 1.9 | 50 |
| 20 $mm/s$ | 12.55 | 0.38 | 561 | 750 | 4.75 | -4.75 | 170 |
| 40 $mm/s$ | 8.56 | 0.172 | 676 | 812 | 8.55 | -2.85 | 50 |

Table 4.12: Boiling and characteristic parameters for influence of plate velocities for single full jet nozzle quenching in case of nickel material

**Nicrofer Material**

Infrared images for the nicrofer material of 5 mm thick material for various water jet velocities were shown in **Fig. 4.51**. The wetting front propagation propagates faster in case of 12 $m/s$ compared to 8.6 $m/s$ since the higher water flow rates clearly dominates the cooling of the plate in width direction. The internal heat conduction lowers due to the lower thermal conductivity of the nicrofer material.
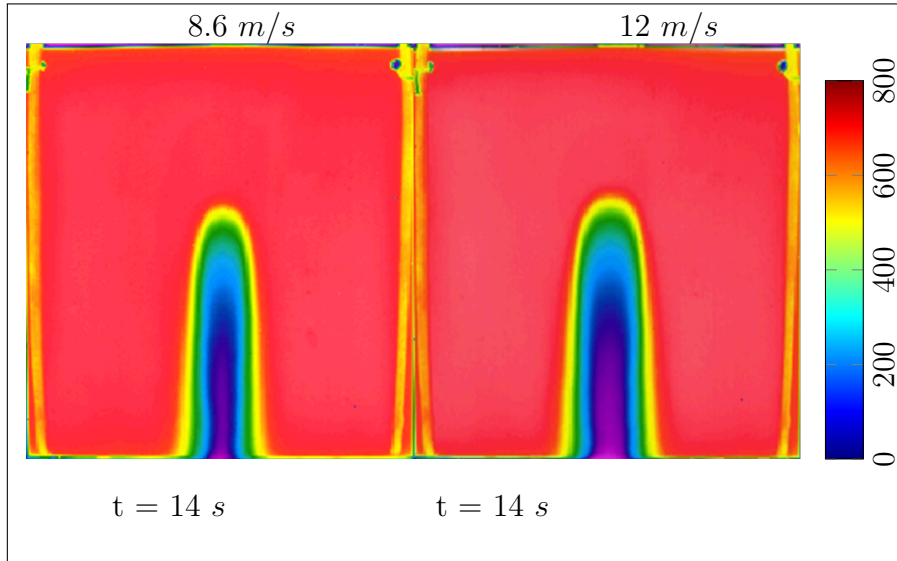


Nicrofer $s = 5mm$, $T_0 = 800°C$, $T_w = 17°C$, $w_j = 12m/s$, $\alpha = 90°$, Tap water, $w_p = 10mm/s$

Figure 4.51:  Infrared images for nicrofer material of different water jet velocities at quasi-steady state - 5 mm thick plate
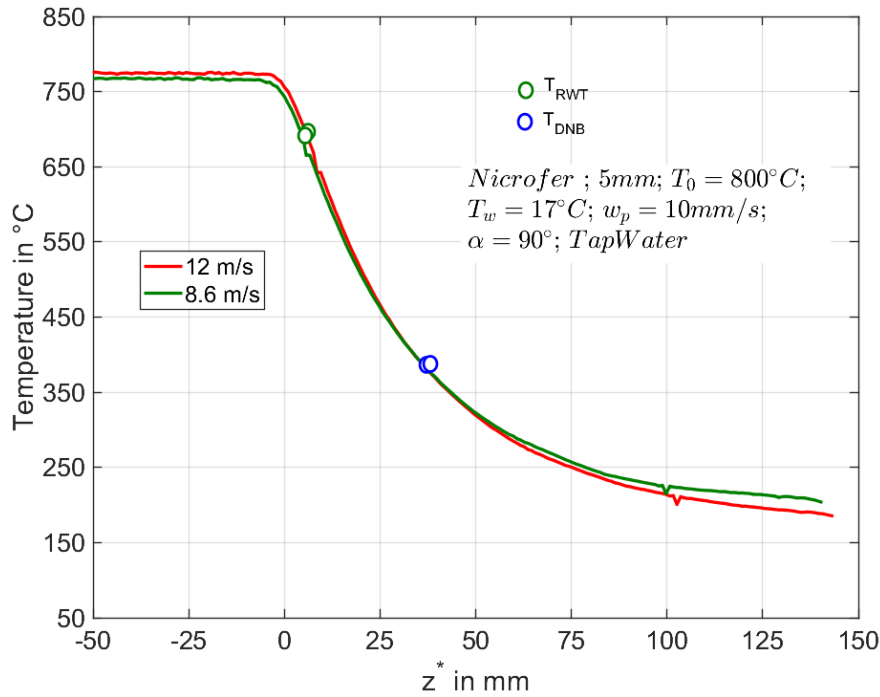
Figure 4.52: Measured surface temperatures for nicrofer material of different water jet velocities at quasi-steady state - 5 mm thick plate

Surface temperature for nicrofer material at quasi-steady state for two different water jet velocities shown in **Fig. 4.52**. The temperature drop in the water impingement region shows a constant temperature drop for two water jet velocities i.e., 8.6 $m/s$ and 12 $m/s$. The water impingement region was the main focus of this study and the heat transfer in the wetting front region should affect the overall heat transfer of the plate.
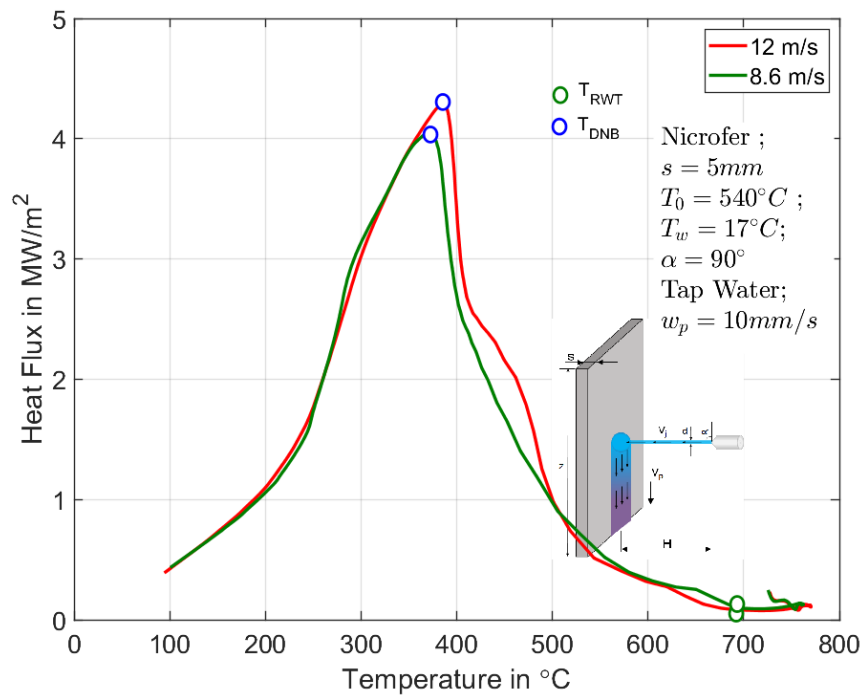


Figure 4.53: Characteristic curves for nicrofer material of different water jet velocities at quasi-steady state - 5 mm thick plate

**Fig. 4.53** and **Tab. 4.13** depicts the boiling curves and boiling parameters for the influence of different water jet velocities in case of nicrofer material with 5 mm thick plate. The boiling curves shows a similar tendency and the heat flux extraction are almost same for the two different water jet velocities i.e., 8.6 $m/s$, 12 $m/s$. Tab. 4.13 shows the peak influencing parameters i.e., $q_{max}$, $T_{DNB}$, $q_{RWT}$, $T_{RWT}$ magnitudes are constant for different water jet velocities.

| $w_j$ | $q_{max}$ in $MW/m^2$ | $q_{RWT}$ in $MW/m^2$ | $T_{DNB}$ in °C | $T_{RWT}$ in °C | $z^*_{DNB}$ in $mm$ | $z^*_{RWT}$ in $mm$ | $w_b = 0.75 * q_{max}$ in °C |
|---|---|---|---|---|---|---|---|
| 8.6 $m/s$ | 4.04 | 0.09 | 373 | 700 | 38.95 | 3.8 | 100 |
| 12 $m/s$ | 4.29 | 0.08 | 386 | 691 | 36.1 | 5.7 | 100 |

Table 4.13: Boiling and characteristic parameters for influence of water jet velocities for single full jet nozzle quenching in case of nicrofer material
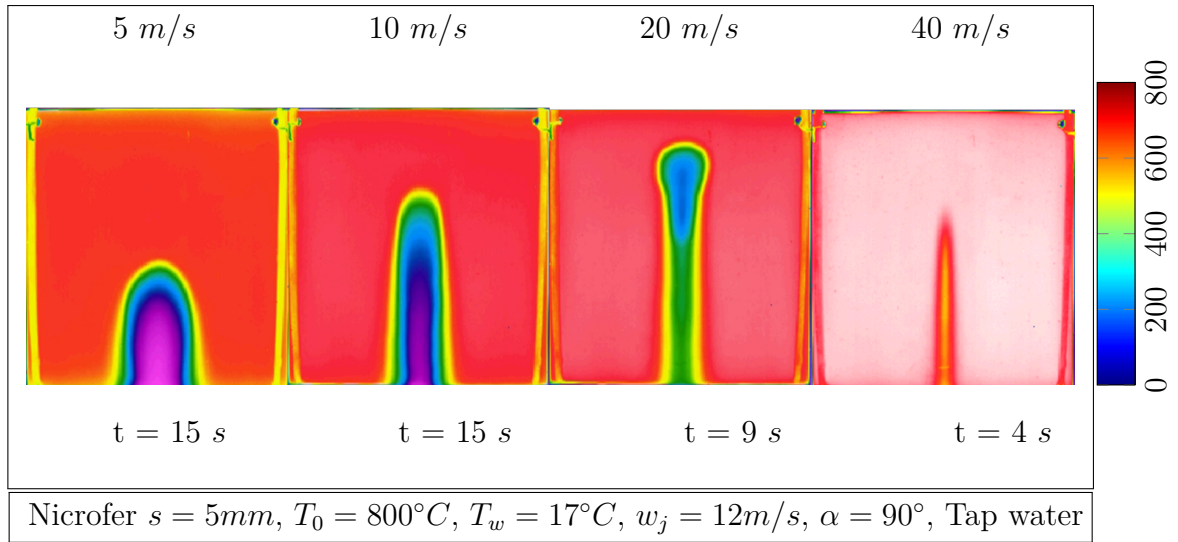


Figure 4.54: Infrared images for nicrofer material of different plate velocities at quasi-steady state - 5 mm thick plate

Infrared images for the different plate velocities in case of 5 mm thick plate for nicrofer material is shown in the **Fig. 4.54**. The influence of plate velocity as usual influences the heat transfer behaviour or temperature drop in the downward region of the plate. For 40 $mm/s$ plate velocity, the surface temperature of the plate stays at higher temperature about more than 700°$C$. Whereas, for lower plate velocity the effect of plate velocity on the temperature drop can be reduced with better and uniform cooling in the water impingement and the downward direction below the nozzle position.
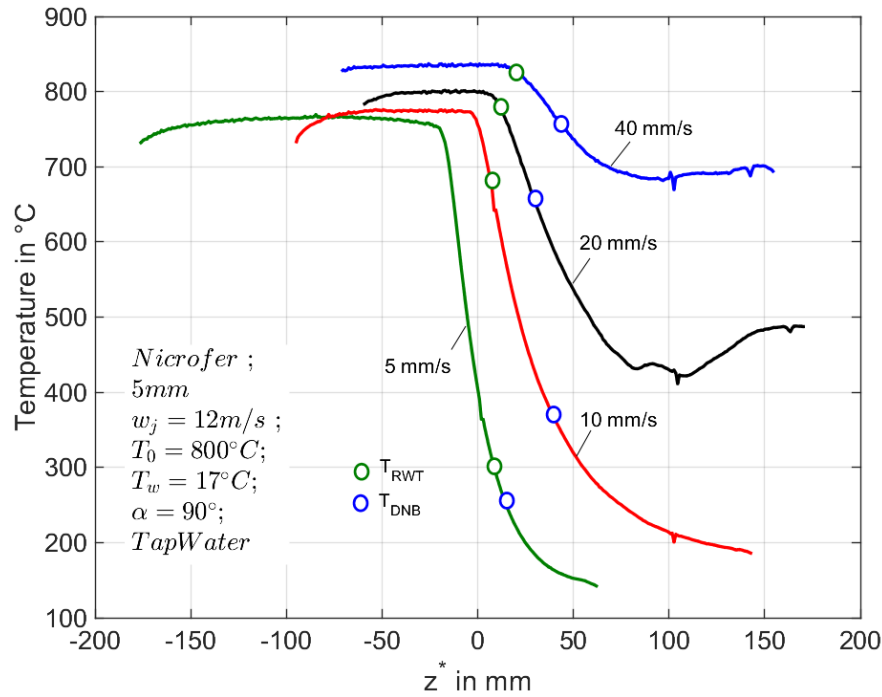
Figure 4.55: Measured surface temperatures for nicrofer material of different plate velocities at quasi-steady state - 5 mm thick plate

Surface temperature for nicrofer material of different plate velocities at quasi-steady state condition for 5 mm thick plate were shown in **Fig. 4.55**. The lower plate velocities shows the better cooling at steady state condition, since the velocity of the plate provides sufficient time for the wetting front or the cooling fluid to stay on the plate. Hence, the uniform temperature drop occurs in the water impingement region. For higher plate velocities i.e., 10 $mm/s$, 20 $mm/s$ and 40 $mm/s$, the temperature of in the upper side of the water impingement region cab be significantly reduced and in the water impingement region influence of the internal conduction can be felt strongly. The propagation of the wetting front in both upward direction and lower direction is restricted due to the strong internal conduction as the contact period of wetting front on the plate changes faster wit the higher plate velocities.
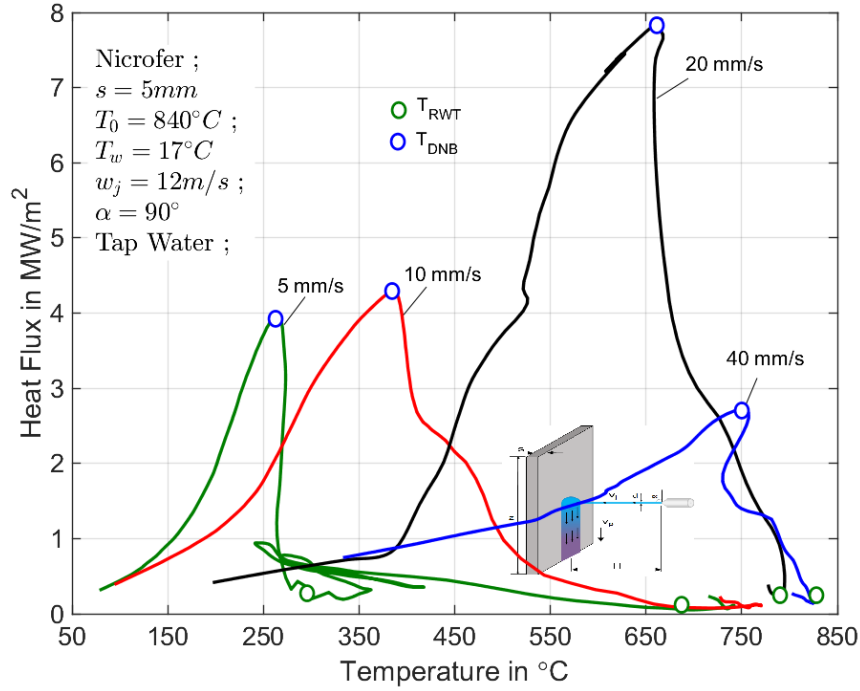
Figure 4.56: Boiling curve and characteristic curves for nicrofer material of different plate velocities at quasi-steady state - 5 mm thick plate

**Fig.  4.56** and **Tab.  4.14** shows the boiling curve and the boiling parameters for the nicrofer material at quasi-steady state condition in case of different plate velocities. The boiling curves clearly indicates that the slight increase of heat flux from 4 $MW/m^2$ to 4.2 $MW/m^2$ for 5 $mm/s$ and 10 $mm/s$ plate velocities and for 40 $mm/s$, we see a drastic increase of maximum heat flux to nearly 8 $MW/m^2$ which is twice as that of 10 $mm/s$ i.e., 4.2 $MW/m^2$. For maximum plate velocity, the heat flux reduces as the surface temperature of the plate stays at higher temperature i.e., $700°C$ to a maximum heat flux value of 2.8 $MW/m^2$. The departure nucleate boiling, re-wetting temperature and heat fluxes were listed in the Tab. 4.14 and were observed to shift to temperature as the position of these peak values are more inclined towards the nozzle position.

| $w_p$ | $q_{max}$ in $MW/m^2$ | $q_{RWT}$ in $MW/m^2$ | $T_{DNB}$ in $°C$ | $T_{RWT}$ in $°C$ | $z^*_{DNB}$ in $mm$ | $z^*_{RWT}$ in $mm$ | $w_b = 0.75 * q_{max}$ in $°C$ |
|---|---|---|---|---|---|---|---|
| 5 $mm/s$ | 3.95 | 0.2 | 263 | 301 | 13.3 | 8.55 | 50 |
| 10 $mm/s$ | 4.29 | 0.08 | 386 | 691 | 36.1 | 7.6 | 100 |
| 20 $mm/s$ | 7.81 | 0.23 | 663 | 793 | 28.5 | 7.6 | 60 |
| 40 $mm/s$ | 2.71 | 0.168 | 754 | 824 | 44.65 | 20.9 | 40 |

Table 4.14: Boiling and characteristic parameters for influence of plate velocities for single full jet nozzle quenching in case of 5 mm thick nicrofer material
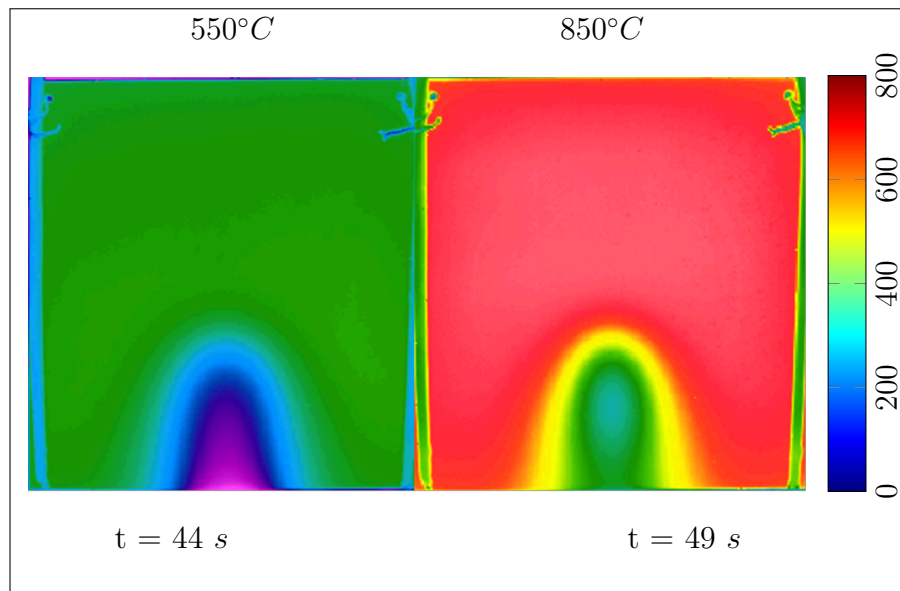
Nicrofer $s = 20mm$, $T_0 = 800°C$, $T_w = 17°C$, $w_j = 12m/s$, $\alpha = 90°$, Tap water, $w_p = 2mm/s$

Figure 4.57: Infrared images for nicrofer material of different initial temperature of the plate at quasi-steady state - 20 mm thick plate

Infrared images for the different initial temperature of the plate were shown in the **Fig. 4.57** at quasi-steady state condition for nicrofer 20 mm thick material. As the start temperature of the plate decreases,the overall thermal energy of the nicrofer plate will reduce. The higher start temperature of the plate restricts the cooling of the plate because of lower internal conduction of the material and thus surface temperature of the plate in the water impingement, downward direction still posses higher values. Whereas, for the lower surface temperature of the plate i.e., $550°C$ better or nearly uniform cooling occurs in the water impingement as well as the downward direction of the plate.
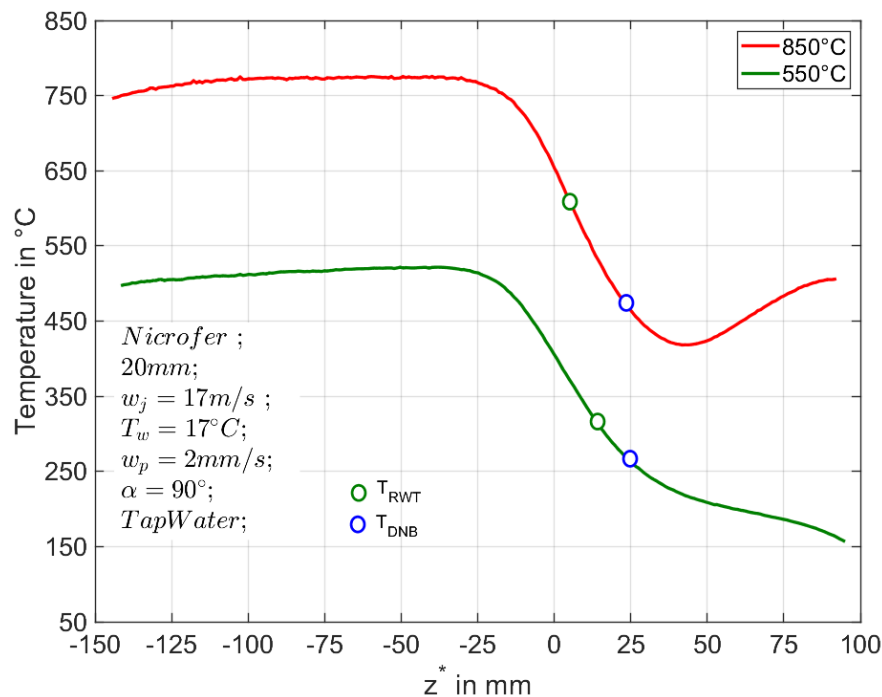


Figure 4.58:  Measured surface temperatures for nicrofer material of different initial temperature of the plate at quasi-steady state - 20 mm thick plate

**Fig. 4.58** shows the surface temperatures for different initial temperature of the nicrofer 20 mm thick plate. The higher thickness of the nicrofer material is strongly felt in the water cooling region and the width of the cooling is strongly seen in case of $550°C$ start temperature. The plate velocity was maintained constant at $2\ mm/s$ with water jet velocity at $17\ m/s$, the start temperature at $550°C$ cools nearly to about $150°C$ plate temperature whereas for $850°C$ start temperature the temperature of the plate still stay at nearly $450°C$. At $850°C$, the temperature of the plate increases again in the downward direction from $450°C$ to $520°C$, the reason for this increase in surface temperatures are mainly due to water ejection from the surface and also the lower thermal conductivity of the plate restricts the wetting front propagation in the downward direction even though the effect of gravity has no role in the cooling of the plate.
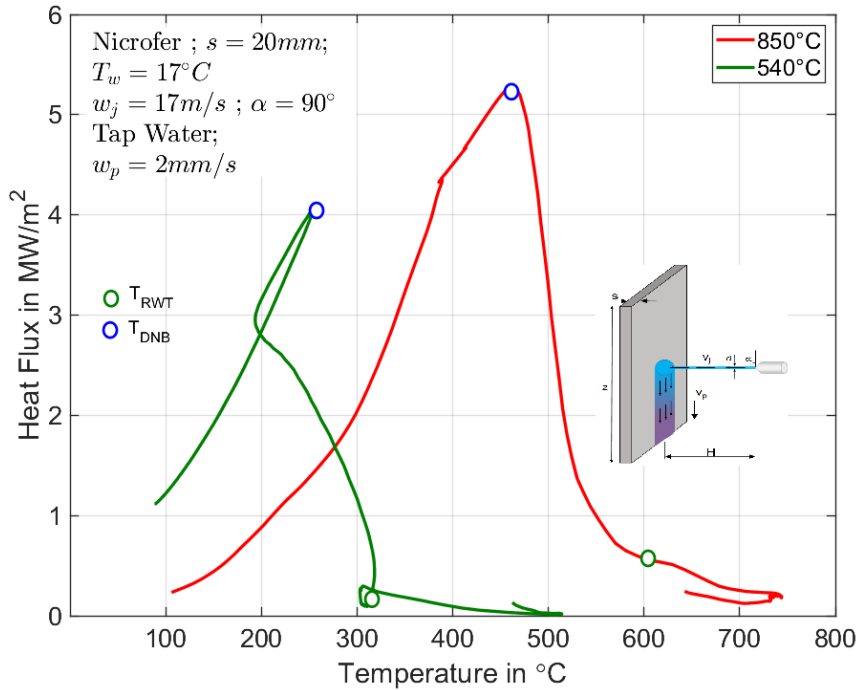


Figure 4.59: Boiling curve and characteristic curves for nicrofer material of different initial temperature of the plate at quasi-steady state - 20 mm thick plate

Boiling curves for nicrofer material for different initial temperatures of the plate at quasi-steady state condition were shown in **Fig. 4.59** for 20 mm thick plate. As we discussed previously the temperatures are mainly influenced with the start temperature of the plate, thickness and the thermal conductivity of the plate. From the observation of heat flux curves, the peak of the departure nucleate boiling shifts towards the lower values for lower start temperature of the plate. **Tab. 4.15** lists the boiling parameters for the two different initial temperature. The higher start temperature of the plate proportionately increases the re-wetting and departure nucleate boiling temperature of the plate.

| $T_{in}$ | $q_{max}$ in $MW/m^2$ | $q_{RWT}$ in $MW/m^2$ | $T_{DNB}$ in °C | $T_{RWT}$ in °C | $z^*_{DNB}$ in $mm$ | $z^*_{RWT}$ in $mm$ | $w_b = 0.75 * q_{max}$ in °C |
|---|---|---|---|---|---|---|---|
| 540 °C | 4.08 | 0.17 | 256 | 314 | 25.65 | 14.25 | 10 |
| 850 °C | 5.279 | 0.557 | 461 | 604 | 24.7 | 5.7 | 120 |

Table 4.15: Boiling and characteristic parameters for influence of initial temperature for single full jet nozzle quenching in case of 20 mm thick nicrofer material

Infrared images for the different water jet velocities in case of 20 mm thick plate were shown in the **Fig. 4.60** for nicrofer material at quasi-steady state condition. The higher water jet velocities directly promotes the better and uniform cooling behaviour in the water impingement region.



Nicrofer $s = 20mm$, $T_0 = 850°C$, $T_w = 17°C$, $\alpha = 90°$, Tap water, $w_p = 2mm/s$
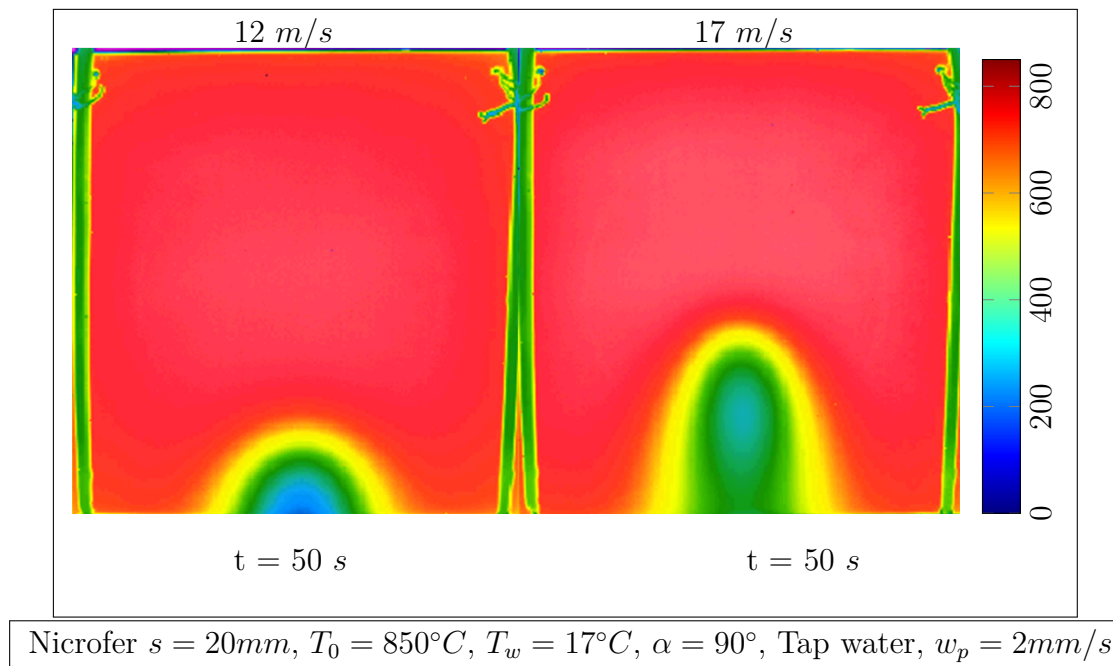
Figure 4.60: Infrared images for nicrofer material of different water jet velocities of the plate at quasi-steady state - 20 mm thick plate

Surface temperature for nicrofer material of different water jet velocities with 20 mm thick plate **Fig. 4.61**. The higher water jet lowers the temperature of the plate at the water impingement region and in the downward direction effect of the re-heating or water ejection becomes stronger. The width of the temperature drop is larger because of the thick material and lower thermal conductivity of the plate.
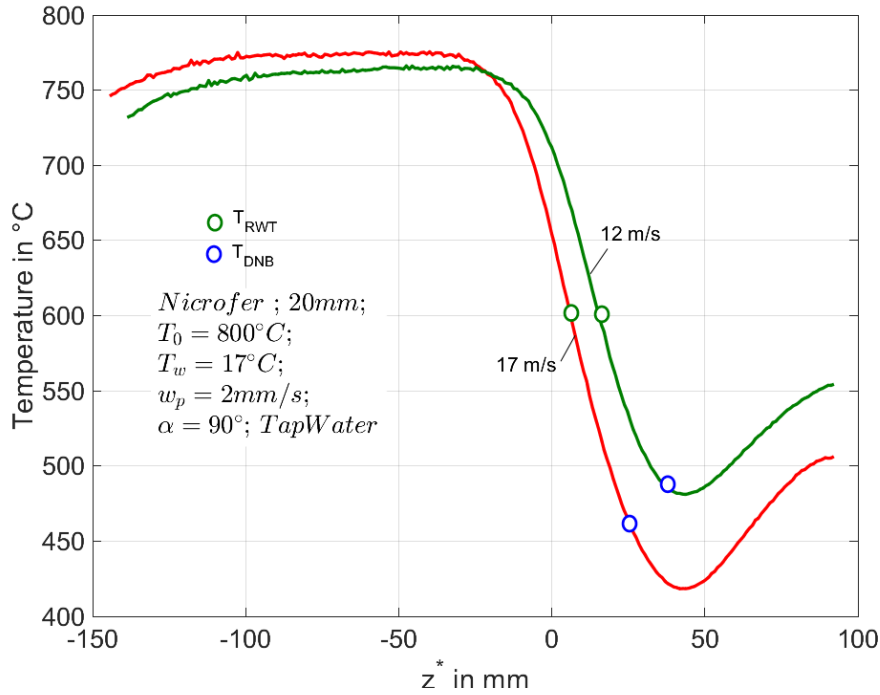
Figure 4.61: Measured surface temperatures for nicrofer material of different water jet velocities of the plate at quasi-steady state - 20 mm thick plate

Boiling curve for the two different water jet velocities i.e., 12 and 17 $m/s$ were depicted in the **Fig. 4.62**. The maximum heat flux slightly increases from 4.5 $MW/m^2$ to 5.2 $MW/m^2$ as listed in the **Tab. 4.16**. The boiling curve for two different water jet velocities shows similar tendency. The larger spatial temperature gradient leads to the higher width of the boiling as can be depicted from the Tab. 4.16.
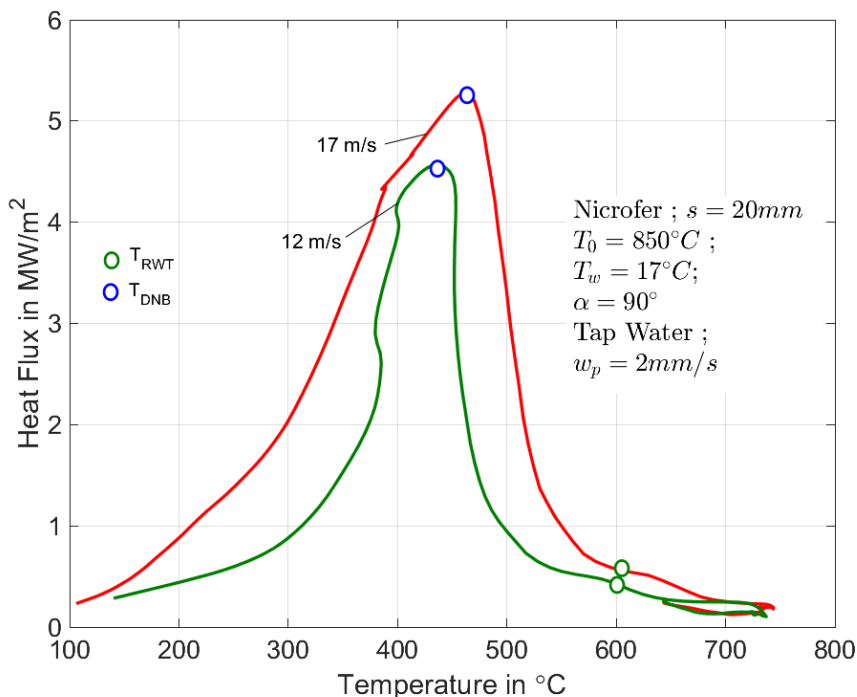


Figure 4.62: Characteristic curves for nicrofer material of different water jet velocities of the plate at quasi-steady state - 20 mm thick plate

| $w_j$ | $q_{max}$ in $MW/m^2$ | $q_{RWT}$ in $MW/m^2$ | $T_{DNB}$ in $°C$ | $T_{RWT}$ in $°C$ | $z^*_{DNB}$ in $mm$ | $z^*_{RWT}$ in $mm$ | $w_b = 0.75 * q_{max}$ in $°C$ |
|---|---|---|---|---|---|---|---|
| 12 $m/s$ | 4.57 | 0.43 | 435 | 599 | 38 | 15.2 | 60 |
| 17 $m/s$ | 5.279 | 0.557 | 461 | 604 | 25.65 | 5.7 | 100 |

Table 4.16: Characteristic parameters for influence of water jet velocities for single full jet nozzle quenching in case of 20 mm thick nicrofer material

Infrared images for the different plate velocities for 20 mm thick nicrofer material are shown in the **Fig. 4.63**. For different plate velocities i.e., 1, 2, and 5 $mm/s$ plate velocities at 50 s quasi-steady state condition were depicted in Fig. 4.63 and the infrared images shows uneven cooling in case of higher plate velocities. For 5 $mm/s$ plate velocity, the water ejection and reheating is stronger and affects the temperature drop in the water impingement as well as in the downward direction.
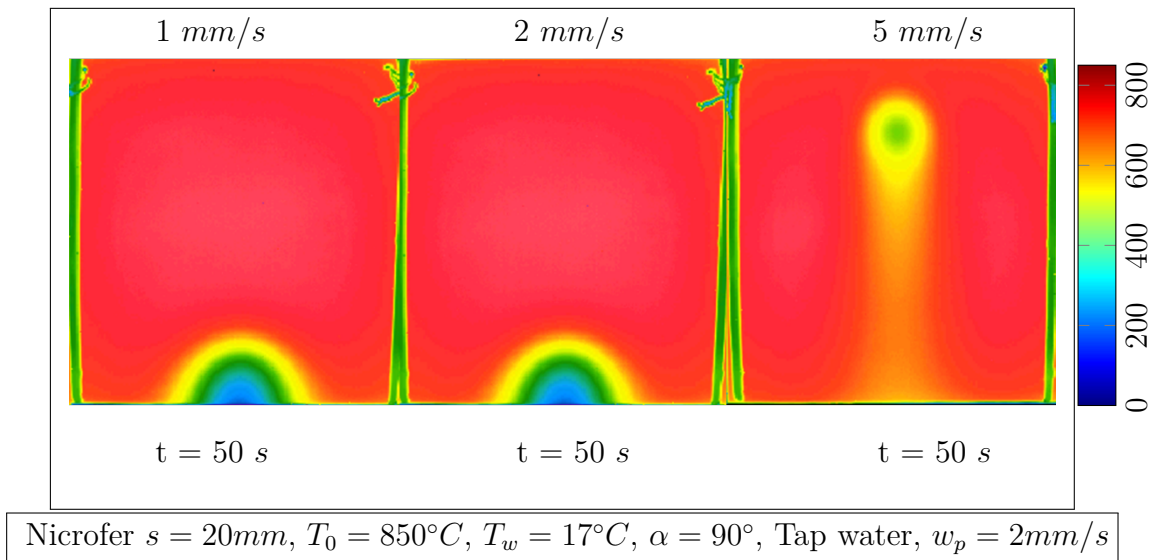


Figure 4.63: Infrared images for nicrofer material of different plate velocities of the plate at quasi-steady state - 20 mm thick plate

The surface temperatures for different plate velocities at quasi-steady state time in case of nicrofer material for 20 mm thick plate is depicted in **Fig. 4.64**. The lower plate velocities directly influences the cooling of the plate and for higher plate velocities the heat conduction, water ejection dominates which lowers the wetting front propagation. The pre-cooling region can be avoided for higher plate velocities. Also, the wetting front movement in both upward and downward direction is strongly restricted due to lower contact time between the moving plate and the stagnant water jet.
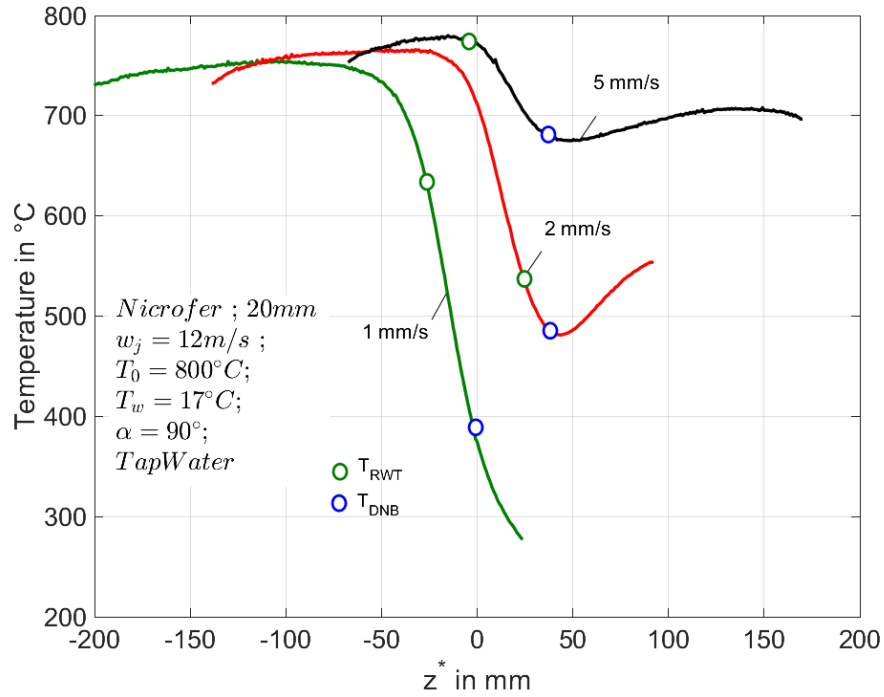
Figure 4.64: Measured surface temperatures for nicrofer material of different plate velocities of the plate at quasi-steady state - 20 mm thick plate

Boiling curves for the different plate velocities were shown in the **Fig. 4.65** at quasi-steady state condition. The lower plate velocity shows a higher value for maximum heat flux at 6.5 $MW/m^2$ and magnitude significantly reduces as the plate velocity is raises. **Tab. 4.17** also lists the peak boiling and re-wetting parameters for different plate velocities in case of 20 mm thick nicrofer material. From the Tab. 4.17 we see an linear decrease in the maximum heat flux value and departure nucleate boiling temperature, similarly the shift of $T_{DNB}$ shifts more towards the lower position away from the nozzle. The typical surface temperature behaviour proportionately influences the width of the boiling and the DNB, RWT shift well below the water impingement region.
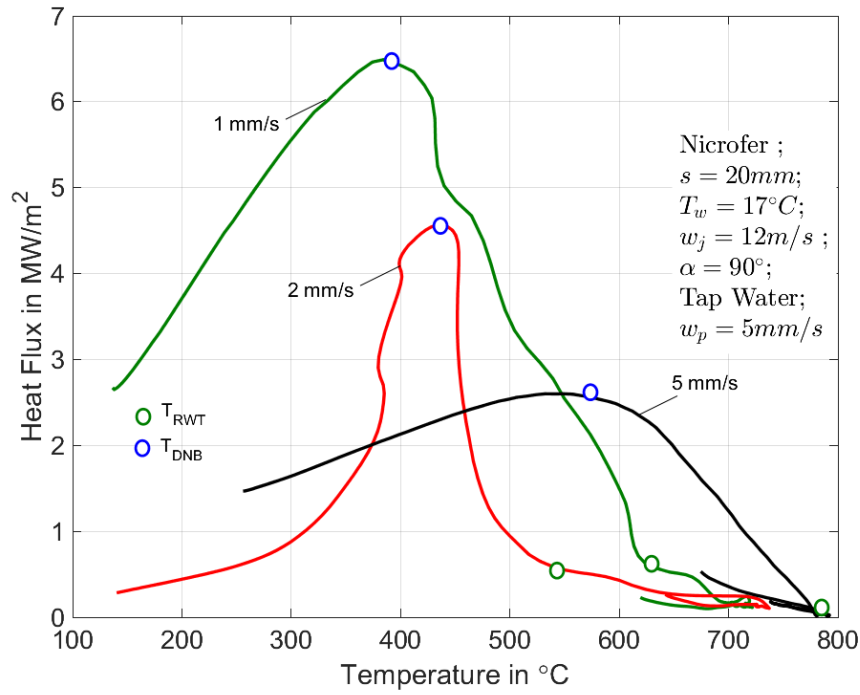
Figure 4.65: Characteristic curves for nicrofer material of different plate velocities of the plate at quasi-steady state - 20 mm thick plate

| $w_p$ | $q_{max}$ in $MW/m^2$ | $q_{RWT}$ in $MW/m^2$ | $T_{DNB}$ in $°C$ | $T_{RWT}$ in $°C$ | $z^*_{DNB}$ in $mm$ | $z^*_{RWT}$ in $mm$ | $w_b = 0.75 * q_{max}$ in $°C$ |
|---|---|---|---|---|---|---|---|
| 1 $mm/s$ | 6.46 | 0.58 | 395 | 629 | -1.9 | -25.65 | 160 |
| 2 $mm/s$ | 4.57 | 0.58 | 435 | 539 | 37.05 | 23.75 | 60 |
| 5 $mm/s$ | 2.56 | 0.01 | 573 | 780 | 40.85 | -9.5 | 250 |

Table 4.17: Characteristic parameters for influence of plate velocities for single full jet nozzle quenching in case of 20 mm thick nicrofer material
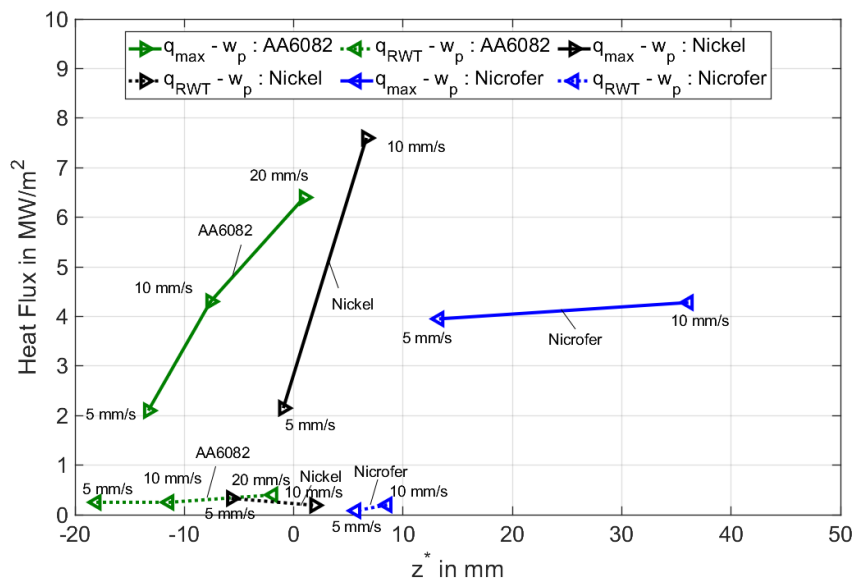


Figure 4.66: Comparison of heat flux with nozzle position for different materials

**Fig. 4.66** shows the variation of the heat flux with respect to the nozzle position for different kinds of material. The variation of the heat transfer is proportionate to the higher magnitude of the process parameters. AA6082 with high conductive material compared to the nickel and nicrofer promotes the stronger diffusion of the heat from the dry region to the wet region. Therefore for lower plate velocity, the position of the maximum heat flux for AA6082 material lies about 10 mm away from the jet position because of stronger advection and with further increase in the plate velocity, the heat flux position shifts towards the nozzle position because of the wall friction between the solid surface and the jet velocity. In case of the nickel material the thermal conductivity is lower compared to AA6082 material and thus the position of the maximum heat flux lies well below the jet position for 5 $mm/s$ plate velocity. Whereas, for 10 $mm/s$ plate velocity the position of the maximum heat flux shifts towards downward position with increase in the magnitude is due to the stronger resistance to diffusion from the metal. The similar phenomena can be well observed in case of the nicrofer material with low thermal conductivity than the nickel and AA6082 material, the intensity of the heat transfer remains constant whereas the position of the maximum heat flux shifts far about 35 mm from the jet position.
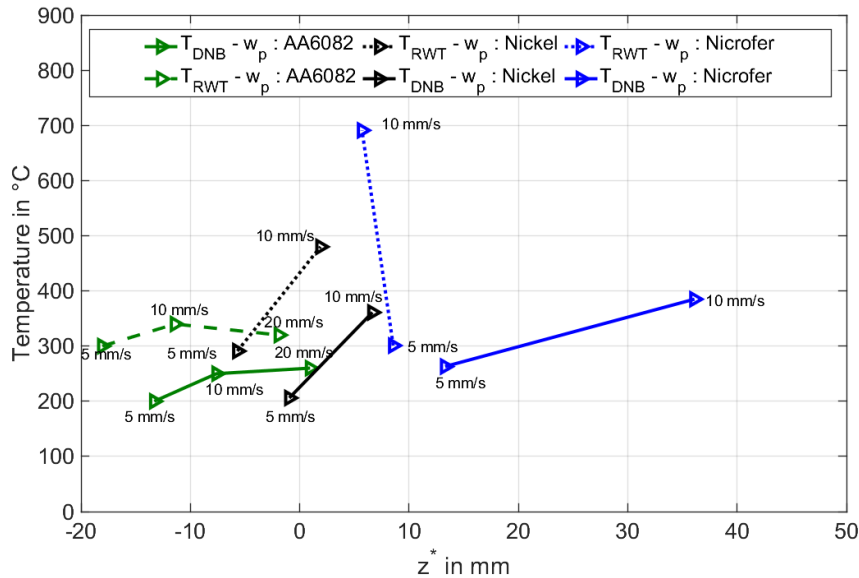


Figure 4.67: Comparison of temperature with nozzle position for different materials

**Fig. 4.67** discuss the variation of the temperature for the different kinds of metals with respect to the nozzle position in case of the plate velocity. The departure nucleate boiling temperature for lower plate velocity i.e., 5 $mm/s$ lies in the range of $200°C$, whereas with the increase of the plate velocity the magnitude increases along with the shift in the position of the departure nucleate boiling temperature to shift near the jet position with decrease in the plate thermal conductivity, increase in the plate velocity both offers stronger resistance to the heat diffusion from dry region to the wet region. In similar situation, the re-wetting temperatures are observed to be around $300°C$ for lower plate velocity i.e., 5 $mm/s$. With the increase in the plate velocity, decrease in the material thermal conductivity the stronger resistance to the thermal diffusion promotes the increase in the re-wetting condition to occur at higher temperature.

## 4.7   Conclusion: Moving Plate

Single full jet quenching with moving plate condition were investigated and furthermore the influence of the process parameters on the heat flux extraction were studied in detail.

The maximum heat flux in relation to the position of the water jet impingement on the hot moving plate observed to be the main influencing parameter for enhancement of the rate of heat transfer in quenching process. Furthermore, we conclude the main key responsible parameters on the heat transfer as stated below:

1. The plate velocity while maintains water jet velocity as constant, significantly influence the rate of heat transfer and the fluid layer movement on the hot moving plate. The maximum heat flux increases with the factor of 3 for plate velocity 5 $mm/s$ to 20 $mm/s$ i.e., 2 $MW/m^2$ to 6.5 $MW/m^2$ respectively. The reason for the increase of the heat flux is the shift of the DNB position towards the water jet impingement position and shift towards higher temperature.

2. Water jet velocity shows a relatively less influence on the maximum heat flux, DNB temperature which remains almost constant.

3. The start temperature highers the internal energy of the plate which alters the magnitude of the maximum heat flux. Higher the start temperature of the plate, the rate of heat transfer gradually increases i.e., for $T_{in}$ of 250°$C$, 450°$C$, 520°$C$ observed to be 2.2 $MW/m^2$, 3 $MW/m^2$, and 4.6 $MW/m^2$. However, with the gradual increase of the start temperature promotes the position of the DNB point toward the water jet impingement with reduction in the length of the pre-cooling region. Although, the DNB temperature falls around 160-230°$C$.

4. The thickness of the plate strongly affects the heat transfer rate and the localized cooling of the plate takes place as the maximum heat flux position shifts away from the nozzle stagnation position. However, the change of the maximum heat flux is in the order of 1 $MW/m^2$. Henceforth, the DNB, and RWT temperature shifts towards the downstream direction because of the stronger advection from the dry region.

5. Nickel with the high heat penetration coefficient and low thermal conductivity obtains the maximum heat flux peak compared to the higher conductive AA6082 material and low conductive nicrofer material for similar experimental conditions. Interestingly, the position of the maximum heat flux and DNB lies almost near the jet impingement location.

As we can conclude from these discussions, that the position of the water jet impingement position plays a crucial role in the heat transfer intensity and proper selection of the experimental conditions favours the rate of heat transfer accurately.

# Chapter 5

# Horizontal Array of Jets (Mold)

## 5.1 Introduction

An array of jets is frequently used for rapid cooling of hot metals in metal processing and casting industries as such a setup can be integrated for continuous production process. Casting process with aluminum can cause several solidification defects such as porosity, inclusion, hot and cold cracks, which harms the quality of the cast produced and reduce the output. The solidifying grain structure determines the final material properties like strength, stiffness, ductility and creep behaviour. The importance of optimization of the casting process for manufacturing high-quality aluminium at low cost becomes necessary. The cooling process in DC casting undergoes two different subprocesses, initially liquid metal experiences a primary cooling, which solidifies the outer shell of the ingot. The heat transfer is effective when the water-cooled mold makes contact with the liquid metal. In a later section, heat transfer is dominant with secondary cooling, because of the direct impingement of water from an array of jets on to the hot partially solidified ingot emerging from the primary cooling and most of the heat is extracted in this section $(80 - 90\%)$ Wells et al. (2001). Consequently, heat transfer analysis in the secondary cooling region is crucial for process optimization. The steady state in the cooling process is achieved after the transient process at a length of $0.5 - 1$ m, while the ingot speed and water flow rate are kept constant. Even though the steady state finds the most productive stage, the depth of the casting pit limits the duration of this stage. To measure the temperature distribution during the DC casting process, the experimental method becomes complicated and highly expensive. Hence, the necessity to perform experiments in the laboratory conditions becomes important. Experimental study helps to quantify the effect of process parameters on the heat transfer and to minimize the dynamic parameters. Therefore, laboratory setup should be similar to the secondary cooling section of the industrial casting process. From the experiments, surface temperature is recorded in time for the motion of the hot plate. A methodology to obtain the heat flux is significant for implementing heat transfer results into the process simulation of DC casting for further investigation.

**Mechanism of Heat Transfer** In a moving metal sheet setup, the mold with a water jet is kept stationary and the hot metal sheet is moved down at a controlled speed, as illustrated in **Fig. 5.1**. The hot metal in motion at the desired speed for the time instants are shown in Fig. 5.1 and the temperature profiles were observed to be in a quasi-stationary state. The snapshots for three-time steps i.e., 11s, 12s, 13s are presented in Fig. 5.1. For each instant, three different images were shown starting from the left is image from GoPro comes at water-quenched side, on the middle is the thermal image recorded from the infrared thermography and on the right next to it is the temperature profile which is obtained from the thermal images at the center of vertical region.

The water jet first comes in contact with the bottom edge of the sheet and the wetting

front moves above and below the water impingement region while the hot plate is in downward motion. Consequently, the water jet cools the hot plate in motion mostly in the impingement region. A water jet has both horizontal and vertical momentum with in the free-falling region. Thus, a water jet impulses a turbulent flow in the impingement zone as the horizontal momentum is completely diminished with short distance. At higher jet angle and jet velocities, the portion of the water flow from the jet will bounce off the hot metal surface. Thus, the definition of the impingement region becomes complicated because of the bounce off phenomena as the water jet makes initial contact at the lower portion of the plate. As water hits the hot plate in motion, turbulent flow occurs with the formation of the vapor film on the metal surface. Consequently, the vapor film acts as a barrier which creates a resisting energy toward the surface in normal direction, which helps to restrict the contact between water and hot surface. The film barrier loses its energy as the plate cools down and at Leidenfrost temperature, the energy of the barrier will become less than that of liquid water. Thus, it causes the water to penetrate the barrier and initial contact with a hot surface in motion exists to higher the rate of heat removal.
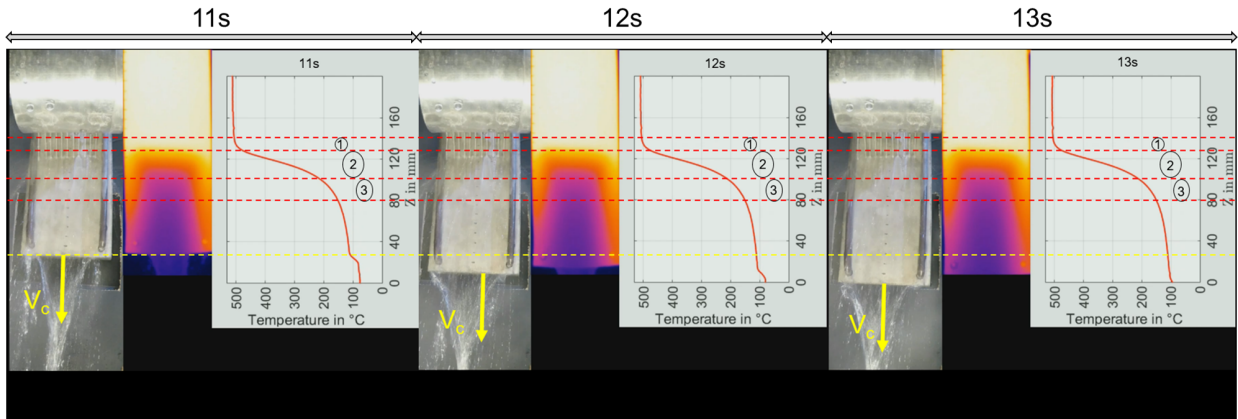


Figure 5.1: Experimental measurements and the phenomena of quenching with mold quenching for moving plate

From the physical understanding, we can hypothesize that the energy of the water stream in the direction normal to the metal surface will be higher and the temperature at which the water stream can penetrate will be higher. The experimental investigation during water jet quenching of hot plate in motion shows the movement of wetting front above the jet impingement portion and this is termed as climbing height. As the water climbs up on the hot moving surface, the diffusion of heat dominates from the dry region to the wetting region, thus promoting the cooling of the plate before water approaches the surface. Thus, the phenomena of heat flow from dry region to wet region are defined as pre-cooling regions. The phenomena as similar to pre-cooling, was named as advanced cooling in the literature from most of the scientific researchers during water cooling process Weckman and Niessen (1982), Bakken and Bergström (1986), Drezet et al. (2000). The focus of the research paper on quenching with a hot plate in motion is limited to the steady state. Since, the authors observed a steady state in transient temperature measurements during quenching of hot moving metal plates. However, the researchers were unable to quantify the length of the hot region to the water impingement region. Consequently, a question arises to determine the width of the pre-cooling region and hence to quantify the pre-cooling region to conduct the experiments for various conditions. The literature on water jet quenching gives information mainly on the determination of the heat flux on the quenching surface. Whereas, the quenched side temperature was rarely discussed. The boiling conditions like $q_{max}$, $T_{DNB}$, $T_{RWT}$, $q_{RWT}$ give the amount of heat transfer in the quenching of a hot plate in motion. This work would present the quenched side temperature profile and the width

of different regions during cooling like pre-cooling, transition, and nucleate boiling were quantified and discussed in detail.

Bakken and Bergström (1986) observed a temperature drop a few millimetres above the jet impingement region during secondary cooling of the DC casting process. Opstelten and Rabenberg (2016) also reported a drop in the surface temperature of the metal through axial conduction. Caron and Wells (2006) integrated phenomena of advanced cooling into the method of inverse heat conduction and the domain of the boundary conditions for the partial differential equation changes. The pre-cooling particularly becomes higher in case of aluminium due to their higher thermal conductivity. Such a situation is particularly seen in the DC casting process when the hot molten metal is supplied continuously from the top and diffusion of heat occurs through axial conduction.

Caron and Wells (2009a) studied the heat transfer in quenching of magnesium alloy AZ31 during secondary cooling in the DC casting process. To understand the influence of several parameters like cooling water flow rate, water temperature, and initial temperature, the heat extraction was quantified. A formulation of an idealized boiling curve to solve the thermo-mechanical behaviour of DC casting was shown. For higher plate velocities, the maximum heat flux does not change, whereas only a shift in DNB temperature occurs. Hnizdil et al. (2015b) studied the effect of impact angle and pressure on the vertically moving plate with a spray nozzle. From the experimental analysis, they observe the increase in heat transfer coefficient and Leidenfrost temperature occurs with the water pressure. In case of lower surface temperature, the heat transfer coefficient is higher for lower impact angle and vice-versa.

The application of different nozzle types during the quenching of hot moving metal plates were found in literature study. **Table. 5.1** lists the experimental conditions and corresponding maximum heat fluxes obtained from the experimental analysis. Table. 5.1 lists the conditions like thickness ($s$) of the metal sample, diameter ($d_j$) of the nozzle, volume flow ($w_j$) of the cooling water, plate speed ($w_p$), the initial temperature ($T_s$) of the sample plate and the maximum heat flux ($\dot{q}_{max}$) obtained during experimental analysis. Since, authors use different conditions for experiments, the obtained results tend to change. An attempt is made to compare the results from different researchers for the study on heat transfer during movement of the hot plate. The **Table. 5.3** gives some significant conclusions based on the experimental and numerical solutions from Table. 5.1.

Table 5.1: Experimental conditions and analysis results from literature work

| Author | $s$ | $d_j$ | $w_j$ or $Q^*$ | $w_p$ | $T_s$ | $\dot{q}_{max}$ |
|---|---|---|---|---|---|---|
| | $mm$ | $mm$ | $m/s$ or $l/min/m$ | $mm/s$ | $°C$ | $MW/m^2$ |
| Caron and Wells (2009a) | 100 | 4.75 | $15 - 150^*$ | 10 - 40 | 500 | 4 - 7.5 |
| Opstelten and Rabenberg (2016) | 130 | - | $100 - 120^*$ | 1.27 - 6.6 | 400 | 4 - 8 |
| Hnizdil et al. (2015a) | 1.5 | - | 3 | - | 900 | 5.2 - 11.6 |
| Gradeck et al. (2009b) | 75 | - | 1 - 1.2 | - | 500 - 600 | 5 - 12 |
| Vakili and Gadala (2013) | - | 1.6 | 18 | 350 - 1000 | 300 - 700 | 10 |
| Sharma and Sahu (2019a) | 0.15 | 1.6 | - | 0 - 40 | $500 \pm 10$ | 6 - 8.5 |
| Modak et al. (2015) | 0.15 | 1.38 | - | 0 | $500 \pm 10$ | 2 - 5 |
| Fujimoto et al. (2015a) | 0.3 | 5 | 0.4 - 1.2 | 500 - 1500 | $500 \pm 10$ | 6 - 8.5 |
| Jha et al. (2015b) | 6 | 5 | $0.025^*$ | 60 | 1050 | 3 - 4 |
| Wang et al. (2019a) | 20 | 2 | $1.5 - 30^*$ | 10 - 15 | 700 | 4 - 5 |

Table 5.3: Conclusion from different authors in literature work

| Author | Remarks |
|---|---|
| Caron and Wells (2009a) | 1. The influence of process parameters like flow rate, water temperature, jet velocity and initial temperature on the boiling curve are discussed. |
| Opstelten and Rabenberg (2016) | 2. Plate speed and different aluminium alloys significantly influences on the boiling curve |
| Hnizdil et al. (2015a) | 3. The study of the water flow rate and impact angle on the heat transfer coefficient were made. |
| Gradeck et al. (2009b) | 4. The movement of maximum heat flux from film boiling to forced convection regime is discussed. |
| Vakili and Gadala (2013) | 5. The study of multiple jets and jet spacing on the impingement heat transfer for higher plate velocity of the plate were carried out. |
| Sharma and Sahu (2019a) | 6. The magnitude of heat flux is higher for stationary plate, compared to higher plate speed. |
| Modak et al. (2015) | 7. The increase in the nano-fluid concentration, maximizes the heat flux extraction. |
| Fujimoto et al. (2015a) | 8.The initial temperature of the plate provokes heat transfer. |
| Jha et al. (2015b) | 9. The surfactant concentration has negative . effect on heat transfer |
| Wang et al. (2019a) | 10. Angle of inclination significantly increases the heat transfer rate |

Opstelten and Rabenberg (2016) investigate the stationary part of the DC casting process; heat flux are estimated as a function of impingement distance. Studies on the influence of plate speed and water flow rate on the heat flux were conducted. With the increase in plate speed, the heat extraction increases for higher surface temperature. In the impingement region, the extraction of heat reduces for larger water flow rates, but in downstream regions, the higher heat flux is observed leading to large water amounts. Gradeck et al. (2012) measured the transient temperature with the help of sensors located in the hot rotating cylinder. The thermal boundary conditions i.e., heat transfer on the impinging surface were predicted using Beck's future time steps. They determined that the maximum heat flux across different positions on the rotating cylinder varies tolerance of $1 \pm MW/m^2$ and with a temperature change of $\pm 20°C$. The maximum heat flux decreases with an increase in plate speed that contradicts the results from Caron and Wells (2009a). Vakili and Gadala (2013) focused on studying the boiling heat transfer on the hot moving plate with multiple impinging jets. The inverse method was developed to estimate the temperature and heat flux on the boiling surface due to water impingement. In the stagger nozzle arrangement more uniform temperature distribution is obtained and with the increase in jet line spacing the uniformity becomes more significant. The effect of plate speed on the heat flux is predominant for higher surface temperature and the heat flux in the impingement region is lower for higher casting speed. Sharma and Sahu (2019a) investigated the effect of water jet impingement on the hot moving surface of $0.15mm$ thick steel material. An infrared camera was used to record the transient temperature distribution and with the use of the energy equation transient surface heat flux was obtained. The local heat fluxes were observed to decrease away from the impingement point. Maximum hot flux reduces for higher plate speed. Jha et al. (2015b) showed the importance of ultrafast cooling of hot moving plates on the heat transfer and compared the water jet and spray nozzle for stationary and moving conditions with the addition of a surfactant to cooling water. In case of jet impingement, the maximum heat flux and the cooling rate will be higher compared to spray impingement technique. Interestingly, the addition of a surfactant to the water decreases the heat extraction for the moving plate condition. Wang et al. (2019a) investigated the effect of heat transfer during slit nozzle impingement on the hot moving plate surface. The intensity of maximum heat flux increases with the impingement angle. Nucleate boiling occurs with reduction in the transition boiling zone for different times at various thermocouple locations. For higher plate speed, the movement of the nozzle shortens the time for plate to the cooling water, which reduces the maximum heat extraction.

Fujimoto et al. (2015a) worked on circular water jet impingement on hot moving sheet transient temperature distribution on the underside of the plate was captured by infrared thermography. The experiments showed a steady-state condition in the transient cooling process and solved a 3D partial differential equation. The sample start temperature has a higher heat flux extraction. The boiling curve for different plate speeds depending on the jet velocity has no significant difference.

Henceforth, this work discusses the heat transfer mechanism on the hot moving metal plate with an array of jets. The results are first compared by superimposing the temperature profiles obtained from the experiments. Temperatures are recorded with an infrared camera on the back of the plate quenching. The comparison of the measured temperatures from the experiments gives us a qualitative idea of influence on the different parameters without the use of any numerical model. The interface temperature is obtained from a 1D analytical solution using the energy balance equation. The temperature profiles are analysed further to obtain the boiling curve i.e., heat fluxes as a function of temperature on the quenching side. Jha et al. (2015b) worked on studying the influence of surfactant additives for hot moving steel plates and found that the addition of surfactant results in a negative effect on the cooling rate and obtained the decrease in maximum heat flux. During the bottom

jet cooling of a steel plate, an increase in the inclination angle results in lower overall heat removal rate from the experimental study by Chester et al. (2012a). Wang et al. (2019a) investigates the heat transfer characteristics of slit nozzle impingement on high-temperature plate surfaces. The impingement angle was varied from 0 to 45°, the intensity of heat transfer improved, while time for nucleate boiling reduced with decrease in the width of the transitional region.

In this work, many experiments have been performed to study the influence of various process parameters during quenching of moving hot metal. The cooling water through an array of jets is impinged on the front side of the heated metal plate; the temperatures are measured with the use of an infrared camera on the other side of the plate surface. The temperature measurements are used as a source for predicting unknown surface heat flux for the inverse heat conduction algorithm. In literature, we find many articles on the heat transfer in steel plates, whereas few authors have discussed the influence of Aluminium alloy. Thus, 4 different metal types were chosen to investigate the heat transfer during the quenching process. Further, Aluminium with high thermal conductivity is preferred and experiments were performed to observe the influence of various process parameters on heat transfer. The inverse heat conduction model is integrated with the Eulerian steady-state model to understand heat transfer with the estimation of surface temperature and correspondingly to quantify the surface heat flux through the boiling curve for different parameters.

## 5.2   Analysis Method
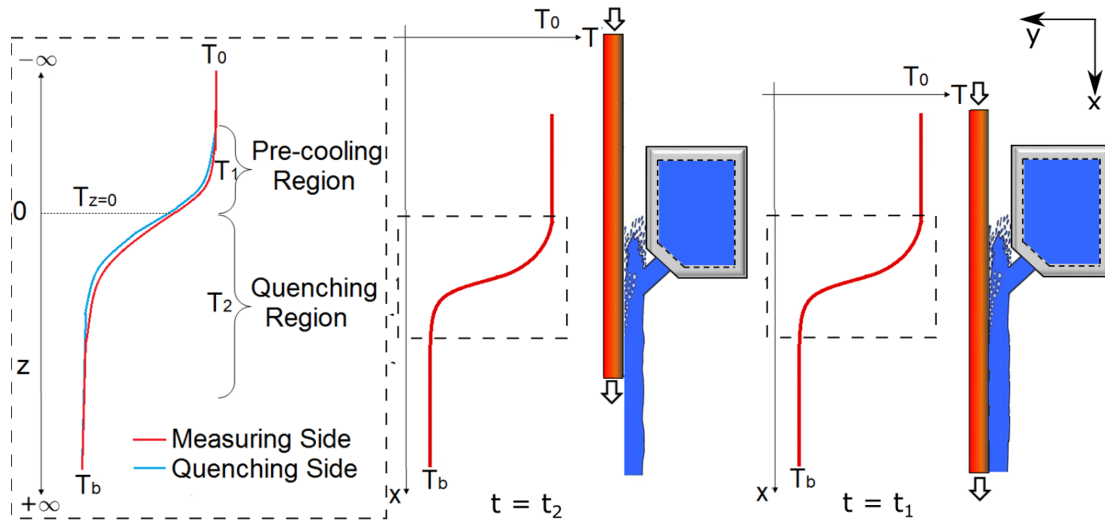


Figure 5.2: Temperature profiles in different regions and different time instants of quenching process under moving sheet setup Kulkarni et al. (2019)

**Fig. 5.2** shows the temperature profiles, which can be distinguished as pre cooling and quenching region and the visualization of the plate movement can be seen at two time instants. Pre-cooling due to the high conductivity of metal as heat diffuses through axial conduction. Quenching region is due to the water impingement on the hot metal plate with the transfer of heat to the cooling water. Fig. 5.2 also shows the position of the metal plate at two time instants. The cooling starts with the impingement of mold jets on the bottom of the metal plate. This instant is set as the start time $t = 0s$. As time elapses, the metal plate moves downward while fixing the spatial position of the jet impingement by mold on the moving plate and is defined as Eulerian coordinate at $z = 0$. The interface temperature $T_{z=0}$ distinguishes the pre-cooling and quenching region. The normalized temperature at the

interface can be approximately calculated using **Eq. 5.1** and a more detailed explanation is given in Kulkarni et al. (2019).

$$\theta_{z=0} = \frac{T_0 - T_b}{T_{z=0} - T_b} = \frac{2}{1 + \sqrt{1 + \frac{4 \cdot Bi}{Pe^2}}} \qquad (5.1)$$

Here, $Bi = hs/\lambda$ and $Pe = V_p s \rho c/\lambda$ are, respectively, Biot and Peclet number. Where, $h$, $s$, $\lambda$ and $\rho$, $c$ are respectively the heat transfer coefficient, thickness of the plate, the thermal conductivity of the plate and density, specific heat capacity of the plate, $V_p$ is the speed of the plate. $Bi$ is a mean value of the quenching region. With this approach, the interface temperature $T_{z=0}$ is determined to distinguish between the quenching region and the pre-cooling using **Eq. 5.2** Kulkarni et al. (2019),

$$T_{z=0} = \frac{(T_0 - T_b)}{\theta_{z=0}} + T_b, \qquad (5.2)$$

where $T_0$, $T_b$ are initial and final temperature of the sample plate during quenching process.
**Pre-cooling Region**
The movement of plate takes place from the top to the bottom with a certain velocity. As the array of jets impinges on the hot moving plate, the cooling water flows down along with the surface motion and also tries climbing up the plate against plate motion. We observe the existence of two regions as shown in Fig. 5.2. The quenching region, where the most effective heat transfer occurs and the maximum heat flux position always belongs to this region for any cooling time. Consequently water reaches a pre-cooling region, where the high temperature gradient between the quenching region and the pre-cooling region leads to the loss of heat from dry region (Pre-cooling) to wet region (quenching region) region, even before the plate experiences water cooling to the dry region. The pre-cooling is typical in high conductivity material with almost constant surface gradient along the axial position. Stationary co-ordinate along the normal, according to the left part of the Fig. 5.2 is called as z-coordinate. At the interface temperature, the z coordinate shows with the value zero. The moving plate gives the co-ordinate x, where $x = 0$ symbolizes the upper part of the plate as shown in the right part of the Fig. 5.2.
**Quasi-Steady Condition**
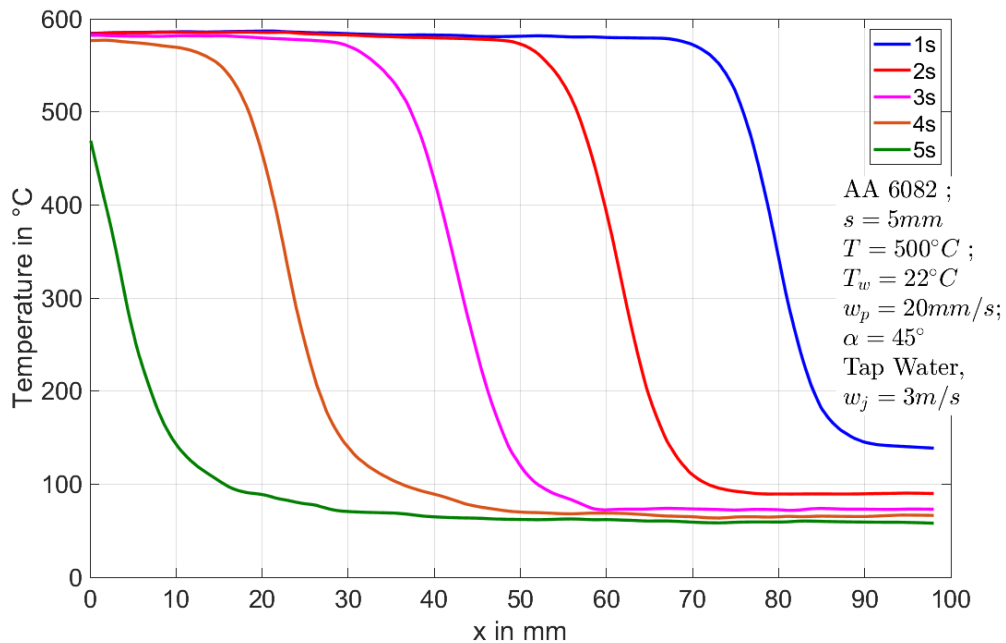


Figure 5.3: Temperature distribution for five different times in Lagrangian coordinates.
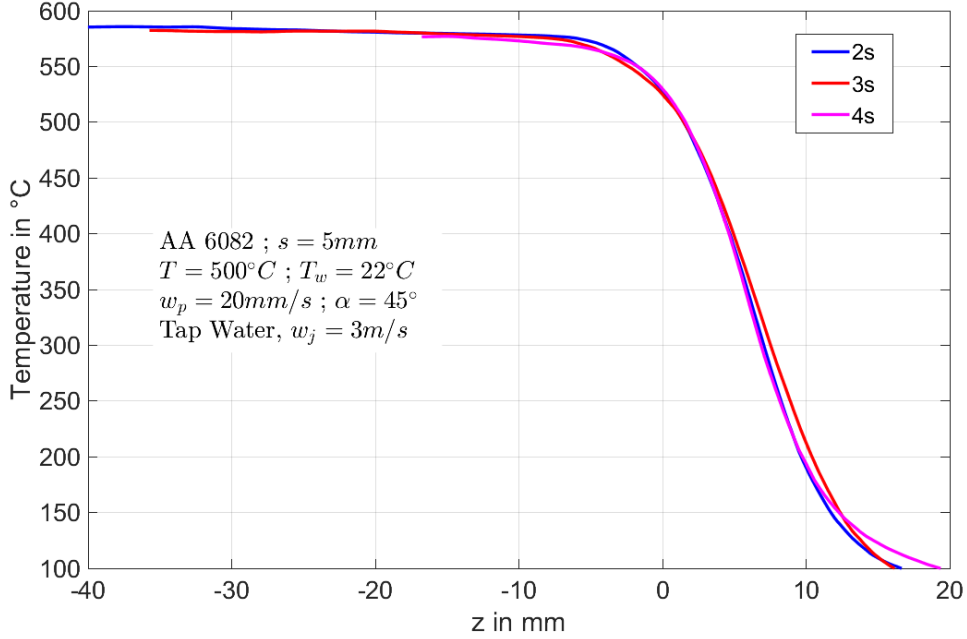
Figure 5.4: Superposition of the temperature distribution for three different times according to Eulerian coordinates.

Stationary coordinates along the normal, according to the left part of Fig. 5.2 is called the z coordinate. At the interface temperature, the z coordinate shows the value of zero. The moving plate gives the coordinate x, while x=0 symbolizes the upper part of the plate, as shown in the right part of 5.2. The surface temperature is shown as a function of z, the higher temperature is obtained in the negative range of z. The interface temperature is obtained in the negative range of z to distinguish between the quenched side and the dry region is immediately identified. The temperature gradient before the water jet contact with the plate is mainly due to the advection. The temperature drops below the water jet contact and results from cooling by mold jets. The quasi-stationary state of temperature in the central region of the metal plate can be observed.

To simplify the experimentally measured temperature during the plate movement. **Fig. 5.3** and **Fig. 5.4** gives an overview of the simplification, where the Lagrangian coordinates were transformed into Eulerian coordinates. Fig. 5.3 shows the temperature as a function of the coordinate x fixed to the plate (i.e., Lagrangian coordinate) at the cooling times of 1, 2, 3, 4 and 5 seconds. The temperature from Fig. 5.3 is superimposed using the coordinate z fixed to the nozzle (i.e., Eulerian coordinate), we obtain the temperature profiles, as shown in Fig. 5.4. Henceforth, it can be clearly seen that after initial startup time, the experimentally measured temperature on a moving metal sample reaches a quasi-steady state condition. The advantage is that in the quasi-stationary range the cooling process can be approximated quite well by a single temperature curve. The quasi-stationary temperature profile are used for the determination of unknown heat flux and surface temperature on the quenched surface. Therefore, the temperature measured is approximated using the Boltzmann function

$$T = A_2 + \frac{A_1 - A_2}{\left[1 + exp\left(\frac{z - z_0}{dz}\right)\right]}, \tag{5.3}$$

where $A_1$, $A_2$, $z_0$, $dz$ are the values of constants obtained by curve fitting the experimental temperature using origin software. The one-dimensional heat flux is obtained from the

energy balance

$$\dot{q}(z) = sw_p\rho C\frac{\partial T}{\partial z} + s\lambda\frac{\partial^2 T}{\partial z^2}. \tag{5.4}$$

The transferred heat flux is equal to the change of stored enthalpy and the conducted heat flow. The stored enthalpy is dominant. This balance assumes that the temperature in the y-direction (thickness) is equal. The solution gives the heat flux (boiling curve) on the measuring side. However, the heat flux on the quenching side is required. Hence, to compute the temperatures during quenching process, the Fourier equation is formulated as in **Eq. 5.5**. The Eq. 5.5 can be further defined as direct problem

$$\rho C w_p\frac{\partial T}{\partial z} = \lambda\left(\frac{\partial^2 T}{\partial z^2} + \frac{\partial^2 T}{\partial y^2}\right). \tag{5.5}$$

The formulation of partial differential equation is based on the assumption that the existence of steady state condition during transient cooling process and thus to reduce the simple steady state problem. The partial differential equation in Eq. 5.5 were numerically solved using finite difference method with appropriate boundary conditions. The boundary conditions in the y-direction are mainly due to the heat flux at the quenching region and on the back side of the quenching region adiabatic condition applies.
The boundary condition in the z-direction consists of the initial temperature at the top of the plate (i.e., at z = -∞) to replicate the continuous hot movement of the plate and the adiabatic at the bottom of the plate (i.e., at z = +∞).

## 5.3 Inverse Heat Conduction Method

The estimation of heat flux and the surface temperature on the boiling surface is realised with the use of inverse heat conduction method. The experimentally measured temperature are available and in order to compute the inverse problem, the regularization method must be implemented. The idea of regularization is to impose the stability on the ill-posed problem to accurately predict the approximate solution. For the ill-posed problem, the general form leads to the minimization of the objective function. The development of the present inverse algorithm was primarily based on the Jarny et al. (1991). Here, we integrated the Tikhonov regularization to the objective function to stabilize the inverse problem as given in **Eq. 5.6**

$$J_{q_j} = \frac{1}{2}\int_0^{t_f}\int_{\Gamma_c}(T - T_{exp})^2 d\Gamma dt + \frac{\gamma_k}{2}\int_0^{t_f}\int_{\Gamma_j}(q_j)^2 d\Gamma dt. \tag{5.6}$$

In **Eq. 5.6**, $T_{exp}$ is from the experimental temperature measurements from the infrared camera and T is the solution obtained from direct heat conduction problem. To regularize the optimization problem, we introduce the term $\gamma_k$ in second part of the equation called as regularization parameter. The selection of the regularisation parameter was based on the work of Bozzoli et al. (2014), where the second order Tikhonov regularization method is used to stabilize the inverse method. The solution of the direct problem are obtained from the computation of partial differential equations as given below

$$\rho C V_c \frac{\partial T}{\partial z} = \lambda \left( \frac{\partial^2 T}{\partial z^2} + \frac{\partial^2 T}{\partial y^2} \right) \qquad (x, t) \in (\Omega) \tag{5.7a}$$

$$\frac{\partial T}{\partial y} = 0 \qquad (z, y = s) \in (\Gamma_c) \tag{5.7b}$$

$$\frac{\partial T}{\partial y} = -\frac{q_j}{\lambda} \; (z, y = 0) \in (\Gamma_j, \tau) \tag{5.7c}$$

$$\frac{\partial T}{\partial z} = 0 \qquad (z = 0, y) \in (\Gamma_b) \tag{5.7d}$$

$$T = T_0 \qquad (z = L, y) \in (\Gamma_t). \tag{5.7e}$$

The governing partial differential equation is solved using 2D-Finite difference method. The boundary condition on the quenched surface were applied as the heat flux obtained from 1D analytical equation as in Eq. 5.4 and on the back of the quenching side similarly on the bottom of the plate adiabatic conditions are applied. To resemble the continuous movement of the plate, Dirichlet boundary condition is applied on the top surface of the plate with constant start temperature. To compute the gradient $\nabla J_{q_j}$ of the objective function for the optimization process, the formulation of adjoint problem becomes necessary.
The gradient of the objective function is defined as

$$\nabla J_{q_j} = \phi + \gamma_k \; q_j. \tag{5.8}$$

To determine the sensitiveness of the direct problem, the sensitive function is derived as described by Jarny et al. (1991). The variation of $q_j(x)$ undergoes a change of $\nabla q_j(x)$ and T is perturbed by $\nabla T$. The sensitivity function is obtained simply by replacing $\nabla q_j(x)$ and $\nabla T$ in place of $q_j(x)$ and T in **Eq. 5.7**. The sensitivity problem is described as

$$\rho C V_c \frac{\partial \theta}{\partial z} = \lambda \left( \frac{\partial^2 \theta}{\partial z^2} + \frac{\partial^2 \theta}{\partial y^2} \right) \qquad (x, t) \in (\Omega) \tag{5.9a}$$

$$\frac{\partial \theta}{\partial y} = 0 \qquad (z, y = s) \in (\Gamma_c) \tag{5.9b}$$

$$\frac{\partial \theta}{\partial y} = P(x) \; (z, y = 0) \in (\Gamma_j, \tau) \tag{5.9c}$$

$$\frac{\partial \theta}{\partial z} = 0 \qquad (z = 0, y) \in (\Gamma_b) \tag{5.9d}$$

$$\theta = 0 \qquad (z = L, y) \in (\Gamma_t). \tag{5.9e}$$

The adjoint problem is described as

$$\rho C V_c \frac{\partial \phi}{\partial z} = \lambda \left( \frac{\partial^2 \phi}{\partial z^2} + \frac{\partial^2 \phi}{\partial y^2} \right) \qquad (x, t) \in (\Omega) \tag{5.10a}$$

$$\frac{\partial \phi}{\partial y} = 0 \qquad (z, y = s) \in (\Gamma_c) \tag{5.10b}$$

$$\frac{\partial \phi}{\partial y} = T(x; q_j) - T_{exp} \; (z, y = 0) \in (\Gamma_j, \tau) \tag{5.10c}$$

$$\frac{\partial \phi}{\partial z} = 0 \qquad (z = 0, y) \in (\Gamma_b) \tag{5.10d}$$

$$\phi = 0 \qquad (z = L, y) \in (\Gamma_t). \tag{5.10e}$$

The step size ($\alpha_k$)and the conjugate coefficient ($\beta_k$) for the estimation of the unknown as suggested in Jarny et al. (1991) are utilized in the present method:

$$\alpha_k = -\frac{\int_{\Gamma_c}(T - T_{exp})\theta_k d\Gamma + \gamma_{k+1}\int_{\Gamma_j} P_k q_j d\Gamma}{\int_{\Gamma_c}\theta_k^2 d\Gamma + \gamma_{k+1}\int_{\Gamma_j} P_k^2 d\Gamma} \tag{5.11}$$

and

$$\beta_k = \{ \begin{matrix} 0 & if\,k = 0 \\ max(0, \beta^{PR}) & otherwise \end{matrix} \tag{5.12}$$

where $\beta^{PR}$ represents the Polak-Ribiere's formulation of the conjugation coefficient

$$\beta^{PR} = -\frac{\int_{\Gamma_j}\nabla J_{q_{j,k}} * \nabla J_{q_{j,k}} d\Gamma}{\int_{\Gamma_j}\left(\nabla J_{q_{j,k-1}}\right)^2 d\Gamma}. \tag{5.13}$$

The conjugate search direction is solved using the following condition

$$P_k = \{ \begin{matrix} \nabla J_{q_{j,k}} & if\,k = 0 \\ \nabla J_{q_{j,k}} + \beta_k P_{k-1} & otherwise \end{matrix}. \tag{5.14}$$

The choice of regularization parameter were chosen from the work Bozzoli et al. (2014):

$$\gamma_{k+1} = \frac{\int_{\Gamma_c}(T - T_{exp})d\Gamma}{\int_{\Gamma_j}\left(q_{j,k}\right)^2 d\Gamma}. \tag{5.15}$$

## 5.4   Computational Algorithm

To solve the partial differential equation, two-dimensional finite difference method with spatial discretization are performed by central difference scheme and Neumann boundary condition with addition of ghost points were developed. To estimate the unknown heat flux, we initially approximate the heat flux as obtained through Eq. 5.4 and the adjoint problem, gradient of the objective function are initialized before the start of iteration. The experimental temperatures are used to find the optimal search direction to find the unknown heat flux through iterative process. The detailed computational algorithm to estimate the surface heat flux and surface temperature distribution can be found in **Algorithm. 1**.

---

**Algorithm 1** Inverse heat conduction algorithm to estimate unknown heat flux

---

1: set $q_j$ as in Eq. 5.4, $\gamma_k = 0$, $\nabla J_{k+1} = 0$, $P_k = 0$,
2: get $\phi$ from **Eq. 5.10**.
3: solve $\nabla J_{q_j}$ from **Eq. 5.8**
4: **while** $T = T_{exp}$ **do**
5:     solve for $T$ based on **Eq. 5.7**
6:     get $\phi$ from **Eq. 5.10**. But use the boundary condition $T(x, t; q_j)$ as in **Eq. 5.10** which is the solution of previous step.
7:     solve $\nabla J_{q_j}$ from **Eq. 5.8**. $\phi$ is the solution from **Eq. 5.10**.
8:     Compute conjugate coefficient $\beta_k$ from **Eq. 5.12**
9:     Compute conjugate search direction as in **Eq. 5.14**
10:     Solve for $\theta$ from **Eq. 5.9**.
11:     Compute for $\gamma_{k+1}$, regularisation term from **Eq. 5.15**.
12:     Compute the optimal step size ($\alpha_k$) from **Eq. 5.11**.
13:     Estimate $q_{j,k+1}$ from the following equation $q_{j,k+1} = q_{j,k} + \alpha_k * P_k$
14: **end while**

---
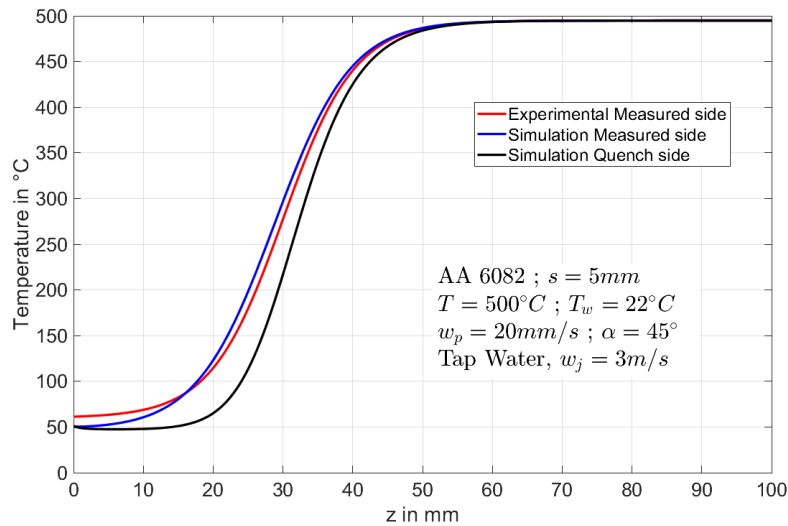
Figure 5.5: Temperature distribution in the measuring and quenching region for quasi-steady state condition
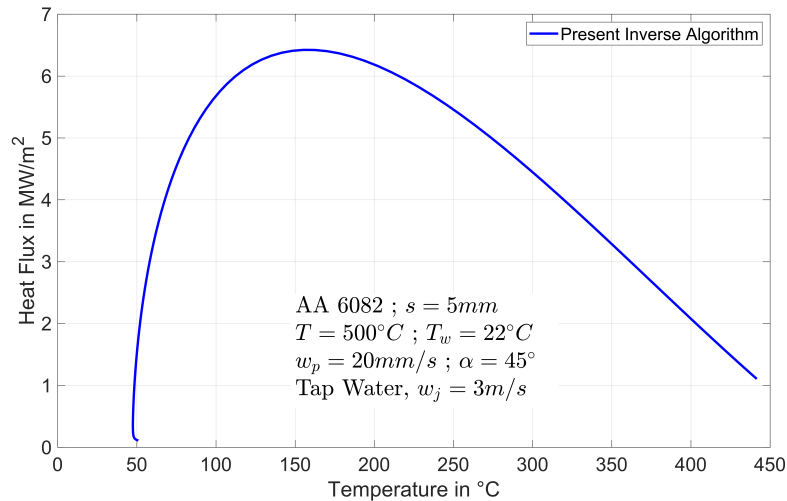


Figure 5.6: Boiling curve at the water jet impingement region for quasi-steady state condition
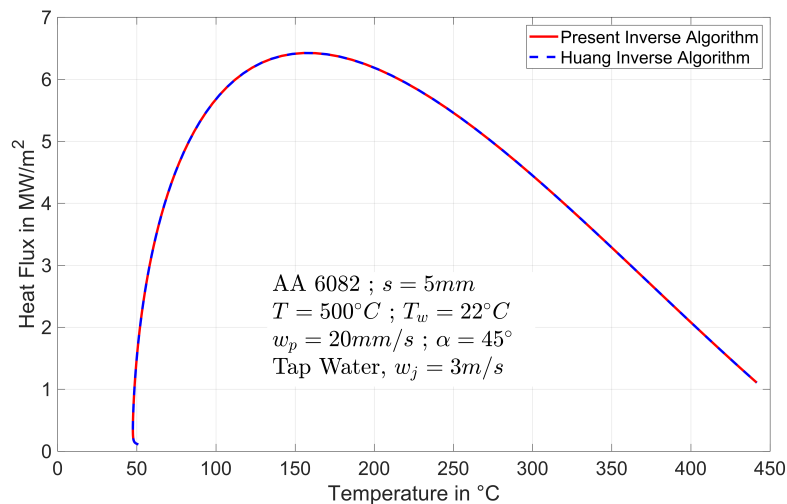


Figure 5.7: Comparison of present 2D inverse solution with Huang and Wang (1999)

**Fig. 5.5** and **Fig. 5.6** shows the numerical validation of the temperature profiles from inverse model with that of the experimental measurements and the typical boiling curve for the hot moving plate were also obtained through 2-dimensional inverse technique. **Fig. 5.7** shows the comparison of two-dimensional inverse solution from the present model with the inverse model from literature without regularization term as proposed by Huang and Wang (1999) for the quasi-steady state condition. The inverse solution from the present method perfectly matches well with the method from Huang and Wang (1999) and efficient use of the present method significantly reduces the fluctuations in inverse solutions and computational time.

## 5.5 Results and Discussion

### 5.5.1 Experimental Repeatability and Water Quality

To verify the experimental repeatability of the quenching process for hot moving metal plates, the experiments were performed with tap water for the similar set of experimental conditions on the same metal sheet for 2 consecutive times. **Fig. 5.8** shows the temperature profiles for the 2 consecutive experimental cases. The experiments were conducted on a 10 $mm$, AA6082 sheet at an initial temperature of around 500 °$C$, jet angle of 45 °, jet velocity of 3 $m/s$, the water temperature of 22 °$C$ and plate speed of 20 $mm/s$. We clearly observe the perfect match for the 2 cases of experimental measurements and thus we can conclude that the experiments are repeatable.
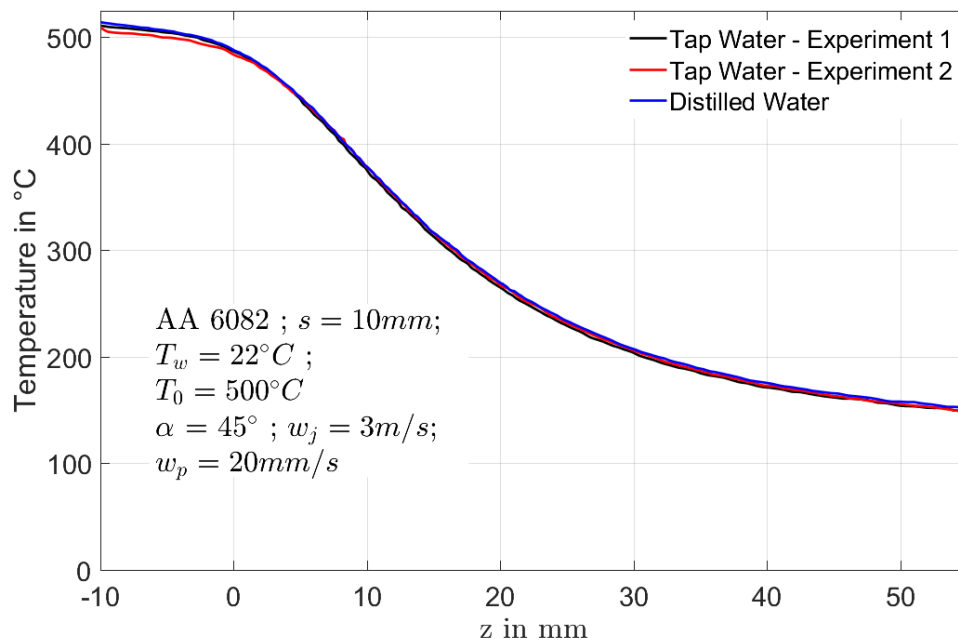


Figure 5.8: Superimposed temperature profile for different water quality Kulkarni (2019)
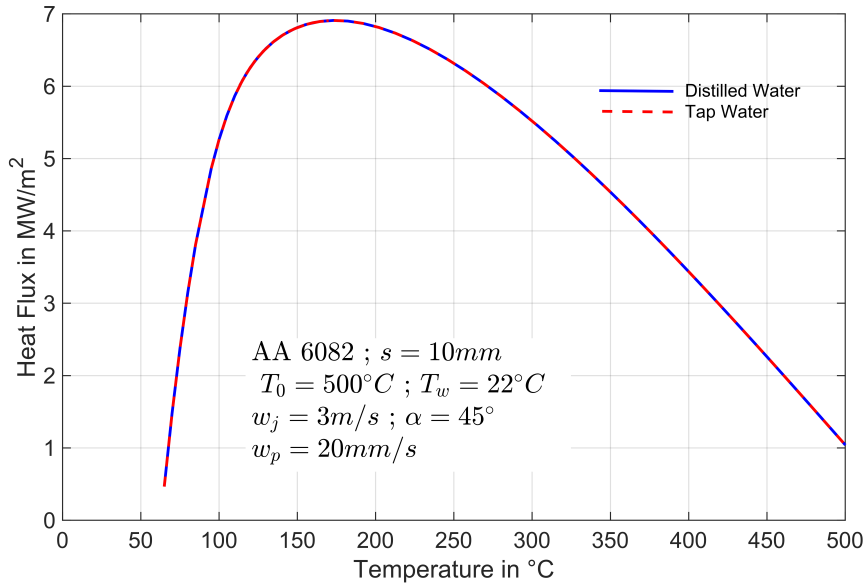
Figure 5.9: Boiling curve for different water quality

Table 5.5: Width of the various boiling regions Kulkarni (2019)

| | |
|---|---|
| Pre-Cooling Region | 5.2 $mm$ |
| Transition Boiling Region | 26.5 $mm$ |
| Nucleate Boiling Region | - |
| $T_s = 0.99 * T_0$ | 509°C |
| $T_{z=0}$ | 485°C |
| $T_{DNB}$ | 172°C |
| $q_{z=0}$ | 1.4 $MW/m^2$ |
| $q_{max}$ | 6.9 $MW/m^2$ |

In contrast, Abdalrahman et al. (2014) and Specht (2017) reported the strong influence of quality of cooling water on heat transfer with the spray nozzle. The authors have conducted an extensive study to determine the influence of the salt content on the Leidenfrost and DNB temperature, maximum heat flux, and heat transfer coefficient. The maximum heat flux, Leidenfrost and DNB temperature increase consistently with the salt content. Henceforth, to identify the influence of water quality on heat transfer during quenching, the experiments were performed for tap water and distilled water. The tap water used for experiments is the water in Magdeburg, Germany. The electrical conductivity of this tap water is measured to be 0.58 $mS/cm$. The distilled water is obtained from the distillation of tap water to remove salts and impurities in water. Therefore, the electrical conductivity of distilled water is 0 $mS/cm$.

Fig. 5.8, shows the superimposed temperature profiles for distilled water and tap water and indicates the identical temperature profiles. Thus, it means that the change in water quality has no influence on heat transfer in the impingement zone. **Fig. 5.9** shows the comparison of surface temperature and corresponding heat fluxes on the quenching region for distilled water tap water. Fig. 5.9, can be typically defined as the characteristic of the boiling curve and the transfer of heat for different boiling phenomena i.e., film boiling, transition boiling, nucleate boiling and saturation boiling are demonstratively the same. In **Tab. 5.5**, the width of the boiling region is summarized. The boiling width of pre-cooling is 5.2 mm and the boiling width of the transition boiling region is above the pre-cooling region. The accurate width of nucleate boiling cannot be determined because the final measurement is

greater than 100°$C$. Although, based on the temperatures from the quenching side, the width of nucleate boiling is approximately determined to be 30 mm. From the observations, we can conclude that the quality of water has no significant influence on cooling at the impingement surface. Henceforth, for further experimental analysis, tap water is used as a cooling agent mainly to remove heat from the hot moving plate.

## 5.5.2   Thickness of Metal Sheet
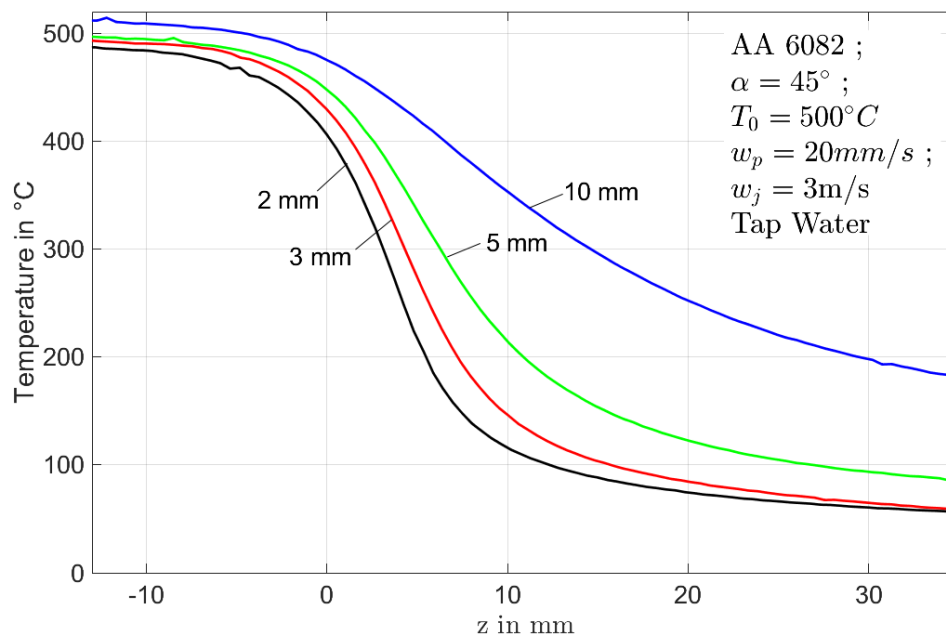


Figure 5.10: Superimposed temperature profile for different thickness Kulkarni (2019)

To study the heat transfer changes during the quenching process for different thicknesses of the metal sheet, experiments were conducted with water at 22 °$C$, jet velocity, and angle of 3 $m/s$ and 45 °$C$ respectively. An AA6082 alloy heated to an initial temperature of around 500 °$C$ and plate speed of 20 $mm/s$ metal sheet with different thickness of 2 mm, 3 mm, 5 mm and 10 mm were used for analysis. **Fig. 5.10** shows superimposed temperature profiles for different thicknesses of the metal sheet. Hypothetically, higher thickness of the plate leads to longer cooling time with these conditions; a 10 mm sheet cannot be cooled to 100 °$C$.

**Fig. 5.11** shows the boiling curve for different metal sheet thickness. The departure nucleate boiling (DNB) temperature for different sample thickness remains constant at nearly 180 °$C$ and the maximum heat flux increases from 5.4 $MW/m^2$ to 6.9 $MW/m^2$ for 2 mm to 10 mm, respectively. Below 100 °$C$ some profiles are crossing over, which has no physical meaning. The reason are the problems in the analysis. The temperature measurements below 100 °$C$ because a little bit inaccurate. Because of high temperature gradient in the region of nucleate boiling the inverse method can have some fluctuations. As a consequence the profiles below 100 °$C$ can be only considered as approximation.

**Tab. 5.6** shows the characteristic values and the widths of various regions during quenching of the metal sheet. The width of the pre-cooling region decreases with increase in metal sheet thickness from 8.3 mm to 5.2 mm. As the pre-cooling region lowers, the interface temperature reaches higher values due to reduced heat transfer from dry region to quenched region. This leads to increase in width of the transition boiling region for higher metal sheet thickness from 5.5 mm to 26.5 mm. Whereas, the width of the nucleate boiling region

seems independent of the thickness. The values for the 10 mm plate can not be determined, because the final temperature is greater than 100 °C.
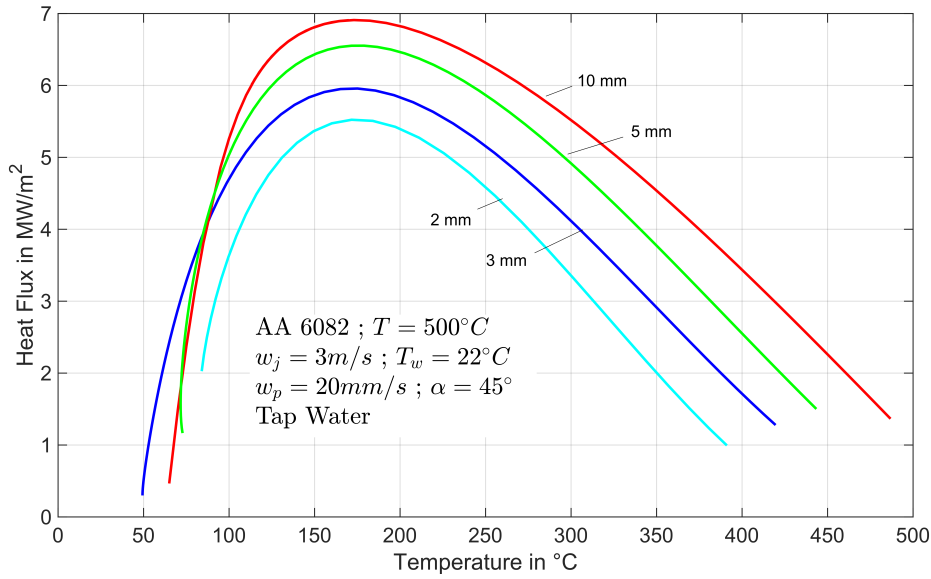


Figure 5.11: Boiling curve for different thickness

Table 5.6: Width of various regions for different thickness Kulkarni (2019)

|  | 2 mm | 3 mm | 5 mm | 10 mm |
|---|---|---|---|---|
| Pre-Cooling Region | 8.3 mm | 7.4 mm | 6.9 mm | 5.2 mm |
| Transition Boiling Region | 5.5 mm | 7.3 mm | 11.0 mm | 26.5 mm |
| Nucleate Boiling Region | 6.8 mm | 5.5 mm | 7.3 mm | > 30 mm |
| $T_s = 0.99 * T_0$ | 495°C | 499°C | 500°C | 509°C |
| $T_{z=0}$ | 407°C | 426°C | 450°C | 485°C |
| $T_{DNB}$ | 171°C | 175°C | 175°C | 172°C |
| $q_{z=0}$ | 0.6 $MW/m^2$ | 1.2 $MW/m^2$ | 1.5 $MW/m^2$ | 1.4 $MW/m^2$ |
| $q_{max}$ | 5.5 $MW/m^2$ | 6.0 $MW/m^2$ | 6.8 $MW/m^2$ | 6.9 $MW/m^2$ |

Caron (2008), also reported an increase in maximum heat flux as the thickness of the plate is raised during the secondary cooling process.

### 5.5.3   Jet Velocity

For constant plate velocity of 20 mm/s, the jet velocities are varied from 2.1 $m/s$ (46 $l/min/m$) to 3.3 $m/s$ (76 $l/min/m$) in the range of 0.3 m/s. **Fig.   5.12** shows the comparison of temperature distribution for various jet velocities at quasi-steady-state condition.  The quenching conditions implemented for the experimentation are given in Fig.  5.12.  For jet velocities, lower than 2 m/s at 45° jet angle, the jet possesses lower momentum to effectively make contact with a hot moving plate.  For the higher jet velocities, the temperature increases slightly while maintaining the same cooling tendency and the temperature profile remains to be at a quasi-steady-state condition. **Fig.  5.13** shows the boiling curve for different jet velocities at quasi-steady-state for the surface temperature as shown in Fig.  5.12.  The effect of gravity on the heat transfer during vertical plate movement from top to bottom occurs, since the cooling water must flow downward after the initial contact with the hot moving plate.  The gravitational phenomena apply to all the jet velocities during experimentation.  Henceforth, from the surface temperature

measurements and the heat flux extraction, profiles are as depicted in Fig. 5.12 and Fig. 5.13. The observation clearly shows that the jet velocity has no consistent influence on the heat extraction from the plate. The maximum heat flux spans approximately 6.5 - 6.7 $MW/m^2$ and the corresponding DNB temperature are about 180°.
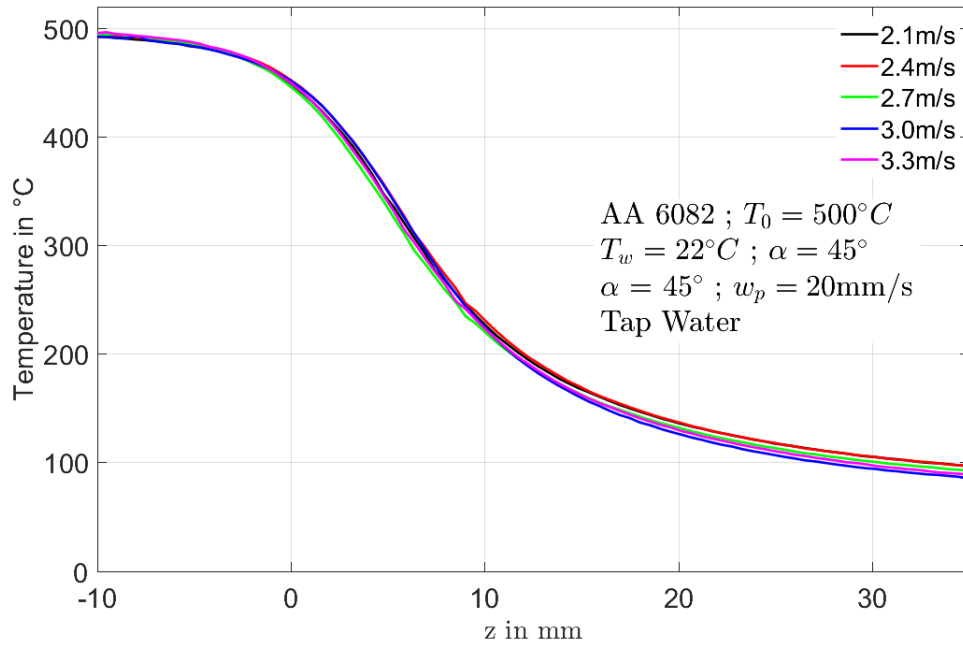


Figure 5.12: Superimposed temperature profile for different jet velocity Kulkarni (2019)
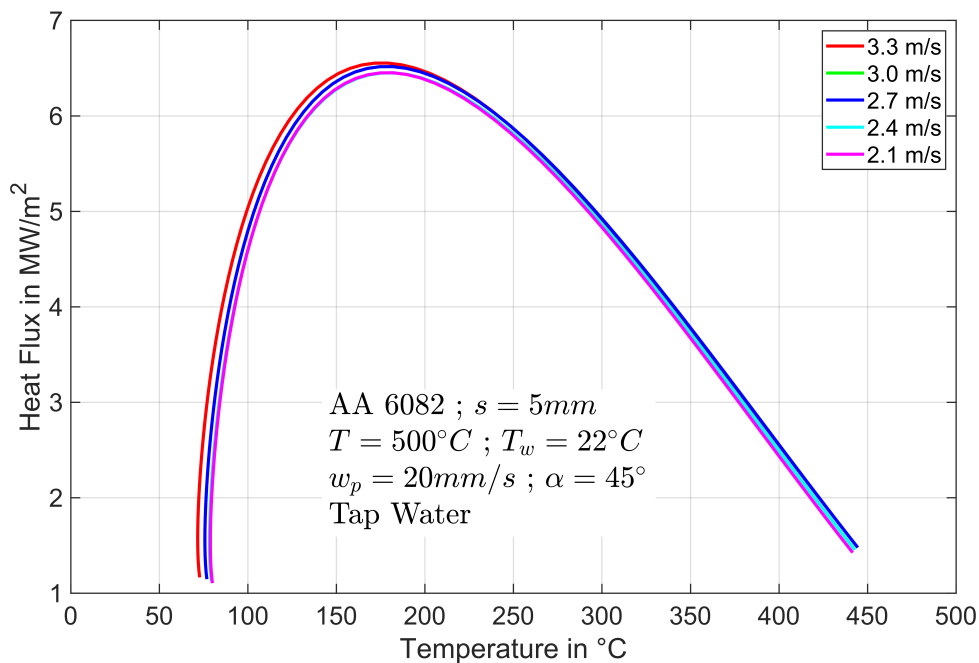


Figure 5.13: Boiling curve for different jet velocity

From the boiling curve, it can be seen that the velocity has no significant change with respect to the maximum heat extraction. Fujimoto et al. (2015a) observed that with an increase in the velocity of a jet the heat flux increases slightly.

### 5.5.4   Jet Impingement Angle
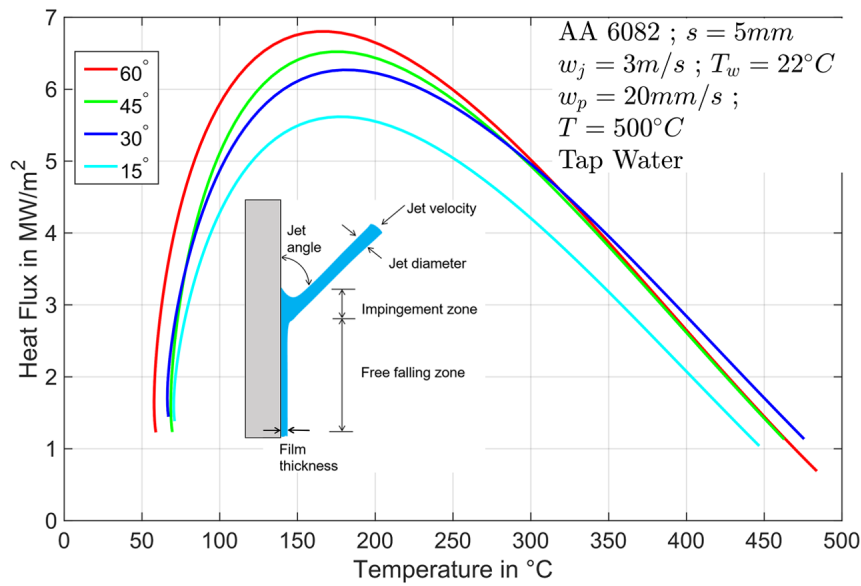


Figure 5.14: Boiling curve for different jet angle

**Fig.   5.14** shows the boiling curve for angles from 60 ° to 15°.   For the variation of
the jet impingement angle, the vertical plate is taken as a reference point with angle 0°.
The boiling curve gives an overview of the heat transfer with the surface temperature
of the quenched plate.   As the angle of the jet impingement is lowered, the peak heat
flux consistently decreases.   The departure nucleate boiling (DNB) temperature remains
constant.   Consequently, the impingement angle significantly weakens the heat transfer in
the impingement region. Wang et al. (2019a) also showed that the maximum heat extraction
increases with an increase in case of slit nozzle impingement angle.

In the downstream side, the higher percentage of heat transfer occurs toward the
aligned nozzle.   The local heat transfer decreases with the increase of impingement angle
perpendicular to the plate, consequently the distance from the plate to the jet increases.
The momentum of the water jet decreases as the jet impingement angle moves away from
the perpendicular.   The water flow in the downstream direction increases along with the
wetting front velocity as the jet impingement angle is raised.   The velocity of the front
decreases in the upward and downward direction as the impingement angle is raised, due
to the considerable decrease in the flow rate.

### 5.5.5 Plate Speed
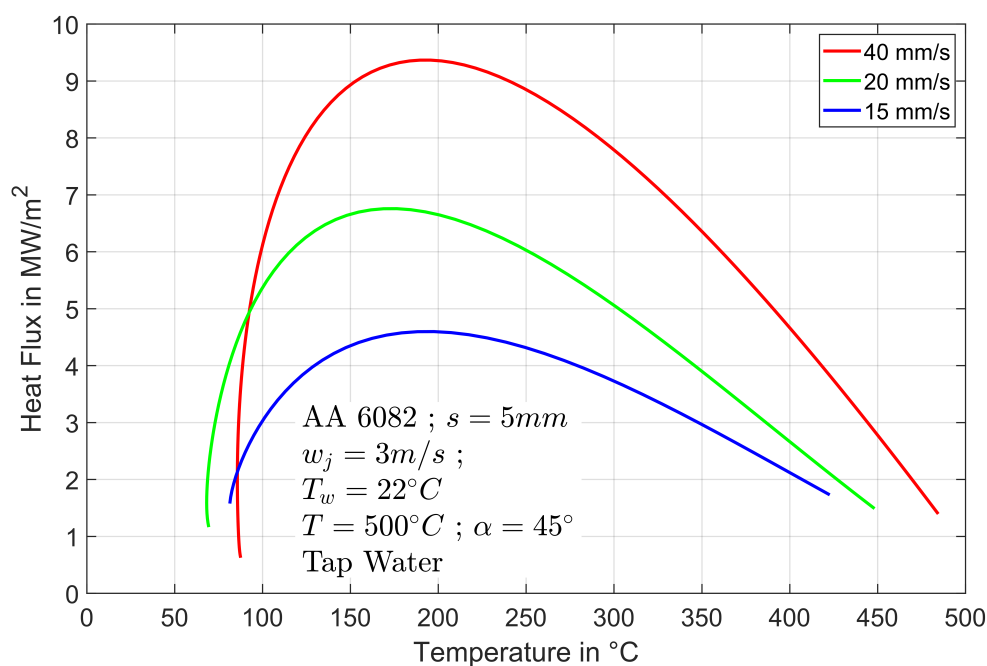


Figure 5.15: Boiling curve for different plate speed

**Fig. 5.15** shows the characteristic boiling curves for different plate velocities. The characteristic data of boiling widths are summarized in **Tab. 5.7**. The observations of the boiling width show that the DNB temperature decreases slightly with the plate speed. For plate speeds of 15 $mm/s$ and 40 $mm/s$, the corresponding DNB temperatures are 201 °C and 192 °C. Whereas, the maximum heat flux increases with the plate speed for 15 $mm/s$ and 40 $mm/s$ are 4.6 $MW/m^2$ and 9.4 $MW/m^2$. Caron and Wells (2006) showed a similar effect of the plate velocity on the boiling curve. The peak heat flux increases with the plate speed for the surface temperature below the Leidenfrost point. Contradictorily they observed that the increase in initial temperature of the test sample above the Leidenfrost point lowers the heat extraction. Caron and Wells (2009a) in their publication on the secondary cooling process of magnesium alloy observed that increase in plate velocity has no significant influence on the maximum heat extraction and found an approximate value of 4.7 $MW/m^2$ with the corresponding DNB temperature of about 200 °C. Researchers in Vakili and Gadala (2013), Sharma and Sahu (2019a), Wang et al. (2019a), Gradeck et al. (2012) reported that with an increase in the plate speed the heat transfer reduces slightly. Opstelten and Rabenberg (2016) and Jha et al. (2015b) shows that with an increase in the plate speed the heat flux increases significantly.

Tab. 5.7 shows the front width of various regions during the quenching process. The front width in the pre-cooling region decreases with an increase in plate speed, for 15 $mm/s$ and 40 $mm/s$ are 10.7 $mm$ and 3.5 $mm$, respectively. The front width in the transition boiling region increases with an increase in plate speed, for 15 $mm/s$ and 40 $mm/s$ it corresponds to 7.9 $mm$ and 23.7 $mm$, respectively. The obtained boiling widths support the hypothesis that the boiling curves depend on the interface temperature and for the same interface temperature, they obtained the same boiling curve for different thicknesses of the plate.

The observations show that with an increase in plate speed, the width of the pre-cooling region is reduced. The lowering of the pre-cooling region is significant for the metal processing industry, where once the metal crosses a critical temperature (like eutectic temperature in case of steel) a lower rate of cooling will lead to the determination of material properties. Hot metal will cross the critical temperature in the pre-cooling region

and will experience slow cooling. To avoid slow cooling, the moving speed of the plate should be increased. Hence, the length of the quenching setup increases with a higher rate of cooling.

Table 5.7: Width of various regions for different casting speed of $5mm$ thick plate Kulkarni (2019)

|  | $15\ mm/s$ | $20\ mm/s$ | $40\ mm/s$ |
|---|---|---|---|
| Pre-Cooling Region | $10.7\ mm$ | $6.9\ mm$ | $3.5\ mm$ |
| Transition Boiling Region | $7.9\ mm$ | $11.0\ mm$ | $20\ mm$ |
| Nucleate Boiling Region | $9.0\ mm$ | $7.3\ mm$ | $> 8\ mm$ |
| $T_s = 0.99 * T_0$ | $506°C$ | $489°C$ | $509°C$ |
| $T_{z=0}$ | $422°C$ | $449°C$ | $485°C$ |
| $T_{DNB}$ | $190°C$ | $170°C$ | $190°C$ |
| $q_{z=0}$ | $1.7\ MW/m^2$ | $1.5\ MW/m^2$ | $1.4\ MW/m^2$ |
| $q_{max}$ | $4.6\ MW/m^2$ | $6.7\ MW/m^2$ | $9.4\ MW/m^2$ |

## 5.5.6 Initial Temperature of Metal Sheet
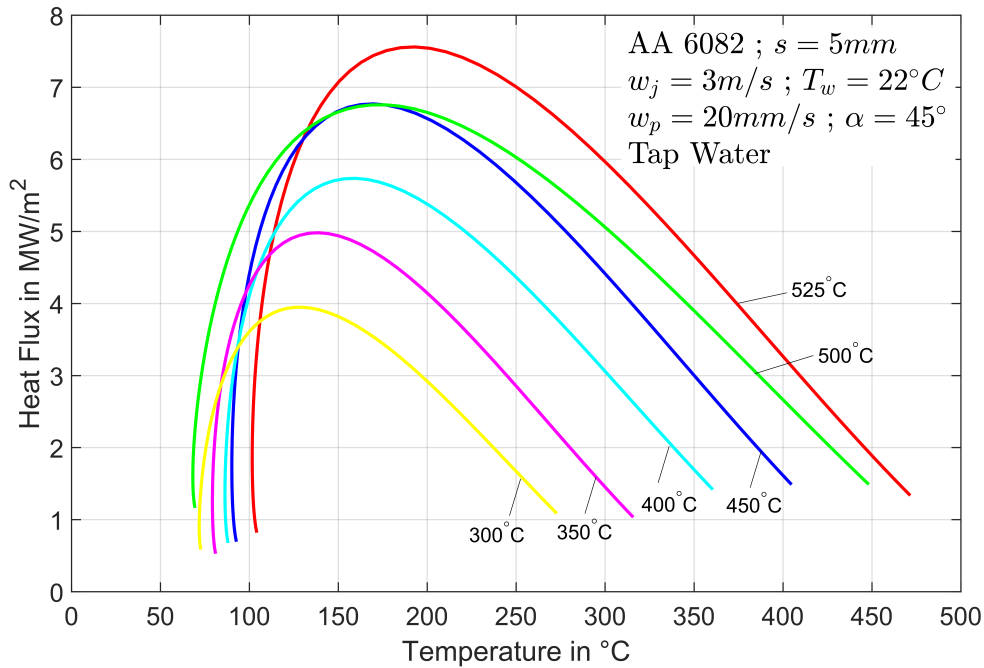


Figure 5.16: Boiling curve for different initial temperature
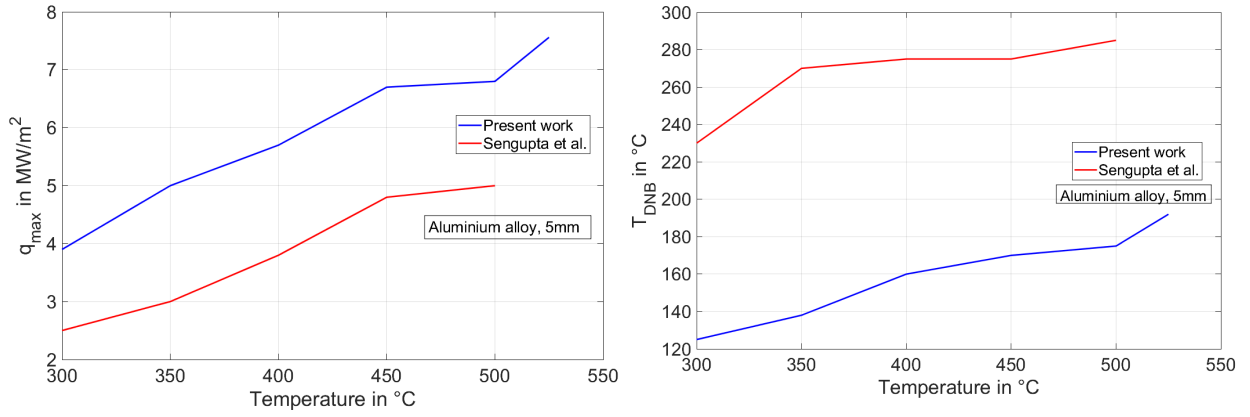
Figure 5.17: Comparison of $\dot{q}_{max}$ and DNB temperature with Sengupta and Wells (2005)

**Fig. 5.16** shows the boiling curve for the different initial temperatures of an Aluminium sheet. The characteristic data for boiling widths are given in **Tab. 5.8**. The intensity of the maximum heat flux strongly depends on the initial temperature on the metal. The magnitude of maximum heat flux increases with the increase in initial temperature and after an initial temperature of $450°C$, the maximum heat flux remains constant. A similar effect occurs for the departure nucleate boiling for an initial temperature of the metal sheet. **Fig. 5.17** shows a comparison of $q_{max}$ and DNB temperature with Sengupta and Wells (2005). The comparison shows a similar tendency as reported in this work.

Table 5.8: Width of various regions for different initial temperature Kulkarni (2019)

| | $300°C$ | $350°C$ | $400°C$ | $450°C$ | $500°C$ | $525°C$ |
|---|---|---|---|---|---|---|
| Pre-Cooling Region | $5.9\ mm$ | $5.5\ mm$ | $5.8\ mm$ | $5.8\ mm$ | $5.8\ mm$ | $5.8\ mm$ |
| Transition Boiling Region | $11.1\ mm$ | $11\ mm$ | $10.7\ mm$ | $10.0\ mm$ | $11.7\ mm$ | $11.4\ mm$ |
| Nucleate Boiling Region | $2.1\ mm$ | $4.1\ mm$ | $4.5\ mm$ | $5.8\ mm$ | $6.9\ mm$ | $> 7mm$ |
| $T_s = 0.99 * T_0$ | $297°C$ | $346°C$ | $396°C$ | $445°C$ | $495°C$ | $520°C$ |
| $T_{z=0}$ | $273°C$ | $315°C$ | $360°C$ | $405°C$ | $450°C$ | $473°C$ |
| $T_{DNB}$ | $125°C$ | $138°C$ | $160°C$ | $170°C$ | $175°C$ | $192°C$ |
| $q_{z=0}\ (MW/m^2)$ | 1.0 | 1.0 | 1.41 | 1.48 | 1.5 | 1.3 |
| $q_{max}\ (MW/m^2)$ | 3.9 | 5.0 | 5.7 | 6.7 | 6.8 | 7.56 |

Tab. 5.8 shows the width of boiling regions during the quenching process. The width of the pre-cooling region remains constant for different initial temperatures, thus it can be concluded that the Biot number and the Peclet number also remain constant, and the analytical solution for the non-dimensional temperature profile will remain constant in the pre-cooling region. The value of the interface temperature decreases with the initial temperature. Whereas, the width of the transition boiling region remains constant. From these interpretations, it can be understood that the metal sheet experiences more thermal gradient in the transition boiling region for higher initial temperature. The width of the nucleate boiling region increases with initial temperature. Whereas, for the lower initial temperature of the plate, the departure nucleate boiling temperature should be decreased.

### 5.5.7   Kinds of Metal

Finally, the influence of such metal on the quenching process will be discussed. Aluminium, Nickel and Nicrofer are used as materials. The thermophysical properties are summarized in **Tab. 5.9** for the temperature of $20°C$. The thickness of the plates was 2 $mm$. The plate speed of 20 $mm/s$, the initial temperature of $500°C$, tap water of $22°C$ and a jet with 3 $m/s$ at an angle of $45°$was kept constant. **Fig. 5.18** shows the temperature drop for the metal samples. Aluminium has the fastest and Nicrofer has the slowest cooling rate. Since the thermal conductivity of the metal sample is higher and the corresponding cooling rate increases proportionally.
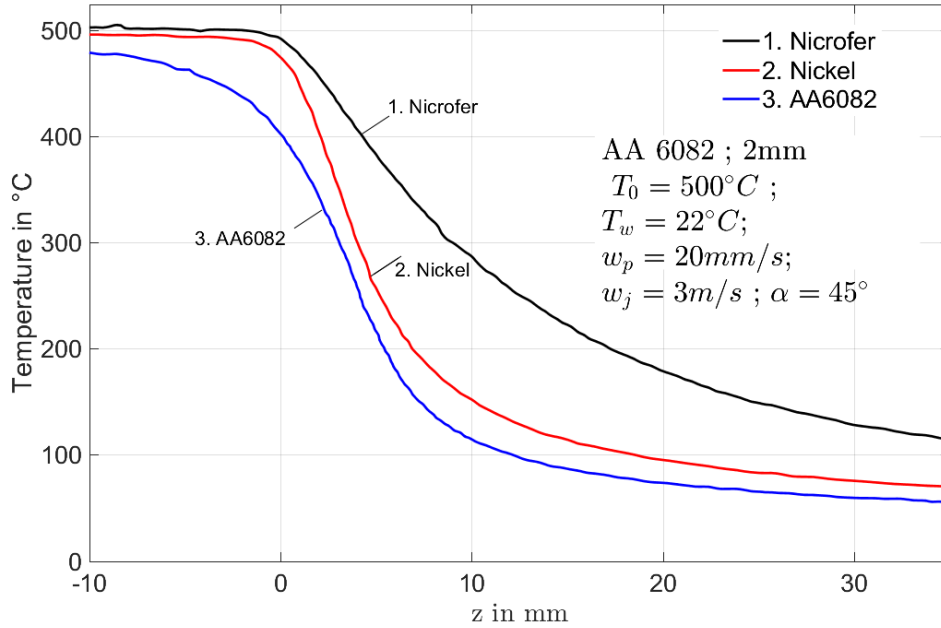


Figure 5.18: Temperature drop for different kinds of metals Kulkarni (2019)

Table 5.9: Material properties for different metals at $20°C$ Kulkarni (2019)

|  | Aluminum | Nickel | Nicrofer |
|---|---|---|---|
| **Density** $(kg/m^3$ $)$ | 2700 | 8908 | 8400 |
| **Thermal Conductivity** $(W/m \cdot K)$ | 170 | 65 | 17 |
| **Specific Heat Capacity**$(J/kg \cdot K)$ | 1050 | 500 | 510 |
| **Thermal Effusivity** $(W\sqrt{s}/m^2 \cdot K)$ | $2.2 * 10^4$ | $1.7 * 10^4$ | $8.5 * 10^3$ |
| **Thermal Diffusivity** $(m^2/s)$ | $6.0 * 10^{-5}$ | $1.45 * 10^{-5}$ | $4.0 * 10^{-6}$ |
| **Thickness (mm)** | 2 | 2 | 2 |
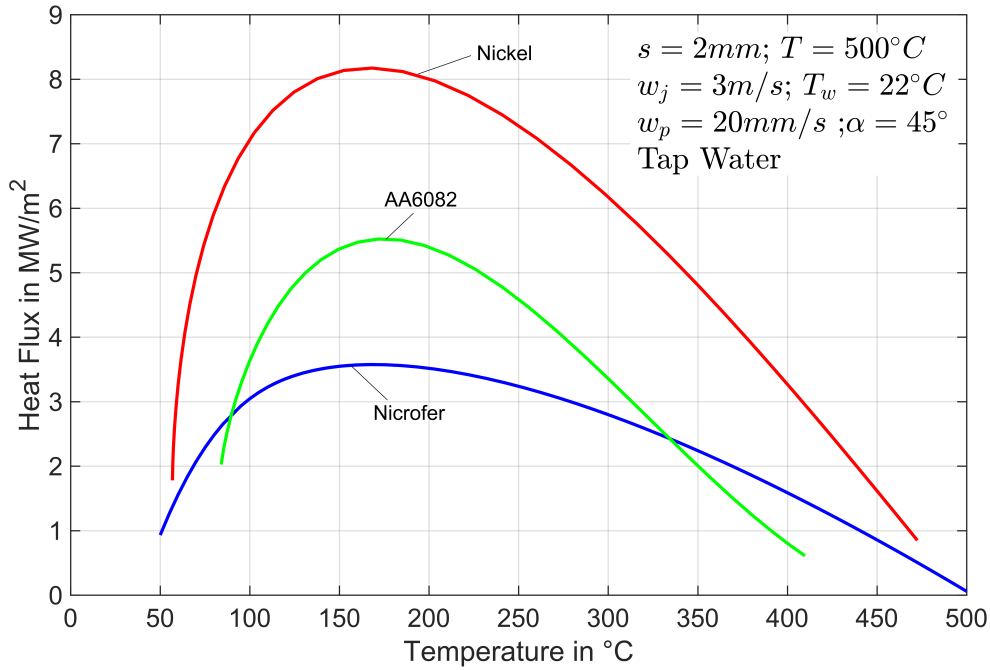
Figure 5.19: Boiling curve for different kinds of metals

Table 5.10: Width of various regions for different metals Kulkarni (2019)

| | Aluminum | Nickel | Nicrofer |
|---|---|---|---|
| Pre-Cooling Region | $8.3\ mm$ | $1.0\ mm$ | $0.2\ mm$ |
| Transition Boiling Region | $5.5\ mm$ | $7.9\ mm$ | $22.0\ mm$ |
| Nucleate Boiling Region | $4.1\ mm$ | $3.8\ mm$ | $4.8\ mm$ |
| $T_s = 0.99 * T_0$ | $495°C$ | $495°C$ | $495°C$ |
| $T_{z=0}$ | $407°C$ | $462°C$ | $493°C$ |
| $T_{DNB}$ | $171°C$ | $170°C$ | $175°C$ |
| $q_{z=0}$ | $0.6\ MW/m^2$ | $15\ MW/m^2$ | $0.1\ MW/m^2$ |
| $q_{max}$ | $5.5\ MW/m^2$ | $8.2\ MW/m^2$ | $3.6\ MW/m^2$ |

**Tab. 5.10** shows the widths of various zones during the quenching process of different metals. It can be observed that the width of the pre-cooling region for metals with low thermal conductivity and high heat capacity is smaller. Hence, during the heat transfer analysis of metals with high thermal conductivity, it is important to quantify the temperature drop because of the diffusion of heat. The initial temperature is in all cases $495°C$. The higher the conductivity the lower is the interface temperature. For nicrofer with the lowest conductivity, the temperature drop is only $2°C$ and for Aluminium with the highest conductivity the drop is $88°C$. The width of the transition boiling region also increases with heat capacity and with decreasing thermal conductivity. Whereas, the width of the nucleate boiling region is the same for Aluminium, nickel and nicrofer.

**Fig. 5.19** shows the boiling curve for these different metals. It can be clearly seen that the boiling curve strongly depends on material properties. The maximum heat flux for nickel is higher than other metals. It has the same tendency as for the full jet nozzle **Fig. 4.66**. The DNB temperature for nickel, Aluminium is $175°C$. The reason for the large fluctuations in the maximum heat flux cannot be given. Contradictorily, Zhao et al. (2015) reported that for quenching of an array of jet Aluminium possesses a higher maximum heat flux value compared to nickel material and the analysis was primarily performed using the one-dimensional analytical model.

## 5.5.8 Mechanism of Heat Transfer
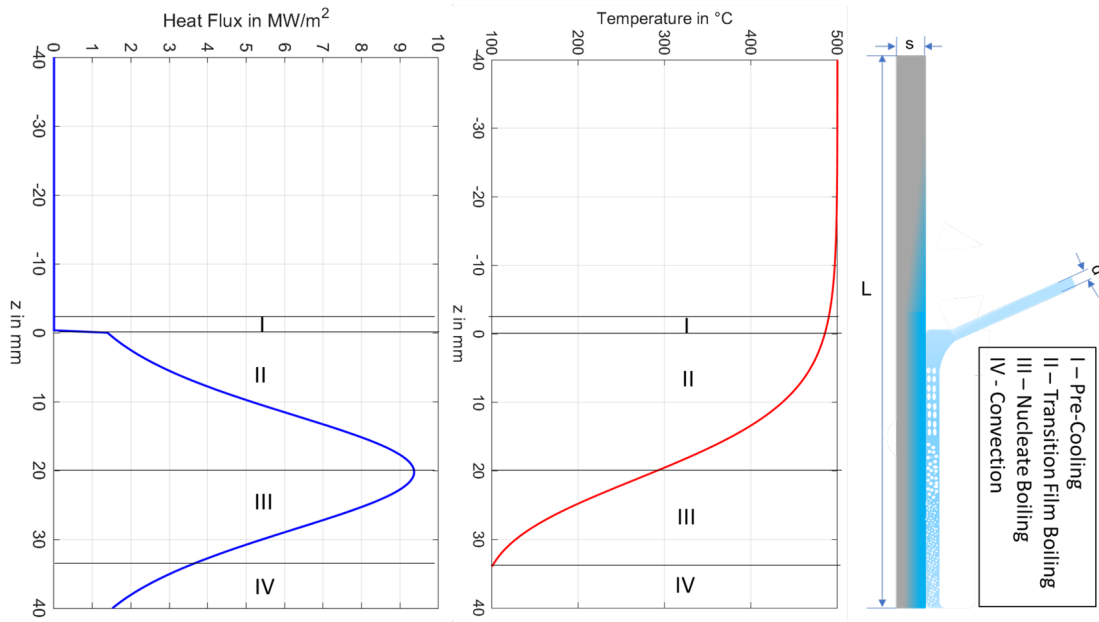


Figure 5.20: Physical mechanism for the high plate speed condition

**Fig. 5.20** shows the schematic of the physical mechanism of the mold quenching with array of jets at high plate velocity i.e., 40 $mm/s$ and the surface measured temperatures, surface quenched side heat fluxes at quasi-steady condition. In the Fig. 5.20, we can distinguish heat transfer mechanism into four regimes based on the surface heat flux profiles obtained from numerical analysis as well as the measured surface temperatures. The axial length in the surface temperatures and heat fluxes are indicated to be $+z$ and $-z$ with 0 mm acts as the interface between the dry region and the water quenching region. Pre-cooling region can be observed above the interface point. As can be seen from Tab. 5.7, the pre cooling length is with 3.5 mm very short. The length of the transition boiling regime is with 24 mm relatively long. The position with the maximum heat flux is at the position $z = 20mm$.
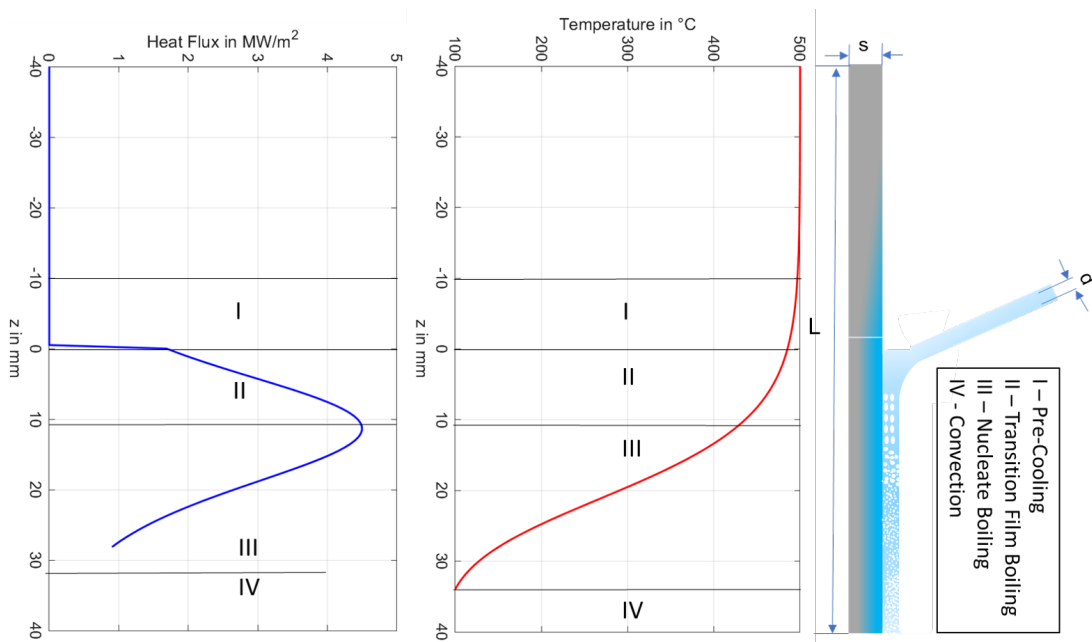


Figure 5.21: Physical mechanism for the low plate speed condition

**Fig. 5.21** shows the schematic of the physical mechanism of the mold quenching with array

of jets at high plate velocity i.e., 5 $mm/s$ and the surface measured temperatures, surface quenched side heat fluxes at quasi-steady condition. The pre-cooling region is with 10.7 mm very long and the transition boiling length with $7.9mm$ relatively short. Therefore, the position with the maximum heat flux is more closer to the impingement point. The results showed, that the maximum heat flux is as larger as the plate speed is. The flow profile of the water film must be independent on the plate speed, because it is much lower as the speed of the water film. As a consequence, this effect can only be explained with a heat transfer depended on the local position. The more the position is away from the impingement point the higher must be the heat transfer. This can be explained with the increasing velocity of the water film due to the gravity. In Fig. 5.22 the maximum heat flux is shown in dependence on the position from the impingement point for the lower plate velocity.

In section 5.5.2 it was shown that the maximum heat flux increases with the thickness. From Tab. 5.6 it can be seen, that the transition boiling region increases with the thickness, that means the distance from the impingement point increases. The heat transfer again depends on the local position. The profile of the water film must be independent on the plate thickness. The maximum heat flux for the low plate thickness are also gives in Fig. 5.22. The value for the the thickness $10mm$ can be considered as not very precise because there is not a complete cooling as can be seen in Fig. 5.10. Fig. 5.23 the DNB temperature is shown versus the distance to the impingement point. It can be concluded, that the DNB temperature is nearly independent on the position. It should be noted that the exact value of the DNB temperature is difficult to describe because of the fluctuating heat flux profile. This result smaller with the heat transfer for the full jet quenching. In **Fig. 4.42** is was shown that the DNB temperature is also independent on the local position for this kind of quenching.

In section 5.5.6 it is shown that the maximum heat flux increases with initial temperature. From Tab. 5.8 it can be seen that the length of the transition boiling region and also the pre-cooling region is independent on the initial temperature. Therefore, the change of the maximum heat flux can not be explained with the local position. However, from Tab. 5.5.6 it can be seen that the DNB temperature significantly decreases with decreasing initial temperature. In all cases discussed before, the DNB temperature always remained in the range of 170 - 190 $°C$. As a consequence, the mechanism of heat transfer must be depend on the initial temperature, because with this temperature the DNB temperature and also the range of nucleate boiling change. In Fig. 4.37 and Tab. 4.10 it would be seen also for the full jet quenching, that the DNB temperature decreases with decreasing initial temperature. Its influence was shown in Fig. 5.17.
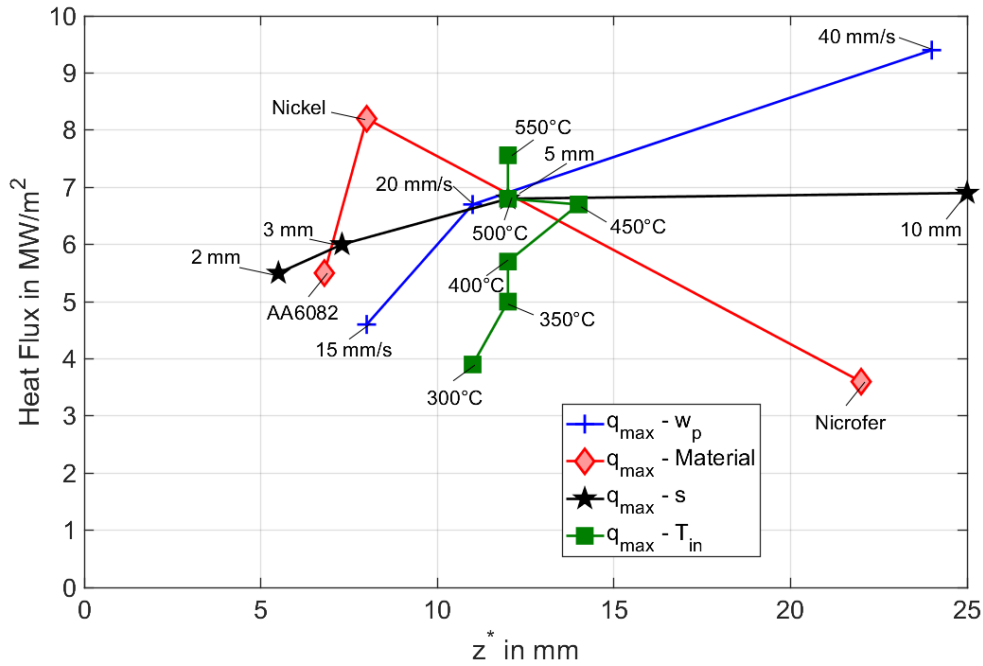
Figure 5.22: Heat flux comparison for different process parameters with respect to plate length

**Fig.  5.22** lists the heat flux with respect to the plate length comparison of different process parameters such as $s$, $T_{in}$, $w_p$, $w_j$, $\alpha$ and different kinds of material. The heat flux profiles discussed were listed with reference to the interface position i.e., at 0 mm. Above the interface position, the region is distinguished as dry region and below it is termed as water cooling region. The maximum heat flux increases with respect any parameter variation as mentioned earlier. The peak of the maximum heat flux lies between 4 $MW/m^2$ and 10 $MW/m^2$ and position of the peak lies within 10 mm between 5 mm and 15 mm plate length. Whereas,for nicrofer material, 40 $mm/s$ plate velocity, and 10 mm plate thickness the maximum heat flux shows large fluctuations and position of the peak shifts towards the lower part of the plate at 20 mm for Nicrofer, 40 $mm/s$, and for 10 mm at around 35 mm distance. In case of nicrofer and 10 mm plate thickness significantly less internal heat conduction because of the lower thermal conductivity and higher thickness offers significantly low heat diffusion and hence the delay in the heat flux extraction can be observed from this discussion. However, the re-wetting heat flux for all the process parameter lies in the range of 1 - 2 $MW/m^2$ and the interface position acts as a barrier between the dry region and the water cooling region.
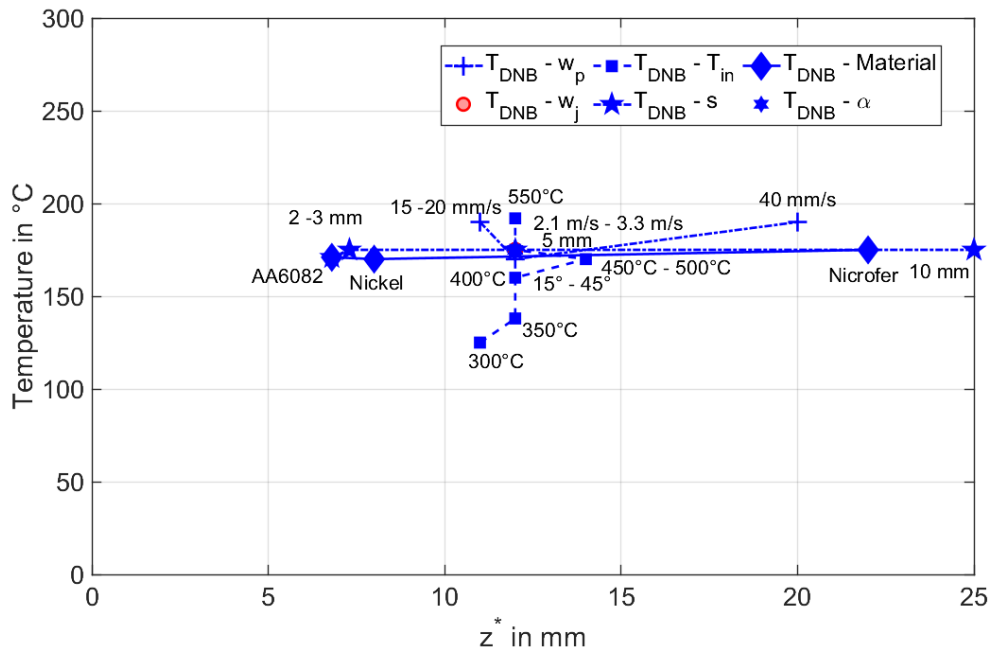
Figure 5.23: Departure nucleate boiling temperature comparison for different process parameters with respect to plate length

**Fig. 5.23** discuss the temperature variation with respect to the plate length for different variation of the process parameters. From the temperature data, we can clearly observe the constant temperature for departure nucleate boiling at around 180 - 200 $°C$. Although the temperature value remains constant at around $200°C$, position of the temperature lies between 5 mm and 15 mm from the interface temperature. But for 40 $mm/s$, nicrofer, 10 $mm$ process parameters position of the temperatures shifts far from the interface position i.e., 20 mm, 22 mm, 35 mm from the interface position. Reason for the shift to lower position could be the resistance to the heat diffusion for thicker body, low thermal conductivity material, and higher plate velocity promotes the resistance to the heat propagation at the impingement position and henceforth the delay in the heat transfer shifts to lower position on the plate. In similar way, the re-wetting temperature also lies at the interface position between the water cooling region and the dry region. For the increase of the surface temperature, the re-wetting temperature raises to higher values while remaining stagnant at the interface position.

### 5.5.9   Application to industrial DC casting process
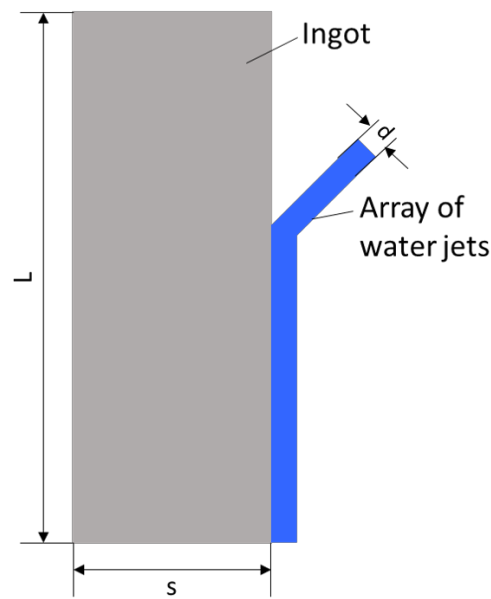


Figure 5.24: Schematic of industrial dc casting process
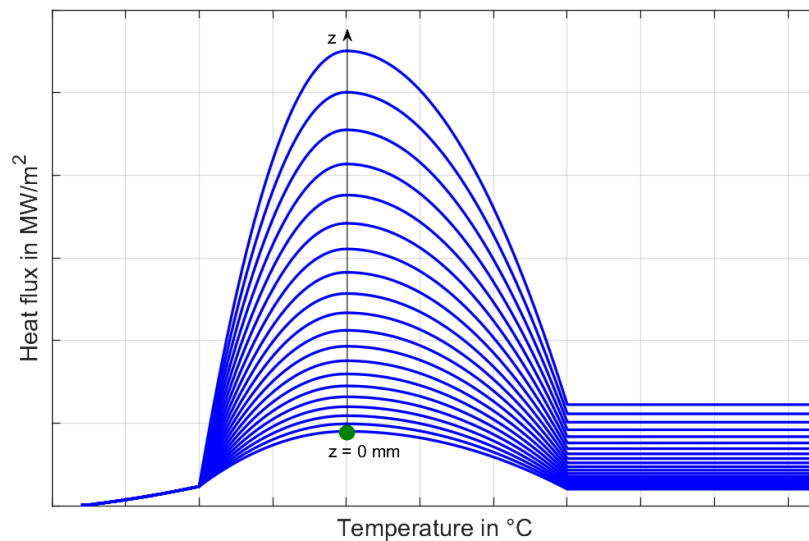


Figure 5.25: Boiling curves for different spatial position along the plate surface

The heat flux as a function of temperature for various spatial location can be implemented based on the present work for every kind of experimental condition. The heat flux profiles should act as a thermal boundary condition for the solution of the partial differential equation. The local heat flux distribution can be further approximated with the usage of boiling curve. Therefore, the surface temperature distribution can be computed in any kind of commercial software with the simplified heat transfer correlation. The heat fluxes can be modified based on the surface temperature for every iteration and the magnitude of the heat flux should be raised accordingly until the surface, core temperature reduces to the below 100 $°C$. As we know from previous discussion, the local heat fluxes position are the sole responsible for the larger surface gradient and therefore to cool the ingot to well below 100 $°C$. The implementation of the heat transfer results from the

laboratory scale can successfully utilized to further understand the cooling of large ingots in industrial DC casting process with computation of two-dimensional and three-dimensional heat conduction problem using heat fluxes as thermal boundary conditions. This kind of temperature calculation is more realistic since the local heat flux were calculated based on the accurate high resolution infrared thermography.

## 5.6   Conclusion

The thermal images from the infrared camera clearly distinguishes three main regions during cooling of a hot moving plate: pre-cooling, transition boiling region, and nucleate boiling region. The various regions are specified in the infrared image and quenching side temperatures obtained from the inverse solutions. The infrared camera with a spatial resolution of 610 x 560 pixels and a temporal resolution of 200 images per second provides a clear view of the temperature distribution in the cooling process and acts as the source for the inverse algorithm. The heat flux estimation is based on the Eulerian steady-state condition with the integration of the inverse heat conduction method along with the formulation of the two-dimensional finite difference method. The experimental temperature is based on analytical expression, i.e. Boltzmann function, since this model is less sensitive to the temperature measurement and numerical errors. From this research work, the following conclusions can be made.

1. The different kinds of metal show a strong influence on heat transfer. The width of the pre-cooling region increases with thermal conductivity of metals, which results in lower interface temperature. The material with a longer temperature drop has a higher transition boiling region resulting in lower $\dot{q}_{max}$.

2. An increase in the initial temperature of the sample plate changes the internal energy stored in the metal sheet, which significantly influences the boiling curve with the change in the interface temperature $\dot{q}_{max}$ and $T_{DNB}$ strongly depends on the initial temperature of the plate. The width of pre-cooling, transition boiling remains constant, while the width of the nucleate boiling region increases with the initial temperature of the plate.

3. The quality of water has no influence on heat transfer, since the temperature profiles for both tap water and distilled water show no significant difference.

4. Jet velocity shows a slightly consistent increase in the heat flux from 6.57 $MW/m^2$ to 6.67 $MW/m^2$. The experiments were performed for small variations of jet velocities 2 $m/s$ to 3.3 $m/s$.

5. The increase in the jet impingement angle and plate velocity heat transfer increases drastically. Consequently, the width of the pre-cooling region reduces for higher plate velocities.

6. The heat transfer increases with the distance to the impingement point, which can be explained with the increasing velocity of the water film due to the gravity. The DNB temperature is independent on the position.

# Chapter 6

# Array of Jets

## 6.1 Introduction

Impingement heat transfer is considered as a promising heat transfer enhancement technique. Among all convection heat transfer enhancement methods, it provides significantly high local heat fluxes. At the surface where a large amount of heat is to be removed/addition, this technique can be employed directly through very simple design involving a plenum chamber and orifices. For instance, in gas turbine cooling, jet impingement heat transfer is suitable for the leading edge of a rotor air foil, where the thermal load is highest and a thicker cross-section enables accommodation of a coolant plenum and impingement holes. This technique is also employed in turbine guide vanes (stators). Other applications for jet impingement could be combustor chamber wall, steam generator, ion thrusters, tempering of glass, electronic devices cooling and paper drying, etc. Jet impingement cooling is a very effective heat transfer mechanism.

## 6.2 Inline Configuration of Full Jet Nozzles

**Phenomena of Inline Jet Quenching**
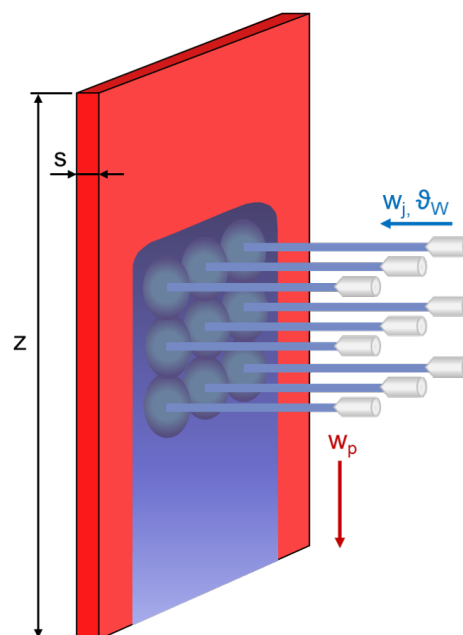


Figure 6.1: Schematic diagram of inline full jet impingement quenching

**Fig. 6.1** shows the full jet impingement quenching in case of the inline configuration, single full jet nozzles are arranged equally at a distance of 35 $mm$ from the centre of each jet in three different rows and in three different columns. The complexity of the jet interaction between the other adjacent jets and the movement of the wetting front influences on the heat transfer during this kind of quenching. As depicted in the Figure 1, the plate with a dimension of 230 $mm$ width x 250 $mm$ length x s $mm$ thickness, the plate moves with a velocity of $w_p$, the water jet possess a velocity of $w_j$ and temperature $\theta_w$. In the following section, the description of the heat transfer during quenching with arrangement of inline configuration will be discussed along with the variation of various influencing process parameters.

## 6.2.1 Fixed Plate Condition
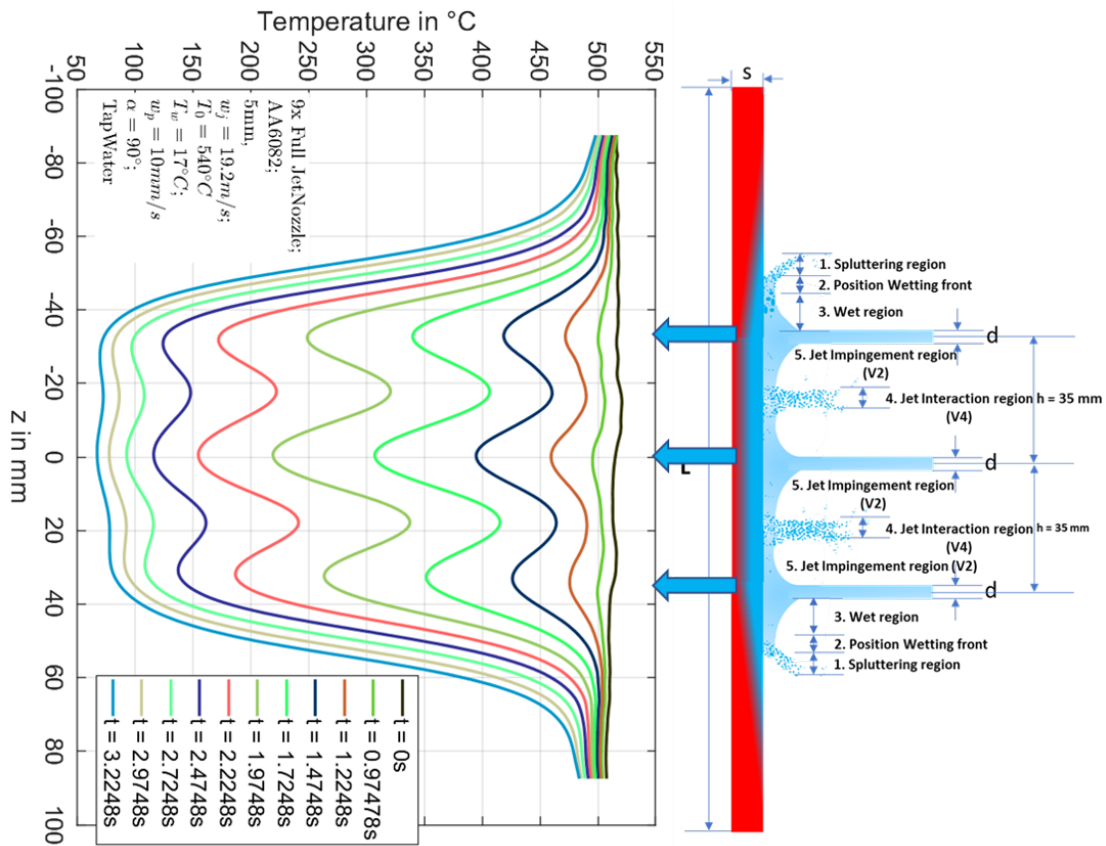


Figure 6.2: Schematic diagram of inline full jet impingement quenching for stationary plate condition

Fixed plate condition involves the stagnant water jet as arranged in a inline configuration as well as the hot metal plate at high temperature are kept constant. The heat transfer mechanism during the configuration of the water jets are schematically provided in the **Fig. 6.2**. The schematic represents the side view of the quenching process with the three row of water jet impinges on the fixed plate and after the jet impingement, the fluid and hot surface interaction causes the formation of different heat transfer regimes. The heat transfer regimes are distinguished based on the state of the water and the surface temperature as sputtering region, position of wetting front, and wet region respectively. In addition, the water jet forced to form a mountain like structure at the interaction between the adjacent jets exactly at halfway through the neighbouring jets and this region is termed as jet interaction region. The left part of the schematic represents the surface measured temperatures on the other side of the plate. The temperature profiles are plotted at the centre vertical line of the

plate, the influence of the water jet can be observed until a quench time of 2.5s. Exactly at the jet impingement position, the heat transfer significantly drops to lower temperature and in the water jet interaction region the temperature of the plate remains to be higher. Although the start temperature of the surface no longer remains constant, since due to the internal heat conduction temperature drops as seen the temperature profiles. For quench time of 1.5s, the local temperatures at the nozzle impingement area between the three jet configuration drops to nearly 400 °C from start temperature of 500 °C. Whereas, the temperature of the surface in the water impingement region soon becomes homogeneous above quench time of 2.5s.

Surface heat flux on the quenched side and the measured side temperature were compared along the plate length in the nozzle impingement region. The surface heat flux and temperature for different times i.e. 0.5s, 1.0s, 1.5s were discussed in **Fig. 6.3**. The surface temperature drops significantly at the water impingement region and show a significant temperature drop of about 100 °C for 1s and further for 1.5s the temperature of the plate attains nearly 200 °C. The higher water jet velocity overcomes the significant wall friction resistance, the fluid able to absorb the heat at faster rate. Henceforth, the heat flux is inverse proportional and for the decrease in the surface temperature of the plate gives rise to the surface heat fluxes for all the consecutive time instants. The peak of the heat flux raised from 1.5 $MW/m^2$ to 3.3 $MW/m^2$ nearly about 2 times from earlier time step. The local heat transfer phenomena is highly prone to larger temperature gradients across the plate surface and consequently in other parts of the plate. The larger temperature gradient gives rise to the generation of the thermal stresses and the deformation in the initial stages of the quenching process.
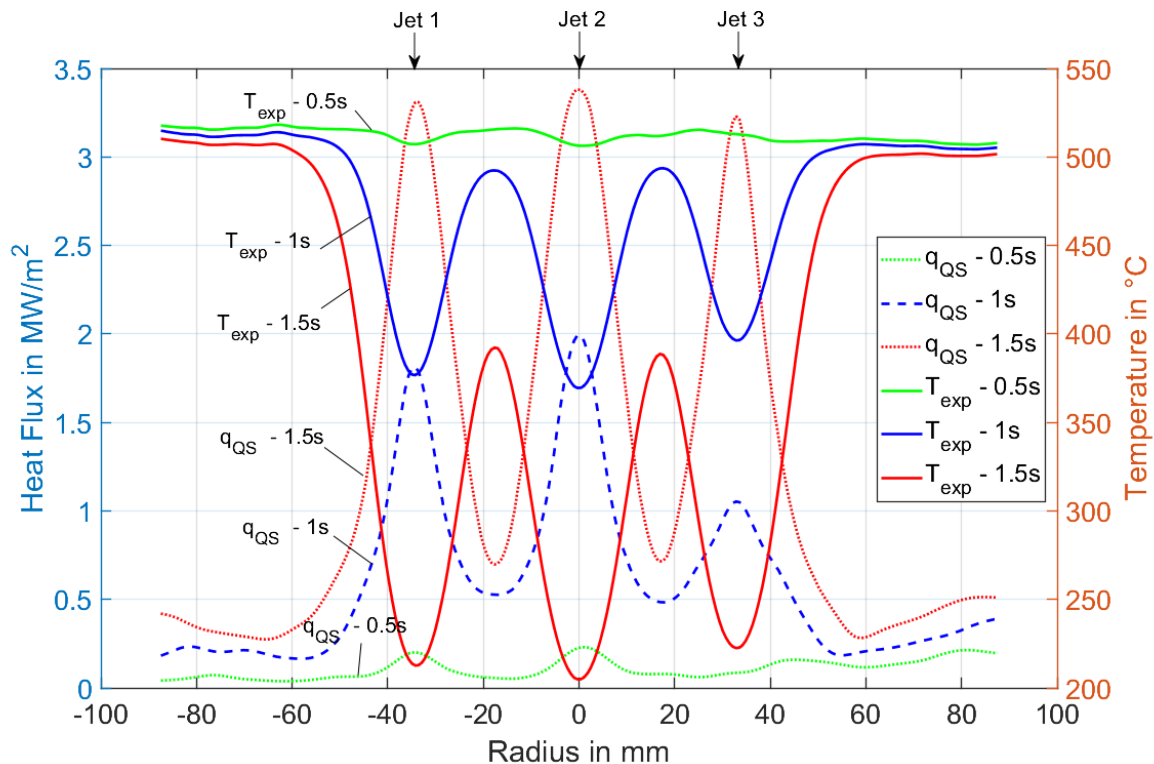


Figure 6.3: Comparison of the surface measured temperatures and the surface heat fluxes on the quenched side for different time steps

**Fig. 6.4** shows the profiles for the heat fluxes ($q_{max}$ and $q_{RWT}$) at jet impingement region ($V_2$) and the jet interaction region ($V_4$). The water impingement region proportionately attains the higher heat fluxes in the nucleate boiling regime of around 4 $MW/m^2$ and decreases in the water interaction region to around 2.3 $MW/m^2$. The heat transfer

extraction is most favourable in the impingement region and maximum heat flux decreases drastically in the water jet interaction region. Although, the heat flux profiles in the outer region of the water impingement for impingement region and interaction region shown to be almost similar and decreases gradually because of the strong internal conduction to resist the water cooling.
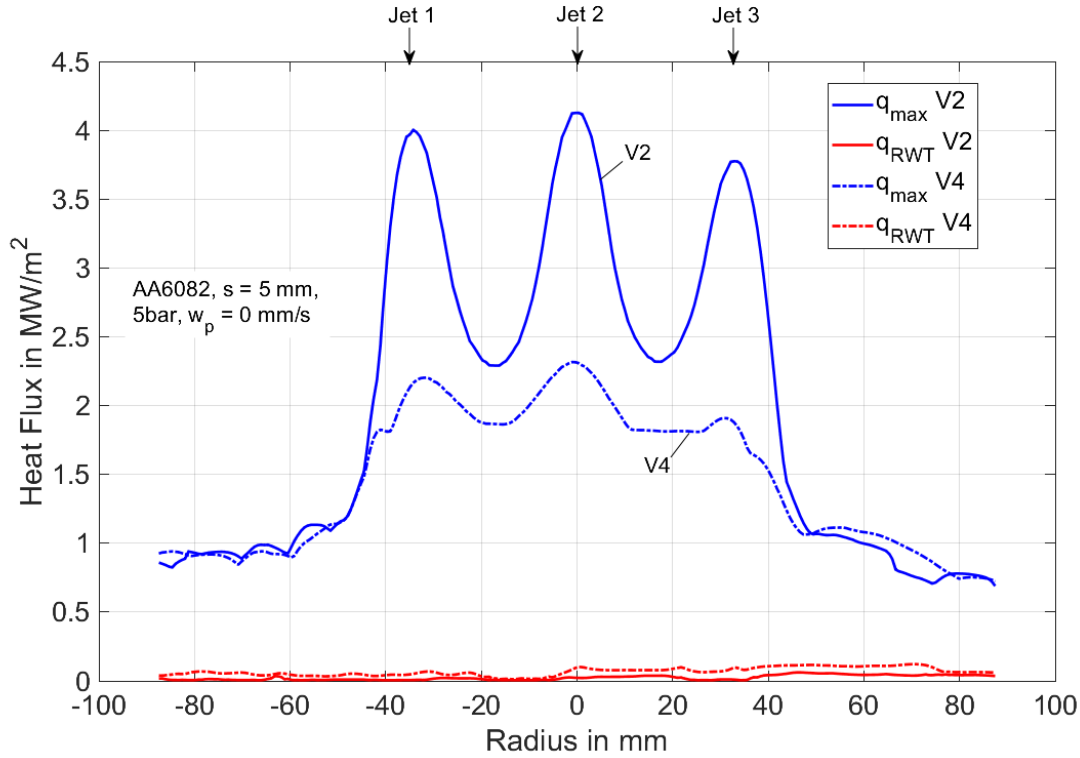


Figure 6.4: Comparison of the heat fluxes ($q_{max}$ and $q_{RWT}$) at jet impingement region ($V_2$) and the jet interaction region ($V_4$)

**Fig. 6.5** shows the comparison of the temperatures ($T_{DNB}$ and $T_{RWT}$) at jet impingement region ($V_2$) and the jet interaction region ($V_4$). The temperatures at the re-wetting condition remains almost constant at around $500\,°C$ although jet interaction region observed to show the slight fluctuations. For the departure nucleate boiling zone, the water impingement region shows a direct proportion to the heat flux profiles and increases at the nozzle position and gradually decreases away from the nozzle position. But, the water interaction ($V_4$) shows no influence of the nozzle position on the heat transfer.
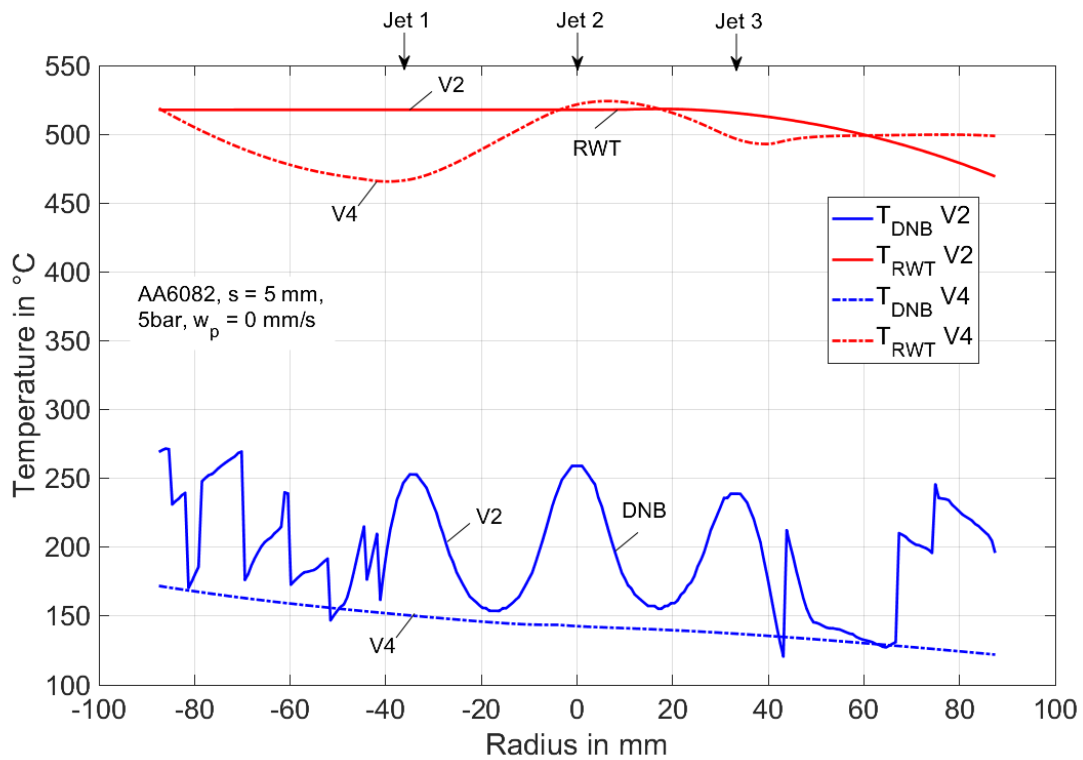
Figure 6.5: Comparison of the temperatures ($T_{DNB}$ and $T_{RWT}$) at jet impingement region ($V_2$) and the jet interaction region ($V_4$)
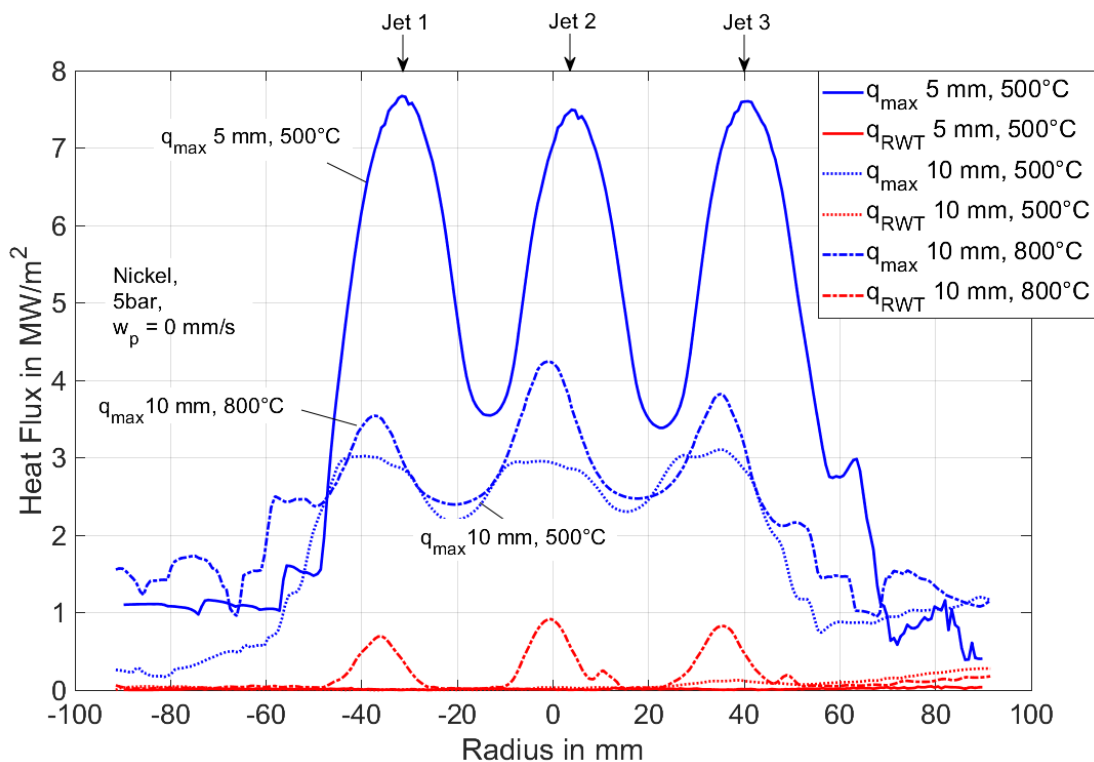


Figure 6.6: Comparison of the heat fluxes ($q_{max}$ and $q_{RWT}$) at jet impingement region ($V_2$) for various thickness and different initial temperatures for nickel material

**Fig. 6.6** depicts the comparison of the heat fluxes at the water impingement region ($V_2$) for various plate thickness i.e., 5 $mm$ and $10mm$ as well as for the start temperature of 500 °C and 800 °C at 10 mm plate thickness for nickel material. The similar phenomena can be observed as compared to the earlier heat flux profiles as in Fig. 6.5, maximum heat flux

for the higher plate thickness drastically decreases to around 4 $MW/m^2$ from 8 $MW/m^2$ for 5 mm plate thickness. The reason for the decrease in the peak of the heat flux is the strong internal conduction against the fluid flow and hence the start temperature of the plate remains at higher temperature. The re-wetting heat flux remains to be as low and no significant influence can be observed except for plate thickness 10 mm at 800 $°C$ start temperature shows slight variation similar to the maximum heat flux profiles.
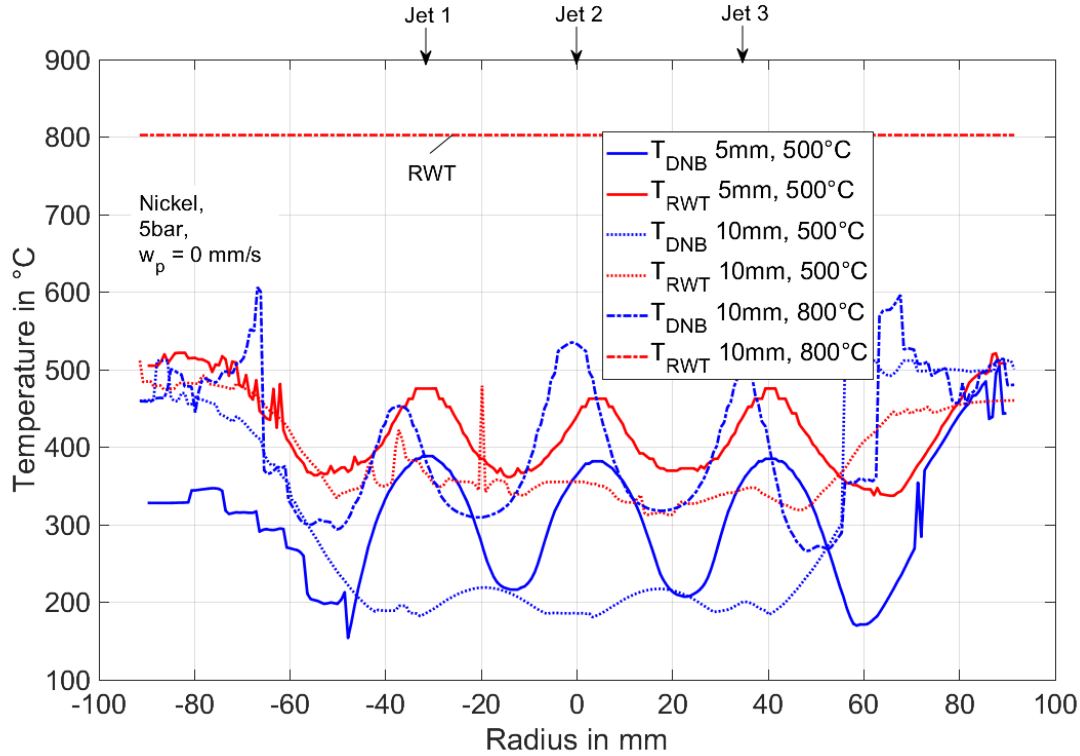


Figure 6.7: Comparison of the temperatures ($T_{DNB}$ and $T_{RWT}$) at jet impingement region ($V_2$) for various thickness and different initial temperatures for nickel material

**Fig. 6.7** shows the temperature for water jet impingement region for different thickness and for different initial temperatures. From the profiles, we can observe the DNB temperature varies of about 200 $°C$ and increases to higher temperature which indicates the higher amount of heat extraction occurs at higher start temperatures. Whereas the re-wetting phenomena occurs around 400 $°C$ for start temperature of 500 $°C$ and for 800 $°C$ start temperature the re-wetting temperature remains 800 $°C$. Low conductive nickel material promotes stronger thermal resistance to the fluid flow and initiates the higher amount of heat flux extraction at higher surface temperatures.

**Fig. 6.8** shows the schematic representation of the measured side surface temperatures from the infrared thermography in two-dimensional region at 5$s$ from the quench time for inline configuration. Experiment performed for AA6082 material with 12 $m/s$ water jet velocity of 5 $mm$ thick plate when the hot plate kept in a fixed condition. The influence of the water jet arranged in inline configuration with 35 mm distance between adjacent jets can be observed in the temperature profiles. In the water impingement region exactly at the centre of the hot plate profiles show a nature of wave with significant decrease in temperature drop. The position of the water jets are the sole responsible for the extraction of the heat and to promote the significant temperature drop. However, the location between the adjacent water jets shows significantly less drop in temperature value and the temperature at the jet interaction region no longer remains to be the initial temperature. The stronger internal conduction and the movement of the water jet reduces the surface temperature lower than the initial temperature of the plate. In the dry region, the plate maintains

the surface temperature nearly at initial temperature even though the water movement from the impingement region propagates towards the outer regions. However, the uniform temperature drop with respect to the 9 water jet can be clearly observed from the surface temperature measurements.
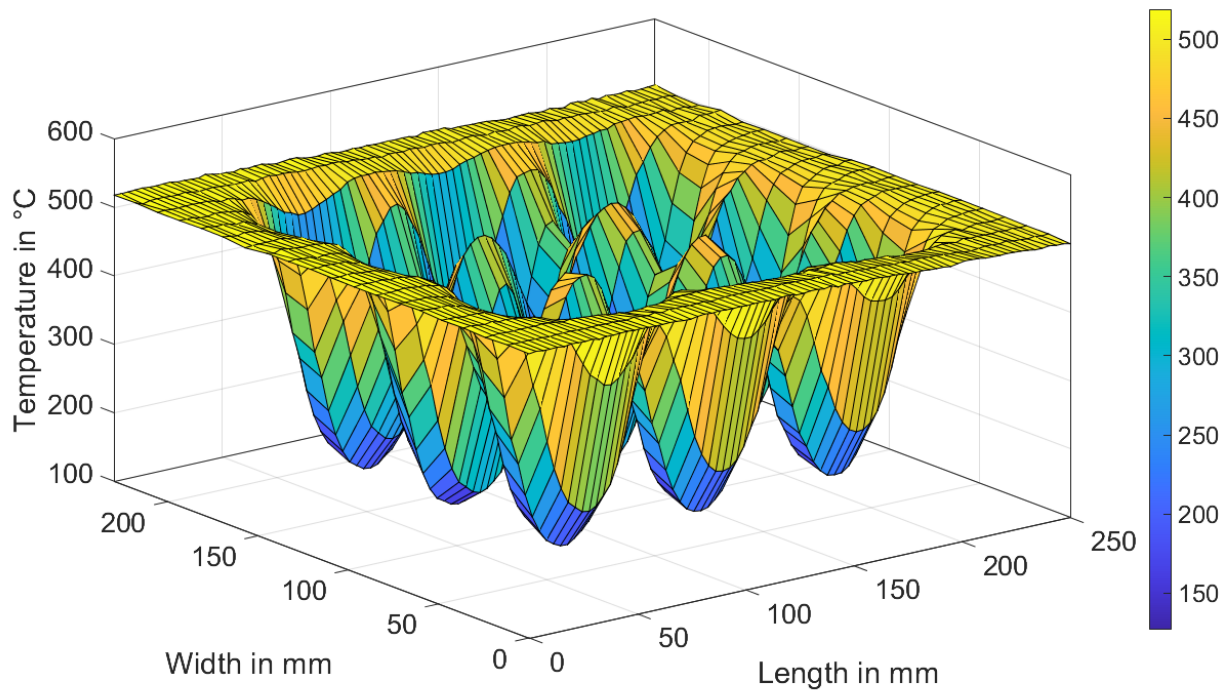


Figure 6.8: Two-dimensional representation of the experimental surface temperatures at 5s obtained from the infrared thermography measurements
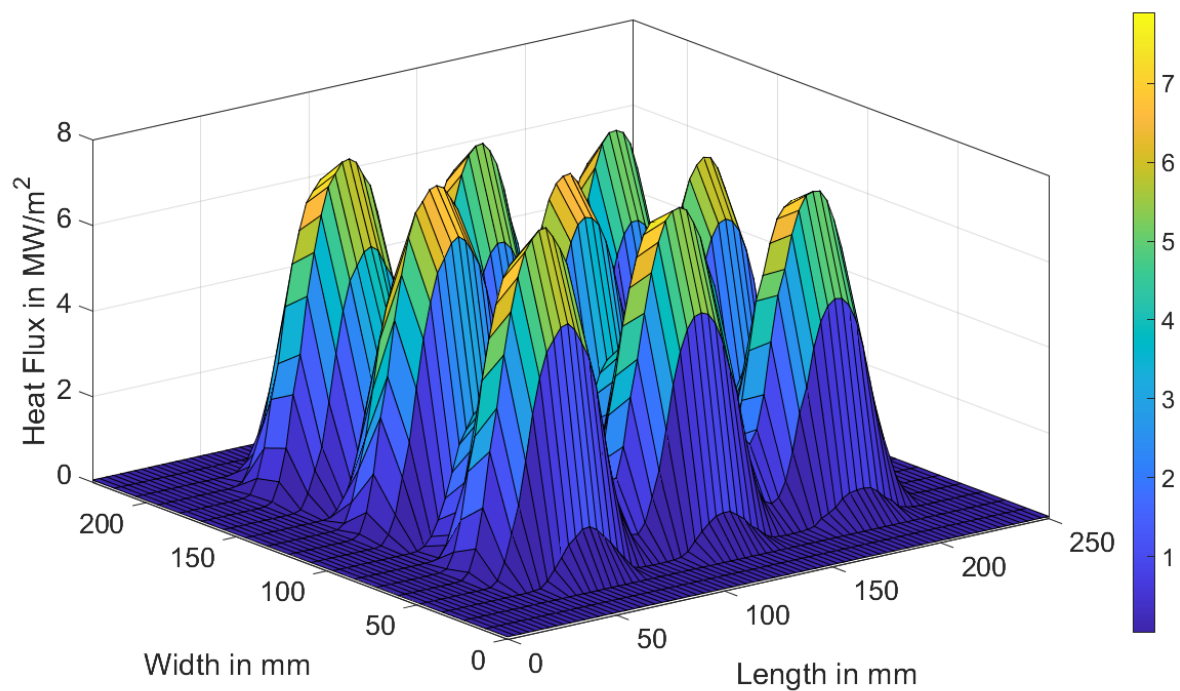


Figure 6.9: Two-dimensional representation of the surface heat fluxes on quenched surface at 5s obtained from the three-dimensional inverse heat conduction problem (IHCP)

s The two-dimensional experimental surface temperatures were utilized for the computation of the surface heat flux in three-dimensional inverse heat conduction model which developed in this present work. **Fig. 6.9** represents the schematic profiles for the surface heat fluxes estimated on the water impingement region for the inline configuration. The heat flux profiles shows a similar peaks at the 9 water jet locations with same heat transfer magnitude of 7.5 $MW/m^2$. The heat transfer intensity is inversely proportional to the surface temperature and henceforth we observe the similar phenomena. The heat flux remains at lower value for the dry surface and the similar condition can be seen in the water jet interaction region.

## 6.2.2   Moving Plate Condition
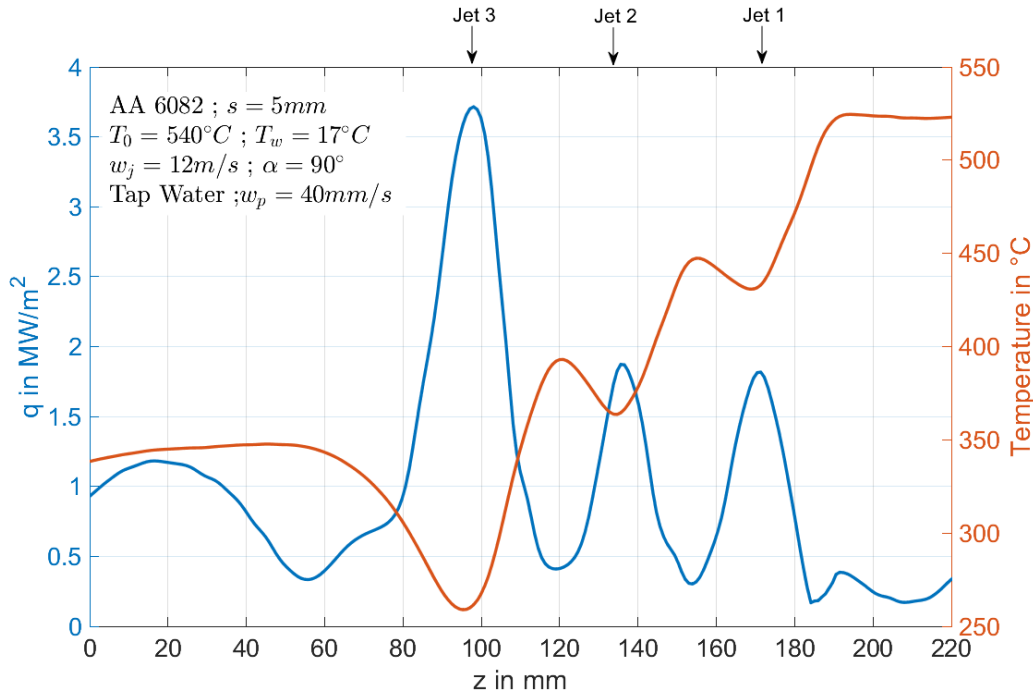


Figure 6.10: Surface temperature distribution and surface heat fluxes for 40 mm/s plate velocity at quasi-steady state condition

**Fig. 6.10** discuss the superimposition of the surface heat flux on the quenched side and the surface temperatures on the measured side during the plate movement condition fo 40 $mm/s$ at quasi-steady state condition. The heat flux inversely proportional to the surface temperature drop and three peaks in the temperatures represents the nozzle impingement position and we can clearly observe the temperature drop of 100 $°C$ between the consequent water jets. The heat transfer at the first two water jet regions shows almost same values of 1.8 $MW/m^2$. The reason for the same peak heat flux should be that heat transfer at the first peak i.e., 440 $°C$ shown to be 1.8 $MW/m^2$ and further at second jet position the temperature drops only about 100 $°C$ the same heat transfer should be extracted and henceforth we observe the similar two peaks. Whereas for the third nozzle position the heat flux raises to maximum at around 3.7 $MW/m^2$ at around surface temperature 250 $°C$ near to the nucleate boiling regime might be the reason for the higher amount of heat extraction.

### 6.2.3   Results and Discussion

In this section, the influence of different process parameters on the heat transfer is discussed with the help of obtained boiling curves from the two-dimensional inverse heat conduction method. The heat fluxes as a function of surface temperature on the water impingement side gives the physical understanding of the real boiling behaviour. The influence of the array of jets on the heat transfer at the quasi-steady state should be well understood. The main objective of the array of jets in an inline configuration is to obtain the homogeneous temperature distribution. The detailed results are shown in the following section and the influence is listed in detail.

### 6.2.4   Influence of Thickness of the material



AA6082, $T_0 = 540°C$, $T_w = 17°C$, $\alpha = 90°$, Tap water, $w_p = 10mm/s$
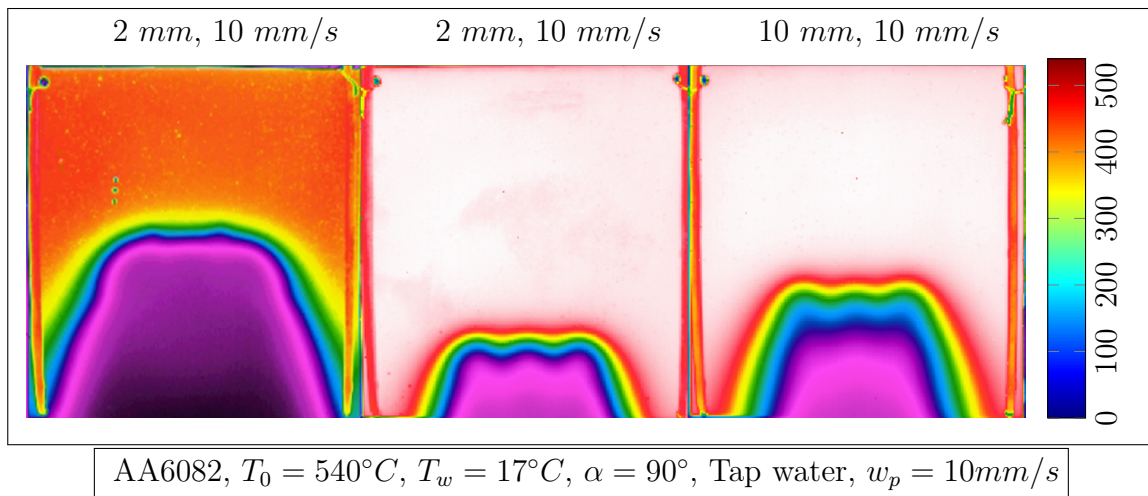
Figure 6.11: Infrared images for different thickness of the material for quasi-steady state condition
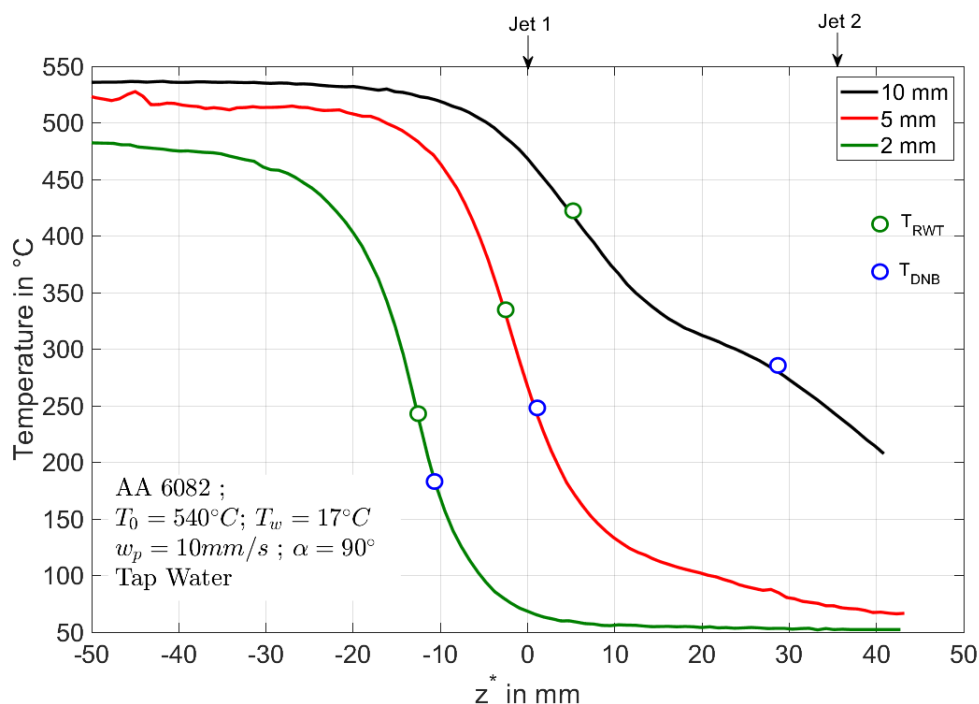


Figure 6.12: Measured surface temperature for different thickness of the material for quasi-steady state condition

**Fig. 6.12**shows the surface temperature distribution for various thickness of the plate at quasi-steady state condition. As seen from the temperature profiles, the cooling is faster in case of the 2 $mm$ thick plate and 5 $mm$ is progressively cools faster than the 10 $mm$ plate. The temperature drop for 2 $mm$ plate is 30 $mm$, for 5 $mm$ is 40 $mm$ and 10 $mm$ the temperature drops above 70 $mm$. For 10 $mm$, the final temperature is around $180°C$, that is still in the nucleate boiling range.
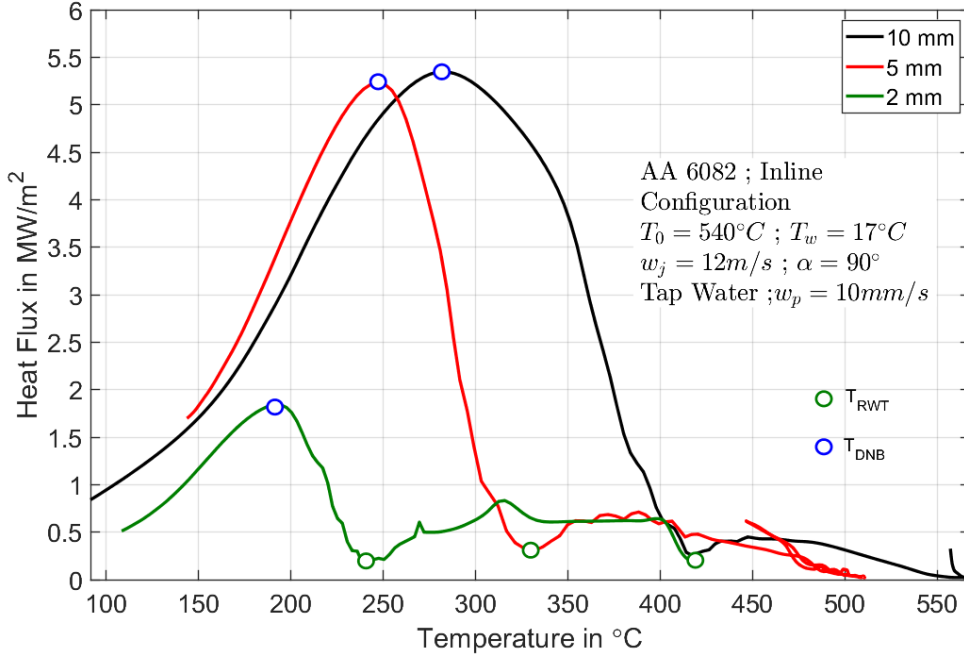


Figure 6.13:  Boiling curve for different thickness of the material at quasi-steady state condition

| $s$ | $q_{max}$ in $MW/m^2$ | $q_{RWT}$ in $MW/m^2$ | $T_{DNB}$ in $°C$ | $T_{RWT}$ in $°C$ | $z^*_{DNB}$ in $mm$ | $z^*_{RWT}$ in $mm$ |
|---|---|---|---|---|---|---|
| 2 $mm$ | 1.84 | 0.19 | 191 | 241 | -10.45 | -12.35 |
| 5 $mm$ | 5.23 | 0.3 | 247 | 331 | 0.9 | -2.7 |
| 10 $mm$ | 5.34 | 0.25 | 281 | 417 | 29.45 | 5.7 |

Table 6.1:  Boiling parameters for influence of plate thickness for 9 full jet nozzle quenching

Boiling curve for the variation of the different plate thickness is shown in the **Fig. 6.13** and **Tab. 6.1** at the quasi-steady state condition. The maximum heat flux $q_{max}$ steeply increases from 1.9 $MW/m^2$ at 2 $mm$ thick plate to 5.2 $MW/m^2$ at 5 $mm$ thick plate and the maximum heat flux remains constant until further 10 $mm$ plate. The shift in the DNB temperature is typically raises for higher thickness of the plate and which corresponds to 190 $°C$, 245 $°C$, 280 $°C$ for 2 $mm$, 5 $mm$ and 10 $mm$ respectively. The re-wetting temperature also increases with the increase in the thickness i.e., 240 $°C$, 330 $°C$, 410 $°C$ for 2 $mm$, 5 $mm$, 10 $mm$ thick plates, as the thermal mass or capacity of the plate higher. Thus, provides more resistance to wet or cool the plate with the same amount of water capacity.

## 6.2.5 Influence of Initial Temperature of the AA6082 Material
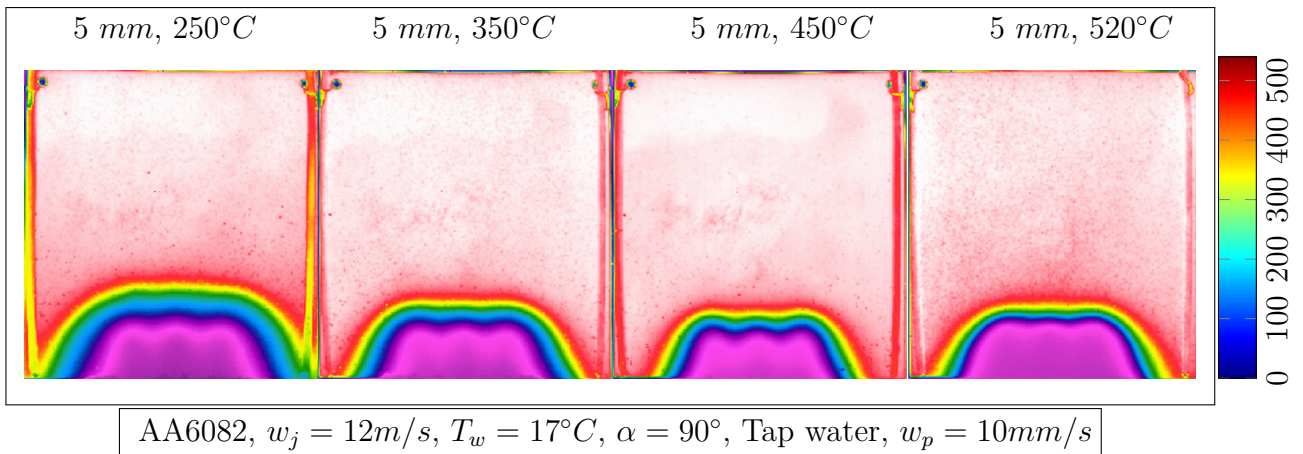


Figure 6.14: Infrared images for different initial temperature of the plate at quasi-steady state condition for 5 mm thick plate
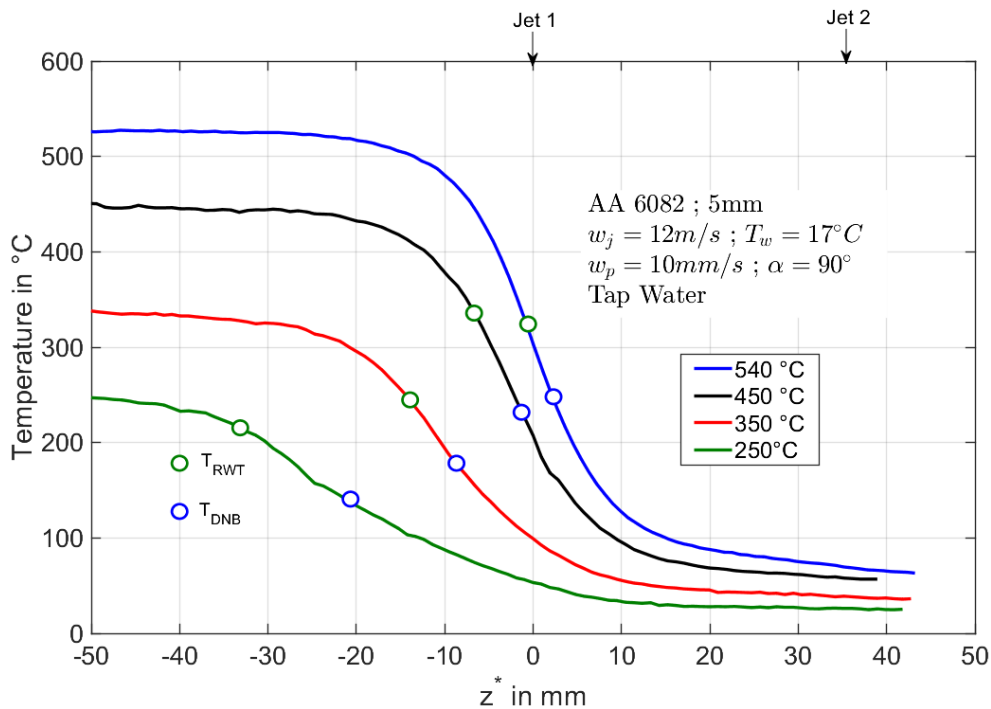


Figure 6.15: Measured surface temperature for different initial temperature of the plate at quasi-steady state condition for 5 mm thick plate

The description of the influence of initial temperature on the surface temperature is shown in the **Fig. 6.15** at quasi-steady state condition. The lower temperature at $250°C$, the wetting region is larger compared to that of the higher initial temperature of the plates i.e., $350°C$, $450°C$ and $540°C$. The corresponding wetting region on the surface of the plates are $40\ mm$, $30\ mm$, $25\ mm$, $25\ mm$ for $250°C - 540°C$ initial temperatures respectively. The DNB and RWT temperature indicate a shift away from the water jet impingement side for the increase in the temperature of the plate, since the higher temperature provides more thermal capacity to resist the water cooling.
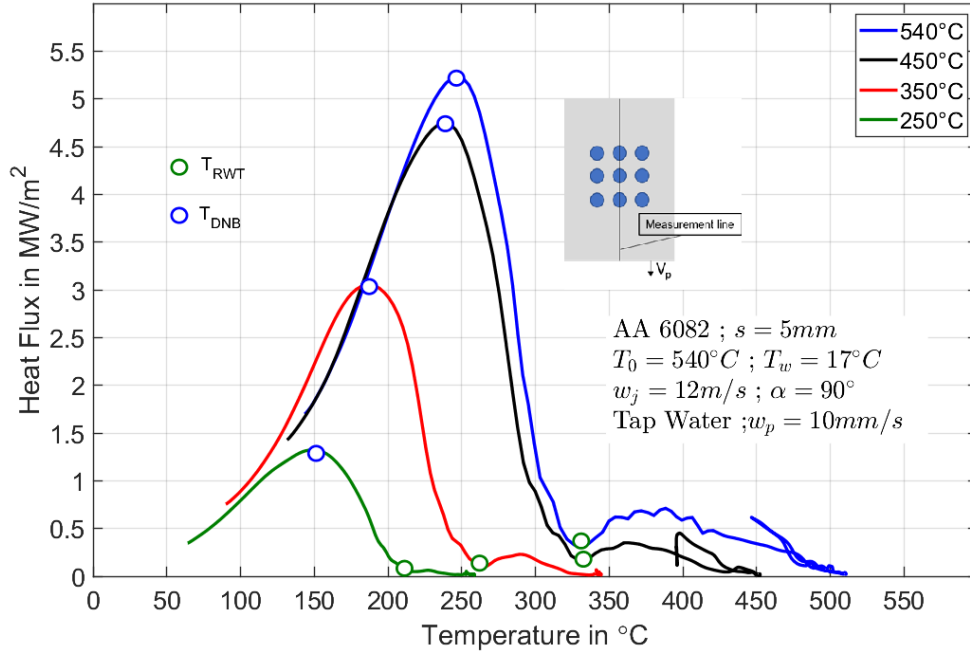
Figure 6.16: Boiling curve for the different initial temperature of the plate at quasi-steady state condition for 5 mm thick plate

| $T_{in}$ | $q_{max}$ in $MW/m^2$ | $q_{RWT}$ in $MW/m^2$ | $T_{DNB}$ in °$C$ | $T_{RWT}$ in °$C$ | $z^*_{DNB}$ in $mm$ | $z^*_{RWT}$ in $mm$ |
|---|---|---|---|---|---|---|
| 250 °$C$ | 1.31 | 0.063 | 151 | 210 | -22.8 | -32.8 |
| 350 °$C$ | 3.05 | 0.13 | 187 | 261 | -9.5 | -16.15 |
| 450 °$C$ | 4.75 | 0.17 | 237 | 332 | -1.9 | -6.65 |
| 540 °$C$ | 5.23 | 0.3 | 247 | 331 | 2.7 | -0.9 |

Table 6.2: Boiling parameters for influence of initial temperature on 5 mm thick plate for 9 full jet nozzle quenching

The typical boiling curve characteristics are shown for the different initial temperatures of the plate in the **Fig. 6.16** and **Tab. 6.2**. at quasi-steady state condition. The higher thermal capacity of the plate at higher temperatures provides more thermal resistant to the water cooling. Thus, the variation of the initial temperatures influences the heat transfer characteristics. Henceforth, the clear shift in the departure nucleate boiling can be seen from 150°$C$, 185°$C$, 240°$C$, 250°$C$, at initial temperatures 250°$C$, 350°$C$, 450°$C$ and 540°$C$ respectively. Consequently, the similar situation arises in the re-wetting phenomena, where the wetting front temperature shifts to higher temperatures away from the nozzle position i.e., 210°$C$, 260°$C$, 330°$C$, 330°$C$ correspondingly for the higher start temperatures from 250°$C$ until 540°$C$. The higher initial temperature with larger thermal mass physically posse's higher internal energy of the plate and thus, the heat extraction or the maximum heat flux also increase correspondingly for the higher start temperatures i.e., 1.4 $MW/m^2$, 3 $MW/m^2$,4.7 $MW/m^2$, 5.3 $MW/m^2$ which corresponds to start temperatures from 250°$C$ until 540°$C$.

### 6.2.6 Influence of Plate Velocity
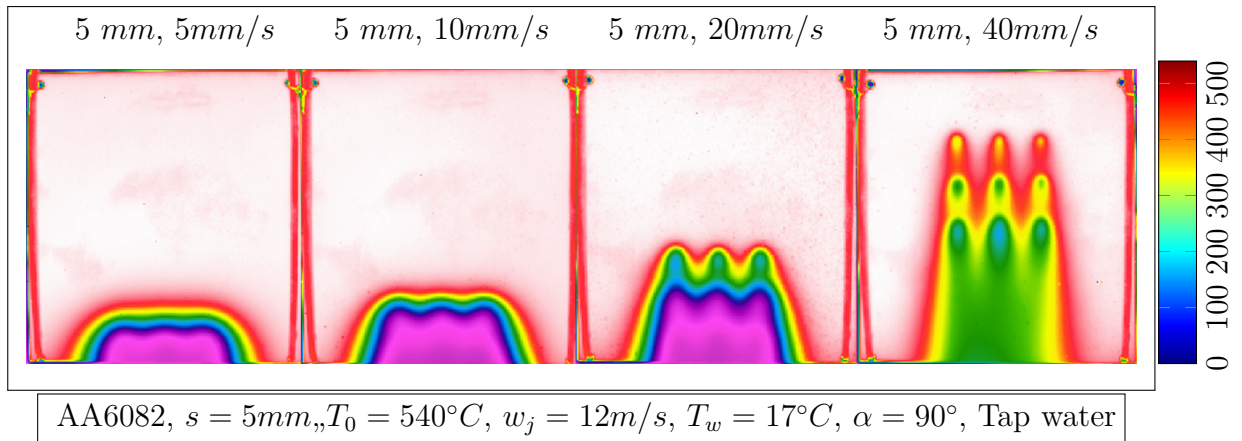
**For 5 mm Thick Plate**



Figure 6.17: Infrared images for different plate velocity at quasi-steady state condition for 5 mm thick plate
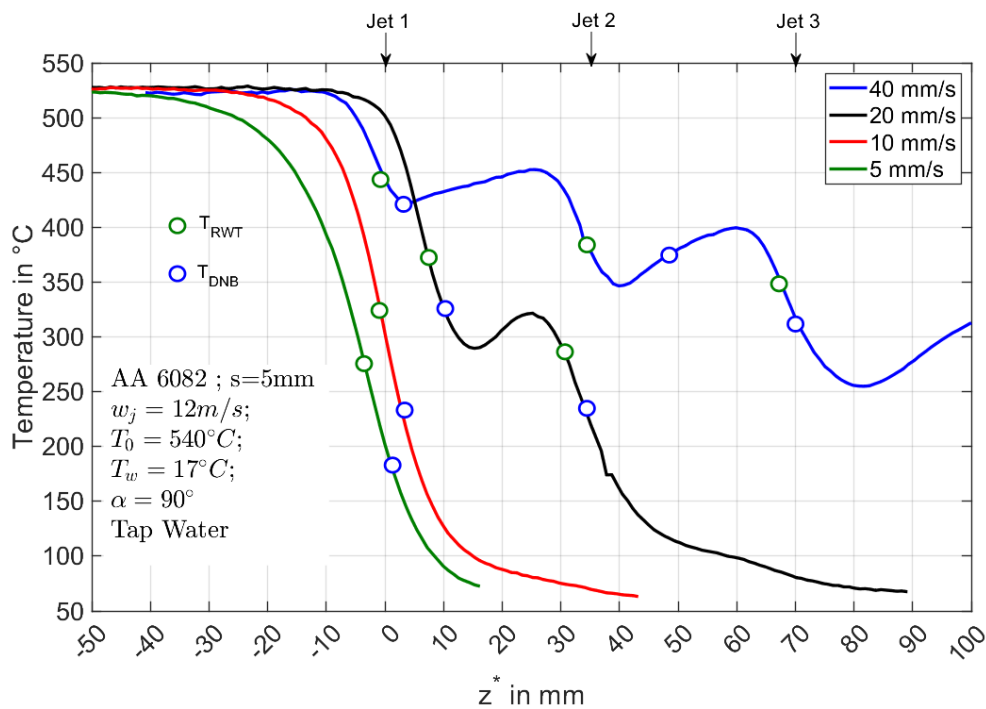


Figure 6.18: Surface temperature for different plate velocity at quasi-steady state condition for 5 mm thick plate

The influence of the plate velocity on the inline configuration in case of 5 mm thick plate is presented in the **Fig. 6.18** at the quasi-steady state condition. The detailed description of the boiling and re-wetting phenomena is indicated for better understanding of the actual quenching process. For $5mm/s$ plate velocity, the slope of the curve is observed to be steep and the wetting front is about 25 $mm$ occupied on the plate length. The similar situation to $5mm/s$ plate velocity is observed on 10 $mm/s$ plate velocity, where the steep of the temperature curves is about 25 $mm$ on the length of the plate. In case of plate velocity 20 $mm/s$ and 40 $mm/s$, the influence of the jets on the temperature distribution can be seen clearly. For 20 $mm/s$ plate velocity, the jet position 1 and jet position 2 shows a steady temperature drop whereas, between the jet position 1 and position 2 the rise in peak is

observed due to the water jet interaction between these two jets. The clear and more heterogeneous temperature distribution is observed in case of the 40 $mm/s$ plate velocity, three jet peaks and the influence of the jet interaction is clearly seen. Since the actual distance between the adjacent jets in the experiments are 35 $mm$, in similar manner, the distance between the jet position 1 and jet position 2 and correspondingly jet position 3 constitutes to be around 35 $mm$. To be precise, the lower temperature corresponds to the jet positions and whereas the increase in temperature due to advection constitutes the jet interaction regions. Since, the temperature is unevenly distributed in case of 40 $mm/s$ plate velocity, the heat transfer characteristics should be analysed at each jet position i.e., Jet:1st row, Jet: 2nd row, Jet: 3rd row.
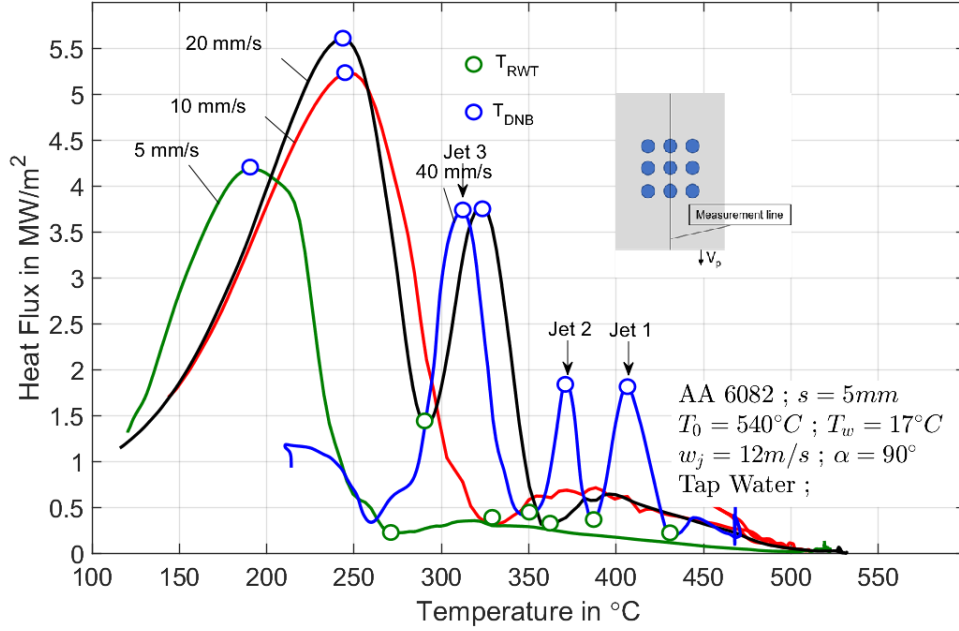


Figure 6.19: Boiling curve and characteristic curve for plate velocities of 5, 10, 20, and 40 mm/s respectively at quasi-steady state condition for 5mm thick plate

| $w_p$ | $q_{max}$ in $MW/m^2$ | $q_{RWT}$ in $MW/m^2$ | $T_{DNB}$ in $°C$ | $T_{RWT}$ in $°C$ | $z^*_{DNB}$ in $mm$ | $z^*_{RWT}$ in $mm$ |
|---|---|---|---|---|---|---|
| 5 $mm/s$ | 4.18 | 0.22 | 190 | 272 | 0.9 | -3.6 |
| 10 $mm/s$ | 5.23 | 0.3 | 247 | 331 | 2.7 | -0.9 |
| 20 $mm/s$ | $Jet_1$ - 3.76 | $Jet_1$ - 0.30 | $Jet_1$ - 324 | $Jet_1$ - 360 | $Jet_1$ - 9.9 | $Jet_1$ - 8.1 |
| | $Jet_2$ - 5.6 | $Jet_2$ - 1.39 | $Jet_2$ - 244 | $Jet_2$ - 291 | $Jet_2$ - 34.2 | $Jet_2$ - 30.6 |
| 40 $mm/s$ | $Jet_1$ - 1.81 | $Jet_1$ - 0.18 | $Jet_1$ - 406 | $Jet_1$ - 431 | $Jet_1$ - 3.8 | $Jet_1$ - 0 |
| | $Jet_2$ - 1.87 | $Jet_2$ - 0.31 | $Jet_2$ - 370 | $Jet_2$ - 387 | $Jet_2$ - 48.45 | $Jet_2$ - 34.2 |
| | $Jet_3$ - 3.71 | $Jet_3$ - 0.41 | $Jet_3$ - 311 | $Jet_3$ - 350 | $Jet_3$ - 70.3 | $Jet_3$ - 67.45 |

Table 6.3: Boiling and characteristic parameters for influence of plate velocity on 5 mm thick plate for 9 full jet nozzle quenching

The heat transfer characteristics for the different plate velocities i.e., 5 mm/s, 10 mm/s, 20 mm/s and 40 mm/s are represented in the **Fig. 6.19** and **Tab. 6.3** at quasi-steady state condition. The homogeneous heat transfer distribution can be observed for the 5 $mm/s$ and 10 $mm/s$ plate velocity in case of 5 $mm$ thick plate. The heat flux increases from 4.2 $MW/m^2$ to 5.3 $MW/m^2$ with the corresponding nucleate boiling temperature of $180°C$ and $250°C$ for 5 $mm/s$ and 10 $mm/s$ respectively. The higher plate velocity, the boiling

activity occurs below the nozzle position with the increase in the nucleate boiling or the nucleate boiling temperature shifts towards the higher temperatures. In similar manner, the re-wetting phenomena changes with corresponding increase in its temperature from 270°C to 330°C for plate velocity 5 $mm/s$ and 10 $mm/s$. For plate velocity 20 $mm/s$ and 40 $mm/s$, the influence of the array of jets can be seen clearly. The two peaks correspond to two jet positions in case of 20 $mm/s$ and correspondingly for 40 $mm/s$, there exists a three jet peaks as indicated in the Fig. 6.19. The heat transfer characteristics at peak one is $q_{max}$: 5.6 $MW/m^2$, $T_{DNB}$: 245°C, $T_{RWT}$: 290 °C and similarly at peak two is: $q_{max}$: 3.7 $MW/m^2$, $T_{DNB}$: 330°C, $TRWT$: 360°C for 20 $mm/s$. In similar way, for 40 $mm/s$ for peak one is: $q_{max}$: 3.5 $MW/m^2$, $T_{DNB}$: 310°C, $T_{RWT}$: 340°C, for peak two is: $q_{max}$: 1.9 $MW/m^2$, $T_{DNB}$: 370°C, $T_{RWT}$: 380°C and for peak three is: $q_{max}$: 1.8 $MW/m^2$, $T_{DNB}$: 410 °C, $T_{RWT}$: 430 °C. The re-wetting phenomena shifts towards higher temperature while keeping its heat extraction same. From the observations, it is clearer that the jet position 1 posses higher heat flux and lower departure nucleate boiling and re-wetting temperature compared to the other jet positions.

**For 10 mm Thick Plate**



AA6082, $s = 10mm$, $T_0 = 530°C$, $w_j = 12m/s$, $T_w = 17°C$, $\alpha = 90°$, Tap water
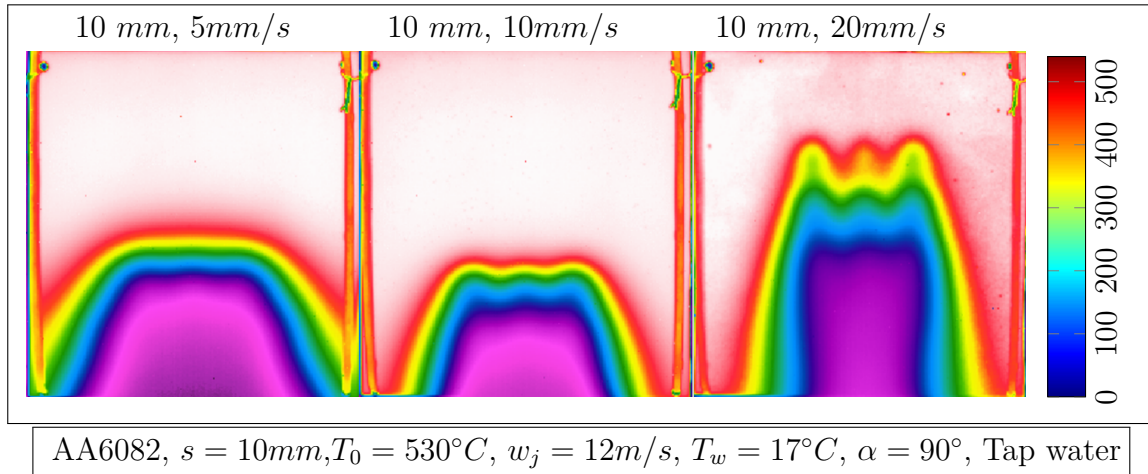
Figure 6.20: infrared images for different plate velocities at quasi-steady state condition for 10 mm thick plate
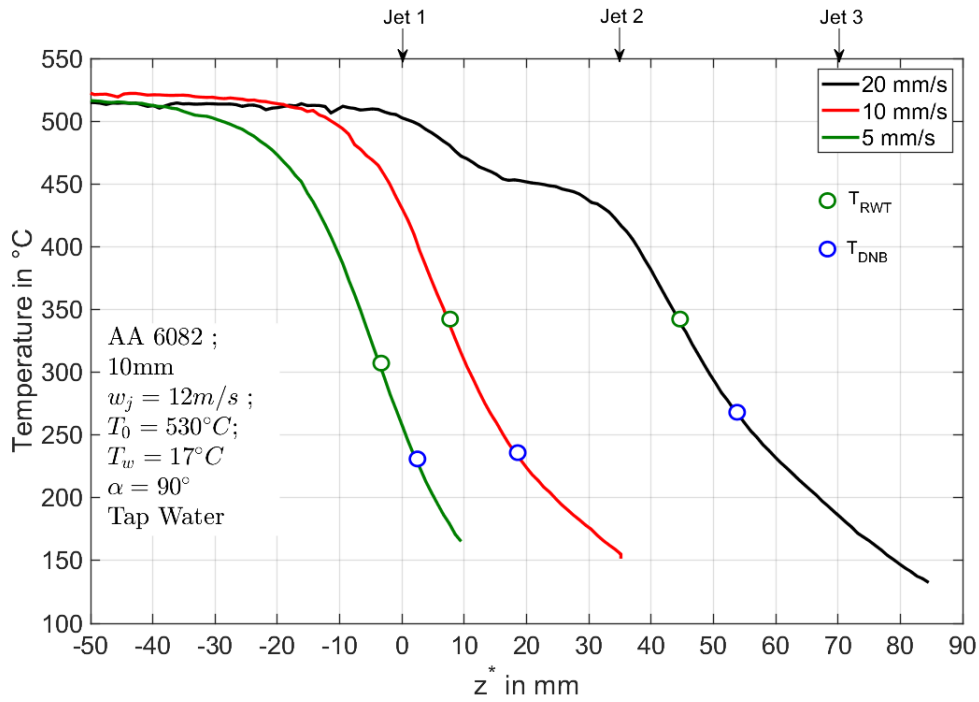
Figure 6.21: Measured surface temperature for different plate velocities at quasi-steady state condition for 10 mm thick plate

**Fig. 6.21**, depicts the surface temperature distribution for various plate velocities in case of 10 $mm$ plate thickness at quasi-steady state region for jet velocity of 12 $m/s$. The temperature profiles provide a homogeneous distribution across the plate length, whereas the effect of the jets on the temperature distributions are completely avoided. The wetting region for the plate velocities 5 $mm/s$ and 10 $mm/s$ are almost constant at about 60 $mm$. Contradictorily, the 20 $mm/s$ posses a higher wetting or cooling region. Due to the higher thermal energy, the jet effect is predominantly lower and the more homogenous temperature distribution can be achieved. From the temperature profiles, we can also state that for 20 $mm/s$ plate velocity, the cooling range is vast in comparison to 5 $mm/s$ and 10 $mm/s$ at about 150 $mm$. The higher cooling range promotes more uniform distribution of temperature across the whole length of the plate. Whereas, for plate velocities 5 and 10 $mm/s$ the temperature drop is steep at a particular length which might promote more thermal stresses leading to deformation and eventually to thermal cracks. The heat transfer characteristics indicates a shift in nucleate and re-wetting temperatures towards higher plate velocities or towards nozzle position.
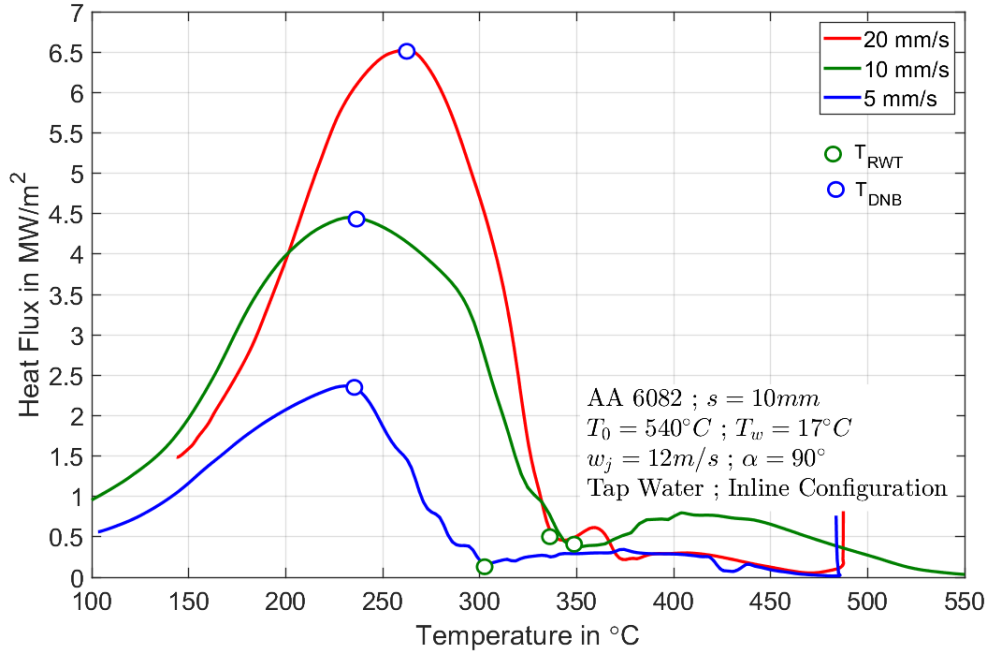
Figure 6.22: Boiling curves for different plate velocities at quasi-steady state condition for 10 mm thick plate

| $w_p$ | $q_{max}$ in $MW/m^2$ | $q_{RWT}$ in $MW/m^2$ | $T_{DNB}$ in °C | $T_{RWT}$ in °C | $z^*_{DNB}$ in $mm$ | $z^*_{RWT}$ in $mm$ |
|---|---|---|---|---|---|---|
| 5 $mm/s$ | 2.36 | 0.163 | 232 | 303 | 1.9 | -3.8 |
| 10 $mm/s$ | 4.45 | 0.38 | 232 | 347 | 19 | 6.65 |
| 20 $mm/s$ | 6.52 | 0.46 | 260 | 340 | 55.1 | 44.65 |

Table 6.4: Boiling parameters for influence of plate velocity on 10 mm thick plate for 9 full jet nozzle quenching

**Fig. 6.22** and **Tab. 6.4** presents the boiling curves for different plate velocities for 10 $mm$ thick plate at quasi-steady state condition. The heat flux gradually increases from 2.5 $MW/m^2$, 4.5 $MW/m^2$, 6.5 $MW/m^2$ for plate velocities 5 $mm/s$, 10 $mm/s$, and 20 $mm/s$ respectively. The steady increase in the peak of the heat flux shifts the DNB temperature to higher value i.e., 230°C, 240°C and 260°C for plate velocities 5 $mm/s$, 10 $mm/s$ and 20 $mm/s$ respectively. Even though the position of the departure nucleate boiling temperature shifts away from the nozzle impingement position, the peak of the heat flux increases drastically. Interestingly, the shift of the DNB temperature takes place between the second row and third row of water jets at position 55 $mm$ from the first row of nozzle position i.e., at 0 $mm$. The water flow from the first, second row of water jets and the local strong cooling occurs at the centre of the nozzle configuration because of several movement of the wetting front. All these influencing experimental conditions promotes stronger cooling of the plate below the first and second row of water jets with the higher amount of heat extraction from the plate. The position of the re-wetting temperature also shifts away from the nozzle position, but the corresponding heat flux remains constant at around 0.3 − 0. 5 $MW/m^2$. Whereas, the re-wetting temperature increases from 300°C for 5 $mm/s$ to 350°C for 10 $mm/s$ and remains constant for 20 $mm/s$ plate velocity.

## 6.2.7   Influence of Water Jet Velocity
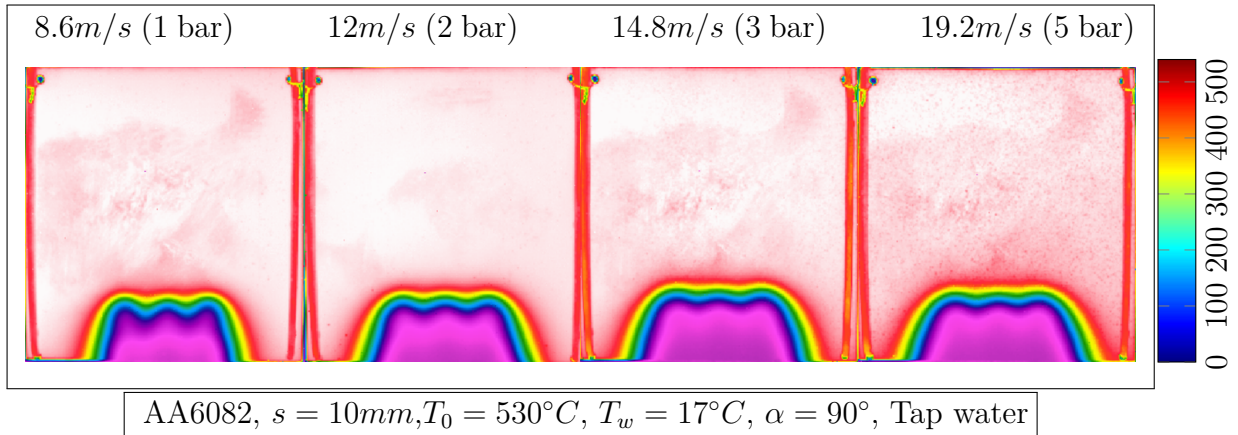
**For 5 mm Thick Plate**



Figure 6.23: Infrared images for different water jet velocities at quasi-steady state condition for 5 mm thick plate

**Fig. 6.24**, shows the infrared images for different water jet velocities for 5 mm thick plate at quasi-steady state condition. From the infrared images, we can clearly see no spatial variation of the temperature in the water jet impingement region and the away from the water jet region as the wetting front propagates across the width or edges of the plate. While comparing the water jet pressure for 1 bar, 2 bar with 3 bar and 5 bar pressures, we can clearly see the wetting front propagation across the edges of the plate. However, the measurement temperatures at the vertical centre line of the plate were chosen for the heat transfer analysis.
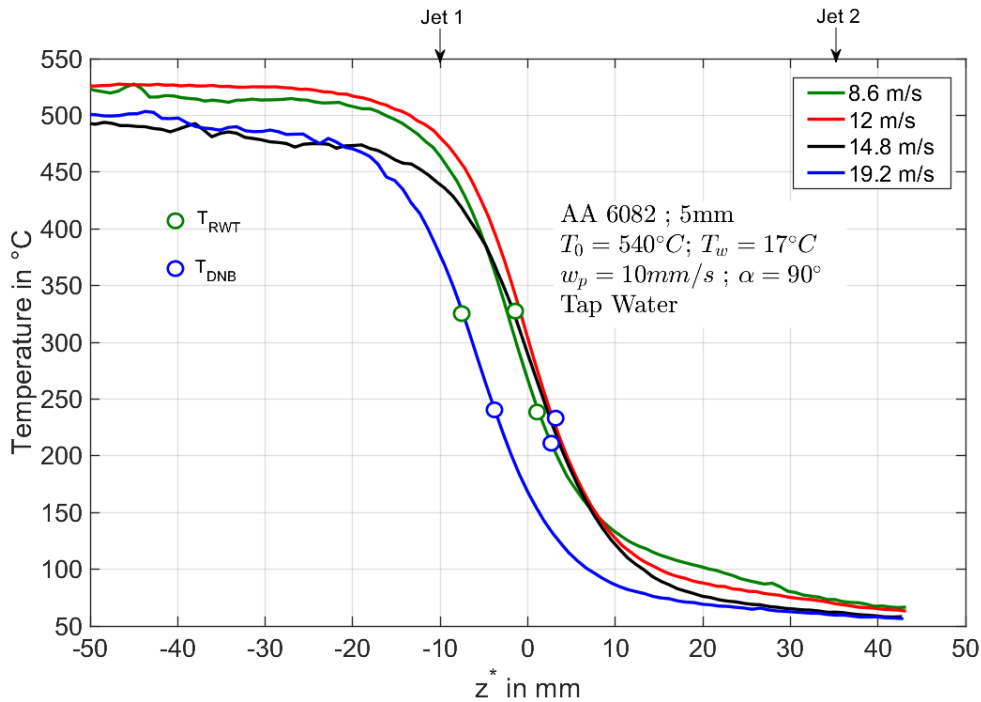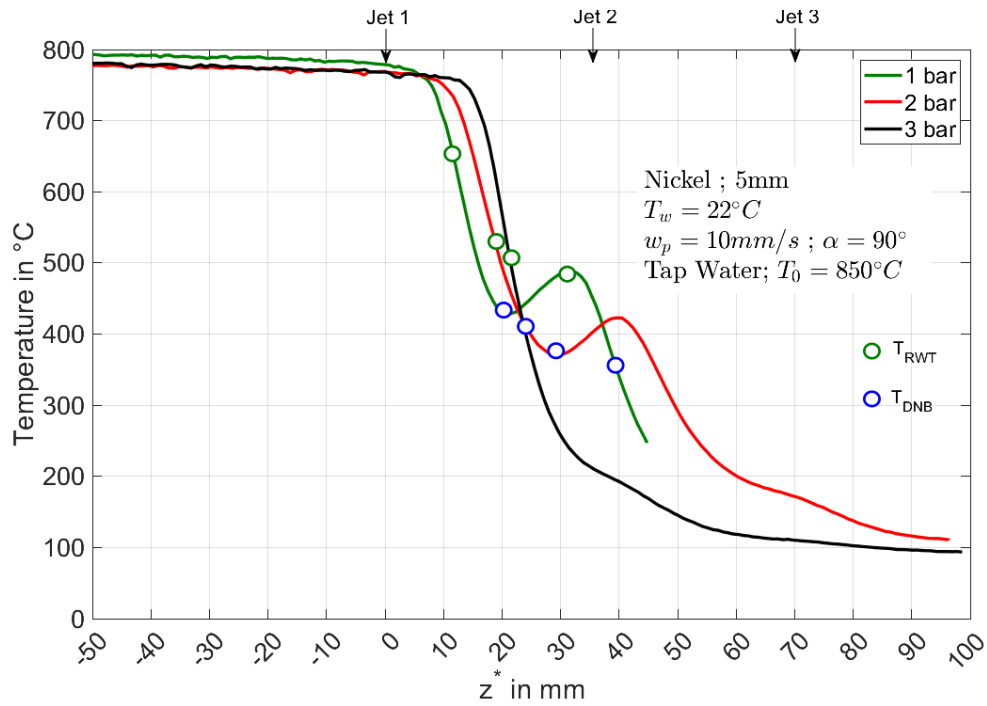


Figure 6.24: Measured surface temperature for different water jet velocities at quasi-steady state condition for 5 mm thick plate

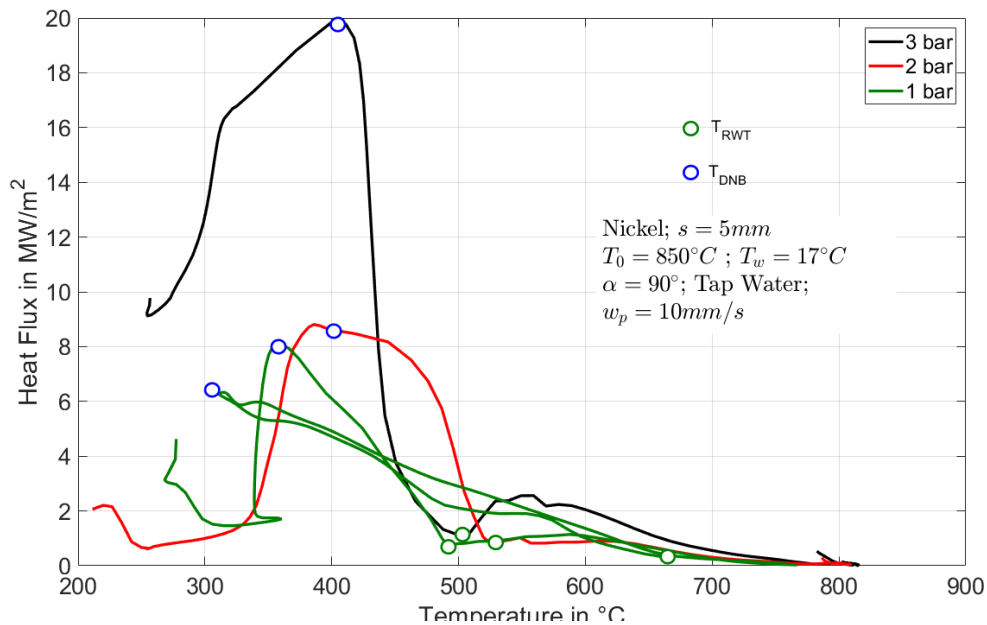The influence of the different water jet velocities on the 5 $mm$ thick plate is depicted in the **Fig. 6.24** at quasi-steady state condition. For water jet velocities or water jet pressures of

1 bar to 3 bar, we can clearly see a steady uniform temperature distribution in the water jet impingement region. Although, for the water pressure of 5 bar, we can observe a better and more faster cooling rate in comparison to the lower water jet pressures. However, the pre-cooling effect is more dominant at the higher water jet pressures and nearly about 20 mm above the water jet impingement position. Whereas for lower water jet pressures i.e., 1 bar, 2 bar, and 3 bar, we seen a uniform reduction of 10 $mm$ in the width of pre-cooling region. Hence, the higher water jet pressures must promote a higher heat transfer in the cooling process.
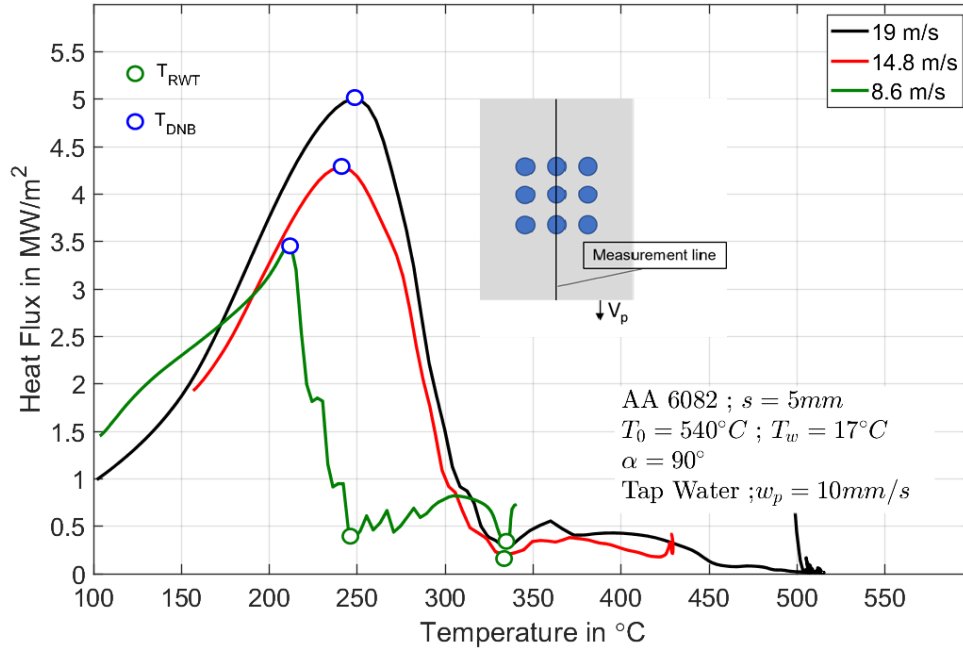


Figure 6.25: Boiling curve for different water jet velocities at quasi-steady state condition for 5 mm thick plate

| $w_j$ | $q_{max}$ in $MW/m^2$ | $q_{RWT}$ in $MW/m^2$ | $T_{DNB}$ in °C | $T_{RWT}$ in °C | $z^*_{DNB}$ in $mm$ | $z^*_{RWT}$ in $mm$ |
|---|---|---|---|---|---|---|
| 8.6 $m/s$ | 3.46 | 0.37 | 212 | 248 | 2.7 | 0.9 |
| 14.8 $m/s$ | 4.27 | 0.20 | 242 | 333 | 1.9 | -1.9 |
| 19 $m/s$ | 5.00 | 0.288 | 247 | 332 | -3.8 | -7.6 |

Table 6.5: Boiling parameters for influence of water jet velocities on 5 mm thick plate for 9 full jet nozzle quenching

**Fig. 6.25** and **Tab. 6.5**, shows the typical boiling curves for different water jet pressures at quasi-steady state condition for 5 $mm$ thick plate. The peak of the maximum heat flux steadily increases from 3.5 $MW/m^2$, 4.4 $MW/m^2$ and 5 $MW/m^2$ with peak temperature of about 210°$C$, 240°$C$, and 250°$C$ respectively for water pressures of 1 bar, 3 bar and 5 bar. The influence of the water jet and the adjacent jets is significantly lowering for 5 mm plate thickness and for higher water jet pressures. Interestingly, temperature of the re-wetting changes for lower water pressure of 1 bar at 250°$C$ and remains constant for higher water jet pressures at around 340°$C$. Also, the minimum heat flux point decreases slightly from 0.4 $MW/m^2$ for 1 bar water jet pressure to remains constant around 0.2-0.3 $MW/m^2$. The reason for higher heat transfer in case of 5 bar water pressure is due to the shift in the position of peak temperature i.e, DNB temperature away from the nozzle position which moves in upward direction as the pre-cooling effect seems to be stronger for higher water jet pressures.
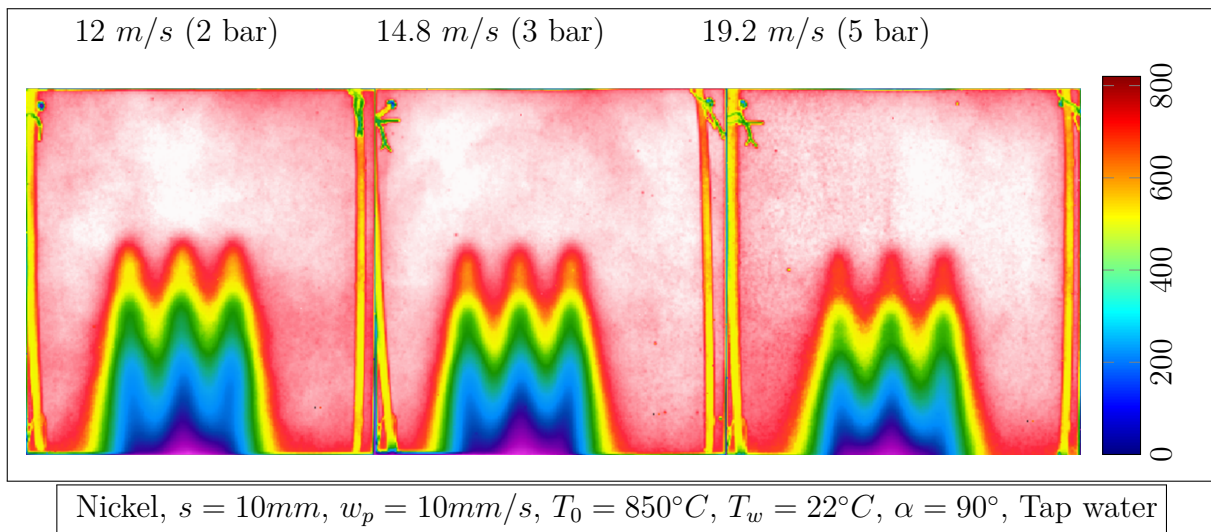
**For 10 mm Thick Plate**
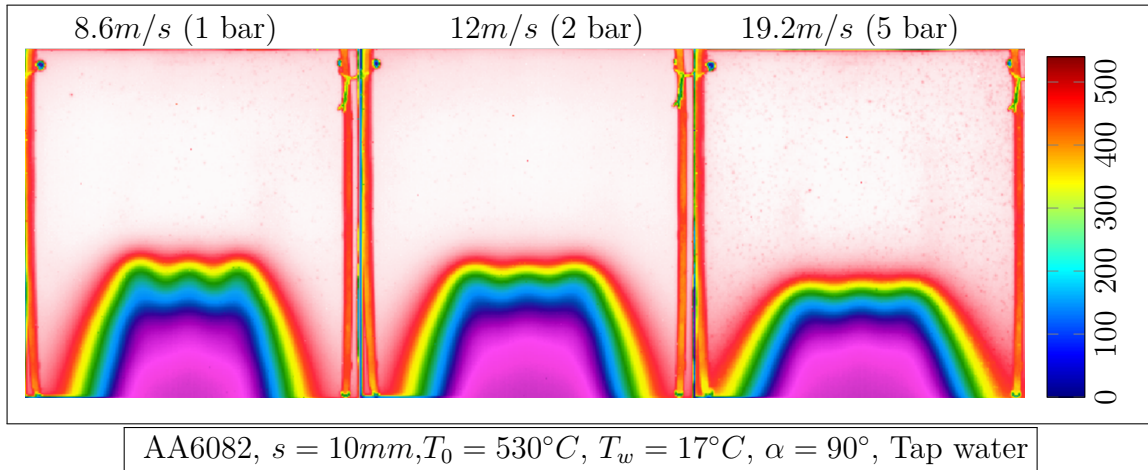


Figure 6.26: Infrared images for different water jet velocities at quasi-steady state condition for 10 mm thick plate

**Fig. 6.26** presents the infrared images for different water jet pressures for 10 $mm$ thick plate at quasi-steady state condition. The Infrared images shows a steady uniform distribution across the spatial direction both in width and length direction. For lower water jet pressures of 1 bar, the temperature distribution in the width direction shows slightly low influence compared to higher water jet pressure at 5 bar. For 5 bar water jet pressure, the wetting front movement becomes strong and the cooling of the plate is more uniform.
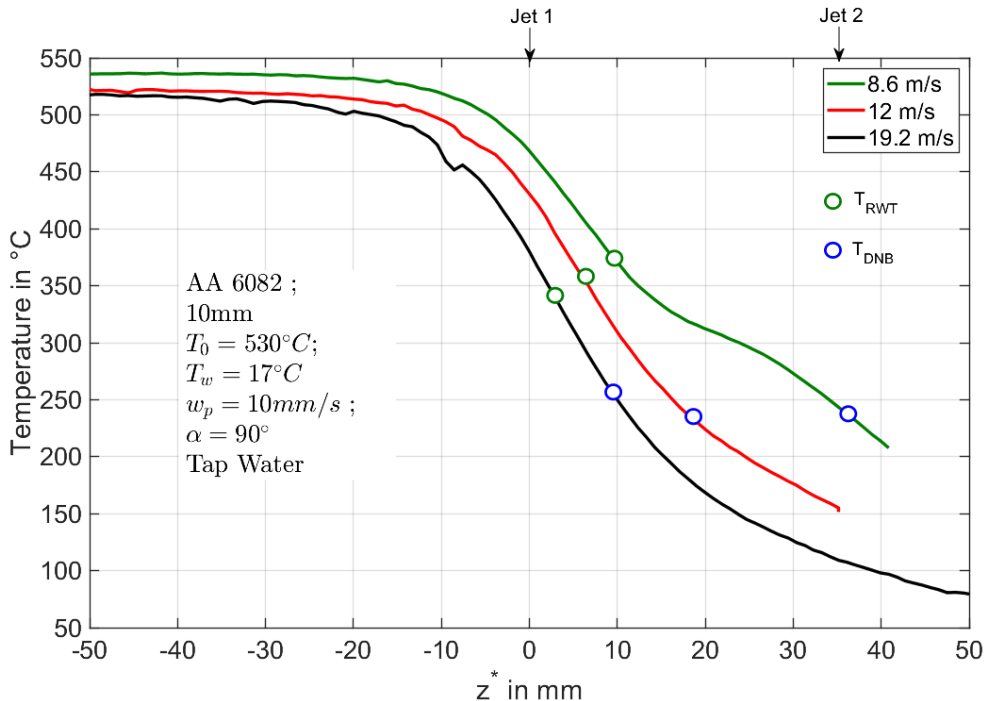


Figure 6.27: Measured surface temperature for different water jet velocities at quasi-steady state condition for 10 mm thick plate

To study the influence of different water jet pressures on the 10 mm thick plate, the surface temperature distribution at quasi-steady state condition were presented in the **Fig. 6.27**. The plate thickness restricts the lower water jet pressures to cool faster and the cooling rate reduces significantly. With the increase in the water jet pressures to 2 bar and 5 bar, the

temperature drop becomes more significant and at the nozzle position, cooling of the plate becomes faster. The low cooling rate promotes a higher temperature gradient across the plate length which induces the uneven development of the thermal stress across the plate surface.
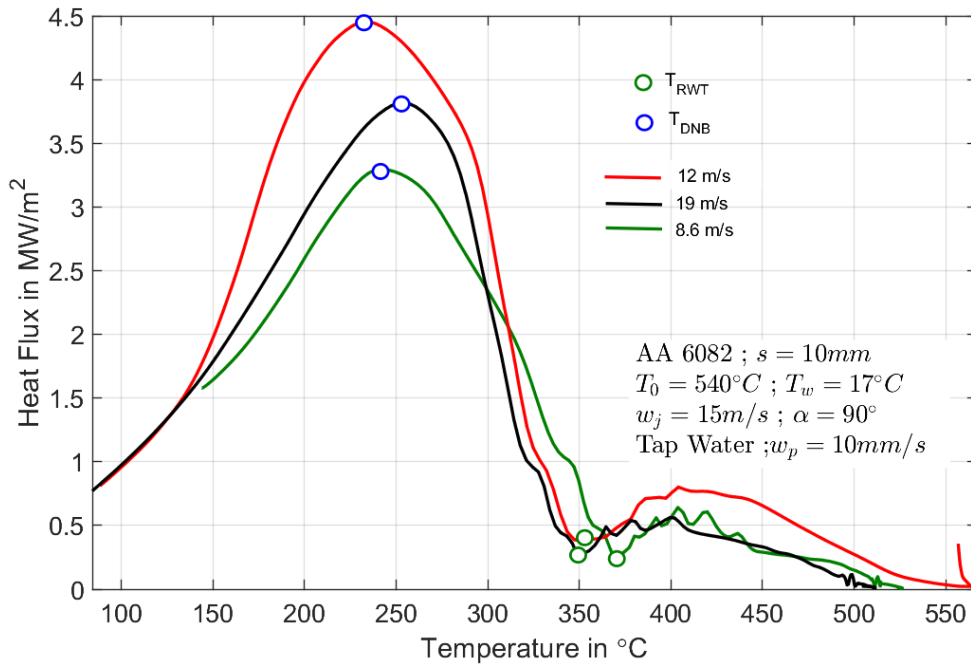


Figure 6.28: Boiling curves for different water jet velocities for quasi-steady state condition for 10 mm thick plate

| $w_j$ | $q_{max}$ in $MW/m^2$ | $q_{RWT}$ in $MW/m^2$ | $T_{DNB}$ in °C | $T_{RWT}$ in °C | $z^*_{DNB}$ in $mm$ | $z^*_{RWT}$ in $mm$ |
|---|---|---|---|---|---|---|
| 8.6 $m/s$ | 3.29 | 0.26 | 243 | 371 | 35.15 | 9.5 |
| 14.8 $m/s$ | 4.45 | 0.37 | 232 | 351 | 19 | 6.65 |
| 19 $m/s$ | 3.81 | 0.27 | 253 | 348 | 9.5 | 2.85 |

Table 6.6: Boiling parameters for influence of water jet velocities on 10 mm thick plate for 9 full jet nozzle quenching

**Fig. 6.28** and **Tab. 6.6**, shows the typical characteristic boiling curve for different water jet pressures for 10 $mm$ thick plate at quasi-steady state condition. The steady increase of the heat flux takes from 1 bar water jet pressure to 2 bar, wherein the maximum heat flux point corresponds to 3.3 $MW/m^2$ for 1 bar water jet pressure to 4.5 $MW/m^2$ at 2 bar water jet pressure. Contradictorily for water jet pressure 5 bar, the peak of the heat flux reduces with the increase in the DNB temperature to 250°C. As the position of the departure nucleate boiling lies near the first row of water jets, the conduction from the incoming hot solid affects the heat extraction from the solid. Whereas for water jet pressure of 2 bar, the position of the DNB temperature lies away from the first row of water jets and the adjacent water jets promotes the higher amount of heat extraction from the hot solid.

**For 20 mm Thick Plate**
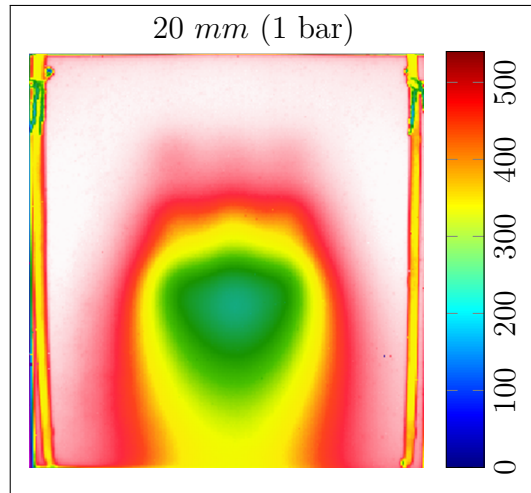


AA6082, $s = 20mm$, $T_0 = 540°C$, $w_j = 8.6m/s$, $w_p = 10m/s$, $T_w = 17°C$, $\alpha = 90°$, Tap water

Figure 6.29: Infrared image for 20mm thick plate at quasi-steady state condition for 8.6 m/s water jet velocity

The infrared image for 20 $mm$ plate thickness is shown in the **Fig. 6.29** for 1 bar water pressure at quasi-steady state condition. The influence of the plate thickness on the cooling process promotes an uneven distribution of the temperatures across the plate surface. The cooling is insignificant in the first and second row of water jets as seen from the infrared image compared to the third row of water jet. Below the third row of water jets, the reheating of the plate surface becomes more pre-dominant because of the higher internal energy, material possess higher thermal conductivity.
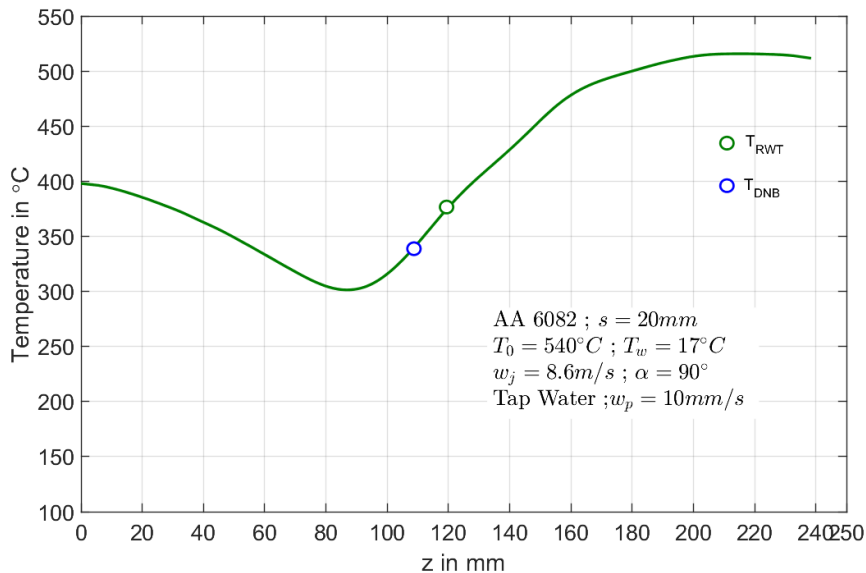


Figure 6.30: Measured surface temperature for 20mm thick plate at quasi-steady state condition for 8.6 m/s water jet velocity

**Fig. 6.30** shows the influence of the plate thickness on the water jet impingement cooling for 1 bar pressure. The higher plate thickness of 20 $mm$ promotes stronger restriction of the water jet to cool the hot moving surface, also the hot incoming solid makes the cooling process complicated. However, at the third row of water jets the cooling of the

plate becomes stronger and the temperature drop of about $300°C$ can be observed. Due to the internal conduction, the material heats up in the lower part of the plate while ejecting the moving fluid from the nozzle position away from the plate surface.
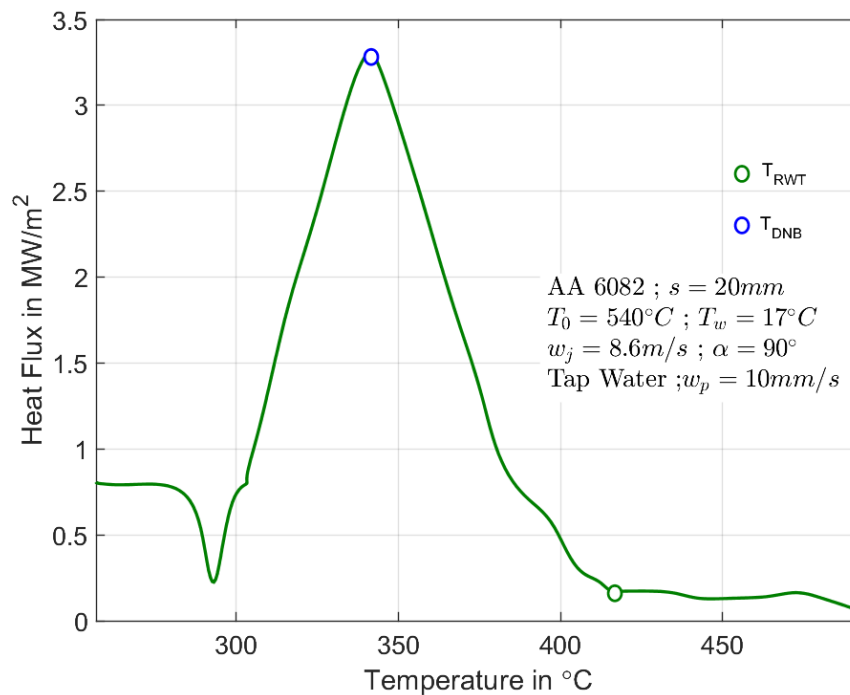


Figure 6.31: Characteristic curve for 20 mm thick plate at quasi-steady state condition for 8.6 m/s water jet velocity

The typical boiling curve for 20 $mm$ plate thickness at quasi-steady state condition for 1 bar water jet pressures are depicted in the **Fig. 6.31**. The heat transfer increases from 450°C steadily reaching a maximum value at 3.4 $MW/m^2$ with peak temperature at 330 °C, due to the effect of internal conduction affect further extraction of heat from the hot surface and heat extraction from the plate surface reduces.
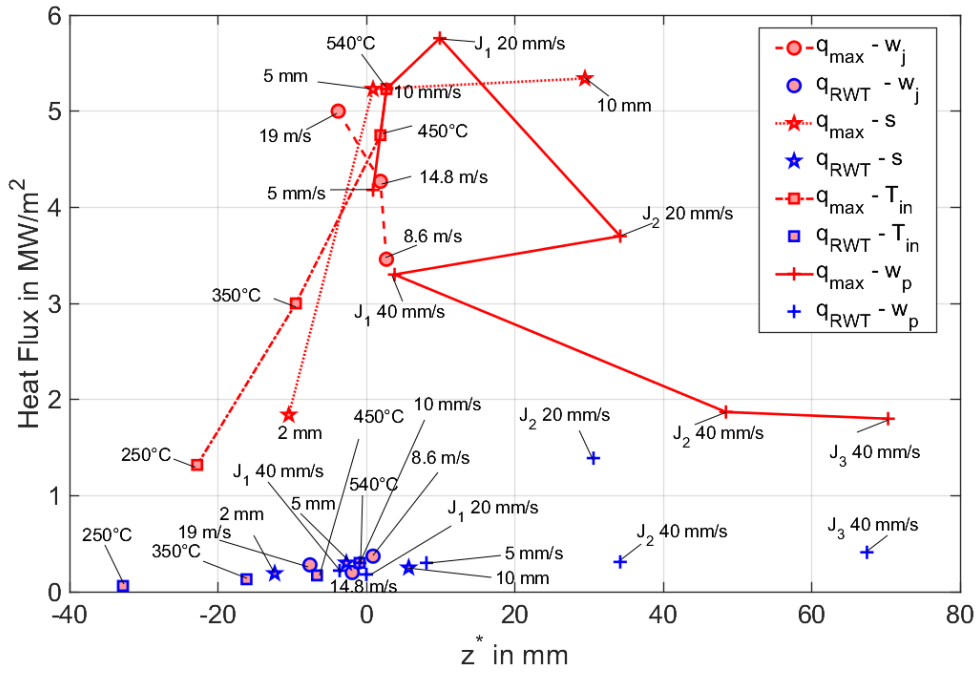
Figure 6.32: Comparison of the heat fluxes with respect to nozzle position for different process parameters for AA6082, 5 mm plate thickness

**Fig. 6.32** discuss the heat fluxes with respect to the nozzle position for different process parameters of AA6082, 5 mm material. With the increase in the process parameters such as $w_j$, $s$, $w_p$, and $T_{in}$ corresponds to the higher heat flux and the heat transfer rate enhances proportionately. The lower start temperature and plate thickness favours the pre-cooling regime and the large amount of heat can be extracted without water cooling. For such kind of applications, the lower plate temperature and plate thickness can be recommended and also the heat transfer decreases largely. As the plate temperature, velocity, water jet were raised the friction between the solid and fluid causes the heat transfer diffusion to raise and shift to the nozzle position. Whereas for the higher plate velocity the strong resistance to the fluid flow and the water jets below the first row of jets influence the heat transfer. Henceforth the peak heat flux at the below first row of jets shifts to the downward direction with respect to the nozzle position from the first row. However, we observe lower heat flux values with higher plate velocities at higher surface temperature becomes nearly constant. The re-wetting surface heat fluxes lies within the range of 1 $MW/m^2$ and the clear understanding of such variables might not influence the overall heat transfer during plate cooling process.
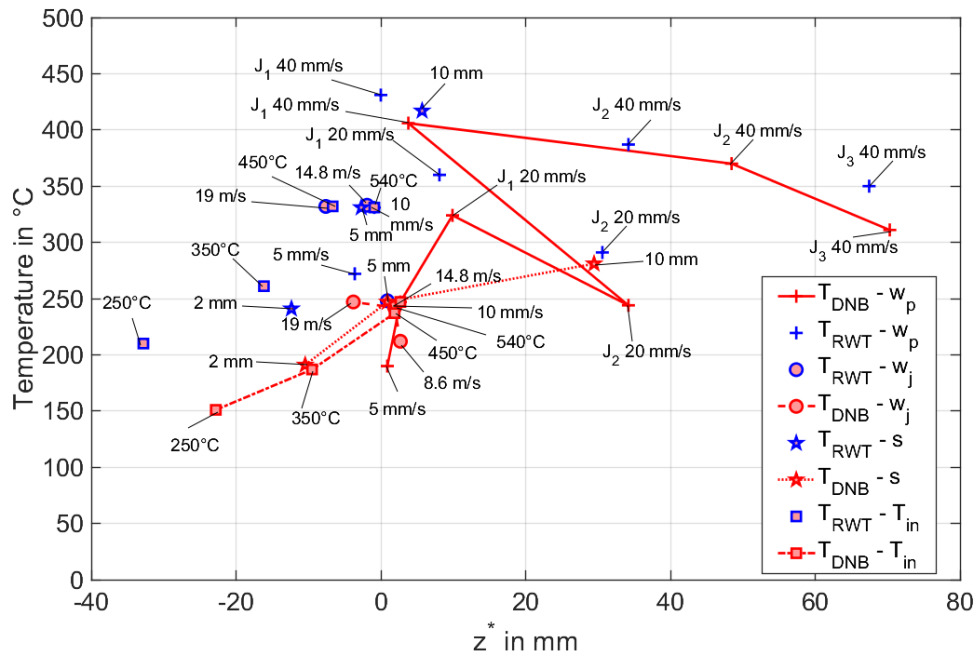
Figure 6.33: Comparison of the temperatures with respect to nozzle position for different process parameters for AA6082, 5 mm plate thickness

**Fig. 6.33** shows the temperatures data points as a function of nozzle position for different process parameters for AA6082, 5 mm plate thickness. The departure nucleate boiling obtains in the range of 150 and 250 °$C$ within the span of 20 mm and the pre-cooling region can significantly reduced with the higher magnitude of the process parameters. In case of the second, third row of water jets offers strong resistant to the fluid flow and due to the higher surface temperature, departure nucleate boiling temperature raises. In case of re-wetting temperature, the position of the temperature shifts towards with respect to higher values of process parameters and lies in the range of 250 and 350 °$C$.
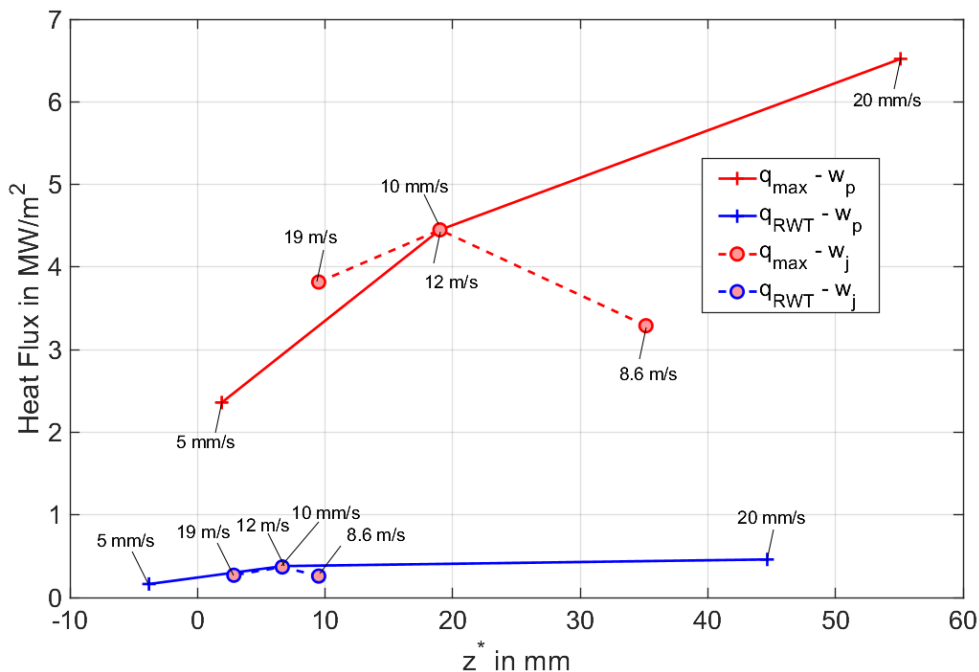


Figure 6.34: Comparison of the heat fluxes with respect to nozzle position for different process parameters for AA6082, 10 mm plate thickness

**Fig. 6.34** shows the profiles for the heat fluxes with respect to the nozzle position for 10

mm plate thickness. The higher plate thickness strongly shifts the peak of the heat flux value to well below the nozzle position and the heat flux value raises higher i.e., from 2 $MW/m^2$ to approximately 6.5 $MW/m^2$ with a spatial shift of 60 mm below the nozzle position. The similar shifts can be observed in case of the re-wetting heat flux although the peak of the heat flux remains at around 0.5 $MW/m^2$.



Figure 6.35: Comparison of the temperatures with respect to nozzle position for different process parameters for AA6082, 10 mm plate thickness

**Fig. 6.35** discuss the comparison of the temperature for different process parameters of 10 mm thick AA6082 material. The departure nucleate boiling temperature remains constant at around 250 $°C$ although the shift in the spatial location can be observed. In similar way, the re-wetting temperature remains around 350 $°C$ because of the stronger resistance to the heat transfer at higher surface temperature as the thickness of the vapour layer induces insulation.

### 6.2.8 Influence of Initial Temperature of the Nickel Material
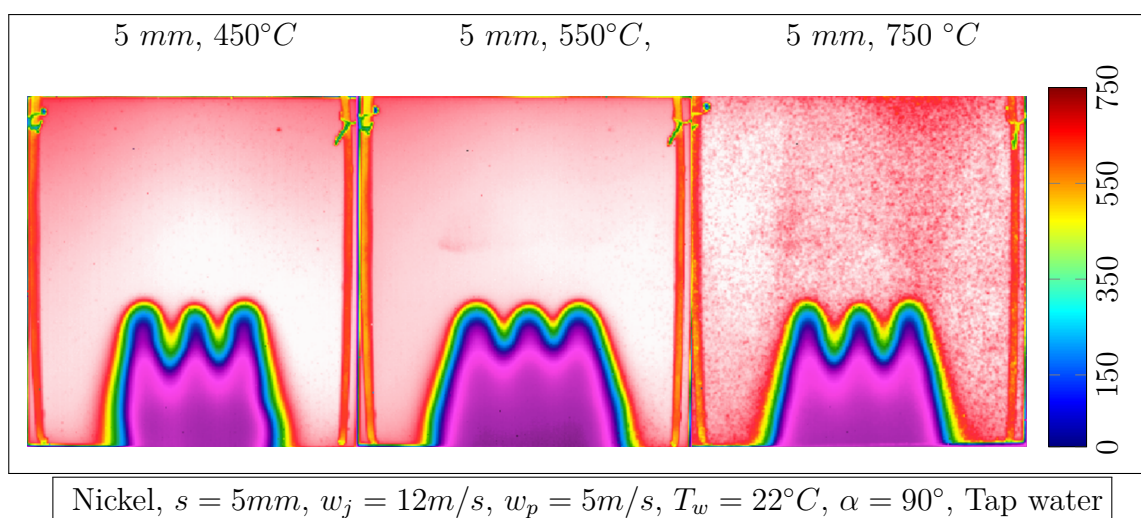


Figure 6.36: Infrared images for different initial temperature at quasi-steady condition for 5 mm thick plate

**Fig. 6.36** shows the infrared images for different initial temperature of the plate for 5 *mm* thick plate at quasi-steady state condition. As we seen clearly from the Fig. 6.36, the start temperature of the plate has no significant influence on the temperature distribution of the plate in two-dimensional space. For start temperature of the 450 °$C$ and 750°$C$, influence of the first row of water jet is strong and the effect of the water jet interaction region can be clearly seen between the centre and the respective adjacent water jets which are symmetrically apart to each other at 35 *mm*. Contradictorily, for start temperature of 550°$C$ effect of the first row of water jets has less significant on the water jet interaction region in comparison to the other plate temperatures. However, for analysis the heat transfer distribution for various initial temperatures, local temperature profiles at the centre of the plate is considered and were referred to further estimation of the heat transfer.
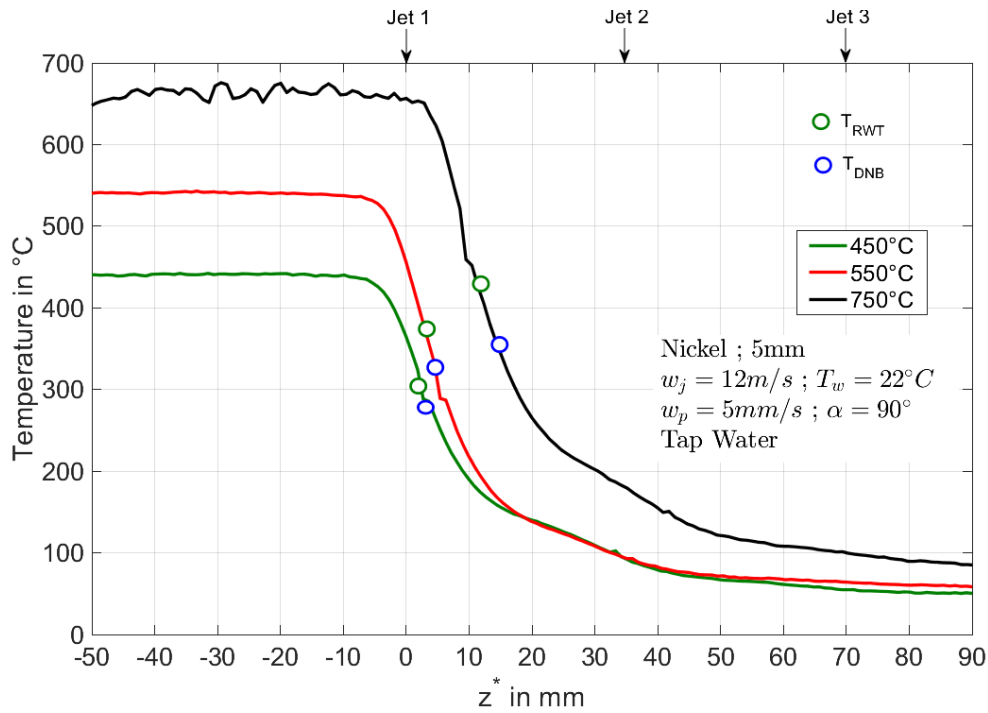
Figure 6.37: Measured surface temperature for different initial temperature of the plate at quasi-steady state condition for 5 mm thick plate

The local temperature distribution for different plate temperatures for 5 $mm$ thick plate at quasi-steady state condition were depicted in the **Fig. 6.37**. For start temperature of $450°C$ and $550°C$, the temperature profiles show a similar tendency and the $450°C$ shows slight faster cooling at the water jet impingement region compared to $550°C$ start temperature. Although, the start temperature above the nozzle position is higher based on the experimental conditions. For plate temperature of $750°C$, the temperature drop shows a delay in the cooling of the plate at the nozzle position in comparison to the lower plate temperature. As we see clearly from the local temperature profiles, the temperature distribution span across the plate length of about 80 mm from the nozzle position. The larger temperature gradient over the plate length are more prone to the thermal deformations and gradual increase in the thermal stresses takes place. Interestingly, the similar temperature tendency can be observed for all the experimental conditions for the initial temperature of the plate. Also, we can clearly see from the temperature profiles, the effect of the pre-cooling is reduced because of the lower thermal conductivity of the material.
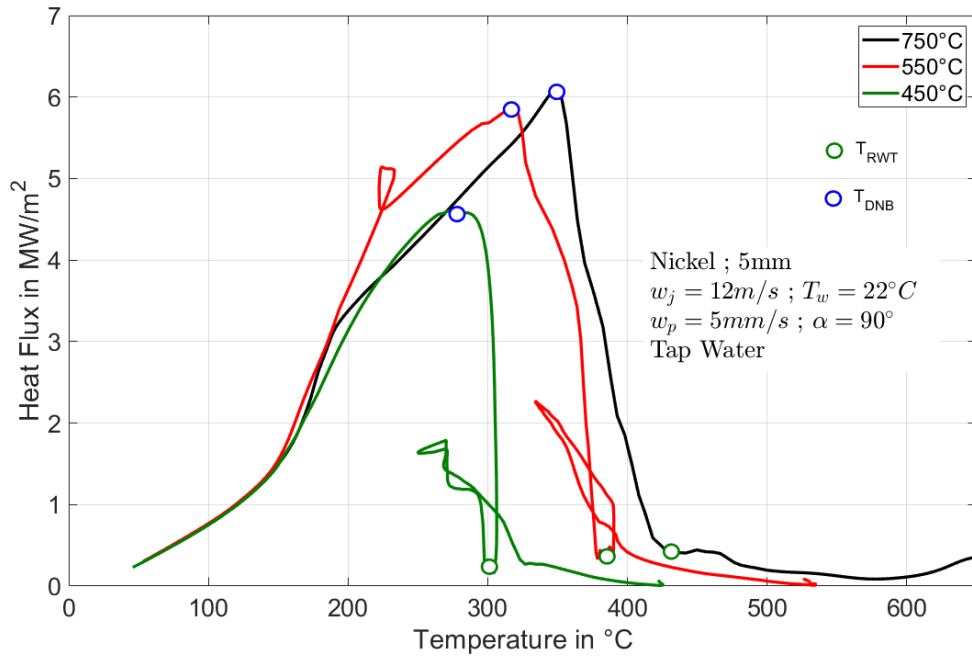
Figure 6.38: Characteristic curve for the different initial temperature of the plate at quasi-steady state condition for 5 mm thick plate

| $T_{in}$ | $q_{max}$ in $MW/m^2$ | $q_{RWT}$ in $MW/m^2$ | $T_{DNB}$ in $°C$ | $T_{RWT}$ in $°C$ | $z^*_{DNB}$ in $mm$ | $z^*_{RWT}$ in $mm$ |
|---|---|---|---|---|---|---|
| 450 $°C$ | 4.58 | 0.22 | 275 | 303 | 4.5 | 1.8 |
| 550 $°C$ | 5.87 | 0.35 | 316 | 380 | 4.5 | 2.7 |
| 750 $°C$ | 6.06 | 0.41 | 346 | 429 | 15.2 | 11.4 |

Table 6.7: Characteristic parameters for influence of initial temperature on 5 mm thick nickel plate for 9 full jet nozzle quenching

The influence of the different initial temperature of the plate with respect to heat transfer estimation can be studied using the **Fig. 6.38** and **Tab. 6.7**. The maximum heat flux and the corresponding temperature shifts towards a higher values and similar tendency can be seen with respect to the spatial location of these values in Fig. 6.38. The maximum heat flux increases from 4.7 $MW/m^2$, 5.8 $MW/m^2$ and 6 $MW/m^2$ respectively for 450$°C$, 550$°C$ and 750$°C$. In similar way, the departure nucleate boiling temperature raises from 280$°C$, 310$°C$ and 330$°C$ for start temperatures of 450$°C$ to 750$°C$ respectively. Interestingly, the re-wetting temperature of the plate shows the increase in its magnitude from 300$°C$, 380$°C$ and 430$°C$ respectively for 450$°C$, 550$°C$ and 750$°C$ start temperatures of the plate. The reason for higher temperature of both the departure nucleate boiling and the re-wetting temperatures is due to the shift in the position of the DNB and RWT point with respect to nozzle positions which can be seen as shown in the Fig. 6.38.

## 6.2.9   Influence of Plate Velocity

**For 5 mm Thick Plate**



Nickel, $s = 5mm$, $w_j = 12m/s$, $T_0 = 820°C$, $T_w = 22°C$, $\alpha = 90°$, Tap water
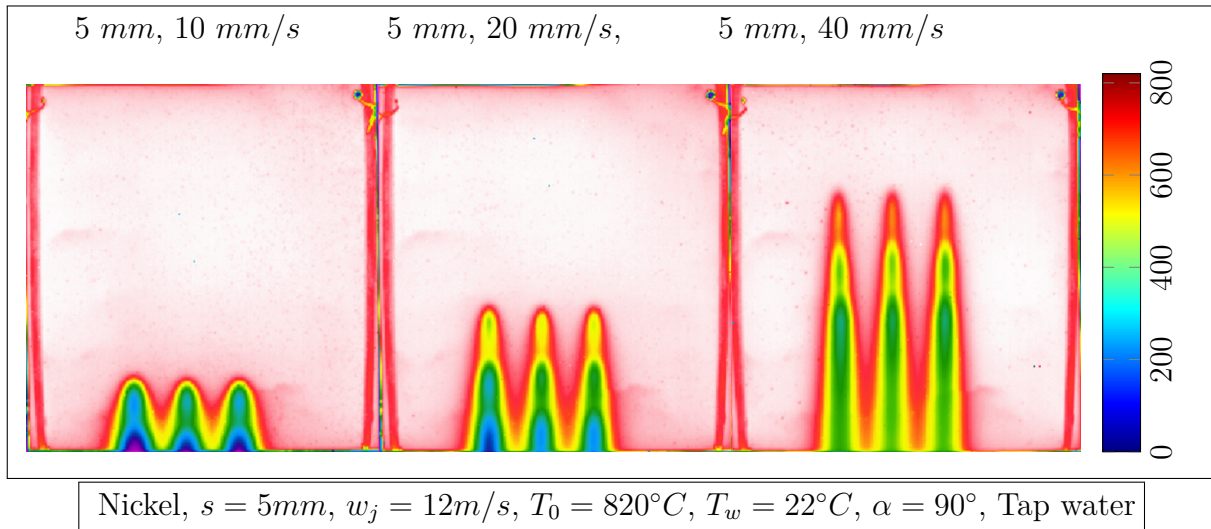
Figure 6.39: Infrared images for different plate velocity at quasi-steady state condition for 5 mm thick plate
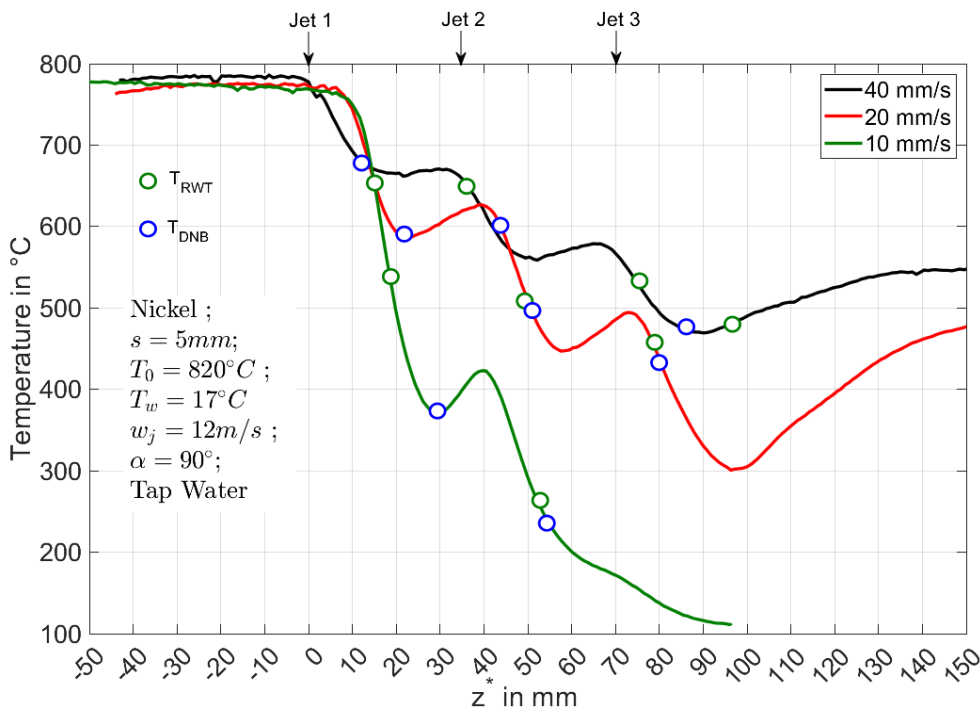


Figure 6.40: Measured surface temperature for different plate velocity at quasi-steady state condition for 5 mm thick plate

**Fig.  6.39** clearly shows the thermal images captured from the infrared thermography for different plate velocities at quasi-steady state condition.  The influence of the nozzle configuration on the temperature distribution across the plate surface can be seen in the infrared images.  For plate velocity 10 $mm/s$, the temperature in the second row of water jet shows lower temperature compared to the first row of water jet.  Whereas for plate velocity of 20 $mm/s$ and 40 $mm/s$, the effect of water jets on the temperature distribution is strong and non-linear temperature gradient exists across the plate surface.  The effect of wetting front movement is restricted at higher plate velocities because of the less contact time between the

water jet and the incoming hot solid at the each of the water jet rows. Lower plate velocities promote a strong wetting front movement between their respective adjacent water jets. For plate velocities of 20 $mm/s$ and 40 $mm/s$, the temperature distribution at each of the water jet location in the longitudinal direction shows an equivalent temperature distribution. So, for further understanding of the heat transfer, we consider the local temperature at the centre of the plate for estimation of the heat transfer. Surface temperature of the 5 $mm$ thick plate for different plate velocities at quasi-steady state condition were depicted in the **Fig. 6.40**. For 10 $mm/s$ plate velocities, the temperature drop is very significant at the first row of water jet because of strong conduction from the region above the nozzle position. The increase of the temperature at location of about 45 $mm$ from the nozzle position occurs due to the reheating effect or the wetting front is yet to reach the adjacent of the water jet locations. In similar way, the temperature drop at location near 25 $mm$ indicates the first row of water jets. For plate velocity 20 $mm/s$ and 40 $mm/s$, the effect of three rows of water jets on the cooling process can be seen in the local temperature profiles at quasi-steady state conditions, the temperature drop and temperature raise after each peak drop in temperature represents the row of water jet.
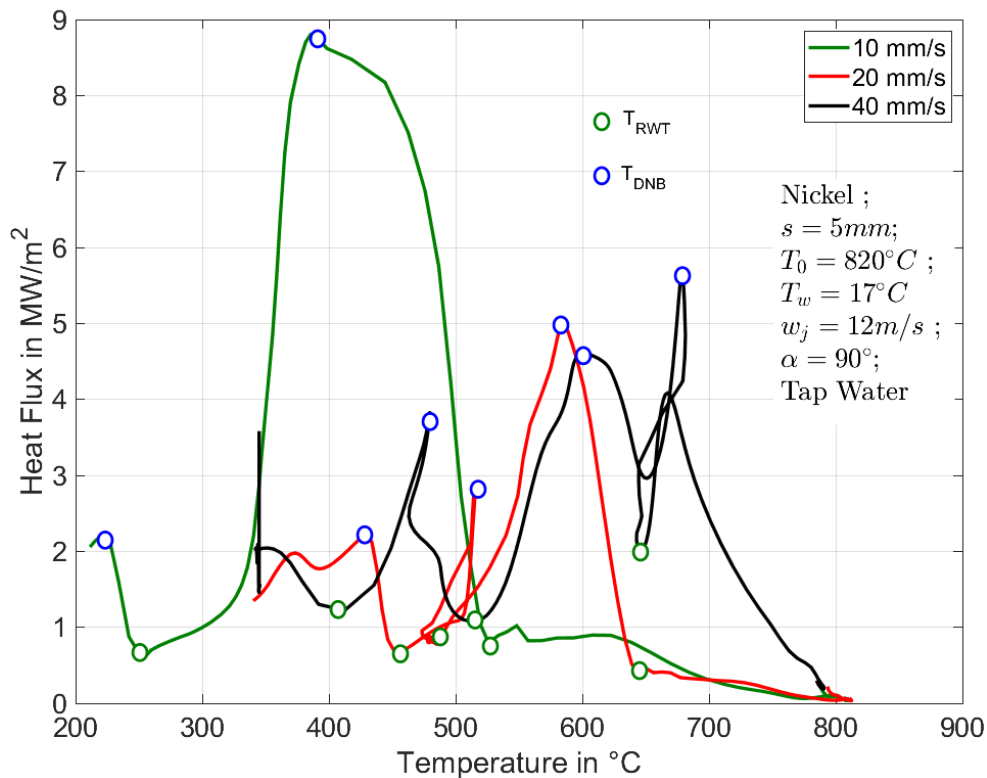


Figure 6.41: Characteristic curve for different plate velocity at quasi-steady state condition for 5mm thick nickel plate

| $w_p$ | $q_{max}$ in $MW/m^2$ | $q_{RWT}$ in $MW/m^2$ | $T_{DNB}$ in °C | $T_{RWT}$ in °C | $z^*_{DNB}$ in $mm$ | $z^*_{RWT}$ in $mm$ |
|---|---|---|---|---|---|---|
| 10 $mm/s$ | $Jet_1$ - 8.76 | $Jet_1$ - 0.79 | $Jet_1$ - 390 | $Jet_1$ - 526 | $Jet_1$ - 30 | $Jet_1$ - 18.9 |
|  | $Jet_2$ - 2.2 | $Jet_2$ - 0.61 | $Jet_2$ - 220 | $Jet_2$ - 254 | $Jet_2$ - 55.8 | $Jet_2$ - 53.1 |
| 20 $mm/s$ | $Jet_1$ - 4.98 | $Jet_1$ - 0.48 | $Jet_1$ - 583 | $Jet_1$ - 644 | $Jet_1$ - 23.4 | $Jet_1$ - 15.3 |
|  | $Jet_2$ - 2.88 | $Jet_2$ - 0.84 | $Jet_2$ - 515 | $Jet_2$ - 488 | $Jet_2$ - 51.3 | $Jet_2$ - 51.3 |
|  | $Jet_3$ - 2.25 | $Jet_3$ - 0.68 | $Jet_3$ - 430 | $Jet_3$ - 455 | $Jet_3$ - 81 | $Jet_3$ - 79.2 |
| 40 $mm/s$ | $Jet_1$ - 5.65 | $Jet_1$ - 2.0 | $Jet_1$ - 679 | $Jet_1$ - 645 | $Jet_1$ - 16.2 | $Jet_1$ - 36.9 |
|  | $Jet_2$ - 4.59 | $Jet_2$ - 1.08 | $Jet_2$ - 603 | $Jet_2$ - 516 | $Jet_2$ - 42.3 | $Jet_2$ - 75.6 |
|  | $Jet_3$ - 3.82 | $Jet_3$ - 1.22 | $Jet_3$ - 479 | $Jet_3$ - 412 | $Jet_3$ - 89.1 | $Jet_3$ - 107 |

Table 6.8: Characteristic parameters for influence of plate velocity on 5 mm thick nickel plate for 9 full jet nozzle quenching

For different plate velocities at quasi-steady state condition of 5 $mm$ thick plate, the typical boiling curve represents the amount of heat transfer during the quenching process as shown in the **Fig. 6.41** and **Tab. 6.8**. The peak of the maximum heat flux decreases drastically from 8.9 $MW/m^2$ to 4.5 $M/m^2$ for 10 $mm/s$ and 40 $mm/s$ plate velocities respectively. The higher maximum heat flux occurs for 10 $mm/s$ plate velocity due to predominant cooling behaviour compared to other plate velocities of 20 $mm/s$ and 40 $mm/s$. The decrease of the heat flux for higher plate velocities agrees with the surface temperature because of the higher end temperature of the plate surface, which stays the plate in the transition and in film boiling region of the cooling process.

**For 10 mm Thick Plate**
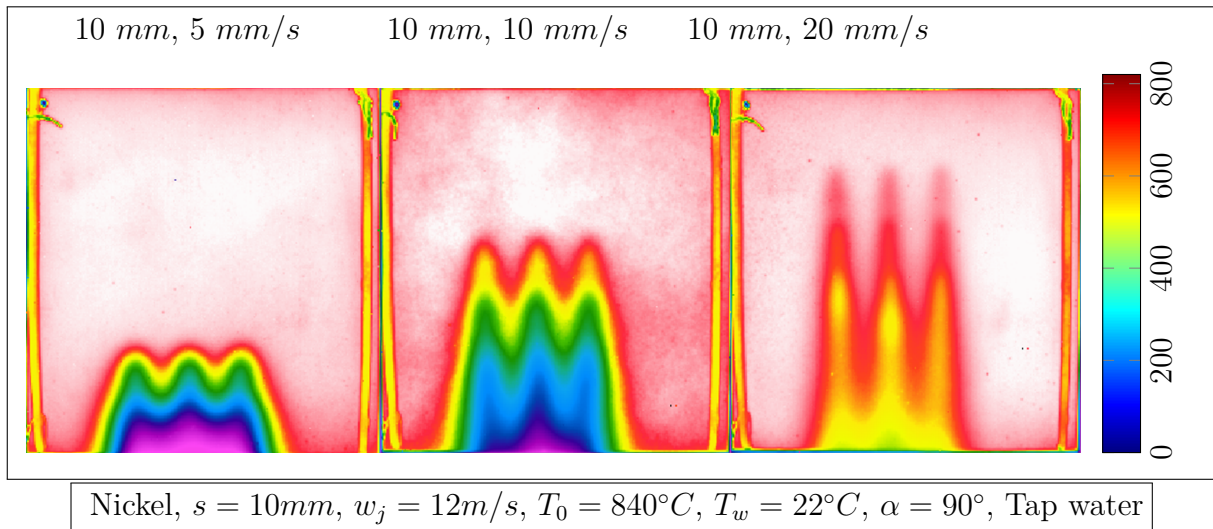


Figure 6.42: Infrared images for different plate velocities at quasi-steady state condition for 10 mm thick plate

The thermal images for plate thickness of 10 $mm$ are shown in **Fig. 6.42**, which presents the infrared images for different plate velocities. For higher plate velocities of 10 $mm/s$ and 20 $mm/s$, the non-uniform temperature distribution occurs in the water jet impingement region wherein the cooling process lies in transition boiling range for 10 $mm/s$ plate velocity and for 20 $mm/s$ plate velocity, cooling of the plate stays in the film boiling region.
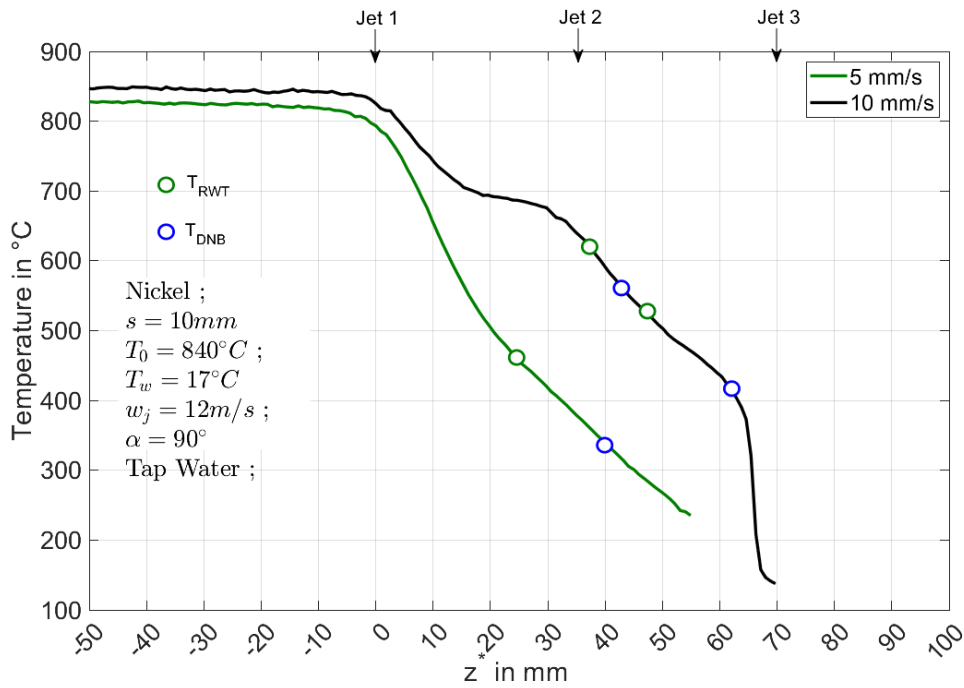
Figure 6.43: Measured surface temperature for different plate velocities at quasi-steady state condition for 10 mm thick plate
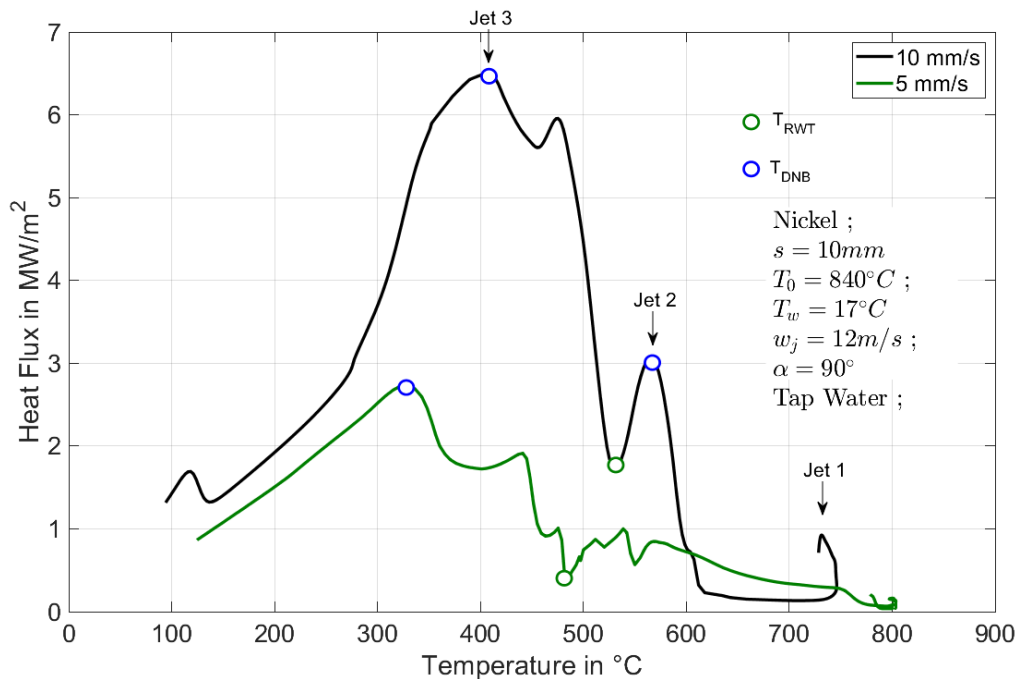
Figure 6.44: Characteristic curves for different plate velocities at quasi-steady state condition for 10 mm thick plate

**Fig. 6.43** depicts the surface temperature distribution for different plate velocities for 10 $mm$ thick plate at quasi-steady state condition. In the temperature profiles, we presented local cooling profiles only for 5 $mm/s$ and 10 $mm/s$ plate velocities. As we see from the infrared images for plate velocity of 20 $mm/s$, the temperature distribution still stays in the film boiling range and thus can't be analysed. The temperature profiles for plate velocity 5 $mm/s$ shows a faster cooling rate compared to plate velocity of 10 $mm/s$. Even though the end temperature of the plate for 10 $mm/s$ plate velocity is well below $100°C$, the significant difference between the two plate velocities can be clearly seen. The effect of the first row

of the water jet on the temperature profiles can be seen in the temperature profiles of 10 $mm/s$ plate velocity.

| $w_p$ | $q_{max}$ in $MW/m^2$ | $q_{RWT}$ in $MW/m^2$ | $T_{DNB}$ in $°C$ | $T_{RWT}$ in $°C$ | $z^*_{DNB}$ in $mm$ | $z^*_{RWT}$ in $mm$ |
|---|---|---|---|---|---|---|
| $5\ mm/s$ | 2.7 | 0.37 | 329 | 485 | 41.4 | 22.5 |
| $10\ mm/s$ | $Jet_1$ - 3.05 | $Jet_1$ - 0.22 | $Jet_1$ - 567 | $Jet_1$ - 617 | $Jet_1$ - 42.5 | $Jet_1$ - 37.4 |
|  | $Jet_2$ - 6.49 | $Jet_2$ - 1.73 | $Jet_2$ - 407 | $Jet_2$ - 532 | $Jet_2$ - 62.05 | $Jet_2$ - 45.9 |

Table 6.9: Boiling parameters for influence of plate velocity on 10 mm thick nickel plate for 9 full jet nozzle quenching

Characteristic boiling curve for different plate velocities for 10 $mm/s$ plate velocity is presented in the **Fig.  6.44** and **Tab.  6.9**. From the typical boiling curves, we can clearly observe the increase in the maximum heat flux from 2.8 $MW/m^2$ to 6.5 $MW/m^2$ for corresponding temperature of 310 $°C$ and 400$°C$ respectively. The increase in the heat flux is mainly due to the larger temperature gradient across the length of the plate, wherein the cooling of the hot plate spans from nozzle position at 0 $mm$ until 60 $mm$ below the first row of water jets. So, the higher temperature gradient across the length of the plate promotes the larger heat flux or maximum heat flux value. The heat flux obtained at the first row of jet in case of 10 $mm/s$ plate velocity shows a higher magnitude of maximum heat flux compared to the 5 $mm/s$ plate velocity heat flux profiles.

### 6.2.10   Influence of Water Jet Velocity

**For 5 mm Thick Plate**



Nickel, $s = 5mm$, $w_p = 10mm/s$, $T_0 = 850°C$, $T_w = 22°C$, $\alpha = 90°$, Tap water
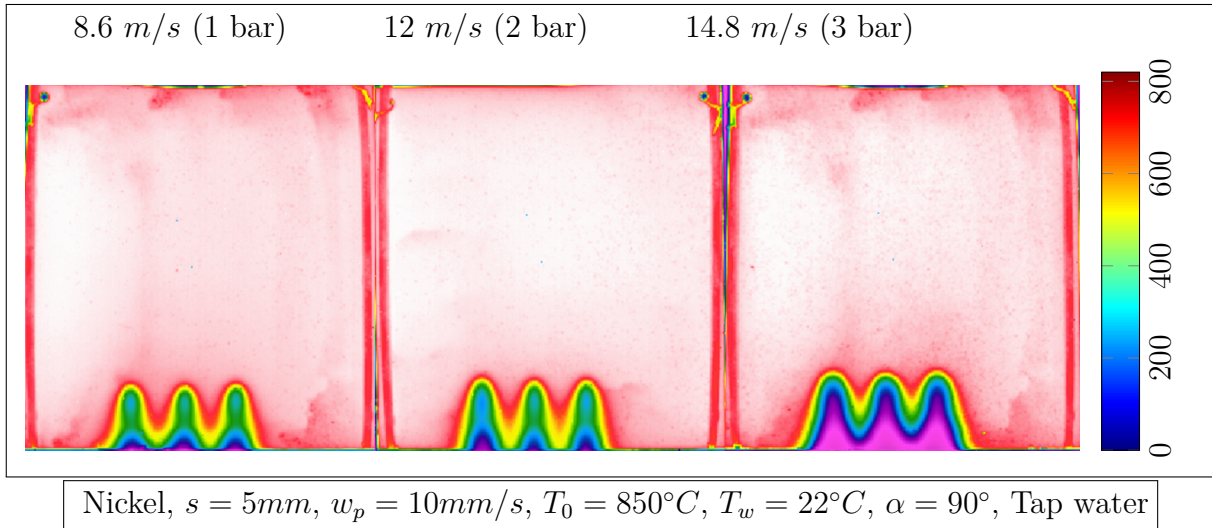
Figure 6.45: Infrared images for different initial temperature of the plate at quasi-steady state condition for 5 mm thick plate

The influence of the water jet velocity on the temperature profiles for 5 mm thick plate for inline configuration of the water jets are shown in the **Fig. 6.45**. For water jet pressure of 1 bar and 2 bar, the uneven cooling of the temperature takes place while the influence of the adjacent water jets on the temperature distribution can be seen clearly. Whereas, for water jet pressure of 3 bar the more even temperature distribution exists in the water impingement region. And the effect of the reheating phenomena can be avoided in case of higher water pressure conditions.

Figure 6.46: Measured surface temperature for different water jet velocities at quasi-steady state condition for 5 mm thick plate
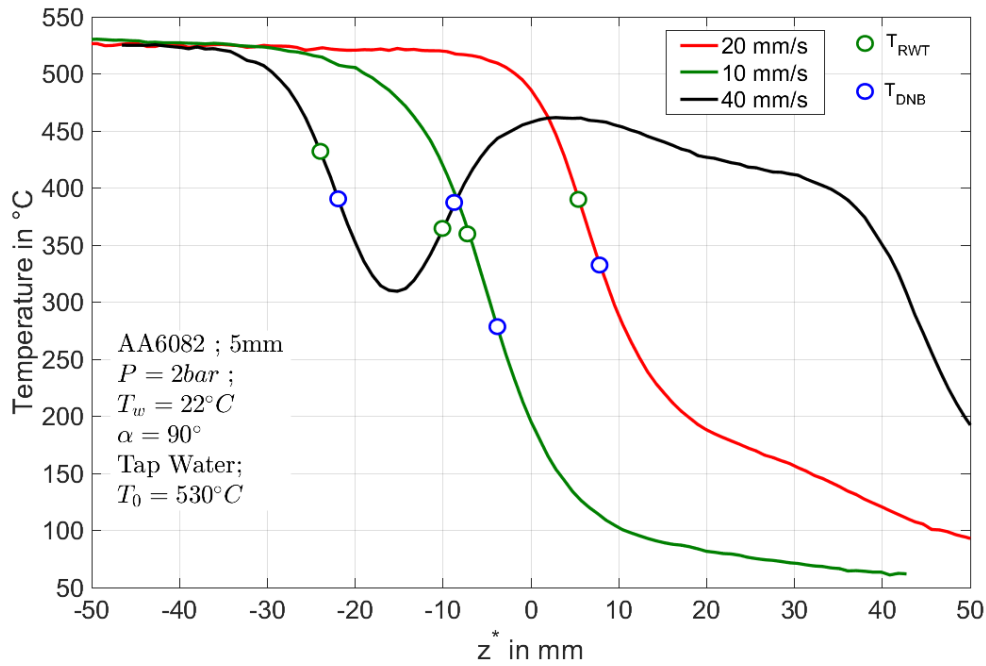


Figure 6.47: Characteristic curve for different water jet velocities at quasi-steady state condition for 5 mm thick plate

Surface temperature distribution for different water pressure are depicted in the **Fig. 6.46** at quasi-steady state condition. For water pressure of 3 bar, the more uniform cooling occurs as seen in the temperature profiles in the water jet impingement region and more non-linear temperature can be observed in cases of lower water pressures i.e., 2 bar and 1 bar, which shows a reheating phenomenon at the adjacent to the water jet region. The width of the cooling increases for the 1 and 2 bar water pressure temperature profiles because of strong internal conduction from the bottom and adjacent water jets region. This non-linear temperature distribution across the water jet impingement mainly affects the local heat transfer and increases the possibility for thermal deformation and induces a higher thermal

stress on the plate.

| $w_j$ | $q_{max}$ in $MW/m^2$ | $q_{RWT}$ in $MW/m^2$ | $T_{DNB}$ in $°C$ | $T_{RWT}$ in $°C$ | $z^*_{DNB}$ in $mm$ | $z^*_{RWT}$ in $mm$ |
|---|---|---|---|---|---|---|
| 8.6 $m/s$ | $Jet_1$ - 6.29 | $Jet_1$ - 0.39 | $Jet_1$ - 312 | $Jet_1$ - 663 | $Jet_1$ - 20.8 | $Jet_1$ - 11.2 |
|  | $Jet_2$ -8.08 | $Jet_2$ - 0.73 | $Jet_2$ - 356 | $Jet_2$ - 492 | $Jet_2$ - 39.2 | $Jet_2$ - 32.8 |
| 12 $m/s$ | 8.62 | 0.79 | 398 | 526 | 26.1 | 18.9 |
| 14.8 $m/s$ | 19.78 | 1.01 | 410 | 505 | 23.8 | 21.25 |

Table 6.10: Boiling parameters for influence of water jet velocities on 5 mm thick nickel plate for 9 full jet nozzle quenching

**Fig. 6.47** and **Tab. 6.10**, shows the typical boiling curve for different water jet pressures for 5 $mm$ thick plate at quasi-steady state condition. The increase in the heat flux for 3 bar water jet pressure takes place because of uniform cooling of the plate at water jet impingement position. Whereas, for water pressures 2 bar and 1 bar relatively shows a lower peak in the maximum heat flux and the peak temperature reduces to the lower values i.e., the peak heat fluxes correspond to 20 $MW/m^2$, 9 $MW/m^2$, 8 $MW/m^2$ and peak temperature corresponds to $400°C$, $390°C$, $360°C$ for water jet pressures of 3 bar, 2 bar and 1 bar respectively. The re-wetting temperature is about $500°C$ with the corresponding heat flux is about 1 $MW/m^2$.

**For 10 mm Thick Plate**



| 12 $m/s$ (2 bar) | 14.8 $m/s$ (3 bar) | 19.2 $m/s$ (5 bar) |

Nickel, $s = 10mm$, $w_p = 10mm/s$, $T_0 = 850°C$, $T_w = 22°C$, $\alpha = 90°$, Tap water

Figure 6.48: Infrared images for different water jet velocities at quasi-steady state condition for 10 mm thick plate

The thermal infrared images for different water jet pressures are shown in **Fig. 6.48**, for 10 $mm$ thick plate at quasi-steady state condition. The thermal infrared images clearly indicate the similar tendency in the temperature distribution across the plate surface for 2 bar and 3 bar water jet pressures. Whereas for water jet pressure 5 bar, first row of water jets shows higher temperatures compared to the water jet pressures for 2 bar and 3 bar. The reason for this kind of cooling behaviour should be the effect of bounce off the water jets from the plate surface. Since for water jet pressure of 5 bar, the fluid motion is very complex involving higher Reynolds number with correspondingly larger turbulent motion of the fluid. However, for the purpose of the heat transfer analysis, temperatures at the centre of the plate is considered.
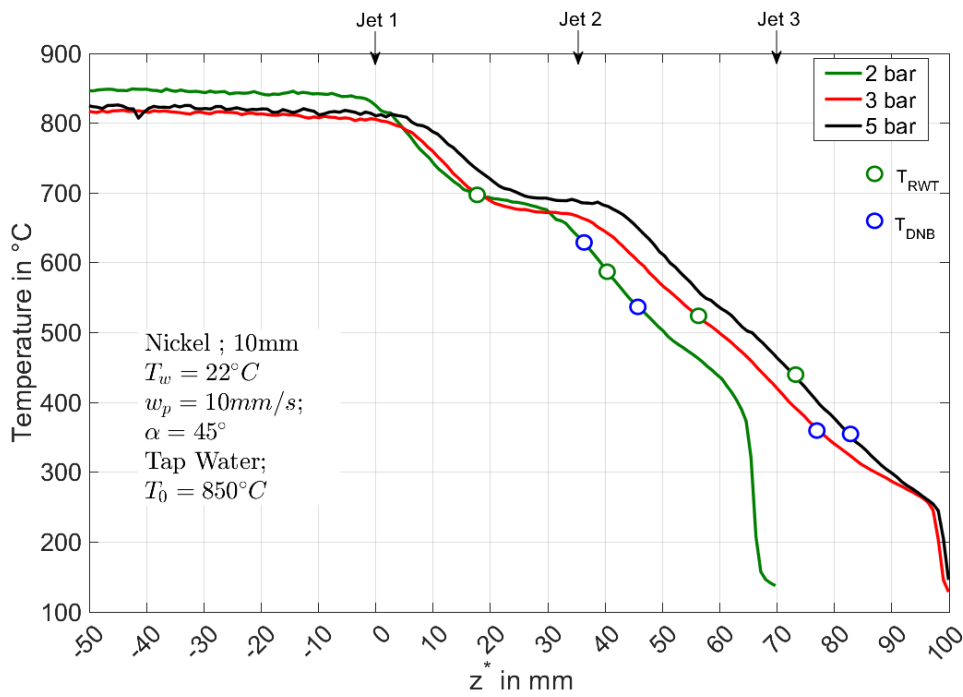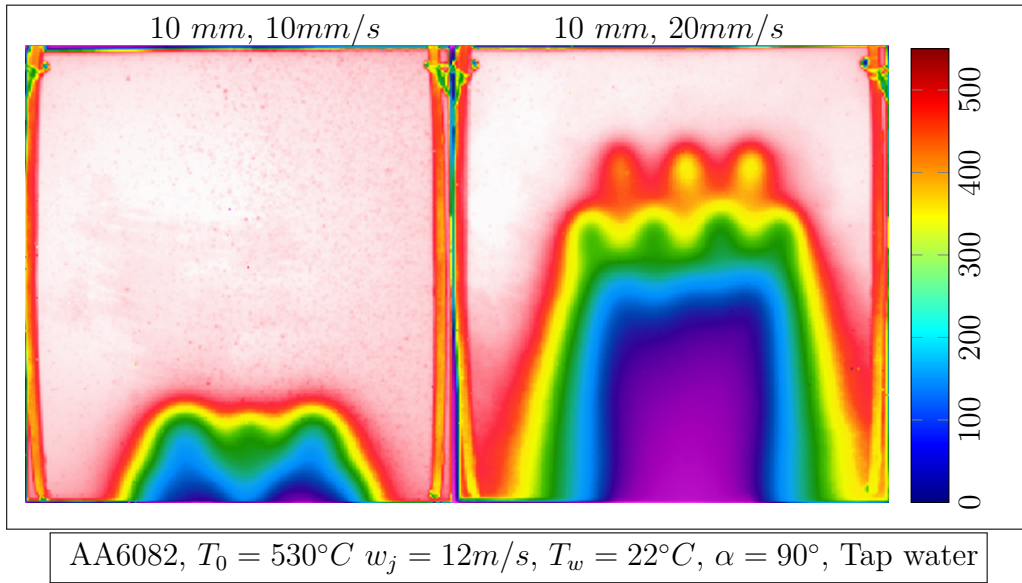
Figure 6.49: Measured surface temperature for different water jet velocities at quasi-steady state condition for 10 mm thick plate
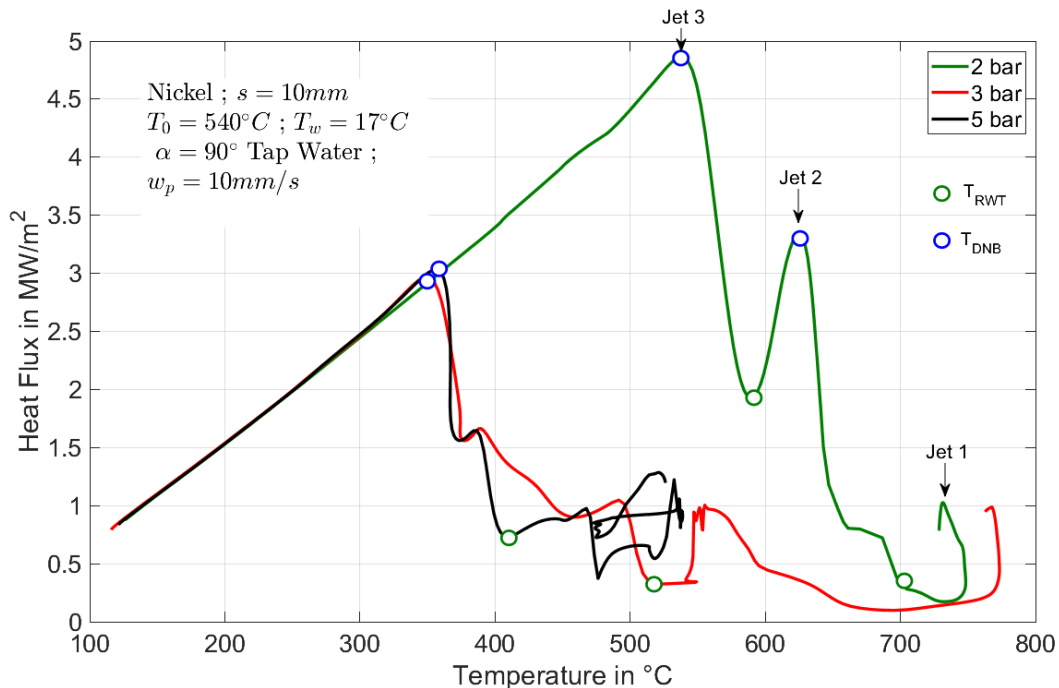


Figure 6.50: Characteristic curves for different water jet velocities for quasi-steady state condition for 10 mm thick plate
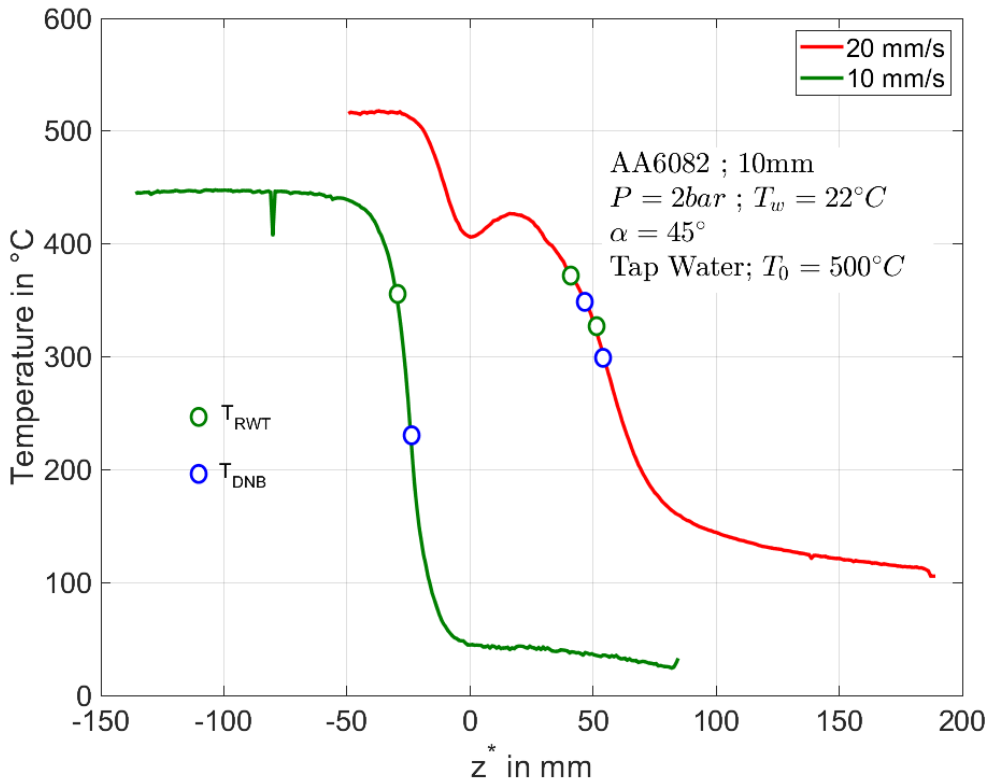
**Fig. 6.49**, shows the surface temperature distribution for different water jet velocities for 10 *mm* thick plate at quasi-steady state condition. The local temperature profiles clearly indicate faster cooling for 2 bar water jet pressure compared to the 3 bar and 5 bar, due to the bounce off phenomenon. The effect of the first row of water jets can be seen below the nozzle impingement position for all the water jet pressures. The heat flux distribution for all these water pressure should reveal more information for understanding the estimation of the heat flux during inline configuration.

| $w_j$ | $q_{max}$ in $MW/m^2$ | $q_{RWT}$ in $MW/m^2$ | $T_{DNB}$ in °C | $T_{RWT}$ in °C | $z^*_{DNB}$ in $mm$ | $z^*_{RWT}$ in $mm$ |
|---|---|---|---|---|---|---|
| 12 $m/s$ | $Jet_1$ - 3.31 | $Jet_1$ - 0.28 | $Jet_1$ - 627 | $Jet_1$ - 704 | $Jet_1$ - 36.55 | $Jet_1$ - 16.15 |
|  | $Jet_2$ -4.86 | $Jet_2$ - 1.92 | $Jet_2$ - 537 | $Jet_2$ - 589 | $Jet_2$ - 45.9 | $Jet_2$ - 40.8 |
| 14.8 $m/s$ | 2.96 | 0.32 | 349 | 518 | 77.4 | 56.7 |
| 19 $m/s$ | 3.03 | 0.73 | 357 | 411 | 82.8 | 75.6 |

Table 6.11: Boiling parameters for influence of water jet velocities on 10 mm thick nickel plate for 9 full jet nozzle quenching

Surface heat flux profiles for different water jet pressures are shown in **Fig. 6.50** and **Tab. 6.11** for 10 $mm$ thick plate at quasi-steady state condition. Due to the effect of the water ejection from the surface of the plate at higher water jet pressures i.e., 3 bar and 5 bar pressures, peak of the maximum heat flux reduces significantly from 4.9 $MW/m^2$ at 2 bar pressure to around 3 $MW/m^2$ at 3 and 5 bar water pressures respectively. With the decrease in the maximum heat flux reduces the peak temperature to lower values i.e., from 520 °C to 350°C for 2 bar and 3, 5 bar water jet pressures respectively. The similar effect can be seen in the re-wetting temperature of the plate i.e., from 590°C, 520°C and temperature decreases finally to 400°C correspondingly for water jet pressures of 2 bar, 3 bar and 5 bar.

## 6.2.11   Influence of Plate Velocity - Nicrofer Material
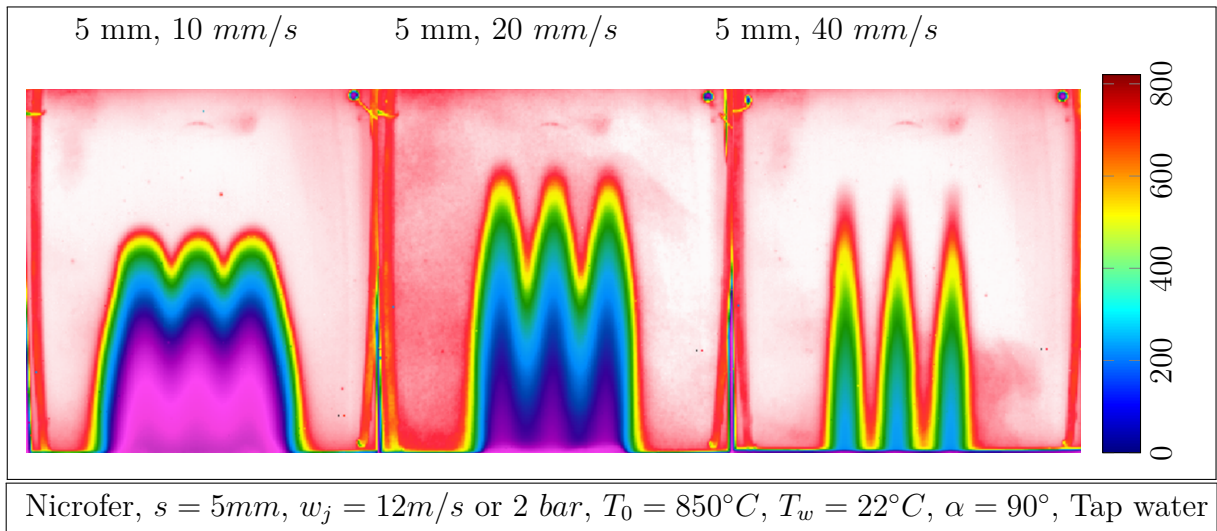


Figure 6.51: Infrared images for different plate velocity at quasi-steady state condition for 5 mm thick plate

**Fig. 6.51** shows a infrared images for different plate velocities for 5 $mm$ thick plate for nicrofer material at quasi-steady state condition. For plate velocity of 10 $mm/s$, the more uniform temperature distribution can be seen in the water jet impingement region for all three rows of water jet configuration. Whereas for 20 $mm/s$ and 40 $mm/s$, the temperature seems to be more non-uniformly distributed across the surface of plate. The effect of nozzle configuration is stronger in case of 40 $mm/s$ plate velocity.
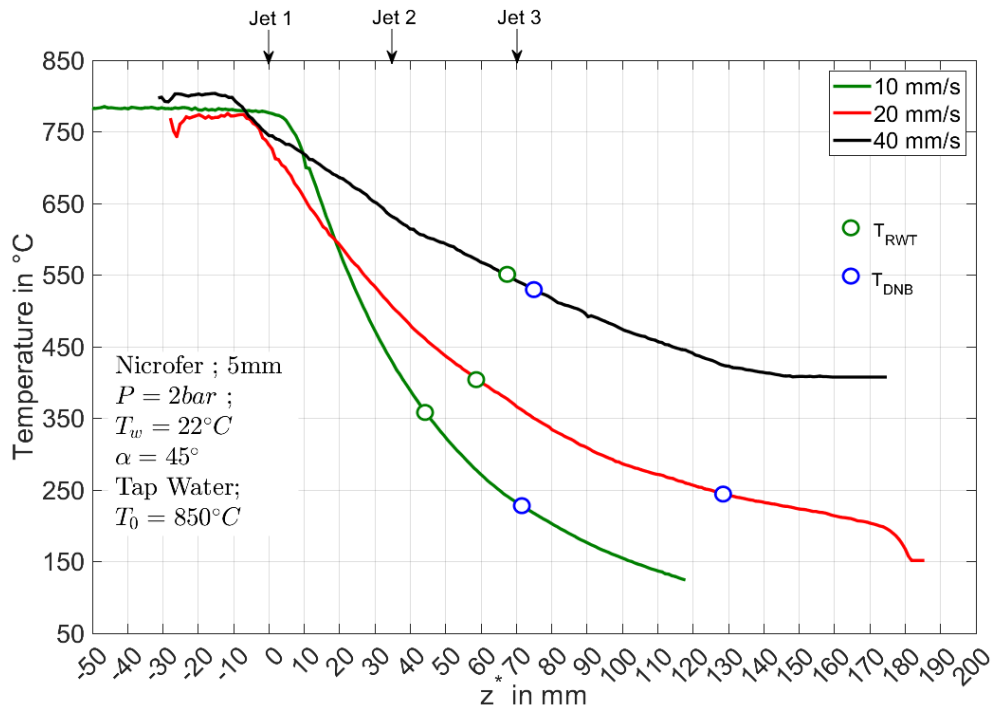
Figure 6.52: Measured surface temperature for different plate velocity at quasi-steady state condition for 5 mm thick plate

Surface temperature distribution for different plate velocities at quasi-steady state condition for 5 $mm$ thick plate is shown in the **Fig. 6.52**. For plate velocities of 10 $mm/s$, the temperature cooling is stronger and plate cools faster compared to the other plate velocities i.e., 20 $mm/s$ and 40 $mm/s$. For more uniform cooling of the plate, plate velocity of 10 $mm/s$ can be chosen. Since the water jet impingement takes place form $0mm$ i.e., nozzle position until the 75 $mm$ of the plate length. The effect of the nozzle positioning can be seen in the surface temperature distribution of the plate. The end temperature of the plate is higher for higher plate velocities, i.e., 110°$C$, 150°$C$ and 400°$C$ for 10 $mm/s$, 20 $mm/s$ and 40 $mm/s$ plate velocities. The effect of the pre-cooling significantly reduces because of lower thermal conductivity of the plate. The temperature drop takes for all the water jet pressures well below the nozzle positions.
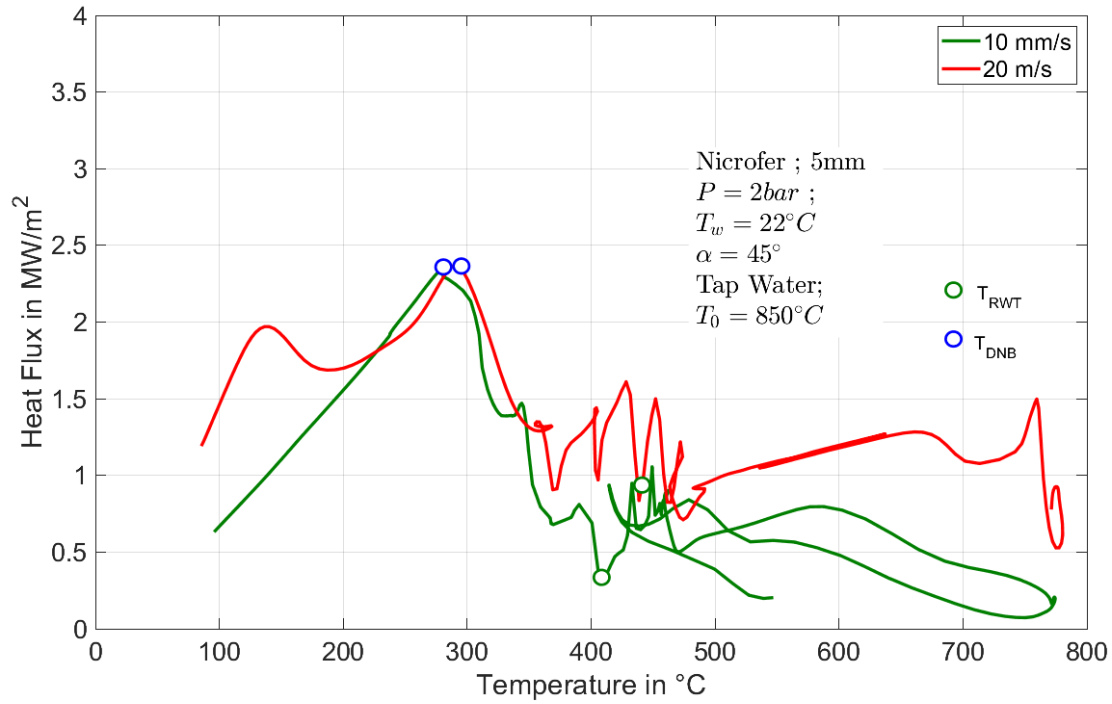
Figure 6.53: Boiling curve for different plate velocity at quasi-steady state condition for 5mm thick plate

| $w_p$ | $q_{max}$ in $MW/m^2$ | $q_{RWT}$ in $MW/m^2$ | $T_{DNB}$ in °C | $T_{RWT}$ in °C | $z^*_{DNB}$ in $mm$ | $z^*_{RWT}$ in $mm$ |
|---|---|---|---|---|---|---|
| 10 $mm/s$ | 2.29 | 0.29 | 280 | 407 | 58.9 | 37.05 |
| 20 $mm/s$ | 2.33 | 0.99 | 296 | 442 | 97.2 | 46.8 |

Table 6.12: Boiling parameters for influence of plate velocity on 5 mm thick nicrofer plate for 9 full jet nozzle quenching

Characteristic boiling curve for different plate velocities of the plate for 5 $mm$ thick plate at quasi-steady state condition is shown in the **Fig. 6.53** and **Tab. 6.12**. From the heat flux profiles, we can clearly observe that for higher plate velocities the peak of the maximum heat flux is drastically increases from 2 $MW/m^2$ at 10 $mm/s$ and 20 $mm/s$ to nearly 14 $MW/m^2$ at 40 $mm/s$ plate velocity. Similarly, the peak temperature also drastically increases form 300°$C$ to 600°$C$ temperature. Whereas, the re-wetting temperature for 10 and 20 $mm/s$ plate velocity remains constant at 400°$C$ and for 40 $mm/s$ it corresponds to higher temperatures of nearly 800°$C$.

### 6.2.12 Influence of Water Jet Velocity - Nicrofer Material
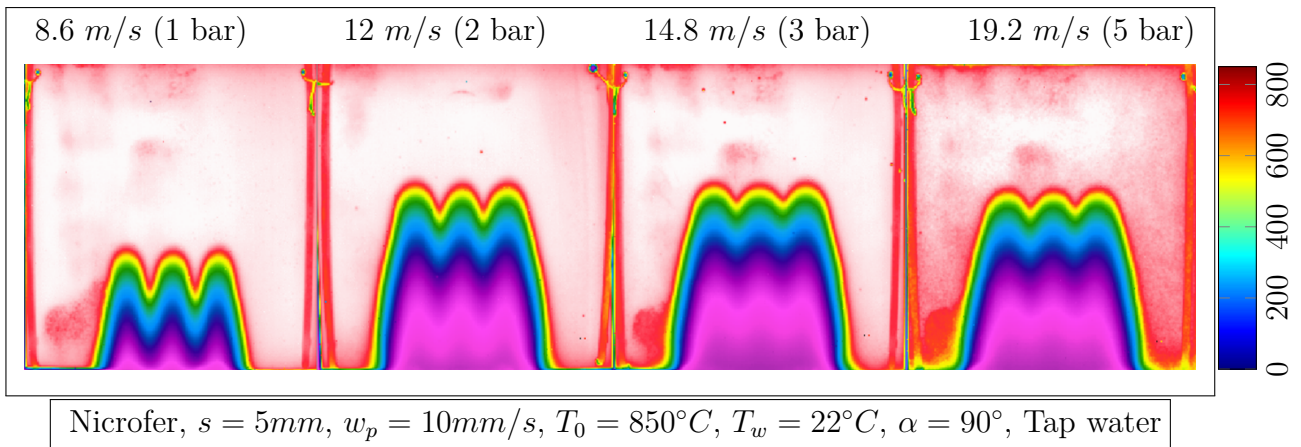


Figure 6.54: Infrared images for different water jet velocities at quasi-steady state condition for 5 mm thick plate

**Fig. 6.54** shows an infrared thermal image for different water jet velocities for 5 $mm$ thick plate at quasi-steady state condition. The infrared images show a similar tendency in temperatures across the plate surface for all the water jet pressures. However, for further understanding of the heat fluxes, the local temperature distribution at the centre of the plate is considered for analysis.
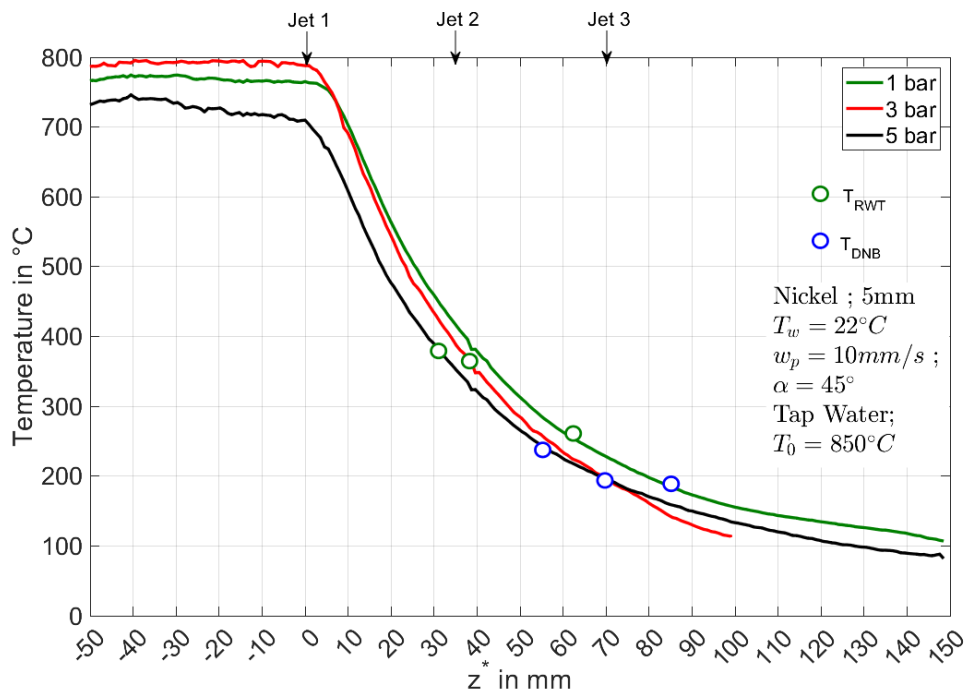


Figure 6.55: Measured surface temperature for different plate velocity at quasi-steady state condition for 5 mm thick plate

Surface temperature distribution for different water jet velocities at quasi-steady state condition for 5 mm thick plate are shown in the **Fig. 6.55**. The temperature distribution for 5 bar water jet pressure shows a faster cooling conditions, where the curve shifts towards the nozzle position. The pre-cooling has no influence with increase in the water jet pressures. The boiling curve or the heat flux curve profiles reveals more accurate information about the amount of heat transfer during the cooling process.
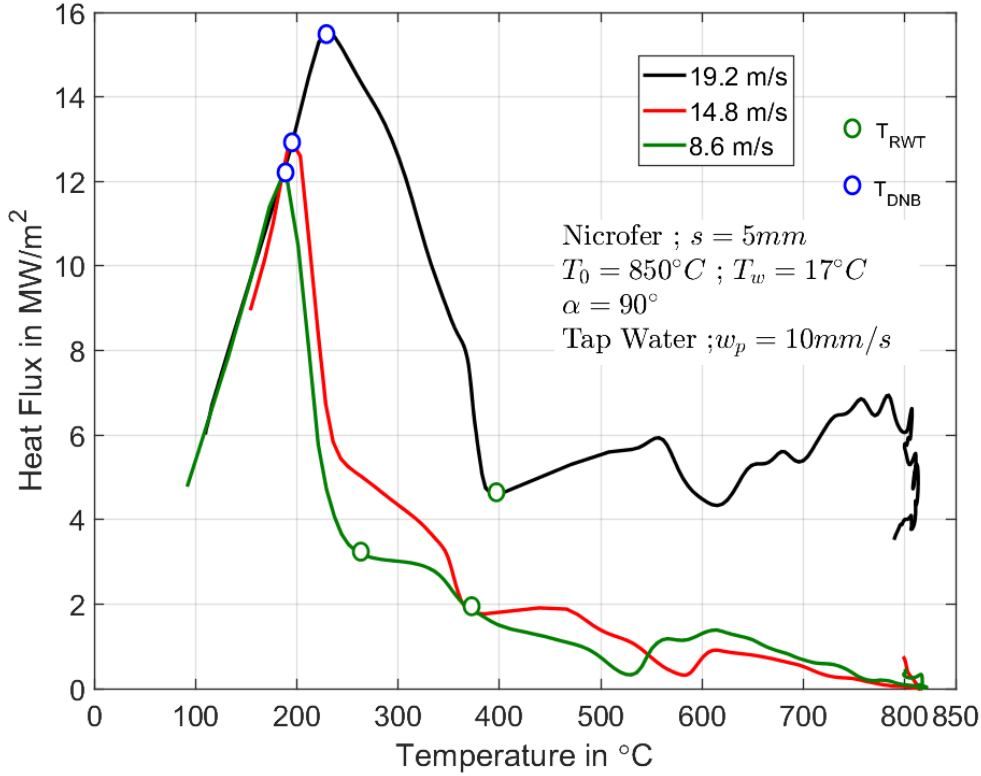
Figure 6.56: Boiling curve for different water jet velocities at quasi-steady state condition for 5 mm thick plate

| $w_j$ | $q_{max}$ in $MW/m^2$ | $q_{RWT}$ in $MW/m^2$ | $T_{DNB}$ in $°C$ | $T_{RWT}$ in $°C$ | $z^*_{DNB}$ in $mm$ | $z^*_{RWT}$ in $mm$ |
|---|---|---|---|---|---|---|
| 8.6 $m/s$ | 12.27 | 3.17 | 188 | 264 | 83.7 | 59.4 |
| 14.8 $m/s$ | 13 | 1.8 | 193 | 372 | 71.1 | 36.9 |
| 19 $m/s$ | 15.5 | 4.63 | 229 | 390 | 58.5 | 29.7 |

Table 6.13: Boiling parameters for influence of water jet velocities on 5 mm thick nicrofer plate for 9 full jet nozzle quenching

The influence of water jet pressures on the 5 mm thick plate at quasi-steady state condition are shown in the **Fig.  6.56** and **Tab.  6.13**. The steady increase in the maximum heat flux takes place from 12 $MW/m^2$, 13 $MW/m^2$ to 15.5 $MW/m^2$ for 1 bar, 3 bar and 5 bar water pressures, respectively. In similarly, the departure nucleate boiling temperature increases from $180°C$, $200°C$ to $220°C$ temperature. Whereas, re-wetting temperature remains constant at $380°C$, but the increase in the maximum heat flux takes place from 2 $MW/m^2$ to nearly 5 $MW/m^2$ for 1 bar, 3 bar and 5 bar water jet pressures respectively.

## 6.3  Staggered Configuration of Full Jet Nozzles

**Phenomena of Staggered Jet Quenching**
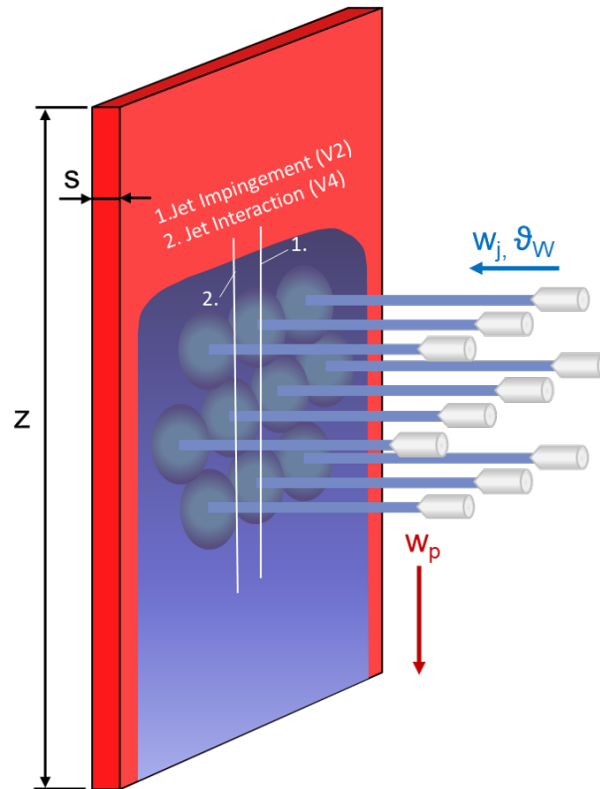


Figure 6.57: Schematic diagram of staggered full jet impingement quenching

**Fig. 6.57** shows the full jet impingement quenching in case of the staggered configuration, single full jet nozzles are arranged equally at a distance of 35 *mm* from the centre of each jet in three different rows and in three different columns and in second row one extra jet is added to mimic the fluid flow thus correspondingly heat transfer. The complexity of the jet interaction between the other adjacent jets and the movement of the wetting front influences on the heat transfer during this kind of quenching. As depicted in the Fig. 6.57, the plate with a dimension of 230 *mm* width x 250 *mm* length x s *mm* thickness, the plate moves with a velocity of $w_p$, the water jet possess a velocity of $w_j$ and temperature $\theta_w$. In the following section, the description of the heat transfer during quenching with arrangement of inline configuration will be discussed along with the variation of various influencing process parameters.

## Staggered Nozzle Configuration

The staggered nozzle configuration differs from the inline in the middle row, staggered has 4 nozzles in the middle row compare to inline which has 3. The process parameters are same as discussed in the inline configuration but main difference is positioning of the nozzle , here the temperature plot is drawn for the line $V_2$ centre (78 mm) on the impingement nozzle and line $V_4$ (at 78 mm) centre is the interaction point for $V_4$ and $V_5$ centre from both sides at 17.5 mm each. The cooling time from 800 °$C$ to saturation water temperature 100 °$C$ is equal for both $V_4$ and $V_2$ with 24 seconds. The major cooling rate difference can be observed from 800 °$C$ to 250 °$C$ with 2 seconds late cooling for $V_2$, since the position of the $V_2$ has a cooling effect from four different impinging nozzles from four dirsctions and once the film layer is breaks down it reaches to saturation temperature with faster cooling rate.
In **Fig. 6.58** depicts the comparison of different time periods for jet impingement and jet interaction region, experiments were carried out at water temperature of 18 °$C$, water
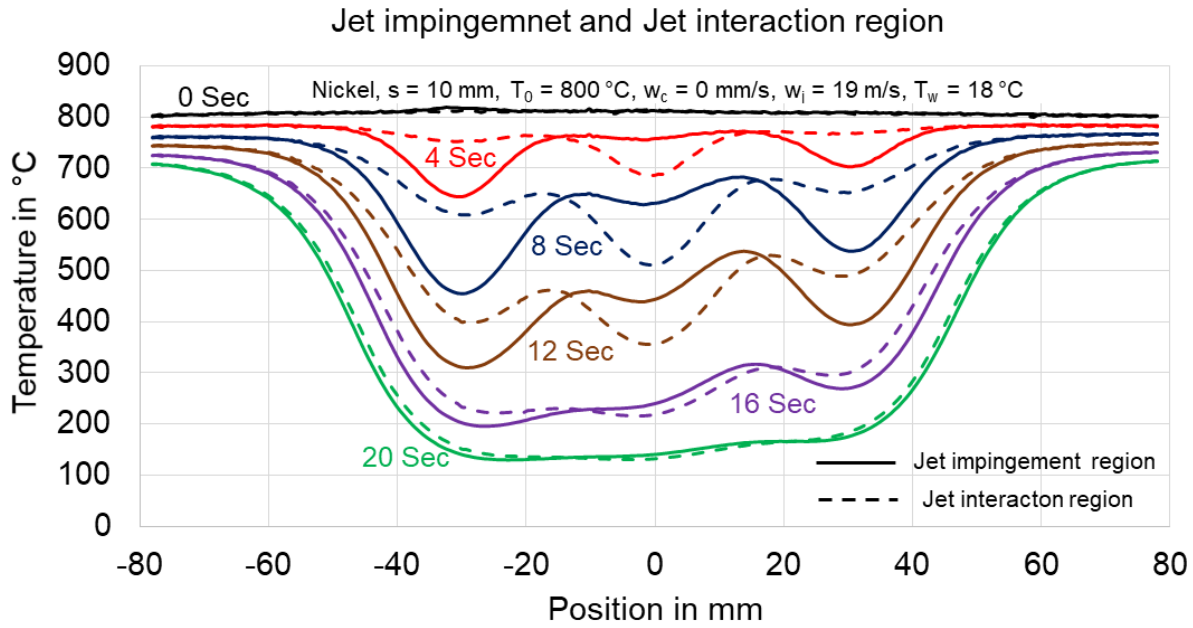
Figure 6.58: Comparison of jet impingement and jet interaction region over different time periods

jet velocity of 19 m/s, and initial temperature of 800 $°C$ for 10 mm thickness plate. It can be observed from the figure that the cooling time required for both impingement and interaction zone to reach saturation temperature are same, but impingement region cools faster than interaction region in the transition zone.
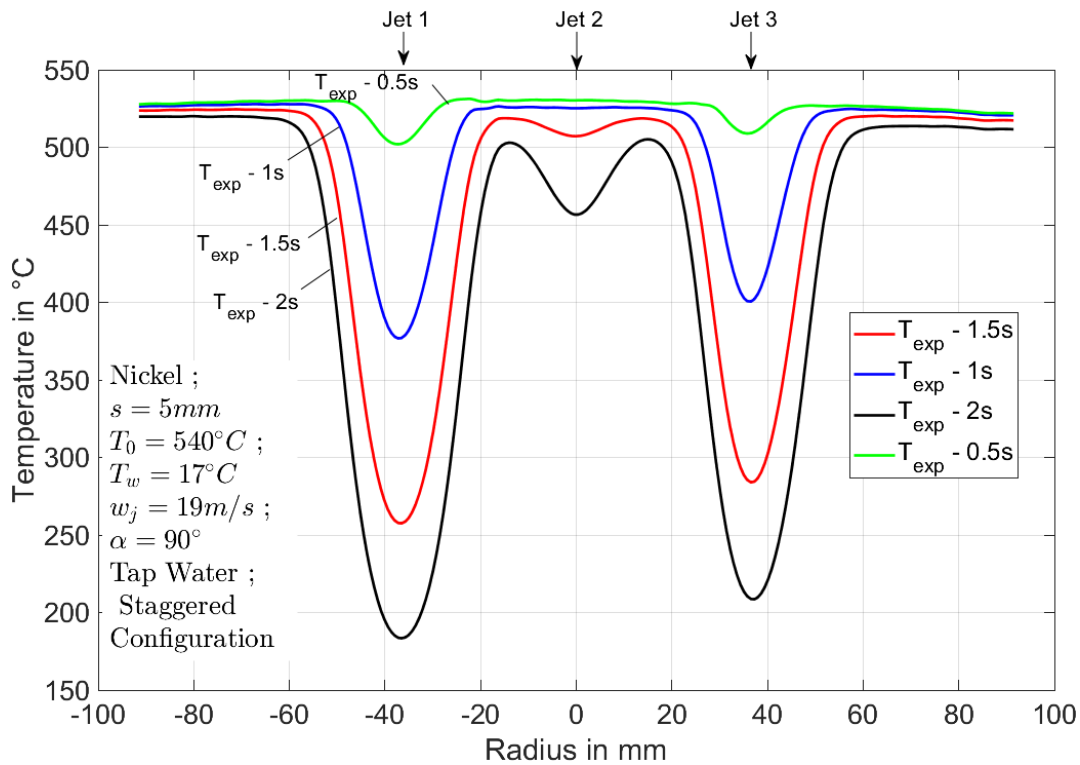


Figure 6.59: Surface measured temperatures for different time periods

**Fig. 6.59** and **Fig. 6.60** discuss the surface quenched side heat fluxes and the measured surface temperatures for different quench times of 0.5, 1, 1.5, and 2s in the centre vertical
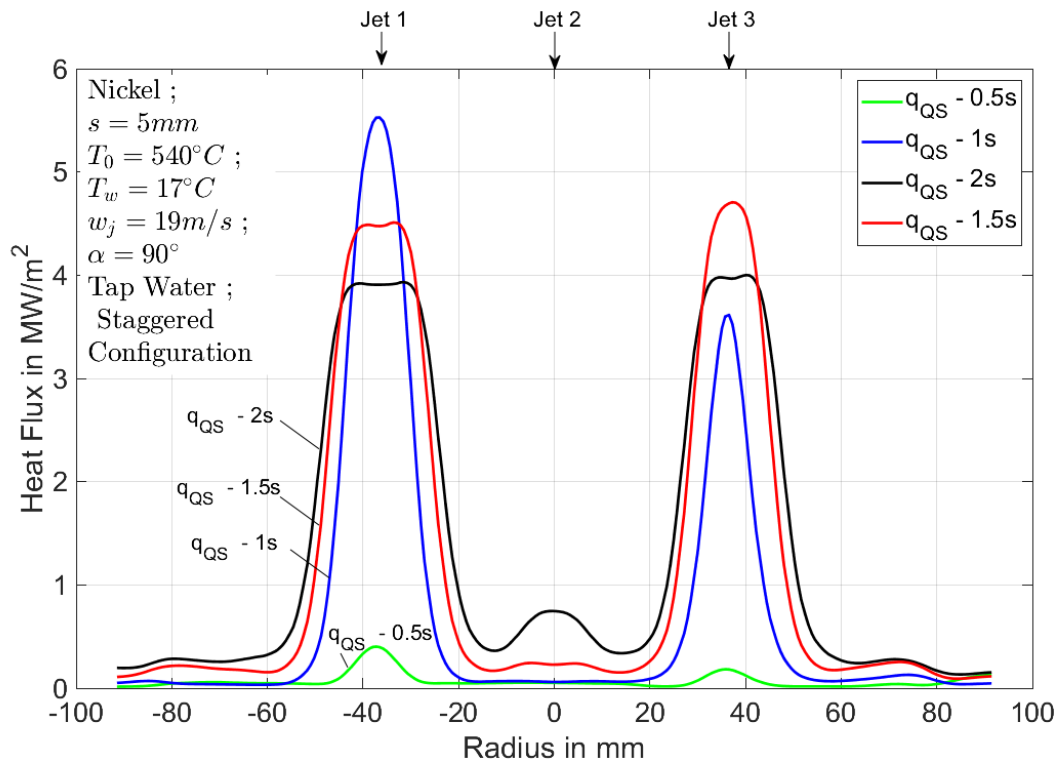
Figure 6.60: Quenched side surface heat fluxes for different time periods

line exactly at plate centre. The measured surface temperature indicates only two peak drop position, since in case of staggered configuration the nozzle is replaced with one extra nozzle and shifts apart. Although the temperature drop clearly indicate the intense cooling within the time span of 2s temperature from 500 $°C$ decreases to nearly 200 $°C$. With such drastic drop in the temperature are mainly caused with the intense heat transfer rate and the profiles discuss the inverse proportion of the heat fluxes with respect to the temperatures. The heat transfer intensity increase to 5.5 $MW/m^2$ at quench time of 1s and decreases gradually for higher quench time of 1.5s, 2s because the start temperature of the plate reduces and the available heat on the surface of the plate reduces to extract. However, the maximum heat flux intensity lies in the range of 4 $MW/m^2$ with reduction of only 2 $MW/m^2$ heat flux magnitude. **Fig. 6.61** shows the plot of heat fluxes with respect to the radius for the water jet impingement region ($V_2$ and $V_3$) and the water jet interaction region ($V_4$). The maximum heat flux at the respective nozzle position shows a higher magnitude and the peak heat flux gradually decreases to away from the nozzle position. The similar phenomena can be observed for the water jet interaction region ($V_4$) wherein the peak in the heat flux shows at the centre of the nozzle position as mentioned earlier, in case of staggered configuration at the interaction region i.e. between the first and second water jet column only one water jet exists. Therefore we observe the peak heat flux profiles exactly at nozzle position 0 mm. Interestingly, the heat flux in the dry region in case of the water jet interaction region, and the water impingement region are observed to be same at around 3 $MW/m^2$ along the spatial location of the plate. **Fig. 6.62** discuss the temperature for the water jet impingement region and the water jet interaction region with respect to the nozzle position. The temperature at the water jet impingement position of both water jet region and water interaction region increases because the heat flux at water jet impingement position promotes the stronger heat extraction. Whereas in the region away from the nozzle impingement lowers the departure nucleate boiling temperature because of lower surface temperature and consequently at the outer circumferential area the temperature raises since the surface remains to approximately at the start temperature. However, the re-wetting
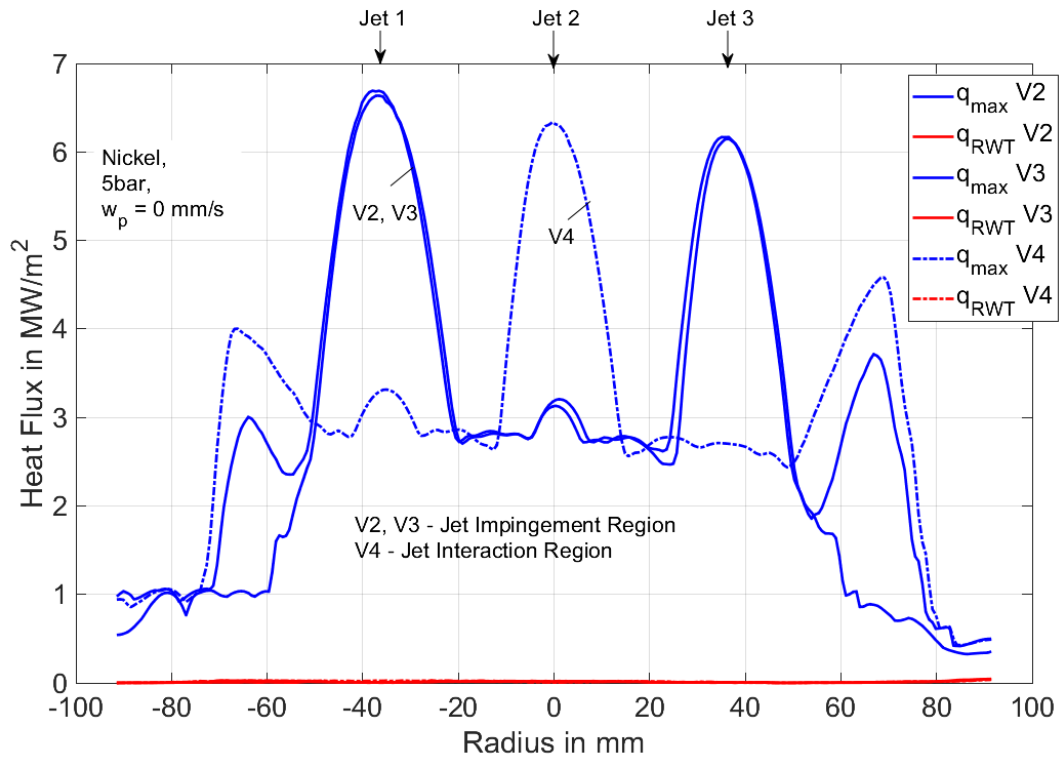
Figure 6.61: Comparison of heat fluxes with respect to the position of the nozzle for water jet impingement region and water jet interaction region
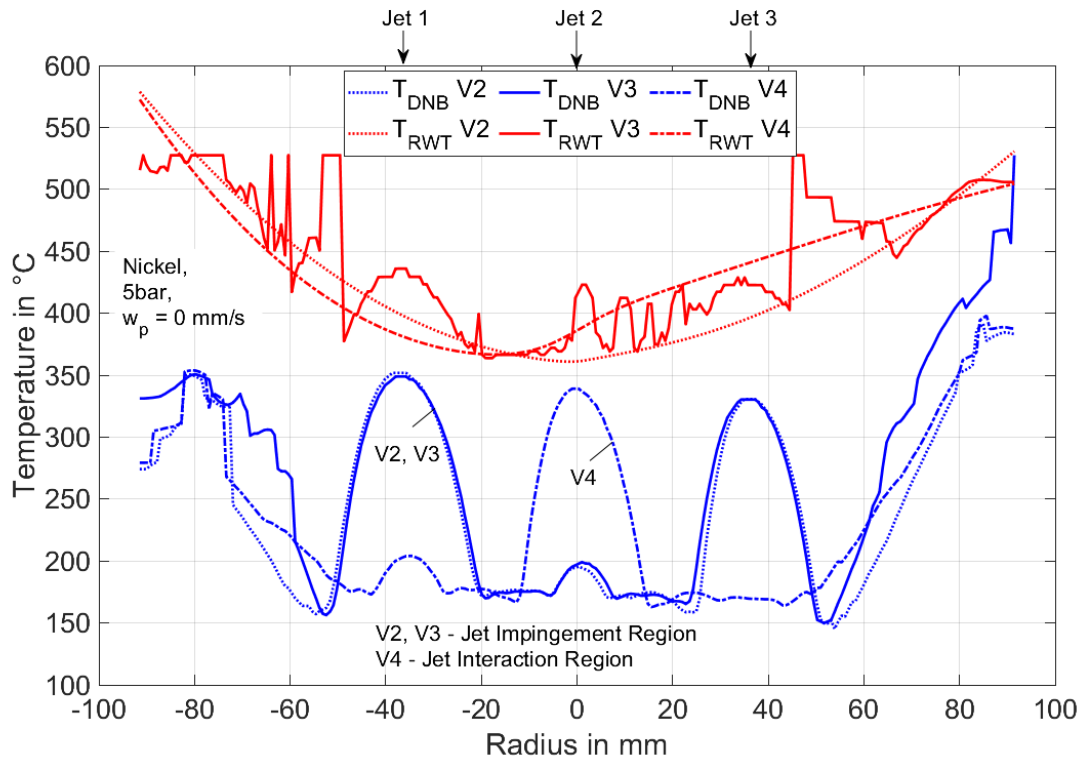


Figure 6.62: Comparison of temperature with respect to the position of the nozzle for water jet impingement region and water jet interaction region

temperature shown to be insignificant to the water jet impingement position even though the lower temperature can be observed in the water impingement region compared to the circumferential region.

### 6.3.1 Influence of Initial Temperature of the Material
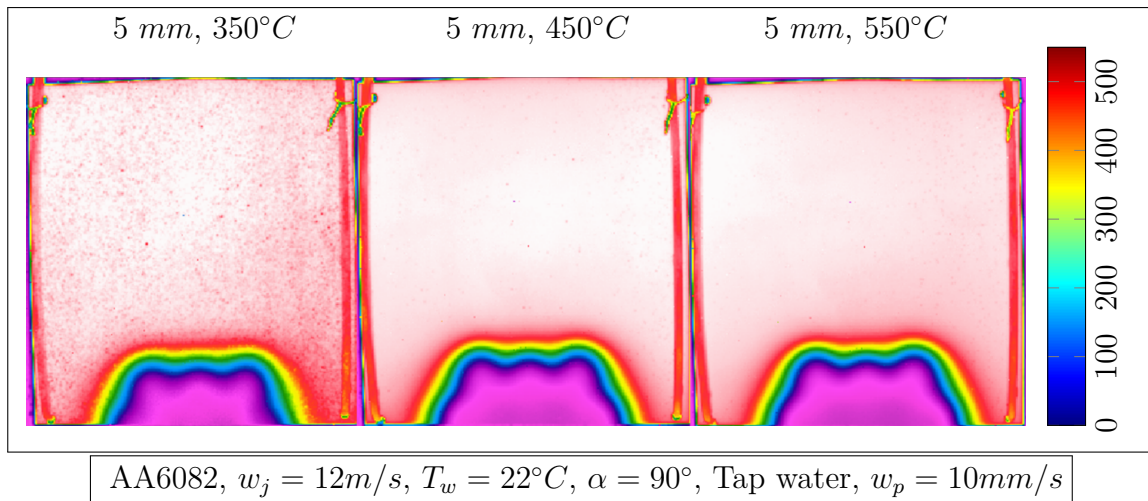


Figure 6.63: Infrared images for different initial temperature of the plate at quasi-steady state condition for 5 mm thick plate

**Fig. 6.63** shows the infrared thermal images for different initial temperature of the plate thickness 5 $mm$ at quasi-steady state condition. The temperature distribution seems to be uniformly distributed in spatial direction across width and length direction. The higher plate temperature leads to higher internal energy of the body, which decelerates the heat extraction from the surface of the plate. The local temperature profiles should reveal the more information about the cooling behaviour more accurately.
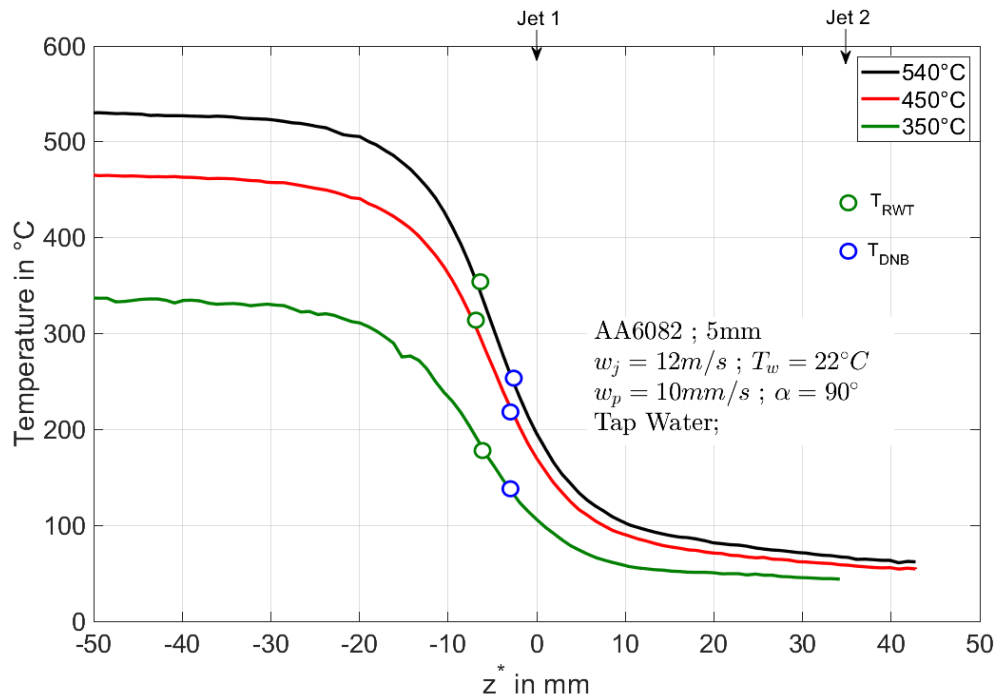


Figure 6.64: Surface temperature for different initial temperature of the plate at quasi-steady state condition for 5 mm thick plate

**Fig. 6.64** shows the temperature profiles for 5 $mm$ thick plate for longitudinal direction at the centre of the staggered configuration. The temperature profiles shown in Figure 5 also shows the influence of different initial temperature on the cooling process. For start

temperature of 350 °$C$, the cooling is stronger as the plate temperature exists already in the transition boiling, which makes the cooling process faster. Whereas for plate start temperatures 450°$C$ and 540°$C$, the temperature drop at the jet impingement point becomes almost same. The width of the pre-cooling or the advection is less significant in case of higher plate temperatures i.e., 450°$C$ and 540°$C$. In contrast, for lower plate temperature the width of pre-cooling region increases. Off course, the temperature above the water impingement region and below the water impingement or nozzle position the temperature of the plate is higher. The end temperature of the plate becomes higher because of strong internal conduction of the plate.
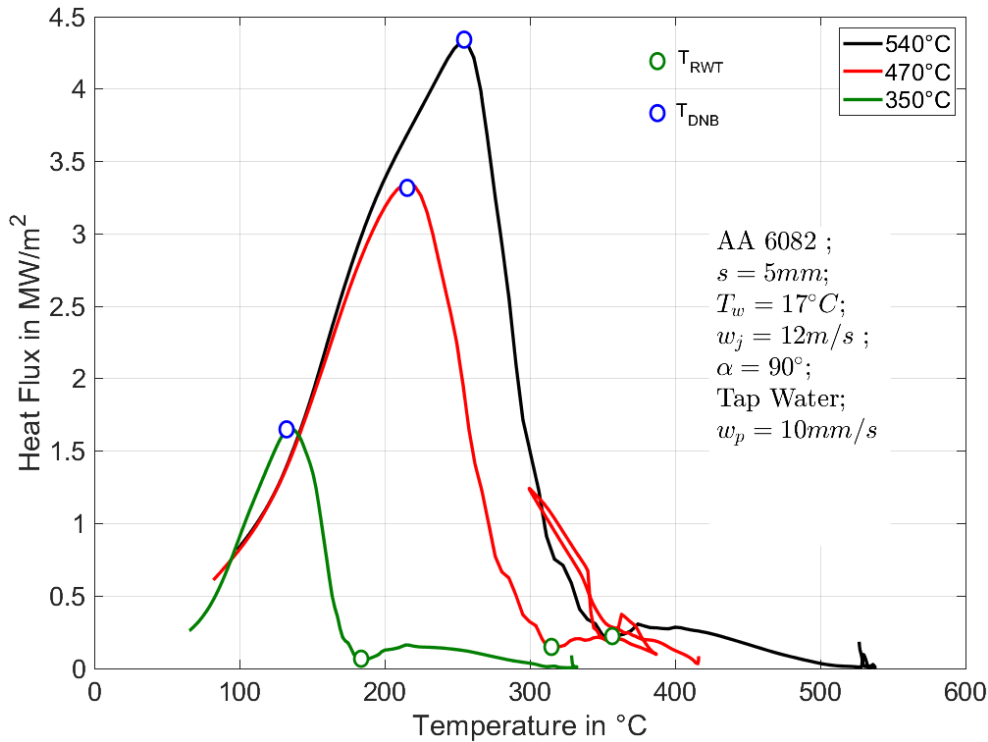


Figure 6.65: Boiling curve for the different initial temperature of the plate at quasi-steady state condition for 5 mm thick plate

The boiling curves for the different initial temperature of the plate for 5 $mm$ thick plate at quasi-steady state condition are shown in the **Fig. 6.65**. As we observe the heat flux distribution for different start temperature of the plate, heat flux gradually increases from the maximum heat flux of 1.6 $MW/m^2$ at 350 °$C$, 3.4 $MW/m^2$ at 470°$C$, 4.4 $MW/m^2$ at 540°$C$ start temperatures respectively. In similar way, the departure nucleate boiling temperature increases from 125°$C$ at 350°$C$, 220°$C$ at 470°$C$, 250°$C$ at 540°$C$ start temperature of the plate. Correspondingly, the thermal energy of the plate affects the temperature of the re-wetting to shifts to higher values and for plate temperature of 350°$C$ it is 180°$C$, for 470°$C$ start temperature is 310°$C$, for 540°$C$ start temperature is 350°$C$ respectively. The increase in the higher heat fluxes and higher departure nucleate boiling and re-wetting temperatures are shift in the position of these values towards the nozzle positions.

## 6.3.2 Influence of Plate Velocity
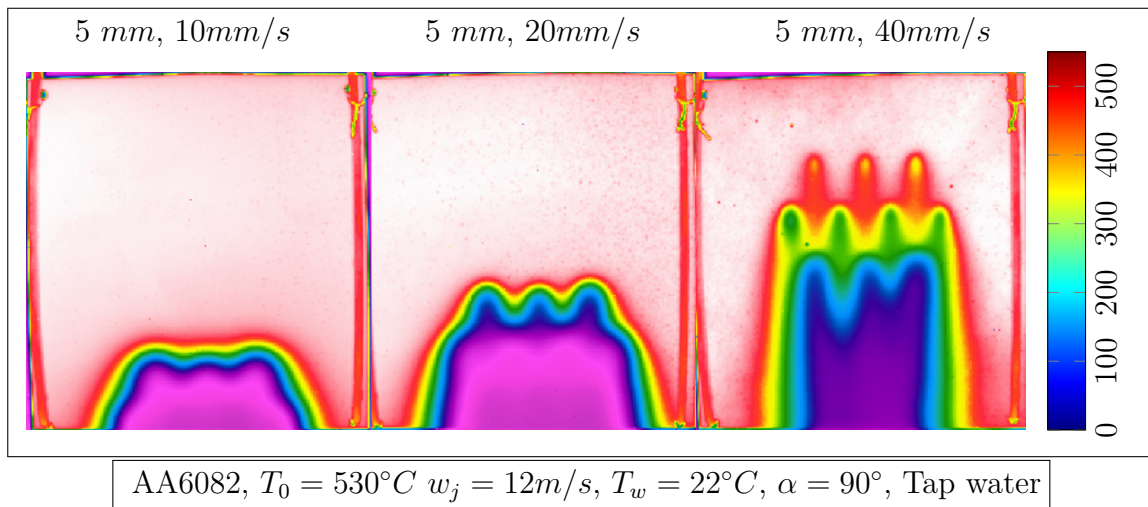
**For 5 mm Thick Plate**



Figure 6.66: Infrared images for different plate velocity at quasi-steady state condition for 5 mm thick plate

The thermal infrared images for different plate velocities at quasi-steady state condition for 5 *mm* thick plate are shown in **Fig. 6.66**. The plate velocity strongly affects the spatial temperature distribution in both width and length direction of the plate. For lower plate velocity 10 *mm/s*, the temperature distribution across the surface of the plate seems to be uniform. Whereas, for higher plate velocities i.e., 20 *mm/s* and 40 *mm/s* the temperature is uneven and non-uniform cooling leads to increase the larger temperature gradient across the surface of the plate. For plate velocity 20 *mm/s*, the temperature below the first row of the full jet staggered configuration of the nozzle is uniform, whereas above the nozzle position the conduction from the top surface leads to affect the cooling and wavy shape of temperature distribution can be observed. The extra nozzle in the second row of the staggered configurations strongly affects the internal conduction and lowers the plate temperature promoting more uniform cooling in the lower part of the plate. For plate speed of 40 *mm/s*, the temperature in the third row of nozzle configuration promotes strong cooling as the fluid flows from the first and second row of the jet due to effect of gravity and at this location temperature of the incoming hot part of the solid is low, since the solid should pass through the first and second row of jets before reaching to the third of row jets. While, the second row seems to be at higher temperature compared to third row of jets because of strong internal conduction from the other parts of the solid and in this region the plate is at transition region. Physically, the temperature of the plate at the first row of the jets should be at higher start temperatures, because of the new incoming hot solid at initial temperature of the plate. To further understand the heat transfer distribution and local phenomena occurring at various locations of the plate, temperature profiles at the centre of the plate is considered for the analysis of heat extraction in this region.

Figure 6.67: Surface temperature for different plate velocity at quasi-steady state condition for 5 mm thick plate

The surface temperature distribution for different plate velocities for 5 mm thick plate at quasi-steady state condition are shown in **Fig. 6.67**. Temperature distribution for plate velocity of 10 $mm/s$ cools faster compared to plate velocity of 20 $mm/s$ and 40 $mm/s$ respectively. As per the physical understanding, the faster cooling in case of the plate velocity 10 $mm/s$ compared to 20 $mm/s$ agree to the real temperature profiles. From the temperature profiles, we observe an increase in the width of the pre-cooling region for lower plate velocities in comparison to the higher plate velocity 20 $mm/s$. Contradictorily, for plate velocity 40 $mm/s$ the pre-cooling is strongly influenced and the plate still lies in the transition boiling range. The reheating or the internal conduction is strongly seen in case of 40 $mm/s$ while this effect is less significant for 20 $mm/s$ and 10 $mm/s$ plate velocities. At plate velocity 40 $mm/s$, the cooling and reheating effect is symmetric in the water jet impingement position. Therefore, the larger temperature gradient can be observed along the longitudinal direction of the plate which spans around 80 $mm$ across the water jet impingement location.
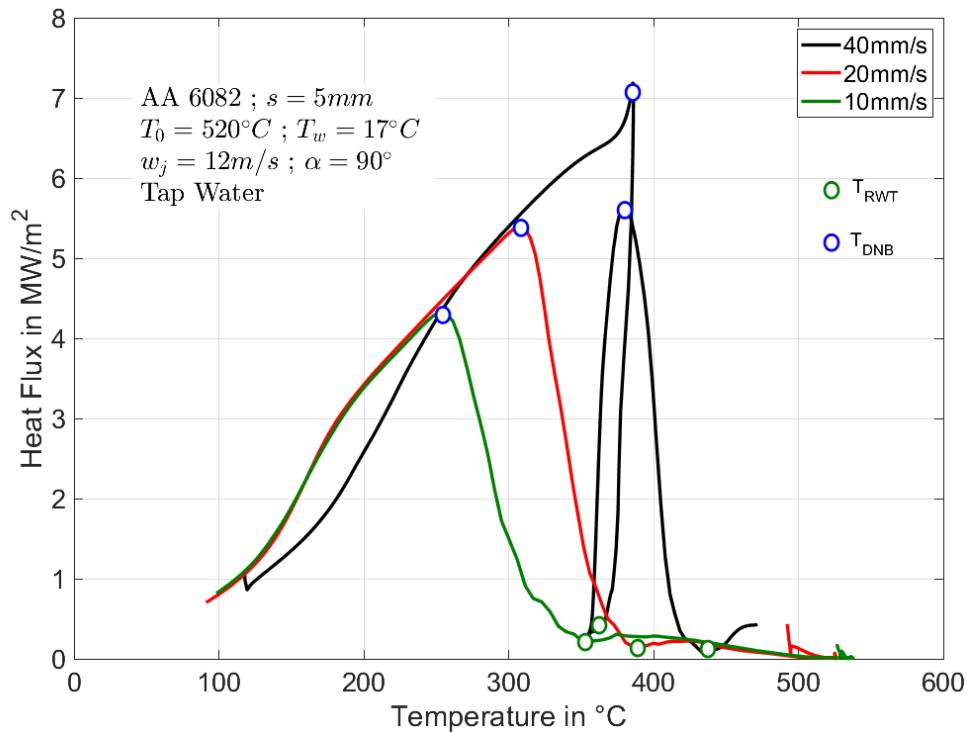
Figure 6.68: Boiling curve and characteristic curve for different plate velocity at quasi-steady state condition for 5mm thick plate

Typical boiling curve for various plate velocities are presented in the **Fig. 6.68** in case of 5 mm thick plate at quasi-steady state condition. For higher plate velocities, the heat transfer is more significant and the maximum heat flux gradually increases from 4.2 $mw/m^2$, 5.4 $MW/m^2$ and 7 $MW/m^2$ for 10 $mm/s$, 20 $mm/s$, and 40 $mm/s$ plate velocities respectively. Similarly, the temperature of the departure nucleates boiling increases form 250 $°C$, 300$°C$ and 380$°C$ for 10 $mm/s$, 20 $mm/s$ and 40 $mm/s$ respectively. Whereas, the temperature of the re-wetting and heat flux lies in the range of 350$°C$ and 0.2 $MW/m^2$. The maximum heat flux increases mainly due to the shift of the corresponding heat flux and temperatures towards the nozzle position. For 40 $mm/s$ plate velocity, there exists two peaks which represents the first two rows of the jets. Starting from the higher temperatures, we can see the first peak at 380$°C$ with 5.7 $MW/m^2$ which corresponds to the jet position 1 and following comes the second jet position at 380$°C$ with 7 $MW/m^2$. After the first peak, the heat flux decreases gradually and in the same way the heat flux starts to increase due to addition of heat from the conduction. We can clearly observe a symmetric cooling and heating behaviour at the first peak of the jet position.

**For 10 mm Thick Plate**



AA6082, $T_0 = 530°C$ $w_j = 12m/s$, $T_w = 22°C$, $\alpha = 90°$, Tap water

Figure 6.69: Surface temperature for different plate velocities at quasi-steady state condition for 10 mm thick plate



Figure 6.70: Surface temperature for different plate velocities at quasi-steady state condition for 10 mm thick plate

**Fig. 6.69** shows the infrared images for different plate velocities at quasi-steady state condition of 10 $mm$ thick plate. The thermal images here depict for plate velocity 10 $mm/s$ and plate velocity 20 $mm/s$, the temperature distribution at the first row of the jet position seems to provide non-uniform thermal gradient. For plate velocity 10 $mm/s$,

the temperature seems to show less fluctuations in the temperature distribution across the surface in comparison to 20 $mm/s$ plate velocity. For plate velocity 40 $mm/s$, the temperature distribution at the third row of the nozzle position shows a more uniform compared to the second and third row of water jets. The local temperature distribution across the surface of the plate is strongly influence with higher plate velocity as well as the plate thickness. Hence, for understanding the heat transfer during this kind of quenching process, temperature at the centre of the plate is considered for analysis of heat transfer. Surface temperature distribution along the length of the plate at the centre location of the plate is presented in **Fig. 6.70** for different plate velocities for 10 mm thick plate. The local temperature profiles shown in Fig. 6.70. Plate velocity at 10 $mm/s$ shows a more uniform cooling of the plate in comparison to the 20 $mm/s$ plate velocity. As we observed from the local temperature profiles that for 10 $mm/s$ plate velocity, the temperature drop takes place in the water impingement position and the effect of pre-cooling is strong. Whereas for plate velocity of 20 $mm/s$, the influence of the first row of jet is clearly seen at the plate surface temperature of $400°C$ and significant drop in temperature takes place below this position. The non-linear distribution of the temperatures takes place across water jet positions of around 80 $mm$. Hence, the mechanical behaviour of the metal plate is strongly influence with the larger temperature gradient across the plate locations.
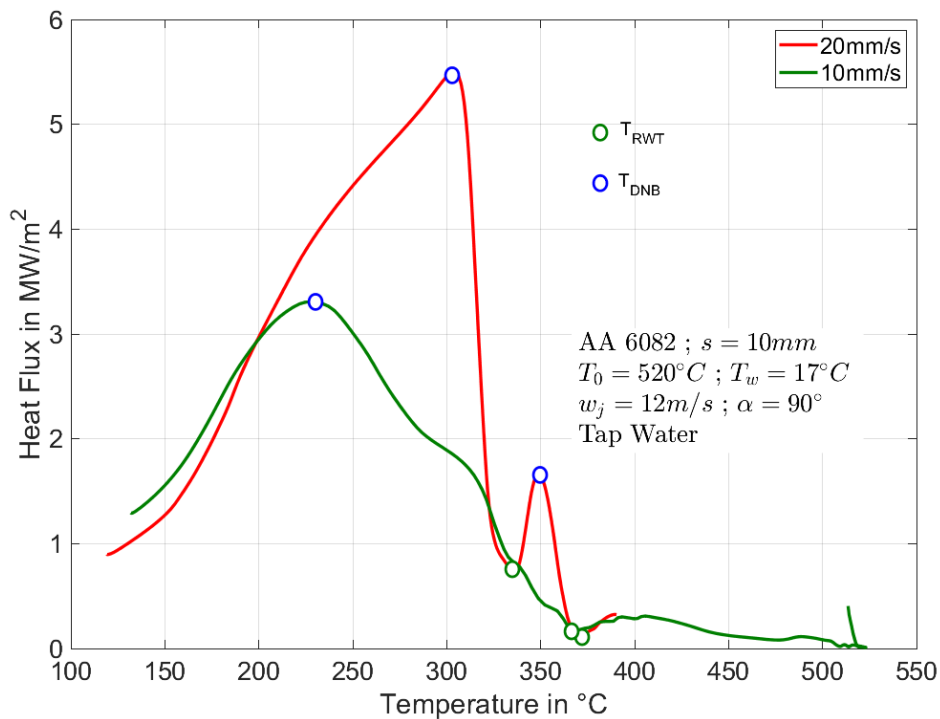


Figure 6.71: Boiling curve and characteristic curve for different plate velocities at quasi-steady state condition for 10 mm thick plate

**Fig. 6.71** shows the boiling curves for different plate velocities for 10 $mm$ thick plate at quasi-steady state condition. The typical heat flux profiles can be seen for two different plate velocities i.e., 10 $mm/s$ and 20 $mm/s$. Increase in the maximum heat flux from 3.2 $MW/m^2$ to 5.5 $MW/m^2$ takes place for 10 $mm/s$ and 20 $mm/s$ plate velocity with corresponding temperature i.e., departure nucleate boiling is around $220°C$ and $300°C$ respectively. Whereas, the re-wetting temperature and the corresponding minimum heat flux are $370°C$ and 0.2 $MW/m^2$ respectively. For plate velocity 20 $mm/s$, the influence of the first water jet can be seen at temperature of around $350°C$ of 1.7 $Mw/m^2$ maximum heat flux values.

### 6.3.3   Influence of Water Jet Velocity
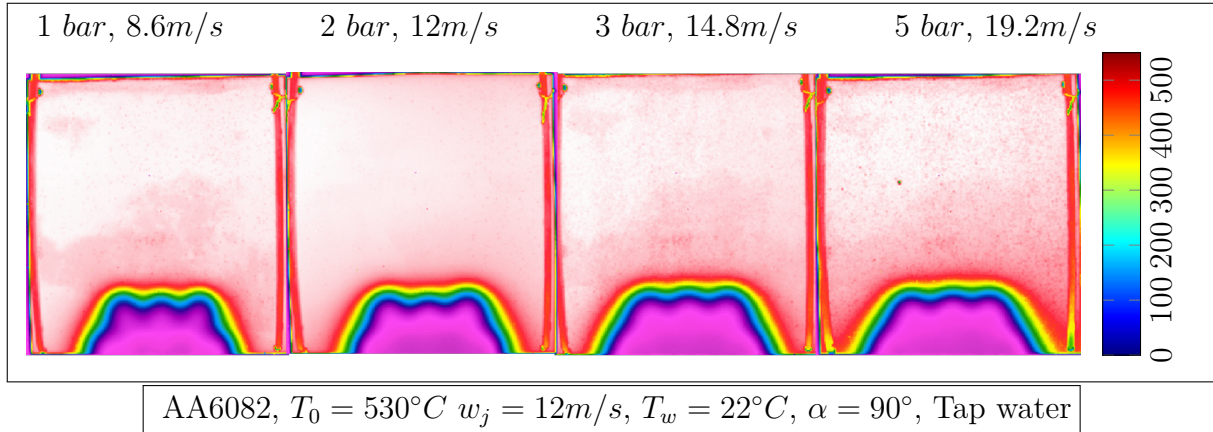
**For 5 mm Thick Plate**



Figure 6.72: Infrared images for different water jet velocities at quasi-steady state condition for 5 mm thick plate

The influence of water jet velocity on the 5 *mm* thick plate are depicted in the infrared images as in **Fig. 6.72**. The water pressures ranging from 1 bar to 5 bar clearly shows no significant difference in the spatial temperature distribution of the plate. The temperature distribution in the width direction is stronger for higher water pressures compared to lower water pressures density. The significant effect of water pressure on the velocity of the wetting front can be seen in the thermal images as the temperature distribution spreads more towards the edges of the plate. The local temperature profiles at the centre location of the plate are considered for further understanding of the heat transfer distribution.
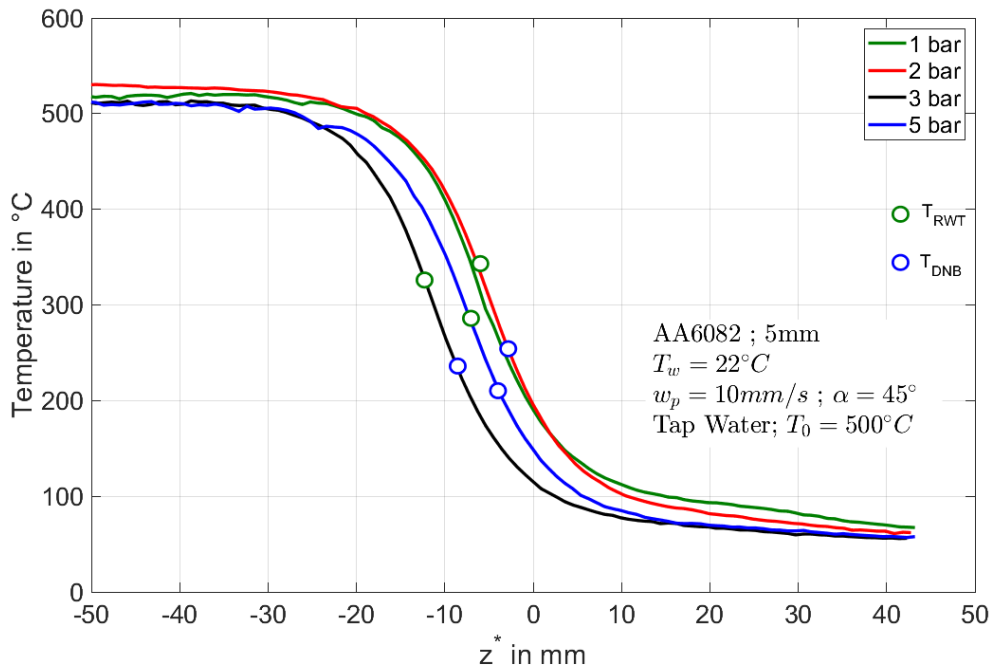


Figure 6.73: Surface temperature for different water jet velocities at quasi-steady state condition for 5 mm thick plate

**Fig. 6.73** shows the surface temperature distribution for different water jet pressures on the 5 *mm* thick plate. For higher water pressure densities, the temperature distribution

or drop shows a similar tendency. More accurately, for water pressure 1 bar and 2 bar no significant difference can be found. Whereas, for water pressure of 3 bar cools faster compared to 1 and 2 bare water pressures. With further increase in the water pressure to 5 bar, the water jet bounces due to complex fluid flow and motion of the fluid becomes more turbulent. The heat flux profiles should provide more accurate analysis of the heat transfer mechanism for different water pressures.
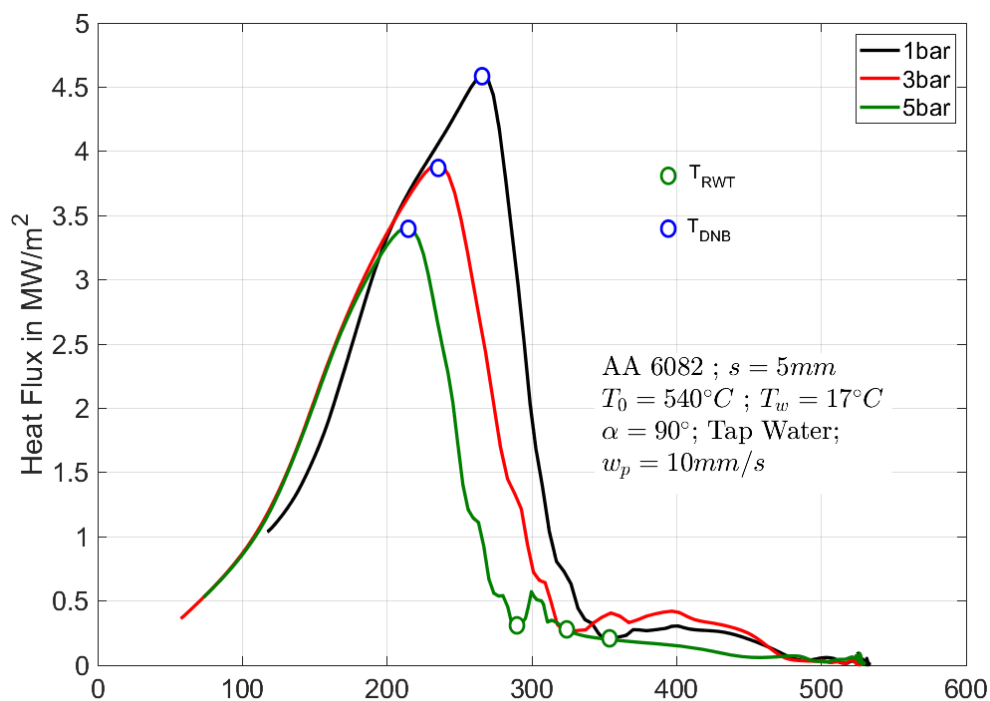


Figure 6.74: Boiling curve for different water jet velocities at quasi-steady state condition for 5 mm thick plate

Typical characteristic boiling curve for different water jet velocities of 5 mm thick plate at quasi-steady state condition are presented in the **Fig. 6.74**. For initial at 1 bar water pressure, the heat flux profiles show a higher value which corresponds to 4.6 $MW/m^2$ with $270°C$ and with further increase in the water jet pressure, the heat extraction lowers due to the bounce off phenomena with higher turbulent fluid flow. The gradual decrease of the maximum heat flux values from 4.6 $MW/m^2$, 4.4 $MW/m^2$, 3.8 $MW/m^2$, 3.4 $MW/m^2$ for water pressures of 1 bar, 2 bar, 3 bar and 5 bar respectively. Correspondingly, the re-wetting temperature and minimum heat flux are between $300°C$ to $350°C$ and about 0.3 $MW/m^2$ respectively.
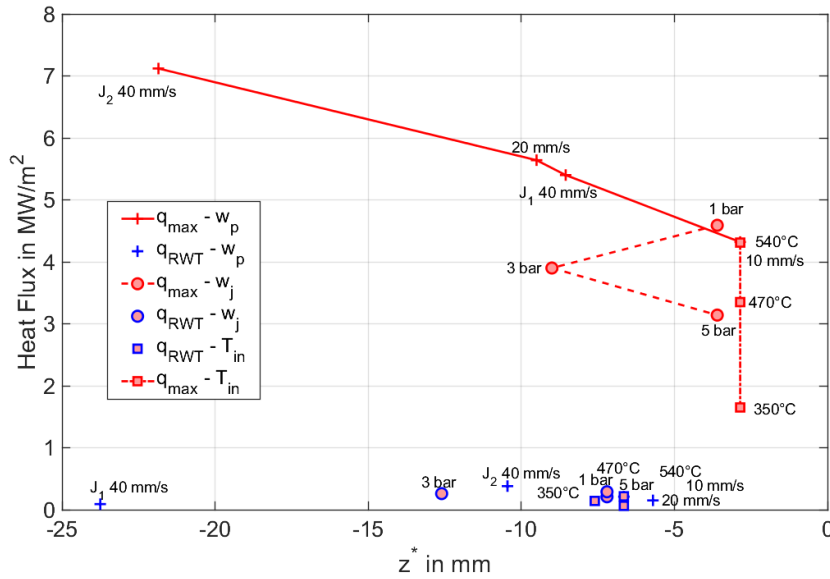
Figure 6.75: Comparison of the heat fluxes for different process parameters in case of AA6082 5 mm thickness

**Fig. 6.75** discuss the heat fluxes for different process parameters such as $w_p$, $w_j$, $T_{in}$ with respect to the nozzle position. The heat flux values for all the process parameters lies above the nozzle position because of the strong conduction from the dry region favours the advanced cooling. The wetting front should climb in the upward direction because of the advanced cooling in the quenching process. The increase in the start temperature increases the heat transfer intensity while the spatial position of the heat flux remain nearly at the same location. In other parameters the shift in the peak of the heat flux to larger position can be observed above 25 mm from the nozzle position. In case of the re-wetting condition, the heat flux remain nearly constant around 0.5 $MW/m^2$.
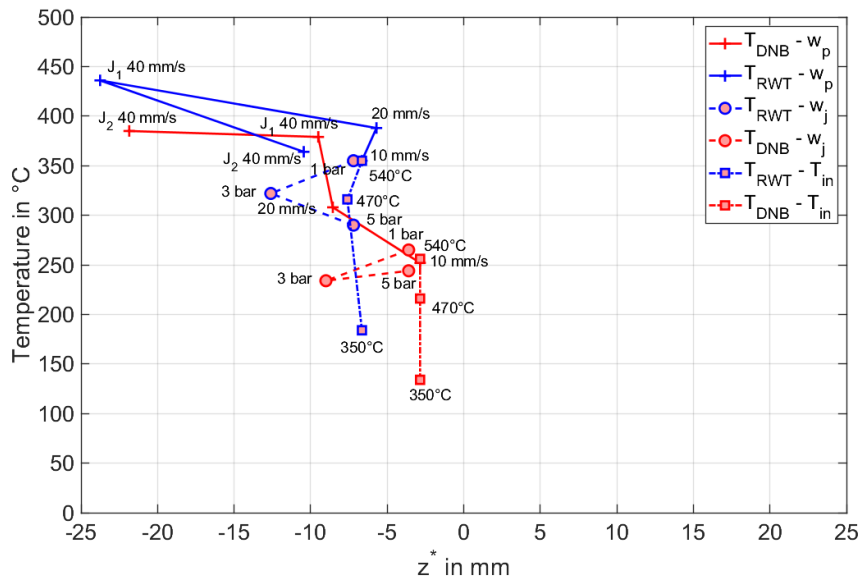


Figure 6.76: Comparison of the temperature for different process parameters in case of AA6082 5 mm thickness

**Fig. 6.76** temperature for the different process parameters lies above the nozzle position and pre-cooling is inevitable for the cooling process. The departure nucleate boiling

temperature lies in the range of 200 °C ± 50 °C while the spatial locations remains in the range of 10 mm above the nozzle impingement position. Surprisingly, the re-wetting temperature also lies within the range of departure nucleate boiling while the temperature shown to be higher than the departure nucleate boiling temperature.

## 6.4 Comparison of Array of Jets and Single Full Jet Nozzle
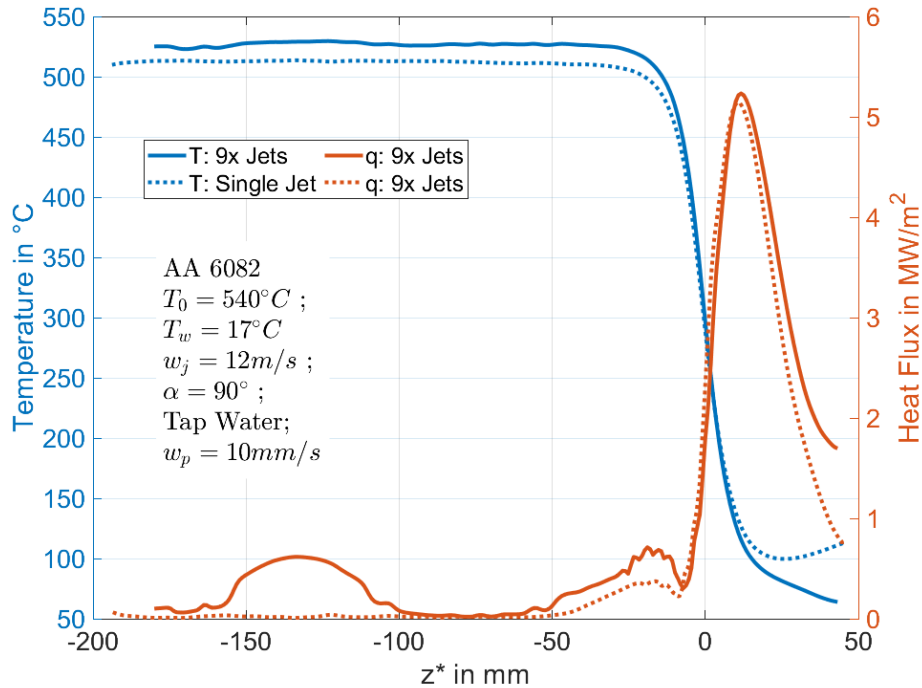


Figure 6.77: Comparison of the surface temperatures and surface heat fluxes for vertical measurement line at the water impingement region for quasi-steady state condition

**Fig. 6.77** depicts the comparison of the single full jet nozzle and the array of jets at quasi-steady state condition for vertical measurement line. The superimposed temperature profiles matches exactly similar at the first row of nozzle position in case of array of jets and at stagnation point for single full jet nozzle. We also observe the similar heat transfer behavior for both the kind of quenching mechanism. We can conclude that the effect of second and third nozzle relatively no influence on the cooling for this set of experimental condition in the vertical local position.
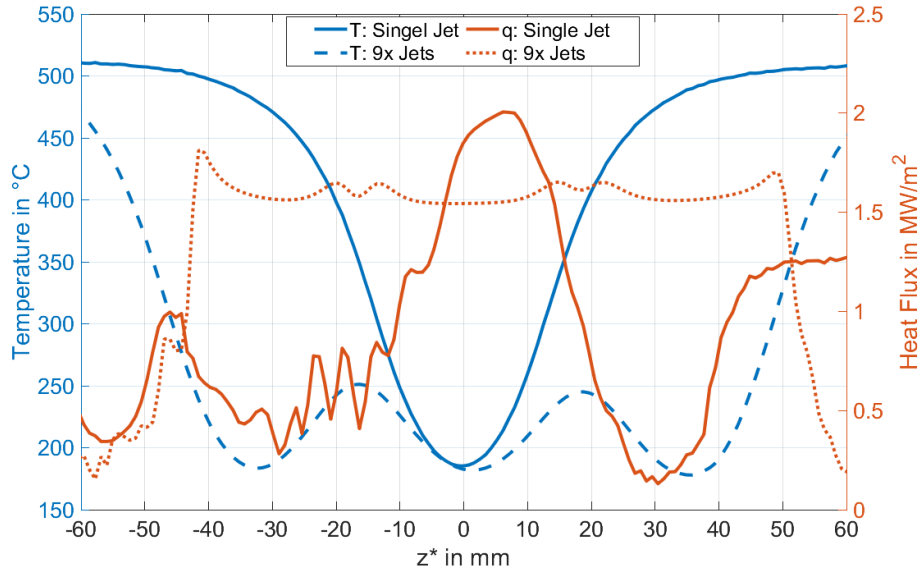
Figure 6.78: Comparison of the temperature for different process parameters in case of AA6082 5 mm thickness

**Fig. 6.78** discuss the heat transfer and surface temperature profiles for the horizontal position for single full jet nozzle and array of jets configuration at quasi-steady state condition. The surface temperature profiles at the measured side are relatively similar at the centre of the plate for single full jet nozzle and the array of water jet i.e., at $z^* = 0$ mm. Relatively for the other jet location surface temperature decreases at the water jet position and the temperature remains relatively higher at water interaction region. In case of surface heat fluxes, the magnitude of heat transfer is almost same in array of jets and single full jet nozzle and varies in the range of 0.25 $MW/m^2$.

## 6.5   Application to Industrial Process

From the discussion in **Chapter 4.6** and **Chapter 6.1**, we strongly observe the influence of the water jet location on the local heat transfer mechanism. In order to cool the plate homogeneously from high temperature to relatively lower temperature below 100 $°C$. The position of the water jet plays a major role in the local heat transfer mechanism as seen in Fig. 6.17 - 6.19 for higher plate velocity, the larger distance between the adjacent jet leads to inhomogeneous cooling and for better cooling the position of the jets should be reduced to enhance the higher rate of cooling. Henceforth, the proper selection of the boiling curve for each set of experimental conditions can be easily chosen from the present analysis and can be implemented for industrial applications. The results reported in the form of boiling curves are effectively used as thermal boundary conditions for the solution of the 3-dimensional heat conduction problem, which can be effectively solved using any commercial software available. Therefore, the reported results can be further utilized to study the local thermal stresses and deformation during quenching process in order to better optimize the industrial process.

## 6.6   Conclusion: Array of Jets

In this chapter, the quenching process with array of 9 full jet and 10 full jet nozzle with inline and staggered configuration was investigated experimentally and the two-dimensional and three-dimensional inverse solution were discussed. At first, the influence of the fixed plate

on the heat extraction from the plate is investigated. The relatively significant temperature gradient exists between the water impingement region and the water interaction region of approximately around 50 °$C$ at the start of the quenching process. Within the quench time of 2 to 3s, surface temperature reaches below 100 °$C$. Also, the influence of the water jets on the heat removal can be observed in a radial manner and maximum heat transfer reduces away from the jet impingement position. However, the heat flux profiles attains homogeneous within the short time of quenching and further lowers the temperature to attain the same. Secondly, the effect of the moving plate on the heat transfer is investigated with the variation of different influencing parameters such as $T_{in}$, $w_j$, $w_p$, and $s$ for inline and staggered configuration are discussed below:

1. The plate thickness offers a stronger resistance to the temperature drop at the nozzle location and the higher temperature values are attained with larger temperature gradient. Henceforth, the shift of the DNB temperature takes place further down the plate.

2. The initial temperature of the plate reduces the width of the pre-cooling region, and the consequently the position of the DNB temperature moves towards the jet impingement position with the increase of the maximum heat flux significantly. For the higher initial temperature of the plate, the larger temperature gradient can be observed in the jet impingement region and for lower start temperature temperature gradient reduces. Although, the spatial temperature gradient exits above the nozzle position.

3. The larger the plate velocity, the heat flux attains higher until 20 mm/s and then decreases for 40 mm/s because of insufficient cooling of the plate. However, the position of the DNB temperature strongly promotes the higher rate of heat transfer in the nozzle impingement position. For the higher plate velocities, the effect of the adjacent nozzles can be clearly felt. Henceforth, the local heat transfer affects strongly.

4. The higher water jet velocities shows insignificant to the rate of heat transfer and the DNB, RWT shows relatively less effect.

# Chapter 7

# Thermal Stresses in Quenching of Hot Moving Plates

## 7.1 Introduction

Thermal stresses during quenching process is inevitable and the reduction of the residual stresses is the main goal of any quenching process in practice. In this chapter, the thermal stresses are determined using the boundary conditions as obtained from the inverse algorithm as discussed earlier in the chapter 3 - 7. The heat flux acts the main cause for the generation of the stresses and thermal deformation of the material. For this, we adopt the two-dimensional thermo-mechanical model and the three-dimensional thermo-mechanical model to obtain the solution of the thermal stresses and the deformation.

Numerical modelling of quenching process is a powerful tool for design, optimization, and understanding the evolution of microstructure and internal stresses which are experimentally complex to acquire. This section provides a comprehensive review of those studies and to present the state of the art and the overview of some literature work to model through multi-physical approach. Heat treatment of metals is essential part of the production of most mechanical products from the raw material up to the final product. The quenching process involves the direct impingement of the water or quench-ant on the material and heat treatment happens through conduction though the bulk of the material. Mostly the final properties of the product take place largely during this stage, which renders the quenching as the most critical stage of production. Although the quench hardening is the vital part of production and consequently the cause of rejected components, production losses, and the components that need to be reworked. The cause of the final product are mainly the distortion, residual stresses, desired distribution of microstructure and properties such as hardness were for a long time considered the most influencing parameter in the quenching of metals.

## 7.2 Literature Review

The review of the literature on thermo-mechanical modelling of quenching process were performed to understand the underlying phenomenon. The research papers provide a vast insight into modelling the appropriate thermal boundary conditions and many mathematical models were solved to understand the internal stress evolution, phase transformations, distortion. Whereas, the present research work only focusses on modelling the residual/thermal stresses and distortion during quenching process.

Y. KaymakKayamak (2007), introduced a themo-mecahnical model and its finite element implementations for simulating the transient fields of temperature, stress, strain, micro structure, displacement during heat treatment process. Many simulations are carried out in

order to investigate the optimum cooling strategies for avoiding the distortion and reducing stresses for various geometries such as long profiles, disks, shafts for various metals. The results shown that by reducing the cooling at thin parts and edges as well as increasing the cooling at thicker parts, the distortion and stresses can be reduced concurrently.

A.K. NallathambiNallathambi et al. (2009), presented a mathematical formulations of the quenching process, the numerical technique and the optimization of the cooling strategies for the selected geometries. The localized heat transfer coefficient during the quenching process plays a crucial role for the evolution of the distortion and residual stresses. It is shown that the with the with an enhanced quenching at the mass lumped regions and with a reduced quenching at the edges and corners, stresses and distortion can be minimized simultaneously. The examples are given for different kinds of metals and geometries such as long profiles (L and T) and disk with a hole.

A.K. NallathambiNallathambi and Specht (2009a), investigated the influence of thermal, metallurgical and mechanical properties on the final distortion and residual stresses during the metal quenching process. The analysis shows that the change in none of the thermal properties simultaneously reduce the distortion and residual stresses. It is found from the investigation that reduced metallurgical properties, yield stress, and bulk modulus simultaneously lower the distortion and residual stresses for an equal cooling.

R. Pietzsch and M. BrzozaPietzsch et al. (2007), introduced a complex thermo-mechanical model for simulating transient field of the temperature, micro structure, stress, strain, and displacement during the quenching of the steel profiles. The model serves as a basis for optimizing the cooling condition for reducing residual stress and distortion. They also suggested the distortion can be reduced by intensified cooling of the mass lumped parts of the cross-section.

M. Brzoza and E.SpechtBrzoza et al. (2006), therm.mechanical model for quenching of the cutting discs and shafts is introduced. According to optimization simulations the shafts were quenched with certain heat transfer coefficient distribution. The larger diameter parts of the shaft were more intensively quenched so that the hardness profiles were equalized and the residual stresses at the edge were significantly reduced.

S.R. Yazdi Yazdi et al. (1998), the quenching process of aluminum alloys is modelled using Finite Element Method. They considered two different boundary conditions in the thermal problem, one with heat transfer coefficients obtained by resolution of the heat conduction equation and the second being the measured temperature exactly at the surface is used as boundary conditions in the thermal problem. The influence of different quenching parameters on the level of residual stresses is studied. To validate the quench modeling, incremental hole drilling, neutron diffraction methods are used to measure the residual stress field in the studied parts.

X. Yang and J. ZhuYang et al. (2013), the quenching process of A357 aluminum alloy large complicated thin wall workpiece were investigated by Finite Element Method simulation on Abaqus software. Heat transfer coefficient were calculated by tradition method of inverse heat transfer. The maximum tensile and compressive residual stress of quenched large complicated thin wall workpiece decreases with increasing water temperature(80 degC), the maximum tensile and compressive residual stresses are much smaller than the values in the other temperatures.

Z. Zhang and W. Wang Zhang et al. (2012), the effect of cooling rate on residual stress, microstructure and mechanical properties of an Fe-6.5 Si alloy were investigated using various quenching medium. The results show the surface residual tensile stress increases and residual compressive stress decreases with the increase in the cooling rate. As the surface residual stress increases with the cooling rate, the average bending fracture deflection of the water and salt quenched are less than that of oil quenched alloy.

J. S. Robinson Robinson et al. (2012), considered two aluminum alloys 7010 and 7075 with

different quench sensitivity to determine if solute loss in the form of precipitation during quenching can significantly affect residual stress magnitudes. The distribution of stress were measured with neutron diffraction and X-ray diffraction were in close agreement.

Y.Liu and S. Qin Liu et al. (2017), implemented finite element method to predict the distribution of internal stress in quenched AISI 440 cylinder used Abaqus to solve coupled temperature, micro structure field and stress field. The comparison with the measured cooling curves were made. Then the micro structure distribution were determined by comparing the theoretical calculation with experiments.

Y.N. Li and Y.A.ZhangLi et al. (2016a), studied the effect of heat transfer coefficient on the quenching residual stresses in 7055 aluminum alloy. The influence of the heat transfer coefficients in different temperature regions on the quenching residual stresses were studied. The heat transfer coefficient in the range of 100-200 degC have a great influence on the residual stresses. The residual stresses decreases as the water temperature increases while increase as the water flow increases. The immersion quenching shows higher stress than that of the spray quenching process.

C. Simir Simir and Gür (2008), FEM based mathematical model capable of predicting temperature, evolution of phase and internal stress for complex 3D engineering components was developed. The results verified with XRD residual stress measurements of eccentrically drilled C60 steel cylinders. The model effectively predicted the trends in the distribution of the residual stress.

Y. Dong Dong et al. (2015), heat transfer calculation was coupled with the hyperbolic sine type constitutive model to simulate the residual stress during the quenching. They suggested the residual stress reduction can be achieved by decreasing the cooling rate during quenching.

Y. Nagasaka Nagasaka et al. (1993), coupled heat flow / phase transformation model and a thermo-elasto-plastic stress analysis model both based on the finite element method developed and applied to spray quenching of steel bars.

S. Bikass Bikass et al. (2012), the effect of non-uniform cooling in three direction was introduced with a focus on different cooling conditions in two zones across the width. Such non-uniformity due to different heat transfer coefficient or due to a difference in the thickness of a section.

Y.N.LiLi et al. (2016b), the effect of dimensional variation on the residual stress distribution was studied and discussed by using different models with different dimensions. The maximum tensile stress and compressive stress increase as the thickness increases.

Y.X.Zhang Zhang et al. (2016), lower cooling rates reduced tensile strength and yield strength due to decrease amount of free precipitates and reduced the residual stress with the reduction of plastic strain and the degree of inhomogeneous plastic deformation. In addition residual stress changed faster than the tensile properties with decreasing cooling rates.

W.J.J. VorsterVorster and Korsunsky (2008), spray and bath quenching were analyzed. Neutron diffraction experiments and finite element analyzes indicate that the use of water spray reduces the depth of permanent deformation in quenched compared to those treated in water bath. As it is the direct consequence of the re wetting condition.

Y. Zhang Zhang et al. (2017), thermal expansion coefficients, yield strength and elastic moduli played key role in determining the magnitude of plastic strains. The cooling rate at high temperature plays an important role in determining residual stresses only reducing the cooling rate at low temperature does not reduce residual stresses.

## 7.3 Thermal model

The temperature field is modelled by the Fourier's law of heat conduction equation. The thermal problem consists of finding the absolute temperature field Nallathambi (2010)

$$\rho C_p(\frac{\partial T}{\partial t}) = k\frac{\partial}{\partial x}(\frac{\partial T}{\partial x}) + k\frac{\partial}{\partial y}(\frac{\partial T}{\partial y}) \tag{7.1}$$

**Eq.** (7.1) represents the energy balance of the heat transfer in solid body.
Where,

$\rho$ is the density in $kg/m^3$
$C_p$ is the specific heat in $J/kgK$
$k$ is the thermal conductivity in $W/mk$
$\frac{\partial T}{\partial t}$ is the cooling rate in T/s
$Q$ is the contains heat sources other than viscous dissipation in $W/m^3$

## 7.4 Mechanical Model

The equilibrium equations for solid mechanics are given by Newton's second law. It is usually written using a spatial formulation in terms of the Cauchy stress tensor $\sigma$ :

$$\rho \, \frac{\partial u}{\partial t} = \nabla_x \sigma + f_v \tag{7.2}$$

Where,

$f_v$ is the body force per unit deformed volume
$\rho$ is the current mass density

**Eq.** (7.2), can be written for second Piola-Kirchoff stress tensor, S as

$$\rho_o\frac{\partial u}{\partial t} = \nabla_x(FS) + F_v \tag{7.3}$$

Where,

F is the deformation gradient

The implementation of the equation is not based on the equation of motion directly, but rather on the principle of virtual work.
Total deformation observed from experimental results are small. Therefore small deformation theory is employed and the total strain E is decomposed in to three components as thermal $\epsilon_{th}$, elastic $\epsilon_e$ and inelastic $\epsilon_{inel}$ strain tensors as follows Nallathambi (2010)

$$S = S_{ad} + C : \epsilon_d \tag{7.4}$$

$$\epsilon_{el} = \epsilon - \epsilon_{inel} \tag{7.5}$$

$$S_{ad} = S_o + S_{ext} + S_q \tag{7.6}$$

$$\epsilon = \epsilon_{th} + \epsilon_e \tag{7.7}$$

$$\epsilon = \frac{1}{2}[(\nabla \vec{u})^T + \nabla \vec{u}] \tag{7.8}$$

For the linear elastic material, Hooke's law relates the strain tensor to the elastic strain tensor:

$$\sigma = \sigma_{ex} + C : \epsilon_{el} = \sigma_{ex} + C : (\epsilon - \epsilon_{inel}) \tag{7.9}$$

Where,

$\sigma_{ex}$ is the extra stress distribution
C is the fourth order elasticity tensor
: denotes tensor product
$\epsilon$ is the total strain
$\epsilon_{el}$ is the elastic strain

The elastic strain energy density is

$$W_s = \frac{1}{2}\epsilon_{el} : (C : \epsilon_{el} + 2\sigma_o) \tag{7.10}$$

Because of the symmetry the strain tensor can be written as the following matrix.

**Thermal Expansion** is the internal strain caused by changes in temperature. The thermal strain depends on the coefficient of thermal expansion (CTE) $\alpha$, the temperature T, and the strain-free reference temperature $T_{ref}$:

$$\epsilon_{th} = \alpha(T - T_{ref}) \tag{7.11}$$

The reference temperature is taken as the initial temperature of the plate, where the thermal strain is zero.

**Viscoplastic strain** or creep strain is the inelastic time-dependent deformation that occurs when a material is subjected to stress typically much less than the yield stress at sufficiently high temperatures. The creep strain rate, in general depends on stress, temperature and time usually in a non-linear manner:

$$\dot{\epsilon_{cr}} = F_{cr}(\sigma, T, t) \tag{7.12}$$

The material model used in is explained in the further sections.

## 7.5 Thermal Boundary Conditions

The thermal boundary conditions are main loading to study thermal stresses and distortion in this study. For this purpose the boundary conditions are divide into three parts in the case of jet quenching which are as follows:

- Radiation Region

- Impingement Region

- Free Falling Region

and the boundary conditions for Jets and Spray quenching are as explained below:
The boundary conditions for the array of jets were moving with time or transient boundary conditions. The thermal loading is updated at every time step which is modelled in *MATLAB* code. The boundary conditions are divided as stated above. The transient boundary conditions implemented is radiation, impingement and free falling region. The boundary conditions are modified once the moving mold reaches the top region, the boundary conditions were modified to act only with impingement and free falling region as static plate condition.

## 7.6 Boiling Curve Used
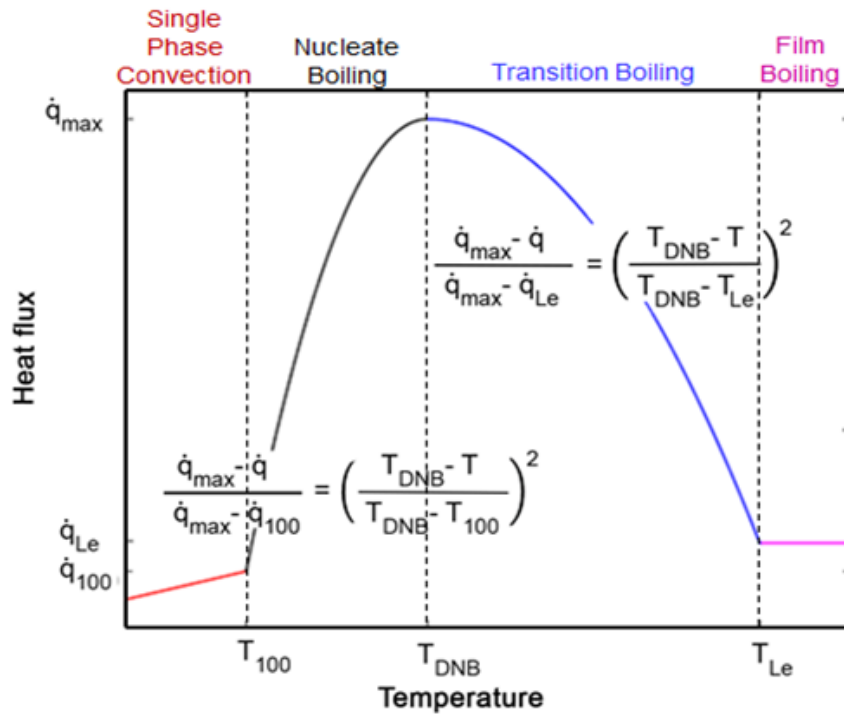


Figure 7.1: Boiling curve with corresponding equation and regimes

Boundary condition for impingement and free falling regions are transient in nature, so for modelling the thermal boundary condition boiling curves are used. Boiling curves are used to evaluate the surface heat flux. In boiling curve, heat flux $\dot{q}$ is the function of the ingot surface temperature T. **Fig. 7.1** illustrates a typical boiling curve and shows the four boiling water heat transfer regimes which can take place in the secondary cooling zone of the DC casting process Caron and Wells (2009b).

The heat fluxes sharply increase at the start of nucleate boiling at saturation temperature $T_{100}$, and reach the maximum heat flux of the boiling curve at departure nucleate boiling temperature $T_{DNB}$. After departure nucleate boiling temperature $T_{DNB}$, the heat flux decrease gradually and reaches the minimum heat flux called Leidenfrost heat flux or film boiling heat flux at Leidenfrost temperature $T_{Le}$. Film boiling occurs for temperature higher than Leidenfrost temperature. At this time, a steady vapour layer covers the hot surface and reduces the heat transfer sharply by repelling the impinging water. For surface temperature below Leidenfrost temperature, the bubble layers will collapse and wetting starts occurring on the hot surface. This phenomenon is called transition boiling.

Film boiling regime can only be observed at the impingement region, where the water jet momentum provides a horizontal force to compensate the pressure associated with the formation of vapour on the ingot surface. In the free falling region, the formation of water vapour is not opposed by any horizontal forces. So there is no possibility of film boiling in the free falling region. The four boiling curve regimes and their governing equations for evaluating corresponding heat fluxes for impingement and free falling regions are given below,

- **Forced convection or single phase convection regime**

For both impingement and free falling region, the plate surface temperature T $\leq T_{100}$ saturation temperature, the heat flux q is given by

$$\dot{q} = (14.6(T + 273) + 68.5(T_f + 273) - 21500)) \sqrt[3]{Q}(T - T_f) \tag{7.13}$$

Where, Q is water flow rate and $T_f$ is water temperature.

- **Nucleate boiling regime**

For both impingement region and free falling region, the plate surface temperature T > $T_{100}$ and T $\leq T_{DNB}$ departure nucleate boiling temperature, the heat flux is given by

$$\dot{q} = \dot{q}_{max}\left(\frac{T_{DNB} - T}{T_{DNB} - T_{100}}\right)^2 (\dot{q}_{max} - \dot{q}_{100}) \tag{7.14}$$

Where, $\dot{q}_{max}$ is the maximum heat flux, $\dot{q}_{100}$ is the saturation heat flux, $T_{100}$ is the saturation temperature and $T_{DNB}$ is the departure nucleate boiling temperature.

- **Transition boiling regime**

For impingement region, the plate surface temperature T > $T_{DNB}$ and T $\leq T_{Le}$ Leidenfrost temperature, the heat flux is given by,

$$\dot{q} = \dot{q}_{max}\left(\frac{T_{DNB} - T}{T_{DNB} - T_{Le}}\right)^2 (\dot{q}_{max} - \dot{q}_{Le}) \tag{7.15}$$

For free falling region, the plate surface temperature T>$T_{DNB}$ and T$\leq T_{Re}$ rewetting temperature, the heat flux is given by,

$$\dot{q} = \dot{q}_{max}\left(\frac{T_{DNB} - T}{T_{DNB} - T_{Re}}\right)^2 (\dot{q}_{max} - \dot{q}_{Re}) \tag{7.16}$$

Where, $q_{max}$ is the maximum heat flux, $\dot{q}_{Le}$ is the Leidenfrost heat flux, $\dot{q}_{Re}$ is the re-wetting heat flux, $T_{DNB}$ is the departure nucleate boiling temperature, $T_{Le}$ is the Leidenfrost temperature and $T_{Re}$ is the re-wetting temperature.

- **Film boiling regime**

For impingement region, the plate surface temperature T> $T_{Le}$ Leidenfrost temperature, the heat flux is given by,

$$\dot{q} = \dot{q}_{Le} \tag{7.17}$$

For free falling region, the plate surface temperature T> $T_{Re}$ re-wetting temperature, the heat flux is given by,

$$\dot{q} = \dot{q}_{Re} \tag{7.18}$$

Where, $\dot{q}_{Le}$ the Leidenfrost heat is flux and $\dot{q}_{Re}$ is the re-wetting heat flux.

## 7.7    Material Model

Plain strain situation in the plate width direction is assumed due to the negligible temperature gradient in that direction. Elasto-Viscoplastic material model is implemented to capture the rate dependency of thermal loading. The Garofalo law best describes the aluminum alloy's mechanical behaviour. Garofalo creep is also a deviatoric creep model with a creep rate proportional to the hyperbolic sine function. It can also be augmented by an Arrhenius type temperature dependency such that

$$\dot{\epsilon}_{cr} \propto e^{\frac{-Q}{RT}} \tag{7.19}$$

Where,
Q is the activation energy in $J/mol$
R is the gas constant
T is the absolute temperature in $°C$

The complete creep rate equation then reads

$$\dot{\epsilon}_{cr} = A \sinh(\frac{\sigma_{eff}}{\sigma_o})^n e^{\frac{-Q}{RT}} \tag{7.20}$$

where,
A is the creep rate in $1/s$
$\sigma_{eff}$ is the reference effective stress level in $Pa$
The **Tab. 7.1** lists the constants defined in the **Eq. 7.20**.

| | | |
|:---:|:---:|:---:|
| A | $28.2 \times 10^{25}$ | $1/s$ |
| $\sigma_{eff}$ | $13.6 \times 10^6$ | $Pa$ |
| n | 7.13 | - |
| Q | $400 \times 10^3$ | $J/mol$ |

Table 7.1: List of the constants for the Garafola law

## 7.8    Material Properties

The material properties are important in modelling the thermo-mechanical fields. In our case temperature dependent properties of the aluminium alloy were used which are shown in the **Fig. 7.2 to 7.9**.
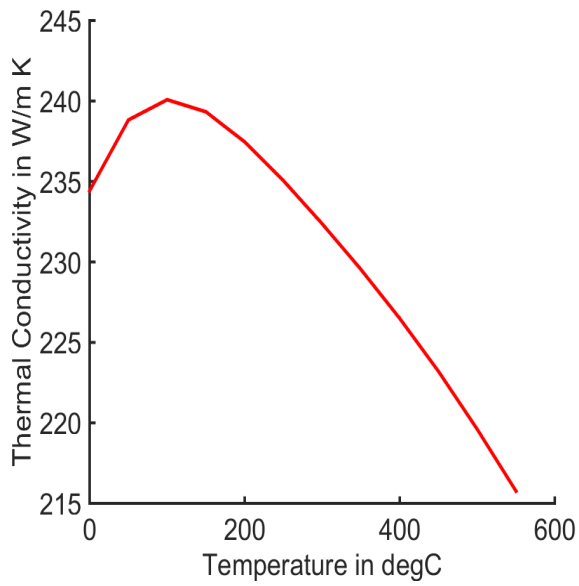
Figure 7.2: Temperature dependent Thermal conductivity
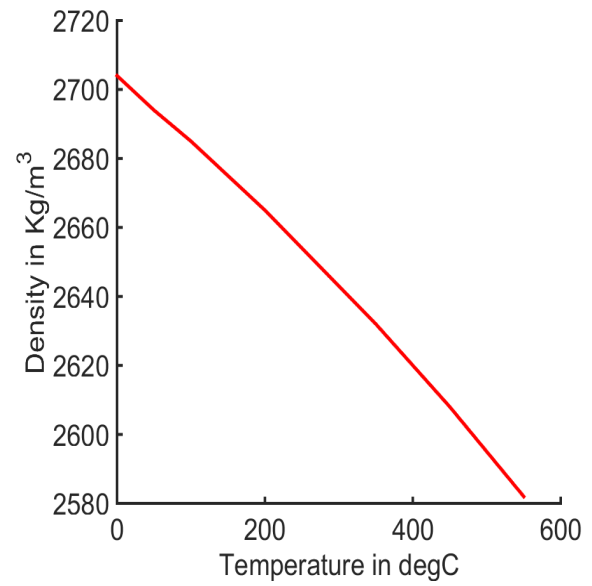


Figure 7.3: Temperature dependent Density
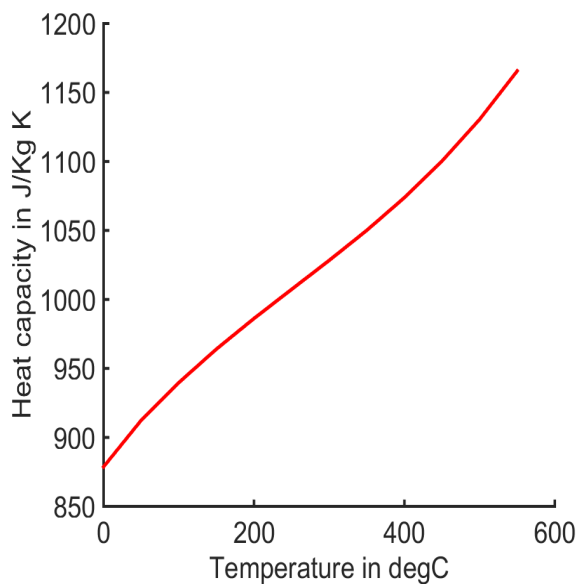


Figure 7.4: Temperature dependent Heat capacity at constant pressure
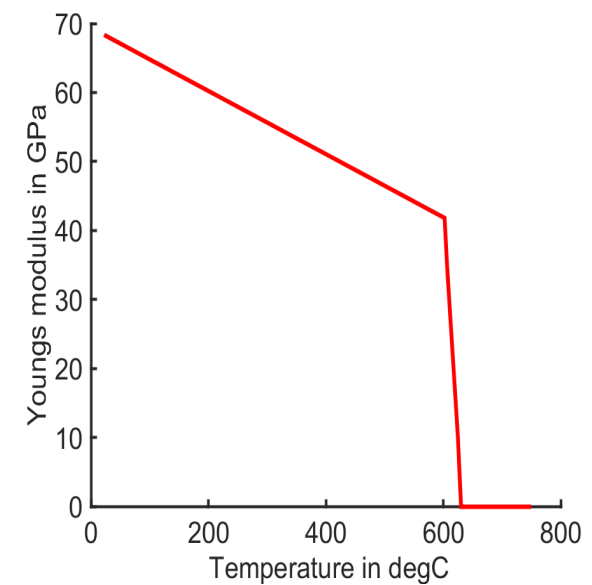


Figure 7.5: Temperature dependent Young's modulus
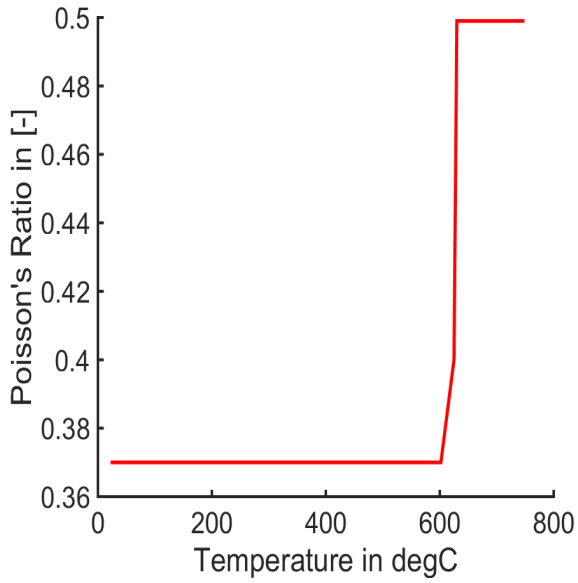
Figure 7.6: Temperature dependent Poisson's Ratio
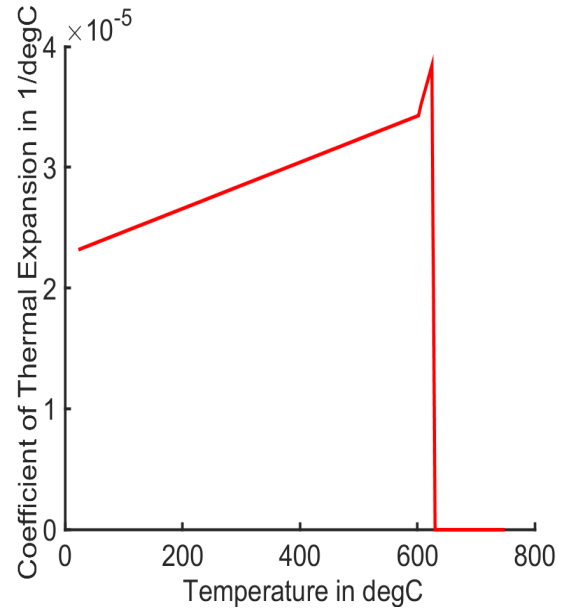


Figure 7.7: Temperature dependent Coefficient of thermal expansion
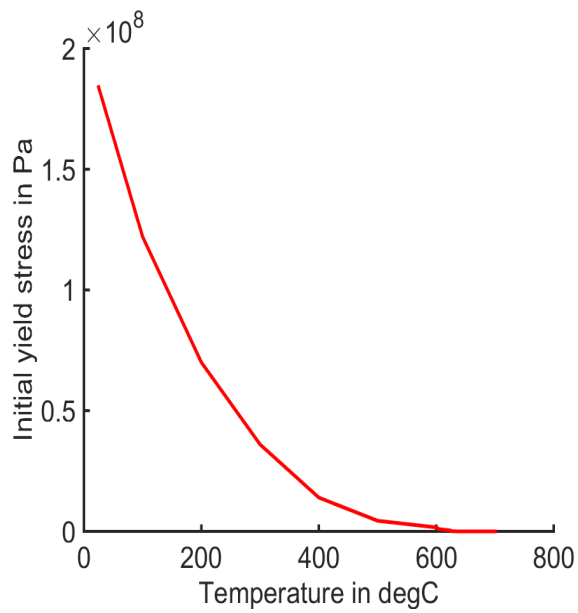


Figure 7.8: Temperature dependent initial yield stress
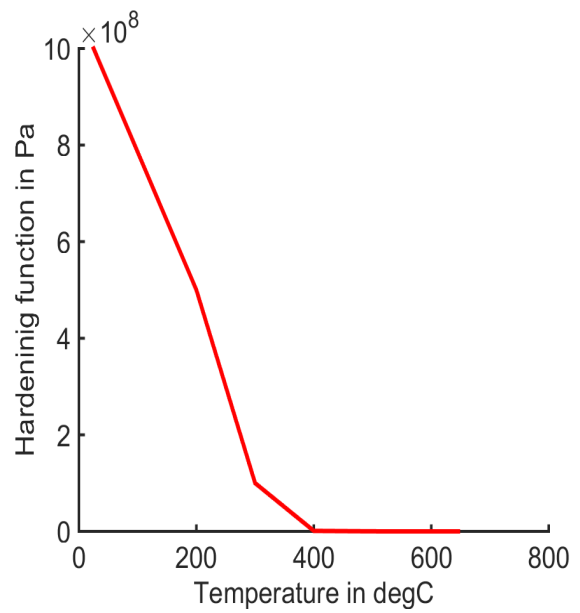


Figure 7.9: Temperature dependent Hardening function

## 7.9   Thermal Results

### 7.9.1   Experimental Surface Temperatures
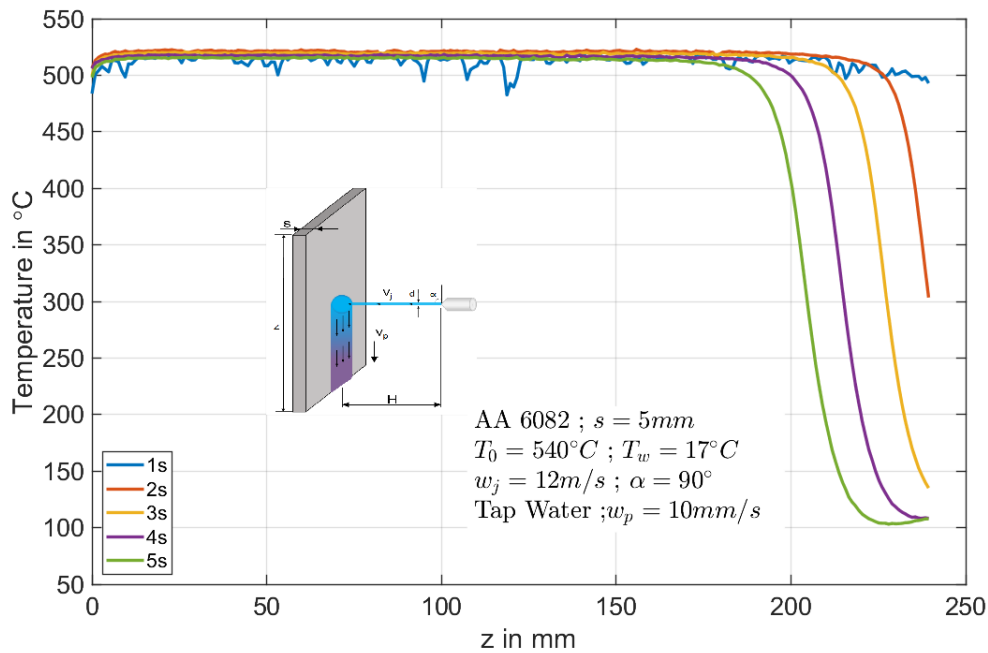


Figure 7.10: Surface temperatures from the infrared measurements for various time instants
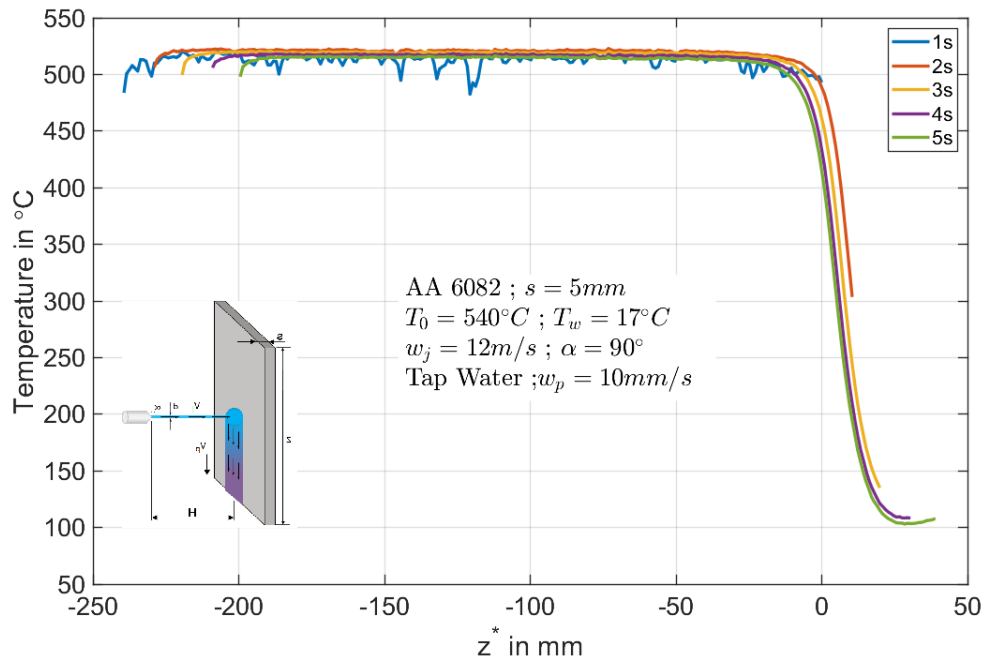


Figure 7.11: Surface temperatures from the infrared measurements for various time instants at nozzle impingement position

Temperature profiles over position during cooling process of AA6082 sheet with Full jet nozzle at 2 bar water pressure, casting velocity of 10 $mm/s$, thickness of 5 $mm$ and initial temperature of $500°C$ for three specific times i.e., 2s, 4s and 6s are shown in **Fig. 7.10**. The temperature profiles along the plate position is extracted for every time step as depicted in Fig. 7.10. For simpler understanding, we can visualize that plate is kept stationary and

the water jet moves with a casting velocity of 10 $mm/s$ on the plate. The quasi-stationary of the temperature profiles after 4s as observed in Fig. 7.10. In jet impingement cooling region, temperature drops faster from 400°$C$ to 100°$C$ in the range of 25 $mm$ between any two successive points. The quasi-steady state simplifies the problem and the estimation of the boiling curve during cooling process becomes easier.
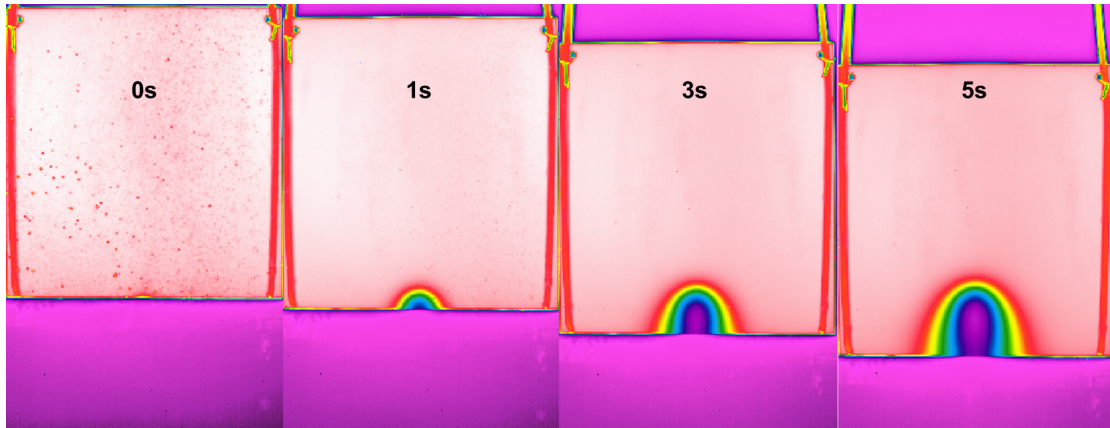


Figure 7.12: Infrared Thermography images for time 2s, 4s, 6s from left to right side

**Fig. 7.12** depicts the measured infrared images for the same experimental conditions as stated above in Fig. 7.10. Water jet is kept stationary and the hot aluminium plate with an initial temperature of 525°$C$ moves continuously from top to bottom. The water jet makes an initial contact with the plate at the bottom and the wetting front moves down with the plate due to gravitational effect, whereas some part of the water jet climbs upward with the initiation of a pre-cooling phenomena. As the plate moves, the jet spreads parabolic-ally with 30 $mm$ at 2$s$ and gradually increases from 60 to 80 $mm$ for 4$s$ and 6$s$ respectively. Surface temperature at the jet impingement region in the range of 40-50 $mm$ which drops below 100°$C$ for 4$s$ and 6$s$ respectively. Therefore, heat transfer analysis was focused only in the jet impingement region.
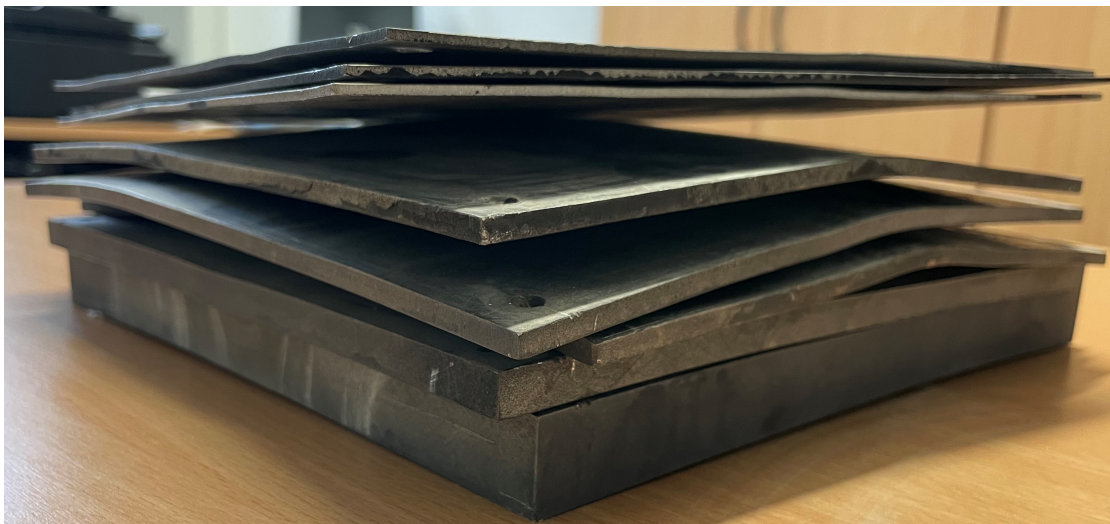


Figure 7.13: Stack of distorted AA6082 aluminium alloy plates after the quenching process
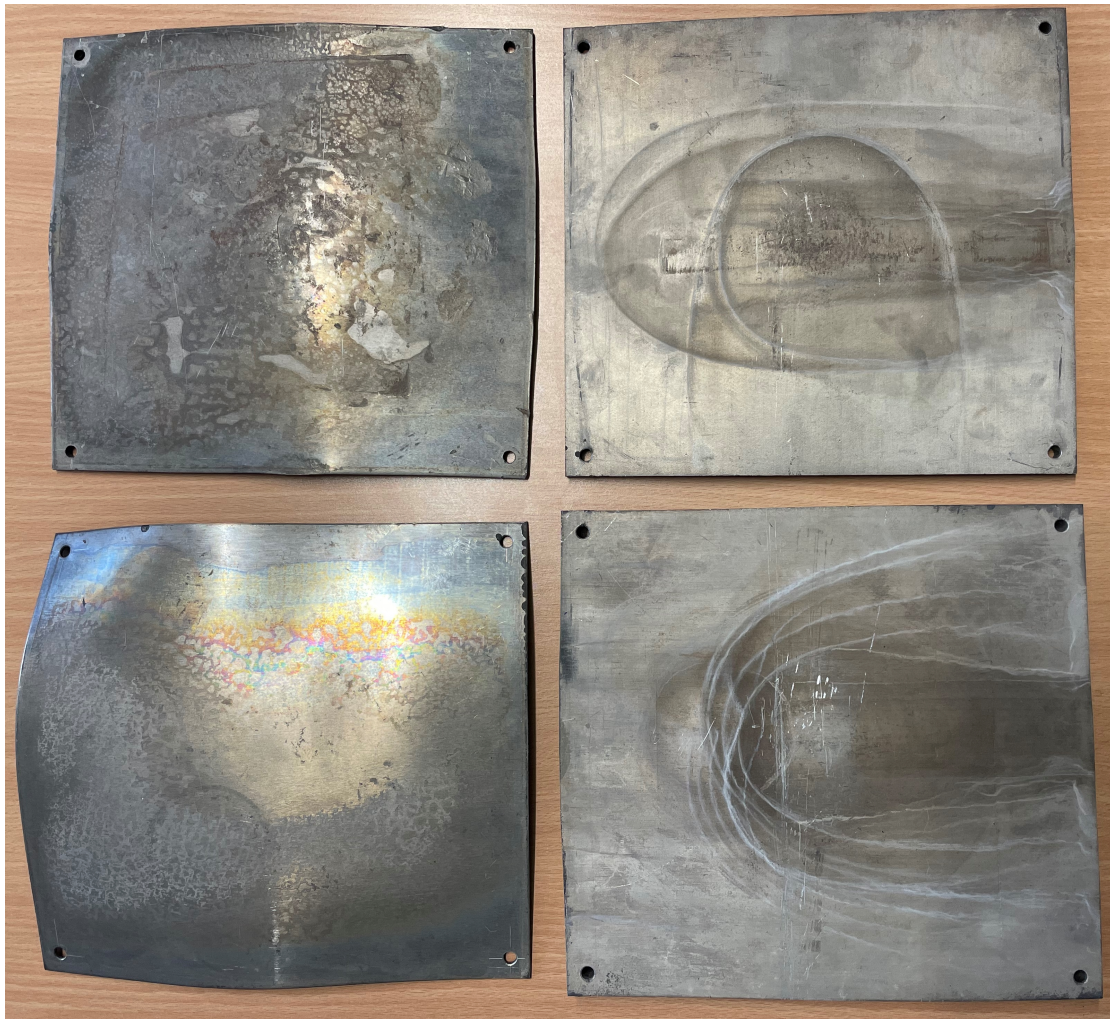
Figure 7.14: Distortion of the AA6082 aluminium alloy plates after the quenching process

**Fig. 7.13** and **Fig. 7.14** shows the distorted plates after the quenching process using array of jet configurations. The experimental conditions for the depicted deformed plates can be referred to Chpater 6.1. Necessity for the understanding of the distortion during quenching process is inevitable. Henceforth, we employ a three-dimensional viscoplasticity analysis during quenching with array of jets and single jet were studied.

## 7.9.2   Modelling and Verification of the Temperature Solution
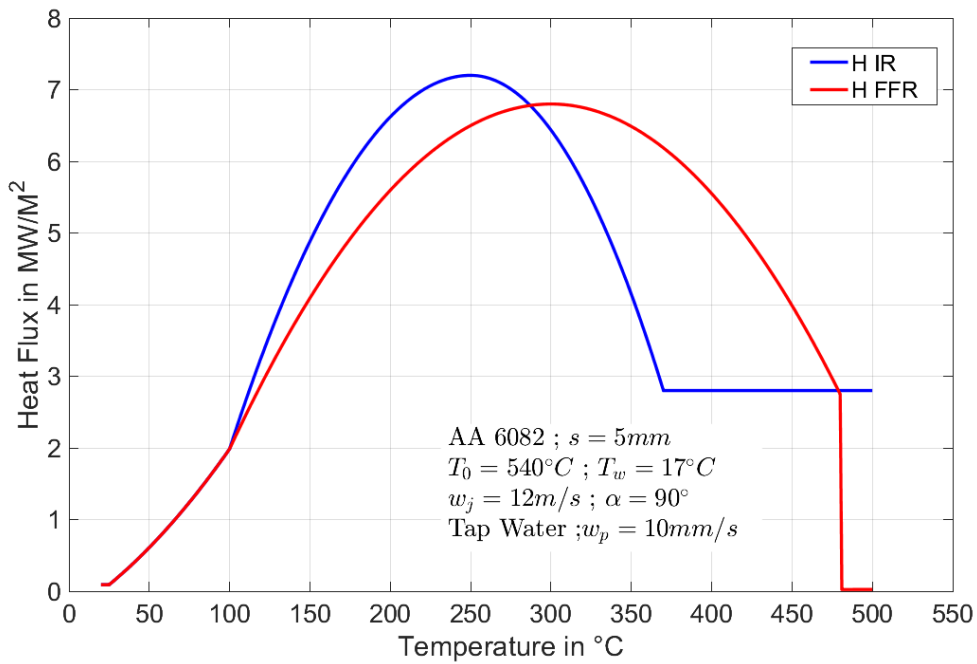


Figure 7.15: Boiling curve for quenching due to full jet nozzle

The heat exchange between the cooling water and the hot moving metal plate can be distinguished into two regions as impingement region and free-falling region.  The heat transfer during the quasi-stationary condition can be quantified as heat flux and are defined with the use of boiling curve as show in **Fig.  7.15**.  The quadratic interpolation between the heat flux and surface temperature is considered in transition and nucleate boiling region which gives a better approximation in comparison to linear approximation.  The heat transfer in the impingement region is higher in comparison to free-falling region with maximum heat flux of 7.2 $MW/m^2$ and 6.8 $MW/m^2$ respectively.  Departure nucleate boiling (DNB), where maximum heat flux occurs between 250 and 300°$C$ with a difference of 50°$C$.  We also observe that heat flux is independent of Leidenfrost and re wetting temperatures respectively in the impingement and free-falling region.
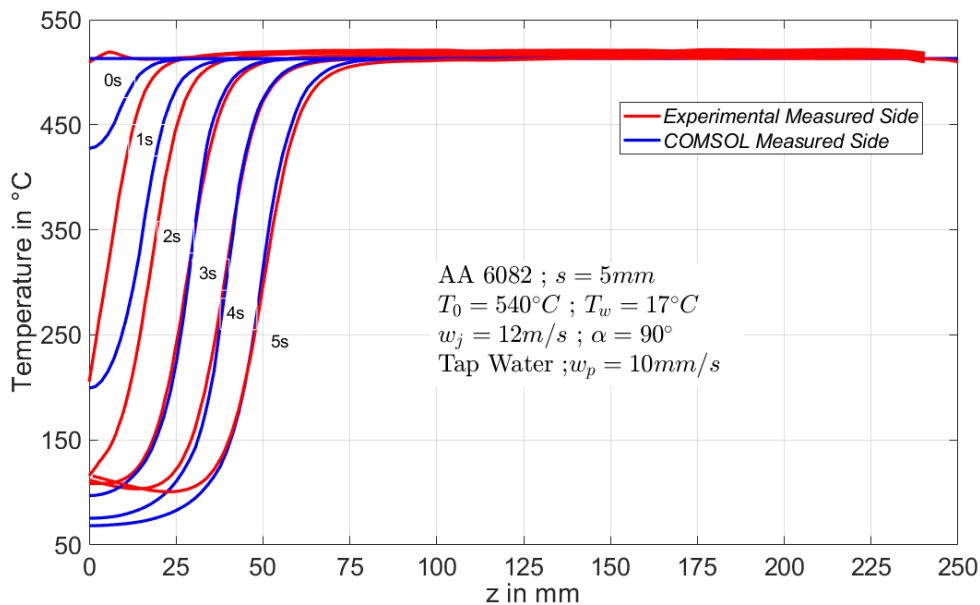


Figure 7.16: Temperature comparison of experiments with 3D numerical solution

**Fig. 7.16**, indicates the comparison of experimental and simulated temperature profiles at different time instants until $5s$. The temperature profiles match perfectly well and error of less than 10% below $200°C$. The temperature profiles at the initial time instant should be neglected because of the water ejection and fluid structural effects the temperature prediction, therefore data can't be accurate. The temperatures below $150°C$ should be neglected, the infrared camera is inaccurate below that temperature. Therefore, the three-dimensional numerical simulation believed to be perfect and further analysis can be done with it.
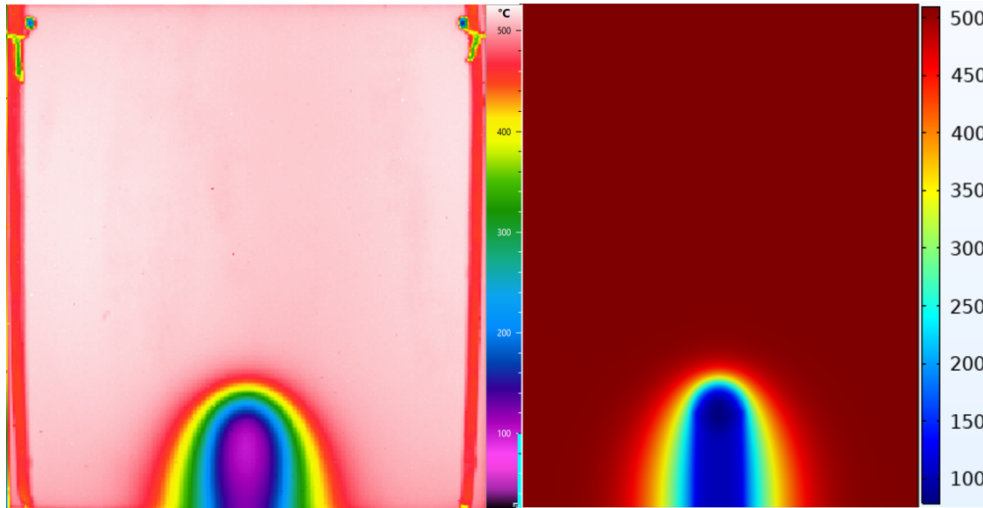


Figure 7.17: Experimental temperature from Infrared Camera (left) and Temperatures from numerical three-dimensional solution (right)

**Fig. 7.17**, shows the temperature contours from infrared measurements and three-dimensional numerical solutions for the quasi-stationary condition. The temperatures images represent from measurement side of the cooling process. From the temperature images, we can clearly see parabolic shaped cooling area in the jet impingement region. The temperature images in Fig. 7.17, shows nearly the same tendency as that of experiments. Hence, the three-dimensional simulation proves to give promising results for the boiling curve approximation.

# 7.10   Mechanical Results

## 7.10.1   Mechanical Results: Single Full Jet Nozzle
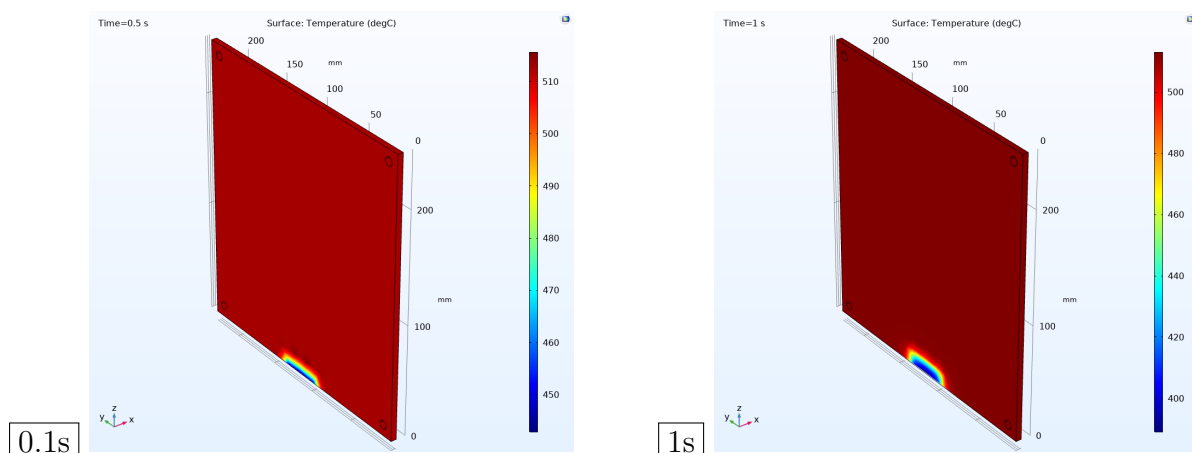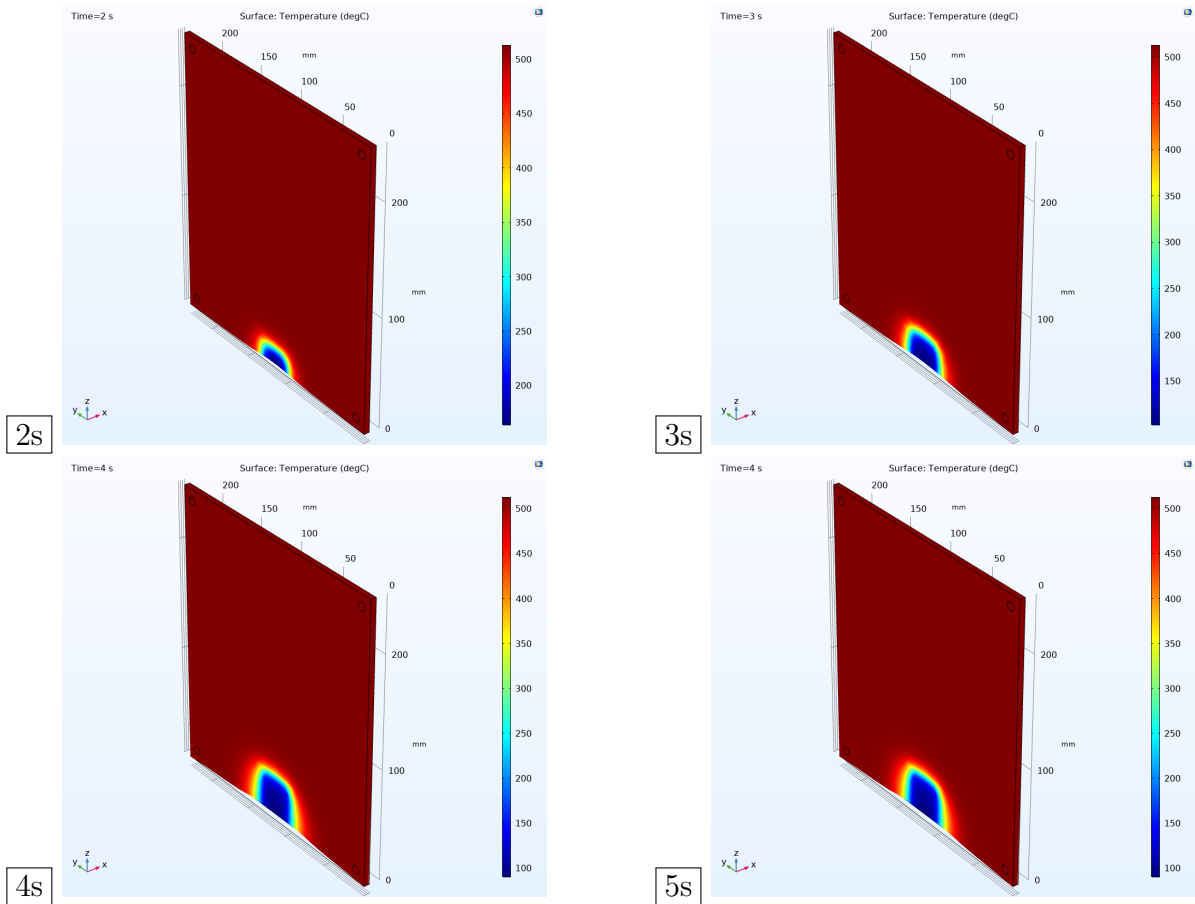
Figure 7.18: Simulation results for single full jet nozzle:Temperature and deformation

The three-dimensional view of the temperatures for different time instants for AA6082 material with $w_j = 12$ m/s, $w_p = 10$ mm/s, $s = 5$ mm thick plate were depicted as shown in the **Fig. 7.18**. The clear movement of the water jet can be seen while the wetting front tries to propagate in the lateral direction and the temperature of the body lowers to below $100°C$. The influence of the water cooling on the mechanical deformation of the plate shown to be less significant with this kind of cooling technique.
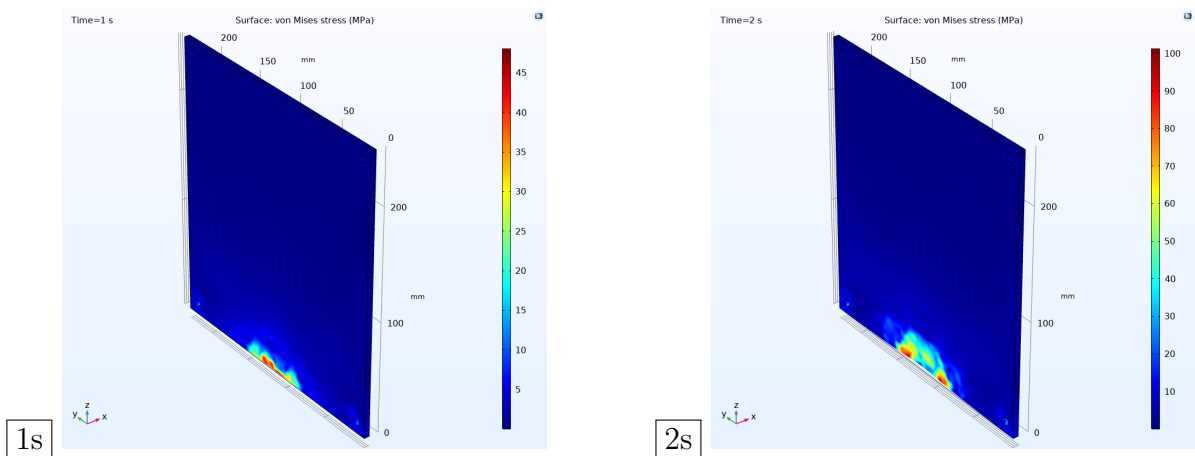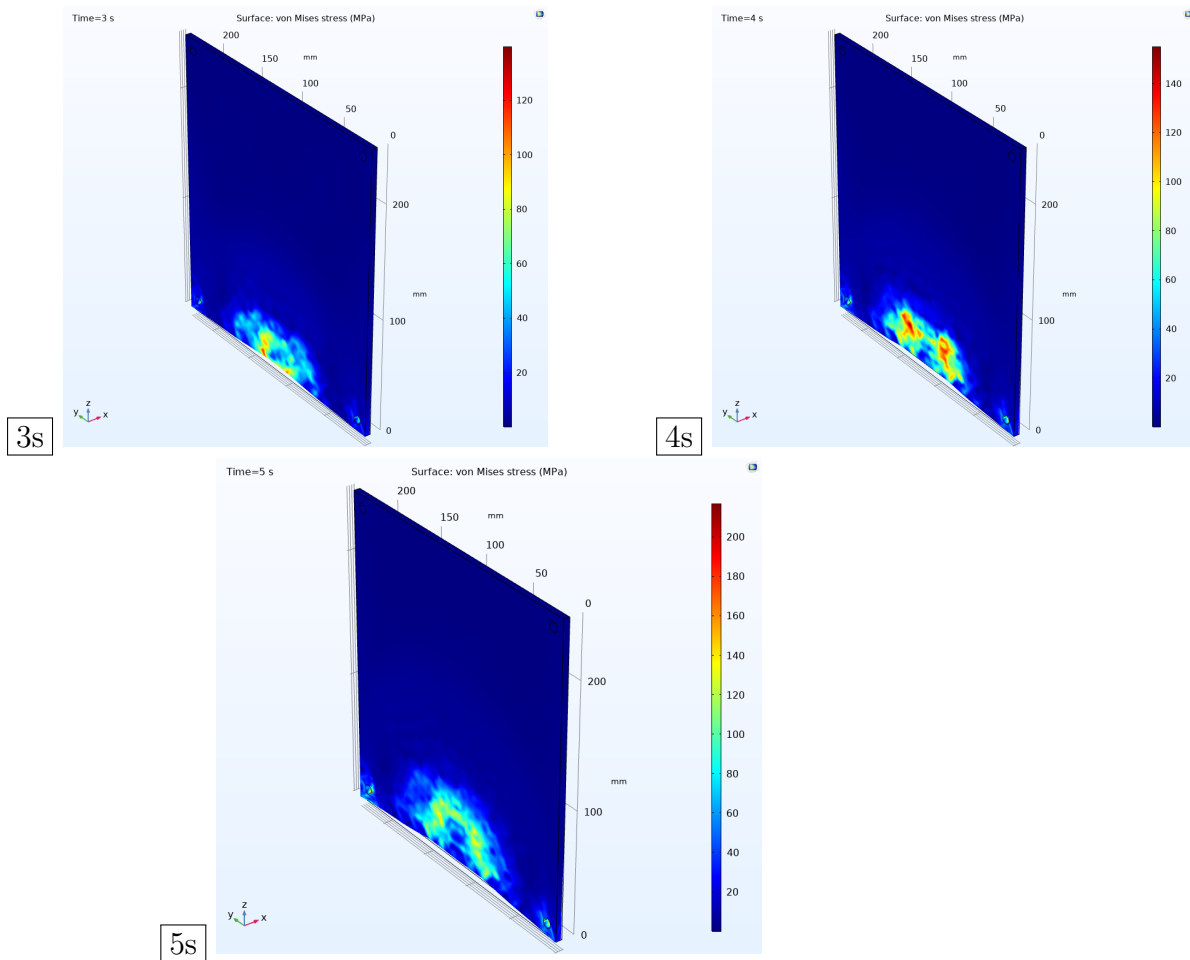
Figure 7.19: Simulation results for single full jet nozzle:von Mises Stresses for different time instants

**Fig.  7.19** shows the von Mises stress profiles for different time instants for the same experimental conditions as described in Fig. 7.18. The evolution of the stress takes place mainly in the water impingement region and the for different time instants the movement of the water jet on the plate surface gradually highers the thermal stresses. The mechanical constraints on the corner of the plates shows not significant influence on the material. However, the water cooling becomes homogeneous below the impingement region which means the no temperature gradient exists and this favours the material to attain the constant stress intensity. Therefore, the larger temperature gradient in the initial phase of the cooling phase leads to larger magnitude of nearly 50 MPa and in the quasi-steady state conditions the stress state remains around 120 $MPa$ after $4s$ from the start of the quenching process.
**For 5 mm/s plate velocity**
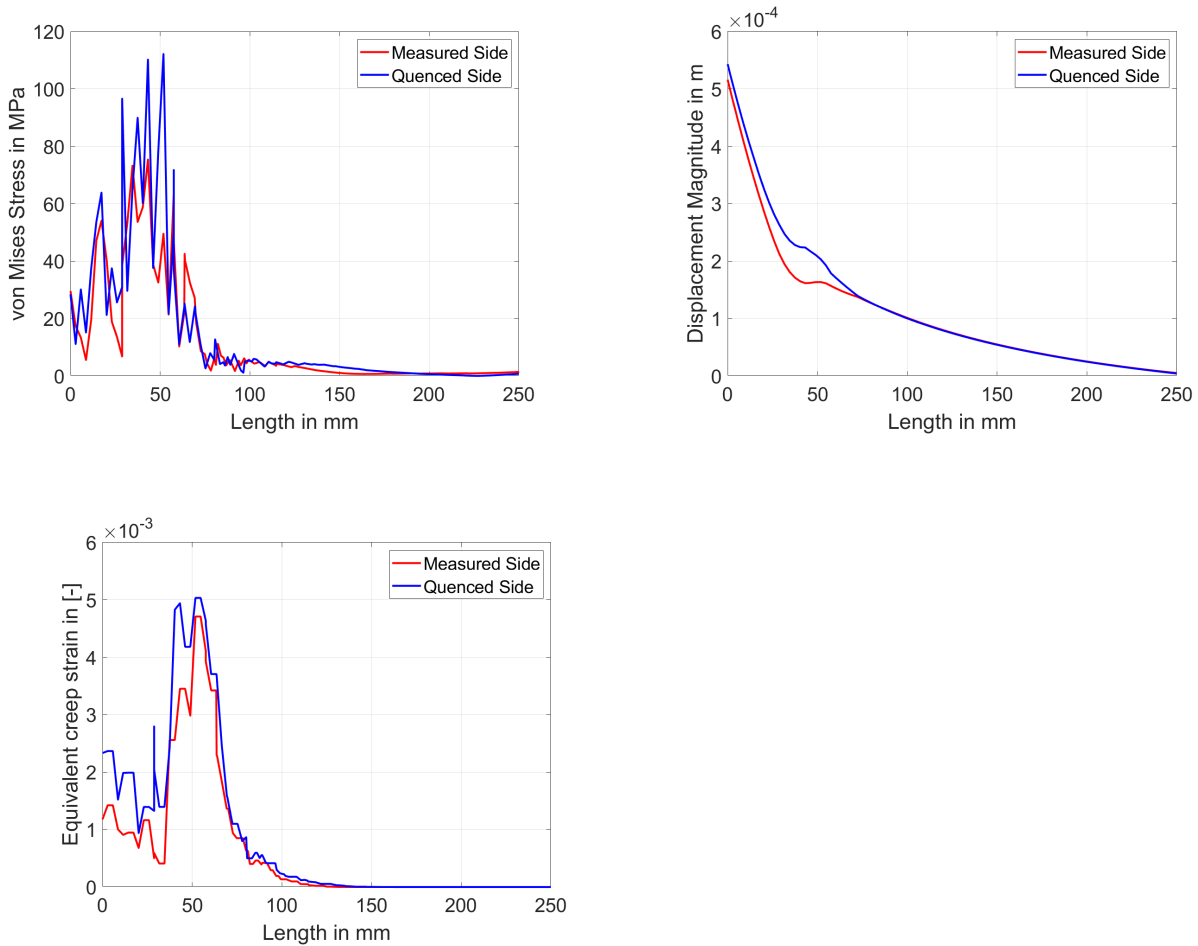
Figure 7.20: Simulation results for single full jet nozzle: Equivalent and stress at quasi-steady state condition

**Fig. 7.20** shows the profiles of the von Mises stress, displacement magnitude, equivalent creep strain over the plate length for quasi-steady state condition on the measured side and quenched side of the plate in case of 5 mm/s plate velocity. The profiles clearly shows no distinction between the measured side and the quenched side and the whole material behaves in a almost uniform manner. The creep strain and displacement magnitude shows a little variation on the quenched side. The quenching process and the experimental condition for these profiles are same as discussed in early sections and the final quench time is 5s which indicates that the water jet travelled up to location nearly 70 mm on the plate surface. From the stress profiles, we can observe a steep increase nearly at 50 mm plate length shows a value of 80 - 100 MPa. The water jet position is mainly responsible of the extraction of the heat from the hot body and the removal of heat promotes the material to undergo change in temperature and in addition the material experiences a thermal load which leads to increase the stress levels in the material. Therefore, the plate deforms and shows a inverse proportionality to the stress state with increase in the downstream region. The change in the plate length to the initial length can be termed as the strain and the equivalent creep strain which accounts the temperature dependency shows a direct proportional to the stress state.

**For 10 mm/s plate velocity**
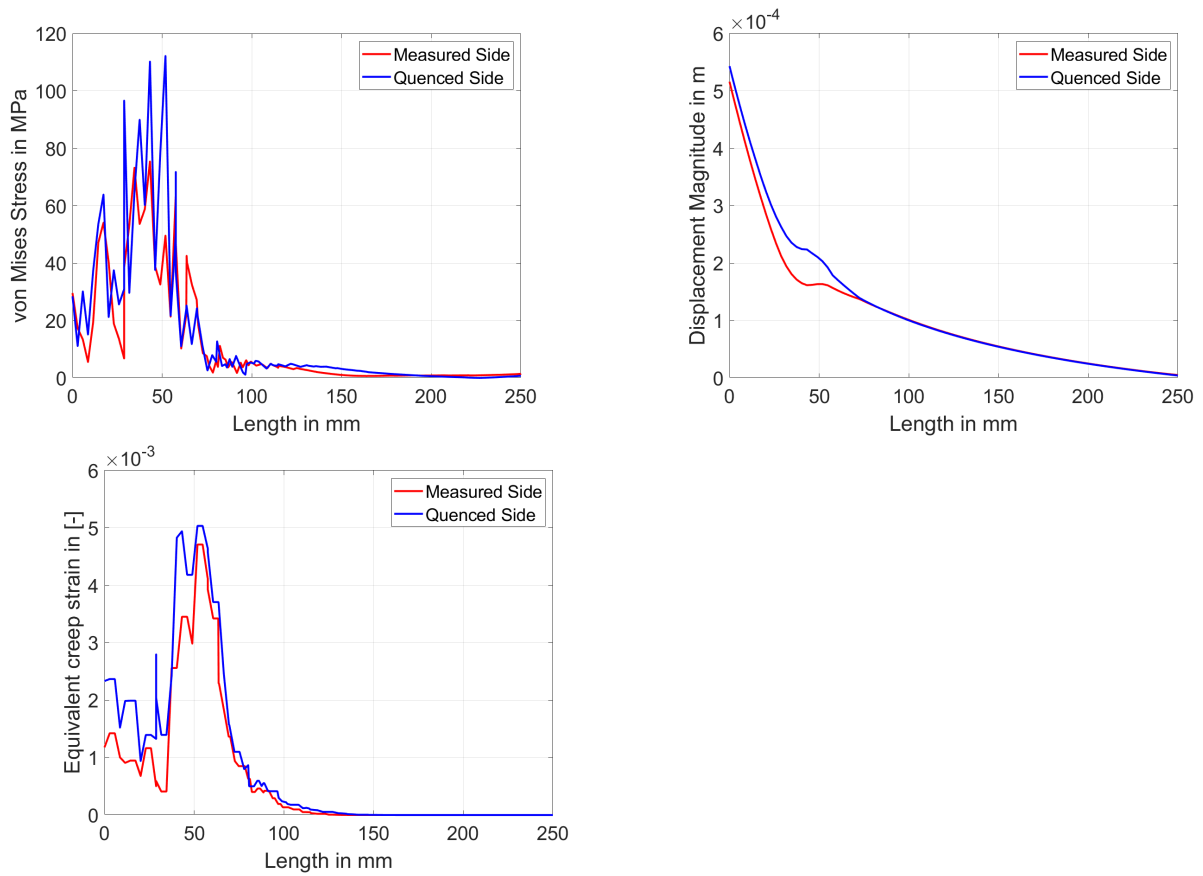
Figure 7.21: Simulation results for single full jet nozzle: Equivalent and stress at quasi-steady state condition

## For 20 mm/s plate velocity
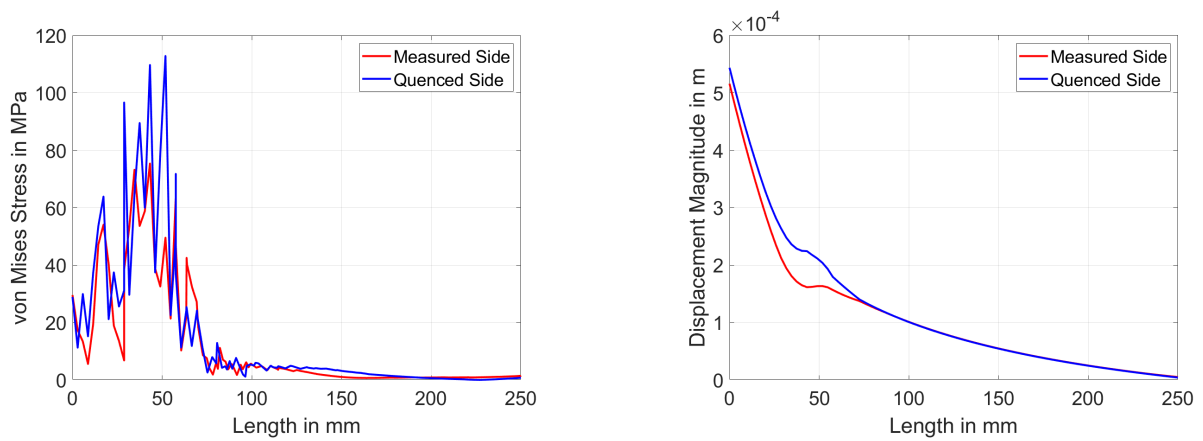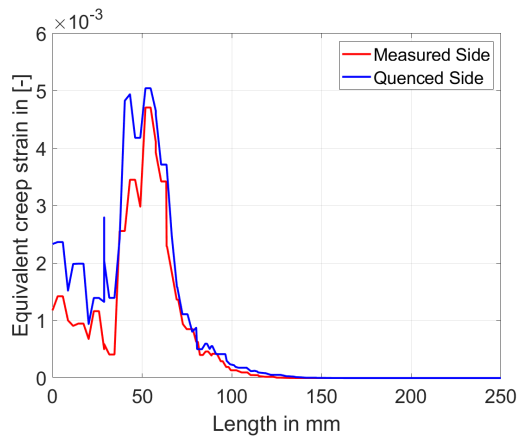
Figure 7.22: Simulation results for single full jet nozzle: Equivalent and stress at quasi-steady state condition

**Fig. 7.21** and **Fig. 7.22** shows the similar range of magnitudes for all the profiles in case of 10 mm/s and 20 mm/s plate velocities. The similar explanation to that of 5 mm/s plate velocity applies.

**For 10 mm thick plate**
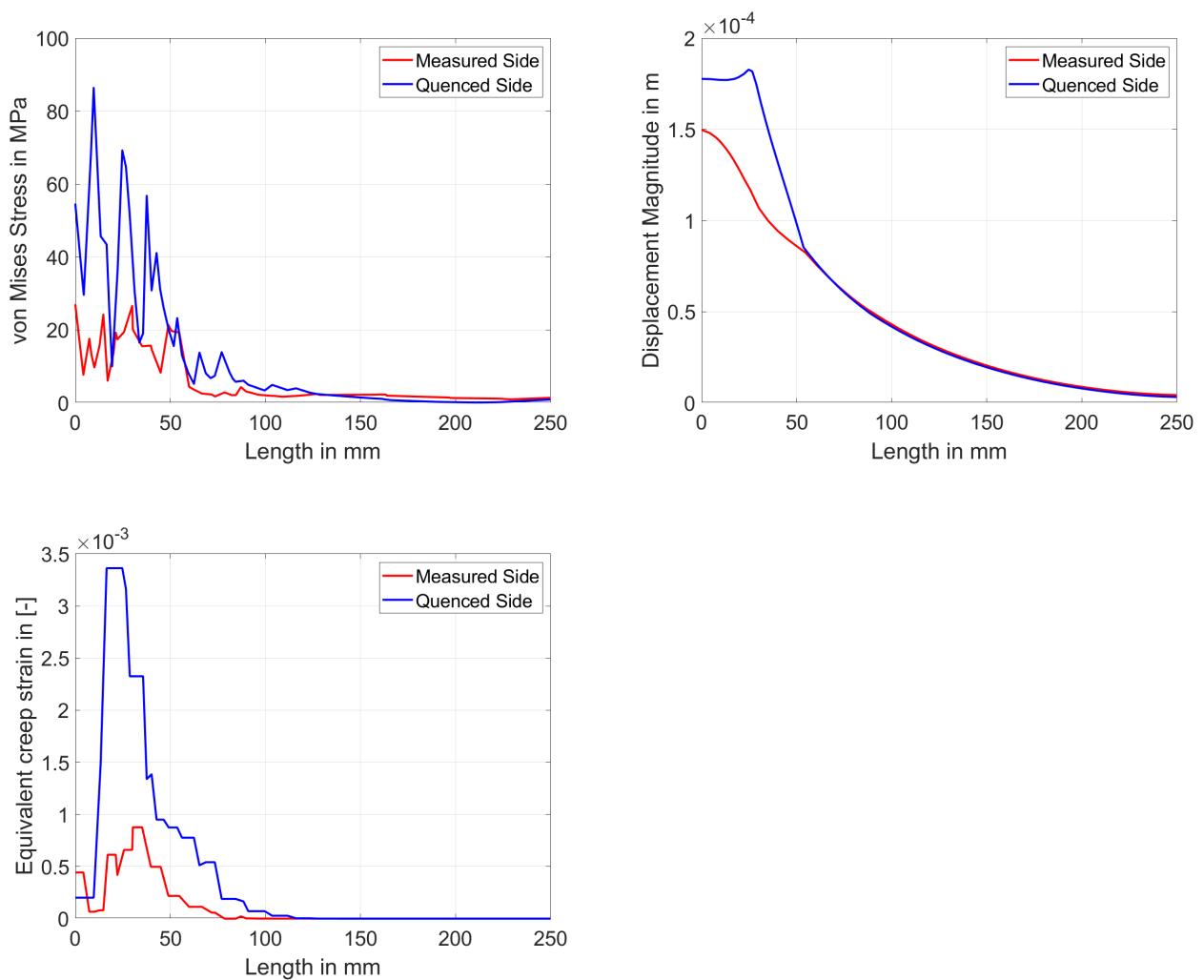




Figure 7.23: Simulation results for single full jet nozzle: Equivalent and stress at quasi-steady state condition

For plate thickness of 10 mm, the profiles for the von Mises stress, displacement magnitude, and equivalent creep strain were shown in **Fig. 7.23** at quasi-steady state condition while

other experimental conditions are maintained the same for the sake of simplicity. The influence of the plate thickness can be strongly observed in all the depicted profiles for stress, strain, and displacements. The water impingement side shows a stronger effect on the stress intensity and peak fluctuates between 40 - 80 MPa, while the measured sides shows nearly independent profiles around 20 MPa. Although the displacement intensity observed to be lower around $2 \times 10^{-4}$ m, the quenched side shows a higher value. In case of creep strain, the quenched side shows a value of 3 times the measured side and the water impingement with the local position of the water jet has a significant influence on the material behaviour.

**For initial temperature of $250°C$**
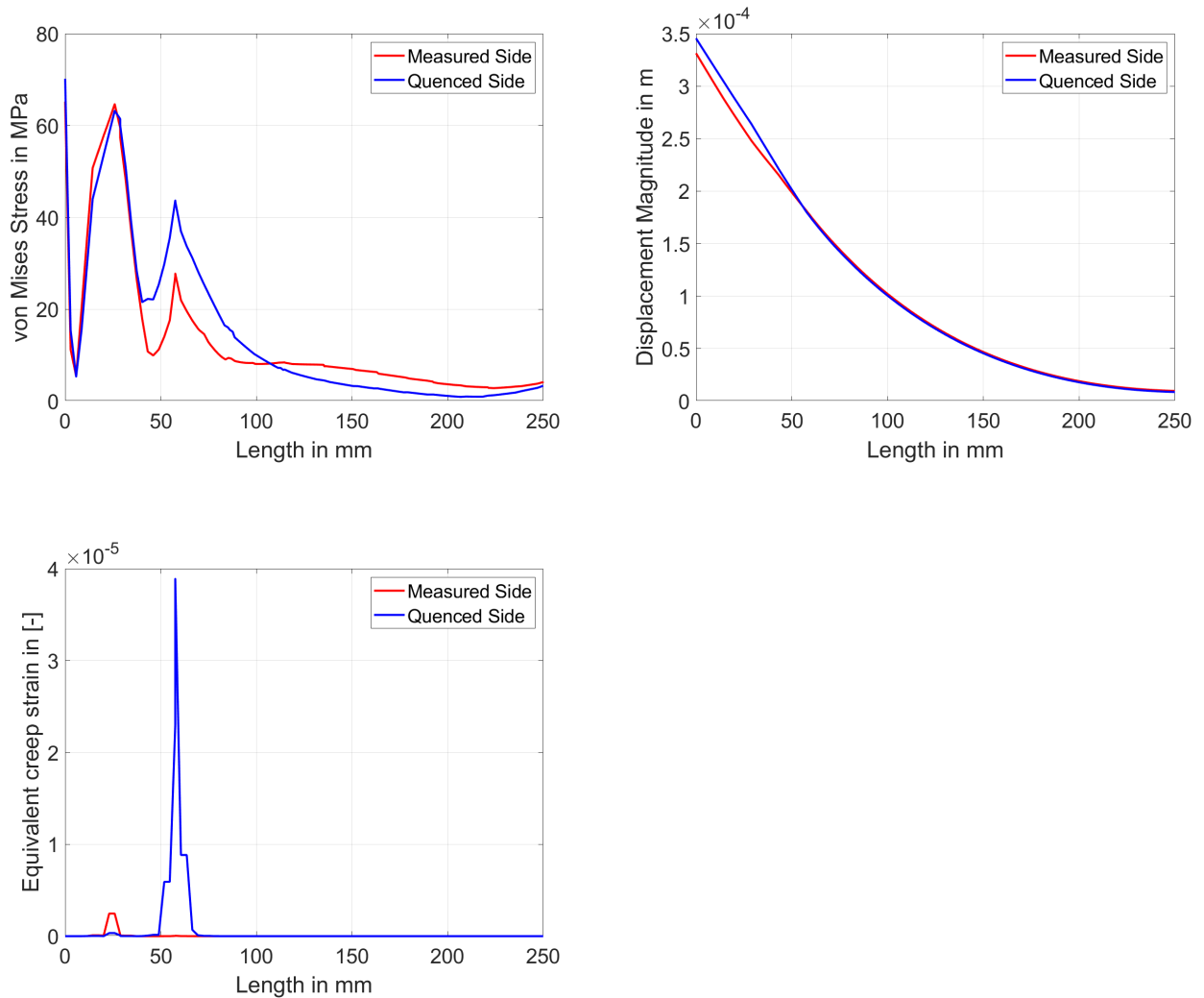


Figure 7.24: Simulation results for single full jet nozzle: Equivalent and stress at quasi-steady state condition

For start temperature of $250°C$, the profiles of the von Mises stress, displacement magnitude, and the equivalent strain are depicted in the **Fig. 7.24** for same experimental condition at quasi-steady state condition. The thermal energy of the body is low compared to higher start temperature and therefore the intensity of heat extraction is reduced. The temperature gradient within the material can also significantly reduces with the low start temperature which promotes the faster heat conduction within the material. Henceforth, the effect of the stress intensity on the water cooled region significantly lowers compared to start temperature of $520°C$. Although the strain show relatively higher value at location 50 mm on the plate length should indicate the larger plate distortion because of strong local internal conduction.

**For initial temperature of 450°$C$**
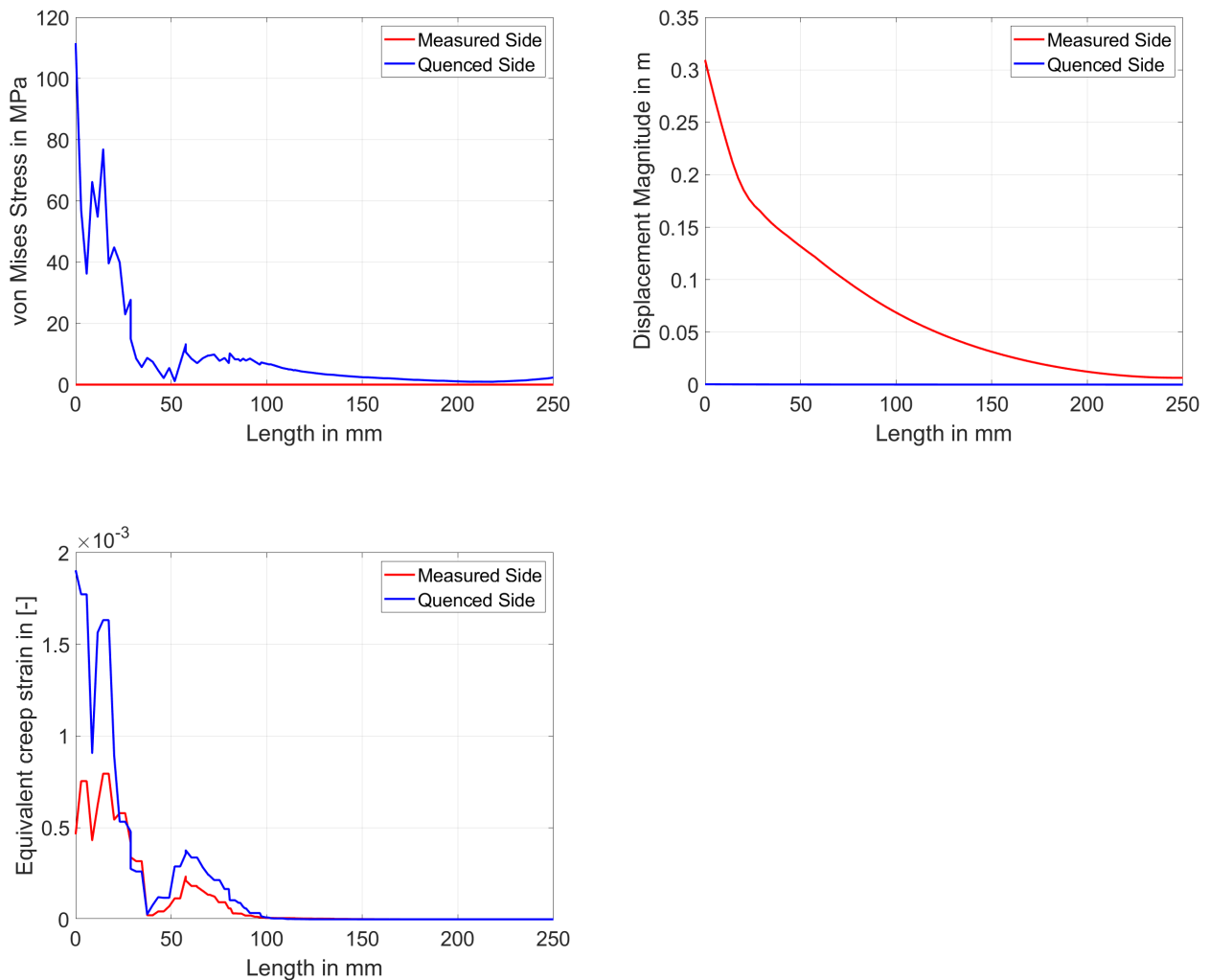






Figure 7.25:  Simulation results for single full jet nozzle:  Equivalent and stress at quasi-steady state condition

Similarly, the higher start temperature highers the magnitude of heat transfer as reported in Chapter 4.6 favours higher stress, strain states as depicted in the **Fig. 7.25**. The effect is strongly seen in the water quenched region and also displacement higher towards the measured side.

## 7.10.2   Mechanical Results: Array of Jets

The mechanical behaviour of the material in case of array of jet quenching is simulated in three-dimension and were shown in the **Fig. 7.26**.  The profiles were shown for different time instants from 0.1s to 5s quench time.  For the higher quench time, the temperature of the plate lowers in the water impingement region and the plate distorts largely.  The temperature of the body attains a steady state after the time instant of 3s and the temperature gradient attains uniform.  The larger temperature gradient exists during the start up phase of the cooling process until 3s, which affects the body to fluctuate largely towards the quenching side and after the homogeneous temperature distribution the plate distorts away. Henceforth, the local temperature distribution within the body should mainly responsible for the non-linear behaviour of the body.  To avoid such distortion in the body, the proper selection of the experimental conditions for cooling of the plate becomes inevitable.
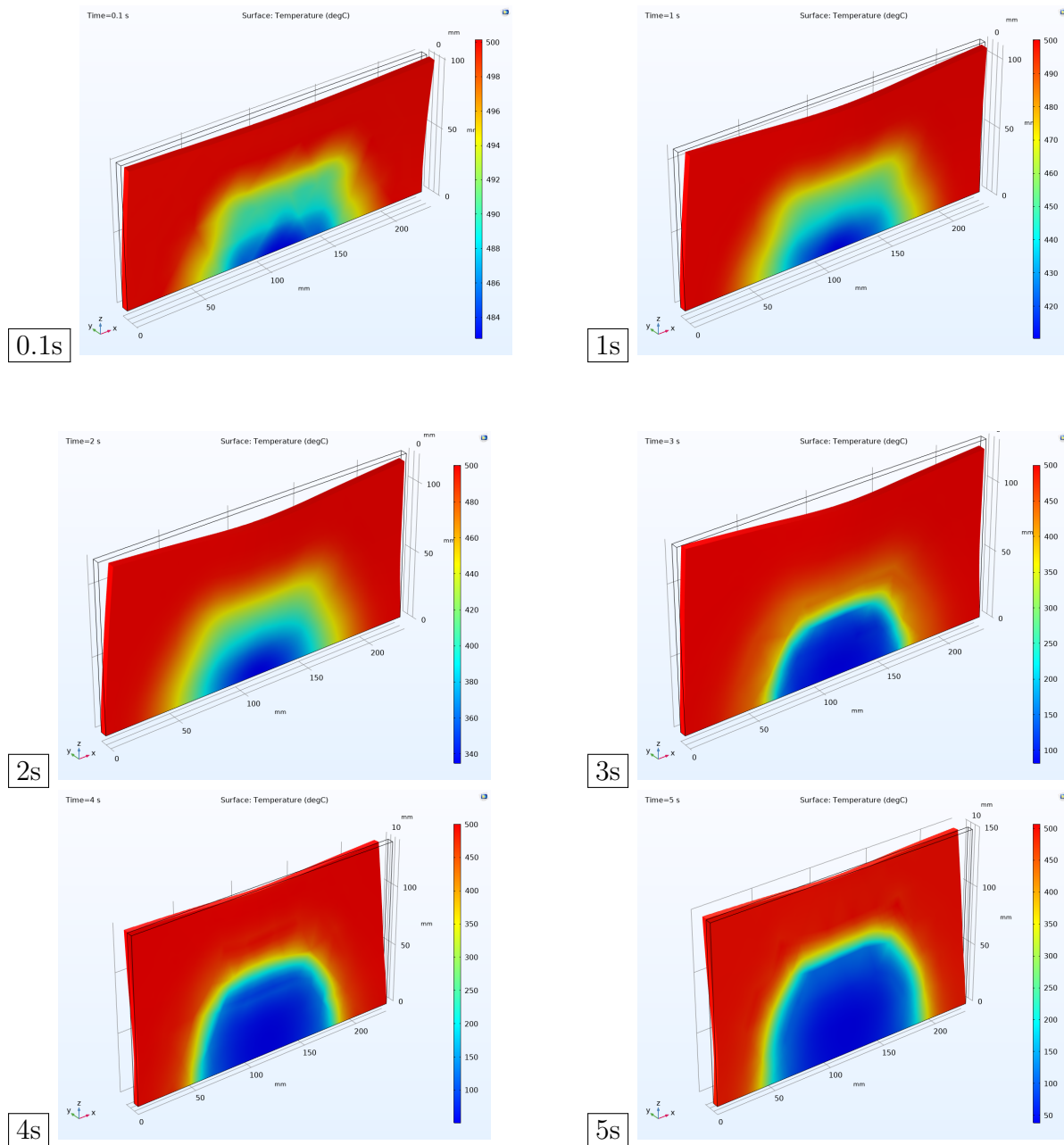
Figure 7.26: Simulation results for array of full jet nozzle:Temperature and deformation

**For 2 mm thick plate**
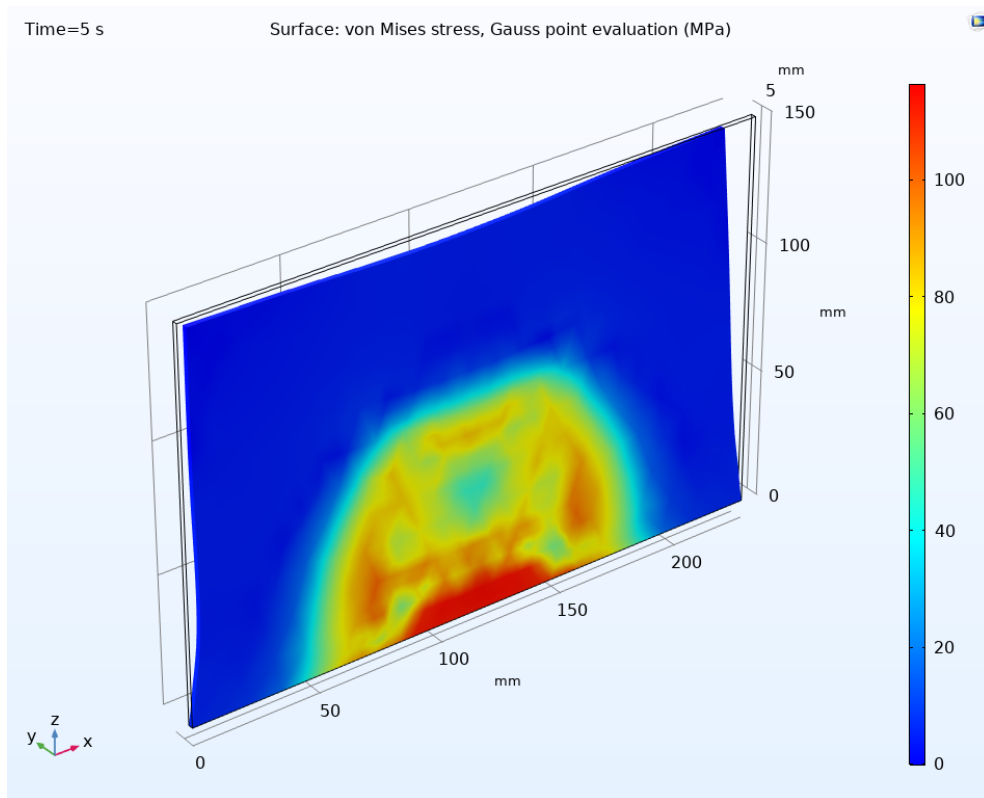
Figure 7.27: von Mises stress at Gauss points for 2 mm plate thickness in case of array of jet quenching at quasi-steady state condition

**Fig. 7.27** shows the von Mises stress, Gauss point evaluation for the 2 mm plate thickness at quasi-steady state condition for the same experimental conditions. The non-linear distribution of the stress state at the water impingement location are the result of the temperature gradients because of cooling. As we can see, a large intensity of stress arises at the centre of the cooling region and the plate deforms largely.
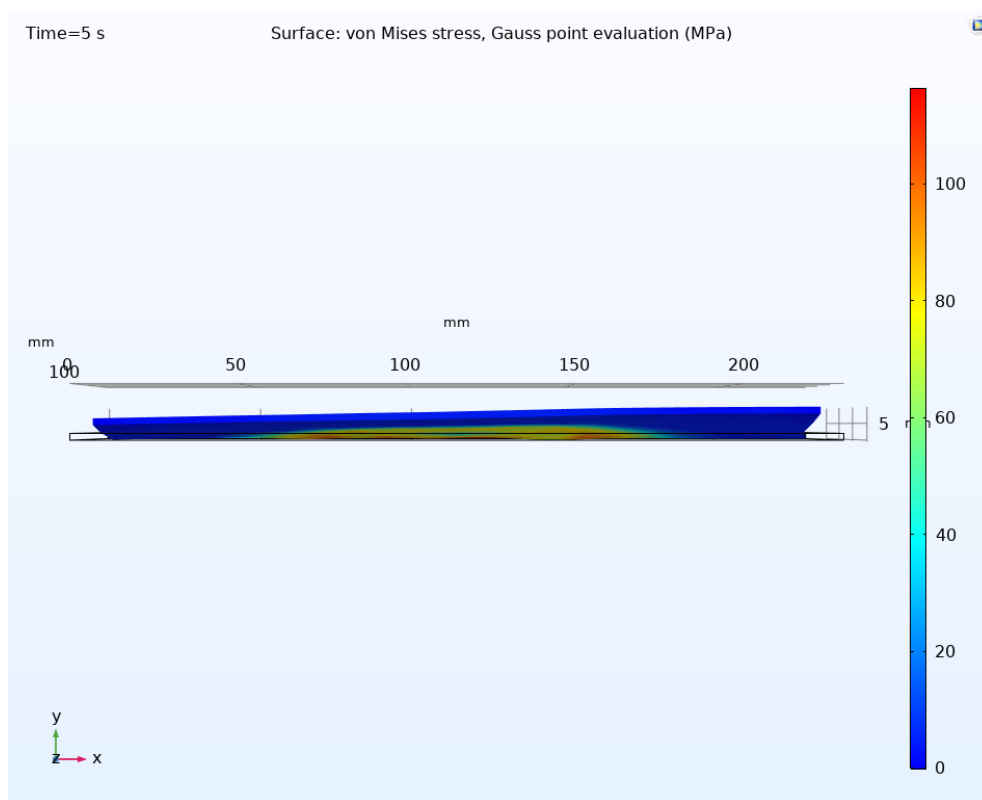
Figure 7.28: von Mises stress at Gauss points for 2 mm plate thickness in case of array of jet quenching at quasi-steady state condition in xy plane
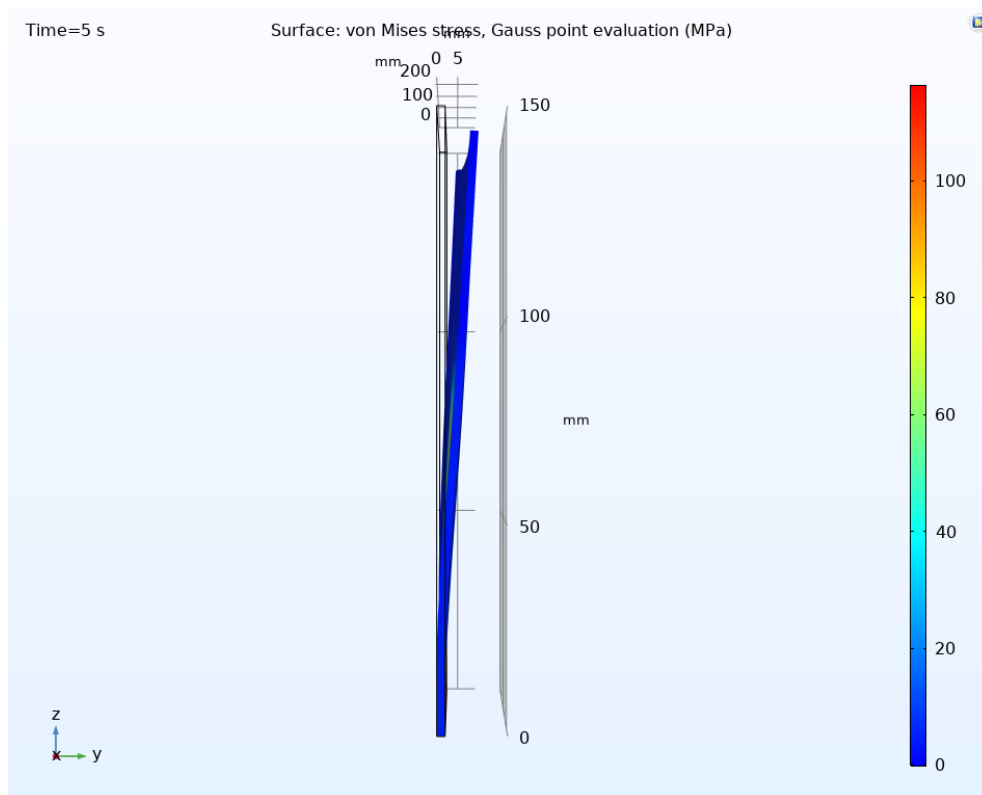


Figure 7.29: von Mises stress at Gauss points for 2 mm plate thickness in case of array of jet quenching at quasi-steady state condition in yz plane

**Fig. 7.28** and **Fig. 7.29** shows a distortion of the 2 mm thick plate in case of the array of jets in xy plane and yz plane respectively. The plane bends towards the measured side in

both the planes since the water jets with high momentum strongly affects the deformation to occur and also low plate thickness.
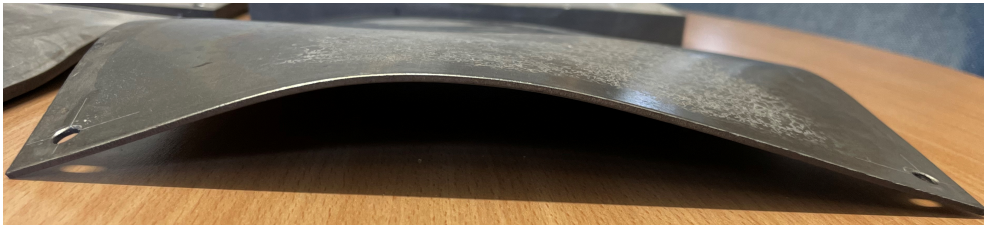


Figure 7.30: Simulation results for single full jet nozzle: Comparison of stress and strain for quenched side temperature at quasi-steady state condition
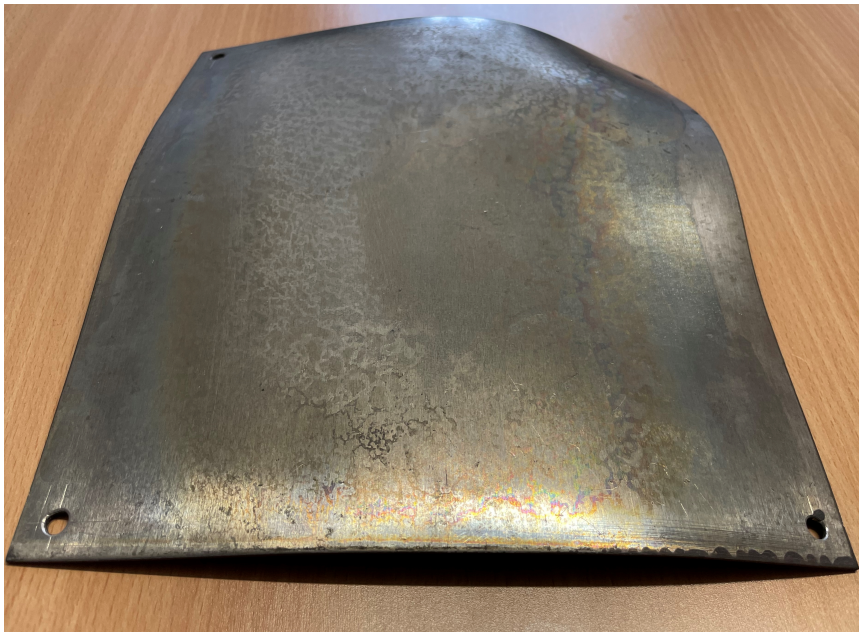


Figure 7.31: Simulation results for single full jet nozzle: Comparison of stress and strain for quenched side temperature at quasi-steady state condition

In similar way, the plate as shown in **Fig. 7.30** and **Fig. 7.31** from the experimental quenching process. From the views, we can clearly see the highly fluctuating behaviour of the plate and from the three-dimensional viscoplastic modelling shows relatively similar effect. Henceforth, the three-dimensional modelling predicts the mechanical behaviour of the quenching process in case of array of jets. However, the stronger local definition of the heat transfer behaviour should be analysed in detail.

# Chapter 8

# Conclusion

The quenching process is replicated in the laboratory setup to study the local heat transfer phenomena with array of water jets. The surface temperature measurements at the back of the water impingement region were measured with high resolution infrared thermography. The two-dimensional surface temperature measurements has more advantage than the conventional thermocouples in order to study the local temperature gradient and further more the heat flux profiles. The obtained thermal measurements are utilized to obtain the local heat transfer distribution on the water impingement region. However, the direct prediction of the heat transfer on the water impingement side is highly complex and the solution of the partial differential equation becomes ill-posed because of the unknown boundary conditions i.e., heat flux. As a consequence, non-linear inverse heat conduction model is developed for the cooling process in two and three dimensions. The 3D IHCP solution are highly beneficial in understanding the local heat transfer phenomena during cooling process. Finite element method is adopted and developed in *MATLAB* programming language for the solution of the partial differential equation and the associated adjoint, sensitivity problems in the inverse heat conduction method. To overcome the instabilities in the inverse heat flux estimation, the well known Tikhonov regularization term were added to the objective function to avoid the divergence and the accurate estimation of the heat fluxes. The inverse model is successfully verified against the measured surface temperatures and the temperatures on the water impingement side can be predicted. In addition, an attempt is made to approximate the boiling curve with the Gaussian analytical equation for simplification.

Experiments were performed for the full jet nozzle with fixed and moving plate condition, horizontal array of jets (mold) with moving plate, and array of jets in case of inline configuration and staggered configuration with moving plate for different influencing process parameters. Initial temperature of the plate, kinds of metals, plate velocity, water jet velocity, plate thickness were the process parameters used for the experimental study. The local heat transfer phenomena during quenching process with array of jets were investigated in detail and the influence of $T_{DNB}$, $T_{RWT}$, $q_{max}$, and $q_{RWT}$ were reported.

**Single Full Jet Nozzle: Fixed Plate**

- The heat transfer is a strong function of the radius and higher heat flux ($q_{max}$) promotes steeper temperature gradient and consequently the width of the boiling reduces and vice-versa.

- Higher thermal conductivity material significantly lowers the rate of heat transfer ($q_{max}$), and low conductive with high heat penetration coefficient material promotes stronger rate of heat transfer ($q_{max}$). Nickel in this manner shows this behaviour.

- Maximum heat flux is a strong function of the start temperature and the rate of heat transfer ($q_{max}$) is increase with 1.5 times for temperature of 500 to 850 $°C$

233

respectively. DNB remains almost same, whereas the RWT shows relatively similar effect with maximum heat flux ($q_{max}$) and increases gradually to higher temperatures.

- The higher internal energy promotes the higher heat extraction ($q_{max}$) and similar effect can be observed for thickness of the plate. Although, DNB and RWT remains constant for all the plate thickness.

The maximum heat flux ($q_{max}$) for all the process parameters are observed to be at the water stagnation position i.e., water jet impingement region and the heat flux gradually decreases in a radial manner away from the water jet position.

**Single Full Jet Nozzle: Moving Plate**

- Increase of plate velocity reduces the pre-cooling region, shifts the DNB, maximum heat flux ($q_{max}$), position towards the nozzle position with increase of rate of heat transfer.

- Water jet velocity shows significantly no influence on the rate of heat transfer ($q_{max}$) and also the DNB, RWT remains similar.

- The start temperature of the plate increases the rate of heat transfer with reduction of the pre-cooling region, as the position of the DNB, maximum heat flux ($q_{max}$) shifts towards jet impingement position where higher temperature gradient exists.

- Higher plate thickness obviously lowers the advection from the dry region, while the DNB, RWT positions are shifted far from the water jet impingement. Thus, the rate of heat transfer ($q_{max}$) shows relatively similar to the 5 mm plate thickness.

- Influence of material with low thermal conductivity and high heat penetration coefficient (thermal effusivity) similar to the fixed plate condition are observed and nickel material obtains the higher rate of heat transfer ($q_{max}$).

**Horizontal Array of Jets (Mold)**

- Kinds of metals increases the pre-cooling with higher thermal conductivity, the material with longer temperature drop attains higher transition boiling region results in lower maximum heat flux ($q_{max}$). Consequently lower temperature drop with higher heat penetration coefficient promotes higher heat transfer.

- The $q_{max}$ and the DNB temperature strongly depends on the initial temperature of the plate, while the width of the nucleate boiling region increases with the initial temperature of the plate.

- Water quality, water jet velocity shows relatively independent on the maximum heat flux extraction.

- The increase of the water jet impingement region, and plate velocity highers the rate of heat transfer. Consequently, the width of the pre-cooling region reduces for higher plate velocities.

We can further conclude, the heat transfer increases with the distance from the impingement position, which can be explained with the increasing velocity of the water film due to the gravity. However, the DNB temperature remains independent on the position.

**Array of Jets**

- Plate thickness offers a stronger resistance to the temperature drop at the nozzle location and the higher temperature values are attained. The maximum heat flux and DNB position shifts downstream from the jet position, where the effect of the other jets affects the heat transfer.

- The initial temperature of the plate reduces the width of the pre-cooling region, and the consequently the position of the DNB temperature moves towards the jet impingement position with the increase of the maximum heat flux significantly.

- The larger the plate velocity, the heat flux attains higher until 20 mm/s and then decreases for 40 mm/s because of insufficient cooling of the plate. However, the position of the DNB temperature strongly promotes the higher rate of heat transfer in the nozzle impingement position.

- The higher water jet velocities shows insignificant to the rate of heat transfer and the DNB, RWT shows relatively less effect.

Henceforth from the local heat transfer analysis with the usage of the various types of quenching technique with array of jets, the influence of the process parameters on the rate of heat removal is significant. As a consequence, the local definition of the water jet position is mainly responsible for the maximum heat flux extraction from the plate. Therefore, the local control of the water jet position, and relevant experimental condition strongly recommended for the control of heat transfer in industrial quenching processes. The heat transfer profiles obtained in the present work can be easily implemented in the real work industrial applications with proper computation based on the experimental conditions. Furthermore, the surface heat flux results obtained from two-dimensional inverse heat conduction problem can be further employed with thermo-mechanical modelling to predict the evolution of thermal stresses and deformation. With the continuation of the two-dimensional inverse heat conduction problem is extended to the three-dimensions and the relevant heat flux profiles were obtained to show the influence of the water jets for accurate prediction to reality.

The thermo-mechanical modelling is done in three-dimensional through *COOMSOL* Multiphysics. The influence of the single full jet nozzle and the array of jets were simulated for different process parameters. The obtained results are observed to match with the real world distorted plates and the local stress profiles increases with decrease in the temperatures as a direct consequence. Therefore, the obtained results can be further employed in the industrial applications to optimize the process and to study the cooling strategies for high heat transfer rate.

# Bibliography

K. H. Abdalrahman, Sabariman, and E. Specht. Influence of salt mixture on the heat transfer during spray cooling of hot metals. *International Journal of Heat and Mass Transfer*, 78:76 – 83, 2014. ISSN 0017-9310. doi: https://doi.org/10.1016/j. ijheatmasstransfer.2014.06.070.

R. Abou Khachfe and Y. Jarny. Numerical solution of 2-d nonlinear inverse heat conduction problems using finite-element techniques. *Numerical Heat Transfer: Part B: Fundamentals*, 37(1):45–67, 2000.

C. Agrawal, R. Kumar, A. Gupta, and B. Chatterjee. Rewetting and maximum surface heat flux during quenching of hot surface by round water jet impingement. *International Journal of Heat and Mass Transfer*, 55:4772–4782, 8 2012. ISSN 00179310. doi: 10.1016/ j.ijheatmasstransfer.2012.04.045.

M. K. Agrawal and S. K. Sahu. Analysis of conduction-controlled rewetting of a hot surface by variational method. *Heat Mass Transfer*, 49:963–971, 2013. doi: 10.1007/ s00231-013-1139-6.

U. Alam, J. Krol, E. Specht, and J. Schmidt. Enhancement and local regulation of metal quenching using atomized spray. *Journal of ASTM International*, 5:1–10, 2008. doi: 10.1520/JAI101805.

J. A. Bakken and T. Bergström. Heat transfer measurements during DC casting of aluminium part i : Measurement technique. *Journal of Light Metals*, pages 883–889, 1986.

J. V. Beck. Nonlinear estimation applied to the nonlinear inverse heat conduction problem. *International Journal of Heat and Mass Transfer*, 13:703–716, 1970.

J. V. Beck, B. Blackwell, and A. Haji-Sheikh. Comparison of some inverse heat conduction methods using experimental data. *International Journal of Heat and Mass Transfer*, 39 (17):3649–3657, 1996.

M. Bergagio, H. Li, and H. Anglart. An iterative finite-element algorithm for solving two-dimensional nonlinear inverse heat conduction problems. *International Journal of Heat and Mass Transfer*, 126:281–292, 2018.

S. Bikass, B. Andersson, A. Pilipenko, and H. Langtangen. Simulation of the distortion mechanisms due to the non.uniform cooling in the aluminium extrution process. *International Journal of Thermal Sciences*, 52:50–58, 2012.

F. Bozzoli, L. Cattani, S. Rainieri, F. S. V. Bazán, and L. S. Borges. Estimation of the local heat-transfer coefficient in the laminar flow regime in coiled tubes by the tikhonov regularisation method. *International Journal of Heat and Mass Transfer*, 72:352–361, 2014.

M. Brzoza, J. Specht, E.and Ohland, O. Belkessam, and U. Lubben, Th.and Fritsching. Minimizing stress and distortion for shafts and discs by controlled quenching in a field of nozzles. *Mat.-wiss. u. Werkstofftech*, 37(1):97–102, 2006.

E. Caron. Secondary cooling in the direct-chill casting of light metals. *Ph.D. Thesis, The University of British Columbia*, 2008.

E. Caron and M. Wells. Secondary cooling in the direct-chill casting of magnesium alloy az31. *Metallurgical and Materials Transactions B*, 40(4):585–595, Aug 2009a. ISSN 1543-1916. doi: 10.1007/s11663-009-9254-y.

E. Caron and M. Wells. Secondary cooling in the direct-chill casting of magnesium alloy az31. *Metallurgical and Materials Transactions B*, 40(4):585–595, 2009b.

E. Caron and M. A. Wells. Effect of advanced cooling front (acf) phenomena on film boiling and transition boiling regimes in the secondary cooling zone during the direct-chill casting of aluminum alloys. *Materials Science Forum*, 519-521:1687–1692, 2006.

S. Chantasiriwan. An algorithm for solving multidimensional inverse heat conduction problem. *International journal of heat and mass transfer*, 44(20):3823–3832, 2001.

S.-J. Chen, J. Kothari, and A. A. Tseng. Cooling of a moving plate with an impinging circular water jet, 1991a.

S.-J. Chen, J. Kothari, and A. A. Tseng. Cooling of a moving plate with an impinging circular water jet. *Experimental thermal and fluid science*, 4(3):343–353, 1991b.

N. L. Chester, M. A. Wells, and V. Prodanovic. Effect of Inclination Angle and Flow Rate on the Heat Transfer During Bottom Jet Cooling of a Steel Plate. *Journal of Heat Transfer*, 134(12), 10 2012a. ISSN 0022-1481. doi: 10.1115/1.4007127. 122201.

N. L. Chester, M. A. Wells, and V. Prodanovic. Effect of inclination angle and flow rate on the heat transfer during bottom jet cooling of a steel plate. *Journal of Heat Transfer*, 134, 2012b. ISSN 00221481. doi: 10.1115/1.4007127.

M. Ciofalo, I. Di Piazza, and V. Brucato. Investigation of the cooling of hot walls by liquid water sprays. *International Journal of Heat and Mass Transfer*, 42(7):1157–1175, 1999.

B. Y. Dong, W.-Z. Shao, L. Xing, J. Tang, and L. Zhen. Numerical simulation of residual stress in an al-cu alloy block during quenching and aging. *Journal of Materials Engineering and Performance*, 24(12):4928–4940, 2015.

J. M. Drezet, M. Rappaz, G. U. Grün, and M. Gremaud. Dertermination of thermophysical properties and boundary conditions of direct chill-cast aluminium alloys using inverse methods. *Metallurgical and Materials Transactions A*, 31A:1627–1634, 2000.

S. Dua and C. Tien. An experimental investigation of falling-film rewetting. *International Journal of Heat and Mass Transfer*, 21(7):955–965, 1978.

P. Duda. Solution of an inverse axisymmetric heat conduction problem in complicated geometry. *International Journal of Heat and Mass Transfer*, 82:419–428, 2015.

J. Evancho and J. Staley. Kinetics of precipitation in aluminum alloys during continuous cooling. *Metallurgical and Materials Transactions B*, 5(1):43–47, 1974.

J. Filipovic, F. Incropera, and R. Viskanta. Rewetting temperatures and velocity in a quenching experiment. *EXPERIMENTAL HEAT TRANSFER An International Journal*, 8(4):257–270, 1995.

G. Franco. *Boiling heat transfer during cooling of a hot moving steel plate by multiple top jets.* PhD thesis, University of British Columbia, 2008.

H. Fujimoto, K. Tatebe, Y. Shiramasa, T. Hama, and H. Takuda. Heat transfer characteristics of a circular water jet impinging on a moving hot solid. *ISIJ international*, 54(6):1338–1345, 2014.

H. Fujimoto, Y. Shiramasa, K. Morisawa, T. Hama, and H. Takuda. Heat transfer characteristics of a pipe-laminar jet impinging on a moving hot solid. *ISIJ International*, 55(9):1994–2001, 2015a. doi: 10.2355/isijinternational.ISIJINT-2015-124.

H. Fujimoto, Y. Shiramasa, K. Morisawa, T. Hama, and H. Takuda. Heat transfer characteristics of a pipe-laminar jet impinging on a moving hot solid. *ISIJ International*, 55(9):1994–2001, 2015b.

H. Fujimoto, N. Hayashi, J. Nakahara, K. Morisawa, T. Hama, and H. Takuda. Boiling heat transfer during impingement of two or three pipe laminar jets onto moving steel sheet. *ISIJ International*, 56(11), 2016.

M. Gradeck, A. Kouachi, M. Lebouché, F. Volle, D. Maillet, and J.-L. Borean. Boiling curves in relation to quenching of a high temperature moving surface with liquid jet impingement. *International Journal of Heat and Mass Transfer*, 52(5-6):1094–1104, 2009a.

M. Gradeck, A. Kouachi, M. Lebouché, F. Volle, D. Maillet, and J. Borean. Boiling curves in relation to quenching of a high temperature moving surface with liquid jet impingement. *International Journal of Heat and Mass Transfer*, 52(5):1094 – 1104, 2009b. ISSN 0017-9310. doi: https://doi.org/10.1016/j.ijheatmasstransfer.2008.09.015.

M. Gradeck, J. A. Quattara, B. Rémy, and D. Maillet. Solution of an inverse problem in the hankel space infrared thermography applied to estimation of a transient cooling flux. *Experimental Thermal and Fluid Science*, 36:56–64, 2012.

S. Groß, M. Soemers, A. Mhamdi, F. Al Sibai, A. Reusken, W. Marquardt, and U. Renz. Identification of boundary heat fluxes in a falling film experiment using high resolution temperature measurements. *International Journal of Heat and Mass Transfer*, 48(25-26): 5549–5562, 2005.

B. Hadała, Z. Malinowski, and A. Szajding. Solution strategy for the inverse determination of the specially varying heat transfer coefficient. *International Journal of Heat and Mass Transfer*, 104:993–1007, 2017.

J. Hammad, Y. Mitsutake, and M. Monde. Movement of maximum heat flux and wetting front during quenching of hot cylindrical block. volume 43, pages 743–752. Elsevier Masson SAS, 2004. doi: 10.1016/j.ijthermalsci.2004.02.014.

J. HAMMAD, M. MONDE, and Y. MITSUTAKE. Characteristics of heat transfer and wetting front during quenching by jet impingement. *Thermal Science and Engineering*, 12 (1):19–26, jan 2004. ISSN 09189963. URL https://ci.nii.ac.jp/naid/10012103106/en/.

N. HATTA, J. ichi KOKADO, and K. HANASAKI. Numerical analysis of cooling characteristics for water bar. *Transactions of the Iron and Steel Institute of Japan*, 23 (7):555–564, 1983. doi: 10.2355/isijinternational1966.23.555.

N. Hatta, Y. Tanaka, H. Takuda, and J. ichi Kokado. A numerical study on cooling process of hot steel plates by a water curtain. *ISIJ International*, 29(8):673–679, 1989a. doi: 10.2355/isijinternational.29.673.

N. Hatta, Y. Tanaka, H. Takuda, and J.-i. Kokado. A numerical study on cooling process of hot steel plates by a water curtain. *Isij International*, 29(8):673–679, 1989b.

M. Hnizdil, M. Chabicovsky, and M. Raudensky. Influence of the impact angle and pressure on the spray cooling of vertically moving hot steel surfaces. *Materiali in Tehnologije*, 49: 333–336, 01 2015a. doi: 10.17222/mit.2013.239.

M. Hnizdil, M. Chabicovsky, and M. Raudensky. Influence of the impace angle and pressure on the spray cooling of vertically moving hot steel surfaces. *Materials and Technology*, 49:333–336, 2015b.

C.-H. Huang and S.-P. Wang. A three-dimensional inverse heat conduction problem in estimating surface heat flux by conjugate gradient method. *International Journal of Heat and Mass Transfer*, 42(18):3387–3403, 1999.

C.-H. Huang and H.-H. Wu. An inverse hyperbolic heat conduction problem in estimating surface heat flux by the conjugate gradient method. *Journal of Physics D: Applied Physics*, 39(18):4087–4096, sep 2006. doi: 10.1088/0022-3727/39/18/020. URL https://doi.org/10.1088/0022-3727/39/18/020.

R. Ishida, A. Mizuta, K. Korida, S. Yasunaga, and K. Takisawa. Basic characteristics of pipe nozzle cooling with retaining water on plate. *ISIJ International*, 29(4):339–344, 1989. doi: 10.2355/isijinternational.29.339.

Y. Jarny, M. Ozisik, and J. Bardon. A general optimization method using adjoint equation for solving multidimensional inverse heat conduction. *International journal of heat and mass transfer*, 34(11):2911–2919, 1991.

Y. Jarny et al. Determination of heat sources and heat transfer coefficient for two-dimensional heat flow–numerical and experimental study. *International Journal of Heat and Mass Transfer*, 44(7):1309–1322, 2001.

J. M. Jha, S. V. Ravikumar, I. Sarkar, S. K. Pal, and S. Chakraborty. Ultrafast cooling processes with surfactant additive for hot moving steel plate. *Experimental Thermal and Fluid Science*, 68:135–144, 2015a.

J. M. Jha, S. V. Ravikumar, I. Sarkar, S. K. Pal, and S. Chakraborty. Ultrafast cooling processes with surfactant additive for hot moving steel plate. *Experimental Thermal and Fluid Science*, 68:135–144, 2015b. doi: 10.1016/j.expthermflusci.2015.04.004.

J. M. Jha, S. V. Ravikumar, I. Sarkar, S. K. Pal, and S. Chakraborty. Jet impingement cooling of a hot moving steel plate: an experimental study. *Experimental Heat Transfer*, 29(5):615–631, 2016.

N. Karwa and P. Stephan. Experimental investigation of free-surface jet impingement quenching process. *International Journal of Heat and Mass Transfer*, 64:1118–1126, 2013. ISSN 00179310. doi: 10.1016/j.ijheatmasstransfer.2013.05.014.

Y. Kayamak. Modeling of metal quenching process and strategies to minimize distortion and stresses. *Otto von Guericke University, Magdeburg*, 2007.

H. Kim and S. Oh. Evaluation of heat transfer coefficient during heat treatment by inverse analysis. *Journal of Materials processing technology*, 112(2-3):157–165, 2001.

G. A. Kulkarni. *Local heat transfer and stress analysis of direct chill casting process.* Docupoint Verlag, 2019.

G. A. Kulkarni, A. K. Nallathambi, and E. Specht. Eulerian steady state solution of boiling curve for impinging water jet on moving hot metal plate. *Heat and Mass Transfer*, 55 (6):1819–1828, 2019.

S. G. Lee, M. Kaviany, C. J. Kim, and J. Lee. Quasi-steady front in quench subcooled-jet impingement boiling: Experiment and analysis. *International Journal of Heat and Mass Transfer*, 113:622–634, 2017. ISSN 00179310. doi: 10.1016/j.ijheatmasstransfer.2017.05. 081.

Y. Lee and W.-Q. Shen. Effect of coolant vapor quality on rewetting phenomena. *International Journal of Heat and Mass Transfer*, 28(1):139–146, 1985. ISSN 0017-9310. doi: https://doi.org/10.1016/0017-9310(85)90015-8. URL https://www.sciencedirect.com/science/article/pii/0017931085900158.

H. Leocadio. Interfaces and heat transfer in jet impingement on a high temperature surface. 2018.

N. Y. Li, Y. Zhang, H. Li, J. Wang, W. Yan, B. Jin, and Q. Xiong. Effects of heat transfer coefficients on quenching residual stresses in 7055 aluminium alloy. *Material Science Forum*, 887:647–654, 2016a.

N. Y. Li, Y. Zhang, H. Li, J. Wang, W. Yan, B. Jin, and Q. Xiong. Quenching residual stress distribution in aluminium alloy plates wit different dimensions. *The Nonferrous Metals Society of China and Springer-Verlag Berlin Heidelberg 2016*, 2016b.

J. Lienhard, X. Liu, and L. Gabour. Splattering and heat transfer during impingement of a turbulent liquid jet. 1992.

Y. Liu, S. Qin, Q. Hao, N. Chen, X. Zuo, and Y. Rong. Finite elemet simulation and experimental verification of internal stress of quenched aisi 4140 cylinders. *The Minerals, Metals Materials Society and ASM International*, 48 A(A):1402–1413, 2017.

T. Lüttich, A. Mhamdi, and W. Marquardt. Design, formulation, and solution of multidimensional inverse heat conduction problems. *Numerical Heat Transfer, Part B: Fundamentals*, 47(2):111–133, 2005.

M. Modak, S. Srinivasan, K. Garg, S. S. Chougule, M. K. Agarwal, and S. K. Sahu. Experimental investigation of heat transfer characteristics of the hot surface using al2o3–water nanofluids. *Chemical Engineering and Processing: Process Intensification*, 91:104 – 113, 2015. ISSN 0255-2701. doi: https://doi.org/10.1016/j.cep.2015.03.006.

K. Morisawa, J.-y. Nakahara, K. Nagata, H. Fujimoto, T. Hama, and H. Takuda. Boiling heat transfer characteristics of vertical water jet impinging on horizontally moving hot plate. *ISIJ International*, 58(1):140–145, 2018.

A. K. Mozumder, M. Monde, and P. L. Woodfield. Delay of wetting propagation during jet impingement quenching for a high temperature surface. *International Journal of Heat and Mass Transfer*, 48(25):5395–5407, 2005. ISSN 0017-9310. doi: https://doi.org/10.1016/j.ijheatmasstransfer.2005.06.034. URL https://www.sciencedirect.com/science/article/pii/S0017931005004722.

A. K. Mozumder, M. Monde, P. L. Woodfield, and I. M. A. Maximum heat flux in relation to quenching of a high temperature surface with liquid jet impingement. *International Journal of Heat and Mass Transfer*, 49:2877–2888, 2006a.

A. K. Mozumder, M. Monde, P. L. Woodfield, and M. A. Islam. Maximum heat flux in relation to quenching of a high temperature surface with liquid jet impingement. *International Journal of Heat and Mass Transfer*, 49(17):2877–2888, 2006b. ISSN 0017-9310. doi: https://doi.org/10.1016/j.ijheatmasstransfer.2006.01.048. URL https://www.sciencedirect.com/science/article/pii/S0017931006001517.

A. K. Mozumder, P. L. Woodfield, M. Ashraful Islam, and M. Monde. Maximum heat flux propagation velocity during quenching by water jet impingement. *International Journal of Heat and Mass Transfer*, 50(7):1559–1568, 2007a. ISSN 0017-9310. doi: https://doi.org/10.1016/j.ijheatmasstransfer.2006.08.035. URL https://www.sciencedirect.com/science/article/pii/S0017931006005199.

A. K. Mozumder, P. L. Woodfield, M. A. Islam, and M. Monde. Maximum heat flux propagation velocity during quenching by water jet impingement. *International Journal of Heat and Mass Transfer*, 50:1559–1568, 4 2007b. ISSN 00179310. doi: 10.1016/j.ijheatmasstransfer.2006.08.035.

Y. Nagasaka, J. Brimacombe, E. Hawbolt, I. Samarasekera, H. Morales, and S. Chidiac. Mathematical model of phase transformations and elasto-plastic stress in the water spray quenching of steel bars. *Metallurgical Tractions A*, 24 A(1):795–808, 1993.

A. K. Nallathambi. Thermomechanical simulation of direct chill casting. *Otto von Guericke University, Magdeburg*, 2010.

A. K. Nallathambi and E. Specht. Estimation of heat flux in array of jets quenching using experimental and inverse finite element method. *Journal of Materials Processing Technology*, 209(12-13), 2009a. doi: 10.1016/j.jmatprotec.2009.04.001.

A. K. Nallathambi and E. Specht. Estimation of heat flux in array of jets quenching using experimental and inverse finite element method. *Journal of Materials Processing Technology*, 209(12-13):5325–5332, 2009b.

A. K. Nallathambi, Y. Kaymak, E. Specht, and A. Bertram. Optimum strategies to reduce residual stresses and distortion during the metal quenching process. *Journal of ASTM International*, 6(4), 2009. doi: 10.1520/JAI101806.

S. Nukiyama. The maximum and minimum values of the heat q transmitted from metal to boiling water under atmospheric pressure. *Journal of the Society of Mechanical Engineers, Japan*, 37:367–374, 1934.

I. J. Opstelten and J. M. Rabenberg. *Determination of the Thermal Boundary Conditions During Aluminum DC Casting from Experimental Data Using Inverse Modeling*, pages 665–671. Springer International Publishing, Cham, 2016. ISBN 978-3-319-48228-6. doi: 10.1007/978-3-319-48228-6_83.

R. Panda and B. Prasad. Conjugate heat transfer from a flat plate with shower head impinging jets. *Frontiers in Heat and Mass Transfer (FHMT)*, 2(1), 2011.

M. Pietzsch, R.and Brzoza, Y. Kayamk, E. Specht, and A. Betram. Simulation of the distortion of long steel profiles during cooling. *Journal of Applied Mechanics*, 74:427–439, 2007.

M. Raynaud and J. Bransier. A new finite-difference method for the nonlinear inverse heat conduction problem. *Numerical Heat Transfer, Part A: Applications*, 9(1):27–42, 1986.

H. Robidou, H. Auracher, P. Gardin, M. Lebouche, and L. Bogdanić. Local heat transfer from a hot plate to a water jet. *Heat and mass Transfer*, 39(10):861–867, 2003.

J. Robinson, D. Tanner, R. Paradowska, and R. Wimpory. The influence of quench sensitivity on residual stresses in the aluminium 7010 and 7050. *Material Characterization*, 65:73–85, 2012.

N. Schweizer. Multi-scale investigation of nucleate boiling phenomena in micro gravity phenomena. *PhD Thesis, Technische Universitat Darmstadt*, 2010.

T. B. Sengupta, J. and M. Wells. The use of water cooling during the continuous casting of steel and aluminum alloys. *Metallurgical and Materials Transactions A Volume*, 36: 187–204, 2005. doi: https://doi.org/10.1007/s11661-005-0151-y.

A. K. Sharma and S. K. Sahu. The thermal and rewetting behavior of hot moving surface by water jet impingement. *Applied Thermal Engineering*, 159:113950, 2019a. ISSN 1359-4311. doi: https://doi.org/10.1016/j.applthermaleng.2019.113950.

A. K. Sharma and S. K. Sahu. The thermal and rewetting behavior of hot moving surface by water jet impingement. *Applied Thermal Engineering*, 159:113950, 2019b.

A. K. Sharma, M. Modak, and S. K. Sahu. The heat transfer characteristics and rewetting behavior of hot horizontal downward facing surface by round water jet impingement. *Applied Thermal Engineering*, 138:603–617, 6 2018. ISSN 13594311. doi: 10.1016/j. applthermaleng.2018.04.050.

C. Simir and H. Gür. 3d fem simulation of steel quenching and investigation of the effect of asymmetric geometry on residual stress distribution. *Journal of Material Processing Technology*, 207:211–221, 2008.

E. Specht. *Heat and mass transfer in thermoprocessing: fundamentals, calculations, processes*. Vulkan Verlag, 2017.

J. Su and G. F. Hewitt. Inverse heat conduction problem of estimating time-varying heat transfer coefficient. *Numerical Heat Transfer, Part A: Applications*, 45(8):777–789, 2004.

W. Suyitno, L. Katgerman, et al. Finite element method simulation of mushy zone behavior during direct-chill casting of an al-4.5 pct cu alloy. *Metall Mater Trans A*, 35:2918–2926, 2004.

H. J. Thevik, A. Mo, and T. Rusten. A mathematical model for surface segregation in aluminum direct chill casting. *Metallurgical and Materials Transactions B*, 30(1):135–142, 1999.

W. Timm, K. Weinzierl, and A. Leipertz. Heat transfer in subcooled jet impingement boiling at high wall temperatures. *International Journal of Heat and Mass Transfer*, 46(8): 1385–1393, 2003. ISSN 0017-9310. doi: https://doi.org/10.1016/S0017-9310(02)00416-7. URL https://www.sciencedirect.com/science/article/pii/S0017931002004167.

S. Vakili and M. S. Gadala. Boiling heat transfer of multiple impinging jets on a hot moving plate. *Heat Transfer Engineering*, 34(7):580–595, 2013. doi: 10.1080/01457632. 2013.730412.

W. Vorster and A. M. Korsunsky. Analysis of residual strain and stress states due to heat treatment and thermal processing. *Jounal of Strain Analysis*, 44:71–91, 2008.

B. Wang, X. Guo, Q. Xie, Z. Wang, and G. Wang. Heat transfer characteristic research during jet impinging on top/bottom hot steel plate. *International Journal of Heat and Mass Transfer*, 101:844–851, 10 2016a. ISSN 00179310. doi: 10.1016/j.ijheatmasstransfer. 2016.05.083.

B. Wang, D. Lin, Q. Xie, Z. Wang, and G. Wang. Heat transfer characteristics during jet impingement on a high-temperature plate surface. *Applied Thermal Engineering*, 100:902–910, 2016b. ISSN 1359-4311. doi: https://doi.org/10. 1016/j.applthermaleng.2016.02.054. URL https://www.sciencedirect.com/science/article/pii/S1359431116301971.

B. Wang, Z. Liu, B. Zhang, Z. Wang, and G. Wang. Heat transfer characteristic of slit nozzle impingement on high-temperature plate surface. *ISIJ International*, 59(5):900–907, 2019a. doi: 10.2355/isijinternational.ISIJINT-2018-576.

B. Wang, Z. Liu, B. Zhang, Z. Wang, and G. Wang. Heat transfer characteristic of slit nozzle impingement on high-temperature plate surface. *ISIJ International*, pages ISIJINT–2018, 2019b.

H. Wang, W. Yu, and Q. Cai. Experimental study of heat transfer coefficient on hot steel plate during water jet impingement cooling. *Journal of Materials Processing Technology*, 212:1825–1831, 9 2012. ISSN 09240136. doi: 10.1016/j.jmatprotec.2012.04.008.

D. C. Weckman and P. Niessen. A numerical simulation of the D. C. continuous casting process including nucleate boiling heat transfer. *Metallurgical Transactions B*, 13B: 593–602, 1982.

M. A. Wells, D. Li, and S. L. Cockcroft. Influence of surface morphology, water flow rate and sample thermal history on the boiling-water heat transfer during direct-chill casting of commercial aluminum alloys. *Metallurgical and Materials Transactions B*, 32B:929–939, 2001.

P. L. Woodfield, A. K. Mozumder, and M. Monde. On the size of the boiling region in jet impingement quenching. *International Journal of Heat and Mass Transfer*, 52(1):460–465, 2009. ISSN 0017-9310. doi: https://doi.org/10.1016/ j.ijheatmasstransfer.2008.05.024. URL https://www.sciencedirect.com/science/article/pii/S0017931008003499.

F. Xu and M. S. Gadala. Heat transfer behavior in the impingement zone under circular water jet. *International Journal of Heat and Mass Transfer*, 49:3785–3799, 10 2006. ISSN 00179310. doi: 10.1016/j.ijheatmasstransfer.2006.03.034.

Q.-W. Xue and H.-T. Yang. A conjugate gradient method for the hyperbolic inverse heat conduction problem with multi-variables. *Chin Jounal of Computational Physics*, 22(5): 417–424, 2005.

C.-y. Yang et al. Inverse estimation of the boundary condition in three-dimensional heat conduction. *Journal of Physics D: Applied Physics*, 30(15):2209, 1997.

X. Yang, Z. Zhu, Y. Liu, D. He, and Z. Nong. Finite elelment analysis of quenching temperature field, residual stress and distortion in a357 aluminium alloy large complicated thin-wall workpieces. *Traction of Nonferrous Metals Society of China*, 23:1751–1760, 2013.

R. Yazdi, D. Retraint, and J. Lu. Study of through-thickness residual stress by numerical and experimental techniques. *Journal of strain analysis*, 33(6):449–458, 1998.

S.-Y. Zhang, Y.-X. Wu, K. Liao, and H. Gong. Effect of quenching and pre-stretching on residual stresses in 2a12 aluminum alloy thick plates. *Cailiao Rechuli Xuebao/Transactions of Materials and Heat Treatment*, 33:47–52, 12 2012.

Y.-x. Zhang, Y.-p. Yi, S.-q. Huang, and F. Dong. Influence of quenching cooling rate on residual stress and tensile properties of 2a14 aliminium alloy forgings. *Material Science and Engineering A*, 674:658–665, 2016.

Y.-x. Zhang, Y. Xi, and H. Huang, S.and He. Influence of temperature-dependent properties of aluminium alloy on evolution of plastic strain and residual stress during quenching process. *Metals*, 228(7):1–13, 2017.

P. Zhao, Sabariman, E. Specht, and X. N. Song. Influence of jet velocities and material properties in quenching of metal with array of jets. In *Energy and Materials Research for the Future*, volume 1090 of *Advanced Materials Research*, pages 63–68. Trans Tech Publications Ltd, 3 2015. doi: 10.4028/www.scientific.net/AMR.1090.63.

# Part I

# Appendix

# Appendix
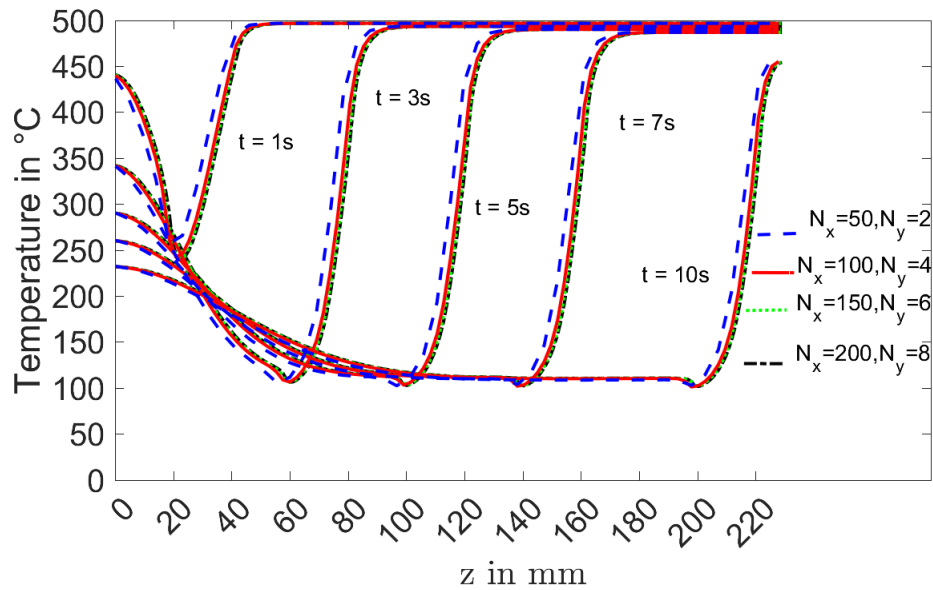


Figure 8.1: Temperature profiles with position for different number of elements.
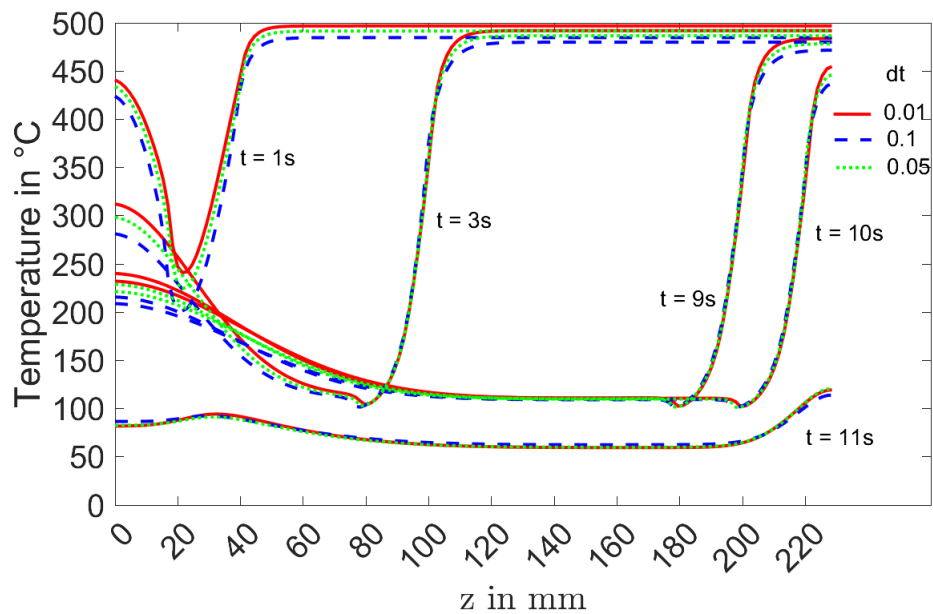


Figure 8.2: Temperature profiles with position with different timesteps
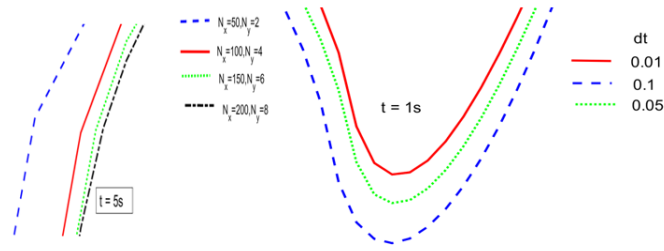
Figure 8.3: Close view of comparison of different number of elements and timesteps.
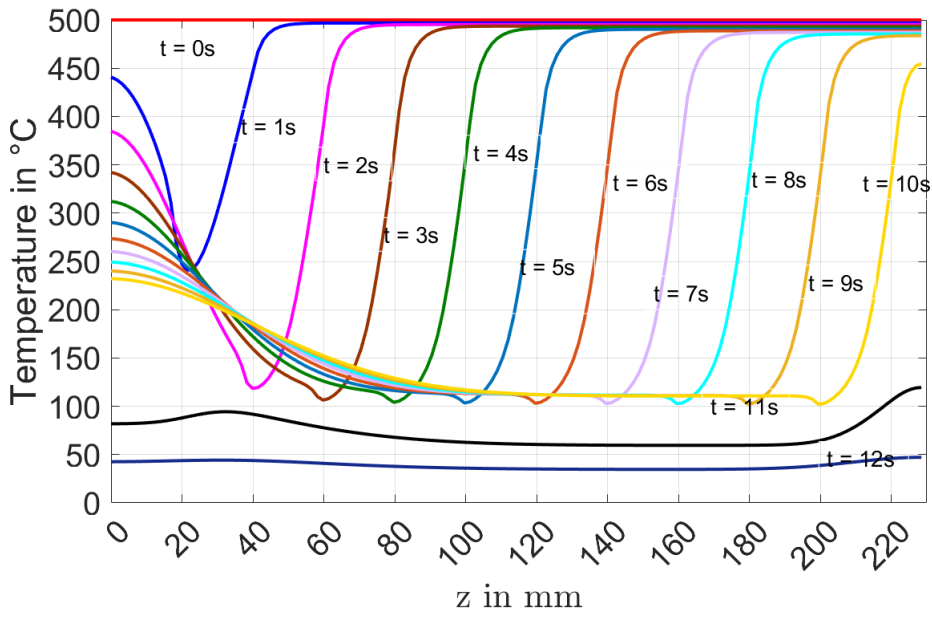


Figure 8.4: Temperature profiles with Nx=150 and Ny=6 with 0.05 dt
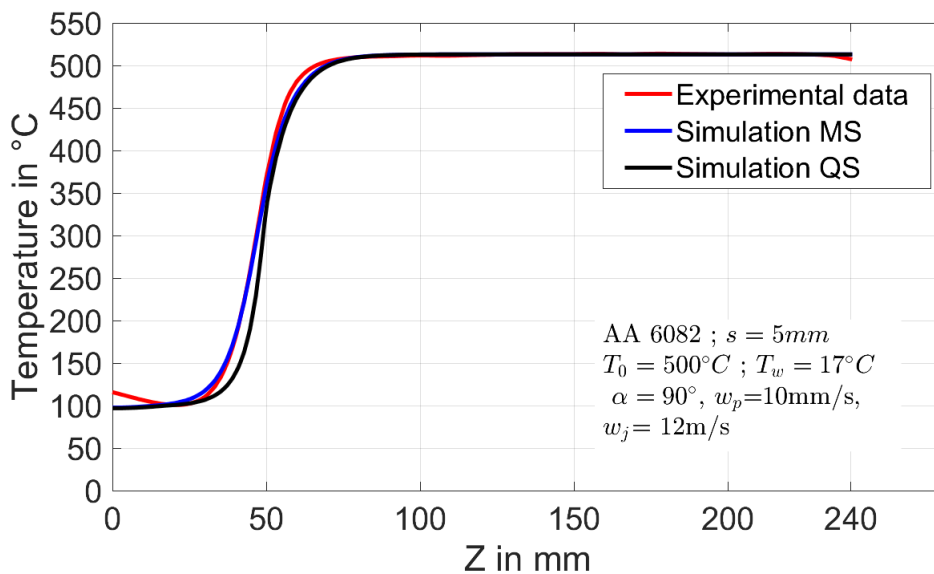


Figure 8.5: Validation of 5mm AA6082 with $T_{in} = 500 \text{ř} C, w_p = 10 mm/s$, $w_j$=12m/s at 5s.
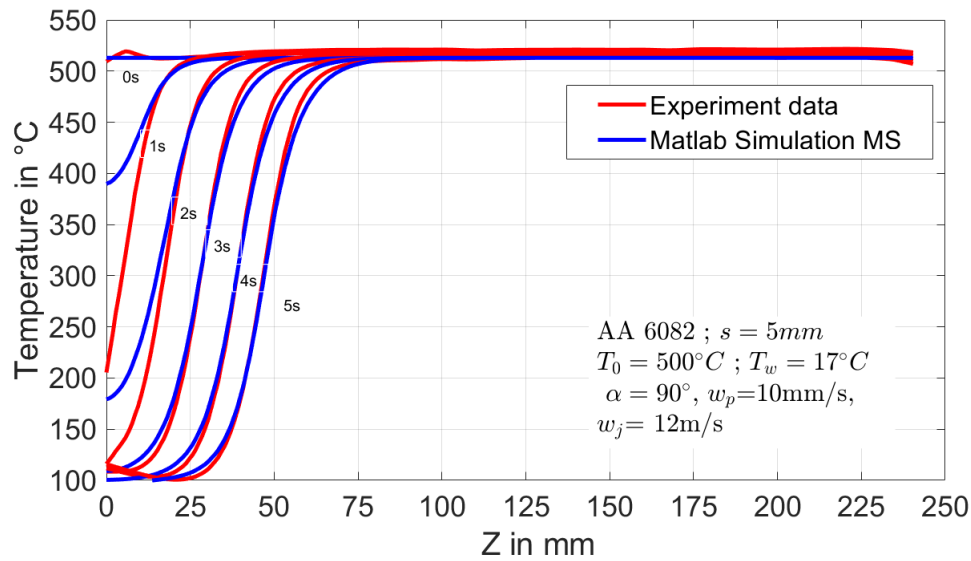
Figure 8.6: Validation at different times with same test parameters as mentioned in Fig 5.5.
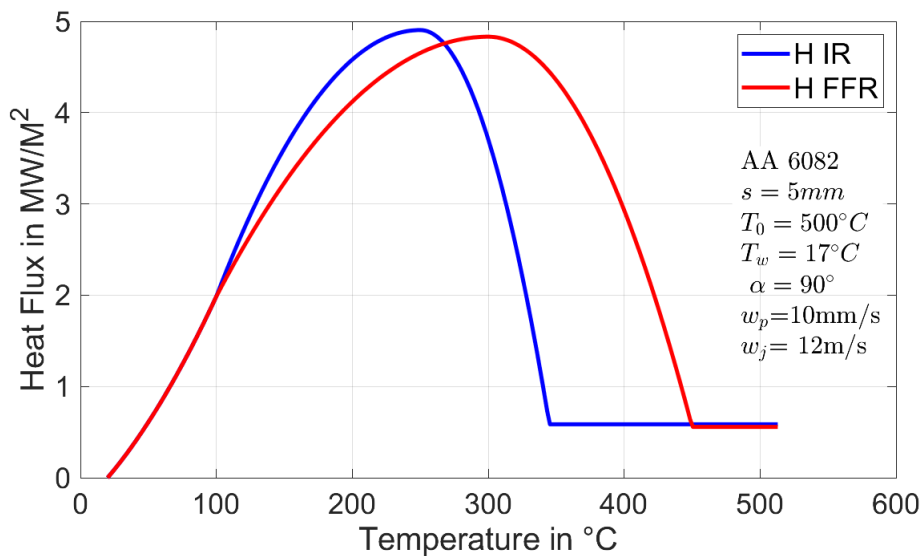


Figure 8.7: Boiling Curve for infrared and free-falling regions with same test parameters as mentioned in Fig 5.5
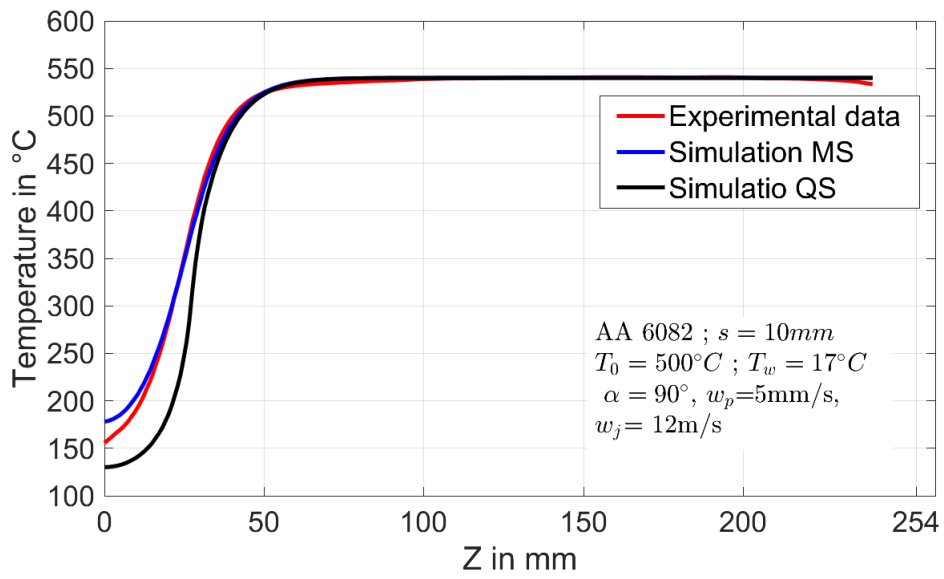
Figure 8.8: Validation of 10mm AA6082 with $T_{in}$=500°C, $w_p$=5mm/s,$w_j$=12m/s at 5s.
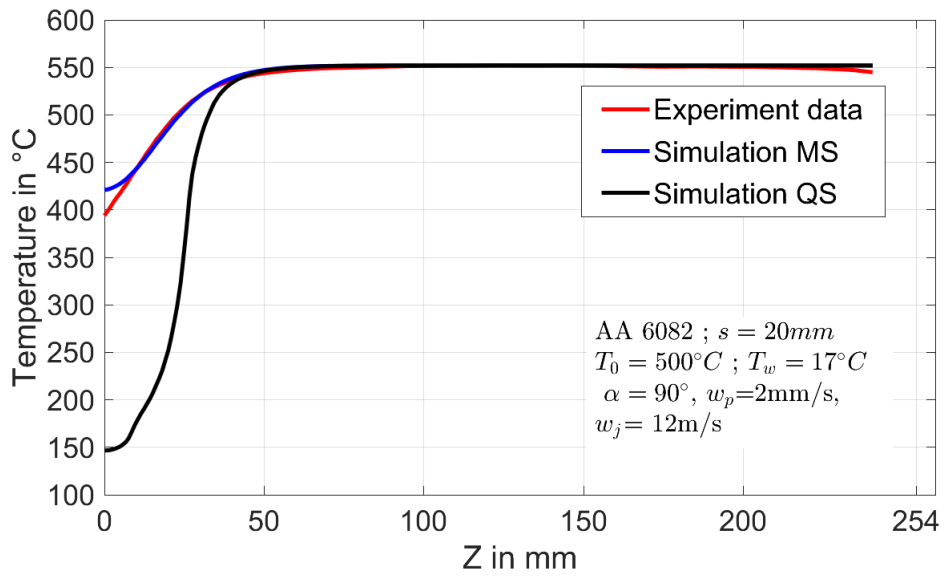


Figure 8.9: Validation of 20mm AA6082 with $T_{in}$=500°C, $w_p$=2mm/s,$w_j$=12m/s at 5s.
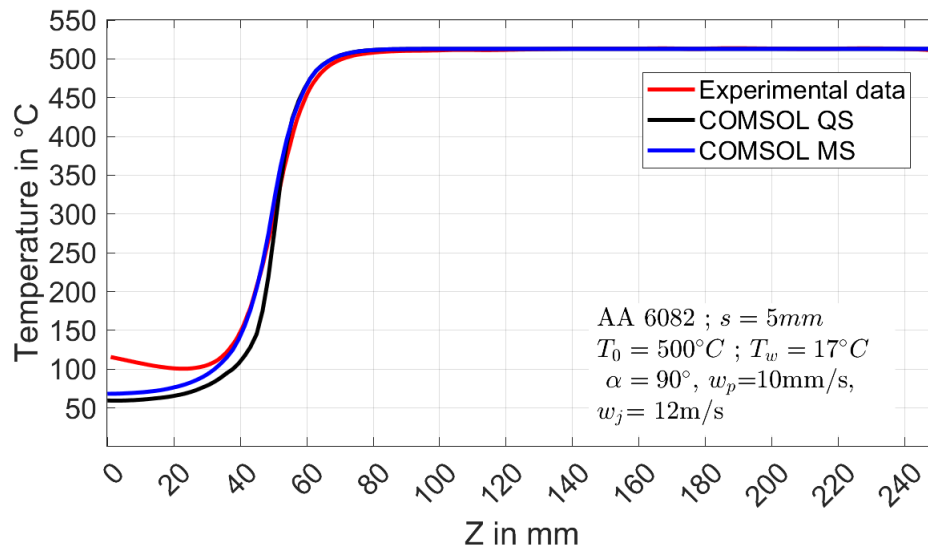
Figure 8.10: 3D analysis validation of 5mm AA6082 with $T_{in}$=500°C, $w_p$=10mm/s,$w_j$=12m/s in COMSOL.
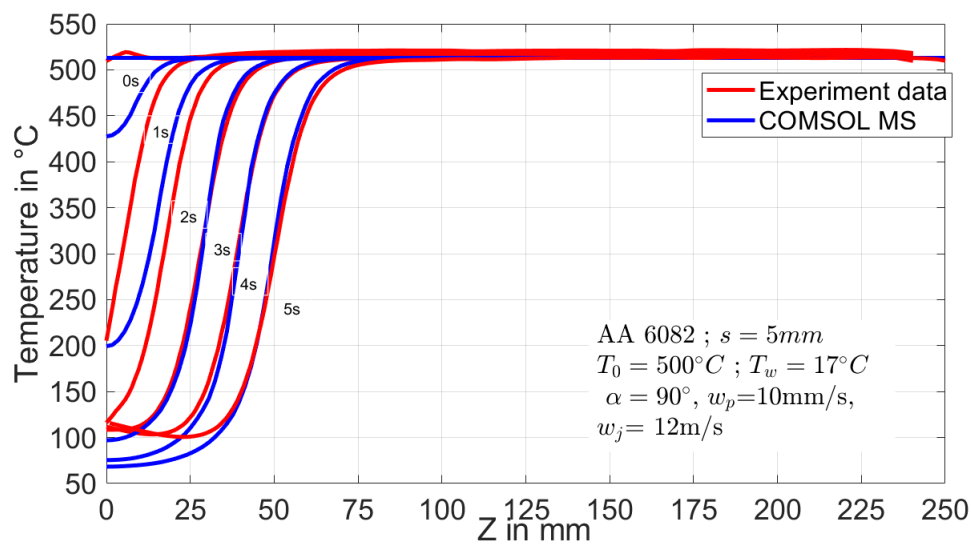


Figure 8.11: 3D analysis validation for different times with test parameters as mentioned in Fig 5.11.
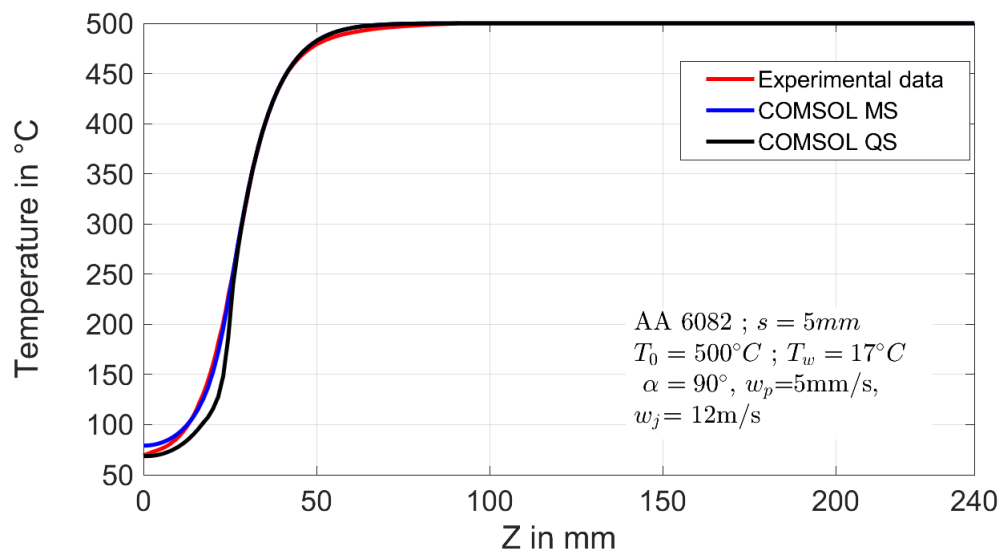
Figure 8.12: 3D analysis validation of 5mm AA6082 with $T_{in}$=500°C, $w_p$=5mm/s,$w_j$=12m/s in COMSOL.

# List of Publications

1. **Suresh Babu Gopalkrishna**, Ashok Kumar Nallathambi, Eckehard Specht, "Inverse Heat Conduction Method to Estimate the Heat Flux during Quenching Process of Hot Metals with Infrared Themrography Measurements", SSRN Electronic Journal, May 2022.

2. Saravanakumar Palaniswamym Saravabab Murugesan, Jiji Prasad Jayaprasad Remani, **Suresh Babu Gopalkrishna**, Ashok Kumar Nallathambi, Daniel Juhre, Eckehard Specht, "Experimental Investigation of Heat Transfer During Quenching of Semi-Solid Aluminium Plate under Hot Cracking Condition", SSRN Electronic Journal, January 2022.

3. **Suresh Babu Gopalkrishna**, Eckehard Specht, "Inverse Heat Conduction Method to Estimate the unknown Surface Heat Flux during Quenching Process", $7^{th}$ Themal and Fluids Engnieering Conference, Las Vegas, USA, MAY 2022.

4. **Suresh Babu Gopalkrishna**, Bilal Mehdi, Hermann Woche, Eckehard Specht, "Local Heat Transfer Analysis in Quenching of Metal Plates with Spray Nozzles", Jahrestreffen der ProcessNet-Fachgruppen Fluidverfahrenstechnik und Wärme und Stoffübertragung, 24 - 26 Febraury 2021, Online-Event.

5. Nithin Mohan Narayan, **Suresh Babu Gopalkrishna**, Bilal Mehdi, Hermann Woche, Udo Fritsching, Eckehard Specht, "Investigation of Heat Transfer in Arrays of Water Jets and Sprays", European Conference on Heat Treatment - Quenching and Distortion Engineering, April 2021.

6. Bilal Mehdi, **Suresh Babu Gopalkrishna**, Nithin Mohan Narayan, Stephan Ryll, Hermann Woche, Eckehard Specht, Udo Fritsching, "Quenching of moving metal plates with flat sprays and single full jet nozzle", 3. Aachnere Ofenbau und Thermprocess Kolloqium, 07 - 08 October 2021.

7. Bilal Mehdi, **Suresh Babu Gopalkrishna**, Hermann Woche, Stephan Ryll, Nithin Mohan Narayan, Eckehard Specht, Udo Fritsching, "Analysis of heat tranasfer in quenching of moving sheets with flat sprays", 7th Themal and Fluids Engineering Conference (TFEC) 2022.

8. Bilal Mehdi, **Suresh Babu Gopalkrishna**, Stephan Ryll, Eckehard Specht, Nithin Narayan Mohan, Udo Fritsching, "Experimental Investigation of Quenching of Moving Hot Metal Plate with Water Using Flat Spray Nozzles", Prodeedings of the 7th World Congress on Momentum, Heat and Mass Transfer (MHMT'22), Virtual Conference, April 07 - 09, 2022.

9. **Suresh Babu Gopalkrishna**, Gaurav Abhay Kulkarni, Ashok Kumar Nallathambi, and Eckehard Specht, "Thermal Stresses in Quenching of Moving Plate by an Array of Jets", Symposium and Workshop for Analytical Youth on Applied Mechanics. 2018. ISBN: 978-9-38676-713-6

10. **Suresh Babu Gopalkrishna**, Gaurav Abhay Kulkarni, Ashok Kumar Nallathambi, Yalcin Kaymak, and Eckehard Specht, "Investigation of Distortion in Quenching of Seamless Tubes", Student techincal conference, Petroleum and Drilling Engineering related Geoscience Geothermics, 2018

11. Hermann Woche, Yuan Fang, **Suresh Babu Gopalkrishna**, Eckehard Specht, "Einfluss der Oberfächenrauheit, der Wasserqualität und der Metallart auf den Wärmeüber-gang bei der Kühlung von Metallen mit unterschiedlichen Düsenarten", 2. Aachener Ofenbau und Thermprocess Kolloqium, 10 - 11 September 2019.

# Conference Presentation

**Suresh Babu Gopalkrishna**, Eckehard Specht, "Inverse Heat Conduction with Tikhonov Regularisation to Estimate the Unknown Heat Flux in Quenching of Metals", *International Conference on Analysis, Inverse Problems and Applications*, July 18-21, 2022, Department of Mathematics, **Indian Institute of Technology Madras (IIT Madras)** , Chennai, India.

# Journal and Conference Reviewer

1. *Materials Today: Proceedings Journal*, Elsevier Publication, since October 2020.

2. $7^{th}$ *Thermal and Fluids Engineering Conference (TEFC-2022)*, American Society of Thermal and Fluids Engineers, May 15-18, 2022.

# List of Thesis Supervised

1. Sravan Kumar Sidrala, "Experimental Investigation during Quenching of Metals with Different Configuration of Full Jet Nozzle Fields", *Master Thesis*, *Otto-von-Guericke Universität Magdeburg*, 2020.

2. Balaji Reddy Pongupalli V., "Experimental Investigation during Quenching of Hot Moving Metal Plate with Spray nozzle fileds", *Master Thesis*, *Otto-von-Guericke Universität Magdeburg*, 2020.

3. Stephan Ryll, "Untersuchung von Modell-Brauseköpfen für die Abschreckung von Metallplatten", *Master Thesis*, *Otto-von-Guericke Universität Magdeburg*, 2020.

4. Meesala Rudra Venkata Santhoshkumar, "Product Development of a Self-Adjusting Degas Valve in an Automobile Vechicle Cooling System", *Master Thesis*, *Otto-von-Guericke Universität Magdeburg* and Schaeffler Group, 2021.

5. Sai Kalyan Kolapally, "Thermal Analysis of Quenching process for Hot Moving Plate: A Numerical Approach", *Master Thesis*, *Otto-von-Guericke Universität Magdeburg*, 2022.

6. Prasanna Selvarajan, "Three-dimensional Inverse Heat Conduction Problem to Estimate the Unknown Heat Fluxes during Quenching Process", *Master Thesis*, *Otto-von-Guericke Universität Magdeburg*, 2022, *In progress.*

# List of Abbreviations and Symbols

## Abbreviations

| | |
|---|---|
| MHF | Maximum Heat Flux |
| ONB | Onset of Nucleate Boiling |
| DNB | Departure Nucleate Boiling |
| DC | Direct Chill Casting |
| EM | Electromagnetic Casting |
| 3D | Three-Dimensional Co-ordinate System |
| CGM | Conjugate Gradient Method |
| FEM | Finite Element Method |
| IHCP | Inverse Heat Conduction Problem |
| 2D | Two-Dimensional Co-ordinate System |

## Symbols

| | |
|---|---|
| $T_{DNB}$ | Departure Nucleate Boiling Temperature in $^\circ C$ |
| $T_{RWT}$ | Re-wetting Temperature in $^\circ C$ |
| $q_{max}$ | Maximum Heat Flux in $MW/m^2$ |
| $q_{RWT}$ | Re-wetting Heat Flux in $MW/m^2$ |
| $q_{Le}$ | Leidenfrost Heat Flux in $MW/m^2$ |
| $T_{Le}$ | Leidenfrost Temperature in $^\circ C$ |
| T | Temperature in $^\circ C$ |
| q | Heat Flux in $MW/m^2$ |
| $\sigma$ | Stress in $MPa$ |
| $\epsilon$ | Strain in [-] |
| $x_e$ | Eulerian Position in $m$ |
| $w_j$ | Water Jet Velocity in $m/s$ |
| $w_p$ | Plate Velocity in $mm/S$ |
| $\lambda$ or $k$ | Thermal Conductivity in $W/mK$ |
| $\rho(T)$ | Density as a function of temperature in $kg/m^3$ |
| c(T) | Specific Heat Capacity as a function of temperature in $J/kgK$ |

| | |
|---|---|
| $T_{initial}$ | Initial Temperature of the Plate in $°C$ |
| $\Omega$ | Domain in $m$ |
| $\tau$ | Time in $s$ |
| $\Gamma_j$ | Boundary of jet impingement region in $m$ |
| $\Gamma_c$ | Boundary of back of jet impingement region or infrared camera side in $m$ |
| x | Spatial direction in $m$ |
| t | Time in $s$ |
| $t_{max}$ | Maximum time in $s$ |
| $q_j$ | Heat flux on jet impingement side in $MW/m^2$ |
| V | Volume of the domain in $m$ |
| $N_e$ | Element Temperature |
| $H_e$ | Temperature gradient interpolation operator |
| $T_{exp}$ | Experimental temperature in $°C$ |
| $J_{qj}$ | Objective function |
| $\gamma_k$ | Regularization parameter |
| $e_m$ | error function |
| $\phi$ | Adjoint function |
| $\theta$ | Sensitivity function |
| $t_f$ | Final time in $s$ |
| $P$ | Conjugate search direction |
| $\beta$ | Conjugate co-efficient |
| $\alpha$ | Optimal step size |
| $\nabla J$ | Gradient of objective function |
| $w_f$ | Wetting front velocity in $mm/s$ |
| $z_{DNB}^*$ | Position of the DNB temperature in mm |
| $z_{RWT}^*$ | Position of the RWT temperature in mm |
| $\theta_w$ | Temperature of the water in $°C$ |
| $d_j$ | diameter of the water jet in $mm$ |
| $Q^*$ | Water flow rate in l/min/m |
| $T_s$ or $T_0$ | Start temperature in $°C$ |
| $s$ | Thickness of the plate in mm |
| $\theta_{z=0}$ | Interface temperature in $°C$ |
| $Bi$ | Biot number |
| $Pe$ | Peclet number |
| $T_b$ | Final temperature in $°C$ |
| $A_1,\ A_2,\ z_0,\ dz$ | Boltzmann function constants |
| $HTC$ | Heat Transfer Coefficient in $W/m^2K$ |

# List of Figures

# List of Tables